STRONG MICROWAVES IN PLASMAS

1996

Volume 1

Institute of Applied Physics
Nizhny Novgorod

RUSSIAN ACADEMY OF SCIENCES
INSTITUTE OF APPLIED PHYSICS

STRONG MICROWAVES IN PLASMAS

PROCEEDINGS
OF THE INTERNATIONAL WORKSHOP

Nizhny Novgorod,
7 – 14 August 1996

Edited by
A.G. Litvak

In two volumes
Volume 1

Nizhny Novgorod – 1997

License No 020235 of 20.01.97

ISBN 5-201-09305-1

Editor's Preface

In August 1996 the International Workshop on Strong Microwaves in Plasmas was held for the third time already. This means that it became a tradition and found its niche in a series of numerous conferences and meetings in the related fields. The success of the Workshop can be also attributed to the unique manner it is conducted in: for the whole week of Workshop duration the participants stay on board a comfortable ship cruising along the Volga river, and have virtually unlimited possibilities for scientific discussions within and beyond the Workshop Program. A rich social program including tours around picturesque ancient Volga cities and evening concerts of classic music performed by musicians specially invited to join the tour makes this trip an unforgettable event both for the participants and members of their families traveling with them.

It is also becoming traditional that along with exchange of new information, which is typical for conferences of that kind, the Workshop on Strong Microwaves in Plasmas is really a workshop: a large number of collaborative scientific projects are discussed here and agreed to be accomplished jointly by Russian laboratories and foreign scientific centers. Progress in the projects initiated at previous meetings is also reviewed and discussed.

The third Workshop took place on 7–14 August, 1996 on board the "Alexander Suvorov" steamer that cruised from Moscow to St. Petersburg. 116 participants from 16 countries attended the Workshop. The scientific program was not overloaded with presentations: in total, there were 94 of them selected by the Program Committee. That made it possible to concentrate on morning plenary sessions and further work in four topical sections, thus making poster sessions unnecessary. Almost a half of the talks were "invited" (21 plenary talks and 21 topical talks), and the time given to each of them was long enough for detailed presentation and discussion.

As previously, four sections worked at this Workshop:

- Current drive and heating of plasma by microwaves in fusion devices;
- Microwave discharges;
- Nonlinear processes in plasmas (theory and microwave experiments);
- Development of high-power microwave sources.

The work of these sections focused mainly on the problems of developing powerful microwave sources and their applications for plasma studies. Among new trends that widen the scientific range of the Workshop one has to mentions the progress in making a short-pulse radar based on a relativistic microwave carsinotron, the study of the possibility to compress powerful microwave pulses actively and passively, experimental modeling and numerical calculations that verify potentiality of using microwave discharges in the atmosphere for its purification from freons and recuperation of atmospheric ozone, and successful start of the studies of physical processes in materials treated with microwave radiation.

This book is the collection of invited lectures and original contributions delivered at the Third International Workshop on Strong Microwaves in Plasmas. These materials give a sufficiently detailed idea of the state-of-the-art and results of studies in the field of development of powerful microwave sources and their applications. We hope that this book will be useful for professionals working in these fields.

A.G. Litvak

CURRENT DRIVE AND HEATING OF PLASMA BY MICROWAVES IN FUSION DEVICES

TOKAMAK AND GYROTRONS IN RRC 'KURCHATOV INSTITUTE'

V. S. Strelkov and Tokamak team

Nuclear Fusion Institute,
Russian Research Centre 'Kurchatov Institute',
Moscow, Russia.

In early 1970s, due to the initiative of Academician L. A. Artsimovich, V. V. Alikaev and K. A. Rasumova with co-workers carried out the first experiments on heating plasma by electron-cyclotron (EC) waves in tokamak TM-3 [1]. The gyrotrons used in these experiments were designed in the Institute of Applied Physics of the Russian Academy of Sciences. The additional heating of plasma (with respect to the ohmic one) enabled to elevate the plasma temperature. Moreover, it was expected that, upon the additional heating, it would be possible to examine the dependence of the energy accumulated in the plasma w_{pl} and of the energy confinement time

$$\tau_E = w_{pl}/P_{tot}$$

on the plasma temperature and heating power P_{tot}. In the experiments with ohmic heating, the heating power and the plasma temperature can be varied only by changing the plasma current I_{pl}. Therefore the results of these experiments are doubtful as the observed change in the energy confinement time is also dependent on the change in the magnetic configuration. The use of the EC resonance heating (ECRH) provided a basis for hope for a reliable scalings $\tau_E=f(P_{tot})$ and $\tau_E=f(T)$. This method does not involve the injection of additional particles into plasma. The absorption zone of the high frequency (HF) power is defined by resonance conditions:

$$\omega - n\gamma\omega_{ce} = k_z V_z$$

Upon the injection of the HF power perpendicular to the magnetic field ($k_z=0$) and fixed gyrotron frequency ω, the absorption zone can shift across the plasma column with small changes in the magnetic field in the tokamak from one discharge to another.

In the case of heating by injection of fast neutral atoms (neutral beam injection, NBI) the zone and amount of absorption of additional power depend on the plasma density and its distribution along the plasma column radius. The injection also results in the increase of plasma density.

The subsequent developments showed several advantages of the use of ECRH. Firstly, it can effectively heat plasma up to the thermonuclear temperatures. Secondly, it enables generation of a stationary current drive. Thirdly, it provides a means of control of distribution profile of the electron temperature $T_e(r)$ and the current density $j(r)$. Finally, upon the use of ECRH the control of stability of the plasma column by changing the profile of $j(r)$ is possible.

Now we will discuss the main results of this work on the T-10 facility and its perspectives on T-10 and T-15.

Electron component heating

The excellent heating of electrons has been shown in the earlier experiments on tokamak T-10 (R=1.5m, $a \leq 0.35$m, $B_T \leq 3.5$T, $I_{pl} \leq 0.4$MA). The HF power up to 2MW has been injected at the first or the second harmonic through 4 horizontal ports from the low-field side. The measurements of spectrum of the X-ray emittance showed that the energetic distribution of electrons was maxwellian. The temperature of electrons was up to 10keV. The preservation of the maxwellian distribution of the electron energy within a fair accuracy means that the power transferred from electrons to ions can be calculated by the conventional formulas for Coulomb collisions [2].

The efficiency of ECRH is defined as the ratio of the power absorbed by plasma P_{ab} to the power injected into tokamak *i. e.* passed through the injection window of the tokamak. The absorbed power P_{ab} is measured by the time derivative of T_e or the time derivative of the diamagnetic signal at the moment when the gyrotrons are switched on or off. These measurements of the time derivative of T_e also enable to define the distribution of P_{ab} over the section of the plasma column *i. e.* to define the heating zone. The measured efficiency of ECRH was up to 80-90%. The observed decrease of the efficiency at the first harmonic with the increase of plasma density is due to the refraction of the HF waves. In this case the plasma frequency approaches the frequency of the HF waves [3].

The study of the plasma heating upon various profiles of the injected power was also done. It showed that the local coefficient of thermoconductivity in a tokamak is not only controlled by the parameters of plasma and magnetic field at a point but it also depends on the distribution of pressure and current density along the plasma column radius. This was first observed in experiments where the increase of the plasma energy did not depend on the zone of the power input within $r \leq r_{cr}$. A similar increase of T_e in the centre of plasma

column was observed in the experiments with various profiles of input power. However, the specific HF power absorbed in the centre of the plasma column varied within several times in these experiments. The increase of the plasma energy as a function of the heating power $P_{tot}=P_{OH}+P_{HF}$ corresponded to the so-called *L*-mode. The energetic time decreased as a function of the heating power:

$$\tau_E \sim \tau_E^{OH} (P_{OH}/P_{tot})^{\alpha},$$

where $\alpha \approx 0.4\text{-}0.6$.

By contrast to experiments with injection heating, the ECRH experiments (like experiments with ohmic heating only) allowed to observe the growth of the energetic time in the *L*-mode with the plasma density [2].

Current drive by EC waves (ECCD)

ECCD is especially attractive for ITER primarily since the EC waves absorb locally and the method does not involve any antennas in direct contact with the plasma. During the last few years, the study of efficiency of ECCD, the comparison of observed value of the current drive with the modelled one and the improvement of the model were the main goals of experiments on the T-10 facility. To determine the current drive, the method of co- and contra-switching on of the plasma current (relative to the direction of propagation of the HF waves) was used. The angle of injection of the HF waves relative to the direction of magnetic field was kept constant. The value of the current drive I_{CD} could be directly calculated from the ratio of difference of the voltage measured along the torus circumference in *co* and *contra* directions to their sum after a stationery condition has been achieved, provided that the total plasma current was kept constant.

Once the current drive is defined and the HF power P_{HF} and the plasma density n_e are measured, the ECCD efficiency can be calculated:

$$\eta_{CD}=n_e R I_{CD}/P_{HF}$$

During the experiments on the T-10 facility, I_{CD} attained was 110kA at the first harmonic. This corresponds to $\eta_{CD}=0.33\times10^{19}$A/W·m^2. At the second harmonic, I_{CD} is only 40kA. In the regime with no saw-toothed oscillations, the experimental values of I_{CD} for the second harmonic meet the calculated ones within 20% accuracy.

The velocity distribution function of electrons deviates from the maxwellian one in the energetic region where the electrons responsible

for the current drive are generated. The observed X-ray spectrum of the superthermal electrons coincides with the calculated one and also fits well the calculated profile of the current drive. Thus the Fokker-Planck calculations give a correct and a fairly compete description of absorbance of the EC waves and of the ECCD [4].

Similar calculations of the ECCD efficiency have been carried out within the framework of the ITER project. They give the maximal value for η_{CD} of $(0.2\text{-}0.3)\times10^{20}$ A/W·m^2 for the ITER parameters. The ambiguity in the value for η_{CD} is caused primarily by the ambiguity of profiles of the temperature and density in the vicinity of the plasma edge in ITER. For the value $\eta_{CD}=0.2\times10^{20}$ A/W·m^2, a current drive of over 2MA can be generated near the centre of the plasma column in ITER, provided that P_{HF}=50MW and $n_e=5\times10^{19}$ m^{-3}.

ECCD enables maintenance of a hollow distribution of the plasma current density that corresponds to configurations with a reversed sheer. These configurations allow a better plasma confinement. In the experiments on TFTR and other facilities, the reversed sheer was created on the stage of increase of the plasma current due to skinning. For the T-10 facility, the parameters of the possible regimes with reversed sheer have been defined on the basis of the Fokker-Planck calculations. The achievement and studies of plasma confinement in such regimes is one of the immediate goals of the T-10 programme.

Stabilisation of plasma instabilities by ECRH and ECCD

On the T-10 facility, experiments on several stabilisation effects were carried out, such as: (*i*) stabilisation of m=2, n=1 mode in the case of local heating in the vicinity of the resonance surface m=2; (*ii*) expansion of the stability region upon the disruption on critical density; (*iii*) influence of the HF heating on the suppression of the 'locked' mode.

If there is a local heating in the vicinity of the resonance surface m=2, a decrease in the oscillation amplitude of signals from magnetic probes is observed. This effect has a resonance feature and corresponds to the heating of the m=2 region [5].

If the plasma density is high, the HF input at $r>r_{m=2}$ prevents the development of the disruption on critical density. This effect is not a resonance one. This can be attributed to the compensation by ECRH of the additional plasma energy loss in the vicinity of the critical density.

In the experiments where so-called 'locked' mode (halt of the plasma column rotation) was observed, the input of the HF power results in the disappearance of the 'locked' mode [6].

T-15 status and perspectives

The T-15 facility (R=2.4m, a=0.65m, B_T=3.5T, $I_{pl}\leq$1.4MA) is potentially suitable for studies of the plasma thermoisolation and other plasma processes with the use of EC waves and/or neutral beams. Both methods can be applied simultaneously or separately and used for the plasma heating and current generation. This provides for the study of processes in plasma with hot electrons or hot ions.

The physical start-up of T-15 (production of the first plasma) was accomplished in 1988. In 1990, the rated design value (3.5T) of toroidal magnetic field produced by superconducting Nb_3Sn coils was achieved. During 1993-1995, ohmic heating discharges with plasma current up to 1MA were studied. The first experiments with ECRH and NBI heating were carried out in 1995. The joint functioning of all T-15 systems was demonstrated [7].

The mail goal of future experiments on T-15 is to obtain discharges with an improved plasma confinement with ECRH and NBI. This plan involves the use of existing gyrotrons as well as putting into operation 4 new 110GHz long-pulse gyrotrons with an output power of up to 1MW each.

References

1. Alikaev V. V., Bobrovski G. A., *et al*, Fiz. Plazmy, 1976, **3**, 390.
2. Alikaev V. V., Bagdasarov A. A., *et al*, Fiz. Plazmy, 1988, **14**, 1027.
3. Alikaev V. V., Bagdasarov A. A., *et al*, Plasma Physics and Controlled Nuclear Fusion Research, 1992, **1**, 627.
4. Esipchuk Yu. V., Alikaev V. V., *et al*, Plasma Physics and Controlled Fusion, 1995, **37**, 267.
5. Kislov D. A., *et al*, to be published in Nuclear Fusion.
6. RRC 'Kurchatov Institute'Annual Report, 1995, **2**, 106.
7. *Ibid.*, p. 105.

ECRH IN ASDEX-UPGRADE
DESCRIPTION OF THE RF SYSTEM AND FIRST RESULTS

H. Brinkschulte

F. Leuterer, M. Münich, F. Monaco, A. Peeters, F. Ryter, W. Suttrop
ASDEX Upgrade team
Max Planck Institut für Plasmaphysik, 85740 Garching, Germany

ECRH groups IPF Stuttgart and IAP Nizhny Novgorod

Abstract

A 140 GHz ECRH system with a maximum power of 2 MW and a pulse length up to 2 s (2.8 MW - 2 s) is being installed at the ASDEX-Upgrade tokamak. A first unit delivering 0.5 MW for 0.5 s is operational since summer 1995. In first plasma experiments, deposition of rf power and propagation of heat waves were studied.

1. Introduction

The main objective of ASDEX-Upgrade (R = 1.65 m, a= 0.5m, ε = 1.6, I_p < 1.6 MA, Bt < 2.8 T) is the investigation of the divertor under conditions prevailing in future fusion machines. The installed additional heating power - 20 MW neutral beam injection and 8 MW at ion cyclotron resonance frequency - is sufficient to achieve heat fluxes to the plasma facing components which are encountered in a fusion reactor. However, the energy transport from the core of the plasma through its boundary to the wall is not well understood. Additional plasma features such as MARFEs, various types of ELMs, the transition from the L-regime to the H-regime of the plasma etc. need further investigation. A great number of problems can be studied with a heating method which allows localised deposition of power and which can be modulated, preferably at frequencies between 10 Hz and 10 kHz.

With high power gyrotrons commercially available, ECRH is suitable to meet the task of localised plasma heating. It was decided to

install at ASDEX-Upgrade 2 MW additional heating power at the 2nd harmonic electron cyclotron resonance which corresponds - at a typical toroidal field of 2.5 T - to a frequency of 140 GHz. The high absorption for that case at electron densities between $1x10^{19}$ and the cut-off density of $1.3x10^{20}$ leads to a narrow absorption zone. By changing the toroidal field, or by tilting a mirror in the vicinity of the plasma around its horizontal axis, the entire cross section of the plasma can be reached. Rotating the mirror around its vertical axis allows current drive studies.

2. The rf system

The rf power will be provided by 4 gyrotrons each specified for 500 kW and 2 s pulse length, or 700 kW and 1 s, respectively. The entire system will be operational early 1997. One unit comprising a 0.5 MW / 0.5 s gyrotron, transmission line and in-vessel mirrors are operational since summer 1995. So far, some plasma pulses with additional ECRH have been achieved.

2.1 First unit with 0.5 MW - 0.5 s

A prototype unit was set up in co-operation with IAP / Nizhny Novgorod to test single components of the system and to gain experience with the operation of a 140 GHz gyrotron. The gyrotron delivers its maximum output power of 500 kW at a beam voltage of 71 kV and a beam current of 26 A. A tetrode in series with the power supply allows the modulation of the beam voltage, and thus of the rf power, up to frequencies of 30 kHz. The originally excited TE 22.6 mode is converted inside the tube into a Gaussian beam TEM-00 which is suitable for the transmission over long distances.

Just behind the output window, ca 85 % of the total power is in the desired mode. The spurious power is dumped in the first mirror box behind the gyrotron. The box contains also shaping mirrors to compensate the astigmatism of the beam. The transmission of power is partly quasi-optically, partly via HE-11 mode inside corrugated wave guides with a diameter of 87 mm. The whole arrangement with all major components is sketched in fig. 1. A pair of polarisers (corrugated mirrors) allows us to rotate the plane of polarisation to any direction and to excite an elliptically polarised beam. Near the torus - where space becomes a problem - the rf is transferred into a wave guide. Just

in front of the torus, transmission returns to quasi-optical mode. The resonance window is made from boron nitride and is similar to the output window of the gyrotron. The length of the transmission line between source and plasma is ca. 35 m.

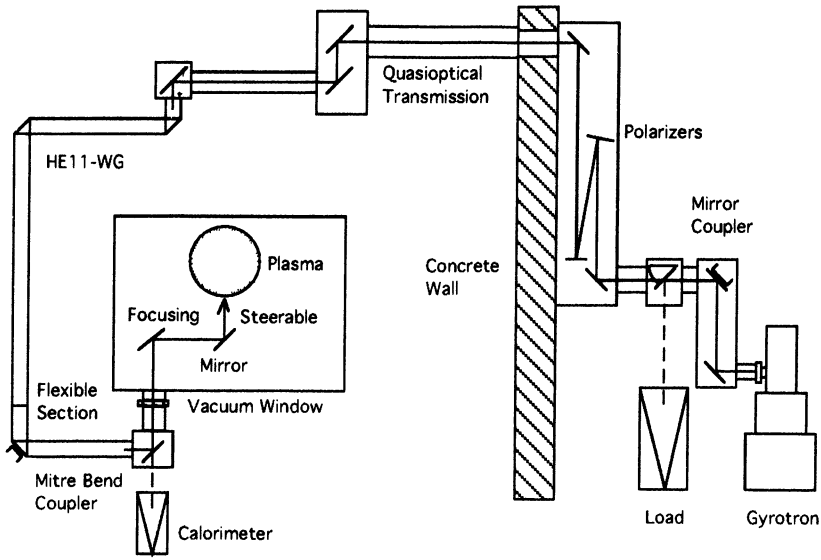

Figure 1. Transmission of rf power from source to plasma; total length is ca. 35 m.

The first mirror of the transmission line and the mitre bend just in front of the torus are equipped with multi-hole directional couplers which enable us to measure the forward and reflected power. The rf diodes at the directional couplers provide very good signals and were calibrated with a calorimetric load near the torus window. Our power measurement is estimated to be accurate within 10 %.

The loss of the transmission line is ca. 7 %, estimated to be mainly due to the 12 mirrors and the 3 wave guide mitre bends, respectively. Thus, about 80 % of the output power is coupled into the ASDEX-Upgrade machine.

During conditioning of the gyrotron, the power is directed into a high power dummy load (by inserting a mirror between the mirror coupler and the polarisers). The load can handle maximum rf power at maximum pulse length and for minimum allowable pulse intervals.

The alignment of the transmission line was executed in 2 steps. Firstly, the quasi optical portion was aligned with a He-Ne laser and small pieces of surface mirrors attached to the centre of each mirror for

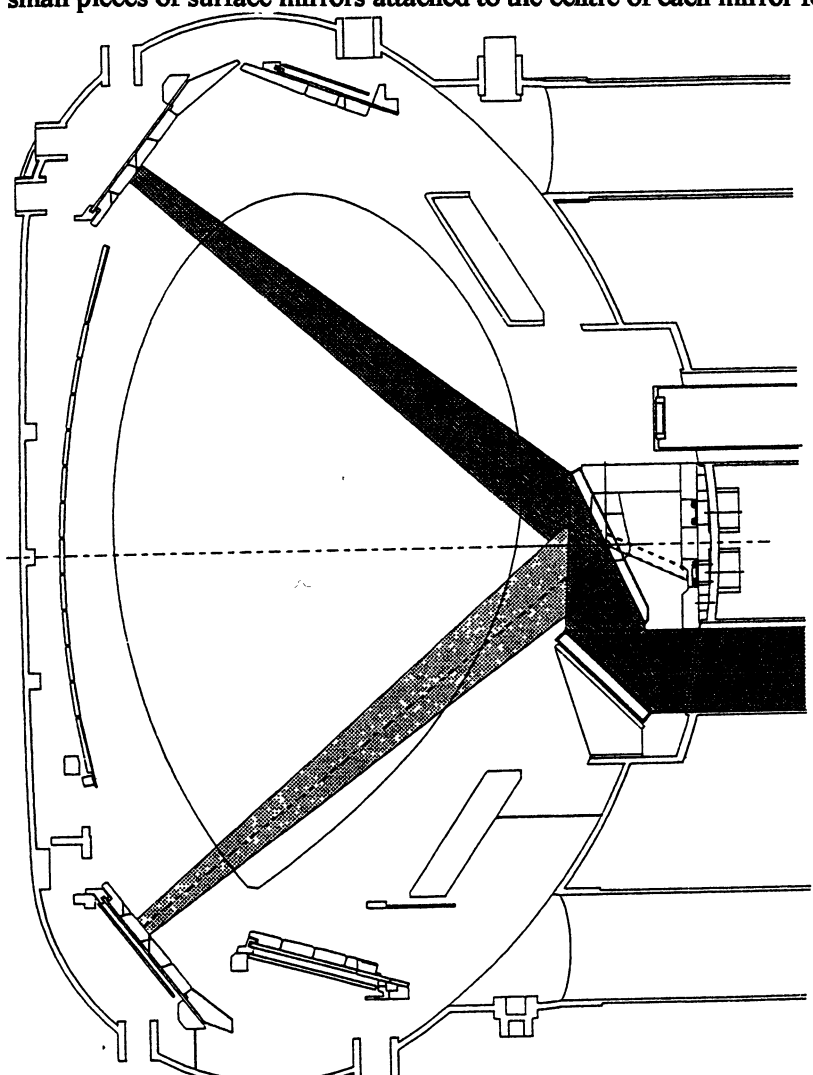

Figure 2. Poloidal cross section of plasma with accessible range for rf beam; $\varphi_{pol} = \pm 35^{0}$

better visualisation of the laser beam. This procedure gives good results as proved with the measured patterns of the rf beam on thermographic foils. In a second step - which turned out to be very tricky - the quasi

optical beam is coupled into the wave guide. For good coupling, the axises of both parts have to coincide with great accuracy. In Addition, slight deviations from a truly Gaussian beam - like a rest of astigmatism - lead inside the wave guide to excitation of additional modes [1]. These modes - although rather weak - can modify the flow of power inside the wave guide substantially. Interferences may lead to a non-uniform power density profile at the end of the wave guide and thus also in the torus window. In our case we were lucky to have the beam centred at the location of the window.

The rf power is launched in the midplane of the vacuum vessel from the low-field side. The in-vessel arrangement is sketched in figure 2. Two mirrors are mounted inside the torus. One mirror is fixed with curved surface to focus the rf beam at a location half way between the centre of the plasma and its boundary on the high filed side. The waist of the beam - calculated without plasma - is $w_0 = 21.14$ mm. A second plane mirror is rotatable around the horizontal, and the vertical axis, respectively. This allows us to scan almost the entire cross section of the plasma ($\varphi_{pol} = \pm 35^0$) and also to direct the beam toroidally in both directions ($\varphi_{tor} = \pm 25^0$). The mirror is made from fine grain graphite with copper coating on its front surface for better reflection of the rf.

2.2 Complete 2 MW - 2 s system

The complete system comprises 4 gyrotrons and 4 separate transmission lines to the experiment. The gyrotrons are made by GYCOM Company in Nizhny Novgorod, Russia. Each gyrotron is designed to deliver 0.5 MW for a 2 s long pulse, or 0.7 MW for only 1 s, respectively. Each two gyrotrons are fed by a common high voltage power supply with a modulator tube in series for switching and modulating of rf power. It is sufficient to reduce the beam voltage by only 30 % to terminate rf oscillation. In this mode, the rf can be modulated up to frequencies of 30 kHz. The gyrotrons emit at 140 GHz $\pm$ 500 MHz.

The gyrotrons are mounted some 15 - 20 m away from the ASDEX-Upgrade machine. At this distance, the magnetic stray field is still up to 30 Gauss. The critical components of the gyrotrons are at the height of the mid-plane of the plasma where the horizontal component of the stray field is minimum. To reduce the horizontal component even further, a 1 cm thick plate of soft iron was mounted above the tubes. Another 2 cm thick iron plate beneath the gyrotrons shields the magnetic stray field from the high current bus bars of the experiment.

For more uniform loading of the collector, the e-beam is swept across its surface with an external magnet (saw tooth at ca. 7 Hz frequency).

The transmission line from the 4 sources to the plasma is ca. 35m long. The rf power from 2 gyrotrons is fed to the plasma through 2 neighbouring ports of the vacuum vessel in sector 6, and 8, respectively, toroidally 22.5^0 apart. The remaining 2 rf beams enter the torus through 2 ports in one ASDEX sector (#14, opposite sector 8).

A critical component of the system is the rf window which separates the transmission line from the torus vacuum. Its relatively high losses around 3 % lead to a strong temperature increase of the window at the end of the 2 s long pulse. To minimise thermal stresses, a mode converter was introduced at the end of the wave guide section which leads - compared to the rather peaked power distribution for the original HE-11 mode - to a more uniform beam pattern at the site of the window.

The construction of the whole system is now (summer 1996) well advanced. 2 gyrotrons are on site and are being commissioned, the remaining 2 tubes are due fall 1996. We are now confident that the complete rf plant and transmission line will be operational and ready for plasma experiments in the first half of 1997. We expect to couple to the plasma 1.8 MW for 2 s, or 2.5 MW for 1s, respectively.

3. First experimental results

During the first year of operation of the 0.5 MW - 0.5 s unit at ASDEX-Upgrade, many plasma pulses with successful electron cyclotron heating were achieved. The maximum injected ECRH power of 0.4 MW is small compared to the ohmic power of ca. 1 MW (for standard 1 MA discharge) and far less than the presently installed 8 MW of ICRH, and 10 MW of NBI power, respectively. Therefore, heating effects can only be studied in low power ohmic discharges. However, the power is sufficient for heat pulse experiments, even in discharges with additional heating. Most experiments so far were done with modulated rf power between 10 Hz and 1 kHz.

During the whole campaign, the system worked very reliably. Most of the pulses were at maximum power and at maximum pulse length of 0.5 s (1 s in case of modulation). The transmission line proved to be very stable and only minute re-alignments were necessary.

3.1 Heating in ohmic discharges

Figure 3 depicts a few signals of a typical 1 MA discharge with ECRH power on between 1.8 and 2.3 s. The stored plasma energy increases with rf power and saturates after ca. 100 ms. The global energy confinement time τ_E as determined by the stored energy divided by the total power $P_{tot} = P_{ohm} + P_{ecrh}$ decreases slightly. We found the

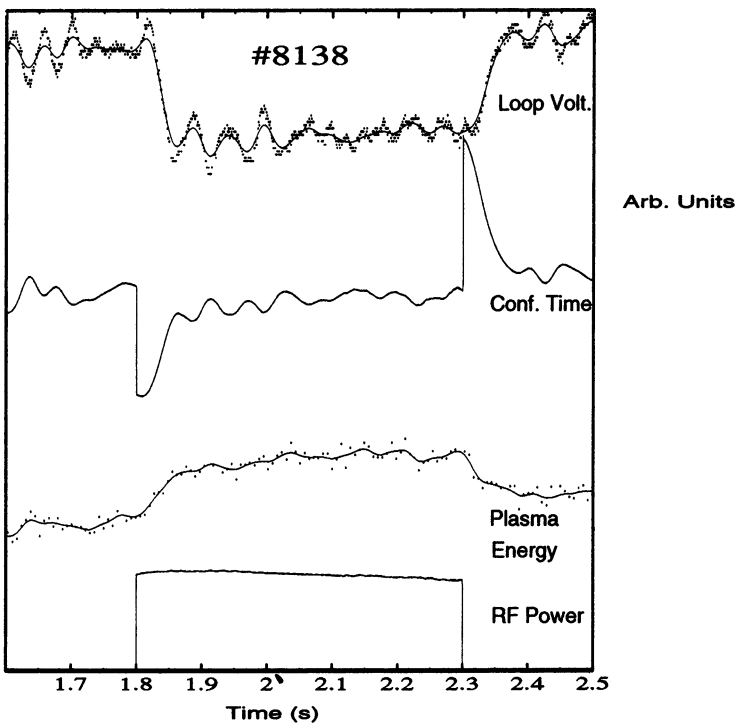

Figure 3. Traces for rf power, plasma energy, confinement time and loop voltage vs. time. Ip = 1MA, $n_e = 4{\cdot}10^{19}$ m^{-3}, $B_t = 2.5$ T

familiar law for the degradation of energy confinement time with power

$$\tau_{E\,oh} / \tau_{E\,oh+ecrh} = (P_{tot}/P_{oh})^{-0.5}$$

For this pulse, the rf beam was launched at an angle of $+35^0$ with respect to the horizontal, i. e. the absorption is far away from the centre of the plasma on a flux surface corresponding to $\rho = 0.8$. We found that the behaviour of the loop voltage, confinement time and electron temperature depends on the location of power deposition [2] (no degradation of τ_E and larger increase of electron temperature for heating near plasma centre). This behaviour needs further study.

3.2 Deposition of rf power

From ray tracing calculations including diffraction and absorption [3] we may expect very localised absorption of rf power. The width of the absorbing zone depends on the angle of incidence of the rf beam with respect to the flux surface: at 90^0 the full half width is minimum at 8 mm while at grazing incidence the deposition profile is only determined by the diameter of the rf beam, i.e. ca 30 mm for our case.

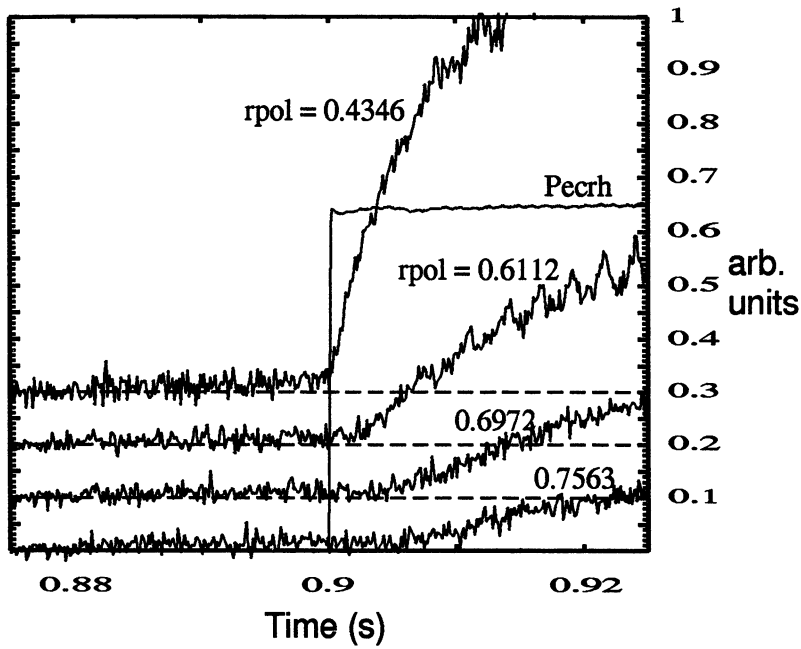

Figure 4. 4 Traces of ECE signals from different radial locations. I_p = 1MA, ne = 2· 10^{19} m^{-3}, B_t = 2.5 T, rf beam +10^0 inclined to horizontal. Pulse # 7494.

ASDEX-Upgrade is well equipped with diagnostics for the measurement of electron temperatures: a 16 beam laser Thomson scattering system delivers electron temperature profiles, 10 per second; ECE diagnostics with 45 channels give a very detailed profile with a maximum time resolution of 10 μs. The latter was extensively used to investigate the response of the plasma to the rf power.

Figure 4 shows 4 ECE signals originating from different radii. Plasma current is 1 MA, electron density $2 \cdot 10^{19}$ m^{-3} and toroidal field is 2.5 T. The rf is launched at an angle of $+10^0$ to the mid plane of the

machine, i.e. absorption is near the plasma centre. The rf is switched on at 0.7 s and T_e increases, fastest and by the largest amount at small r_{pol} and slower and to smaller values further out. For r_{pol} >0.6, even a

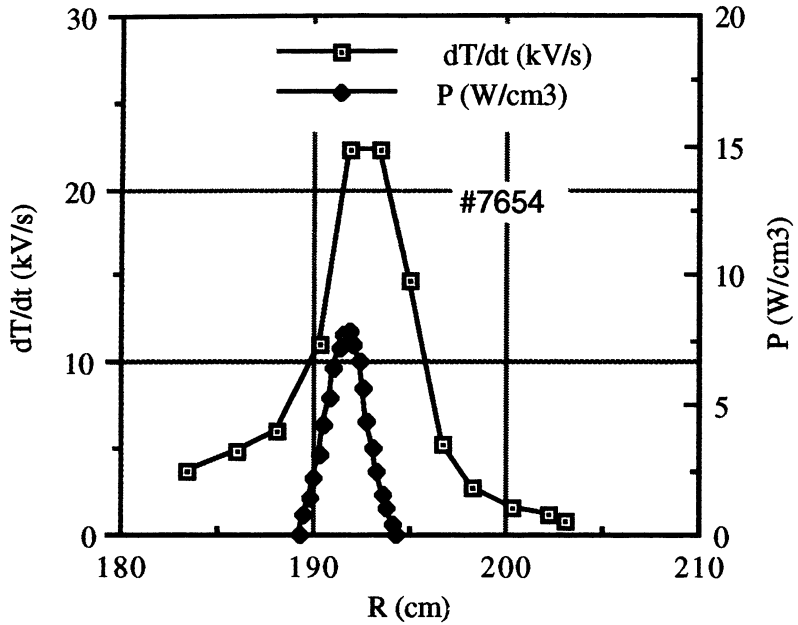

Figure 5. Calculated deposition profile and measured dT/dt versus ρ. I_p = 1 MA, ne = 4 · 10^{19} m^{-3}, B_t = 2.5 T, φ_{pol} = +30°.

measurable delay for the onset of the temperature increase can be seen.

We have measured the rise time of the electron temperature dT_e/dt at the onset of the rf. This gives us the location of maximum absorption and should also yield some hints with respect of the power deposition profile. Figure 5 gives the results for a 1 MA - 2.5 T plasma with the rf beam at +30° to the flux surfaces. In this case, the power is absorbed on the high field side of the machine while the ECE signals originate from the low field side. Also shown is the calculated power deposition for this case. The curve for dTe/dt is much broader than the calculated curve for the deposited power. (The sites of the maxima deviate by ca. 2 cm which may be due to improper calibration.) The broadening can be understood if diffusion effects are taken into account. The characteristic diffusion time τ depends on the characteristic length λ and the diffusivity χ as

$$\tau = \lambda^2/4\cdot\chi$$

At an electron temperature of 1 keV, it takes about 50 μs to fill a flux surface uniformly which corresponds to $\lambda = 1.5$ cm (taking a typical $\chi = 1\ m^2/s$). To determine dT_e/dt properly, a measuring time of 1 ms is needed, leading further to an apparent broadening. Thus, dT_e/dt profiles appear considerably broader than the actual power deposition profile.

3.3 Heat wave experiments

The knowledge of the thermal conductivity of a plasma is fundamental to understand plasma confinement. The thermal conductivity is proportional to the diffusivity χ which can be determined directly with various methods. Most widely used is the measurement of the propagation of saw teeth which yields the electron thermal diffusivity [4]. However, a saw tooth is usually correlated with a large change in electron temperature thus leading to a strong perturbation of the plasma. The corresponding power can reach MW levels and the deduced values for χ may be misleading.

With ECRH one can excite heat waves at much smaller power levels causing only small perturbations of the plasma to be analysed. The origin of the heat wave is very localised and its location and the frequency of the heat pulses can easily be changed. By following the amplitude of the heat wave - represented by the electron temperature -

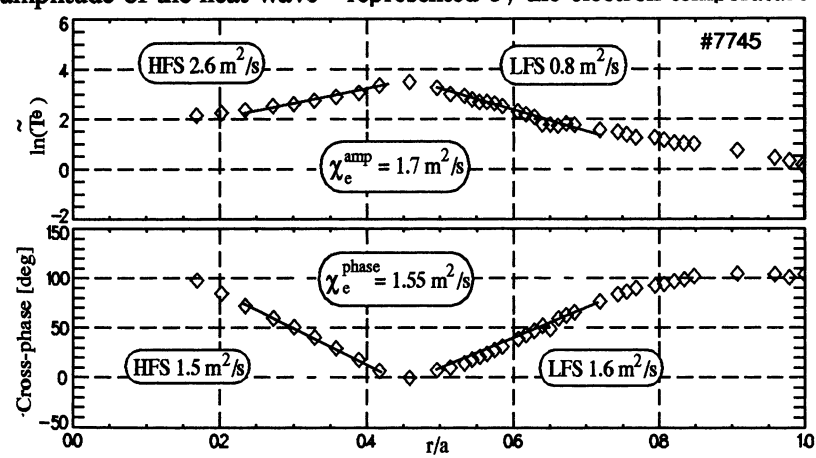

Figure 6. Example for determination of electron thermal diffusivity χ_e from heat pulse measurements. $I_p = 0.8$ MA, $B_t = 2.5$ T. RF power of 400 kW modulated with 29.41 Hz, deposited at $\rho = 0.5$, $\varphi_{pol} = +27^0$.

as it moves away from its origin, one can determine the electron diffusivity χ_{Ampl}. Measuring the time delay, or phase, respectively, one obtains χ_{Phase}. χ_e is defined as

$$\chi_e = (\chi_{Ampl} \cdot \chi_{Phase})^{0.5}$$

Figure 6 gives the results for a typical measurement of χ_e. We did not find a dependence of χ_e on rf power and on modulation frequency. Power was changed between 50 kW and 400 kW, modulation frequency between 10 Hz and 1 kHz. For discharges with saw teeth one has to choose a modulation frequency for which the interference from the saw teeth is minimum. Most measurements were performed at 30 Hz modulation frequency. The χ_e values obtained from ECRH measurements were compared with those from power balance and saw teeth measurements [5].

4. Conclusions

The experiences gained with the prototype ECRH system were very satisfying during the first year of operation. The gyrotron worked very reliably and only minor re-adjustments of its operating parameters were necessary, mainly of the strength of the magnetic field and the emission current. The transmission line - partly quasi-optical, partly wave guide - is very stable and needs only little attention. However, the inner walls of the wave guides have to be kept clean and free of dust to avoid break down at high power levels.

The results obtained so far are very promising. Most experiments were done with modulated rf power to measure transport properties under various plasma conditions. The measured electron thermal diffusivity differs still somewhat in comparison with the data gained from different methods and the whole complex needs further study. With the complete 2.8 MW system operational in the near future, we will start exploring heating effects, the effects on MARFEs, ELMs and on MHD modes [6].

References

[1] G. Denisov, 8th Russian-German Meeting on ECRH and Gyrotrons, Nizhny Novgorod, June 1996

[2] Leuterer, F. et al., 23 rd Conference on Controlled Fusion and Plasma Physics, Kiew 1996, in print
[3] Peeters, A. G., ibid.
[4] Lopes-Cadorzo, N. J., Plasma Phys. Contr. Fus. 37 (1995), 799
[5] Ryter, F., 23 EPS Conference on Controlled Fusion and Plasma Physics, Kiew 1996, in print
[6] Morris, A. W. et al., Plasma Physics and Controlled Nuclear Fusion Research, Seville 1994

Plasma Heating Experiments with an 88 GHz Gyrotron on the WT3 Tokamak

*M. Asakawa, T. Izuhara, K. Tanabe, K. Matsunaga**, S. Yoshimura, S. Kubo***, K. Ohkubo***, H. Asano****, T. Simozuma*****, T. Kikunaga****, T. Maekawa* and Y. Terumichi*

Department of Physics, Faculty of Science, Kyoto university, Kyoto 606-01, Japan

** Department of Fundamental Energy Science, Graduate School of Energy Science, Kyoto university, Kyoto 606-01, Japan*

*** Present address: Mitsubishi Electric Corporation, Hyogo 661, Japan*

**** National Institute for Fusion Science, Nagoya 464-01, Japan*

***** Mitsubishi Electric Corporation, Hyogo 661, Japan*

****** Present address: National Institute for Fusion Science, Nagoya 464-01, Japan*

1. Introduction

Electron cyclotron heating (ECH) is a possible method for controlling the plasma profile. On the WT3 tokamak (R=65 cm, a=20 cm), the effect of ECH on the MHD instabilities has been investigated using an ECH system with 56 GHz gyrotron.[1,2,3] It was found that the MHD activities and the sawtooth oscillations were suppressed or enhanced according to the location of ECH layer. Furthermore these effects of ECH were remarkable when the EC wave was focused strongly.

To study the effect of the highly localized plasma control more extensively, we installed new ECH system using an 88 GHZ gyrotron and a quasi-optical transmission system on WT3. The frequency almost correspond to the second-harmonic cyclotron frequency at the maximum toroidal magnetic induction of WT3 (1.75 T), thus the plasma confinement will be improved compared with previous experiments performed in the magnetic induction range around 1.0 T. Also the density range can be increased without defocusing EC wave due to the refraction to 2×10^{13} cm^{3}, where the cyclotron cut-off appeared with the 56 GHz ECH system.

The quasi-optical transmission system was targeted for focusing the EC wave into a small focal spot with the radius less than tenth of the plasma radius. By the cold test on the transmission system, we confirmed an elliptical Gaussian focal spot profile with radii of 1.85 cm and 1.55 cm in poloidal direction and toroidal direction, respectively. Furthermore, we confirmed that the EC wave was absorbed in the narrow region in plasma. These result will be reported in the following sections.

2. Quasi-optical ECH system using 88 GHz gyrotron

Figure 1 shows the schematic view of the quasi-optical ECH system. The system consists of an 88 GHz gyrotron and the transmission line with eight mirrors. The EC wave is injected into the torus with the vertical polarization for the second-harmonic X- mode injection from low field side.

The operational parameters of the gyrotron are listed in table 1. This gyrotron is designed to work in TE8,2 mode at the cavity. The EC wave is, then, launched into a built-in Vlazov converter consisting of two elliptic focusing mirrors and two flat mirrors. The output is a well defined horizontally polarized Gaussian beam with a radius of 2.3 cm. The available power is still as low as 270 kW and the efficiency is 19 % at this time. The optimization of the operational parameters, especially "tapering", is now underway.

The quasi-optical transmission system was designed with the "constant phase concept" [4]. The basic idea of this concept is illustrated in figure 2 for the symmetric Gaussian beam. The surface of mirror coupling the beam waists w_{in} and w_{out} is defined so that the sum of the phase front functions of the beams incoming and outgoing remains constant at all the point on its surface. One can design the mirror as defining the locations and the sizes of the incoming and outgoing beams. For simplicity, the mirrors designed with the phase concept will be called matching mirrors.

The transmission line is divided into three parts: seven meter long transmission line consists of two pairs of matching mirrors, polarization converter consists of a pair of flat mirrors and the launcher consists of a pair of matching mirrors. The total length of the transmission line is 11 m along the beam propagation. All the mirrors are made of aluminum without the special surface coating.

The pair of M1 and M2 mirrors expands the beam to minimize the diffraction loss through the seven meter propagation, then the pair of M5 and M6 focus the beam again to send the beam to the launcher inside a vacuum vessel installed on the torus. This line is required to separate the gyrotron and the torus with a certain distance, about 6 m in this case, so that the leakage field of the torus dose not affect the operation of the gyrotron.

The pair of M3 and M4 is installed between the transmission line in order to convert the polarization of gyrotron output into vertical polarization for the X-mode injection. The beam is deflected at a right angle from its original path toward the torus, simultaneously.

The launcher, pair of M7 and M8, strongly focus the beam. The focal spot was designed to be located at 62.5 cm in major radius with 1/e radii of 1.2 cm and 1.6 cm in poloidal direction and toroidal direction, respectively. Because the strongly focused beam expands rapidly, the launcher is placed inside the vacuum vessel installed on the torus to minimize the distance between the M8 and focal spot. M8 mirror can be

tilted in both toroidal and poloidal direction to electron cyclotron current drive experiment and to adjust the heating zone. The launching angle can vary from 50° to 90° in toroidal direction.

All the mirror size are designed to be larger than the mode radius of beam by a factor of 1.7 to reduce the diffraction losses at each mirrors. For example, size of M1 is 32×32 cm^2.

3. Test on the transmission line

The characteristics of the transmission line were measured by a cold test using a gyrotron emulating gunn oscillator. The gunn oscillator with scalar cone and a pair of matching mirrors simulate the gyrotron beam in frequency, polarization, and both the size and the location of the waist. We measured the propagation of this gyrotron simulating beam to align and to test the transmission line using a microwave diode. The diode was set as following a E-band waveguid and was installed on a remote controlled movable stage to measure the cross-sectional profile of the beam. By changing the setup angle of the diode, we could also confirm the polarization.

After the cold test, the gyrotron beam was injected into the transmission line. The beam size was evaluated from thermal images on teflon screens located at several point along the transmission line. The focal spot size, located near the center of the torus, was measured from the burn pattern.

The beam sizes measured along transmission line were plotted in figure 3. The solid line represents the design value, and the solid circle and open circle denote the results of the cold and high power tests, respectively. The result of the cold test agrees well with the design and the profile at the focal spot, shown in figure 4, was well defined Gaussian. The radii of the focal spot was 18.5 mm and 15.5 mm in poloidal direction and toroidal direction, respectively. The radius in poloidal direction is larger than that of design, but is still less than tenth of the minor radius of WT3.

The result of the high power test deviates from the design in the seven-meter long transmission line. This deviation arise mainly from the uncertainty of the measurement. The burn pattern at the focal spot near the center of the torus, however, shows a well focused profile with radii of 13.5 mm and 10.5 mm in poloidal and toroidal direction, respectively.

Figure 5 shows the transmission efficiency along the transmission line evaluated from the result of the cold test. Total efficiency was to be 83 %. The output of gyrotron was measured by a water load in front of the entrance window to the launcher vessel. Maximum power transmitted through the transmission line is 220 kW at this time.

4. Plasma heating experiment

To confirm if the EC wave is deposited locally in plasma as expected,

we performed a preliminary heating experiment on WT3. Five arrays of soft-X-ray (SXR) detectors were used to observe changes in the SXR emission caused by ECH deposition in plasma. Arrangement of the SXR detector arrays are shown in figure 6. Each array has twenty SXR diodes detecting the photon energy range from 3 keV to 27 keV. These SXR data of one-hundred line of sight are used to reconstruct the SXR emission profile in plasma by the means of computerized tomography (CT).

Experiments were performed on plasma with relatively low current of 60 kA and line-average density of 1.4×10^{13} cm^{-3} to eliminate the MHD activities, sawtooth oscillations and their associated heat transport. The toroidal magnetic induction was 1.6 T, locating the resonant surface through the plasma center. The ECH power of 150 kW was injected in a time interval from 60 to 70 ms, where the plasma parameters, current, line-average density, SXR emission and loop voltage, began to be stationary. Figure 7 shows the typical response of the plasma. While the line-average density through the plasma center, fig. 7 (c), dropped from 1.4×10^{13} to 1.2×10^{13} cm^{-3} in 4 ms after ECH injection, the SXR signal of the center chord, fig. 7 (e), increases in 1ms, and then starts to decrease. The ECH injection causes to move the plasma slightly toward outer side. The amount of the shift of plasma center was estimated to be only 5 mm by analyzing the magnetic probe signals. Thus this shift is not essential to decrease in the center chord SXR signal, when we consider the width of line of sight. (And the SXR detector viewing at 10 mm outside from the center showed a similar response to the response shown in fig. (e). The increase in SXR signal possibly resulted from the decrease in the center density.) The SXR signals viewing outer side, fig. 7 (f), (g) and (h), begin to increase slowly compared with that of the center chord, and saturate in 3 ms after the ECH injection.

To find the deposition profile of ECH wave, evolution of the profile of the SXR emission on the equatorial plane immediately after the ECH injection is shown in figure 8. These SXR profiles were computed by CT method. Increase in SXR signals, in fig. 8 (a), viewing near the plasma center indicates the increase of temperature by ECH, because the line-average density through the plasma center decreases monotonically in the time range considering here. Change in the SXR emission from immediately before the ECH injection, fig. 8 (b), demonstrates that the EC wave is absorbed in a narrow region from r/a = -0.05 to r/a = 0.25. Corresponding deposition width is 6 cm at most, because this result includes the heat transport.

Similar narrow deposition profiles were observed on the experiments of outside heating, locating the resonant layer at 58 cm and 62 cm in major radius. These results suggest that the refraction in plasma is insignificant up to the density of 1.4×10^{13} cm^{-3}, thus the EC wave is still focused strongly in the presence of plasma.

Table 1 Gyrotron parameters

Frequency	88 GHz	
Cavity mode	TE8,2	
Output mode	linearly polarized Gaussian	
Beam Voltage	80 kV	
Beam current	20 A	
Output power	350 kW	(measured: 270 kW)
Efficiency	29 %	(measured: 19 %)
Pulsewidth	100 ms	(measured: 50 ms)

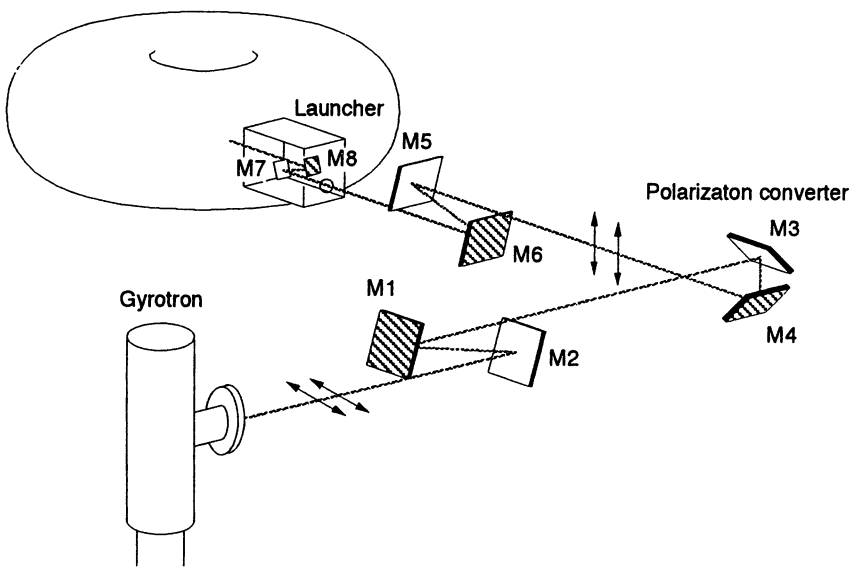

Figure 1. Schematic view of the quasi-optical ECH system for WT3. Total path length from gyrotron exit window to the center of torus is 11 m. The horizontally polarized gyrotron output is converted into vertical polarization at the polarization converter (M3 and M4) placed between the transmission line (M1, M2, M5 and M6). The EC wave is, then, coupled to the launcher (M7 and M8) inside the vacuum vessel through the ceramic window.

Phase function

$$\psi(r)=k\left(z+\frac{x^2}{2R(z)}\right)-\phi(z) \qquad \phi(z)=\tan^{-1}\frac{kw_0^2}{2z} \qquad R(z)=z\left(1+\frac{k^2w_0^4}{4z^2}\right)$$

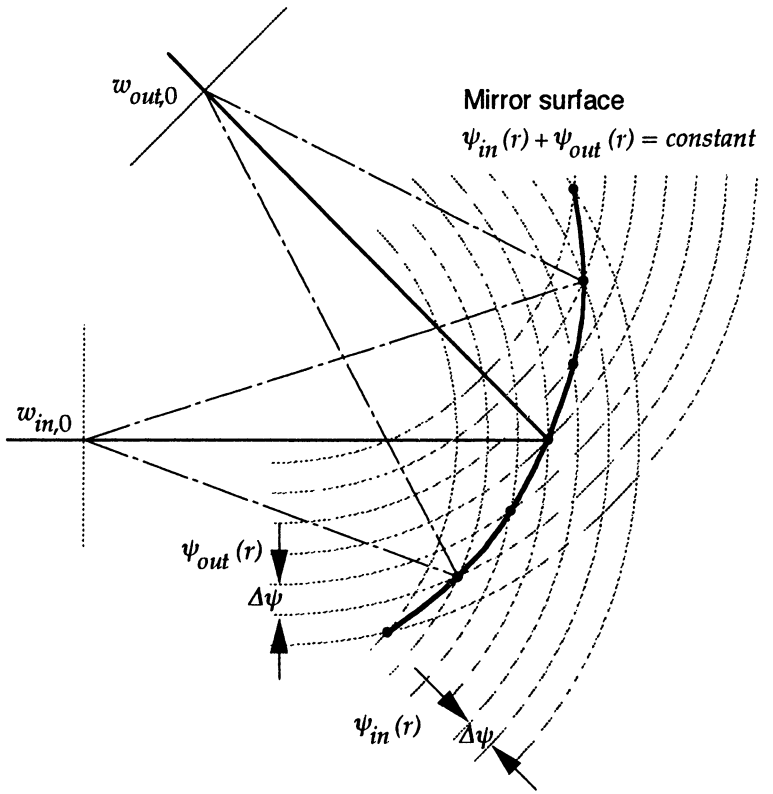

Figure 2. Matching mirror and the constant phase concept. The dashed lines represent the phase fronts of beams incoming and outgoing. Both these phase fronts are drawn by each $\Delta\psi$, such as ψ_{In}, $\psi_{In}+\Delta\psi$, $\psi_{In}+2\Delta\psi$. The mirror surface satisfies the matching condition given by $\psi_{In}(r)$ + $\psi_{out}(r)$ = constant.

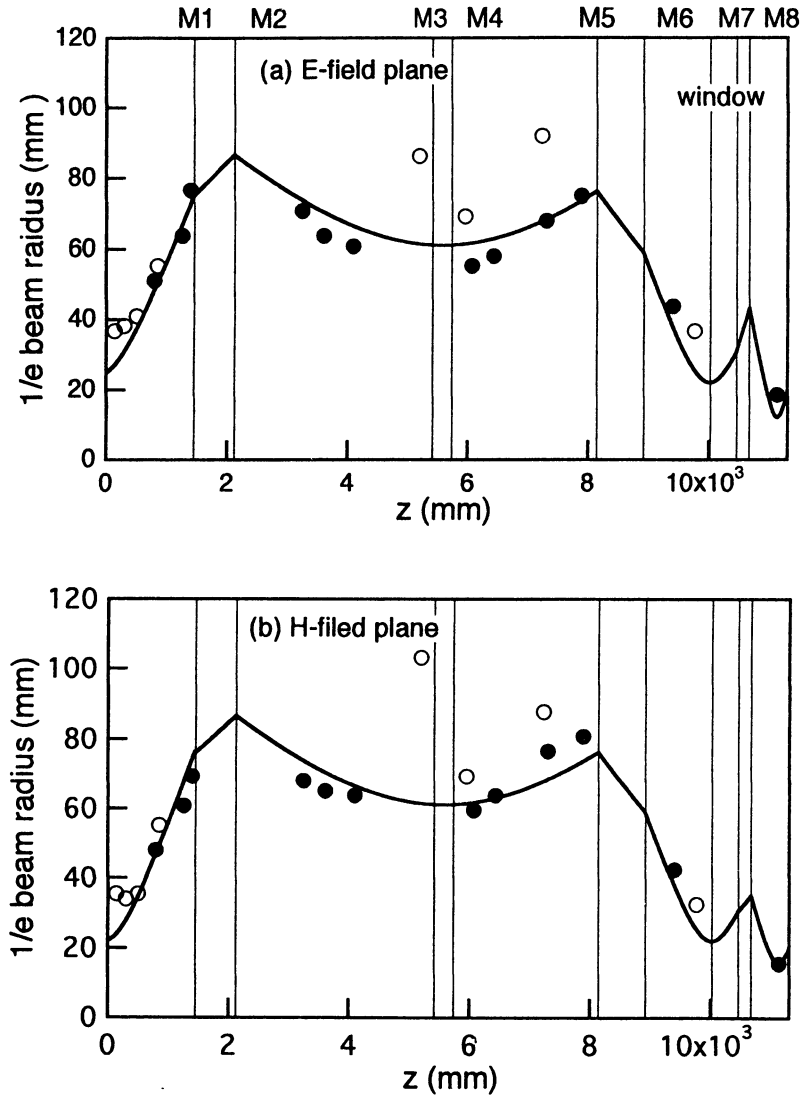

Figure 3. Evolution of the beam radius along the ECH system. Solid and open circles denote the result of the cold test and the high power test, respectively. Solid line represents the design value. Thin lines indicate the positions where mirrors are placed. Fig. (a) is the results measured on E-plane of EC wave, while fig. (b) is the results on H-plane.

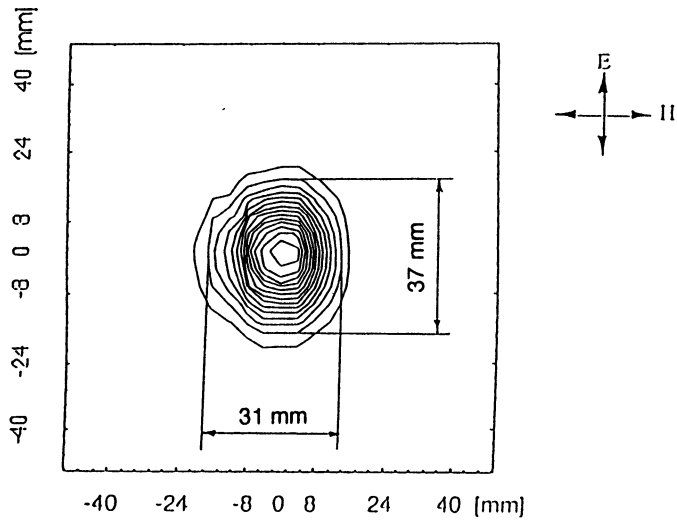

Figure 4. Profile of the EC wave at the focal point near the center of torus. The elliptical Gaussian beam with radii of 18.5 mm in poloidal direction and 15.5 mm in toroidal direction was obtained.

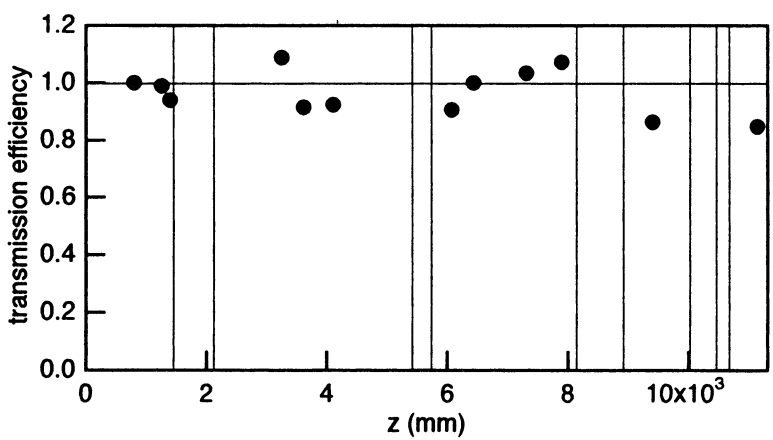

Figure 5. Transmission efficiency as a function of the propagation distance along the ECH system. The transmitted power at each point was calculated by integrating the beam profile measured by the cold test.

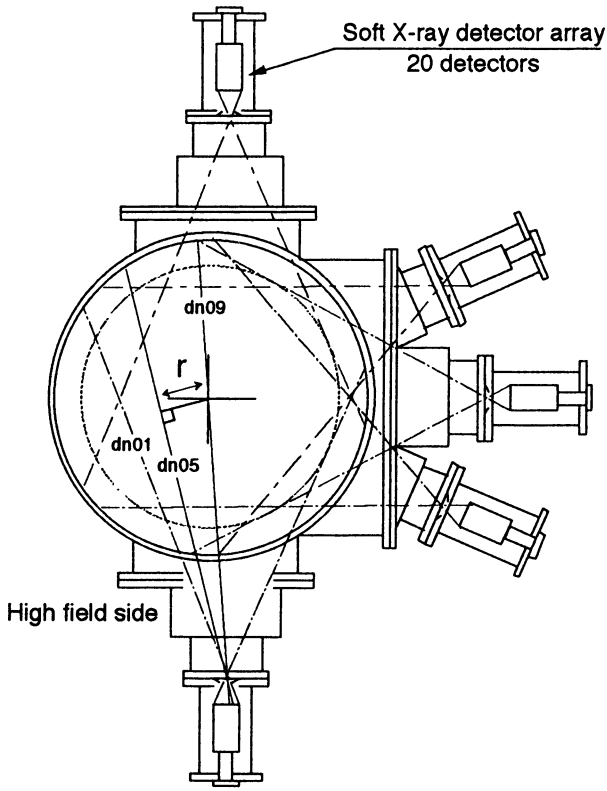

Figure 6. Arrangement of SXR detector arrays. An array consists of 20 detectors. Five arrays are placed on a poloidal plane. The viewing position of the each detector is defined as the length of the perpendicular dropped from center of the torus to its line of sight.

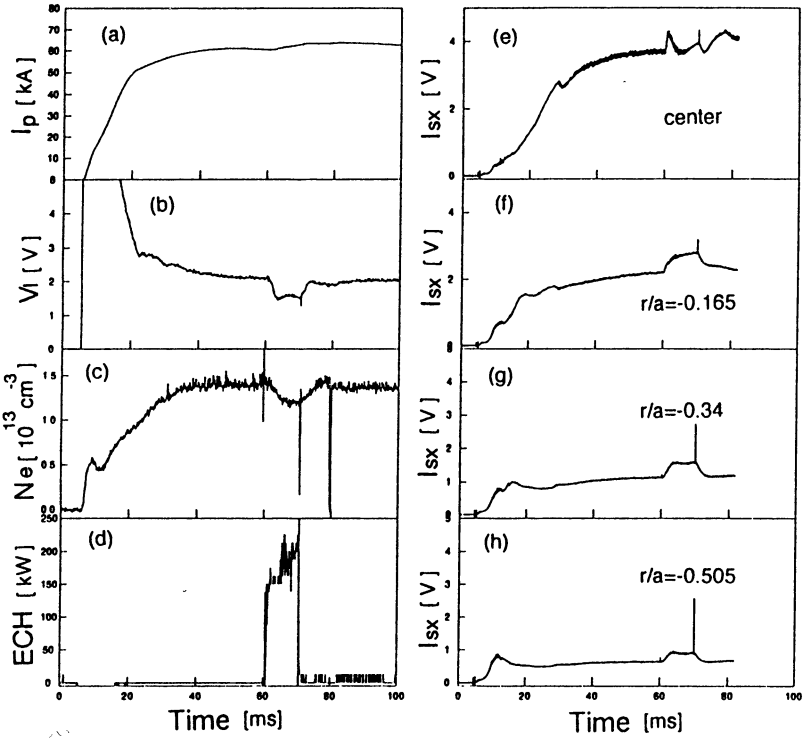

Figure 7. Typical plasma response for the center heating. Fig. (a), (b) and (c) indicates the plasma current, loop voltage and the line average density through the center of plasma, respectively. Fig. (d) is the waveform of ECH. The gyrotron starts to oscillate from 60.1 ms, and the EC wave is injected for 10 ms. Fig. (e) to (h) show the SXR signals. The viewing positions are indicated in figures.

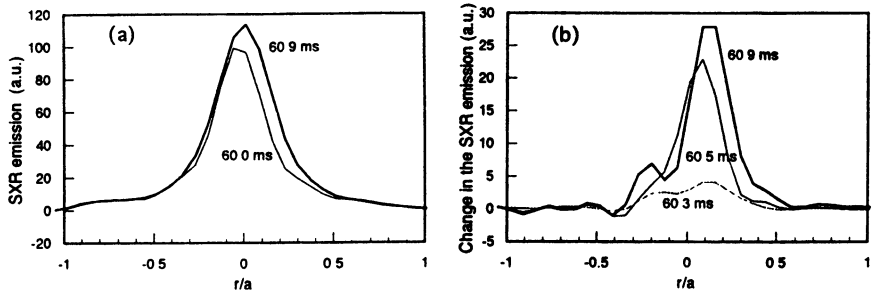

Figure 8. Profile of the SXR emission at 60.0 ms (immediately before the ECH injection) and at 60.9 ms is shown in fig. (a). Change in the SXR profile from that at 60 ms, i.e. Isx(t)-Isx(60ms), for 60.3 ms, 60.5 ms and 60.9 ms is shown in fig. (b). These profiles were computed by the CT method. Fig. (b) suggests that the plasma is heated in a narrow region from r/a=-0.05 to r/a=0.25.

5. Conclusion

A quasi-optical ECH system using an 88 GHz gyrotron was installed on the WT3 tokamak. We confirmed that a well defined Gaussian beam was focused near the center of the torus with a small spot size of 1.85 cm in poloidal direction. The transmission efficiency of the system was measured to be 83 %, and the maximum power injected into the torus was 220kW. For the current drive experiment, we plan to install the polarization converter to produce an elliptically polarized beam. The preliminary ECH experiments suggested that the EC wave was absorbed in the narrow region around the resonant plane. We will make use of this ECH system to investigate the effect of the highly localized plasma control on the MHD phenomena.

Acknowledgment

This work was supported by a Grant-in Aid for Scientific Research from the Ministry of Education in Japan.

References

One K. Hanada et al et al., Phys. Fluids, B4 1992, 3675

Two S. Yoshimura et al, Fusion Engineering and Design 26, 1995, 77

Three Y. Terumichi, et al., in Plasma Physics and Controlled Nuclear Fusion Research 1994 (Proc. 15th Int. Conf. Seville), Vol. 2, IAEA, Vienna (1995) 189.

Four S. Kubo et al., Fusion Engineering and Design 26, 1995, 319.

ELECTRON CYCLOTRON RESONANT HEATING IN THE TOKAMAK T C V

T. Goodman, M. Henderson, A. Pochelon, S. Alberti, M.Q. Tran

Centre de Recherches en Physique des Plasmas
Association Euratom - Confédération Suisse
Ecole Polytechnique Fédérale de Lausanne
PPB-Ecublens, CH-1015 Lausanne, Switzerland

Introduction

The objective of the tokamak TCV (Tokamak à Configuration Variable) at the Centre de Recherches en Physique des Plasmas is to study the influence of elongation κ (κ = b/a = (half height of plasma /minor radius)) and strong shaping on tokamak performances. The importance of elongation clearly stems out from the various energy confinement scalings which all bear a strong dependence on plasma current I^{α} and elongation κ^{β}, where α and β are of order unity. The maximum current I being a quadratic function of κ, there is a very strong interest in assessing the validity of the scaling laws as a function of κ in particular, but also in general as a function of the plasma shape. Note also the scarcity of the data base in the regime of high elongation ($\kappa > 2$).

Since the plasma in TCV can be created with a large variety of shapes (elongation κ from 1 up to 3, D and inverse-D shapes, etc....), the auxiliary heating must be insensitive to the plasma configuration. Of all the heating methods (Alfvén Wave Heating, Ion Cyclotron Resonant Heating, Neutral Beam Injection, and Electron Cyclotron Resonant Heating (ECRH)), ECRH has the best operational flexibility for heating of a wide-range of different configurations, relying on steerable mirrors to deliver the power locally to the plasma. Moreover, mode control, current drive and current profile modifications by off-axis heating are other features which can be achieved with Electron Cyclotron Wave (ECW).

In this report, we shall present the theoretical predictions for the absorption of and current drive (CD) efficiency due to ECW in TCV (Section 2). The description and the status of the implementation of the ECW system is described in Section 3.

Electron Cyclotron Resonant Heating and Current Drive Calculations for TCV

a) *The Tokamak TCV*

The main characteristics of the tokamak TCV are given in Table I.

Major radius R	0.88 m
Minor radius a	0.25 m
Aspect ratio R/a	3.5
Maximum plasma height 2b	1.50 m
Maximum elongation $\kappa = b/a$	3
Maximum design plasma current I	1.2 MA
Operating Magnetic field B_T	1.43 T

TABLE I
Main Characteristics of TCV

To allow the creation of a large variety of plasma configurations and their control, sixteen independent poloidal coils are installed in TCV (Fig. 1). A set of internal coils connected to a fast power supply will be put into operation to control the plasma position at high elongation [1]. Scenarios for obtaining various plasma configurations have been elaborated. For example, it was shown that ITER-like shapes ($\kappa \sim 2$), fully elongated ($\kappa \sim 3$) as well as multiple magnetic axes configuration [2] (Doublets) could be created in TCV. Experimentally elongation κ up to 2.05 and plasma current of 0.81 MA were achieved [3]. Both limited and diverted plasma were also produced during the different experimental campaigns [4]. More recently, a Doublet configuration was obtained during about 10 ms [2].

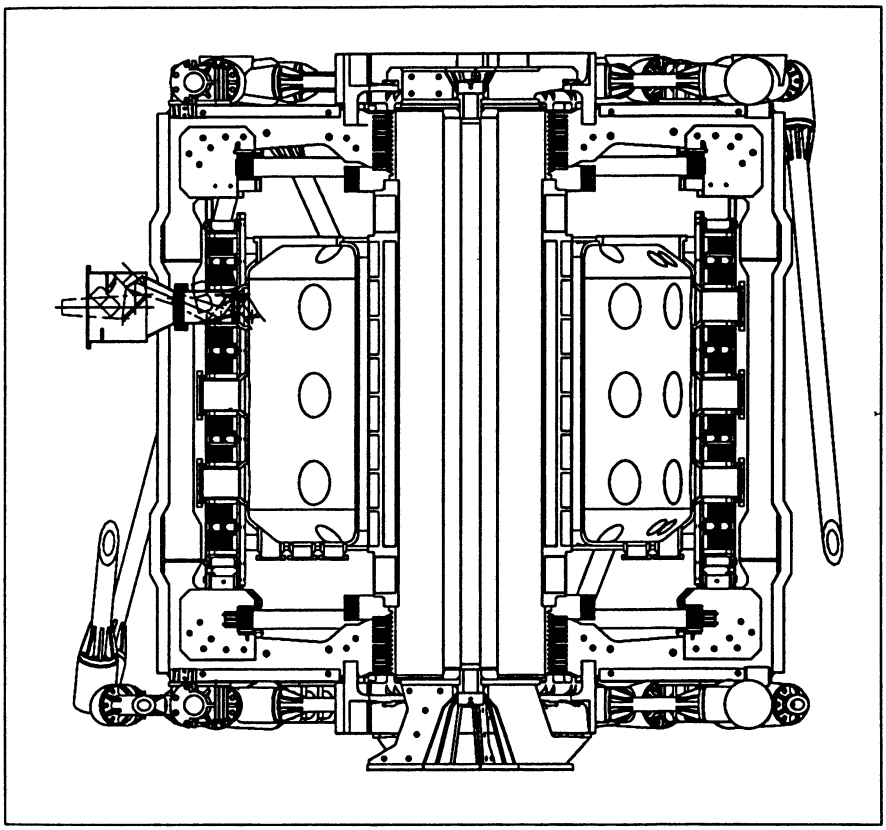

Figure 1

Schematic of TCV. A launcher for the X2 system
is shown on the low-field side on the left of the machine.

b) *Parameters of the ECWS*

The frequencies of the ECW system have been chosen to maximize the density which can be reached below cut-off. Second harmonic at 82.7 GHz and third harmonic at 118 GHz, both in the extraordinary mode X (called hereafter X2 and X3) allow heating at the operating field $B_T = 1.43$ T in high density plasmas: the cut-off density for X2 and X3 are respectively 4.3×10^{19} m^{-3} and 1.15×10^{20}m^{-3}. As will be shown in the next sub-section, the use of combined X2 and X3 modes allow to heat plasmas with central density n_{eo} up to $7\text{-}8 \times 10^{19}$m^{-3}.

A total power of 3 MW in X2 and 1.5 MW in X3 will be installed. The pulse length of the gyrotron is 2 s, so that the heating pulse is longer than the expected current diffusion time (0.2 s for a 0.2 MA circular plasma, about 1 s for a fully elongated ($\kappa = 3$) 1 MA plasma).

c) *Heating and current drive simulations*

Ray-tracing simulations of the accessibility of the resonance from the low field side of TCV through lateral and top ports (Fig. 1) was computed using the codes BANDIT 3-D [5] and TORAY [6]. The equilibrium magnetic field corresponding to the desired configuration and a parabolic density and temperature profiles were used in the calculations. A value of about 1 keV was used as the central temperature T_{eo} in the Ohmic regime. A RF beam divergence of about 2^o was assumed. In the calculations the accessibilty and heating of plasma configurations with elongation κ of 1 (circular plasma), 2 and 3 were assessed.

Heating at the second harmonic extraordinary mode X2 can be performed in all regions of the plasma by injecting the ECW from the upper lateral and middle ports from the low field side [7] by adjustment of the poloidal launch angle. Technically a system of steerable mirrors could be installed on the low field side of the tokamak. 100% first pass absorption in the central region ($x = r/a \leq 0.4$) is achieved if the density is below cut-off on axis (Fig. 2). An X2 wave launched from an upper lateral port is also efficiently absorbed close to plasma edge ($x \gtrsim 0.7$) for central density above the cut-off density (Fig. 3). The localization of the normalized radius x of the absorption region at different central density is also given in Fig. 3.

(a)

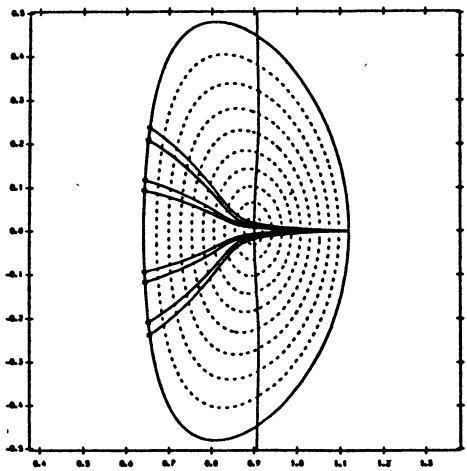

(b)

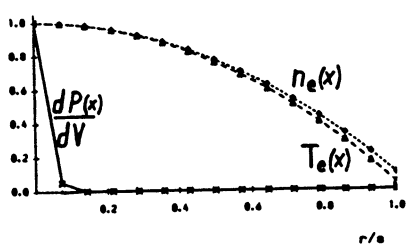

Figures 2a) and 2b)

Ray-tracing (a) and power deposition just below cut-off ($f = 82$ GHz, $n_{eo} = 4 \times 10^{19} m^{-3}$).

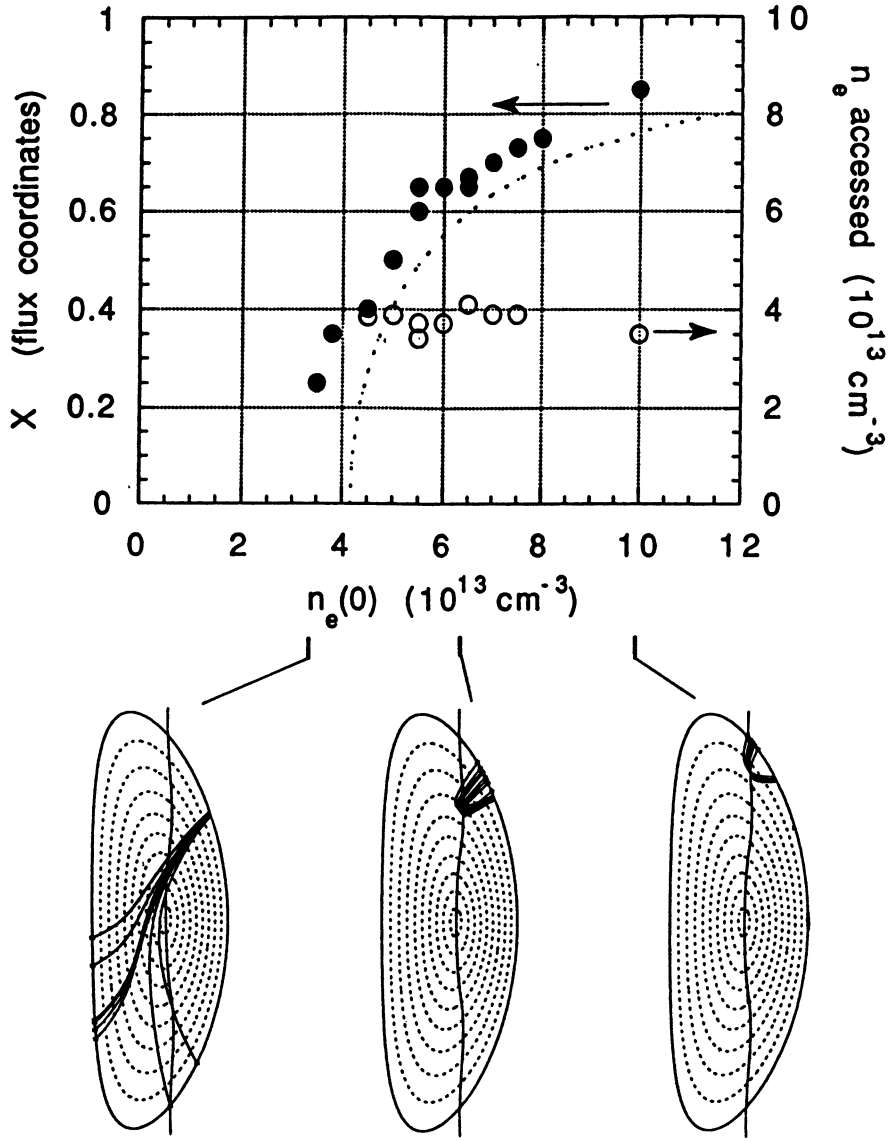

Figure 3

Upper lateral X2 launch into a fully elongated plasma ($\kappa = 3$, 82GHz, 1.5T). The position of power deposition is shown as a function of central density. The dotted line represents the flux coordinate, x, of the cut-off density.

Heating at the third harmonic extraordinary mode X3 is used to increase the accessible density. For the TCV plasma parameters (B_T = 1.43 T), the optimum frequency range is around 125 GHz with the final frequency choice for the X3 gyrotron being at 118 GHz. Since absorption of third harmonic wave is reduced compared to the one of the second harmonic, it is necessary to increase the path over which the RF beam interacts with the resonant layer. This is achieved by a quasi-vertical launch from a top port (Fig. 1). Moreover, since the optical depth τ of the X3 wave is proportional to $n_e T_e^2$, the interaction should occur close to the temperature maximum. The computed value of the optical depth was found to be in excellent agreement with measurement performed at low power in the tokamak Tore-Supra [8]. With the frequency of the X2 wave being 82.7 GHz, the third harmonic resonance is located on the low-field side of the second harmonic layer. The two layers are separated by $\Delta r/a = 0.2$ and central heating is thus possible using RF waves at both frequencies. This could be exploited in heating scenarios where firstly a low density plasma is brought to high temperature with the help of the X2 and X3 waves and secondly the density is raised and central heating performed by the X3 wave. In such heated plasma, the absorption is nearly complete (>95% for temperature above 2 keV) even at moderate elongation, $\kappa = 2$, and at density n_{eo} less than 4.3×10^{19} m^{-3} (Fig. 4).

Current drive efficiency at the second harmonic was computed using the codes BANDIT-3D and the package CQL3D and TORAY [9]. Both codes show that with electron temperature about 1.5 keV and at an electron density of 2×10^{19} m^{-3}, one can obtain 0.05 — 0.06 A/W, corresponding to a normalized efficiency $\gamma_{20} = n_{eo,20}\, RI_{CD}/P = 0.05$ A/(Wm^2). With the full available power in X2, it is therefore possible to drive the total plasma current for a circular shape plasma. Note however that at the power level P of 3.0 MW non-linear effects might have an influence on the CD efficiency since the ratio P[W cm^{-3}] / n^2_{13} [10^{13} cm^{-3}]^2 (= 10 — 30 W/cm^{-3}) largely exceeds the threshold (0.5 W/cm^{-3}) for electron tail formation given in Ref. 10. This subject is also discussed in Ref. 11.

$\kappa = 2$

T_eOH $2 \times T_eOH$

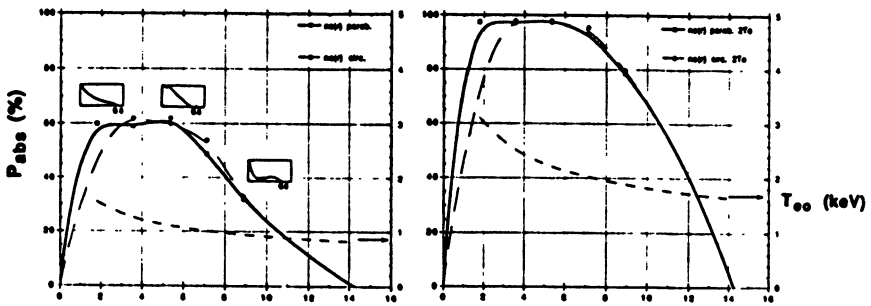

$\kappa = 3$

T_eOH $2 \times T_eOH$

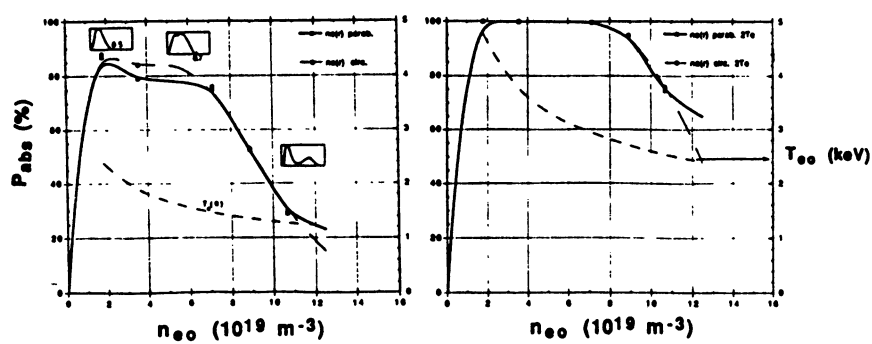

Figure 4

First pass absorption at third harmonic X3 at ohmic temperature (T_eOH ~ 1 keV) and at twice this temperature (2 keV). The dashed line (------) shows the target plasma temperature.

The Electron Cyclotron Wave System

The Electron Cyclotron Wave System (ECWS) [12, 13] is distributed in three clusters delivering 1.5 MW each, two clusters being at 82.7 GHz and the third one at 118 GHz. The system is designed to meet the following physics requirements. For the X2 system the RF beam must be elliptically polarized and be steerable in the poloidal direction (between about -7^{o} and -55^{o} to reach the center of the plasma for all elongations from an upper lateral port) and toroidal direction (in the same range) for current drive. The design beam divergence in the plasma from the launcher is 2^{o} — 3^{o}. For the X3 system, the antenna shoud be movable in the radial direction to adjust the beam location with respect to the resonance layer in the plasma.

An evacuated transmisson line (0.5 MW per line) was chosen because of the requirements caused by the design of windows capable of handling high power in long pulse.

Each cluster of 3 gyrotrons is energized by a single regulated high voltage power supply (RHVPS) delivering 85 kV and 80 A. The RHVPS is a solid state power supply based on the Pulse Step Modulator technology developed and built by Thomcast AG [12, 14].

a) *The X2 system at 82.7 GHz*

The gyrotrons are manufactured by Gycom and deliver 0.5 MW in pulse of 2 s and are described in Ref. 15. They were developed from the existing short pulse (0.5 s) 0.5 MW gyrotrons made by Gycom. The cavity mode is the $TE_{10,\,4}$, which is converted internally into a mode which is compatible with the use of a BN window (Diameter: 104 mm) which is cooled at the edge by water. This mode is then converted to a Gaussian beam matching the input of a 63.5 mm diameter corrugated waveguide. The design beam diameter at 1/e in power is 20.4 mm; the measured values show some asymmetry in the beam shape with two values for the diameter across two perpendicular axis, respectively 22.9 mm and 20.4 mm The matching optics include two focussing mirrors and two flat, corrugated mirrors used as polarizers [16]. The whole optics is enclosed in a vacuum vessel. The stray RF beam is absorbed by plates coated with TiO_2 (Thickness: about 0.3 mm). High power measurements of the Gaussian content η_g of the beam after the matching optics gives a value around 95%. The power measured after two meters of corrugated waveguide is 552 kW for a beam current and voltage

of 70 kV and 22.5 A, respectively.

The schematic of the transmission line is presented in Fig. 5. The typical length of a full line is about 30 m. The main elements are straight sections of Al corrugated waveguides, miter bends with and without power monitor, bellows, DC breaks, pumping Tee, microwave switch and a high power load capable of sustaining 0.5 MW in pulse of 2 s. These components have been designed and manufactured by Spinner Gmbh (Germany) and General Atomic (USA). The computed ratio of transmitted power to input power is 95% The waveguides have lengths up to 2.1 m and are supported at distance about 3 m using simple holders on which the waveguides rest. The alignment was performed using a simple three axis laser device and was referenced to fixed points with respect to the tokamak. The burn patterns obained at the input of the transmission line and at its end are shown in Fig. 6. They are well centered and show no deformation along the line. High power test of the line was performed first with the line under air, then in vacuum. In test under atmosphere, 0.5 MW was transmitted through the whole line during pulse of 0.1 s without any need of conditioning and without arcing. The measured ratio of the input power to the transmitted power is estimated around 93%. The line was then pumped down using a 500 l/s turbo-molecular pump located at the vacuum vessel of the matching optics unit (another turbo-molecular pump is located near the tokamak, downstream from the microwave switch but was not used in this experiment). Typical base pressure is in the range of 4×10^{-5} mbar after one day of pumping. At the time of writing of this paper about 310 kW was transmitted through the line into the load during pulses of 2s. We are presently extending the total energy delivered to the load aiming towards the full specifications, namely 0.5 MW, 2 s. In this process, a conditioning is necessary since the large energy (in the order of 0.6 MJ) absorbed in the load gives rise to a pressure increase in the line ($\Delta p = 10^{-3}$ mbar).

The launcher consists of four mirrors and meets all the physics specifications given above. The mirrors are made out of OFHC copper except for the last one which is TZM. TZM, a Molybdenum alloy, is selected since it has low sputtering and good electrical and thermal properties and is machinable. During a 2 s pulse at 0.5 MW, the temperature increase of the TZM mirror is about 470 ^{o}C, but due to the low duty factor (about 0.3%) the mean temperature is computed to be around 110 ^{o}C with radiative cooling only. The characteristics of the output beam from the launcher were measured at low power and good agreement was found between theory and experiments.

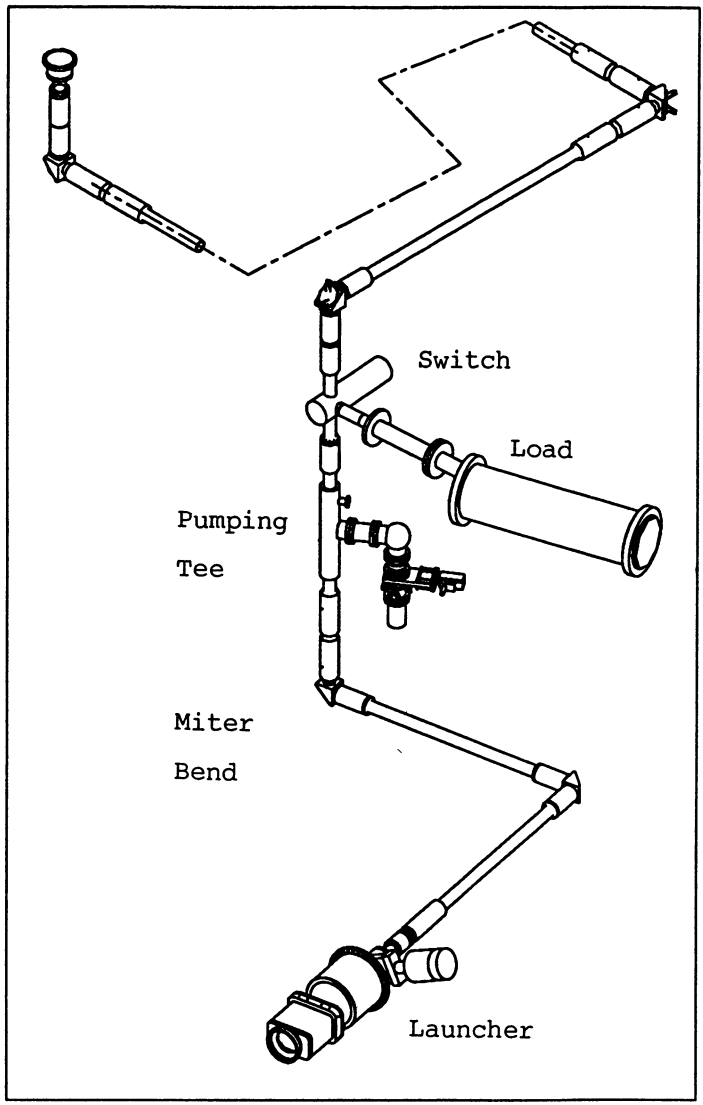

Figure 5

Schematic of the transmission line from the MOU to the launcher at TCV.

(a) at input

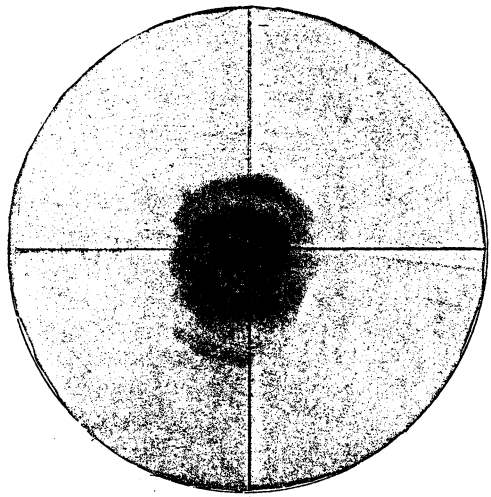

(b) after 20 m

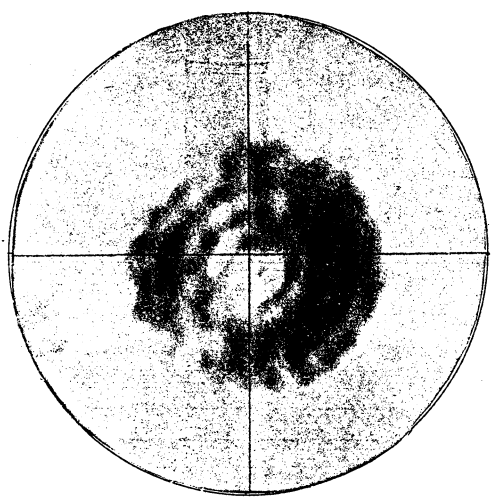

Figures 6 a) and b)

Burn patterns in unevacuated transmission line.

Presently the first cluster is already installed and experiments could be performed as the commissioning of the gyrotrons and the transmission lines progresses.

b) *The X3 system at 118 GHz*

The main element of the X3 system is the 118 GHz gyrotron, for which a development programme is running in collaboration between the Associations CEA-Cadarache (France), CRPP (Switzerland), FZK (Germany) and the industry Thomson Tubes Electroniques (France). The parameters of the 118 GHz gyrotron are given in Table II. This tube will be used for the ECWS of both TCV and the CEA superconducting tokamak Tore-Supra (TS), for which the specification on pulse duration is 210 s.

Frequency	118 GHz
Output power in a HE_{11} waveguide	0.5 MW
Pulse length	2 s (for TCV) 210 s (for TS)
Cathode voltage	80 kV
Modulation anode voltage	30 kV
Electron beam current	22 A

Table II
Characteristics of the 118 GHz gyrotron

A description of the gyrotron design and the status of the high power tests are given in Ref. 17. The main design features of the tubes are: operating mode $TE_{22,6}$, window: sapphire cooled at the edge by liquid Nitrogen [18], pattern at the window: gaussian, spent electron beam swept along the collector. The coupling of the output beam into a corrugated waveguide (diameter: 63.5 mm) is performed via a matching optics consisting of three mirrors, two polarizers and a focussing mirror. We have recently achieved 0.5 MW as measured in a calorimeter after 2 m

of corrugated waveguide in pulses of 2 s. During these tests no attempt was performed to maximize the efficiency. In spite of this, the measured efficiency is about 28%, close to the minimum specified value of 30%. The optimization and characterization of the prototype gyrotron is presently underway and factory acceptance test is foreseen in the very near future.

Conclusion

The main features of the ECRH and ECCD on the tokamak TCV were reviewed. Numerical calculations show that good absorption is achieved at X2 (82.7 GHz) and X3 (118 GHz). The implementation of the ECWS requires the development of long pulse gyrotrons at both 82.7 GHz and at 118 GHz. Of significant importance is the development programme related to the 118 GHz which paves the way to the obtention of CW gyrotron at higher power level. Test on TCV is expected in the next months.

Acknowledgements

The contributions of Drs. A. Kritz (Lehigh University), M. O'Brien (UKAEA), O. Sauter and G. Smith (University of California, Lawrence Livermore National Laboratory) in the ECRH and ECCD calculations are gratefully acknowledged.

The design, fabrication and operation of the ECWS have benefitted form the expert work and assistance of all the engineers and technical teams of the CRPP. The participation of Dr. I. Roy (Kurchatov Institute, Russian Federation) during part of the high power test of the first cluster is gratefully acknowledged. The measurement of the output pattern from the Gycom gyrotron was performed by M. S. Wochner (FZK).

The development of the 118 GHZ gyrotron is performed in the frame of a joint contract between Associations Euratom - CEA Cadarache, Euratom - Confédération Suisse, and the industry Thomson Tubes Electroniques. The project has benefitted from the active contribution of FZK and the contribution of Prof. M. Thumm and M. O. Braz is gratefully acknowledged.

This work is partially supported by the Swiss National Science Foundation.

References

[1] Favre A. et al., to be presented at the 19th Symposium on Fusion Technology, Lisboa, Portugal, Sept. 1996.

[2] Hofmann F. et al., Contributed paper at the 23rd EPS Conf. on Controlled Fusion and Plasma Physics, Kiev, Ukraine, June 1996 (to be published). See also Lausanne Report LRP 550/96.
Hofmann F. et al., Plasma Phys. Control. Fusion, 1995, 36, B277.

[3] Lister J.B. et al., Proceeding of the 15th IAEA Int. Conf. on Plasma Phys. and Contr. Nuclear Fusion Research, Seville, Spain, Sept./Oct. 1994, Vol. 1, 627.

[4] Weisen H. et al., Proc. IAEA Techn. Committee Meeting on H-Mode Physics, Princeton University, Sept. 1995, to be published in "Plasma Physics and Controlled Fusion".

[5] O'Brien M.R. et al., Proc. IAEA Techn. Committee Meeting on Advances in Modelling Plasmas, Montreal, 1992, 527.

[6] Myer M.C. et al., Nucl. Fusion, 1989, 29, 2155.
Yue et al., 10th Topical Conf. on Applications of RF power to Plasmas, Boston, 1993, 273.

[7] Pochelon A. et al., Proceedings of the 20th EPS Conf. on Controlled Fusion and Plasma Physics, Lisboa, Portugal, 1993, Vol. 17c Part III, 1020.

[8] Ségui J. L. et al., Nucl. Fusion, 1996, 36, 237.

[9] Harvey R.W. et al., Proc. IAEA Techn. Committee Meeting on Advances in Modelling Plasmas, Montreal, 1992, also in General Atomic Report GA-A 20978 published in 1992

[10] Harvey R.W., Phys. Rev. Lett. 1989, 62, 426.

[11] Kuyanov A. Yu. et al. Paper H - 17, in Proceedings of this conference.

[12] Fasel D. et al. to be published in the Proceedings of the 19th Symposium on Fusion Technology, Lisboa, Portugal, Sept. 1996.

[13] Goodman T. et al. to be published in the Proceedings of the 19th Symposium on Fusion Technology, Lisboa, Portugal, Sept. 1996.

[14] Besson G. et al. in Proceedings of the 18th Symposium on Fusion Technology, Karlsruhe, Germany (1994), K. Hershbach, W. Maurer and J.E. Vetter editors, North Holland, p. 517.

[15] Bogdanov S.D. et al. Paper S-35, in Proceedings of this conference.

[16] Smits F.M.A. in Proceedings of the 7th Joint Workshop on ECE and ECRH (Hefei, China) 1989.

[17] Pain M. et al. in Proceedings of the 18th Symposium on Fusion Technology, (1994) Karlsruhe, K. Hershbach, W. Maurer and J.E. Vetter editors, North Holland, p. 489.
Giguet E. et al. Conference Digest of the 20th International Conference on Infrared and Millimeter Waves, Lake Buena Vista (Orlando), December 1995, R.J. Temkin editor, 339-340.

[18] Garin P. et al. Conference Digest of the 20th International Conference on Infrared and Millimeter Waves, Lake Buena Vista (Orlanda), December 1995, R.J. Temkin editor, 271-272.

[19] Alberti S. et al., Conference Proceedings of the 21th International Conference on Infrared and Millimeter Waves, Berlin, Germany, July 1996, M. von Ortenberg and H.U. Mueller editors, p. AF1.

STATUS OF LOWER HYBRID HEATING AND CURRENT DRIVE RESEARCH ON TORE SUPRA

D. Moreau

Association Euratom-CEA
Département de Recherches sur la Fusion Contrôlée
Centre d'Etudes de Cadarache
13108 St Paul lez Durance Cedex, France

Abstract

The TORE SUPRA long-pulse lower hybrid (LH) system coupled up to 6.5 MW at 3.7 GHz through two multijunction launchers, and power densities of 24 MW/m^2 were achieved during 75 seconds. Successful experiments on high-power wave coupling at distances up to 15 cm from the plasma have provided new potentialities concerning far-distance coupling in a reactor environment.

In the longest plasma discharge (2 minutes - 3.9 Teslas - 0.8 MA), the total injected LH energy reached a record value of 270 MJ during a 110 s LH pulse, at a power level of 2.5 MW. Thanks to a feedback control of the primary flux, fully non-inductive discharges have been sustained during 70 s (3.9 Teslas - 0.62 MA - 2 x 10^{19} m^{-3}).

These plasmas belong to the so-called "lower hybrid enhanced performance" (LHEP) category in which the (flat or hollow) central current density profile and (peaked) electron temperature profile are fully decoupled. They exhibit a large improvement of the global confinement (60% during 2 minutes) with respect to conventional auxiliary heated plasmas. Heat transport and MHD stability in LHEP plasmas is discussed. Lower hybrid current drive (LHCD) has also been combined with fast wave electron heating experiments. This has produced stationary improved confinement with improvement factors up to 2. With a combined power of 6.3 MW, the LH-driven and bootstrap currents accounted for 70% of the total current.

Progress in the understanding and modelling of LH power deposition profiles are also reported, and possible applications of LHCD in near-term fusion research are mentionned.

1. Introduction

During the last few years, thermonuclear fusion research has made remarkable progress with the observation that transient modifications of the current density profiles could lead to strong improvements in the confinement and stability of large tokamak plasmas [Hugon,

1992 ; JET Team, 1994 ; Levinton, 1995 ; Kimura, 1996 ; Rice, 1996]. Performance is generally measured with respect to empirical scaling laws which have been pushing tokamak reactor designs towards higher and higher dimensions and plasma current operation. Now that significant departures from these scaling laws are commonly being observed, an advanced reactor concept has emerged, with lower plasma current and with a potential for steady-state operation since a large fraction of the total current could be self-generated by the bootstrap effect [Kikuchi, 1990].

Lower hybrid waves have for a long time been recognized as the most efficient means for generating non-inductive currents in moderate temperature plasmas. They are therefore a potential candidate for controlling the current profile in an advanced steady-state reactor, especially in the low-β early phase of the discharge, when most of the current shaping would have to be made to ensure high-Q fusion gain and stability during the burn.

A large part of the TORE SUPRA program is dedicated to long-pulse non-inductive operation with emphasis on current profile control and its effect on plasma confinement and stability both during transients and *in steady-state*. We shall give here an overview of the status of this research and conclude with near-term perspectives regarding the possible use of LH waves in ITER. Reviews of earlier results regarding LH-assisted current ramp-up, sawtooth stabilization, and fast electron transport can be found for example in [Equipe TORE SUPRA, 1995] and references therein.

2. The TORE SUPRA Lower Hybrid System

The 3.7 GHz / 8 MW lower hybrid system installed on TORE SUPRA is made of 16 cw klystron amplifiers delivering up to 500 kW each [Tonon, et al., 1993]. The power is transmitted to the launcher through oversized waveguides over about 20 m with a measured transmission factor reaching 94 %. Transmission lines are terminated by a 3 dB hybrid junction which divides the power delivered by each klystron and allows to power simultaneously an upper and a lower antenna module.

The LH power is coupled to the plasma via two multijunction launchers made of 16 modules (8 juxtaposed in the upper row and 8 in the lower row), and mounted on two adjacent ports of the machine. Each module consists of 2 rows of 4 reduced-size waveguides whose electrical lengths are successively shifted by 90 degrees and whose front end is coated with a thin layer of boron carbide. Spectrum flexibility is obtained by phasing the modules. This allows to launch a travelling wave whose peak refraction index ($n_{//}$) in the direction

parallel to the static magnetic field can be chosen between 1.4 (- 90° phasing) and 2.3 (+ 90° phasing). In each antenna, the number of reduced waveguides facing the plasma is 128 (32 in each row) and therefore the $n_{//}$ spectrum is quite narrow (full width at half maximum $\Delta n_{//} \approx 0.2$).

A maximum power of 6.5 MW has been coupled to the plasma during short pulses and during long-pulse operation, the LH energy injected into the plasma reached a world record value of 270 MJ (about 2.5 MW during 110 s). This corresponds to a moderate steady-state average power density of 15 MW/m^2 on the two launchers. This was not the limiting factor, however, since in other experiments 2 MW were launched during 75 s with only one launcher which then corresponds to 24 MW/m^2 (the power in the second launcher was then reduced to 0.5 MW) [Froissard, *et al.*, 1996 ; Rey, *et al.*, 1996]. The results and limitations of these long-pulse experiments will be discussed in more detail in section 3.

Global reflection coefficients in the range 1-3 % are obtained routinely in a wide range of plasma edge densities for phase shifts between modules ranging from $\delta\phi = - 90°$ to $\delta\phi = + 90°$. The various scattering matrix elements of the multijunction waveguide array have been measured together with the plasma density in front of the launchers (Langmuir probes). When the density at the waveguide apertures is at least around 3 to 4 x 10^{17} m^{-3}, i.e. roughly twice the cutoff density, good coupling is achieved, and the linear theory describes fairly well the observed reflected and cross-coupled signals [Litaudon, *et al.*, 1992]. Such a density readily exists at distances of the order of 1-2 cm from the plasma edge, but in view of reactor applications, experiments on far-distance coupling have been recently performed [Froissard, *et al.*, 1996]. It was found that the LH power produces in front of the launcher a plasma density increment $\Delta n_e \approx 1.5 \pm 0.7$ x 10^{17} m^{-3}/MW, rather independently of the distance to the last closed plasma flux surface and of the pre-existing density at the launcher before the power is applied. This was observed at sufficient power even when the launcher aperture was positioned in the underdense layers (i.e. below cutoff). The overall LHCD efficiency was then independent of the coupling distance. Figure 1 illustrates this phenomenon and shows the clear density increase (from below to slightly above cutoff density) and the concommitant drop in the average reflection coefficients (from nearly 40% to a few percents) when the LH power was raised above 0.5 MW in both launchers at a constant distance of 14 cm from the main plasma. Thanks to this technique, up to 4 MW have been launched while the antennas were 15 cm away from the plasma edge.

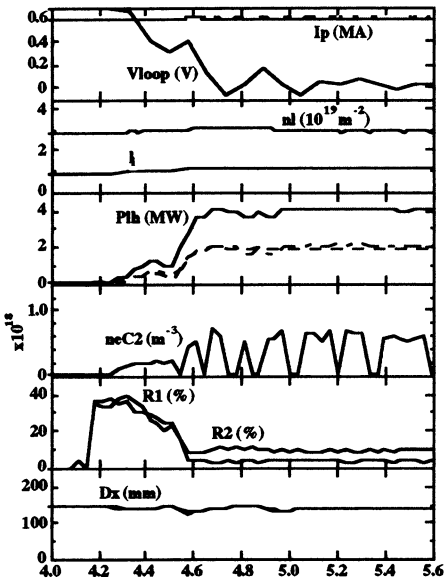

Fig. 1. Time evolution in seconds of the plasma current (Ip), loop voltage (Vloop), line-integrated density (nl) in 10^{19} m^{-2}, internal inductance parameter (li), LH powers in both launchers and total power (Plh), electron density at the launcher apertures (neC2) in 10^{17} m^{-3}, reflection coefficients in both launchers (R1, R2), and distance from the launcher apertures to the last closed plasma flux surface (Dx).

Far-distance coupling can be beneficial in TORE SUPRA to reduce or eliminate some very localized heat loads which have been observed during high power experiments. Power handling and coupling are sometimes affected by the appearance of hot spots on the guard limiters of the antennas or on other plasma facing components which are magnetically connected to the various rows of waveguides composing the launchers. Such hot spots, which were observed mainly at low plasma current, are thought to be due to the acceleration of nearly thermal electrons in the very proximity of the waveguide apertures, up to energies of a few keV [Goniche, *et al.*, 1996]. The numerous high-$n_{//}$ electrostatic components generated by the relatively sharp edges between waveguides and the large oscillating electrostatic fields thus excited could indeed produce stochastic acceleration of electrons from the 100 eV range to several keV, especially when the field lines make a small angle with the waveguide arrays (high-q operation). Suprathermal electrons would therefore stream within very narrow beams originating at mid-height of each row of waveguides, where the HF fields are maximum, and following the magnetic field lines until they encounter some material structure. Such high-$n_{//}$ components exist in both toroidal directions ; they carry very little power (a few %) and should rapidly decay a few millimeters away radially from the antenna precisely because of their resonant interaction with edge electrons. The strong poloidal and radial localizations of the phenomenon would indeed be

consistent with experimental observations not only on TORE SUPRA but also on TdeV [Mailloux, *et al.*, 1996]. More detailed analyses are being pursued both through self-consistent quasi-linear calculations and particle-in-cell simulations [Rantamäki, *et al.*, 1996] to assess its validity and dependence upon plasma edge parameters (temperature, density, safety factor, ...).

3. Long-Pulse TORE SUPRA Operation

With its superconducting toroidal field coils, the TORE SUPRA tokamak has been designed for long-pulse operation and one of the main research program of the Euratom-CEA Association for Fusion is indeed related to the physics and technology aspects of high-power steady-state tokamak operation. During the last 1996 experimental campaign, a record discharge duration of 2 minutes (fig. 2) was achieved in a partially non-inductive regime [Equipe TORE SUPRA, 1996] by combining the LH power drive (which accounted for 90% of the total 0.8 MA current) with a slow consumption, up to its full exhaustion, of the available 15 Wb primary flux (loop voltage of 0.1 V). These long-pulse discharges were performed with deuterium plasmas at volume-averaged densities of 1.2×10^{19} m^{-3} and a toroidal field of 3.9 T. The plasma was maintained against the 12 m^2 water-cooled graphite inner wall. Pre-conditionning of the chamber by boronization and

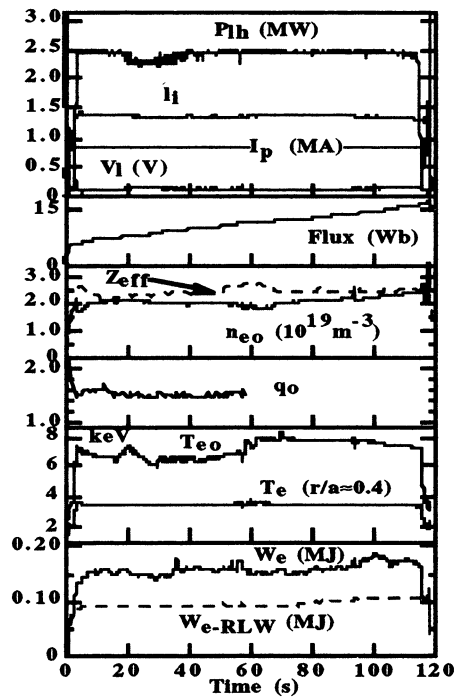

Fig. 2. Two-minute-long LHEP discharge (#19980) : Time evolution in seconds of the LH power (Plh), internal inductance parameter (li), plasma current (Ip), loop voltage (Vl), primary flux consumption, Zeff, central density (neo), central safety factor (qo), central electron temperature (Teo) and temperature at r/a = 0.4, electron energy content (We) and Rebut-Lallia-Watkins prediction (We-RLW).

helium discharge cleaning insures a good pumping capability of the walls, and the plasma density remained nearly constant despite a continuous D_2 gas injection at the rate of 2×10^{20} particles per second.

Present limitations to the long-pulse performance of the machine are sometimes due to the limited primary flux swing, but also to the steady-state power exhaust capability of the plasma facing components for powers above 2.5 MW. Furthermore, various internal parts of the chamber which are not specifically designed to handle large power fluxes are not actively cooled. They may suffer a continuous temperature increase and, during long discharges, this may lead to some uncontrolled outgassing and/or impurity production. In fact, a slight density increase can be seen on fig. 2, starting at 65 s, which can be attributed to such a phenomenon. Z_{eff} is around 2.4 ± 0.3 during the whole discharge and less than 30% of the power input is radiated. The main impurity is carbon, but, simultaneously with the density increase, small amounts of oxygen and silver impurities appear and also increase continuously.

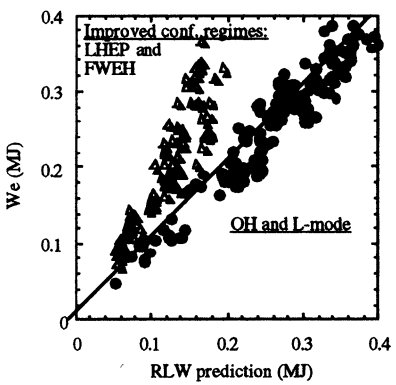

Fig. 3. Electron energy content of various plasma discharges versus RLW prediction. Ohmic and auxiliary heated L-mode plasmas (circles) and improved confinement regimes obtained either by nearly full lower hybrid current drive (LHEP), or by fast wave electron heating (FWEH), or combinations of both (triangles).

To conclude this section, let us note that the global electron energy content of this discharge was enhanced by a factor H_{RLW} = 1.6 as compared with the Rebut-Lallia-Watkins (RLW) prediction [Rebut, *et al.*, 1989]. The RLW global scaling was found to be quite representative of a large variety of TORE SUPRA discharges, from those with ohmic heating only, to those with up to about 8 MW of ion cyclotron and/or lower hybrid additionnal heating [Hoang, *et al.*, 1994]. Electron heated plasmas which significantly depart from this scaling and exhibit an improved confinement are those in which the current density profile is strongly altered in the outer half of the discharge (increase of the magnetic shear), either by transient phenomena (current ramps) or, more interestingly, by an important non-inductive drive which led to

H_{RLW} factors up to 2 (fig. 3). The latter were therefore obtained at low plasma currents by two independent means :

- with nearly full LHCD (the so-called lower hybrid enhanced performance, "LHEP", mode) which tends to produce current density profiles which are steep in the temperature gradient region and flat in the center, with an overall increase of the plasma self-inductance parameter (l_i) but also an increase of the central safety factor (q_0),
- with strong central electron heating by fast magnetosonic waves in the electron Landau damping/transit time magnetic pumping mode [Bécoulet, et al., 1996], which tends to generate large fractions of bootstrap current and significant drops of the loop voltage (fast wave electron heating, "FWEH", mode).

The record two-minute-long discharge was indeed of the LHEP type, with a central electron temperature varying between 6 and 8 keV while the ion central temperature was 1.5 keV. It demonstrates the steady-state potential of this "hot electron" improved confinement mode. Further analyses related to heat transport and MHD stability in the LHEP regime will be developed in section 5.

4. Fully Non-Inductive Operation and Plasma Control

To overcome the pulse length limitations which are due to the primary transformer flux exhaustion, and realize genuine steady-state discharges in a systematic and reproducible way, various modes of operating TORE SUPRA have been studied.

In conventional tokamak operation, the plasma current is controlled and maintained to a reference value through a feedback loop on the external voltage applied on the ohmic primary circuit, V_{oh}. To obtain non-inductive discharges over durations of several minutes the loop voltage must vanish with a fair degree of precision so that no flux is consumed on the average. This would therefore require a prior knowledge of the efficiency of the LH current drive system and of the bootstrap current fraction in the resulting and evolving plasma conditions. To cope with uncertainties on the non-inductive current sources (profile dependences, non-linearities in the driven current and heat transport, ...) one can, in order of increasing complexity :

i) fix V_{oh} and the LH power, P_{lh}, to constant values and let the coupled plasma/poloidal field (PF) system slowly evolve to an equilibrium in which all currents (I_p, I_{oh}) are steady ;

ii) vary V_{oh} such that the primary flux is constant, and let the plasma current float at a value determined by the LH power, the effective current drive efficiency and the bootstrap current ;

iii) simultaneously vary V_{oh} and P_{lh} so as to control the primary flux and the plasma current, respectively, through two independent feedback loops.

These scenarios have been modelled [Kazarian-Vibert, *et al.*, 1996] and new feedback loops have been implemented in the machine operation software for experimental investigations [Wijnands, *et al.*, 1996]. In the first "open loop" scenario (*i*) the time scale required to reach the equilibrium is the longest characteristic time scale of the coupled plasma/PF system, namely about 60 s. Since the plasma parameters keep evolving during this time, this is of little interest for routine operation and plasma physics studies. On the other hand, varying V_{oh} for constant flux operation (*ii*) amounts to adjust the equilibrium current in the ohmic transformer coils in such a way that further evolution towards equilibrium takes place along the eigenmode of the coupled system which has the shortest characteristic time scale since it is precisely the flux-conserving time scale. Internal ohmic current relaxation within the plasma still requires several seconds in this mode. The third mode of operation (*iii*) is even faster since the required LH current is created in situ and almost instantaneously replaces the ohmic current if the feedback gain is large enough. The effective loop voltage inside the plasma then nearly vanishes at the same time as the surface one is kept zero. Resistive diffusion then only has to smooth out second order radial modes in order to adjust the current density profile to the non-inductive one.

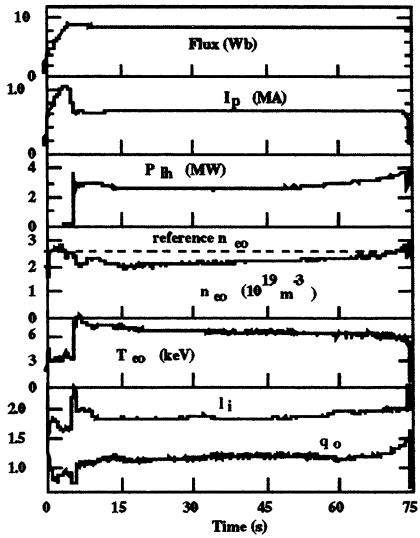

Fig. 4. 70-second-long fully non-inductive LHEP plasma (#19249): Time evolution in seconds of the consumed primary flux, plasma current (Ip), LH power (Plh), central density (neo), central electron temperature (Teo), internal inductance parameter (li), and central safety factor (qo).

Using this last feedback control scenario (*iii*), an MHD-stable fully non-inductive LHEP discharge (H_{RLW} = 1.4) has been sustained at 0.62 MA for 70 s, with a -45° LH antenna phasing ($n_{//o}$ = 1.5) (Fig. 4). The discharge termination was programmed at 75 s and the

total injected energy was 195 MJ. In the initial ohmic phase, the plasma current was first ramped up to a plateau of 1 MA. At t = 5 s, the feedback control was switched to constant flux operation (*ii*) with $P_{lh} = 0$. This led to a rapid decrease of the plasma current at a rate of about 0.5 MA/s. The LH power ($P_{lh} \approx 2.5$ MW) was then applied at t = 5.7 s using the control scheme (*iii*) with proportionnal gains only, and it rapidly stabilized and maintained the plasma current close to the reference value which was set at 0.65 MA. Towards the end of the discharge, the power increased in response to a continuous density increase (cf. section 3). The improved confinement character of such discharges will be discussed in the following sections.

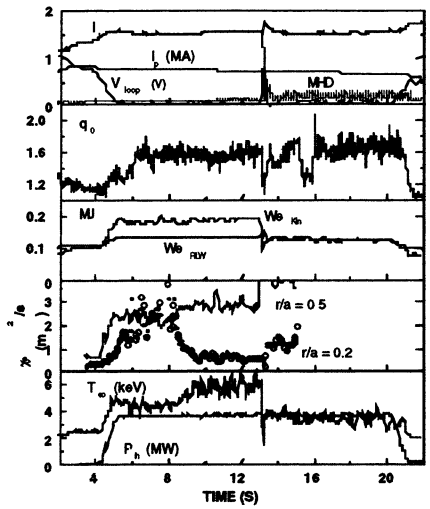

Fig. 5. Fully non-inductive discharge (cf. §4, operation mode *ii*) with 0° LH phasing) showing a transition to a "hot core LHEP phase" and a temperature collapse (#16337). Time evolution of the internal inductance parameter (l_i), plasma current (I_p), loop voltage (V_{loop}), MHD activity signal, central safety factor (q_o), electron energy content (W_{ekin}) and RLW prediction (W_{eRLW}), electron thermal diffusivity at normalized radii r/a = 0.2 and r/a = 0.5, central electron temperature (T_{eo}) and LH power (P_{lh}).

5. LHEP Discharges and Hot Electron Core LHEP Transitions

A stationary improved confinement regime named "LHEP" has been observed when the current density and electron temperature profiles are strongly decoupled [e.g. Equipe Tore Supra, 1995]. This occurs when sufficient LH power drives most of the plasma current non-inductively ($P_{lh} \geq 2.5$ MW for $I_p \leq 0.8$ MA, $n_e(0) \approx 2.5 - 3 \times 10^{19}$ m^{-3}). This regime, which is characterized by current density profiles which differ from those observed during inductive operation, was already defined at the end of section 2 where the global confinement time of the 2-minute pulse was discussed.

One of the most interesting characteristic of this regime is an apparent multi-valuedness of the electron temperature profiles (and hence thermal diffusivity) in the inner part of the plasma. Indeed,

spontaneous transitions to what we now call a "hot core LHEP phase" often occur when the magnetic shear vanishes or is even negative due to the off-axis character of the LH power and current deposition [Litaudon, *et al.*, 1996]. Such an event is seen on fig. 2 at t ≈ 60 s and also more typically on fig. 5 at t ≈ 8 s. It can be reproduced rather reliably during constant flux operation (cf. section 4) when the plasma and LH wave parameters are chosen in the appropriate range. It must be said for clarification that reference to the acronym "LHEP" was originally restricted to this phenomenon [Moreau, *et al.*, 1993] and was later extended in the Tore Supra database to all LH-driven discharges with improved global confinement (cf. fig. 3). In fact the already high global electron energy content of the plasma is hardly enhanced further by these transitions since, up to now, they affect only a small volume in the plasma core. Non-linear couplings between the current density profile, electron heat diffusivity, bootstrap current and LH wave deposition profiles (cf. section 6) are almost certainly responsible for this behaviour.

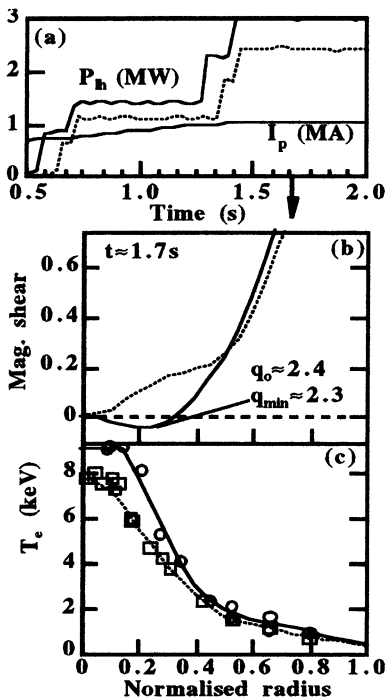

Fig. 6. Comparison of magnetic shear and electron temperature (T_e) profiles at time t = 1.7 s for discharges #19646 (dotted lines) and #19648 (full lines) with the same current ramp and different LH power waveforms (P_{lh}). The central and minimum values of the safety factor (q_o, q_{min}) are indicated for the discharge with negative shear.

The direct link between the reduction of the heat diffusivity and the weak central magnetic shear was recently assessed by specific experiments including various simultaneous power and current ramps in order to modify the transient evolution of the q-profile [Equipe Tore Supra, 1996]. Fig. 6 shows a comparison between two such scenarios in which the LH power differed by only 20% while the electron energy content was following the RLW scaling on one case and was 30% above in the case with slightly negative

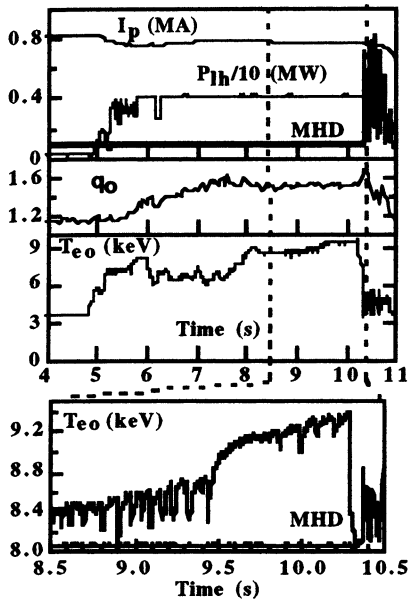

Fig. 7. "Constant-flux" non-inductive discharge (#20035) showing a transition to a "hot core LHEP phase" followed by temperature relaxation oscillations and collapse. Time evolution of the plasma current (I_p), LH power (P_{lh}), MHD activity signal, central safety factor (q_o) and central electron temperature (T_{eo}). The bottom frame shows a zoom between t = 8.5 s and t = 10.5 s.

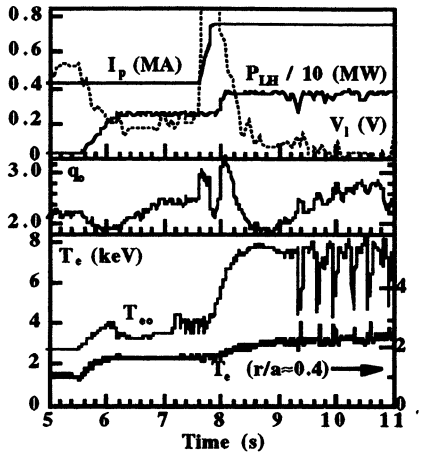

Fig. 8. LHEP phase after a fast current ramp during a heating phase to "freeze" the evolution of the central safety factor (#19649). Time evolution of the plasma current (I_p), LH power (P_{LH}), loop voltage (V_l), central safety factor (q_o), central electron temperature (T_{eo}) and temperature at normalized radius r/a ≈ 0.4 (T_e).

shear. The plasma rotation was measured to be similar in both cases and therefore the negative shear seemed to be the only cause for the large difference in confinement. It was found from the whole set of experiments that the electron diffusivity at r/a ≈ 0.2 continuously decreases when the local shear (s_m) decreases from about 0.15 down to - 0.15, and it reaches neo-classical values for $s_m \approx -0.15$.

MHD stability of the LHEP discharges, especially after several seconds in the hot core phases, is often a problem. The high electron temperature sometimes collapses while low-n modes appear, destroying the good confinement properties of the plasma which returns to the normal L-mode regime. Nice illustrations are shown on fig. 5 and 7. The latter discharge was conducted at constant flux and 4 Teslas and shows a first transition from $T_{e0} \approx 6$ to 8.4 keV at t ≈ 7.5 s. Although $q_0 \approx 1.6$ and is therefore significantly above 1, this phase exhibits "sawtooth-like" temperature relaxations while low amplitude m/n = 2/1 and 3/1 modes are present. After a short (0.4 s) quiescent

phase, the temperature rises above 9 keV and the collapse appears, followed by a steady, MHD-active, degraded phase with sawtooth-like relaxations inverted near the q = 2 surface [Equipe TORE SUPRA, 1996]. In an attempt to eliminate the q = 2 resonant surface, simultaneous power and current ramps (1.2 MA/s) were applied on a 0.4 MA plateau with 2.2 MW of pre-heating LH power with poor directivity (180° phasing), when q_0 was about 2.5 (fig. 8). The LH phasing was switched to - 60° for good current drive efficiency while the power was raised to 3.5 MW and the current to 0.8 MA. This resulted in a fully driven plasma (zero loop voltage) with $T_{e0} \approx 8$ keV and q_0 between 2 and 3, but regular relaxation oscillations were still present, with an even larger amplitude ($\approx$ 4 keV) and an inversion radius at r/a $\approx$ 0.4 where q $\approx$ 3. Further analyses and research will be required to fully understand these phenomena and adequately control the current density profile. Ballooning modes are expected to be stable [Equipe Tore Supra, 1995], but tearing, double tearing or infernal modes can be possible triggers.

Reversed shear LHEP plasmas provide steady-state access to the second ballooning stability regime. They are an ideal target for applying strong central heating power in the ion or electron cyclotron frequency range in the aim of increasing both the normalized beta and the bootstrap current fraction and driving the required seed current to demonstrate steady-state advanced tokamak operation. Recently, LHCD has been combined with fast wave (FW) electron heating. The maximum injected power was 7.2 MW (2 x 3.6 MW). An example is shown on fig. 9 (B_t = 2.8 T, I_p = 0.6 MA, $n_{e0} = 3.9 \times 10^{19} m^{-3}$) in which the confinement improvement factor reached $H_{RLW} \approx 2$ and $\beta_p \approx 0.6$. The LH driven and bootstrap currents were 250 kA and 180 kA, respectively, and accounted for 70% of the total current ($V_{loop} \approx$

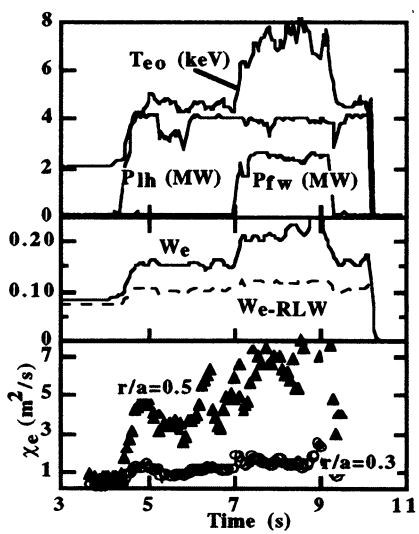

Fig. 9. Combined LHEP/FWEH discharge #19383. Time evolution of the central electron temperature (T_{eo}), lower hybrid and fast wave powers (P_{lh}, P_{fw}), electron energy content (W_e) and RLW prediction (W_{eRLW}), electron thermal diffusivity (χ_e) at normalized radii r/a = 0.5 and r/a = 0.3.

0.14 V). The fact that the heat diffusivity remains small and nearly constant in the central part of the plasma, despite the strongly peaked deposition of the FW power (2.3 MW) is a clear signature of the good confinement in the internal weak shear region.

6. LH Wave Deposition Profiles and Multiple-pass Absorption

Since the early days of LHCD physics research, one has had to cope with the uncertainties inherent to the propagation of the wave along trajectories which are spiralling a long way around the torus before the power is absorbed. The absence of a wave resonance makes it difficult to predict the radial and spectral power deposition profiles. One generally relies on ray-tracing/Fokker-Planck models and careful comparisons of the results with hard X-ray measurements and other experimental data have to be made before assessing the validity of the modelling. Although toroidal couplings seem dominant in modifying the wave spectrum such that strong quasi-linear interaction with the electron population can take place, other effects such as the magnetic field ripple [Peysson, *et al.*, 1996], or density fluctuations [e.g. Baranov, *et al.*, 1996] can alter the predictions.

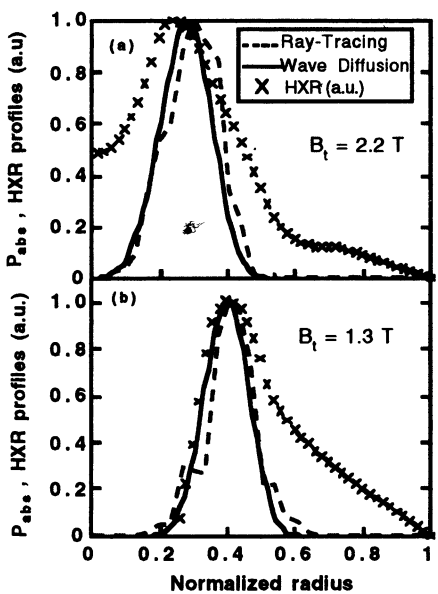

Fig. 10. Comparison of the absorbed power density profiles calculated by the wave diffusion model (full lines) and ray-tracing (dotted lines). Results are shown for two discharges, at 2.2 Teslas (#14386, top) and 1.3 Teslas (#14409, bottom). Abel-inverted hard X-ray emissivity profiles are also shown for 75 keV photons (x).

For usual tokamak aspect-ratios, the orbits of the launched LH rays are chaotic in the Hamiltonian sense, so that, in situations of weak single-pass damping, the wave energy diffuses in phase space within a domain which is determined by the LH dispersion relation. During this process, the well-known spectral gap between the phase velocity of the launched waves and the velocity of maxwellian electrons is nearly always bridged, sometimes at the

expense of finite parasitic edge damping which can reduce the current drive efficiency at low temperatures [Kupfer, *et al.*, 1992]. For the parameter regimes typical of many present day LHCD experiments, including those on TORE SUPRA, part of the power can be absorbed after one or two bounces on the plasma edge cutoff, but often the whole spectrum of waves can be involved in the diffusion process, e.g. in situations when the central hot plasma is hardly accessible to the waves (low magnetic field or high density).

In the former case, the predicted power deposition profiles can be strongly sensitive to all perturbations, and modelling requires that proper account be taken of many different effects such as those mentionned above, and that the excited wavenumber spectrum be divided into a sufficiently large number of rays [Bizarro, *et al.*, 1993]. Although this is rather costly in terms of CPU time, it is often the only way of obtaining predictions which are stable with respect to small variations of the various plasma or wave parameters.

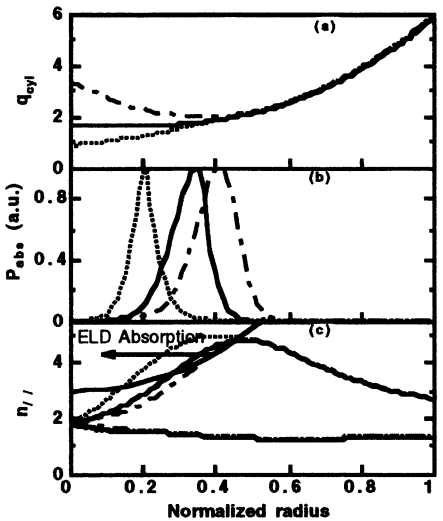

Fig. 11. Wave diffusion/Fokker-Planck calculations for three different q-profiles (a) during an evolution towards reversed shear (pulse #14386). Corresponding absorbed power densities and limits of the wave propagation domains are shown in (b) and (c), respectively. A constant $n_{//}.T_e^{1/2}$ curve (bold) is also shown in (c). The parameters for the calculation are $n_{//o} = 1.8$, $B_t = 2.2$ T, $I_p = 0.4$ MA and $T_{eo} = 3.5$ keV.

The latter case of full multiple-pass damping is simpler in a sense since a statistical description can be made [Moreau, *et al.*, 1989 ; Kupfer, *et al.*, 1993], so that the results are insensitive to small perturbations. The problem amounts to solving two coupled quasilinear equations for the wave energy density and the electron distribution function, and the so-called wave diffusion/Fokker-Planck numerical code (WDFP) has been written for this purpose. Many of the experiments of the LHEP type can indeed be modelled using this theory and in particular those with significant shear reversal for which the wave and plasma parameters

have been carefully selected in order to prevent wave penetration near the core [Litaudon, *et al.*, 1996]. A comparison between WDFP predictions and ray-tracing calculations including a very large number of rays can be seen on fig. 10 for two discharges, and the measured hard X-ray emission profiles are also shown to be quite consistent with the calculated power deposition profiles. Because the wave parallel index is determined from the toroidal (n) and poloidal (m) numbers through the safety factor ($n_{//} \propto n + m/q$), there can be an important non-linear coupling between the q-profile evolution and the power deposition profile when a reversed shear configuration is established. This is illustrated in fig. 11 where one sees clearly that power absorption takes place at the intersection between the domain accessible to wave propagation, which varies with the q-profile, and a curve determined by a local Landau damping condition ($n_{//}.T_e^{1/2}$ = constant). This dependence of the power deposition profile on the q-profile has been verified through the simulation of the time evolution of many LHEP discharges. It was indeed necessary in order to reproduce consistently the transient variations of the measured Faraday rotation angles as well as other magnetic data, and also the resistive relaxation of the ohmic current density profile.

7. Summary of Progress and Future Prospects

We have presented here a brief overview of the main areas of LH research which are being pursued on TORE SUPRA. Encouraging results have been obtained and important progress have been made in many domains, from the technology involved in high-power density HF transmission and coupling to the plasma, to the physics of wave propagation and absorption, current profile modifications and their influence on tokamak transport.

Far-distance coupling seems to be efficient at high power density, which is encouraging for the prospect of applying LHCD to reactor-grade plasmas.

Stationary enhanced plasma performance has been achieved in weak - and/or reversed - shear discharges for up to 2 minutes, and the control of fully non-inductive LHEP plasmas over long durations is now possible. A comprehensive understanding of plasma transport and stability in this regime is still lacking, but further investigations and analyses will surely bring new advances and lead to the implementation of new feedback loops for current profile control.

As far as modelling of the wave power deposition profiles is concerned, recent progress have been decisive for the understanding of TORE SUPRA experiments and the conceptual differences between the extreme régimes of (*i*) strong single-pass damping and (*ii*) full

multiple-pass damping are now well understood and implemented in numerical codes. Some difficulties remain in the intermediate regime where the predictions can be sensitive to small changes in the parameters. Even though present day experiments either fall in this category or in (*ii*), large 10-30 keV plasmas considered in reactor studies are mostly in regime (*i*) so that reliable predictions can be made more easily.

An upgrade of the steady-state power exhaust capability of TORE SUPRA, including the design of a pumped toroidal bottom limiter is under study, and operation at higher density will be necessary to benefit from edge radiation and for particle control purposes. The LH physics program will aim at the demonstration of steady-state operation with intense ICRH/FWEH heating, improved confinement, and high bootstrap current. A major question to be investigated will be the MHD stability and profile control of such plasmas at higher β.

The benefits of using LH waves in ITER are also being investigated through european collaborations [Eur. CCLH, 1994]. With about 50 MW of installed power, such an LH system could serve three functions :

- extend the pulse length in the non-reactive commissioning phase of operations for long-pulse divertor studies,
- avoid the occurence of sawteeth during the first 500 s (or more) of the burn phase in the standard 21 MA scenario by inducing a deep reversed-shear configuration during the current ramp-up, before the α-particle heating "freezes" the profile on a resistive time scale,
- perform and possibly control steady-state "advanced tokamak" discharges with high bootstrap fractions and large scale shear reversal at reduced currents (< 15 MA) so as to study the potentialities of this concept.

For the design of an ITER launcher [Eur. CCLH, 1994, Rey, *et al.*, 1996], a robust, efficiently cooled, and remotely replaceable plasma facing structure has been proposed [Bibet, *et al.*, 1995], in which high individual waveguides (oversized in the poloidal direction) are separated by relatively thick walls which allow for active heat removal and neutron shielding. In order to excite slow waves which can radiate into the plasma, the edge of the thick septa are grooved to form short passive waveguides which act as reflectors of an adequate depth ($\approx \lambda/4$). The result was called a "reflector array" or an "active-passive antenna" because the waves in the reflector (passive) waveguides combine coherently with those in the driver (active) waveguides so as to build up the desired high-directivity wavenumber spectrum. Numerical calculations using the SWAN code show that such a reflector LH antenna should have a coupling efficiency and a

directivity similar to those of present multijunction launchers ($\approx$ 75 %). This concept would have to be tested, possibly on TORE SUPRA, in the near future if it was to be considered for ITER.

Acknowledgements

The results discussed here have been made available by the dedicated work of the whole TORE SUPRA Team and particularly of the LH physics and technology groups. A special contribution by X. Litaudon to the analysis and processing of the data presented in this manuscript is warmly acknowledged.

References

Baranov Y. F., *et al.*, Report JET-P (95) 27 (1995), JET Joint Undertaking, England ; submitted to Nuclear Fusion.

Bécoulet A., *Invited paper at the 23rd Eur. Conf. on Controlled Fusion and Plasma Physics, Kiev (1996)* ; to appear in Plasma Phys. Control. Fusion.

Bibet P., Litaudon X., Moreau D., Nuclear Fusion **35** (1995) 1213.

Bizarro J. P., Moreau D., Phys. Fluids **B 5** (1993) 1227.

Equipe TORE SUPRA, Fusion Engineering and Design, **26** (1995) 29.

Equipe TORE SUPRA, *Invited paper at the 23rd Eur. Conf. on Controlled Fusion and Plasma Physics, Kiev (1996), presented by X. Litaudon* ; to appear in Plasma Phys. Control. Fusion (1997).

European Coordinating Committee on Lower Hybrid Waves, NET Report EUR FU/XII-163/106-94 (1994) ; also Report EUR-CEA-FC-1529, Centre d' Etudes de Cadarache, France (1994) ; and Kaye A. S., *et al.*, Report JET R (94) 07, JET Joint Undertaking, England (1994).

Froissard P., *et al.*, to appear in *Fusion Technology 1996*, Proc. of the 19th Symposium, Lisbon (1996).

Goniche M., *et al.*, in *Proc. of the 23rd Eur. Conf. on Controlled Fusion and Plasma Physics, Kiev (1996).*

Hoang G. T., *et al.*, Nuclear Fusion **34** (1994) 1.

Hugon M., *et al.*, Nuclear Fusion **32** (1992) 33.

JET Team *(presented by F. X. Söldner)*, in *Plasma Physics and Controlled Nuclear Fusion Research 1994 (IAEA, Vienna, 1995)*, Proc. of the 15th International Conference, Seville, Vol. I, p. 423.

Kazarian-Vibert F., *et al.*, Report EUR-CEA-FC-1574, Centre d' Etudes de Cadarache, France ; to appear in Plasma Phys. Control. Fusion (1996).

Kikuchi M., Nuclear Fusion **30** (1990) 265.

Kimura H., *et al.*, Physics of Plasmas, **3**, Part 2 (1996), 1943.

Kupfer K., Moreau D., Nuclear Fusion **32** (1992) 1845.

Kupfer K., Moreau D., Litaudon X., Phys. Fluids **B 5** (1993) 4391.

Levinton F. M., *et al.*, Phys. Rev. Lett. **75** (1995) 4417.

Litaudon X., *et al.*, Nuclear Fusion **32** (1992) 1883.

Litaudon X., *et al.*, Report EUR-CEA-FC-1565, Centre d' Etudes de Cadarache, France ; to appear in Plasma Phys. Control. Fusion (1996).

Mailloux J., *et al.*, in Proc. of the 12th Int. Conf. on Plasma Surface Interaction in Controlled Fusion Devices, St Raphaël, France (1996).

Moreau D., Rax J. M., Samain A., Plasma Phys. Control. Fusion **31** (1989) 1895.

Moreau D., *et al.*, in *Plasma Physics and Controlled Nuclear Fusion Research 1992* (IAEA, Vienna, 1993), Proc. of the 14th Int. Conf., Würzburg, Vol. 1, p. 649.

Peysson Y., *et al.*, Report EUR-CEA-FC-1572, Centre d' Etudes de Cadarache, France ; to appear in Plasma Phys. Control. Fusion (1996).

Rantamäki, K. M., *et al.*, in *Proc. of the 23rd Eur. Conf. on Controlled Fusion and Plasma Physics, Kiev (1996).*

Rebut P. H., Lallia P. P., Watkins M. L., in *Plasma Physics and Controlled Nuclear Fusion Research 1988 (IAEA, Vienna, 1989)*, Proc. of the 12th Int. Conf., Nice, Vol. 2, p. 191.

Rey G., *et al.*, to appear in *Fusion Technology 1996*, Proc. of the 19th Symposium, Lisbon (1996).

Rice B. W., *et al.*, Physics of Plasmas, **3**, Part 2 (1996), 1983.

Tonon G. and Equipe Tore Supra, Plasma Phys. Control. Fusion, Suppl. **A35** (1993) A105.

Wijnands T., Martin G., Report EUR-CEA-FC-1573, Centre d' Etudes de Cadarache, France ; to appear in Nuclear Fusion **36** (1996) issue 9 or 10.

OVERVIEW ON ECRH AND ECCD EXPERIMENTS AT THE W7-AS STELLARATOR

V. Erckmann, H.P. Laqua, H. Maaßberg, M. Romé, W7-AS Team

Max-Planck-Institut für Plasmaphysik, EURATOM Ass.,
D-85748 Garching, Germany

W. Kasparek, G.A. Müller, P.G. Schüller

Institut für Plasmaforschung, Universität Stuttgart, Germany

Borschegovsky, A., V.I.Il'in*, V.I. Malygin***

* Kurchatov Inst., Moscow, Russia, ** IAP, Nizhny Novgorod, Russia

Abstract

ECRH physics experiments at W7-AS are performed with a two frequency system running at 70 GHz and 140 GHz. Three distinct topics are discussed: In the first section we focus on ECR-heating of low density plasmas and the experimental and theoretical investigation of mechanisms, which determine the power deposition profile. In particular the role of trapped particles is investigated.

In the second section we focus on the heating of high density plasmas beyond the limitations given by the cut-off condition for standard heating scenarios. Mode conversion heating via the Ordinary mode-Extraordinary mode-Bernstein mode (O-X-B conversion) is a candidate and was successfully applied. Effective plasma heating was measured in W7-AS far beyond the X2 cut-off density and in the absence of the EC-resonance. The different steps of the mode-conversion were identified.

In the third section we report experimental results on the response of the energy confinement on magnetic shear in the almost shearless vacuum configuration of W7-AS. Stationary profiles of the rotational transform with positive or negative magnetic shear are inferred by inductive and/or EC-driven currents in the direction co-and counter to the confining magnetic field. The role of resonant values of ι under different shear conditions is discussed.

1. Introduction and experimental set up

Net current free plasma build-up and heating is achieved at W7-AS with up to 0.4 MW microwave power at 70 GHz and 0.9 MW at 140 GHz in long pulse operation (< 3 s). The corresponding resonant magnetic induction is 2.5 T, with a cut-off density of $n_{e,crit} = 6.2 \times 10^{19}$ m^{-3} for 1st harmonic O-mode (O1) at 70 GHz and $n_{e,crit} = 1.25 \times 10^{20}$ m^{-3} for 2nd harmonic X-mode (X2) at 140 GHz operation. The 70 GHz System was operated also at 1.25 T (X2) at a reduced cut-off density of $n_{e,crit} = 3.1 \times 10^{19}$ m^{-3}. Two microwave beams at 70 GHz (0.2 MW each) and two beams at 140 GHz (0.45 MW each) are combined at one poloidal plane and each beam can be steered independently by movable launching mirrors inside the vacuum vessel. The beams can be adjusted to toroidal launch angles of up to 40° with respect to perpendicular and poloidal launch angles which provide off-axis heating up to r/a = 0.6. The polarization of each beam can be individually adjusted from O- to X-mode launch. This experimental flexibility together with a high quality of the launched microwave beams is a necessary prerequisite for the investigations presented below. We have operated W7-AS in different magnetic field configurations with different magnetic mirrors to modify the number and drift orbits of trapped particles, which influence the ECRH power deposition. In the same framework we have studied the absorption of O- and X-mode polarized waves which have different absorption properties in phase space.

The experiments on power deposition under various launching conditions and the theoretical modelling are presented in Section 2. Experiments on mode conversion heating with the O-X-B process (Ordinary to Extraordinary to Electron Bernstein Modes) are presented in Section 3. Here we make full use of the capability to launch the waves in a narrow beam with plane phase fronts at high oblique angles. The O-X-B mode conversion process was proposed in 1973 and provides a possibility to operate beyond the density limit for electron cyclotron resonance heating (ECRH). It is shown, that the cut-off restrictions and the restriction given by the resonance condition for EC-wave absorption can be overcome by mode conversion heating. Finally EC-current drive experiments were performed to investigate the effect of shear on the confinement in W7-AS. Some selected experimental results are reported in Section 4.

2. Power Deposition in low density plasmas

The absorption of electromagnetic waves at the ECR-frequencies depends sensitively on the mechanism of the wave-particle interaction.

We have followed two experimental scenarios to investigate the absorption process by i) modification of the wave polarization from O- to X-mode and ii) variation of the fraction of trapped particles.

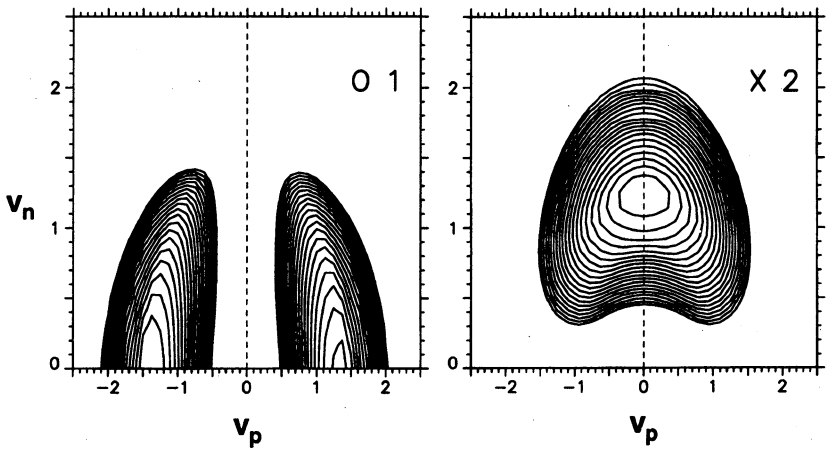

Fig. 1. Level curves of the quasi-linear diffusion coefficient from ray-tracing calculations (averaged within $r \leq 2$ cm). Left: Fundamental O-mode. Right: Second harmonic X-mode.

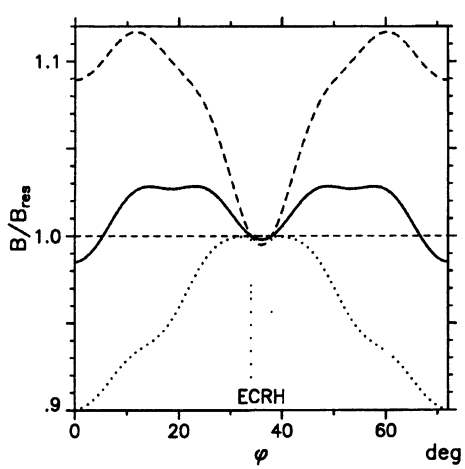

Fig. 2. Magnetic field strength on-axis, normalized to the resonant field at the ECRH launching position, versus the toroidal angle within one field period for $\iota_a \sim 0.345$. The solid line refers to the "standard" configuration of W7-AS, the dashed and the dotted lines correspond to the "minimum B" and the "maximum B" launching scenarios, respectively.

The ECRH is characterized by the quasilinear diffusion coefficient, which has significantly different contours in the velocity space for different heating scenarios (O1 and X2) as seen in Fig. 1. The fraction of trapped particles was changed by changing the toroidal ripple on the magnetic axis in the toroidal position of power launching as seen in Fig. 2. We have restricted the analysis and the experiments to the case of perpendicular, on-axis heating.

2.1 Results of the power deposition analysis

The deposition profile in low density, high temperature plasmas, was derived from the analysis of the electron heat transport in ECRH power modulation experiments, with the time dependent electron temperatures from ECE measurements (see Fig. 3). The ECRH-power was modulated with an amplitude of 10 - 30 % and different frequencies from 0.05 - 5 kHz. This kind of analysis requires a proper modelling of the transport effects in the transient energy balance. The heat transport was described by a purely diffusive model. No evidence for a significant convective contribution was found. Moreover, it has been pointed out that neither a clear dependence of the heat diffusivity on the electron temperature nor on its gradient is indicated [2].

Peaked deposition profiles are usually obtained for both O- and X-mode heating from a 3D Hamiltonian ray-tracing code based on the assumption of a Maxwellian electron distribution function (single pass absorption). From the heat transport analysis of modulation experiments we obtain similarly peaked absorption profiles, but additionally a much broader contribution is present (see Fig. 3), whose width and relative integral contribution with respect to the "thermal" peaked part depends on the particular heating scenario and magnetic configuration. Taking the broader component of the power deposition profile into account, the input power is recovered by the heat transport analysis within the errors, i.e. no indication of "missing power" has been found.

The effect of the magnetic configuration on the electron distribution function in the different heating scenarios being considered, was clearly shown by means of a non-linear 2D bounce-averaged Fokker-Planck (FP) code, which is well suited for the simplified magnetic field geometry close to the magnetic axis of W7-AS [1]. In a heuristic approach, the broadening of the thermal power deposition profile is expected to be related to the radial transport (determined by the ∇B-drift) of the locally trapped suprathermal electrons generated by the ECRH. The particles drift vertically in the

local magnetic ripple, becoming passing particles by pitch angle scattering, and therefore contributing to the energy flux in the outer plasma region without direct ECRH deposition, through thermalization on the flux surfaces.

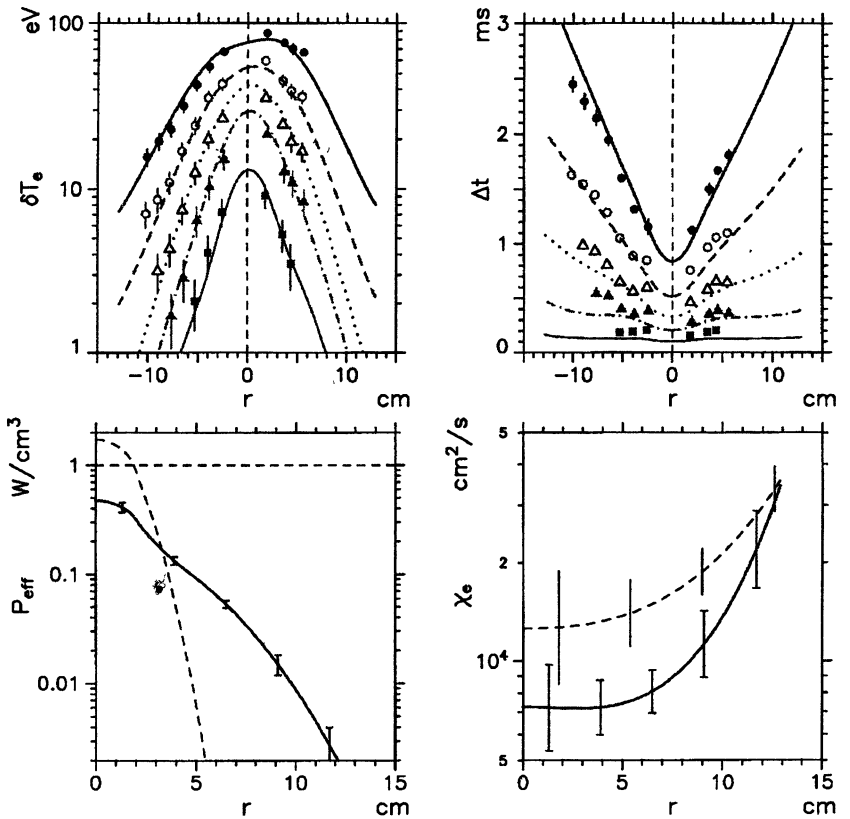

Fig. 3. *The temperature modulation amplitudes, $|\tilde{T}_e|$, and the time delays, Δt, versus radius, r, for different modulation frequencies, f_{mod} = 92, 200, 400, 800 and 2000 Hz (upper left and right plots) from ECRH power modulation experiments at B_0 = 2.5 T (O1-mode, 70 GHz) with on-axis deposition, $n_e \simeq 10^{19}\,m^{-3}$. The power deposition profile (on the lower left) consists of a highly peaked part, corresponding to the "ray-tracing profile" shape (dashed line) and a much broader part. The plot on the right gives the "effective" heat conductivity, $\chi_e(r)$ (solid line). For comparison, the $\chi_e(r)$ profile obtained from the stationary power balance analysis, with the power deposition profile from the ray-tracing calculation is also shown (dashed line).*

The results of the power deposition analysis for scenarios in the "standard" magnetic configuration with B_0 = 2.5 T (see Fig. 2) are summarized in Fig. 4a. The measured power deposition profiles with O1-mode (70 GHz) and X2-mode (140 GHz) are shown for two plasma densities. The power deposition is clearly broadened for the lower density case both for the O1-mode and the X2-mode launch. These findings support the picture of significant heat transport by suprathermal ripple trapped electrons since both the level of the suprathermal tail decreases and the collisional detrapping increases with increasing density. The formation of the suprathermal tail in the ripple trapped electron distribution is expected to be more pronounced for X-mode launch [2] (see Fig. 1), leading to a stronger broadening of the "effective" power deposition profile. For the O-mode scenarios, however, the lower single pass absorption and the effect of wall reflections may lead also to an enhanced broadening of the power deposition profile.

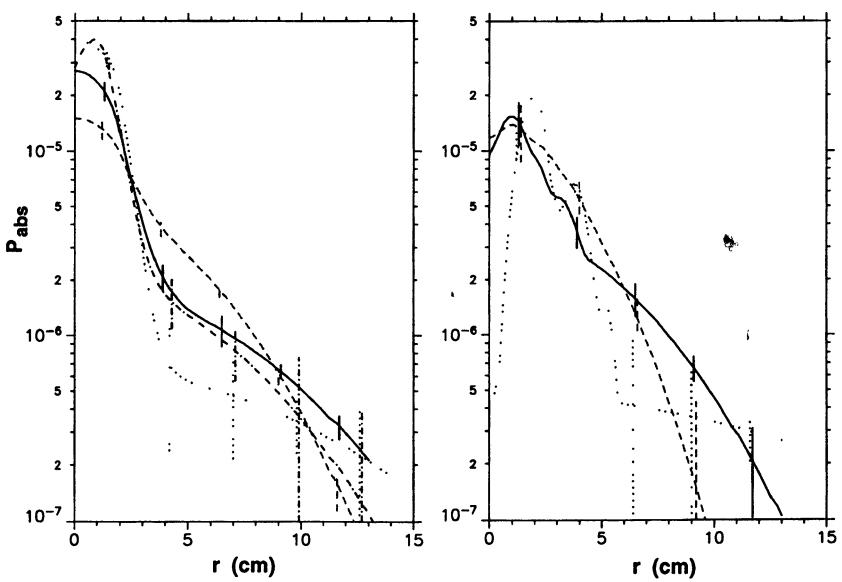

Fig. 4. Power deposition profiles from ECRH power modulation experiments versus the effective radius r. a: B_0 = 2.5 T. The solid and the dashed lines refer to O1-heating (70 GHz), for $n_e = 2 \times 10^{19}$ m^{-3} and $n_e = 10^{19}$ m^{-3}, respectively. The dotted and the dash-dotted lines are the corresponding results for X2-heating (140 GHz). b: B_0 = 1.25 T, and $n_e = 2 \times 10^{19}$ m^{-3}. The solid line refers to the "standard" configuration, the dashed and the dotted lines to the "minimum B" and the "maximum B " magnetic configurations, respectively.

The effect of direct heating of ripple trapped electrons becomes more clear from Fig. 4b, which shows the results of a scan of the toroidal ripple at $B_0 = 1.25$ T with X2-mode launch. In the "standard" configuration, the deposition is broadened as compared to the case of X2 launch (140 GHz) at 2.5 T shown in Fig. 4a, and this effect may be attributed to the stronger ∇B-drift of the trapped electrons. In the "maximum B" scenario, where trapped particles are expected to play a minor role in the power deposition region, the deposition profile derived from the heat wave analysis is fairly close to the ray-tracing results (assuming inherently a Maxwellian distribution), and the broadening of the deposition is of minor importance. For the "minimum B" scenario, a stronger broadening is found. All results on the power deposition are consistent with the heuristic model given above.

2.2 Convective Fokker-Planck model

In order to simulate the broadening of the thermal power deposition profile, a simple FP model has been used, which describes the radial ∇B-drift of the toroidally trapped suprathermal electrons generated by the ECRH. In a first approach, collisional or collisionless detrapping can be treated as a loss term, i.e., the detrapped electrons are assumed to thermalize on the flux surfaces. Taking further trapping of these detrapped particles into account leads to a kind of diffusive modelling (with inward and outward ∇B-drifts). Neglecting this effect gives a convective model and the ECRH driven deviation of the trapped particle distribution from the Maxwellian defines the initial value for this convective FP model. Both an analytical model and the solution of a time-dependent bounce-averaged FP code [1] are used for the initial distribution function. The drift of the suprathermal trapped electrons generated by the ECRH is described by means of the FP equation

$$\langle (v_{\nabla B})_z \rangle_b \frac{\partial f_e^t}{\partial z} = \langle C^{lin} (f_e^t) \rangle_b = C_w(f_e^t) + C_\lambda(f_e^t) \qquad (1)$$

where f_e^t represents the bounce-averaged distribution function of the trapped particles, $v_{\nabla B}$ the drift velocity due to the gradient of the magnetic field, and the angular brackets denote the bounce-averaging procedure, $\langle \ldots \rangle_b \equiv \oint \ldots (ds/v_{||})/\oint (ds/v_{||})$, s being the coordinate along the magnetic field lines.

Stationary conditions are assumed. The presence of a radial electric field is omitted, so that the drift of the toroidally trapped

electrons is mainly in the vertical direction z. The model is thus valid in the central part of the plasma, where the radial electric field is negligible. Note that the experiments were performed with on-axis heating to meet this constraints. The collision operator is linearized by assuming a Maxwellian background which is quite reasonable outside of the ECRH deposition zone. The linearized collision operator, C^{lin}, is written as the sum of a diffusive term in $w \equiv mv^2/2T_e(z=0)$ ($\propto$ energy), and a diffusive term in $\lambda \equiv v_\perp^2 B/v^2 B_0$ ($\propto$ magnetic moment)

$$C_w(f_e^t) =$$

$$= \frac{2\nu_c(z)}{\sqrt{w}} \frac{\partial}{\partial w} \left\{ [2\eta(w_z) - \bar{\eta}(w_z)]\, f_e^t + \frac{T_e(z)}{T_e(0)} \sqrt{w} \frac{\partial}{\partial w} \frac{\eta(w_z)}{\sqrt{w}} f_e^t \right\},$$

$$C_\lambda(f_e^t) = 2\nu_c(z) \frac{\bar{\eta}(w_z) + Z_{eff}}{w^{3/2}} \frac{\partial}{\partial \lambda} \left[\left\langle \frac{1 - \lambda\beta}{\beta} \right\rangle_b \lambda \frac{\partial f_e^t}{\partial \lambda} \right],$$

respectively, with $\beta(s) \equiv B(s)/B_0$.

$$\nu_c(z) = \pi \sqrt{2}\, e^4\, n_e(z)\, \log \Lambda \,/\, m^{1/2}/2\, T_e^{3/2}(0)$$

is the (local) collision frequency, with $\log \Lambda$ the Coulomb logarithm, $w_z = mv^2/2T_e(z)$, and

$$\eta(w_z) = \mathrm{erf}\,(\sqrt{w_z}) - \frac{2}{\sqrt{\pi}} \sqrt{w_z}\, \exp(-w_z),$$

$$\bar{\eta}(w_z) = \mathrm{erf}\,(\sqrt{w_z}) - \frac{\eta(w_z)}{2w_z}\ .$$

Eq. (1) is solved with difference schemes in w and λ (implicit difference formalism in z). The boundary condition $f_e^t(\lambda=\lambda_{lc}) = 0$ is used, where the function $\lambda_{lc}(z) = 1/\beta_M(z)$, represents the width of the trapped particle region, for different vertical positions z, β_M being the maximum value of the normalized magnetic field strength β. The derivative of the distribution function at the loss cone boundary, $\partial f_e^t/\partial\lambda(\lambda=\lambda_{lc})$, measures the collisional loss of the trapped electrons, while the collisionless detrapping is determined by the rate of changing of the function $\lambda_{lc}(z)$.

This model is well suited to describe the effect on the "broadening" of the ECRH power deposition profile of the loss cone size (i.e., the impact of the different magnetic field configurations),

the magnetic field strength ($v_{\nabla B} \propto 1/B$), and the electron density, which enters via the initial value problem as well as via the loss rate due to collisional detrapping (the collisional slowing-down is of minor importance).

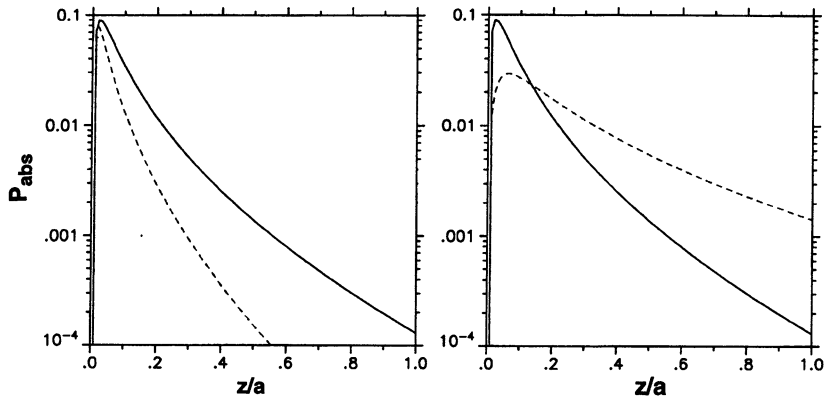

Fig. 5. *Fraction of the absorbed power deposited at the outer radii. a: "Standard " configuration. The solid line is the result for* B_0 *= 1.25 T, and* $n_e = 10^{19}$ m^{-3} *the dashed line for* $B_0 = 2.5$ *T and* $n_e = 10^{19}$ m^{-3} *and the dotted line for* $B_0 = 2.5$ *T and* $n_e = 2 \times 10^{19}$ m^{-3}. *b:* $B_0 = 1.25$ *T and* $n_e = 10^{19}$ m^{-3}. *The solid and the dashed lines are the results for the "standard" configuration and the "minimum B" scenario, respectively.*

2.3 Simulations of the experiments

In the computations for W7-AS scenarios, the loss-cone width λ_{lc} has been assumed constant. Fig. 5a shows the power, normalized to the initial absorbed power, which is deposited at outer radii, in dependence of various parameters. The results are relevant to the "standard" configuration ($\lambda_{lc} \approx 0.97$). The behaviour can be simply explained by the dependence of the ratio between the drift time, τ_D, and the collision time, $\tau_c = 1/\nu_c$ on the magnetic field strength and plasma parameters

$$\tau_D/\tau_c \propto n_e B_0 / T_e^{5/2} w^{5/2} \quad , \qquad (2)$$

having neglected the variations with z of temperature and density, and the weak dependence of the Coulomb logarithm on the electron density. The broadening of the power deposition turns out to be larger in the case of low density and high temperature, and for decreasing magnetic field strength. Moreover, from Eq. (2) it results

that the power deposition profile has a very strong dependence on the energy localization of the initial suprathermal trapped particles distribution function. The higher the velocity, where the EC resonance region is localized, the bigger is the effect of broadening of the power deposition profile.

The "standard" configuration ($\lambda_{lc} \approx 0.97$) and the "minimum B" cases ($\lambda_{lc} \approx 0.90$), are compared in Fig. 5b. For increasing loss cone width, the power is deposited on a broader radial range, and the particles could even be lost at the plasma boundary, before being thermalized. In the opposite limit of a narrow loss cone, the particles are detrapped by the pitch-angle scattering in a very short time, and in our model contribute to the power deposition only in a narrow region close to the axis. The theoretical predictions of this simplified model for the broadening of the power deposition profile, in particular its dependence on the plasma parameters and the magnetic field strength, are therefore consistent with the experimental findings.

3. Mode conversion heating via the O-X-B Process

The commonly used ECRH scenarios provide a good single pass absorption and are 1st harmonic O- or X-mode and 2nd harmonic X-mode launch. These scenarios have intrinsic density limitations by the cut-off condition, which is, e.g. for the 140 GHz system in X2-mode, given by 1.2×10^{20} m^{-3}. In view of reactor relevant conditions it may be desirable to have ECRH-access to even higher densities. This is provided by O2-mode launch, which has a weak absorption at W7-AS parameters, but is a promising candidate at W7-X [4]. Another candidate is the O-X-B mode conversion process [5] as a possibility to overcome the density limitations. Here O, X, and B are the ordinary, extraordinary and Electron-Bernstein-Mode. The essential part of this scheme is the conversion of the O-wave launched by an antenna from the low field side into an X-wave at the O-wave cut-off layer. This mode conversion requires an oblique O-wave launch near an optimal angle.

As shown in Fig. 6 the transverse refractive indices N_x of the O-wave and X-wave are connected at the optimal launch angle with a corresponding longitudinal (parallel B) index $N_{z,opt} = \sqrt{Y/(Y+1)}$ with $Y = w_{ce}/w$ (w is the wave frequency, w_{ce} is the electron cyclotron frequency) without passing a region of evanescence ($N_x^2 < 0$). For non-optimal launch an evanescent region always exists near the cut-off surface whose geometrical size depends on the density scale length $L = n_e/(dn_e/dx)$. A considerable fraction of the energy flux, however, can be transmitted through this region, if L becomes small [6].

Density fluctuations generally lead to a reduced O-X conversion efficiency and are taken into account in the modelling. A significant heating efficiency is obtained only at a very small density scale length (i.e. steep gradients) or a very low fluctuation amplitude. After the O-X-conversion the X-wave propagates back to the upper hybrid resonance (UHR) layer where the refractive index of the X-wave is connected to that of the electron Bernstein waves (EBW) as shown in Fig. 6 and conversion into EBW's may take place. The EBW's propagate then towards the plasma centre where they are absorbed near the electron cyclotron resonance layer or in the nonresonant case by collisional multiple pass damping.

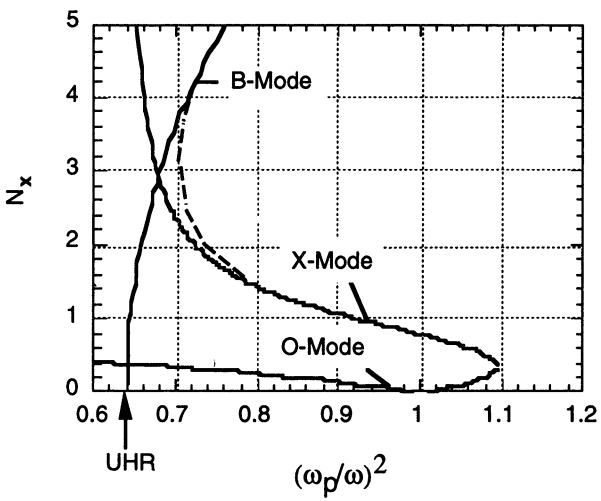

Fig. 6: *Refractive index N_x versus $(\omega_p/\omega)^2$ for the O-X-B conversion process at optimum launch angle.*

The experiments were performed with two 70 GHz beams launched into a neutral beam (NBI) sustained target plasma at resonant (1.25 T) and nonresonant (1.75 T, 2.0 T) magnetic fields. The launch angle of the incident O-mode polarised wave was varied at fixed heating power (220 kW). An example of the nonresonant case is shown in Fig. 7. Due to technical limitations of the maximum launch angle, only the left part of the reduced transmission function could be proved experimentally. The increase of the total stored plasma energy (from the diamagnetic signal) depends strongly on the launch angle, which is typical for the O-X-conversion process, and fits well to the calculation. Here the power transmission function was normalised to the maximum energy increase. The central density was 1.5×10^{20} m^{-3},

which is more than twice the cut-off density for 70 GHz, the central electron temperature was 500 eV. Resonant heating at the plasma edge could be excluded since for 1.75 T no electron cyclotron resonance exists inside the plasma.

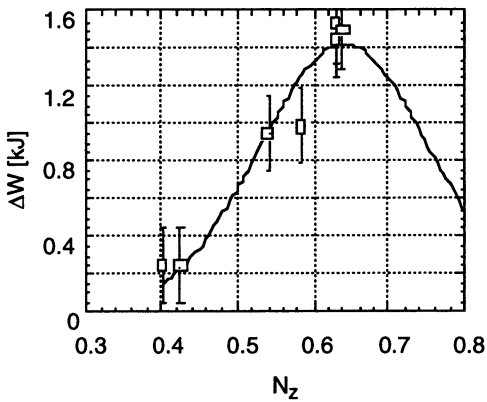

Fig. 7: Measured plasma energy increase by O-X-B heating versus the parallel refractive index N_z of the launched O-mode for nonresonant conditions (B_0 = 1.75 T).

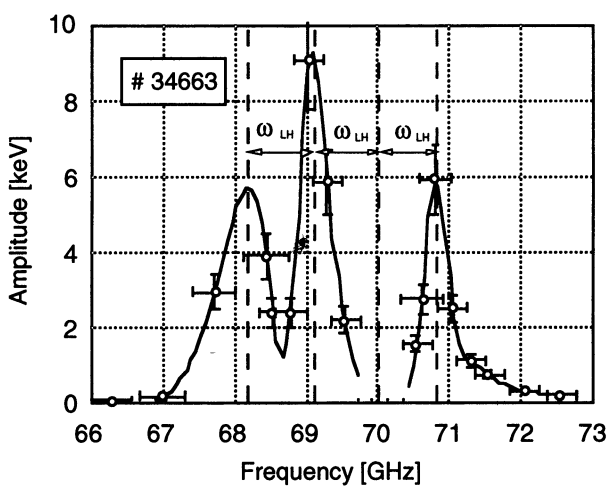

Fig. 8: High frequency spectrum of the parametric decay waves generated in the X-B-process. The incident wave frequency is 70 GHz and the LH frequency is about 900 MHz. The spectrum is measured with the ECE receiver.

In the X-B-conversion process near the UHR parametric instabilities are expected, which allow to identify the X-B process. Decay waves are generated with frequencies of the incident pump wave ω plus and minus the harmonics of the lower hybrid frequency ω_{LH} and the low frequency lower hybrid (LH) wave itself. With the electron cyclotron emission (ECE) receiver a spectrum of the decay waves with maxima at $\omega \pm n\omega_{LH}$ was measured for a resonant magnetic field of 1.25 T and is shown in Fig. 8.

The pump wave is suppressed and the ECE-spectrum is clearly nonthermal since the density was twice the 70 GHz cut-off density. The low frequency LH-wave itself could be detected with a broad band loop antenna and is shown in Fig. 9. A high degree of correlation between the high frequency decay waves and LH-wave was measured.

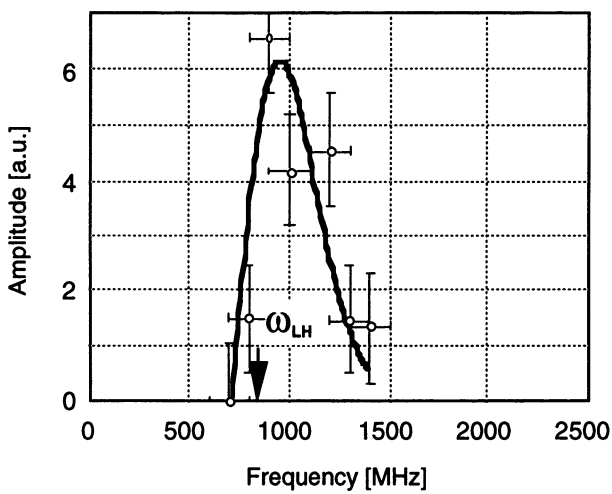

Fig. 9: Low frequency spectrum of the lower hybrid decay wave as measured with a loop antenna.

EBW's experience a cut-off layer at the upper hybrid resonance (UHR) surface (see Fig. 1), which in the nonresonant or higher harmonic ($n > 1$) field totally encloses the inner plasma. The radiation is then trapped inside the plasma and can escape only in the small angular window for O-X- and X-O-conversion, respectively. In the absence of an electron cyclotron resonance in the plasma the EBW's may be absorbed due to finite plasma conductivity after some reflections at the UHR-layer. In both the resonant (1.25 T) and nonresonant cases (2.0 T) efficient heating was observed. Two 70 GHz beams in O-mode polarisation (110 kW power each) were

launched with an oblique angle of 40° into a NBI (700 kW) sustained target plasma with a central density of 1.6×10^{20} m^{-3} and temperature of 560 eV. More than 70 % of the heating power was found in the plasma taking into account the power scaling of the energy confinement time ($P^{-0.6}$).

4. Confinement and shear

The confining magnetic field in the W7-AS Stellarator is generated by a modular set of external coils with a 'built in' flat profile of the rotational transform, ι. The shear, d ln ι/d ln r is weakly positive (up to + 2 %) above $\iota = 0.4$ and weakly negative below (up to - 2%). Low order rational values of ι can thus be excluded from the confinement region by a proper choice of ι. A wide range of $0.25 < \iota < 0.65$ is accessible by additive or subtractive superposition of a purely toroidal magnetic field to the modular magnetic field which has a built-in rotational transform of 0.4. The global confinement depends sensitively on ι and exhibits excursions of about 30 % with maxima in the close vicinity of the low-order rationals ι = 1/2, 1/3...[1,2]. The total stored energy from the diamagnetic signal is shown in Fig. 10 as a function of the edge value of ι(a) for ECR heated plasmas with low β and zero net current.

Under such conditions one may expect to operate close to the vacuum field conditions. The low shear configuration of the vacuum magnetic field is, however, modified by the pressure driven bootstrap current and Pfirsch-Schlüter (PS) currents under finite-β conditions [8]. By far most of the W7-AS data are obtained under net current free plasma operation, where the edge ι is feedback controlled by compensating the bootstrap current with small inductive currents (OH transformer). It should be noted, that although the plasma net current is zero, the internal plasma currents do not cancel locally and thus modify the internal profile of the rotational transform. This is quite obvious for cases where the bootstrap current, which is peaked in the pressure gradient region, is compensated by an inductive current, which is peaked on the plasma axis where the electron temperature is highest. An elegant tool to provide externally-controlled plasma currents is Electron Cyclotron Current Drive (ECCD), because the radial location of the driven current profile can be controlled by tuning the resonance layer or steering of the microwave beams. The EC-driven current is decoupled from the plasma conductivity profile even under steady state conditions in contrast to the inductive current. The magnitude of the EC-driven current is controlled by the launch angle of the incident microwave beam [9,10]. The experiments

reported here are performed with an edge rotational transform around $\iota(a) = 0.34$ in an optimum confinement regime at $B_0 = 2.5$ T (140 GHz, X2) in a wide range of densities from $n_{e0} = 0.17 \times 10^{20}$ m^{-3}) up to $n_{e0} = 0.75 \times 10^{20}$ m^{-3}. Note that the current drive efficiency scales like T_e/n_e. With increasing density both the EC-driven current as well as the bootstrap current become smaller, whereas the PS currents become more important. In the experiments reported here the plasma net current was feedback controlled ($I_p = 0 \pm 200$ A) by compensating both the bootstrap current and the EC driven current component with an inductively driven current.

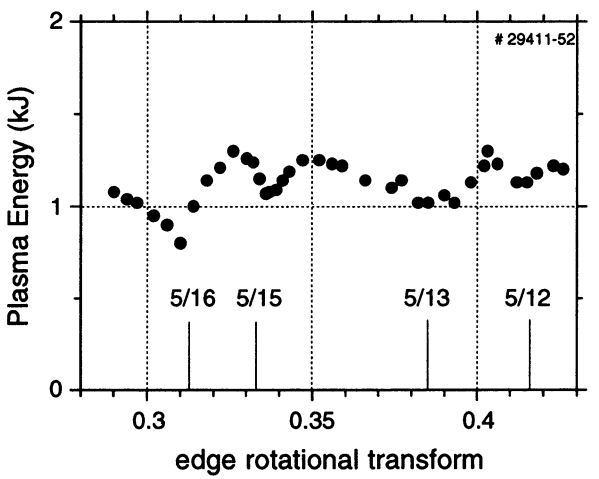

Fig. 10: *Total stored plasma energy as a function of the edge rotational transform for low-β plasmas in W7-AS. The density is 0.2 $\times$ 10^{20} m^{-3}, the ECRH power is 0.2 MW, the plasma net current is zero. Some rational values of ι are indicated.*

The modelling of the radial plasma current distribution, which defines the profile of the rotational transform, is based on the assumption of a linear superposition of the different current contributions. The bootstrap current is calculated by the DKES code [11] and the inductively driven current is calculated assuming neoclassical conductivity, both current components are calculated for each discharge based on the measured profiles of temperature and density. The EC- driven current is calculated in the framework of the linear theory [12] within the 'adjoint approach' [13] taking into account the measured profiles of n_e and T_e and trapped particle effects with a 3D Hamiltonian ray tracing code. The modelling of the

different current contributions was investigated in specially tailored experiments [e.g. 9,10] with respect to magnitude, radial distribution and plasma parameter dependence. Because the internal current density distributions cannot be measured with a sufficient accuracy, the comparison of modelling and experiment is done by the current balance. The balance of theoretically predicted currents is in reasonable agreement with the measured net currents. The basic features of the ι-profile are, however, insensitive to the uncertainties in the modelling of the different current contributions.

Inductive compensation of both the EC-driven current and the bootstrap current allows an easy control of the edge value of ι. It should be noted that the modification of the ι-profile by finite pressure effects (diamagnetic currents and PS-currents) needs to be included in the analysis and becomes important already at moderate β-values (about 0.5 %). In general, with increasing ß the ι-value increases in the plasma centre and decreases in the outer plasma region as compared to the vacuum case [8]. Typical profiles from net-current-free discharges with 0.4 MW ECRH power at 140 GHz (B_0 = 2.5 T, X2) at high ($n_{e0} = 0.75 \times 10^{20}$ m^{-3}) and low density ($n_{e0} = 0.17 \times 10^{20}$ m^{-3}) with β on axis of 0.6 and 0.3, respectively, are shown in Fig. 11.

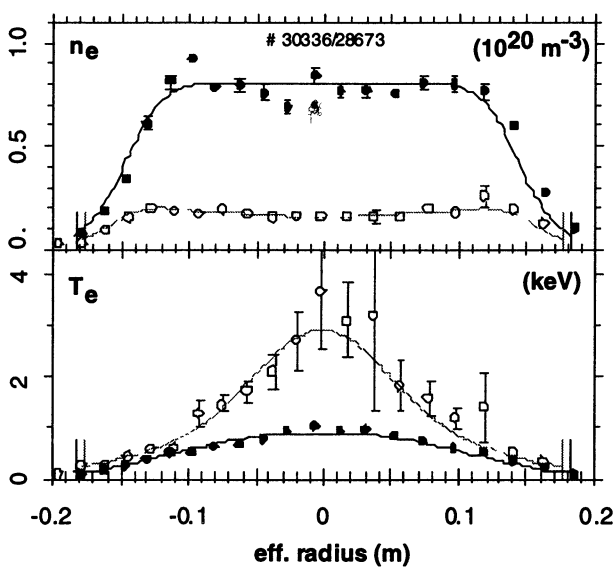

Fig. 11: Radial profiles of n_e and T_e from Thomson scattering for ECR-heated discharges with 0.4 MW input power at high and low density.

For both types of discharges a launch angle scan, i.e. a scan of the EC-driven current, was performed to modify the balance between the contributing internal plasma currents while maintaining zero net current. Fig 12 shows the calculated EC-driven current and the total stored plasma energy as a function of the launch angle for both types of discharges.

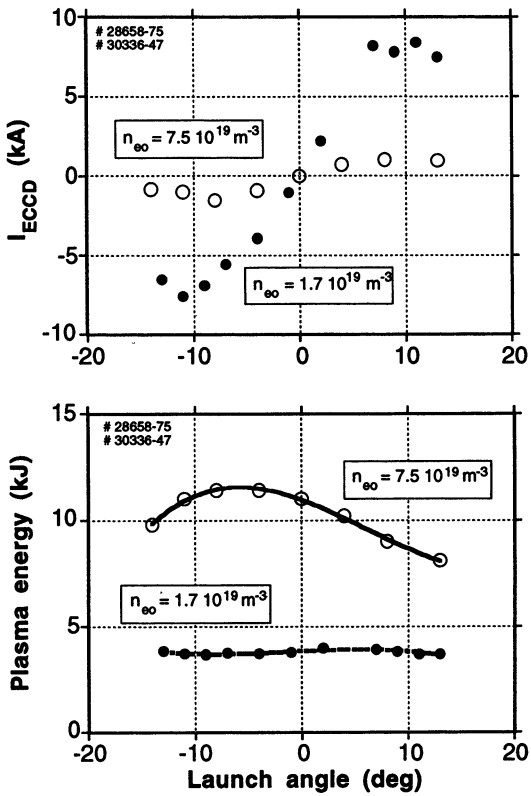

Fig. 12: Calculated EC-driven current (top) and total stored plasma energy (bottom) vs. the toroidal launch angle of the microwave beam for low and high plasma density.

The total stored energy and thus the global confinement changes from 11.5 kJ at full counter current drive to about 8 kJ at full co-current drive in the high density case. Note, that the bootstrap current is compensated by the inductive current alone at perpendicular launch (no ECCD). The increase of the stored energy is due to a steepening of both the density and electron temperature gradients. The density

profiles are typically flat in the centre and thus the gradient region is localized close to the plasma edge (see Fig. 11). In the low density case a much smaller (7 %) but reproducible dependence of the stored plasma energy on the EC-driven current is observed, which points into the opposite direction, i.e. slightly better confinement at co-CD as compared to counter-CD. Whereas, in the high density case, the edge value ι(a) is somewhat below 1/3 due to the finite β effect, it was set to 0.345, slightly above 1/3 in the low density case. As a consequence, the resonance is crossed under counter-CD conditions in the low density case and at co-CD conditions in the high density case, which supports the hypothesis of confinement degradation due to rational values of ι. Both the bootstrap and EC driven currents are of comparable magnitude and much larger in the low density case (about 6-8 kA) than in the high density case (about 2-3 kA). Thus higher shear is introduced in the low density case, which reduces the degradation due to rationals (stabilization of resonant modes or reduction of island width). The calculated ι-profiles in the high density discharges for three cases with co, counter and no ECCD are shown in Fig. 13. In contrast to the corresponding low density discharge, the resonant ι = 1/3 is met with weak shear in the co-CD case giving rise to a flattening of the stationary temperature profile. In the case of no ECCD, ι is almost constant over the minor radius and low order rational values of ι are avoided. In this sense this discharge represents an ideal example for the shearless stellarator. Good confinement is achieved under this condition (see Fig. 12, launch angle 0°), however, the discharge is difficult to control and sensitive to

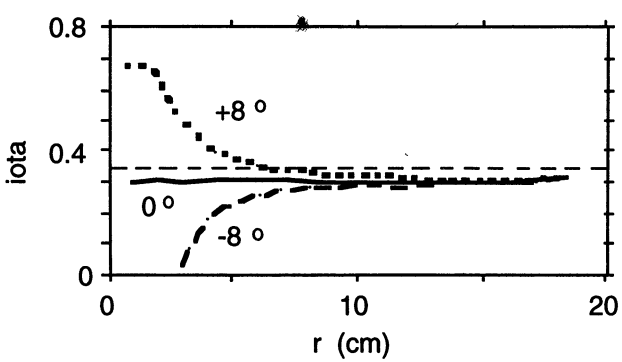

Fig. 13: *Radial profiles of ι for the high density case of Fig. 11 at maximum co-CD (launch angle +8°), no CD (launch angle 0°) and maximum counter-CD (launch angle -8°).*

minor changes of the discharge parameters. For counter-CD a more robust situation is achieved, but it has to be accepted, that the natural resonance at $\iota = 5/16$ with its influence on the confinement (see Fig. 10) appears at the plasma periphery.

5. Conclusions

The deposition profile of ECRH in low density, high temperature plasmas is affected by the wave interaction with trapped particles. The measured profiles consist of a very narrow peaked component, which contains the main power fraction (70 - 100 %) and is consistent with the ray-tracing results. This part is attributed to absorption by the thermal bulk of the electron distribution function. A second component contains up to 30 % of the total power and is much broader. This part is strongly influenced by the number and distribution of trapped particles as derived from experiments with different magnetic mirror configurations, density and magnetic field strenght. Theoretical modelling of the experiments with a bounce averaged FP-code have verified, that the measured broadening of the deposition profile is attributed to the fast transport via the drift orbits of trapped electrons in the long mean free path regime. It is worth noting, that taking into account this effect results in a full power accountability of the launched power.

Mode conversion heating via the Ordinary- to Extraordinary to Electron Bernstein Modes (O-X-B) was investigated experimentally. This heating scheme extends the ECRH application towards high densities, because it inherently works only at densities beyond the cut-off density of the O-mode. Efficient O-X-B heating was clearly demonstrated for the first time for resonant and nonresonant fields at W7-AS. Both, the angular dependence of the O-X-conversion and the parametric instability which is typical for X-B-conversion could be experimentally verified. The efficiency of the process is determined by the density gradient scale length as well as density fluctuations at the O-X-conversion layer. The steep density gradients, which are typical for W7-AS are favourable. By a rough estimate assuming a confinement time scaling like $P^{-0.6}$ we obtained 70 % heating efficiency under optimized conditions.

Electron cyclotron current drive together with inductive current drive was used to control the local current densities and to modify the rotational transform profile. The influence of rational numbers of ι on the energy confinement was investigated under different shear conditions. It is shown that low order rational values in the ι-profile affect the confinement properties as indicated by a flattening in the

stationary electron temperature profiles. Nearly shearless operation with optimum confinement was shown at high densities, if major resonances are avoided in the rotational transform. In cases, where the $\iota = 1/3$ resonance is inferred with small shear, a confinement degradation of about 30 % occurs. Plasma bifurcation was observed under weak shear conditions in the neighbourhood of low order resonant ι-values. With strong shear, however, this effect is much less pronounced. The measured behaviour supports the strategy of advanced stellarators with intermediate shear, where the internal currents (PS and bootstrap) are minimized and the ι-profile remains almost unchanged even at high β.

References

[1] N. Marushchenko et al, Proc. of the 23rd EPS Conference on Controlled Fusion and Plasma Physics, Kiev (1996), in press

[2] M. Romé et al, Plasma Phys. Control. Fusion, in press

[3] A.S. Sakharov and M.A. Tereshchenko, Plasma Phys. Rep. 21, 93 (1995)

[5] J.Preinhaelter and V.Kopecký, J. Plasma Phys. 10 (1973) 1;

[6] E.Mjølhus, J. Plasma Phys. 31 (1984) 7;

[7] H.P. Laqua et al, Proc. of the 23rd EPS Conference on Controlled Fusion and Plasma Physics, Kiev (1996), in press

[8] Renner, H, Ringler, H., Kisslinger, J., Kühner, G., W7-AS Team, NBI-Group, ECRH Group, Intern. Conf. on Plasma Physics, Vol. 16C, Part 1, (1992) 501

[9] Erckmann, V., Gasparino, U., Maassberg, H., Renner, H., et al., Plasma Physics and Controlled Nuclear Fusion Research, (Proc. 13th Conf., Washington) Vol. 2 (1990) 555

[10] V. Erckmann, U. Gasparino, Plasma Phys. Control. Fusion 36 (1994) 1869

[11] S.P. Hirshman and W.I. van Rij, Phys. Fluids B1, (1989) 563

[12] Fisch, N.J., Boozer, A.H., Phys. Rev. Lett. 45 (1980) 720

[13] Anthonsen, T.M., Chu, K.R., Phys. Fluids 25 (1982) 1295

SECOND HARMONIC ECH EXPERIMENT ON HELIOTRON-E

K. Nagasaki, S. Kobayashi, K. Sakamoto, F. Sano, T. Mizuuchi, H. Okada, K. Kondo[A], H. Zushi[A], S. Besshou[A], Y. Kurimoto[B], H. Funaba[B], T. Obiki, A. Ejiri[C], K. Ohkubo[C], M. Kawaguchi[D], G. Denisov[E], A. Goldenberg[E], V. Kurbatov[E], V. Orlov[E], D. Vinogradov[E]

Institute of Advanced Energy, Kyoto University, Uji, Kyoto 611, Japan

A. Faculty of Energy Science, Kyoto University, Uji, Kyoto 611, Japan

B. Faculty of Engineering, Kyoto University, Uji, Kyoto 611, Japan

C. National Institute for Fusion Science, Nagoya 464-01, Japan

D. The Furukawa Electric, Ltd., Hiratsuka, Kanagawa 254, Japan

E. Institute of Applied Physics, Nizhny Novgorod, Russia

Abstract

A new 106.4GHz electron cyclotron resonance heating (ECH) system has been installed and operated for second harmonic extraordinary-mode plasma heating in the Heliotron-E helical device. The waveguide transmission line is effective for high power and high frequency ECH as well as the quasi-optics transmission line. Plasma experiments using this 106.4GHz ECH showed that the accessible electron density was doubled, and plasma parameters such as electron temperature and energy confinement time were improved. Focused Gaussian beam and good single pass absorption allow us to study the plasma response to the change in the power deposition profile and the effect of magnetic shear on the wave propagation. Plasma production is also discussed in terms of the difference between fundamental and second harmonic ECH breakdowns.

1. Introduction

Electron cyclotron resonance heating (ECH) has been applied in many magnetic confinement fusion devices for the purpose of direct electron heating, current drive, plasma start-up, plasma profile control and transport study. Past works on experiments and theory of ECH and ECCD are reviewed in several papers [1-3]. In helical systems, particularly, ECH has been an essential tool for producing high electron temperature plasmas. In the Heliotron-E device which belongs to heliotron/torsatron configurations (H/T), we have been conducting fundamental and second harmonic plasma heating experiments using 28GHz, 35GHz and 53.2GHz ECH. Energy and particle confinement of ECH plasmas and ECH effects on the ion confinement in NBI plasmas have been studied [4].

Most of the plasma experiments in Heliotron-E have been performed using 53.2GHz ECH. The accessible electron density was limited up to $3.5 \times 10^{19} m^{-3}$, which is the cut-off density for fundamental ordinary (O)-mode, giving rise to the difficulty in heating the high density plasma locally. In order to overcome this density limit and make the power deposition easily controlled, we have introduced a new 106.4GHz second harmonic ECH system by replacing the 53.2GHz modules. The launched Gaussian beam is focused, and its polarization can be controlled. The advantages of 106.4GHz second harmonic ECH are that the cut-off density for the extraordinary (X)-mode is high, $ne^c = 7.0 \times 10^{19} m^{-3}$, which is twice as much as for the O-mode in the 53.2GHz fundamental ECH, and that it has a good single pass absorption nearly 100% in usual Heliotron-E plasmas where the optical depth at the core region is larger than unity. Thus the power deposition can be localized at the desired resonance region. Possibility of controlling the resonance position and polarization would give us a clear sight on the plasma response to the change in the power deposition profile.

It is important to study the launching condition for optimum heating in

H/T. The effect of the magnetic shear on the wave propagation has been investigated from the viewpoint of plasma diagnostics such as electron cyclotron emission diagnostics [5], reflectrometer [6], polarimetric measurements [7]. The numerical calculation method used for above diagnostics is applicable to investigate how the launched wave for ECH can access the resonance region. Polarization control experiments can be performed by using a polarizer installed in the transmission line, and the results are compared with the theory.

In this paper, we will present the technological development in the new 106.4GHz ECH system using waveguide transmission line in Heliotron-E, and the second harmonic plasma experimental results, comparing with the previous fundamental and second harmonic ones. Heliotron-E and its ECH system will be described in Sec. 2. Plasma experimental results related to the improvement of plasma parameters, plasma production, plasma response to the power deposition control and magnetic shear effect will be described in Sec. 3. Conclusion is found in Sec. 4.

2. Heliotron-E and ECH System

2.1 Heliotron-E Device

Heliotron-E is a non-axisymmetric helical system, which has a winding law of l=2, m=19, strong magnetic shear, and built-in divertor configuration [8]. The major and minor radii are 2.2m and 0.21m, respectively, for standard configuration, and the maximum magnetic field strength is 1.96T. Parameters of the magnetic surface such as plasma radius, magnetic well, magnetic shear and resonance position can be controlled by using additional vertical, toroidal and perturbation (m/n=1/1) coils. Hydrogen and deuterium gases are used for plasma production, and the density is varied by gas puffing or hydrogen pellet injection. Recently the boronization by 2.45GHz ECH discharge has been introduced for wall conditioning [9][10]. The boronization is more effective than the titanium

gettering for reducing light impurities, making it possible to sustain not only high density ECH plasma but also low density collisionless NBI plasma.

2.2 ECH system for Heliotron-E

ECH system which has been used for Heliotron-E is summarized in Table 1. Four different frequencies of ECH, 28GHz, 35GHz, 53.2GHz and 106.4GHz, were applied for fundamental and second harmonic ECH. Note that all the injection positions of the outside, inside and top corresponds to the low field side injection in heliotron/torsatron configurations. First currentless plasmas were successfully produced and heated by the 28GHz fundamental ECH [11]. The plasma parameters were Te(0)=500eV, Ti=100eV and $\bar{n}_e = 0.4 \times 10^{19} m^{-3}$. Then the powerful 53.2GHz ECH were carried out to extend the plasma parameter regime [12]. The accessible density reached the O-mode cut-off density, $3.5 \times 10^{19} m^{-3}$, and Te(0) was increased to 2.0keV at the low density regime. The 35GHz gyrotron, which

Frequency	Injection Mode	Injection Position	Power	Pulse Width
28GHz	TE02	outside	160kW	0.04sec
35GHz	TE01	outside	130kW	0.2sec
53.2GHz	TE02 / non-focused Gaussian	outside / inside / top	800kW	0.1sec
106.4GHz	focused Gaussian	outside / top	550kW	0.2sec

Table 1 Summary of ECH system for Heliotron-E

was loaned from Oak Ridge National Laboratory, was used mainly for edge heating [13] and high β [4] experiments. The transition phenomena were observed during the second harmonic edge ECH, in which the detached-like state was formed and the particle confinement was improved.

Though the 53.2GHz ECH produced the high Te plasma, the experiments were limited up to the O-mode cut-off density, and the launched waves were TE_{02} circular mode or non-focused linear polarized Gaussian beam [14]. Since the single pass absorption was not good and the power deposition was expanded to the edge region, it was difficult to heat the plasma locally and effectively. In order to sophisticate the launching condition, that is, to focus the wave beam and to control the polarization, we have introduced a new ECH system. Of course, such a system improvement has been accompanied with great progress in millimeter wave sources, gyrotrons [15][16].

2.3 Waveguide line for 106.4GHz ECH

There are two concepts for high-power long-distance transmission line. One is closed, oversized, corrugated or dielectrically lined, HE_{11} mode waveguide, and the other is open, quasi-optical TEM_{00} transmission using metallic reflectors as phase correcting elements [17]. In Heliotron-E, we have been developing the waveguide line and using it for the 106.4GHz ECH system [18][19]. Figure 1 illustrates a schematic view of 106.4GHz ECH system. The system consists of a gyrotron with 0.5MW 0.2sec Gaussian beam output, matching optics unit (MOU), waveguide line, launching system and vacuum window for Heliotron-E. The transmission line is operated at atmosphere pressure with a small amount of CO_2 gas flowing. The whole system is so perfectly closed for human safety that spurious modes do not escape into the free space but are absorbed within the system. The transmission efficiency measured in the high power test is about 85%, so that the power of 0.4MW can be launched into the plasma. Combining the previous 106.4GHz ECH system, total power of 0.6MW

power is possible to launch into a plasma for the second harmonic heating.

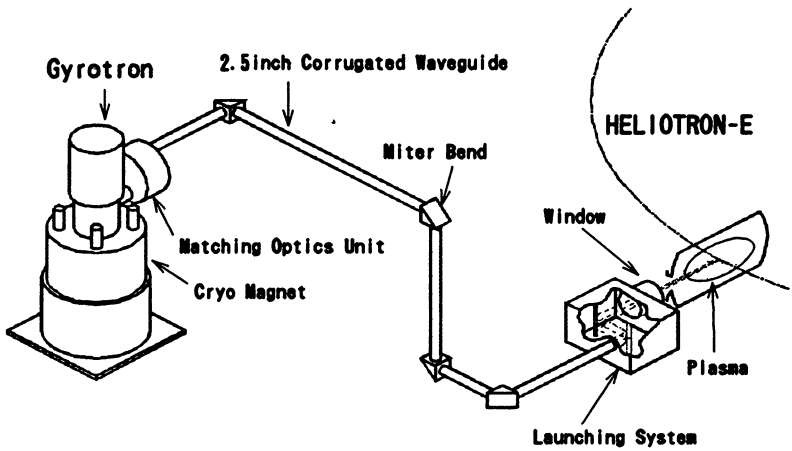

Fig.1 Schematic view of 106.4GHz ECH system for Heliotron-E

The diode type gyrotron is equipped with a built-in quasi-optical converter transforming the cavity output mode, $TE_{15,4}$, into the Gaussian beam. To couple with the HE_{11} waveguide mode effectively and filter the wavebeam irradiated from the gyrotron, the MOU including two adjustable mirrors is placed between the gyrotron and the corrugated waveguide. The power is transported from the MOU to the Heliotron-E device through waveguide line using 15m corrugated waveguides and four miter bends with flat mirrors. Since the waveguide is highly oversized, $a/\lambda=11.3$, the plane reflector can be used at the miter bend. The corrugations are continued up to the mirror, reducing the mode conversion loss be half compared with the case without the corrugations [20]. Polarizer is easy to install in the HE_{11} waveguide line by replacing the flat mirror for the one having sinusoidal grooves rotatable with accuracy of 0.5°. The wave radiation is launched from the outside horizontal port of the Heliotron-E device after being focused by the two adjustable mirrors in the launching system. Since the Heliotron-E port is too small to set the movable mirror

system into the vacuum chamber, the focused beam is launched almost perpendicularly to the plasma in the experiment.

The beam pattern at the launcher output is measured with an infrared camera, and it is confirmed to be circular through the propagation path. Figure 2 shows the beam trajectory in the poloidal cross section. The beam waist is 1.4cm, which is much smaller than the averaged plasma radius, 21cm, so that the power deposition can be localized at the desired resonance position. The power is expected to be absorbed at $r/a_p \leq 0.1$ in case of on-axis heating, where a_p is the averaged plasma radius.

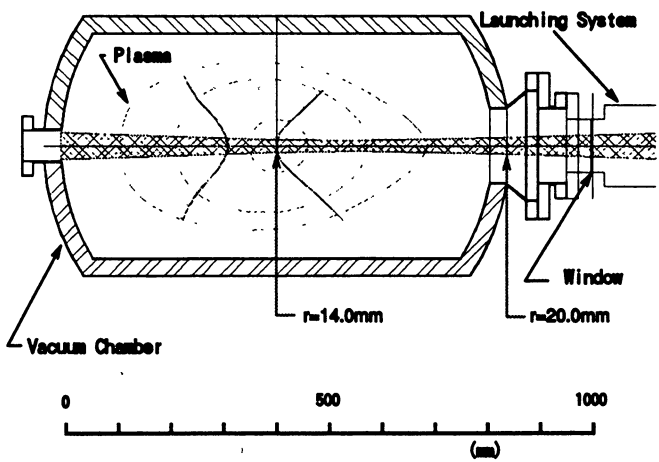

Fig.2 Poloidal cross-section for standard magnetic configuration of Heliotron-E and launched beam trajectory.

The total transmission efficiency from the MOU output to the launcher output measured in the high power test is 86%. This suggests that the waveguide transmission line effectively works as well as the quasi-optical transmission line. Most crucial power losses may be caused by the coupling between the Gaussian beam and HE_{11} waveguide mode, and the mode conversion at miter bends. The TEM_{00} free space mode is known to

have a good coupling to the HE11 mode, ideally 98%, because of similar field distribution. However, the imperfection in the system, especially, tilting and offset of the injected beam, gives rise to a reduction of the coupling efficiency. Figure 3 indicates the ratio of the HE11 and higher modes as a function of the tilting angle and offset distance. The numerical calculation is based on the mode matching method using orthogonal normalization [21]. It is assumed that the injected beam is purely Gaussian, the beam waist is 26mm diameter experimentally measured, and the waist point is 3mm from the waveguide mouth (inside the MOU). In ideal case of no tilting and offset, the fraction of the modes is HE11 97.12% and HE12 2.3%. The coupling efficiency is slightly reduced ~1% due to a smaller beam waist than the optimal one. At the tilting angle experimentally adjusted, α=0.3°, with no offset, the calculated ratio is HE11 95.7%, HE12 2.45%, HE21 0.63% and TM02 0.62%. At the offset distance, 2mm, with no tilting, the HE11 fraction is 96.1%. Combining both tilting and offset effects, the coupling efficiency under the actual imperfection is estimated as 94.8%.

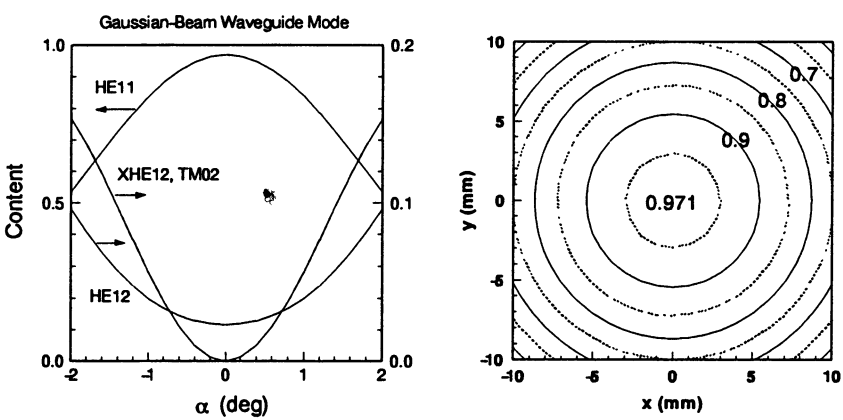

(a) (b)

Fig.3 Power fraction of waveguide modes, (a) dependence on tilting angle of injected beam and (b) dependence on offset distance.

Theoretical power losses in the 106.4GHz ECH system are summarized in Table 2. Summation of the theoretical power losses, 15%, is in good agreement with the high power experimental results, 14%.

Losses	Values
Non-Gaussian beam content	3%
Coupling loss to HE11 mode	5.20%
Losses in waveguides (15m)	
ohmic loss	0.02%
mode conversion losses	
radius change	0.54%
radius offset	0.50%
elliptical offset	0.17%
tilt	0.54%
curvature	0.35%
Losses in miter bends (4 pieces)	
ohmic loss	2.05%
mode conversion loss	0.56%
Losses in launching system	3%
Total loss	14.95%

Table 2 Theoretical power losses in 106.4GHz ECH system

3. Experimental Results

3.1 Improvement of plasma parameters

Second harmonic plasma heating experiments using the 106.4GHz ECH are mainly performed at B=1.90T standard or -2cm shifted configurations in which the resonance layer is located around the magnetic axis. In this section, we will show the plasma experiments using only the new 106.4GHz ECH. Figure 4 shows the density dependence of the central

electron temperature, Te(0), and averaged ion temperature, $\overline{Ti}$. Here $\overline{ne}$, Te(0) and $\overline{Ti}$ are measured with far-infrared interferometer (FIR), Thomson scattering system and neutral particle analyzer (NPA), respectively. The accessible line-averaged density is extended to $\overline{ne}=5.0\times10^{19}m^{-3}$ at P_{ECH}=250-350kW, where ne(0) reached the X-mode cut-off density, $7.0\times10^{19}m^{-3}$. The density profile is broad or slightly hollow, as usually observed in tokamaks and helical systems [22]. Te(0) is improved over the operational density regime. It reaches 2.8keV in the low density ($\overline{ne}=0.5\times10^{19}m^{-3}$) inward shifted ($\Delta v$= -2cm) plasma. $\overline{Ti}$ is not increased with the electron density, but kept constant around 250eV in contrast to the theoretical prediction of collisional coupling between electrons and ions.

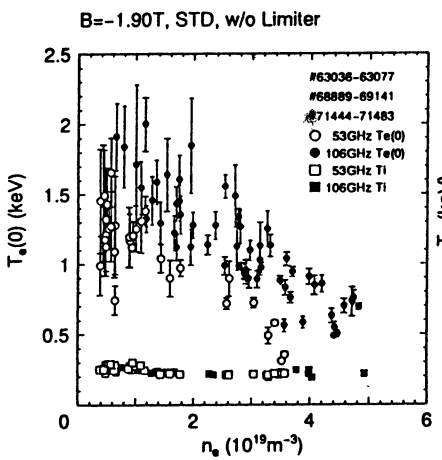

Fig.4 Density dependence of Te(0) and $\overline{Ti}$ at standard configuration.

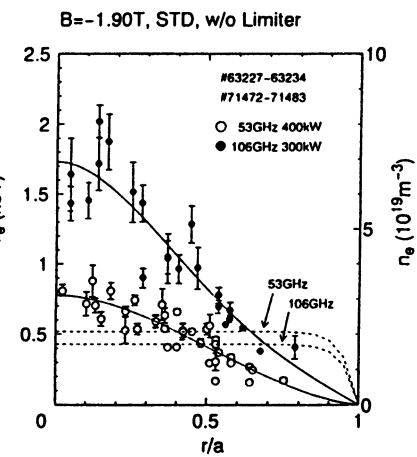

Fig.5 Comparison of ne and Te profiles.

Figure 5 shows the comparison of ne and Te profile at the low density, $\overline{ne}=1\times10^{19}m^{-3}$. The Te profile is more peaked than in the similar power of 53.2GHz fundamental ECH. The peaking factor, η=Te(0)/Te(a/2), is

2.6±0.6 in the 106.4GHz ECH, while it is 2.0±0.5 in the 53.2GHz ECH, implying that the single pass absorption is higher and the power deposition is localized in the central region. The global stored energy, Wp, calculated from measured profiles, increases with the electron density up to $\bar{n}e=3.0\times10^{19}m^{-3}$, then saturates around 8kJ in a similar way in the SOC regime of tokamaks. The energy fraction deposited in the ions increases from 15% at the low density, $\bar{n}e=0.8\times10^{19}m^{-3}$, to 30% at the high density, $\bar{n}e=4.0\times10^{19}m^{-3}$. The energy confinement time, τ_E, is found to be improved by 10–50%, compared to the LHD scaling [23] as shown in Fig.6. Here τ_E is underestimated because the launched power is used as an input power. The improvement of the energy confinement may be associated with the fact that the power is deposited in the central region where the local confinement is better.

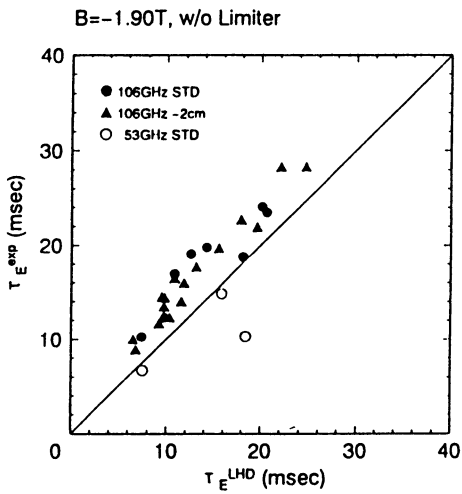

Fig.6 Comparison of global energy confinement with LHD scaling.

3.2 Plasma production

Build-up of the electron density during the plasma breakdown shows different aspects between the fundamental and second harmonic ECH. Figure 7 shows the time evolution of the electron density profile measured with a seven channel FIR. At the second harmonic ECH, the breakdown occurs near the magnetic axis, then expands to the edge region. The electron density is peaked until the density clamping happens. The time

delay of the edge density rise is also observed at other frequencies of second harmonic ECH. At the fundamental ECH, on the other hand, the edge density rises up as soon as the breakdown starts.

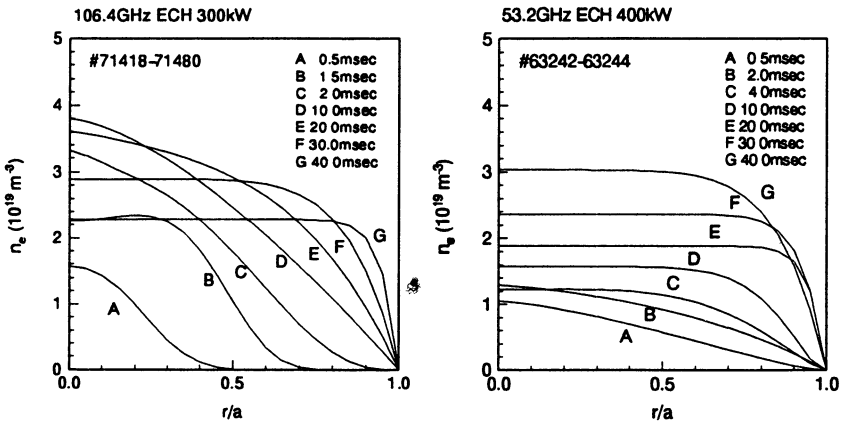

(a) (b)

Fig.7 Time evolution of electron density profile, (a) 106.4GHz second harmonic ECH and (b) 53.2GHz fundamental ECH.

The second harmonic ECH has a narrower magnetic field regime for plasma production. This property is commonly observed in all the frequencies of ECH as shown in Fig.8. The accessible magnetic field regime is the narrowest in the 106.4GHz ECH. This is because the launched beam is a focused Gaussian, which easily uncrosses the resonance layer as decreasing the magnetic field strength. The density build-up is fastest when the resonance layer is placed on the magnetic axis. Therefore the best conditions for plasma production in H/T is that the launched beam should cross the resonance layer at the magnetic axis.

The fact that the breakdown firstly occurs at the central region in the second harmonic ECH may be related to the confinement of accelerated

electrons. It is considered that the nonlinear interaction of a cold electron with the wave plays a role in the second harmonic plasma breakdown [25]. The nonlinear interaction is very large if the electron is trapped near the resonance in a saddle point of the magnetic field. The resonance layer should be tuned in the central region so that the accelerated electron can be well confined.

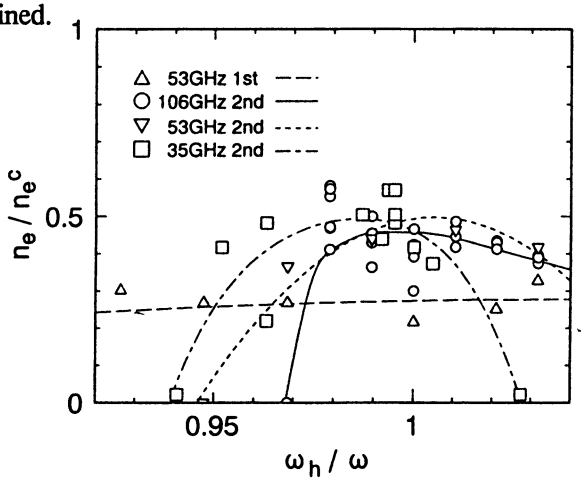

Fig.8 Magnetic field regime for plasma production. n_e^c, ω_h and ω are cut-off density, central resonance and wave frequencies, respectively.

3.3 Response of Te profile to the change in power deposition

Since the magnetic field contour is a saddle geometry at the plasma central region, control of the total field strength makes the injected beam propagate with/without crossing the resonance layer. When the central magnetic field strength is larger than 1.88T, the resonance layer is located in the low field side, so that the launched beam crosses it directly. The lower the field strength is, the less the focused beam crosses the resonance layer, resulting that the one-pass dominant absorption is changed into the multi-pass dominant one. Figure 9(a) shows the Te profile at several magnetic field strengths. The profile is changed from a peaked one (η=2.4 at B(0)=1.90T) to a broad one (η=1.4 at B(0)=1.86T). When the magnetic

field is in the range of 1.90T–1.96T, the resonance position weakly moves, and the Te profile is not much changed. The marginal field strength agrees with a drastic decrease of the single pass absorption from 98% (B(0)=1.90T) to 2% (B(0)=1.86T) evaluated from the ray tracing calculation.

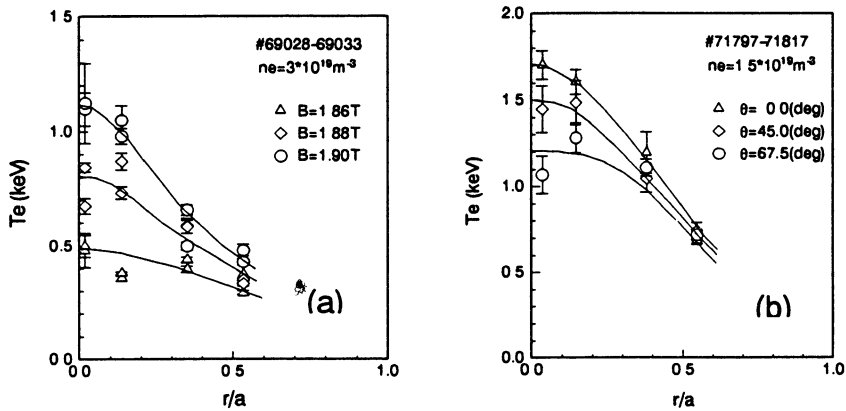

Fig. 9 Te profile change (a) by moving the resonance layer at $\bar{n}_e = 3.0 \times 10^{19} m^{-3}$. *profiles and (b) by controlling the polarization at* $\bar{n}_e = 1.5 \times 10^{19} m^{-3}$.

The difference between one–pass and multi–pass absorptions can also be investigated by controlling the polarization of the launched wave. The polarizer rotates the electric field of the launched wave. Figure 9(b) shows the dependence of the Te profile on the mirror rotation angle. The Te profile is changed from a peaked one to a broad one as observed in the B scanning experiment. The reason why the profile change is weaker than in B scanning experiment is that the launched wave does not become a pure O–mode due to the magnetic shear effect which will be discussed in Sec. 3.4

Localized off–axis heating is conducted by moving the magnetic axis or tilting the launching angle. The magnetic axis is shifted by 8cm inwardly,

or the launching angle is slightly tilted by 2°, corresponding that resonance position is moved to r/a=0.43 in the former and r/a=0.24 in the latter. Figure 10 shows the Te profiles in NBI and NBI+ECH plasmas. They become hollow, and their peak positions are shifted to the resonance position.

From these experimental results, it is concluded that the Te profile is closely associated with the power deposition profile determined by the resonance position and single pass absorption rate. Modification of the power deposition leads to a change in the Te profile.

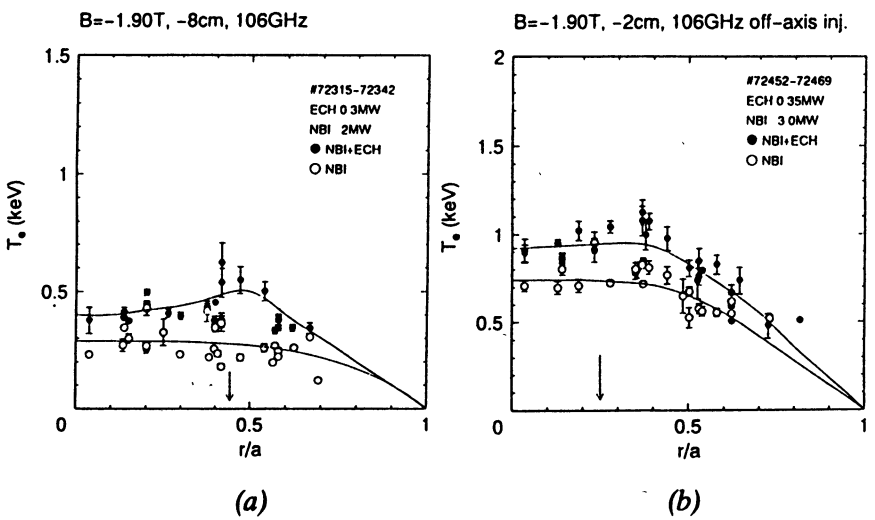

(a) *(b)*

Fig.10 Te profiles at off-axis heating (a) by shifting the resonance layer and (b) by tilting the injection angle. Open and closed circles denotes NBI and NBI+ECH plasmas, respectively.

3.4 Magnetic shear effect on wave propagation

From the viewpoint of wave propagation through a plasma, the most important difference between tokamaks and H/T is that the toroidal and poloidal components of the magnetic field are of comparable magnitude in H/T. The difference of the magnetic field direction between the resonance region and the plasma boundary is quite large. In Heliotron-E, for example,

the magnetic field at the last closed magnetic surface is tilted by 45°. Furthermore, the space-dependent magnetic field affects the wave propagation. The O- and X-modes, which rotate with the magnetic field, do not propagate independently, resulting that their fraction is changing through the propagation path.

To analyze the magnetic shear effect on the wave propagation, the following second order coupled equations [25] [26] are solved for both the O- and X-modes,

$$\frac{d^2E_{//}}{dz^2} + (\frac{\omega^2}{c^2}N_O^2 - \phi^2)E_{//} = 2\phi\frac{dE_\perp}{dz} + \frac{d\phi}{dz}E_\perp \qquad (1)$$

$$\frac{d^2E_\perp}{dz^2} + (\frac{\omega^2}{c^2}N_X^2 - \phi^2)E_\perp = -2\phi\frac{dE_{//}}{dz} - \frac{d\phi}{dz}E_{//} \qquad (2)$$

where ω is wave frequency, $E_{//}$ and $E_\perp$ are parallel and perpendicular components, N_o and N_x are refractive indices for the O- and X-modes in a cold plasma, respectively. The shear, $\phi = d\theta/dz$, is defined to be angular gradient of the magnetic field.

Figure 11 shows one example of the electric field of a 106.4GHz wave through the Heliotron-E plasma. The wave number vector and electric field are set to be perpendicular to the resonant magnetic field. The launched wave is coupled to plasma propagating modes at the boundary, then the X-mode is strongly damped around the second harmonic resonance. The numerical calculation results show that the magnetic shear can not be neglected for a good single pass absorption in H/T, and the launched wave should be elliptically polarized even in the conventional perpendicular launching case. As shown in Fig.12, the calculated optimum conditions for Heliotron-E are tilting angle, 30°, ellipticity, 15°, and right-hand rotation at the medium density regime.

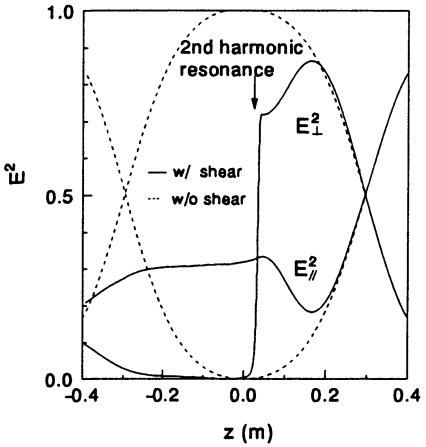

Fig.11 Envelope of the square of the launched electric field through the propagation path.

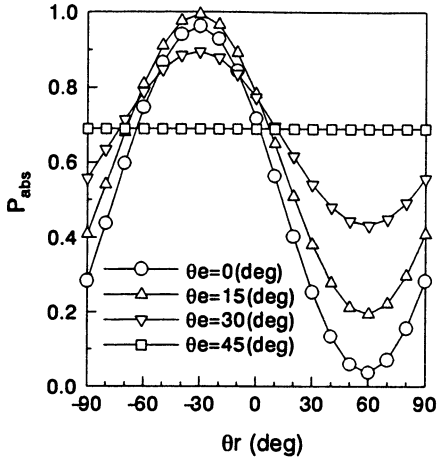

Fig.12 Dependence of absorbed power on launching parameters. θ_r and θ_e denote the rotation angle and ellipticity, respectively.

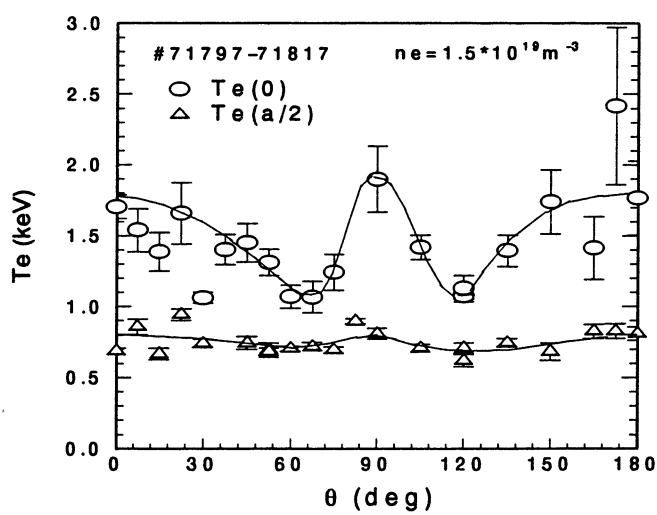

Fig.13 Dependence of Te on mirror rotation angle in ECH plasma. The electron density is $\bar{n}_e = 1.5 \times 10^{19} m^{-3}$.

It is possible to examine the magnetic shear effect experimentally by controlling the polarization of the launched wave. One mirror is used for a linear polarizer [27]. Figure 13 shows the dependence of Te on the mirror rotation angle. Te(0) drastically decreases from 2keV to 1keV, while Te(a/2) is almost constant. This means that the absorption is changed from a single-pass localized heating to a multi-pass uniform one. The mirror rotation angles, Φ=0°, 90°, correspond to 62° tilting of the electric field in respect to the resonant magnetic field. These optimum angles are in good agreement with above mentioned theory including the magnetic shear. Dependence of the polarization of the launched wave on the mirror rotation angle is not experimentally determined in the cold test yet. More detailed comparison between the experiment and the theory is underway.

4. Conclusion

The 106.4GHz ECH system has been installed and operated for Heliotron-E. The 0.5MW high power millimeter wave from the gyrotron source can be effectively transmitted through the waveguide line, and the focused Gaussian beam is injected into a Heliotron-E plasma. The second harmonic heating experiments were made and compared with the previous experimental results. Te(0) increased to 2.8keV in the low density plasma, and ne(0) up to $7.0\times10^{19}m^{-3}$ was accessible. The global energy confinement time was improved up to 50%. The difference of plasma production between fundamental and second harmonic ECH was also discussed. The magnetic field regime for plasma production is narrower in the second harmonic ECH, which may be related to the confinement of accelerated electrons. It was clearly shown that the power deposition can be changed by controlling the resonance position and polarization. The Te profile is sensitive to how the ECH power is deposited. The magnetic shear has an important role in the wave propagation in H/T. It was experimentally and theoretically shown that the launched wave should be elliptically polarized even in the conventional perpendicular launching case.

Acknowledgment

Authors would like to thank the Heliotron–E staff for operating the Heliotron–E device. They are grateful to Drs. K. Ida, M. Sato and Mr. M. Iima of National Institute for Fusion Science for fruitful discussions.

References

[1] A. C. Riviere, Plasma Phys. Control. Fusion 28 (1986) 1262

[2] A. C. England, et al., Nucl. Fusion 29 (1989) 1527

[3] V. Erckmann and V. Gasparino, Plasma Phys. Control. Fusion 36 (1994) 1869

[4] T. Obiki, et al., in Proceedings of 15th Int. Conf. on Plasma Physics and Controlled Nuclear Fusion Research, Seville, 1994 (IAEA, Vienna, 1995) Vol.I, p.757

[5] G. L. Bell, et al., Nucl. Fusion 33 (1993) 875

[6] M. Brambilla and M. Moresco, Plasma Phys. Control. Fusion 29 (1987) 381

[7] A. Airoldi, et al., Phys. Fluids B 1 (1989) 2143

[8] T. Obiki, Fusion Technol. 17 (1990) 101

[9] M. Yamage, et al., J. Nucl. Mater. 220-222 (1995) 743

[10] K. Kondo, et al., J. Nucl. Mater. 220-222 (1995) 1052

[11] A. Iiyoshi, et al., Phys. Rev. Lett. 48 (1982) 745

[12] O. Motojima, et al., in Proceedings of 12th Int. Conf. on Plasma Physics and Controlled Nuclear Fusion Research, Nice, 1988 (IAEA, Vienna, 1989) Vol.I, p.551

[13] K. Nagasaki, et al., Fusion Eng. and Design 26 (1995) 159

[14] H. Zushi, et al., Nucl. Fusion 28 (1988) 1801

[15] V. A. Flyagin, A. L. Goldenberg, V. E. Zapevalov, Conf. Digest 19th Int. Conf. Infrared and Millimeter Waves, Oct. 17-20, 1994, Sendai, p.77

[16] S. D. Bogdanov, E. A. Solujanova and gyrotron team, Conf. Digest 19th Int. Conf. Infrared and Millimeter Waves, Oct. 17-20, 1994, Sendai, p.351

[17] M. Thumm and W. Kasparek, Fusion Eng. and Design 26 (1995) 29

[18] K. Nagasaki, et al., Fusion Technol. 25 (1994) 419

[19] K. Nagasaki, et al., submitted to Fusion Technol.

[20] J. L. Doane and C. Moeller, Int. J. Electronics 77 (1994) 489

[21] K. Ohkubo, submitted to Int. J. Electronics

[22] H. Zushi, et al., "Density Clamping Phenomena in Electron Cyclotron Resonance Heated Plasmas on Heliotron-E", PPLK Report, PPLK-R-27 (1988)

[23] S. Sudo, et al., Nucl. Fusion 30 (1990) 11

[24] M. D. Carter, D. B. Batchelor and A. C. England, Nucl. Fusion 27 (1987) 985

[25] T. Fidone and G. Granata, Nucl. Fusion 11 (1971) 133

[26] K. Nagasaki and A. Ejiri, Nucl. Fusion 35 (1995) 609

[27] K. Nagasaki, A. Isayama and A. Ejiri, Rev. Sci. Instrum. 66 (1995) 3432

RECENT DEVELOPMENTS IN THEORY OF WAVE SCATTERING IN PLASMAS

H. Bindslev

JET Joint Undertaking, Abingdon, UK

Abstract. Recent developments in kinetic/microscopic theory of wave interaction and scattering in plasmas is outlined and quantitative predictions are compared to those of earlier models.

1 Introduction

The theory of collective Thomson scattering (CTS) integrates several distinct areas of plasma physics which are interesting in their own right and relevant to a range of applications other than CTS. They are primarily the theory of microscopic fluctuations and the theory of bilinear wave interaction. The latter includes the problem of wave emission. When CTS is used as a diagnostic the modelling also includes the propagation of waves in inhomogeneous anisotropic media (magnetized plasmas).

In CTS a powerful monochromatic *incident* wave (i) is scattered by spontaneously occurring broadband fluctuations (δ) in the plasma. The spectrum of fluctuations, and with them the spectrum of scattered waves, depend on a wide range of plasma parameters. Detection of the scattered waves (s) thus potentially provides a highly versatile diagnostic, sensitive to many aspects of the confined plasma. Its wide range of sensitivities is a major strength, but also a serious difficulty when analyzing the detected spectrum [1].

The incident wave generally has a frequency which is high compared with the ion plasma and cyclotron frequencies. It thus primarily interacts with the fluctuating electron distribution and associated fields. CTS diagnostics are, nonetheless, potentially very good diagnostics of the ion distribution. This is because an ion, when traveling through the sea of electrons, draws a wake much like a swan traversing a pond; with a proper model of the wake a swan leaves we may be able to deduce the phase space density of swans from the fluctuations in the surface of the pond.

To model CTS we first need an appropriate theory of the fluctuations. They are driven by the thermal motion of the discrete charged particles in the plasma and are therefore sometimes referred to as thermal fluctuations, though this does not imply that we limit our considerations to plasmas in thermal equilibrium. The ensemble average of the fluctuating fields and distributions are zero unlike the ensemble averages of their products, implying that the fluctuations are microscopic. We can only measure macroscopic quantities, so computable expressions for the fluctuations need only cover ensemble averages of quadratic terms; a considerable simplification, without which tractable expressions could not be provided.

Having a model of the fluctuations we need a model of their interaction with the incident wave. This problem is most conveniently split into two parts accounting for: a) the *source current* arising from the interaction and b) the scattered wave that results from the source current. Here it should be noted that because the fluctuations are microscopic the scattered wave is also microscopic, so the theory of the interaction must be derived from a microscopic model.

Finally the incident and scattered waves need to propagate in and out of the inhomogeneous plasma. Modelling of this part of the problem is required to establish where and with what geometry the scattering takes place. If the spectrum of detected fluctuations includes propagating waves, the spectrum of received scattered light is very sensitive to the beam intensity distributions of the emitter and receiver, in which case this part of the modelling becomes critical, generally requiring that beam diffraction also be taken into account.

Existing collective Thomson scattering (CTS) experiments for diagnosing fast ion distributions in fusion plasmas [2, 3, 4] have stimulated a range of theoretical developments in the modelling of CTS. They include dielectric coupling effects in cold [5] and relativistic plasmas [6], scattering from electromagnetic fluctuations [7, 8, 9] and kinetic models of scattering [8, 10, 11]. In the course of this review discrepancies between cold fluid and kinetic models of wave interaction have received considerable attention [10, 12–18].

Here we seek to outline a model of CTS which includes many of the recent developments, which is valid for most ranges of interest in magnetically confined fusion plasmas and which has been implemented in codes and proven to be an effective tool for predicting per-

formance and analyzing CTS data. The model presented here does not accommodate scattering from propagating waves with damping lengths larger than the linear dimensions of the plasma, considered by Piliya et al. [19], nor is it accurate for scattering at the electron cyclotron resonance and its lowest harmonics. The model is outlined, indicating its physics basis, and where appropriate comparisons are made with earlier models.

2 Microscopic description of the plasma

The behavior of electromagnetic waves and fluctuations in plasmas are described by Maxwell's equations for the microscopic fields,

$$\nabla \times \mathbf{E}^{\mathrm{M}} = -\partial_t \mathbf{B}^{\mathrm{M}} , \quad \nabla \times \mathbf{B}^{\mathrm{M}} = \mu_0 \left(\varepsilon_0 \partial_t \mathbf{E}^{\mathrm{M}} + \mathbf{j}^{\mathrm{M}} \right) , \qquad (1)$$

where $\mathbf{j}^{\mathrm{M}}$ is the microscopic plasma current,

$$\mathbf{j}^{\mathrm{M}} = q_e \int \mathbf{v} f^{\mathrm{M}} \, d\mathbf{p} , \qquad (2)$$

and $f^{\mathrm{M}} = \sum_i \delta(\mathbf{x} - \mathbf{x}_i(t))$ $(\mathbf{x} = (\mathbf{r}, \mathbf{p}))$, the microscopic distribution function, is governed by the dynamic equation [20, Section 24]

$$\mathcal{L} f^{\mathrm{M}} = -\mathbf{F}^{\mathrm{M}} \cdot \partial_{\mathbf{p}} f^{\mathrm{M}} . \qquad (3)$$

Here

$$\mathcal{L} = \partial_t + \mathbf{v} \cdot \partial_{\mathbf{r}} + q_e (\mathbf{v} \times \mathbf{B}^{(0)}) \cdot \partial_{\mathbf{p}} , \qquad (4)$$

is the linear operator representing the total derivative along unperturbed orbits in phase space, $\mathbf{B}^{(0)}$ is the static magnetic field and

$$\mathbf{F}^{\mathrm{M}} = q_e \left(\mathbf{E}^{\mathrm{M}} + \mathbf{v} \times (\mathbf{B}^{\mathrm{M}} - \mathbf{B}^{(0)}) \right)$$

is the force electromagnetic fields exert on an electron. It is assumed that there is no static electric field.

Macroscopic quantities are ensemble averages of microscopic quantities, $f = \langle f^{\mathrm{M}} \rangle$, $\mathbf{E} = \langle \mathbf{E}^{\mathrm{M}} \rangle$, $\mathbf{B} = \langle \mathbf{B}^{\mathrm{M}} \rangle$. They are approximately identical to the time or space averages over scale lengths separating microscopic and macroscopic descriptions. Microscopic fluctuations are the differences between the microscopic and macroscopic: $\tilde{f} = f^{\mathrm{M}} - f$, $\tilde{\mathbf{E}} = \mathbf{E}^{\mathrm{M}} - \mathbf{E}$, $\tilde{\mathbf{B}} = \mathbf{B}^{\mathrm{M}} - \mathbf{B}$. It follows from the

definition that the ensemble average of a microscopic fluctuation is identical zero while the average of the product of two microscopic fluctuations in general is not. This is significant here because much of the present considerations are concerned with the observation of microscopic fluctuations by diagnostic methods which involve spatial and temporal integration over scale lengths which are large compared with the scale lengths separating microscopic and macroscopic descriptions.

Taking the ensemble average of (3) gives

$$\mathcal{L}f + \mathbf{F} \cdot \partial_{\mathbf{p}} f + \left\langle \tilde{\mathbf{F}} \cdot \partial_{\mathbf{p}} \tilde{f} \right\rangle = 0\,, \tag{5}$$

which governs the macroscopic distribution. The last term represents the effect of binary interactions and is consequently often referred to as the collision integral. Neglecting this term (5) reduces to the Vlasov equation.

Subtracting (5) from (3) we get

$$\mathcal{L}\tilde{f} + \mathbf{F} \cdot \partial_{\mathbf{p}} \tilde{f} + \tilde{\mathbf{F}} \cdot \partial_{\mathbf{p}} f + \tilde{\mathbf{F}} \cdot \partial_{\mathbf{p}} \tilde{f} - \left\langle \tilde{\mathbf{F}} \cdot \partial_{\mathbf{p}} \tilde{f} \right\rangle = 0\,, \tag{6}$$

which governs microscopic fluctuations. Neglecting collisions eliminates the last two terms.

3 Bilinear wave interaction

We start with this topic to set out which fluctuating quantities we will need to derive expressions for.

3.1 Kinetic description of two wave interaction

The system of equations describing waves in plasma is bilinear due to the term on the right hand side of (3), which causes waves in plasmas to interact. The fact that the nonlinearity is limited to second order implies that the interaction of a larger number of waves can be considered as a sequence of two wave interactions. Integrating (3) along the characteristics of $\mathcal{L}$ (the unperturbed orbits) and inserting the result in (2) we find the plasma current $\mathbf{j}^{\mathrm{M}}$ expressed as a linear integral operator, σ, acting on the bilinear term, $\mathbf{F}^{\mathrm{M}} \cdot \partial_{\mathbf{p}} f^{\mathrm{M}}$:

$$j_i^{\mathrm{M}} = \sigma_i \{ \mathbf{F}^{\mathrm{M}} \cdot \partial_{\mathbf{p}} f^{\mathrm{M}} \}\,. \tag{7}$$

Eliminating $\mathbf{B}^{\mathrm{M}}$ from Maxwell's equations we obtain the wave equation

$$\Lambda_{ij}\mathbf{E}_j^{\mathrm{M}} = \frac{-i}{\omega\varepsilon_0} j_i^{\sigma\mathrm{M}} \tag{8}$$

$$\Lambda_{ij} = \varepsilon_{ij} + N^2\left\{\hat{k}_i\hat{k}_j - \delta_{ij}\right\}, \quad N = \frac{kc}{w},$$

where $\varepsilon_{ij} = \delta_{ij} + \chi_{ij}$. χ_{ij} accounts for the plasma response associated with fields acting on the macroscopic equilibrium distribution, $f^{(0)}$,

$$-i\omega\varepsilon_0\chi_{ij}\mathbf{E}_j^{\mathrm{M}} = \sigma_{ij}\mathbf{E}_j^{\mathrm{M}} = \sigma_i\{\mathbf{F}^{\mathrm{M}}\cdot\partial_{\mathbf{p}}f^{(0)}\},$$

while the *source current*, $j^{\sigma\mathrm{M}}$, is due to the interaction of the fields with the distribution function perturbations

$$j_i^{\sigma\mathrm{M}} = \sigma_i\{\mathbf{F}^{\mathrm{M}}\cdot\partial_{\mathbf{p}}(f^{\mathrm{M}} - f^{(0)})\}. \tag{9}$$

The inhomogeneous wave equation (8) together with the expression for the source current (9) and the dynamic equation (3) completely describe wave interactions in plasmas.

Note that expression (9) retains the complete microscopic description of the plasma. If we are concerned only with the interaction of macroscopic waves we require only the macroscopic source current which is given by the ensemble average of (9),

$$j_i^{\sigma} = \sigma_i\{\mathbf{F}\cdot\partial_{\mathbf{p}}(f - f^{(0)}) + \left\langle\tilde{\mathbf{F}}\cdot\partial_{\mathbf{p}}\tilde{f}\right\rangle\}. \tag{10}$$

The last term represents the effect of collisions. Neglecting this term the expression reduces to that which could be derived from the Vlasov equation, and has the same form as the microscopic expression (9).

The interaction of a macroscopic wave with a microscopic fluctuation gives rise to a scattered wave which is also a microscopic fluctuation, driven by the microscopic fluctuating source current,

$$\tilde{j}_i^{\sigma} = \sigma_i\{\tilde{\mathbf{F}}\cdot\partial_{\mathbf{p}}(f - f^{(0)}) + \mathbf{F}\cdot\partial_{\mathbf{p}}\tilde{f} + \tilde{\mathbf{F}}\cdot\partial_{\mathbf{p}}f - \left\langle\tilde{\mathbf{F}}\cdot\partial_{\mathbf{p}}\tilde{f}\right\rangle\}. \tag{11}$$

The last two terms represent the fluctuations in the collision integral. Neglecting these terms (11) also attains the form of expression (9). Because of the similarity when collisions are neglected we do not distinguish between microscopic fluctuations and macroscopic waves in the rest of this section.

Assuming now that the bilinear interactions represented by the source current (9) are weak we can usefully approximate the solution with a perturbation expansion. Taking this expansion to second order we describe the bilinear interaction of two waves a and b in the first Born approximation. The field, $\mathbf{E}^{\mathrm{s}}$, of the resulting scattered wave s is then given by

$$\Lambda_{ij}\mathbf{E}^{\mathrm{s}}_j = \frac{-i}{\omega\varepsilon_0} j^{\sigma}_i \tag{12a}$$

$$j^{\sigma}_i = \sigma_i\{\mathbf{F}^{\mathrm{a}} \cdot \partial_{\mathbf{p}} f^{\mathrm{b}} + \mathbf{F}^{\mathrm{b}} \cdot \partial_{\mathbf{p}} f^{\mathrm{a}}\}\,. \tag{12b}$$

This set of equations describe the bilinear wave interaction of arbitrary waves a and b and makes no assumptions about s other than that its amplitude must be much smaller than those of a and b. If this is not an acceptable assumption higher order Born approximations may be obtained by considering a sequence of bilinear interactions involving scattered waves.

Although it is straight forward to write down the expression for the operator σ [21, 10] it remains numerically intractable.

3.2 Low Temperature Kinetic model

The complexity of the kinetic expression for the source current (12b) is connected with the fact that it involves the full detail of the distribution function perturbations, f^{a} and f^{b}, associated with the interacting waves. Its complexity can, however, be significantly reduced by assuming that thermal effects are small at the frequency and wave vector, $(\mathbf{k}^{\mathrm{s}}, \omega^{\mathrm{s}})$, of the *scattered* wave, or more precisely that $\langle f^{\sigma} f^{\sigma}\rangle$ ($\mathcal{L} f^{\sigma} = \mathbf{F}^{\mathrm{a}} \cdot \partial_{\mathbf{p}} f^{\mathrm{b}} + \mathbf{F}^{\mathrm{b}} \cdot \partial_{\mathbf{p}} f^{\mathrm{a}}$) is significant only when

$$\frac{v}{c} \ll 1\,; \qquad \frac{v_{\|} k^{\mathrm{s}}_{\|}}{\omega^{\mathrm{s}} + n\omega_c} \ll 1\,, \quad n \in Z\,; \qquad \frac{v_{\perp} k^{\mathrm{s}}_{\perp}}{\omega_c} \ll 1\,, \tag{13}$$

where $\omega_c = -q_e B^{(0)}/m_e$ and $\|$ and $\perp$ indicate components parallel and perpendicular to $\mathbf{B}^{(0)}$. With these assumptions the expression for the source current reduces to a numerically tractable expression which involves only the zeroth and the first order moments of the distribution perturbations associated with waves a and b [10],

$$j^{\sigma}_i = \frac{\sigma^{\mathrm{s}}_{il}\delta^{\mathrm{ab}}_{\alpha\beta}}{n^{(0)}} \left\{ n^{\alpha} E^{\beta}_l + \epsilon_{lmn} \overline{v}^{\alpha}_m B^{\beta}_n + Y^{\mathrm{s}}_{lmn} \frac{1}{c} \overline{v}^{\alpha}_m E^{\beta}_n \right\}\,. \tag{14}$$

Here $\delta^{ab}_{\alpha\beta} = \delta_{a\alpha}\delta_{b\beta} + \delta_{b\alpha}\delta_{a\beta}$,

$$n^\alpha = \int f^\alpha \, d\mathbf{p} \,, \quad \overline{v}^\alpha_j = \int v_j f^\alpha \, d\mathbf{p} \,,$$

and σ^s is the cold electron conductivity at the frequency of the scattered wave, while

$$Y^s_{imn} = \frac{k^s_j c}{\omega^s} \Gamma^{-1}_{ijab} (\delta_{an}\delta_{bm} + \delta_{am}\delta_{bn}) \,,$$

$$\Gamma^{-1}_{ijab} = \frac{-i\Omega\,(\eta_{ia}\xi_{jb} + \xi_{ia}\eta_{jb}) - 2\Omega^2\xi_{ia}\xi_{jb} + (1 - 2\Omega^2)\eta_{ia}\eta_{jb}}{1 - 4\Omega^2}$$

$$+ \frac{\eta_{ia}\zeta_{jb} + \zeta_{ia}\eta_{jb} - i\Omega(\zeta_{ia}\xi_{jb} + \xi_{ia}\zeta_{jb})}{1 - \Omega^2} + \zeta_{ia}\zeta_{jb} \,,$$

and $\Omega = \omega_c/\omega^s$, $\eta_{ij} = \delta_{ij} - \delta_{i3}\delta_{j3}$, $\xi_{ij} = \epsilon_{ij3}$, $\zeta_{ij} = \delta_{i3}\delta_{j3}$.

It is remarkable that although the low temperature kinetic (LTK) expression for the source current (14) involves only the zeroth and first order moments of f^a and f^b it nonetheless introduces no new assumptions about the nature of the interacting waves a and b relative to the full kinetic expression which involves the full detail of f^a and f^b.

Till this point the source current expression has been symmetrical with respect the interacting waves a and b. We now break this symmetry by assuming that the plasma dielectric response is cold at the frequency and wave vector $(\mathbf{k}^i, \omega^i)$ of one of the interacting waves, hence forth referred to as the incident wave, i, while maintaining the generality for the other wave which we will refer to as the fluctuations, δ.

This permits us to use the cold plasma relations to express $\mathbf{B}^i$, $\mathbf{j}^i$ and n^i all in terms of $\mathbf{E}^i$. We then find that the source current is given by [10]

$$j^\sigma_i = \frac{\sigma^s_{ij}}{n^{(0)}} E^i_l \left\{ \delta_{jl} n^\delta + \frac{1}{c}\left(\epsilon_{jkm}\epsilon_{mnl} N^i_n + Y^s_{jkl}\frac{1}{c}\right)\overline{v}^\delta_k \right. \qquad (15)$$

$$\left. + \frac{\sigma^i_{ml}}{q_e}\left[\epsilon_{jmk} B^\delta_k + \frac{1}{c}\left(\delta_{jk} N^i_m + Y^s_{jmk}\right) E^\delta_k\right]\right\} \,,$$

where σ^{i} is the cold electron conductivity at the frequency of the incident wave and $N_j^{\mathrm{i}} = k_j^{\mathrm{i}} c/\omega^{\mathrm{i}}$ is the refractive index of the incident wave.

In a wide range of scattering experiments in laboratory plasmas the frequencies of the incident and the scattered waves are sufficiently high that the plasma can be treated as cold for these waves. The phase velocity of the observed fluctuations are, however, typically of the same order or smaller than the thermal velocities of the electrons and uncorrelated motion may also have to be taken into account, both of which makes it unacceptable to regard the fluctuations as cold collective oscillations. In this case we can make use of the low temperature kinetic model of scattering with the source current given by (15).

Solving for $\tilde{\mathbf{E}}^{\mathrm{s}}$ in (12a), taking the ensemble average of the square of $\tilde{\mathbf{E}}^{\mathrm{s}}$ and accounting for the transfer of power through an anisotropic inhomogeneous plasma in the WKB approximation [22] we find the equation of transfer for a scattering system [23, 10] giving the power received by a diffraction limited receiver:

$$\frac{\partial P^{\mathrm{s}}}{\partial \omega^{\mathrm{s}}} = P^{\mathrm{i}} O_b \left(\lambda_0^{\mathrm{i}}\right)^2 r_e^2 n^{(0)} \frac{1}{2\pi} \Sigma \,. \tag{16}$$

$\lambda_0^{\mathrm{i}} = \omega^{\mathrm{i}}/c$, $r_e = q_e^2/4\pi\varepsilon_0 m_e c^2$ is the classical electron radius and O_b is the beam overlap which is defined in terms of the normalized beam intensities, $\mathcal{I}$, for the transmitter and receiver beams and which, in the case of uniform beam intensities and perfect intersection, is identical to the ratio of the scattering volume, V, to the product of the beam cross sectional areas, A:

$$O_b = \int_{R^3} \mathcal{I}^{\mathrm{i}}(\mathbf{r}) \mathcal{I}^{\mathrm{s}}(\mathbf{r})\, d\mathbf{r} \approx \frac{V}{A^{\mathrm{i}} A^{\mathrm{s}}} \,. \tag{17}$$

O_b will have some frequency dependence due to varying refraction but most of the spectral variation of the received scattered power, P^{s}, is due to the scattering function, Σ, defined as

$$\Sigma = \sum_{\alpha\beta} \Sigma_{\alpha\beta} \,, \quad \Sigma_{\alpha\beta} = \frac{(\omega^{\mathrm{s}})^4}{\omega_p^4} \frac{1}{\mathcal{S}^{\mathrm{i}} \mathcal{S}^{\mathrm{s}}} \widehat{\mathbf{G}}_i^{(\alpha)} \left\langle \alpha_i \beta_{i'} \right\rangle \widehat{\mathbf{G}}_{i'}^{(\beta)*} \,, \tag{18}$$

with $\alpha_i, \beta_i = E_i, B_i, j_i, n$ and the *dielectric coupling* operators, $\widehat{\mathbf{G}}$, defined as

$$\widehat{\mathbf{G}}^{(n)} \;=\; (e_i^{\mathrm{s}})^* \chi_{il}^{\mathrm{s}} e_l^{\mathrm{i}} \tag{19}$$

$$\widehat{\mathbf{G}}_k^{(B)} = -(e_i^{\mathrm{s}})^* \chi_{ij}^{\mathrm{s}} \epsilon_{jmk} \frac{i\omega^{\mathrm{i}}\varepsilon_0}{q_e} \chi_{ml}^{\mathrm{i}} e_l^{\mathrm{i}} \tag{20}$$

$$\widehat{\mathbf{G}}_k^{(j)} = (e_i^{\mathrm{s}})^* \frac{1}{q_e} \left(\chi_{ij}^{\mathrm{s}} \epsilon_{jkm} \epsilon_{mnl} \frac{k_n^{\mathrm{i}}}{\omega^{\mathrm{i}}} + X_{ikl}^{\mathrm{s}} \frac{1}{c} \right) e_l^{\mathrm{i}} \tag{21}$$

$$\widehat{\mathbf{G}}_k^{(E)} = -(e_i^{\mathrm{s}})^* \left(\chi_{ik}^{\mathrm{s}} \frac{i\varepsilon_0}{q_e} k_j^{\mathrm{i}} \chi_{jl}^{\mathrm{i}} + X_{ijk}^{\mathrm{s}} \frac{i\omega^{\mathrm{i}}\varepsilon_0}{cq_e} \chi_{jl}^{\mathrm{i}} \right) e_l^{\mathrm{i}} . \tag{22}$$

The normalized flux and field of the incident radiation is defined by

$$\mathcal{S}^{\mathrm{i}} = N^{\mathrm{i}} |\widehat{\mathbf{k}}^{\mathrm{i}} - \mathrm{Re}\{(\widehat{\mathbf{k}}^{\mathrm{i}} \cdot \mathbf{e}^{\mathrm{i}})(\mathbf{e}^{\mathrm{i}})^*\}| \, , \mathbf{e}^{\mathrm{i}} = \mathbf{E}^{\mathrm{i}}/|\mathbf{E}^{\mathrm{i}}| \, , N^{\mathrm{i}} = k^{\mathrm{i}} c/\omega^{\mathrm{i}} \, , \widehat{\mathbf{k}}^{\mathrm{i}} = \mathbf{k}^{\mathrm{i}}/k^{\mathrm{i}} \, .$$

Similar expressions for $\mathcal{S}^{\mathrm{s}}$ and $\mathbf{e}^{\mathrm{s}}$ relate to the received scattered radiation. All quantities in Σ refer to conditions in the scattering volume.

$\langle \alpha_i \beta_{i'} \rangle$ is the ensemble average of the product of two microscopic fluctuating quantities, i.e. the correlation function, which is macroscopic. The diagonal elements, such as $\langle \tilde{n}\tilde{n} \rangle$, are the power spectra of the microscopic fluctuations in the particular quantities. It is important to note that the scattered power depends also on cross correlations between fluctuating quantities represented by off diagonal elements such as $\langle \tilde{B}_i \tilde{n} \rangle$.

We have now outlined in which form we need to derive expressions for the microscopic fluctuations. This is the subject of the next section.

4 Kinetic model of electromagnetic fluctuations

Kinetic models of electrostatic microscopic fluctuations have been studied extensively (see for instance [25, 24, 20, 26]). Using Liouville's theorem ROSENBLUTH and ROSTOCKER [25] established the much–used dressed particle approach in the electrostatic approximation. This approach has also been applied to electromagnetic fluctuations [21, 7, 8]. Liouville's theorem cannot readily be applied to such fluctuations. It is, however, straightforward to extend the microscopic kinetic discussion of electrostatic fluctuations due to KLIMONTOVICH [20] to allow for electromagnetic interactions. We give a brief sketch of this here, which will serve to outline the physics basis of the model we use and confirm the validity of the dressed particle approach also

for electromagnetic fluctuations under appropriate assumptions. The discussion follows our development in [9] closely.

The microscopic fluctuations, $(\tilde{f}, \tilde{\mathbf{E}}, \tilde{\mathbf{B}})$, are governed by Maxwell's equations and the dynamic equation (6). Neglecting collisions eliminates the last two terms in (6). Neglecting the influence of other waves on the fluctuation spectrum, f and $\mathbf{F}$ simplify to $f = f^{(0)}$, $\mathbf{F} = 0$, where $f^{(0)}$ is the unperturbed macroscopic distribution function. Equation (6) then takes the form

$$\mathcal{L}\tilde{f} + \tilde{\mathbf{F}} \cdot \partial_{\mathbf{p}} f^{(0)} = 0 \,. \tag{23}$$

Integrating along characteristics we find that $\tilde{f} = \tilde{f}_T^{(0)} + \tilde{f}_T^{(1)}$, where the complementary function,

$$\tilde{f}_T^{(0)}(\mathbf{p}, \mathbf{r}, t) = \tilde{f}(\mathbf{p}'(T), \mathbf{r}'(T), T) \,, \tag{24}$$

is the soloution of

$$\mathcal{L}\tilde{f}_T^{(0)} = 0 \,, \tag{25}$$

and

$$\tilde{f}_T^{(1)}(\mathbf{p}, \mathbf{r}, t) = \int_T^t \tilde{\mathbf{F}}(\mathbf{r}'(\tau), \tau) \cdot \partial_{\mathbf{p}} f^{(0)}(\mathbf{p}'(\tau))\, d\tau \,, \tag{26}$$

is the particular integral. The characteristics, $(\mathbf{r}'(\tau), \mathbf{p}'(\tau))$, are the solutions to the coupled equations

$$\partial_\tau \mathbf{r}'(\tau) = \mathbf{p}'(\tau)/m \,, \quad \partial_\tau \mathbf{p}'(\tau) = q(\mathbf{v} \times \mathbf{B}^{(0)}) \tag{27}$$

$$\mathbf{p}'(t) = \mathbf{p} \,, \quad \mathbf{r}'(t) = \mathbf{r} \,.$$

We have chosen $\tilde{f}_T^{(1)}(\mathbf{p}, \mathbf{r}, T) = 0$, so $\tilde{f}_T^{(0)}(\mathbf{p}, \mathbf{r}, T) = f(\mathbf{p}, \mathbf{r}, T)$.

We note that the fluctuation in the distribution function naturally splits into two parts, $\tilde{f}_T^{(0)}$ and $\tilde{f}_T^{(1)}$. $\tilde{f}_T^{(0)}$ represents the evolution of the microscopic distribution $\tilde{f}$ from time T if particle interactions were neglected, i.e. the free streaming of fictitious particles along characteristics given by (27). In the following discussion we consider $\tilde{f}^{(0)} = \tilde{f}_{T'}^{(0)}$ where $t - T'$ is much larger than all characteristic times associated with the plasma dielectric response, and only formally let T' tend to minus infinity after ensemble averages have been taken. $\tilde{f}^{(1)} = \lim_{T \to -\infty} \tilde{f}_T^{(1)}$ given by expression (26) is the dielectric response of the plasma to the microscopic fields $(\tilde{\mathbf{E}}, \tilde{\mathbf{B}})$. Writing the

current $\tilde{\mathbf{j}}^{(1)} = q\int \mathbf{v}\tilde{f}^{(1)}\,d\mathbf{p}$ as the dielectric response, $-i\omega\varepsilon_0\boldsymbol{\chi}\tilde{\mathbf{E}}$, and letting $\tilde{\mathbf{j}}^{(0)} = q\int \mathbf{v}\tilde{f}^{(0)}\,d\mathbf{p}$ be the current associated with the motion of non–interacting charges, we have

$$\Lambda_{ij}\tilde{E}_j(\mathbf{k},\omega) = \frac{-i}{\omega\varepsilon_0}\sum_a \tilde{j}_i^{(a0)}(\mathbf{k},\omega) \tag{28}$$

where $\varepsilon_{ij} = \delta_{ij} + \sum_a \chi_{ij}^{(a)}$ and a indicates charged particle species. In the dressed particle picture $\tilde{f}^{(0)}$ represents the unscreened test particles while $\tilde{f}^{(1)}$ represents the screening of the test particles.

Inverting (28) and making use of the relations $\omega\tilde{\mathbf{B}} = \mathbf{k}\times\tilde{\mathbf{E}}$, $\tilde{\mathbf{j}}^{(e)} = \tilde{\mathbf{j}}^{(e0)} - i\omega\varepsilon_0\boldsymbol{\chi}^{(e)}\tilde{\mathbf{E}}$ and $\omega q_e\tilde{n}^{(e)} = \mathbf{k}\cdot\tilde{\mathbf{j}}^{(e)}$, we have

$$\tilde{\alpha}_i = \hat{\mathbf{S}}_{ik}^{(\alpha i)}\sum_{a\neq e}\tilde{j}_k^{(a0)} + \hat{\mathbf{S}}_{ik}^{(\alpha e)}\tilde{j}_k^{(e0)}\,, \quad \alpha_i = E_i,\, B_i,\, j_i,\, n\,, \tag{29}$$

where we have introduced the *fluctuation operators*:

$$\hat{\mathbf{S}}_{ik}^{(E)} = \Lambda_{ik}^{-1}\frac{-i}{\omega\varepsilon_0} \tag{30}$$

$$\hat{\mathbf{S}}_{ik}^{(B)} = \frac{k}{\omega}\epsilon_{ijl}\hat{k}_j\hat{\mathbf{S}}_{lk}^{(E)} \tag{31}$$

$$\hat{\mathbf{S}}_{ik}^{(ji)} = -\chi_{ij}^{(e)}\Lambda_{jk}^{-1}\,, \quad \hat{\mathbf{S}}_{ik}^{(je)} = \hat{\mathbf{S}}_{ik}^{(ji)} + \delta_{ik} \tag{32}$$

$$\hat{\mathbf{S}}_k^{(na)} = \frac{k_i}{\omega q_e}\hat{\mathbf{S}}_{ik}^{(ja)}\,, \quad a = i,\, e\,. \tag{33}$$

The transform of the correlation of any pair of the set of field and fluid variables can now be written

$$\left\langle\tilde{\alpha}_i\tilde{\beta}_{i'}\right\rangle = \hat{\mathbf{S}}_{ik}^{(\alpha i)}\left\langle\tilde{j}_k^{(i0)}\tilde{j}_{k'}^{(i0)}\right\rangle\hat{\mathbf{S}}_{i'k'}^{(\beta i)*} + \hat{\mathbf{S}}_{ik}^{(\alpha e)}\left\langle\tilde{j}_k^{(e0)}\tilde{j}_{k'}^{(e0)}\right\rangle\hat{\mathbf{S}}_{i'k'}^{(\beta e)*}\,, \tag{34}$$

so for instance

$$\left\langle\tilde{E}_i\tilde{E}_{i'}\right\rangle = \hat{\mathbf{S}}_{ik}^{(E)}\left\langle\tilde{j}_k^{(0)}\tilde{j}_{k'}^{(0)}\right\rangle\hat{\mathbf{S}}_{i'k'}^{(E)*} = \frac{\Lambda_{ik}^{-1}\Lambda_{i'k'}^{-1*}}{(\omega\varepsilon_0)^2}\left\langle\tilde{j}_k^{(0)}\tilde{j}_{k'}^{(0)}\right\rangle. \tag{35}$$

Here $\langle\tilde{j}_k^{(i0)}\tilde{j}_{k'}^{(i0)}\rangle = \sum_{a\neq e}\langle\tilde{j}_k^{(a0)}\tilde{j}_{k'}^{(a0)}\rangle$ and $\langle\tilde{j}_k^{(0)}\tilde{j}_{k'}^{(0)}\rangle = \langle\tilde{j}_k^{(i0)}\tilde{j}_{k'}^{(i0)}\rangle + \langle\tilde{j}_k^{(e0)}\tilde{j}_{k'}^{(e0)}\rangle$. In numerical calculations it is generally most efficient to retain the operator form.

The correlation tensor for the unscreened currents,

$$\left\langle \tilde{j}_k^{(a0)} \tilde{j}_{k'}^{(a0)} \right\rangle = q^2 \int v_k v_{k'} \left\langle \tilde{f}^{(a0)}(\mathbf{p}) \tilde{f}^{(a0)}(\mathbf{p}') \right\rangle d\mathbf{p} d\mathbf{p}' , \qquad (36)$$

can, for a homogeneous and stationary plasma, be expressed in terms of the unperturbed macroscopic distribution function for species a, $f^{(a0)}$, by solving expression (25) in the form

$$\mathcal{L}_{x,t} \left\langle \tilde{f}^{(a0)}(\mathbf{x}, t) \tilde{f}^{(a0)}(\mathbf{x}', t') \right\rangle = 0 \qquad (37)$$

with the initial condition

$$\left\langle \tilde{f}^{(a0)}(\mathbf{x}, t') \tilde{f}^{(a0)}(\mathbf{x}', t') \right\rangle = \delta(\mathbf{x} - \mathbf{x}') f^{(a0)}(\mathbf{x}) . \qquad (38)$$

The latter assumes that initial correlations at time T can be ignored as $(t' - T) \to \infty$. This is reasonable bearing in mind that the correlations are due to particle interactions which are absent for the fictitious test particles that $f^{(a0)}$ represents. The test particles are identical to the real particles at time T, so some time must pass before the correlations existing at that time are lost. Carrying out the integrations we find

$$\left\langle \tilde{\mathbf{j}}^{(a0)} \tilde{\mathbf{j}}^{(a0)} \right\rangle = (2\pi)^2 \frac{m_a q_a^2}{|k_{||}|} \int dp_\perp \, p_\perp \sum_{l=-\infty}^{\infty} \mathbf{c}_l \mathbf{c}_l^* f^{(a0)}(p_\perp, p_{||}) \qquad (39)$$

where

$$\mathbf{c}_l = \begin{Bmatrix} \frac{l\omega_{ca}}{k_\perp} J_l(k_\perp \rho) \\ -i v_\perp J_l'(k_\perp \rho) \\ v_{||} J_l(k_\perp \rho) \end{Bmatrix} , \qquad p_{||} = m_a \frac{\omega - l\omega_{ca}}{k_{||}} . \qquad (40)$$

Here $||$ and $\perp$ indicate the components of a vector parallel and perpendicular to $\mathbf{B}^{(0)}$, J_l are Bessel functions of the first kind of order l and J_l' their derivatives, $\rho = v_\perp / \omega_{ca}$ and $\omega_{ca} = q_a B^{(0)} / m_a$.

5 Comparative investigation of scattering model

The model of microscopic fluctuations, bilinear interactions and scattering, developed in the preceding sections is in many respects more comprehensive than earlier models. In this section we investigate the significance of the various physics aspects which have been included here and compare with simpler and earlier models.

5.1 Scattering from density, current and field fluctuations

In the present model we have included scattering due to density, current and field fluctuations. Frequently only scattering due to density fluctuations is included. This is in many situations an excellent approximation. Under certain conditions, which are of present experimental interest, scattering due to fluctuations in the other quantities is important and the phase relations between the fluctuations, accounted for by the cross correlations, is essential. To see this we note that the scattering function, Σ, consists of diagonal elements such as Σ_{nn} and Σ_{BB} and off diagonal elements such as Σ_{nB}. All elements satisfy the symmetry $\Sigma_{\alpha\beta} = \Sigma^*_{\beta\alpha}$, so $\Sigma_{\alpha\beta}$, considered as a matrix with indexes (α, β), is Hermitian. It follows that the diagonal elements and the sums $\Sigma_{\alpha\beta} + \Sigma_{\beta\alpha}$ are all real. While the diagonal elements are positive definite the real parts of the off diagonal elements may be either positive or negative. The off diagonal element $\Sigma_{\alpha\beta}$ has a maximum magnitude of $(\Sigma_{\alpha\alpha}\Sigma_{\beta\beta})^{1/2}$ and can thus significantly affect the scattering function when scattering from for instance density and magnetic field fluctuations are both important. Depending on the phase between the fields scattered from these fluctuations Σ may in some conditions be much smaller than the trace, $\Sigma_{nn} + \Sigma_{BB}$, or indeed twice that. The scattering function and diagonal elements plotted in Figure 1 demonstrate the former for near perpendicular scattering for parameters relevant to the CTS at TFTR.

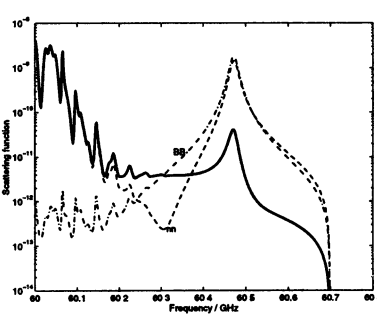

Figure 1: Σ, (solid curve) and Σ_{nn} and Σ_{BB} (broken curves, nn and BB), versus ν^s. $\nu^i = 70$ GHz, $B^{(0)} = 5$ T, $n_e = 10^{20}\,\mathrm{m}^{-3}$, $n_D = n_T = 0.48\,n_e$, $n_\alpha = 0.02\,n_e$, $T_e = 20$ keV, $T_D = T_T = 30$ keV. Alpha particles: classical slowdown distribution, $E_b = 3.5$ MeV, $v_c = 0.07\,v_{T_e}$. $\theta = \angle(\mathbf{k}^i, \mathbf{k}^s) = 20°$, $\phi = \angle(\mathbf{k}^\delta, \mathbf{B}^{(0)}) = 86°$. X to X mode scattering.

The structure at low frequencies is due to damped ion–Bernstein modes while the peak at $\nu^s \approx 60.47$ GHz is due to the fast magne-

tosonic wave. We note that there is a range of frequencies in which Σ is smaller than Σ_{nn} by up to two orders of magnitude and that in this range $\Sigma_{nn} \approx \Sigma_{BB}$ while $\Sigma_{nB} + \Sigma_{Bn} \approx -(\Sigma_{nn} + \Sigma_{BB})$, resulting in near cancellation of scattering from $\tilde{n}$ and $\tilde{\mathbf{B}}$.

5.2 Electromagnetic contra electrostatic

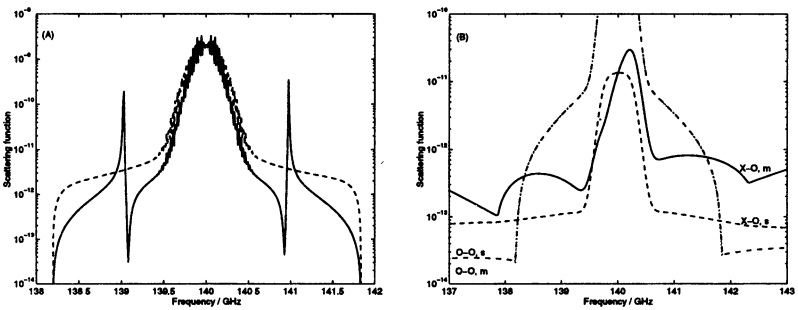

Figure 2: Electromagnetic and electrostatic versions of Σ versus ν^s. $\nu^i = 140\,\mathrm{GHz}$, $B^{(0)} = 3.4\,\mathrm{T}$, $n_e = 6{\times}10^{19}\,\mathrm{m}^{-3}$, $n_D = n_T \approx 0.5\,n_e$, $n_\alpha = 0.003\,n_e$, $T_e = 12$ keV, $T_D = T_T = 20$ keV. Alpha distribution as in Figure 1. $\theta = 20°$. (A): $\phi = 88°$, O to O mode, electromagnetic (solid curve), and electrostatic (broken curve). (B):$\phi = 70°$, X to O (X-O) and O to O (O-O) for electromagnetic (m) and electrostatic (s) models.

Another common simplification is to compute the microscopic fluctuations in the electrostatic approximation, that is, the screening of the test particles (we are referring here to the dressed particle picture discussed briefly in the preceding section) which is due to the dielectric response of the plasma is accounted for only in the electrostatic approximation as opposed to the full electromagnetic description used here. Again this is an acceptable approximation in many situations. It is not acceptable if the spectrum of fluctuations includes weakly damped electromagnetic waves, such as the fast magnetosonic wave, as demonstrated in Figure 2(A). It is also not generally acceptable for cross mode (eg. X to O) scattering as shown in Figure 2(B). For the O to O mode scattering, also shown in this figure, the electrostatic approximation is very good.

5.3 Moments models

The last difference we will discuss here between the present model and earlier models is the derivation of the source current used in the modelling of the bilinear interaction of waves. Until recently the most comprehensive and tractable model was derived from the cold fluid set of equations. Our model is based on a microscopic or kinetic description. There is no computational saving in the cold fluid model. Whether it is conceptually simpler is a matter of debate. The cold fluid model does, however, have important limitations in its range of validity which have only recently been uncovered [10, 12–18]. In particular it does not correctly describe scattering from microscopic fluctuations, a use to which it has often been put.

The fact that the low temperature kinetic expressions for the source current, (14) and (15), involve only zeroth and first order moments of the distribution functions of the two interacting waves suggests that the source current may be derived with the same generality from a sequence of moments of the kinetic equation (5). The simplest set of equations we will consider consists of the zeroth and the first moments of (5) (with $\langle \tilde{\mathbf{F}} \cdot \partial_{\mathbf{p}} \tilde{f} \rangle = 0$). In order to truncate the sequence of connected moments equations we assume that the second moment of the distribution function,

$$\overline{v_i v_j} = \int v_i v_j f \, d\mathbf{p} \,, \tag{41}$$

is related to the lower moments as

$$\overline{v_i v_j} = \frac{\overline{v}_i \overline{v}_j}{n} \,. \tag{42}$$

This is in fact the cold fluid model which Sitenko [27] and others used for deriving expressions for the source current. In these derivations the solution was found by a perturbation expansion of the fluid velocity $u_i = \overline{v}_i / n$. The result is

$$j_i^{\sigma} = \delta_{\alpha\beta}^{\mathrm{ab}} \left\{ \frac{\sigma_{ij}^{\alpha} E_j^{\alpha} n^{\beta}}{n^{(0)}} + \sigma_{il}^{\mathrm{s}} \epsilon_{lmn} u_m^{\alpha} B_n^{\beta} - \frac{i m_e}{q_e} \sigma_{il}^{\mathrm{s}} u_l^{\alpha} k_j^{\alpha} u_j^{\beta} \right\} . \tag{43}$$

Replacing a and b by i and δ and then using the linearized continuity equation, the linearized momentum equation, $u_i^{\mathrm{i}} = \sigma_{ij}^{\mathrm{i}} E_j^{\mathrm{i}} / (q_e n^{(0)})$,

and Faraday's law, all for i, expression (43) can be written as

$$j_i^\sigma = E_l^{\mathrm{i}} \left(\frac{\sigma_{il}^{\mathrm{i}} n^\delta}{n^{(0)}} + \frac{\sigma_{ij}^{\mathrm{s}} \epsilon_{jkm} \sigma_{kl}^{\mathrm{i}} B_m^\delta}{n^{(0)} q_e} + \frac{1}{c} \left\{ \sigma_{kl}^{\mathrm{i}} N_k^{\mathrm{i}} \delta_{im} \right. \right. \tag{44}$$

$$\left. \left. + \sigma_{ij}^{\mathrm{s}} \left[N_j^{\mathrm{i}} \delta_{lm} - \delta_{jl} N_m^{\mathrm{i}} - \frac{\omega^{\mathrm{i}}}{c\omega_p^2} \chi_{kl}^{\mathrm{i}} \left(\delta_{jk} k_m^{\mathrm{i}} + \delta_{jm} k_k^\delta \right) \right] \right\} u_m^\delta \right) ,$$

where $\omega_p^2 = n^{(0)} q_e^2 / (m_e \varepsilon_0)$. This expression for the source current of the scattered field in a magnetized plasma is identical to [28, expression (20.3)] and [27, expression (11.5)], except that we have used SI units. This model is accurate in the limit where the two interacting waves (in the case of scattering, the incident wave and the fluctuations) and the resulting scattered wave all are cold collective oscillations [13]. In this limit the predictions of the cold fluid model coincide with the predictions of the low temperature kinetic model. When one or both the interacting waves are not cold collective oscillations, as in the case of scattering from thermal fluctuations, then the cold fluid expressions (43) and (44) are not guaranteed to be accurate [10], indeed large errors may occur for collective scattering experiments in fusion plasmas [14]. For these situations the low temperature kinetic model given by expressions (14) and (15) should be used instead.

In [10] we noted that the failure of the cold fluid model in describing the interaction of arbitrary waves is due to the fact that the set of equations is solved by expansion in electron fluid velocity rater than electron flux and that the sequence of moments equations was truncated too early by assuming (42). We further showed that if the sequence of moments equations is truncated by assuming instead that the third moment of the distribution is zero,

$$\overline{v_i v_j v_k} = \int v_i v_j v_k f \, d\mathbf{p} = 0 , \tag{45}$$

so that the second moment $\overline{v_i v_j}$ is given by the second moment equation, and replacing the expansion in fluid velocity with an expansion in flux we recover the low temperature kinetic expressions (14) and (15).

We now consider in turn the effect of the early truncation (42) and the expansion in fluid velocity. Carrying out the expansion in

flux but applying the early truncation (42) we have [10, equation 96]

$$j_i^\sigma = \frac{\sigma_{il}^{\rm s}\delta_{\alpha\beta}^{\rm ab}}{n^{(0)}}\left\{ n^\alpha E_l^\beta + \epsilon_{lmn}\overline{v}_m^\alpha B_n^\beta - \frac{ik_j^{\rm s}m_e}{n^{(0)}q_e}\overline{v}_l^\alpha\overline{v}_j^\beta \right\}. \qquad (46)$$

The derivation of the low temperature kinetic expression for the source current (14) is based on an expansion in powers of velocity of the kernel of the integral operator σ_i (c.f. equation (12b)). The zeroth order terms of this expansion led to the terms $n^{\rm b}E_l^{\rm a} + n^{\rm a}E_l^{\rm b} + \epsilon_{lmn}\left(\overline{v}_m^{\rm b}B_n^{\rm a} + \overline{v}_m^{\rm a}B_n^{\rm b}\right)$ in (14), which we note have been recovered in (46). The first order terms in the expansion of the kernel of σ_i led to the term $Y_{lmn}^{\rm s}\left(\overline{v}_m^{\rm b}E_n^{\rm a} + \overline{v}_m^{\rm a}E_n^{\rm b}\right)/c$ which is not recovered in (46). We thus find that the difference between (46) and (14) is of first order in the small variables introduced in (13). Therefore, provided the conditions imposed by the inequalities in (13) are sufficiently well satisfied that the first order terms can be neglected the expression (46) like (14) is valid for arbitrary interacting waves a and b. When first order terms cannot be neglected (46) and (14) coincide in the limit where a and b are cold collective oscillations but not for arbitrary a and b.

To see the effect of expanding in fluid velocity rather than flux we turn now to comparing (46) with the cold fluid result (43). First we note that for arbitrary fluctuations the two expressions differ even in the lowest order terms. Making use of the relation $\mathbf{k}^{\rm s} = \mathbf{k}^{\rm a} + \mathbf{k}^{\rm b}$ we can rewrite (43) on the form

$$j_i^\sigma = \frac{\sigma_{il}^{\rm s}\delta_{\alpha\beta}^{\rm ab}}{n^{(0)}}\left\{ \frac{\Pi_{lj}^{\rm s}}{i\omega_p^2}\omega^\alpha\chi_{jk}^\alpha E_k^\alpha n^\beta + \frac{im_e}{q_e n^{(0)}}\overline{v}_l^\alpha k_j^\beta v_j^\beta \right. \qquad (47)$$

$$\left. + \epsilon_{lmn}\overline{v}_m^\alpha B_n^\beta - \frac{ik_j^{\rm s}m_e}{n^{(0)}q_e}\overline{v}_l^\alpha\overline{v}_j^\beta \right\},$$

where $\Pi_{ij}^\alpha = -i\omega^\alpha\delta_{ij} + \omega_c\epsilon_{ijk}\mathbf{B}_k^{(0)}/|\mathbf{B}^{(0)}|$. Note $(\omega^\alpha/i\omega_p^2)\Pi_{ij}^\alpha\chi_{jk}^\alpha = \delta_{ik}$.

In the limit where both interacting waves a and b are cold collective oscillations $\mathbf{E}_i^\alpha = (q_e/\varepsilon_0\omega_p^2)\Pi_{ij}^\alpha\overline{v}_j^\alpha$, α = a, b, and we have

$$\frac{1}{i\omega_p^2}\Pi_{lj}^{\rm s}\omega^{\rm a}\chi_{jk}^{\rm a}E_k^{\rm a}n^{\rm b} + \frac{im_e}{q_e n^{(0)}}\overline{v}_l^{\rm a}k_j^{\rm b}\overline{v}_j^{\rm b} = E_i^{\rm a}n^{\rm b}$$

and similarly with a and b interchanged. When these relations hold, (43) and (46) coincide. It thus appears that the effect of expanding in

fluid velocity rather than flux is to limit the range of validity of even the lowest order terms to the interaction of cold collective oscillations.

To understand where the difference between the two expansions arises we observe that the flux is linearly related to the distribution perturbation f while the fluid velocity is non–linear in f. Thus the fluid velocity perturbation, $\mathbf{u}^{\mathrm{s}}$, with frequency and wave vector of the scattered wave involves also the velocity distribution perturbations associated with the interacting waves, a and b:

$$\mathbf{u}^{\mathrm{s}} = \frac{\mathbf{v}^{\mathrm{s}}}{n^{(0)}} - \frac{\mathbf{v}^{\mathrm{a}} n^{\mathrm{b}} + \mathbf{v}^{\mathrm{b}} n^{\mathrm{a}}}{(n^{(0)})^2} \,. \tag{48}$$

By perturbation expansion of the first moment equation in $\overline{\mathbf{v}}$ we find that the flux associated with the scattered wave satisfies the relation

$$\begin{aligned} &\partial_t \overline{v}_i^{\mathrm{s}} - \frac{q_e}{m_e}(n^{(0)} E_i^{\mathrm{s}} + \epsilon_{ijk} \overline{v}_j^{\mathrm{s}} B_k^{(0)}) \\ &\quad = -\partial_{r_j} \overline{v_i v_j}^{\mathrm{s}} + \frac{q_e}{m_e}\left[n^{\mathrm{a}} E_i^{\mathrm{b}} + n^{\mathrm{b}} E_i^{\mathrm{a}} + \epsilon_{ijk}\left(\overline{v}_j^{\mathrm{a}} B_k^{\mathrm{b}} + \overline{v}_j^{\mathrm{b}} B_k^{\mathrm{a}} \right) \right] \end{aligned} \tag{49}$$

This equation can also be obtained as the first moment of

$$\mathcal{L} f^{\mathrm{s}} = -\mathbf{F}^{\mathrm{s}} \cdot \partial_{\mathbf{p}} f^{(0)} - \mathbf{F}^{\mathrm{a}} \cdot \partial_{\mathbf{p}} f^{\mathrm{b}} - \mathbf{F}^{\mathrm{b}} \cdot \partial_{\mathbf{p}} f^{\mathrm{a}} \tag{50}$$

which is the second order perturbation of the kinetic equation (5). When solving (49) with (42) for the scattered wave instead of (50) we approximate the detailed behavior of f^{s} by the behavior of its lowest moments and thereby introduce the low temperature approximation for the scattered wave. This does not prevent us from letting the interacting waves be governed by the first order kinetic equation

$$\mathcal{L} f^{\alpha} = -\mathbf{F}^{\alpha} \cdot \partial_{\mathbf{p}} f^{(0)} \,, \quad \alpha = \mathrm{a},\, \mathrm{b} \,. \tag{51}$$

In contrast to this, when expanding in $\mathbf{u}$ we find that the fluid velocity perturbation with the frequency and wave vector of the scattered wave is given by

$$\partial_t u_i^{\mathrm{s}} - \frac{q_e}{m_e}(E_i^{\mathrm{s}} + \epsilon_{ijk} u_j^{\mathrm{s}} B_k^{(0)}) = \delta_{\alpha\beta}^{\mathrm{ab}} \left\{ -\frac{u_k^{\alpha} \partial_{r_k} u_i^{\beta}}{n^{(0)}} + \frac{q_e \epsilon_{ijk}}{m_e} \overline{v}_j^{\alpha} B_k^{\beta} \right\} \tag{52}$$

from which the cold fluid source current is derived. Expression (52), unlike (49), does not in general permit the interacting waves to be

governed by (51). To see this we multiply (52) by $n^{(0)}$, subtract (49) and make use of (42) to find

$$\delta^{ab}_{\alpha\beta} n^{\alpha} \left\{ \partial_t \overline{v}_i^{\beta} - \frac{q_e}{m_e} \left(n^{(0)} E_i^{\beta} + \epsilon_{ijk} \overline{v}_j^{\beta} B_k^{(0)} \right) \right\} = 0 . \qquad (53)$$

As n^{a} and n^{b} are independent the identity in (53) generally only holds when the content of the curly bracket is identically zero,

$$\partial_t \overline{v}_i^{\beta} - \frac{q_e}{m_e} \left(n^{(0)} E_i^{\beta} + \epsilon_{ijk} \overline{v}_j^{\beta} B_k^{(0)} \right) = 0 , \quad \beta = \mathrm{a}, \mathrm{b} . \qquad (54)$$

(54) is the truncated first moment of (51) which holds only for cold collective oscillations. Hence we see that expanding in $\mathbf{u}$ rather than $\overline{\mathbf{v}}$ has the consequence of imposing the approximation implicit in the truncated sequence of moments equations not only on the scattered wave, but also on the two interacting waves. It is possible to show the more general result that if the expansion is carried out in a set of variables which is non–linear in f and the kinetic equation is approximated e.g. by a truncated sequence of moments then the limitations implicit in this approximation apply not only to the scattered wave but also to the interacting waves, while the limitations apply only to the scattered wave if the expansion is linear in f. It therefore matters which set of variables the expansion is carried out in, except when the complete kinetic model is applied.

References

[1] Bindslev H, Manuscript in preparation, see also Bindslev, *Proc. 7th Int. Symp. on Laser–Aided Plasma Diagnostics*, Fukuoka, Japan 60 (1996) (JET preprint JET–P(95)66) and Bindslev et al. this proc.

[2] Machuzak J S et al., *Rev. Sci. Instrum.* , **66**, 484 (1995).

[3] Hoekzema J A, et al., *Proc. 22nd EPS Conf. Contr. Fusion Plas. Phys.* (Bournemouth) **19C**, II, 445. EPS JET, UK (1995).

[4] Suvorov E V, et al., *Plasma Physics and Controlled Fusion*, **37**, 1207 (1995).

[5] Hughes T P and Smith S R P, *J. Plasma Physics*, **42**, 215 (1989).

[6] Bindslev H, *Plasma Physics and Controlled Fusion*, **33**, 1775 (1991).

[7] Chiu S. C., *Phys. Fluids B*, **3**, 1374-1380 (1991).

[8] Aamodt R E and Russell D A, *Nuclear Fusion*, **32**, 745 (1992).

[9] Bindslev H, *J. Atmospheric and Terrestrial Physics*, **58**, 983 (1996).

[10] Bindslev H, *Plasma Physics and Controlled Fusion*, **35**, 1615 (1993).

[11] Heikkinen J A and Dumbrajs O, *Proc. 22nd EPS* (see [3]) III 181.

[12] Bindslev H, *Plasma Physics Reports*, **20**, 33 (1994).

[13] Sitenko A G, *Plasma Physics and Controlled Fusion*, **37**, 163 (1995).

[14] Bindslev H, *Plasma Physics and Controlled Fusion*, **37**, 169 (1995).

[15] Sitenko A G, *Ukrainian Journal of Physics*, **40**, 450 (1995).

[16] Bindslev H, *Ukrainian Journal of Physics*, **40**, 457 (1995). (JET preprint JET-P(94)71).

[17] Sitenko A G, *Plasma Physics and Controlled Fusion*, **38**, 627 (1996).

[18] Bindslev H, *Plasma Physics and Controlled Fusion*, **38**, 639 (1996).

[19] Piliya A D, et al., *Phys. Plasmas*, **2**, 2314 (1995).

[20] Klimontovich Yu. L., *Kinetic Theory of Nonideal Gases and Nonideal Plasmas*. Pergamon Press, Oxford (1982).

[21] Sitenko A G and Kirochkin Yu A, *Sov. Phys. Uspekhi*, **9**, 430 (1966).

[22] Bekefi G, *Radiation Processes in Plasmas*. John Wiley and Sons, New York (1966).

[23] Bindslev H, *On the Theory of Thomson Scattering and Reflectometry in a Relativistic Magnetized Plasma*. D. Phil. Thesis, Oxford University, also available as Risø report: Risø–R–663(EN). (1992).

[24] Lifshitz E M and Pitaevskii L P, *Physical Kinetics 1st edition*. Pergamon press, Oxford (1981).

[25] Rosenbluth M N and Rostoker N, *Phys. Fluids*, **5**, 776-788 (1962).

[26] Sitenko A G, *Fluctuations and Non-linear Wave Interactions in Plasmas*. Academic Press, New York (1982).

[27] Sitenko A G, *Electromagnetic Fluctuations in Plasma*. Academic Press, New York (1967).

[28] Akhiezer A I, et al., *Collective Oscillations in a Plasma*. Pergamon Press, Oxford (1967).

EXPERIMENTS ON THE COLLECTIVE THOMSON SCATTERING OF POWERFUL 140 GHZ RADIATION AT W7-AS

E.V. Suvorov, A.B. Burov, Y.A. Dryagin, A.A. Fraiman, L.M.Kukin, A.V.Kostrov, L.V. Lubyako, D.A. Ryndyk, A.M.Shtanyuk, N.K. Skalyga, O.B. Smolyakova, V. Erckmann, H. Laqua*, T. Geist*, M. Kick*, W VII-AS Team*, ECRH Team*, NBI Team*, E. Holzhauer†, W. Kasparek†*

Institute of Applied Physics, Nizhny Novgorod, Russia
*Max-Planck-Institute für Plasmaphysik, Garching, Germany
†Institute für Plasmaforschung, Universitet Stuttgart, Germany

Powerful gyrotrons have a good principle prospects for using in collective Thomson scattering (CTS) experiments aimed to the investigation of ion distribution function. Their advantage as compared to e.g. CO_2 radiation sources is the possibility to use 90 degree scattering (instead of practically forward scattering) with good spatial resolution. Among other sources D_2O have demonstrated very good ability for ion temperature measurements in moderate size tokamaks [1,2], but these sources have very limited pulse duration which strongly reduces the sensitivity of CTS technique based on them. Powerful gyrotrons developed for electron cyclotron heating and current drive at present reached pulse duration of order of few seconds and now are challenging cw operation. This gives opportunity to increase essentially the sensitivity of CTS systems based on gyrotrons due to averaging procedure by so called radiometric gain $G = \sqrt{\Delta f \bullet \tau}$, where Δf is the bandwidth of the spectral channel and τ is the averaging time. With the typical bandwidth of order of hundred *MHz* the gain of 2-3 orders of magnitude and even more can be reached. This is the main reason why CTS experiments with the gyrotron as radiation source were planned and performed at a number of fusion installations [3-5]; the other reason is the fact that at present gyrotrons are available in many laboratories being involved in ECRH and ECCD experiments. In the present communication taking as an example CTS experiment at W7-AS we discuss the main problems related to using gyrotron as a radiation source in a moderate size installations. Some estimates will be given for possible gyrotron application to α-particle diagnostics in reactor-scale tokamak using CTS technique.

Installation, plasma parameters, scattering geometries

W7-AS is one of the biggest stellarators which may be considered as a moderate size fusion installation (major radius about 2 *m*, averaged minor radius about 0.2 *m*). Operating regimes of the installation are related to existing ECRH system based on gyrotrons delivering powerful radiation at 70 and 140 *GHz* (see more in detail e.g. Paper **H6** of the present volume), this implies that magnetic field in the stellarator is around the values 1.25 *T* (the second cyclotron harmonic for 70 *GHz*) and 2.5 *T* (the first harmonic for 70 *GHz* and the second harmonic for 140 *GHz*). Microwave power is injected into stellarator in sections where plasma column has elliptical cross-section strongly elongated in vertical direction; the magnetic field structure in these sections is close to that of a tokamak with rather low shear and radial variation with a scale length about 1.5 *m*. The typical plasma parameters are: $n_e = (0.2-1) \bullet 10^{14}$ cm^{-3}, T_e = (1-2) *keV*, T_i = (0.2-0.4) *keV*.

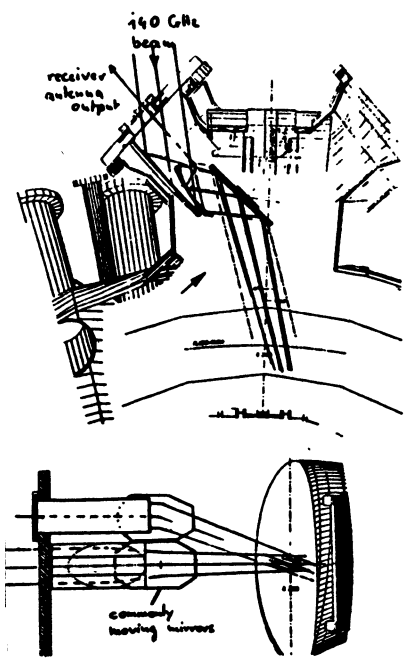

Fig. 1

CTS geometry in Section I.

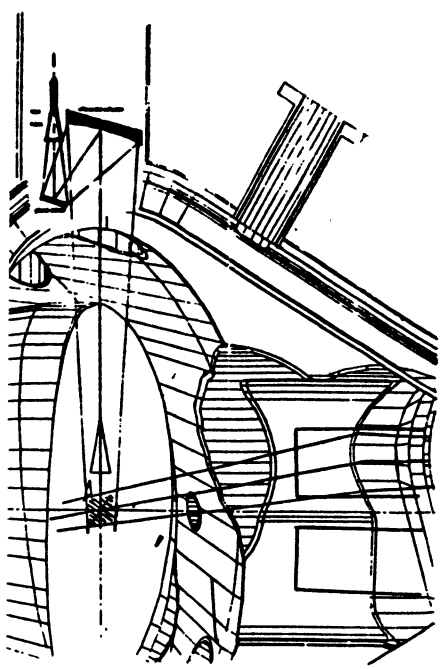

Fig. 2

CTS geometry in Sectrion II.

Two antenna blocks for CTS at 140 *GHz* are installed in two ECRH sections; both of them are using existing launching antenna systems for ECRH at 140 *GHz*. Receiving CTS antennae installed at present are essentially different from each other. Antenna installed in Section I is a circular monomode waveguide surrounded by reflecting mirror to form quasioptical rf beam in the plasma volume (see Fig.1) which introduces rather strong additional attenuation (25-30 dB) into receiving transmission line. This antenna is rigidly attached to the movable mirror of launching antenna for powerful gyrotron radiation thus forming a fixed scattering geometry close to back-scattering; this fixed antenna beam crossing geometry may be scanned both in vertical and horizontal directions. Receiving antenna installed in Section II is the conical horn with two reflecting mirrors (one is focusing and other is flat) with rather low losses and practically immovable vertical receiving radiation pattern (see Fig.2). Two 140 *GHz* gyrotrons are installed in this section; both of them provide scanning of horizontally launched rf beams in vertical and horizontal directions and may be used in principle for CTS with approximately 90 degree scattering geometry.

The polarization of radiation launched into the plasma is controlled by the universal polarizer in every rf beam. The scattered radiation may be analyzed in two orthogonal linear polarizations in Section I; in Section II only linear polarization corresponding to O-mode propagating transverse to the magnetic field may be analyzed. All rf beams (probing and receiving) are quasioptical with the circular cross-sections in the plasma, beam diameters are about 4 *cm*. This means that in Section I there is no spatial resolution along major radius of a torus, while in Section II there is a possibility to provide local measurements with the dimension of scattering volume about 4 *cm*.

Gyrotrons for CTS experiments at W7-AS

At present gyrotrons used in collective scattering experiments are designed as powerful microwave sources for plasma heating. However there are some essential differences in gyrotron parameters required for plasma heating and for collective scattering. For ECRH it is necessary to provide high power in a long pulse at the frequency corresponding to ECR condition. For collective scattering usually it is enough to have moderate power with moderate (sometimes even short) pulse duration, but additional rather strong requirement are: the mode purity, low frequency drift during the measurements and very high from-shot-to-shot stability of gyrotron operat-
9*

ing regime. Besides in order to diminish the level of ECE noise accompanying the scattering signal it is highly desirable that the frequency of probing radiation should be somewhere between electron cyclotron harmonics.

A rather serious problem for the moderate size installations is high level of the stray radiation. It has a few aspects. First of all it is necessary to protect the mixer of the detection system; to provide this notch-filters are very useful, in order to avoid overloading in some cases it is necessary to introduce additional attenuation at the input of the receiver which, of course, diminishes the level of scattered signal as well. Another problem is CTS measurements in ECRH regimes of W7-AS operation. As it was discovered in experiments, it is impossible to perform measurements of CTS signal in ECRH regimes when a number of tubes are operating simultaneously. Because of slight difference in operation frequencies of various tubes these frequencies are as a rule within detection system band of analysis and outside the suppression band of notch-filter; stray radiation of these tubes result in overloading of the detection system under arbitrary experimental conditions. Moreover even the operation of 70 *GHz* ECRH system overloads detection system due to scattered radiation at the second harmonic of tube operation frequency. The best solution of this problem would be using for collective scattering a specially designed tube at the different frequency; another approach is the construction of step-tunable tube which in the main regime provides powerful long pulsed radiation for ECRH and in auxiliary regime provides output power at slightly different (by 10-15 %) frequency with moderate power and pulse duration satisfying all necessary conditions for probing radiation. And, finally, with the stray radiation at the probing frequency an eigen noise generated by the gyrotron besides the main line comes to the detection system as a parasitic signal which cannot be eliminated by the notch-filter; the only way to minimize this noise is to provide as good as possible decoupling between emitting and receiving antennae.

Investigations of frequency drift and of from-shot-to-shot stability of operation regimes were performed for four 140 *GHz* gyrotrons with possess rf pulse parameters presented in the Table I

Table I

Gyrotron	Power	Pulse duration	Section
ALPHA I	0.5 *MW*	0.5 *sec*	I
ALPHA II	0.4 *MW*	1.1 *sec*	I
CHARLY	0.5 *MW*	3.0 *sec*	II
ECHO	0.5 *MW*	3.0 *sec*	II

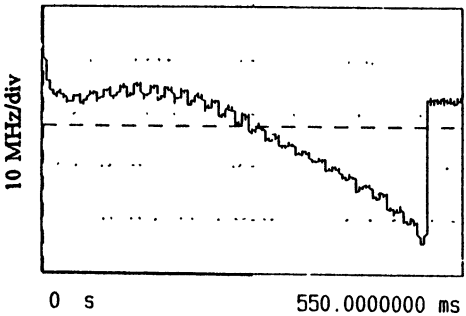

a) ALPHA I

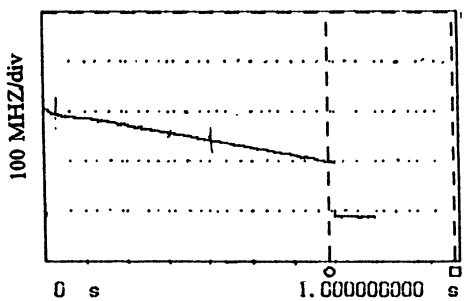

b) ALPHA II

Fig. 3

Evoluion of radiation frequency of "short" pulse tubes.

The frequency variation for tubes ALPHA I and ALPHA II are presented in Fig.3 (*a* and *b*). It can be seen that these tubes demonstrate two different types of frequency evolution during rf pulse: the total frequency variation for ALPHA I does not exceed 25 *MHz* during 0.5 *sec* pulse; for ALPHA II there is practically linear frequency drop during 1 *sec* pulse with the rate -100 *MHz* per second. Both tubes have very high from-shot-to-shot stability of operation regime (within few *GHz* of frequency deviation). For long pulse tubes CHARLY and ECHO three-dimensional plots spectrum versus time are presented in Fig.4. For these tubes programmed establishing of quasi-steady-state regime of microwave power generation is provided; during this stage rather fast frequency drift of the main line takes place. These transient regimes are strongly different for two tubes: for CHARLY during transient time about hundred *ms* the variation of central line frequency is about 600 *MHz*; the corresponding values for ECHO are $\approx$ 70 *ms* and $\approx$ 70 *MHz*. From-shot-to-shot stability in the transient regime for CHARLY is not satisfactory; so it is practically impossible to use this for CTS measurements in a short pulse. With ECHO this is possible due to higher repetition stability. In a quasi-steady-state stage of rf pulses repetition stability is satisfactory for both tubes.

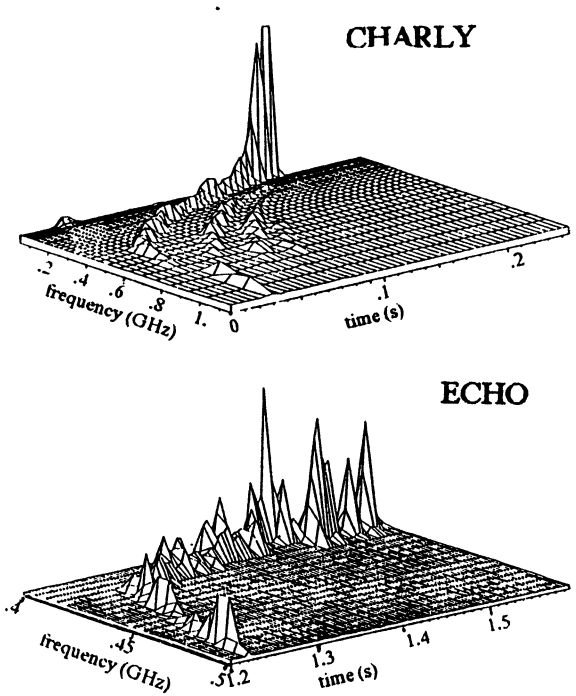

Fig. 4

Spectrum evolution of radiation of long pulse tubes.

Detection system

The detection system is based on the superheterodyne receiver with the Shottkey balanced mixer and BWO local oscillator with the output power about 50 *mW* tunable within frequency range 110-170 *GHz*; nominal heterodyne power needed for the mixer operation is about 5 *mW*. The noise temperature of the receiver referred to the mixer is about 0.2 eV. LO phase locking system proides relative frequency stability better than 10^{-8}.

At the receiver input notch-filter for suppression of stray radiation and high-frequency attenuator are introduced. Tunable notch-filter based on the monomode rectangular waveguide with a number of cylindrical cavities coupled to it [6] provides attenuation more than 40 *dB* in the ± 20 *MHz* band from the line center; attenuation outside ± 100 *MHz* band from the line center in not more than 3 *dB*. Electrically controlled attenuator at the receiver input increases the dynamical range of the detection system operation within 0 - 50 *dB*. It also provides protection of the mixer (by means of programmed gating at -50 *dB* level) from the stray radiation which may be presented outside the notch-filter suppression band in some regimes of stellarator operation or in transient regime of gyrotron operation.

In spite of syperheterodyne receive the main regime of the detection system operation is based on the "homodyne scheme" in which LO frequency coincides with the frequency of probing radiation. This scheme

assumes that the scattered radiation spectrum is symmetric with respect to the probing radiation line and up- and down- shifted frequencies after mixing are summed into the same IF range. So the analysis of scattered spectrum is performed at intermediate frequencies. IF spectrum analyzing system includes two filter banks. The main frequency analyzer cover the range of analysis from 50 to 1200 *MHz* and consists of 32 closely packed channels with the relative bandwidth of every channel and the relative frequency difference between adjacent channels being about 10 %. Decoupling between centers of adjacent channel is better than 20 *dB*. The main frequency analyzer is capable to cover the thermal ion feature in a rather wide range of plasma parameters (D and H plasmas, ion temperatures from 0.1 to 2 *keV*, scattering angles from 60 to 180 *deg.*) "Zoom" frequency analyzing covers total band of analysis about 100 *MHz*. It consists of 20 identical channels with the bandwidth about 5 *MHz* and the same separation between adjacent channels. "Zoom" system is tunable within total band of the main frequency analyzing system and provides principle opportunity to investigate possible fine structures in the spectrum of scattered radiation. Intrinsic integration time of the detection system is about 1 ms which provides "radiometric gain" from ≈50 (in narrow channels) to ≈200 (in wide channels).

Analog outputs from all 52 channel comes to data acquisition system in which ADC with high sampling rate (essentially higher than inverse natural integration time of the system) provides storage of digital information during the whole plasma shot up to 1 sec duration. A number of routines provide data processing of stored information, in particular, it is possible to increase "radiometric gain" using long gyrotron pulses for CTS.

Calibration of the detection system

The laboratory calibration of the detection system was performed using gas discharge noise source and demonstrated that expected sensitivity was achieved.

The experimental results obtained up to now are mainly related to the scattering geometry in Section I with using ALPHA II tube. Due to the fact that the receiving antenna in this Section is looking practically in the direction of major radius there is a very nice possibility to perform absolute calibration throughout the whole receiving transmission line (including receiving antenna) using black-body plasma radiation at the second electron cyclotron harmonic as a calibration source. In order to avoid all disturbances from the gyrotron operation the calibration was performed with

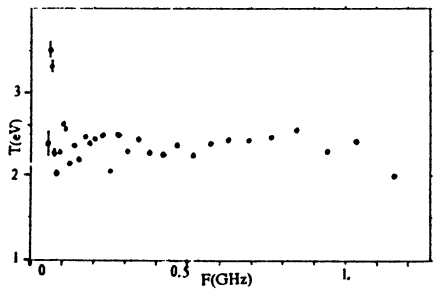

Fig. 5

Spectrum of ECE at the 4-th harmonic registered by CTS detection system.

the plasma supported by NBI heating system only. Comparing output signals from gas discharge noise tube and from the plasma gives opportunity to estimate the signal attenuation in the transmission line which is within 30-35 *dB*.

Fig.5 presents the result of ECE measurements at the fourth cyclotron harmonic. It can be clearly seen that in spite of strong attenuation in the transmission line flat ECE spectrum is registered at a rather low level (about 2 *eV*) which confirms the sensitivity of the registration system. Absolute value of ECE radiation temperature at the fourth harmonic is also confirmed by independent measurements with routine ECE diagnostic system operating at W7-AS.

Unfortunately the possibility of absolute calibration does not exist in the scattering geometry in Section II. Relative calibration can be performed there using either gas discharge noise source or "grey-body" ECE at the second harmonic. Only some indirect considerations can be used for estimates of the absolute values of scattered signal.

Experimental results

The main aim of CTS experiments at W7-AS is the detection of thermal ion features in the scattered signal. The signal value in terms of noise equivalent temperature may be estimated as (see also [7]):

$$T_s(eV) = 350 G_p G_b P_0(MW) \bullet \left(\frac{L}{20cm}\right) \bullet \left(\frac{4cm}{d}\right)^2 \left(\frac{n_i}{10^{14}}\right) \sqrt{\frac{m_i}{m_p}} \frac{1}{\sqrt{T_i(keV)}}$$

where G_p and G_b are polarization factor and emitting-receiving antenna beam crossing factor respectively, P_o is the probing radiation power in *MW*, L is the length of scattering volume in the direction of probing beam propagation, d is the diameter of emitted and receiving beams; the remaining values are quite evident. The estimate is presented for the probing radiation frequency 140 *GHz* used in W7-AS CTS experiment. Due to un-

certainty of G_p and G_b factors the expected signal level is uncertain as well and may be estimated as being equal from ten to few tens of *eV*. So in order to avoid strong ECE background CTS measurements were performed with magnetic field value 1.25 *T*. This resulted however in the enhanced level of stray radiation because it was practically not absorbed by the plasma which circumstance limited pulse duration of the probing radiation.

To minimize the stray radiation level a number of gyrotron pulses were fired into the empty chamber with the different orientations of launching-receiving antenna block. In the optimal position the stray radiation level at the receiving antenna input was less than 100 *W* which corresponded to antenna decoupling about up to 40 *dB*.

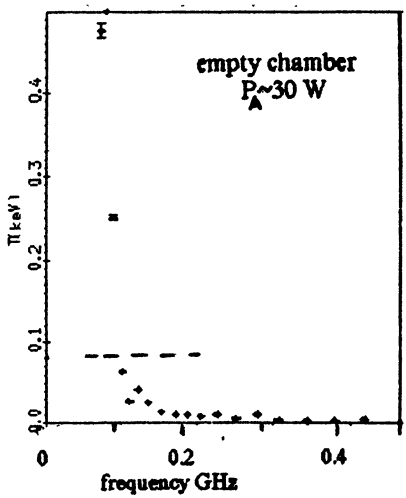

Fig. 6

ALPHA II noise spectrum (crosses) together with ALPHA I noise spectrum from [8] (dashed line).

Shots to the empty chamber were used for the measurement of the spectrum of eigen gyrotron noise in the band of the detection system analysis. The resulted spectrum for optimal antenna position is presented in Fig.6. The dashed line presents the spectrum of eigen noise of ALPHA I tube normalized to the same power which was measured in IAP [8] using quite different high-voltage power supply and different measurement procedure. These noises are comparable by the order of magnitude but possess rather different spectra. The reason of this discrepancy is not clear; it may be due to different power supply or due to difference of two tube designs or even possibly due to additional amplitude noises resulted from the detection of phase noises at the slope of notch-filter characteristics which was not the case in the first measurement presented in [8]. CTS measurements in the half magnetic field regimes may be performed only with short enough rf pulses because launching of high power in a long pulse into the empty chamber (or into nor absorbing plasma) is not desirable. The duration of pulses used in reality was not longer than $\approx$ 50 *ms*.

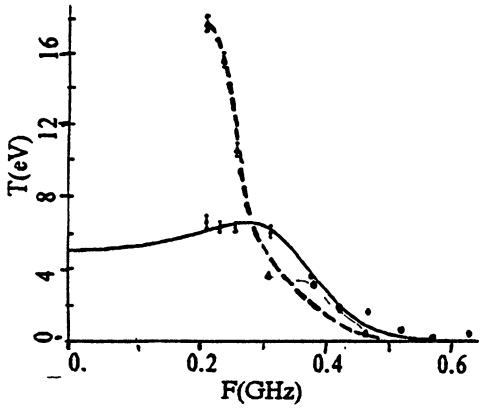

Fig. 7

Examples of ion feature in CTS spectra for plasma densities $4 \bullet 10^{13}$ cm^{-3} (solid line) and $7 \bullet 10^{13}$ cm^{-3} (dashed line).

Measurements of CTS thermal spectra were performed in alternative sequences of gyrotron shots into the empty chamber and into NBI supported plasma with toroidal magnetic field 1.25 *T*. The spectra resulted due to scattering of probing gyrotron radiation by the plasma were obtained as the difference between signals measured with and without plasma with the same position of antenna block. An example of CTS spectra obtained with this subtraction procedure [9] is presented in Fig.7 for two different plasma densities. The signal level is higher for higher density as it should be expected. Slight decrease in the total bandwidth of measured spectrum with the density increase together with more than proportional increase in the signal amplitude may be qualitatively understood basing on the refraction effect. Another example with more careful fitting procedure [4] to provide the best coincidence with theoretically calculated spectrum is presented in Fig.8.

Attempts to detect ion feature in scattering signal on the strong ECE background in the full magnetic field regimes of machine operation were not successful. Instead quite unexpectedly a very strong narrow-band scattered signal was discovered in the lower-hybrid frequency range. The signal arose simultaneously with the launching into the plasma

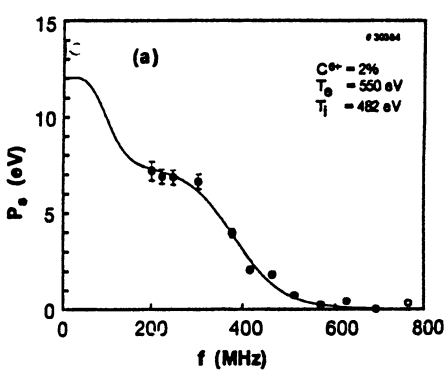

Fig. 8

Experimental (dots) and fitted (solid line) spectra: fitting by T_i variation with its relative profile fixed.

of hydrogen neutral beam for charge exchange diagnostics. This peculiarity was carefully investigated with the "zoom" system in a wide range of plasma parameters and was interpreted as LH wave instability triggered by transverse ion beam arriving in the plasma with the launch of diagnostic NB into it. An example of measured spectrum is given in Fig.9. For more details on the experimental and theoretical investigations of this phenomenon see Paper N5 presented to this Conference.

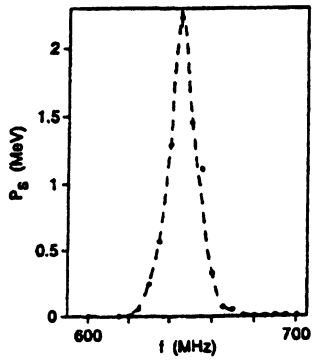

Fig. 9

CTS spectrum from LH turbulence.

Prospects for alpha-particle diagnostics

Due to long pulse operation gyrotrons in the frequency range 140-200 GHz seem to be rather attractive for α-particle diagnostics in reactor scale installations. First experimental results from CTS experiments at JET are presented in the Paper **H12** in this volume. The main and pleasant difference of large installations from moderate size one considered in the present communication is an extremely low level of stray radiation. This removes the problem of gyrotron noise subtraction from the measured spectra and essentially increases reliability of the data obtained in experiments. The main noise source remaining in CTS spectra obtained from large installations is ECE back ground. The estimate of CTS signal from α-particles may be obtained from the given above formula for 140 *GHz* probing radiation frequency. Taking beam diameters 4 *cm*, and scattering angle 30° (which means L = 20 *cm*) for typical α-particle energy $T_\alpha \approx 2.5\ MeV$ one gets the full bandwidth of scattered signal about 4 *GHz*. With the moderate bandwidth of analyzing channel 100 *MHz* and gyrotron pulse duration about 1 *sec* it is possible to obtain "radiometric gain" about 10^4. This gives that with 1 % of α-particle content in D-T plasma with the density $10^{14}\ cm^{-3}$ signal-to-noise ratio is about unity for $T_{ECE} \approx 10\ keV$. So the principle possibility of α-particle detection exists taking into account higher α-particle content in the burning plasma. However it is a matter of very careful investigation to search for probing radiation frequency, scattering geometry and types of normal waves in probing and scattering radiation which provide low enough ECE background coming to the receiving antenna and low cyclotron absorption of

both probing and scattered beams between antennas and scattering volume. This should be done using ray-tracing technique with the detailed and exact modeling of the density, temperature and magnetic field distributions in the real installation but preliminary investigations on the rough models point to some possible solutions.

Conclusions

Both thermal and nonthermal CTS spectra were registered at W7-AS in the proof-of-principle experiment using gyrotron as a source of microwave radiation. As it became clear at moderate size installation such as W7-AS a special care should be provided to diminish the level of stray radiation which introduced additional parasitic signal to that resulted from scattering by plasma density fluctuations. It has beed demonstrated also that a separate tube with the radiation frequency different from EC harmonics should be used in CTS exepriments with the intense ECR plasma heating. Another possibility is to design step-tunable gyrotron which may be used both in the full power long pulse regime for plasma heating and in CTS experiments with the different (by 10-15 %) frequency. In the last regime extremely high power and long pulse are not needed, but instead it is necessary to provide high mode purity, low frequency drift during diagnostic rf pulse and high from-shot-to-shot stability of spectral parameters of probing radiation.

The next step in W7-AS CTS experiments will be change for Section II with another tube as source of probing radiation and another (90 *deg.*) scattering geometry which provides localization of scattering volume and therefore more explicit model for fitting with culculated spectra.

The work has been supported by German Bundesministerium fur Forschung und Technologie.

References

1. R.Behn, D.Dicken, J.Hackmann et al., *Phys.Rev.*, 1989, **v.62**, No 24, p.2833.
2. M.Born, H.-D.Dicken J.Hackmann et al., *Plasma Phys.& Contr.Fusion*, 1993, **v.34**, pp. 391-396.
3. S.Cirant, *et.al.*, 1991, "Feasibility of an Ion Temperature Diagnostics for the High Magnetic Field FTU Plasma using Collective Scattering of mm-waves", Preprint IFP FP 91/8, Milano-Italy.

4. E.V.Suvorov, *et.al.*, *Plasma Phys. and Control.Fusion*, 1995, **v.37**, pp.1207-1213.
5. J.A.Hoekzema, *et.al.*, 1995, 22-nd EPS Conf. on Contr.Fusion and Plasma Phys., Contributed Papers, Part II, pp.445-448, Bournemouth, 3rd-7-th July, 1995.
6. Yu.Dryagin, N.Skalyga and T.Geist, *Int.J. of Infrared and MM Waves*, 1995, **v.17**, N 7, pp.1199-1204.
7. E.V.Suvorov, 1991, High Power Microwave Generation and Applications, Proc. of the Course and Workshop, pp.79-99, Villa Monastero - Varenna, Italy.
8. A.N.Kuftin, L.V.Lubyako and N.K.Skalyga, Scientific-Technical Meeting on MM and subMM Wave Propagation and Applications, Kharkov, 1992, Abstracts, p.35.
9. E.V.Suvorov, *et.al.*, 1995, Proc. of the 9-th Joint Workshop on ECEand ECH, Borrego Springs, California, 23-26 January 1995, ed. by John Lohr, pp.501-508.

COLLECTIVE THOMSON SCATTERING OF MILLIMETRE WAVES IN JET

H Bindslev, J Egedal, J Fessey, J Hoekzema, T Hughes

JET Joint Undertaking, Abingdon, UK

Abstract

Initial results from The JET Collective Thomson Scattering diagnostic are presented along with estimates of its full diagnostic capability. It is shown that for diagnosis of alpha particle distributions electron cyclotron emission (ECE) received via wall reflections must be reduced by installation of a viewing dump and that at the highest temperatures down shifted ECE radiation in direct view of the receiver is a serious limitation. Finally it is shown that significant anisotropies must be expected in the distributions of thermo–nuclear fusion products. Methods of diagnosing such anisotropies are being considered.

1 Introduction

The JET Collective Thomson Scattering (CTS) diagnostic is expected to be fully operational shortly, providing spatially resolved measurements of the fusion alpha particle and other fast ion velocity distributions. During initial short pulse operation the bulk ion feature was observed, with traces of ICRH driven tails. The signal to noise ratios were in good agreement with theory, indicating that, when fully operational, the diagnostic should be able to measure fast ion distributions.

A 500 kW, 140 GHz gyrotron generates the probing radiation. The frequency of 140 GHz was chosen because the spectrum of scattered light remains sensitive to the fast ion distribution at relatively large scattering angles, refraction is tolerable and a source with sufficiently high power and long pulse length was available. The injected power has to be modulated to discriminate between the scattered radiation and the much brighter (by 2 to 3 orders of magnitude) background radiation from electron cyclotron emission (ECE). Fluctuations on the background radiation are the main source of noise.

For standard plasmas with toroidal magnetic fields of 3.4 Tesla, ECE at 140 GHz emanates primarily from the inner and outer edges of the plasma where 140 GHz corresponds to the fundamental and second harmonic of the cyclotron frequency respectively. The ECE background is consequently at a minimum at the probing frequency. The launch and receive antennas, placed at top and bottom of the torus respectively, can both be rotated about two axes providing variable scattering geometry and permitting the localized measurement to be shifted spatially.

2 Diagnostic system

A schematic overview of the diagnostic is given in Figure 1. Only a brief description is given here with emphasis on the initial performance. A more detailed description of the system can be found in COSTLEY ET AL. (1988) and HOEKZEMA ET AL. (1992, 1993).

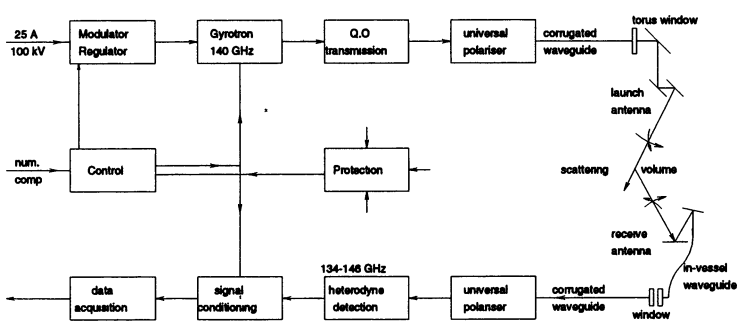

Figure 1: Schematic overview of the diagnostic

The gyrotron can generate 500 kW RF at 140 GHz for 0.5 s. It is important that the RF output is spectrally clean (i.e. power in spurious frequencies in the spectral range of interest > 80 dB down on power in the main frequency) because radiation in spurious frequencies, entering the receiver as stray light, cannot be discriminated from scattered radiation. Spurious frequencies were observed during switch-on and switch-off but not during the flat top of the pulse except at the highest power levels. For the initial operation the gyrotron was switched on at 120 Hz for a number of pulses of 1 ms duration.

The output of the gyrotron is mainly (> 90%) in a Gaussian beam. The high power transmission line (Figure 2) uses a combination of quasi-optical and waveguide propagation. The first part of the transmission system is quasi-optical. Most of the non-Gaussian power is lost from the beam in this section which includes a polariser to produce the desired elliptical polarisation to couple to either the Ordinary or the eXtraordinary mode in the plasma. The Gaussian beam is then coupled into oversized (ID 88.9 mm) corrugated waveguide in which the radiation propagates in the $HE_{1,1}$ mode. Proper alignment of the beam into the waveguide and of the waveguide itself is crucial to avoid significant mode conversion, which would affect the quality of the beam at the end of the waveguide.

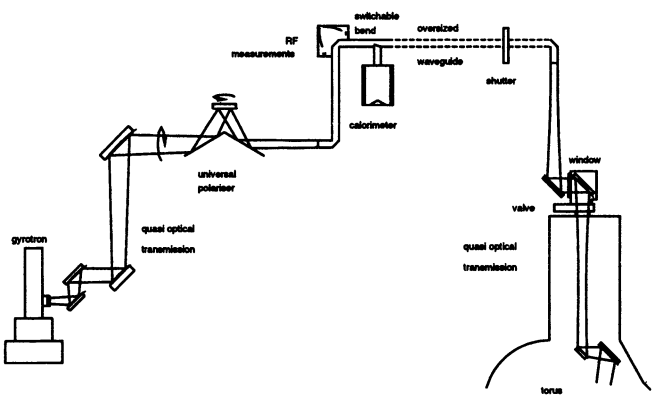

Figure 2: The high power 140 GHz transmission system

With correct alignment, the transmission efficiency of the 60 m. long waveguide run, which includes 7 mitre bends, was extremely good and the burn pattern on thermosensitive paper at the end of the waveguide was closely Gaussian. The RF power level at the torus was about 370 kW.

The last part of the high power transmission line is again quasi optical and a focused Gaussian beam, with a waist radius of 30 mm at the plasma centre, is launched into the torus via a steerable mirror from a top port. For the antenna orientations used in the first measurements, only about 10 mW was coupled to the receiver as stray light.

The receive beam also has a waist radius of 30 mm in the plasma centre and the spatial resolution for the measurement is therefore around 100 mm, dependent on the chosen scattering angle. Via a steerable mirror, the receive beam is focused into corrugated waveguide, which initially has a small diameter (ID 10 mm) to allow curvature around the divertor systems in the bottom of the torus. It is tapered up to 31.75 mm in the bottom port and is continued for $\approx$ 40 m to the detection system where the radiation is coupled into fundamental waveguide via a polariser. The attenuation in the main receive waveguide run is only a few dB. For the initial experiments, relative calibration was obtained by assuming the radiation from the plasma (ECE) is constant in the spectral range of interest and approximate absolute calibration by comparing these signals with those measured by a calibrated ECE diagnostic (although this has a different viewing line through the plasma). Optimum overlap of emitter and receiver beam patterns was established by scanning the main receiver beam from shot to shot. Before the detection system, 2 fundamental waveguide notch filters in series removed the stray light. The stray light attenuation at the centre frequency was at least 80 dB and the full notch width 200 MHz at -3 dB. The heterodyne detection system measures the spectrum between 134 and 146 GHz in 32 channels. The channel bandwidth is chosen to be proportional to the frequency shift. For the measurement of the thermal ion feature only 10 channels closest to the central frequency are of interest. Of these, calibration of the most central 2 or 3 channels is somewhat uncertain due to the effect of the notch filters.

2.1 Results

For the initial measurement the O-mode was selected both for injection and detection. Ray tracing calculations were done to calculate the required antenna directions and polariser settings for an expected plasma. The scattering volume was placed in the centre of the plasma and a scattering vector $|k| = 1500\,\mathrm{m}^{-1}$ was chosen. The scattering angle $\theta = \angle(\mathbf{k}^{\mathrm{i}}, \mathbf{k}^{\mathrm{s}}) = 32°$ while $\phi = \angle(\mathbf{k}^{\delta}, \mathbf{B}) = 122°$. $\mathbf{k}^{\mathrm{i}}$ and $\mathbf{k}^{\mathrm{s}}$ are the wave vectors of the incident and scattered radiation respectively. In operation, only the viewing direction of the receiver beam was adjusted to optimise the overlap. The scattering geometry is slightly different for different plasma parameters, due to the effect

of refraction, and was recalculated using the actual plasma parameters. In practice, optimum overlap of the launch and receive beams was lost whenever the plasma magnetic configuration or the density was significantly changed. Generally, a number of similar plasmas were required to optimise the overlap. It should be easier to find the optimum overlap when the slave receivers are operational.

Clear scattering signals were seen from plasmas with $B_0 > 3$ T [HOEKZEMA ET AL. (1995)]. A sample of the raw data is given in Figure 3. These data were taken shortly after a sawtooth collapse. It is seen that the background radiation is going down (cooling of the outer region where this radiation is emitted) while the scattering signal goes up (re-heating of the central region where the scattering volume is located). For this particular discharge, the scattered radiation in the centremost channels was higher than expected, indicating there may still be an effect of scattering off non–thermal fluctuations up to a frequency shift of 100 MHz.

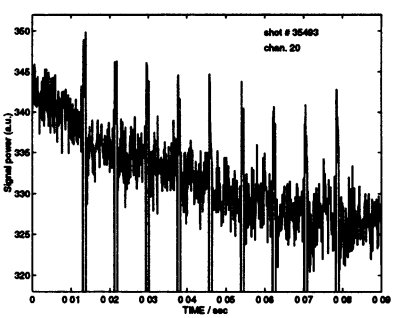

Figure 3: Raw data at $\Delta\nu \approx$ 600 MHz from a plasma with $B = 3.1$ T, $n_e = 3 \times 10^{19}\mathrm{m}^{-3}$, $T_e = T_i = 3$ keV, 1.4 MW hydrogen minority heating (ICRH). Nine 1 ms pulses are injected at 120 Hz.

It is also clearly seen from Figure 3 that during switch-on and switch-off of the gyrotron the receiver is saturated. This is due to spurious frequencies generated during switch-on and switch-off which are outside the notch and enter the receiver as stray light. In some channels, at frequencies where spurious signals are present, positive spikes are seen during these periods. Although the receiver seems to recover quickly from these spikes, detailed analysis shows that there are still some saturation effects during the gyrotron pulse. It is possible that this is due to a relatively high power level at frequencies where the detection system is blind, i.e. at frequency shifts around 50 MHz where the notch filters start to transmit. For fast ion measure-

ments, when much smaller scattering signals have to be detected, it will be important to avoid these effects (by using a wider notch filter and clipping the power during switching). At magnetic field values below 3 T no clear scattering signals were found. This was expected since 2nd harmonic absorption starts to interfere around 3 T.

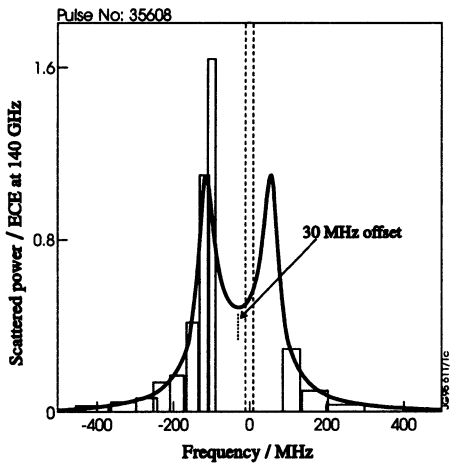

Figure 4: Spectral intensity of scattered light normalized to spectral intensity of ECE at 140 GHz. Shot # 35608 at 57.5 sec. with 5 MW ICRH, $T_{\mathrm{ECE}} \doteq 325$ eV. **Histogram**: Measured signal integrated over 2 gyrotron pulses (1.6 ms).
Curve: theoretical fit. Given: $B = 3.1$ T, $n_e = 4.1 \times 10^{19}\mathrm{m}^{-3}$, $T_e = 3.0$ keV. $\theta = 32°$, $\phi = 122°$. Fitted: $n_{D1} = 1.2 \times 10^{19}\mathrm{m}^{-3}$, $T_{D1} = 3$ keV, $n_{D2} = 0.8 \times 10^{19}\mathrm{m}^{-3}$, $T_{D2} = 20$ keV, $n_N = 0.3 \times 10^{19}\mathrm{m}^{-3}$, $T_N = 3$ keV.

An example of a scattering spectrum is given in Figure 4. The histogram represents the measured spectral intensity in each channel normalised to that of ECE at 140 GHz, which in this case was at a rather low level of 325 eV (for comparison, the alpha feature will only have a radiation temperature of a few eV). A theoretical fit is also given, based on B, n_e and T_e values from other diagnostics while the ion parameters are fitted. The fit is only illustrative. It assumes that the central peaks are due to Nitrogen. The shift of ≈ 30 MHz could be induced by a toroidal drift velocity of 1.6×10^5 m/s. Power accountability is quite good (although the absolute calibration is only approximate): The absolute level of the measured spectral intensity is $\approx 70\%$ of that predicted by theory for perfect beam overlap. The post detection signal to noise ratio, defined as the ratio of the scattered signal to the fluctuations on the total signal, varies over the spectrum between ≈ 10 and ≈ 100. Similar values are found for other spectra.

3 Assessing diagnostic capability of the JET CTS

Collective Thomson Scattering (CTS) spectra, while sensitive to the distribution of fast ions, depend on a wide range of plasma parameters. In the presence of noise in the measured spectra, these do not provide sufficient information to estimate all the relevant parameters with acceptable accuracy; indeed *masking*, where certain variations in parameters lead to no change in the predicted spectrum, makes it impossible to settle the parameters without imposing external constraints, even in the most ideal conditions. These constraints can take the form of parameters measured by other diagnostics or estimated on the basis of theoretical considerations. When assessing whether it is possible to resolve a certain feature, in for instance the fast ion distribution, it is not sufficient that the spectrum be sensitive to this feature, there must not be any other unconstrained perturbation of parameters which gives rise to the same spectral variation. Such masking would lead to large uncertainties in the estimate of the particular feature. Inaccuracies in the constraints can significantly affect the diagnostic capability of CTS, and must be accounted for when analyzing data and assessing diagnostic capability.

Extraction of fast ion distributions and other plasma parameters from CTS spectra is generally done by some fitting procedure. For the best use of the data this fitting should be based on a maximum likelihood estimator which takes into account not only the spectral noise but also uncertainties in constraints. Such an estimator was presented in BINDSLEV (1995) and discussed in detail in BINDSLEV (1996 b). The spectral noise and uncertainty in constraints gives rise to uncertainties in the estimated parameters. This uncertainty can be represented by an error distribution in the space of estimated parameters, which can be visualized as the normalized density of an ensemble of estimates. Directions in which the distribution is narrow are well determined parameter combinations while directions in which it is wide are poorly determined. The best resolved feature in the fast ion distribution corresponds to the direction in parameter space in which the error distribution for the fast ion parameters is narrowest. This is the direction of the first principal component of the distribution. The next best resolved feature, statistically independent of the first, is represented by the direction of the second principal component, etc. The directions and variances of the prin-

cipal components of the error distribution provide a complete set of independently estimated features and associated uncertainties, and thus provides considerable insight into the diagnostic capability of the system. A detailed analysis of the diagnostic capability of CTS and other complex diagnostics can be based on the error distribution and its principal components, and their relation to noise and uncertainties. We will employ some of these relations here but for a more detailed discussion of the method and its applications the reader is referred to BINDSLEV (1996 b). A brief discussion of the underlying mathematics is also given in BINDSLEV (1995, Section 4).

3.1 Principal components and L_α

In this analysis we base theoretical predictions of the spectral intensity of the received scattered light, $\partial P^s/\partial \nu^s$, on the equation of transfer [BINDSLEV, 1993],

$$\frac{\partial P^s}{\partial \nu^s} = P^i O_b (\lambda_0^i)^2 r_e^2 n^{(0)} \Sigma \,, \tag{1}$$

where the scattering function, Σ, [BINDSLEV, 1996 a] depends on the scattering geometry and plasma parameters.

A realistic list of parameters on which the JET CTS spectra depend is given by the set in Table 1 and parameters describing the fast ion distribution (the list could be extended arbitrarily by assuming more complicated plasma conditions). In the present study we assume that the parameters in Table 1 are constrained with the uncertainties given there.

In addition to the constraints given in Table 1 the bulk ion species (deuterium, tritium and impurity ions) are assumed to have the same temperature, the alpha particle distribution, f_α, is assumed to be isotropic and features in f_α occurring on velocity scales less than $v_b/7$ are ignored. The free parameters are those which describe the alpha particle distribution, excluding the low energy range which is masked by uncertainties in the bulk ion feature. For the numerical analysis the parameters in Table 3.1 are used. These parameters are at present the best estimate of the conditions expected for the coming deuterium, tritium experiments.

To investigate which departures of the fusion alpha particle distribution from the classical slowdown distribution can be detected

Constrained parameter		Δ	σ
θ	scattering angle	90°	0.02
ϕ	$\angle(\mathbf{k}^\delta, \mathbf{B})$	90°	0.02
ψ	see caption	90°	0.02
B	$\|\mathbf{B}\|$, modulus of magnetic field	1 Tesla	0.1
n_e	electron density	$4.5 \times 10^{19} m^{-3}$	0.1
T_e	electron temperature	12 keV	0.05
N_i	n_i/n_e, normalized carbon density	0.03	0.3
R_T	$n_T/(n_d + n_T)$, fuel ratio	0.5	0.3
T_i	bulk ion temperature	10 keV	0.2
O_b	beam overlap	5.8 ($\theta = 20°$)	0.5
$f_{\alpha i}$	$f_\alpha(v_i)$, $i = 0, \ldots, 3$	$f_{\alpha i}$	0.5

Table 1: Set of constrained parameters. Δ is the dynamic range of the parameter and σ is the uncertainty of the constrained parameter relative to its dynamic range. ψ = azimuthal angle of $\mathbf{B}^{(0)}$ when $\hat{\mathbf{z}} \parallel \mathbf{k}^\delta$ and $\hat{\mathbf{x}} \parallel \mathbf{k}^i \times \mathbf{k}^s$. $f_\alpha(v) = f_\alpha(0)/(1 + (v/v_c)^3)$, is the classical slowdown distribution with $v_c = 0.09 \times (T_e/2m_e)^{1/2}$. $v_i = (i/14) \times v_b$, where v_b is the birth velocity. O_b is a measure of the extent to which the emitter and receiver beam patterns overlap.

with JET's CTS, the principal components of the error distribution for the free alpha parameters were computed.

Figure 5 shows the first four of a typical set of principal components. In each subfigure the central solid line is the unperturbed classical slowing down distribution. The dotted and dash–dotted lines above and below the central line are the classical distribution plus or minus the perturbation represented by the dynamic range of the principal component [1]. The dashed lines are the distribution plus or minus one standard deviation along the principal component and thus indicate the accuracy to which this feature is resolved. The standard deviation increases with increasing structure (number of oscillations in the perturbation to the velocity distribution). This ordering of best to worst resolved feature persists throughout the range of relevant parameters.

[1]The definition of the dynamic range of principal components is discussed in detail in BINDSLEV (1996 b). Here it is sufficient to note the graphical representation of the range given in Figure 5. The relative errors, and hence the signal to noise ratios for principal components, refer to the absolute error in relation to the dynamic range of the principal component.

parameter	value
θ	10° to 30°
ϕ	80°
ψ	0°
B	3.4 Tesla
n_e	$4.5 \times 10^{19} m^{-3}$
T_e	12 keV
N_i	0.03
R_T	0.5
T_i	20 keV
N_α	3×10^{-3}
$f_{\alpha i}$	$f_\alpha(v_i)$, $i = 0, \ldots, 14$
E_m	4 MeV
P^{i}	400 kW
O_b	$18.8 m^{-1}/\lvert \sin(\theta) \rvert$

Table 2: Parameters used in numerical analysis of diagnostic potential. $N_\alpha = n_\alpha / n_e$ is the normalized alpha density, P^{i} is the power into the plasma. $f_\alpha(v) = f_\alpha(0)/(1 + (v/v_c)^3)$, $v_c = 0.09 \times (T_e/2m_e)^{1/2}$. $v_i = (i/14) \times v_b$, $v_b = (E_b/2m_\alpha)^{1/2}$, $E_b = 3.5$MeV

In Figure 6 are plotted the inverse of the normalized standard deviations, $1/\sigma_{\alpha i}$, which can be interpreted as the signal to noise levels on each of the principal components. The ratios between uncertainties in different principal components (i.e. the relative heights of the bars in Figure 6) are, like the principal components themselves, fairly constant over the range of parameters relevant for JET.

A good measure of the ability of CTS to resolve features in the alpha particle and other fast ion distributions is the *effective signal to noise ratio*, L_α, defined as

$$L_\alpha = \left(\sum_i 1/\sigma_{\alpha i}^2 \right)^{1/2} \qquad (2)$$

L_α takes into account not only the effect of noise in the spectra but also the effect of uncertainties in constraints, masking and the sensitivity of the spectrum to variations in the fast ion distribution. L_α therefore provides a more reliable estimate of the diagnostic capability of the system than the spectral signal to noise ratio which is often quoted for CTS systems.

If we are interested in detecting departures from the classical slowdown distribution it is desirable that principal components 2 and 3 be determined with some accuracy. $L_\alpha \approx 45$ corresponds to relative

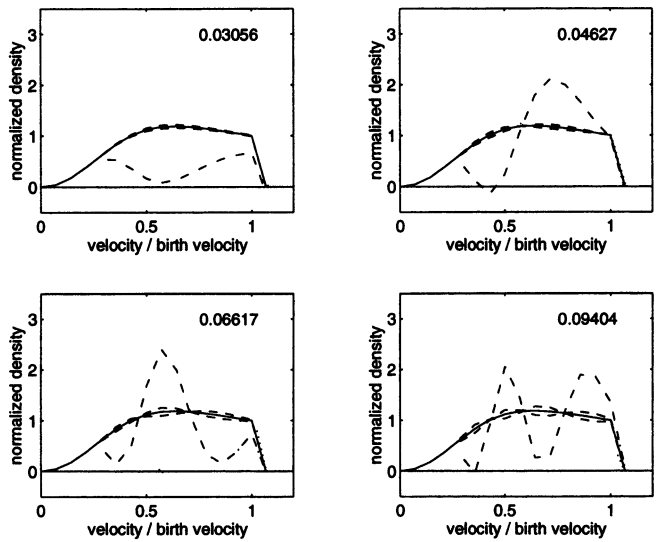

Figure 5: Principal components of alpha particle distribution perturbations. In each subfigure the central solid line is the unperturbed classical slowing down distribution integrated over a surface of constant velocity $((v/v_b)^2 \times f_\alpha(v)/f_\alpha(0))$. The dotted and dash–dotted lines above and below the central line are respectively the classical distribution plus and minus the perturbation represented by the dynamic range along the particular principal component while the dashed lines represent the standard deviation of the component. The standard deviation normalized by the dynamic range is given in the upper right corner of each subfigure. Here $T_N = 100$ eV, $\tau = 200$ ms, $\theta = 20°$ and $N_\alpha = 0.003$. Other parameters and uncertainties are given in Table 3.1 and Table 1 respectively.

errors on components 2 and 3 of respectively 5 and 7 %. This would appear to be adequate for detecting even moderate departures from the slowdown distribution. $L_\alpha \approx 10$ corresponds to relative errors on components 2 and 3 of respectively 30 and 50 %. At this level only gross departures from the slowdown distribution would be detectable. At $L_\alpha \approx 3$ no useful information on the shape of the alpha distribution function is obtained. In this case the high energy alpha density is estimated with a relative error of approximately 40 %.

L_α clearly depends on the uncertainties in the constraints, on the spectral noise, the integration time and on many other parameters.

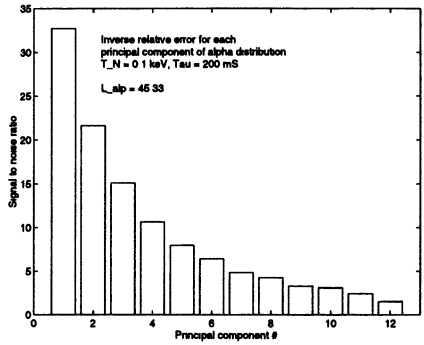

Figure 6: Inverse standard deviations, $1/\sigma_{\alpha i}$, of principal components perturbations to alpha particle distribution function. $1/\sigma_{\alpha i}$ can also be interpreted as the signal to noise ratio on the i'th principal component. Parameters are as in Figure 5.

Some of these vary only slightly while variations in others have only a small impact on L_α. Here investigation of the functional dependence of L_α is limited to variations in the scattering angle, θ, and in the normalized spectral signal to noise ratio, $s = (\sqrt{\tau/100\text{ms}}) \,/\, (T_N/1\text{keV})$, where T_N is the spectral noise temperature and τ is the total integration time. The results are displayed in Figure 7. Here we assumed the uncertainties given in Table 1 and the parameters given in Table 3.1.

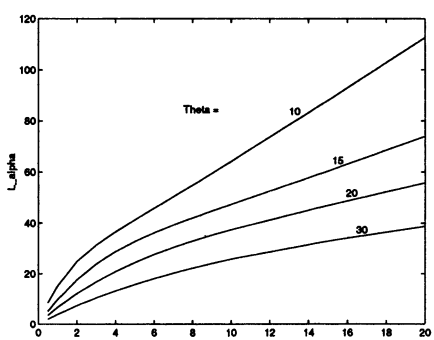

Figure 7: The functional dependence of L_α on normalized spectral noise, $s = (\sqrt{\tau/100\text{ms}}) \,/\, (T_N/1\text{keV})$, for a range of scattering angles, θ.

From the curves in Figure 7, L_α can be estimated for any combination of spectral noise temperature, integration time and scattering angle relevant to the CTS system at JET. The expected variation in magnetic field will have only minor effect on the spectral intensity of the scattered radiation. It will, however, significantly affect the spectral noise temperature which is investigated in the next subsection.

3.2 Spectral noise

On the basis of modelling using TRANSP on shot number 33643 it is projected that a similar shot with 50 % tritium would yield a maximum alpha density of $0.003 \times n_e$ with other parameters as in Table 3.1. For this alpha density and specified scattering angle, integration time and spectral noise temperature, L_α can be read directly from Figure 7. For instance, with a noise temperature of 1 keV and an integration time of 1 second, corresponding to $s \approx 3$, L_α would be greater than 30 for scattering angles less than 10°, making it possible to detect, in the alpha distribution, substantial departures from the classical slowdown distribution (see discussion in the previous section). At a noise temperature of 100 eV and an integration time of 0.1 second ($s = 10$) the same would be achievable with a scattering angle of 20°, and at $\theta = 15°$ L_α would be near 50 making it possible to distinguish even moderate departures from classical slowdown. Clearly a low spectral noise temperature is all important for the performance of this diagnostic. It must also be concluded that at noise temperatures above 1 keV it is virtually impossible to extract information about the shape of the alpha distribution at the projected alpha density.

The principal source of spectral noise is the electron cyclotron emission (ECE) from the plasma in the frequency range 135 GHz to 145 GHz. At moderate electron temperatures ($T_e < 5$ keV) the ECE originates from a narrow region around the cold resonance surfaces where $B = 5\,\text{Tesla}/n$. Here $n = 1$ or 2 for the fundamental and the second harmonic. Figure 8 shows the locations of the cold resonances for a range of central magnetic fields.

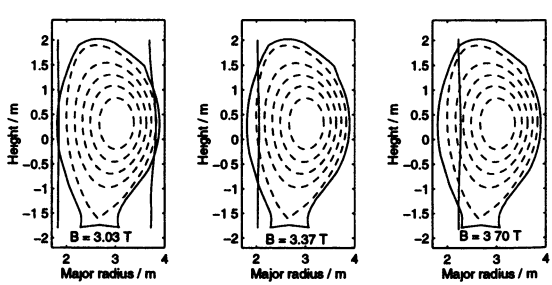

Figure 8: Locations of the cold ECE resonances for a range of magnetic fields.

The surfaces shift outward with increasing magnetic field. It is seen that from 3.1 to 3.3 Tesla both cold resonances are outside the plasma. At 3.4 Tesla the fundamental resonance enters the plasma on the inboard side. Although the receiver does not view a resonance layer directly, radiation still enters the receiver via wall reflections unless the receiver is viewing a dump. At moderate electron temperatures there would thus be a minimum in spectral noise for fields in the range 3.1 to 3.3 Tesla with a sharp rise at fields of 3.4 Tesla and above. At this minimum the noise temperature can be below 100 eV. At higher fields the noise temperature depends on plasma shape and temperature profile, but generally rises rapidly above 1 keV in the absence of a viewing dump.

At fields below 3 Tesla the second harmonic cold resonance enters the plasma from the outboard side increasing the ECE radiation and eventually blocking the receivers view of the centre of the plasma. The fields at which the cold resonances enter the plasma do of course depend on the radial extent of the plasma.

When intense ECE is emitted from a region, which is not in direct view of the receiver, substantial reduction in spectral noise temperature can be achieved by directing the receiving beam at a viewing dump. A viewing dump, for installation at the top of the torus, is presently being constructed. It will be installed with the centre of its aperture at a major radius of 3.25 metres and displaced toroidally relative to the gyrotron radiation launch mirror, to give a scattering angle of approximately 16°, with $\mathbf{k}^{\delta}$ near parallel to the magnetic field. In the absence of ECE radiation being emitted from regions in direct view of the receiver (see discussion below), this setup could reduce the spectral noise temperature dramatically, possibly to 100 eV. With an integration time of 200 ms this would yield $L_{\alpha} \approx 60$ implying that even moderate departures from classical slowdown in the alpha distribution would be detectable.

An alternative approach is to use the low temperature region of the fundamental electron cyclotron resonance as a viewing dump. Two examples of how such a cyclotron viewing dump may be exploited are shown in Figure 9. In the first example the cold yet fully absorbing region of the resonance is viewed directly. In the second example the resonance is viewed after reflection in the roof tiles. The latter approach, which carries the benefit of a reduced scatter-

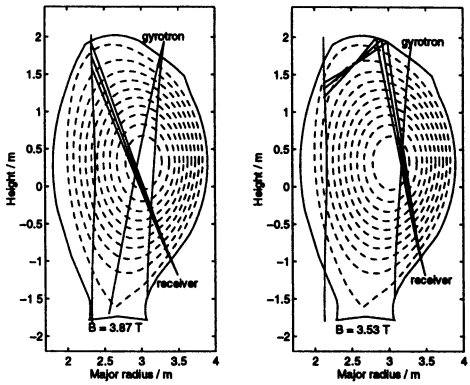

Figure 9: Scattering geometries permitting the low temperature part of the fundamental electron cyclotron resonance to be used as a viewing dump, either directly or via specular reflection in the roof tiles. Only a narrow range of poloidal angles can be used for the receiver.

ing angle, depends on specular reflection in the roof tiles. Use of the cyclotron resonance as a viewing dump is only effective at fields above 3.4 Tesla, which does coincide with the fields at which the ECE emission would become unacceptably high in the absence of a beam dump. The option of using reflection in the roof tiles is not suitable at fields above 3.6 Tesla for fully elongated plasmas because the resonance is then viewed too far into the plasma. A detailed investigation by relativistic ray tracing suggests that with direct viewing the spectral noise temperature can be kept below 1 keV. The calculations are, however, very sensitive to the shape of the temperature and density profiles at the edge. The need to view a limited region of the resonance restricts the scattering geometry such that the scattering angle must be approximately 40° if the centre of the plasma is to be probed when $B = 3.53$ Tesla. Assuming $N_\alpha = 0.003$ and $\tau = 200$ ms, this results in $L_\alpha \approx 3$. If the scattering volume is placed further out at a normalized flux of 0.4 the scattering angle can be reduced to around 30° improving L_α to approximately 4. The option which makes use of reflection in the roof tiles before reaching the resonance dump generally results in slightly higher radiation temperatures (typically 1.5 keV at $B = 3.4$ Tesla) even when specular reflection is assumed. This is because of the different angle at which the dump is viewed. Non-specular reflection will increase the radiation temperature further. This geometry results in a scattering angle of approximately 15°. Assuming $N_\alpha = 0.003$ and $\tau = 200$ ms this results in $L_\alpha = 9$. These values of L_α can be improved by a little more than a factor

of two by extending the integration time to the 1 second which the gyrotron is capable of.

Thus far the discussion has been confined to moderate electron temperatures ($T_e < 5$ keV). At high temperatures ($T_e > 10$ keV) an additional problem appears. Due to relativistic Doppler shift (includes non-relativistic Doppler shift and the effect of relativistically increased mass), the radiation emitted by energetic electrons is displaced from the locations of the cold resonances. In JET significant cyclotron radiation is emitted from regions displaced by a considerable fraction of the minor radius when the electron temperature is above about 10 keV. The consequence is that at 3.2 Tesla and a central electron temperature of 11 keV (as achieved in shot 33643) a strongly emitting cloud appears in the middle of the plasma resulting in a radiation temperature of 1 keV or more. This radiating cloud is downshifted second harmonic radiation.

Because this source of ECE is in direct view of the receiver, the radiation temperature cannot be reduced by any form of viewing dump. The optical thickness of the cloud, and hence intensity of radiation emitted from it, is reduce when the field is increased because the second harmonic resonance moves further out and hence fewer electrons are sufficiently energetic to radiate at the required frequency. The optical thickness of the cloud varies rapidly with temperature. For a given field there is therefore a sharp upper limit on the central electron temperature above which CTS provides little or no information on the alpha distribution. The received radiation temperature is plotted in Figure 10 as a function of central magnetic field and central electron temperature for a viewing direction which could see a dump installed in the roof. It is noted that the temperature limit increases with increasing field and decreases when viewing further out.

The central electron temperature in shot 33643, which is a model for the high performance deuterium–tritium discharges, was recorded by ECE to be 12.6 keV. Modelling by relativistic ray–tracing of relativistically downshifted second harmonic radiation appearing in the detected ECE spectrum suggests a central electron temperature of approximately 11.5 keV.[2] This central temperature is in accord with

[2]The hump appearing below the second harmonic in the ECE spectrum appears to be explainable as relativistically downshifted second harmonic radiation. If this is the case it may provide a good estimate of the absolute level of the temperature profile at high temperatures because from theoretical modelling this

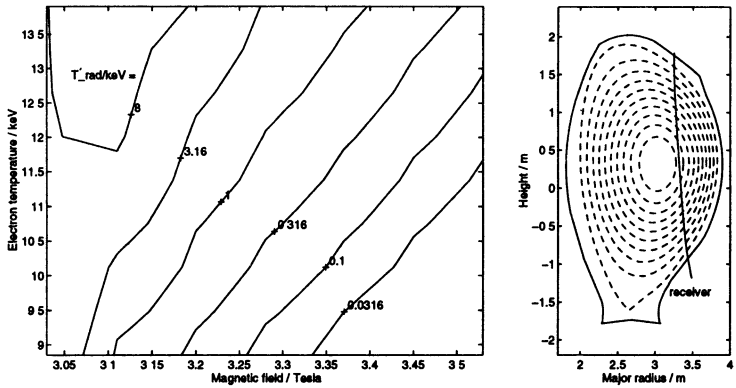

Figure 10: Temperature of received electron cyclotron radiation as a function of central magnetic field and central electron temperature. The wall is assumed cold and completely absorbing so the received radiation is emitted in direct view of the receiver. The radiation is received in O-mode at 140 GHz for a viewing direction of $\theta^s = 11°$ and $\phi^s = 170°$, where (θ^s, ϕ^s) are polar coordinates with vertical as the polar direction and the azimuthal angle ϕ^s being measured relative to the horizontal radial vector through the first receiver mirror. This viewing direction sees the plasma inside the $\Psi = 0.2$ normalized flux surface and the region of the roof where an artificial viewing dump could be installed. See right figure. The plasma equilibrium is based on shot 33643 at 53.3 seconds with scaled magnetic field (including the poloidal field) and scaled electron temperature.

the estimate obtained if the the electron temperature measured by ECE is reduced to agree with the temperature measured with Lidar (the central electron temperature could not be obtained directly from lidar because it does not view the plasma centre). The electron temperature should not be expected to be less in the high performance DT discharges. This means that during the heating phase of high performance shots CTS would not benefit from a reduction of the field to 3.2 Tesla and it appears that CTS would then only provide useful information on the alpha distribution at fields of 3.4 Tesla or above. Operation under these conditions would require a viewing

feature appears to be very sensitive to temperature. It should, however, be noted that this method of analyzing the ECE spectrum has only been conceived in connection with investigations for this report and is thus not fully developed.

dump as discussed above.

An alternative approach is to take the CTS measurement in the afterglow when the main external heating has been switched off and the electron temperature has dropped, yet before the alpha population has had time to decay significantly. On the basis of shot 33643 and TRANSP modelling it appears reasonable to assume that the electron temperature is reduced to below 8 keV in the afterglow. At this temperature there is no significant relativistically downshifted second harmonic radiation in O–mode. The intensity of radiation emitted from the cold resonance layers is, however, still significant and precautions, as discussed above, must therefore be taken also in the afterglow if a cold resonance is in the plasma, as it will be at 3.4 Tesla and above.

4 Predicted distribution of fusion alpha particles

The velocity distribution of alpha particles in devices such as JET will generally be anisotropic. Often, a significant part of the anisotropy is a consequence of the orbit motions of the fusion products. This becomes apparent when considering the expression in KOLESNICHENKO (1995) for the steady state velocity distribution of α–particles slowing down on electrons through Coloumb collisions.

Here, we pay special attention to the distribution function at the birth velocity v_α (E_α = 3.5 MeV). Since pitch angle scattering is negligible for particle energies above $\sim E_\alpha/10$, the anisotropy in the α distribution found at $v = v_\alpha$ is also present at lower energies. Evaluating the expression in KOLESNICHENKO (1995) with $v = v_\alpha$ for the case of a monoenergetic, isotropic source profile, $S_\alpha(\mathbf{r})$, we find:

$$f_\alpha(v_\alpha, \mathbf{r}, \chi) = \frac{1}{4\pi v_\alpha^3} \frac{\langle S_\alpha \rangle}{\langle \tau_s^{-1} \rangle} \quad , \tag{3}$$

where

$$\tau_s = \frac{3\pi^{(3/2)} \epsilon_0^2 v_e^3 m_e m_\alpha}{q_e^4 Z_\alpha^2 n_e \ln \Lambda_e} \tag{4}$$

is the Spitzer slowing down time [SPITZER 1962].

The quantities inside the angled brackets are averaged over an

orbit bounce time, $\tau_b = \oint dt$:

$$\langle(\ldots)\rangle = \frac{1}{\tau_b}\int_0^{\tau_b} dt'\,(\ldots) \quad . \tag{5}$$

The integrations in (5) are taken along the guiding centre orbit specified by the arguments, $(v_\alpha, \mathbf{r}, \chi)$, in equation (3). As we shall see the path of integration is highly dependent on the cosine of the pitch angle, $\chi = \mathbf{v}\cdot\mathbf{J}/(vJ)$, where $\mathbf{J}$ is the current. Consequently, in tokamak plasmas with inhomogeneous profiles of S_α and τ_s the distribution f_α becomes a function of χ, i.e. anisotropic.

The plasma obtained in the high performance D–D shot # 33643 in JET has been given much attention. It is hoped that the performance of this shot can be reproduced with a 50:50 Deuterium/Tritium fueling ratio in the current experimental campaign at JET. As a numerical example we have calculated f_α by using the plasma profiles measured in this shot. The Spitzer time and the orbits of integration were obtained using the profiles measured at the time of the peak performance ($t = 53.2s$). The source profile used was calculated by the TRANSP analysis code [GOLDSTON ET AL. 1981] with the assumption of a 50:50 Deuterium/Tritium fueling ratio.

In Figures 11.A and 11.B the α production rate and Spitzer time are shown as a functions of the position on the horizontal midplane at the low field side of the magnetic axis. The profiles are assumed to be functions of the flux variable. The poloidal projections of guiding centre orbits through the point $(r, Z) = (0.3, 0.0)$ are given in Figure 11.D. The trajectories correspond to different initial values of the pitch angle: $\chi \in \{-1.0, 0.9, \ldots, 1.0\}$. The distribution shown in Figure 11.C is obtained from expression (3) with $\langle S_\alpha\rangle$ and $\langle\tau_s^{-1}\rangle$ being the orbit averages over the trajectories in Figure 11.D.

In the interval $\chi \in [-1.0, -0.51]$ the α–density does not vary significantly since the trajectories corresponding to counter circulating particles are all very similar. For $\chi \in [-0.51, 0.0]$ trapped particles orbits exist. The particles contributing to the α density at $\chi = -0.5$ are all born along the trajectory marked by -0.5 in Figure 11.D. This trajectory intersects regions with very low α–particle production which causes a low average value of the source strength. Furthermore, in the outer regions of the plasma, where the electron temperature is low, the α–particles slow down more effectively on the electrons,

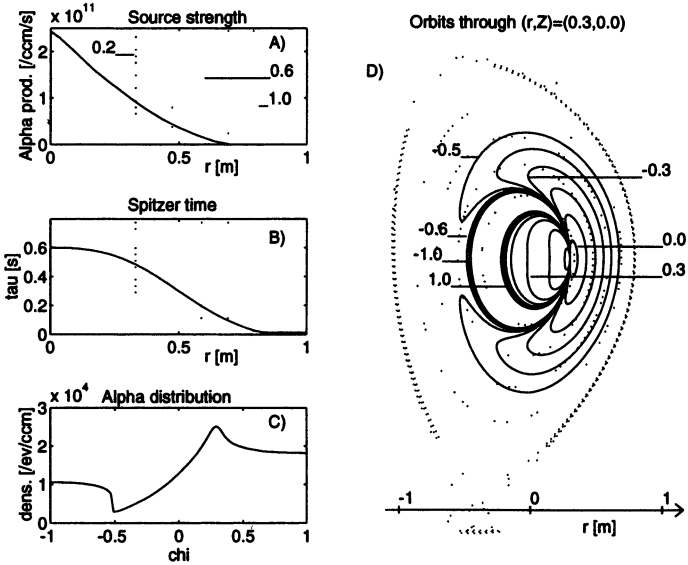

Figure 11: The graphs shown in this figure are all calculated by using the profiles measured in shot # 33643 in JET, assuming 50:50 D/T fueling ratio.
A) Profile showing the alpha particle production at the horizontal midplane.
B) Spitzer time profile on the horizontal midplane. The profiles in A) and B) are assumed to be functions of the flux variable. The positions of the flux surfaces $\Psi \in \{0.2, 0.4, 0.6, 0.8, 1.0\}$ are indicated by dotted lines.
C) Velocity distribution of α–particles at the point $r = 0.3$ on the horizontal midplane. The anisotropy seen in this distribution is closely related to the geometry of the α–particle orbits through the considered point.
D) The poloidal projections of guiding centre orbits for 3.5 MeV α–particles. The trajectories correspond to values of $\chi \in \{-1.0, -0.9, \ldots, 1.0\}$. The dotted lines indicate the positions of the flux surfaces: $\Psi \in \{0.2, 0.4, 0.6, 0.8, 0.99, 1.0, 1.01\}$.

resulting in a short effective Spitzer time, $\langle \tau_s^{-1} \rangle^{-1}$. Hence, the density of α–particles falls dramatically at the point of transition from counter circulating orbits to trapped particle orbits ($\chi \simeq -0.50$). As χ is increased from -0.5 to 0.3 the trajectories approach the centre region. In this interval the α density increases by a factor of eight. As χ is increased further the trajectories start circulating the central region, rather than intersecting it. Consequently, as χ approaches unity the α–density decreases by a small amount from its maximal value.

Due to the differences in trajectories through different points in the plasma, the anisotropic features change with the position. In Figure 12, the distribution f_α at the horizontal midplane ($Z = 0$) is shown as a function of (r, χ). The graphs in Figure 12 indicate that even in the central region of the plasma, where there are no direct losses of α–particles to the wall, orbit effects may well introduce significant anisotropy in the velocity distribution of these particles.

The TRANSP analysis code provides a comprehensive simulation of a range of plasma parameters including the velocity distribution function for the α–particles. A TRANSP simulation was carried out for a 50:50 DT plasma where the input profiles were those measured in shot # 33643. In Figure 13 the α distributions provided by TRANSP at the positions $(r, Z) = (-0.3, 0.0)$ and $(r, Z) = (0.3, 0.0)$ are shown together with the distributions found by equation (3) at the specified locations. The α distribution in TRANSP is obtained by Monte–Carlo techniques, which introduces a significant amount of Monte–Carlo noise on the outputs. In order to limit this noise, the raw TRANSP distribution has been averaged over 0.4 s in time and integrated over the energy range 3.0–3.6MeV. The distributions calculated by TRANSP and by use of equation (3) match each other within the Monte–Carlo noise on the TRANSP distributions. The close match is remarkable considering the simplicity of the model inherent in expression (3).

The Collective Thomson Scattering diagnostic has the potential to provide spatially resolved information from which the one–dimensional distribution of ion velocities in the direction of the fluctuation wave vector, $\mathbf{k}^\delta$, may be found. One such measurement is sufficient to characterize isotropic distributions. In contrast, determination of an arbitrary three–dimensional distribution requires a

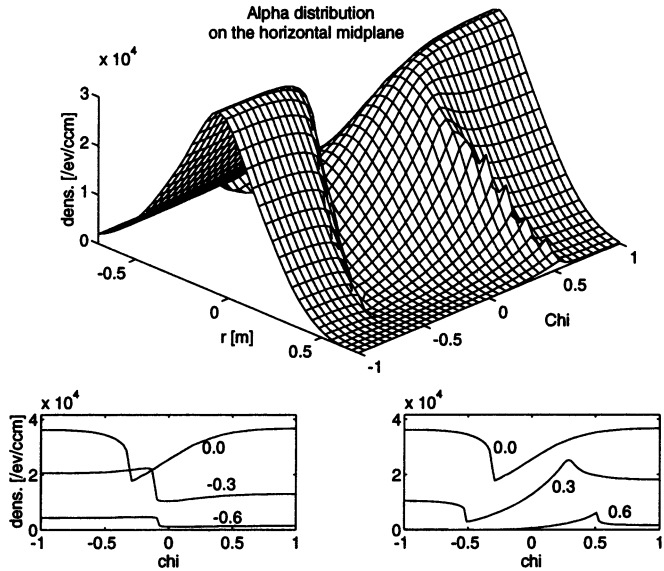

Figure 12: The alpha distribution, f_α, on the horizontal midplane as a function of position and pitch angle. The two subplots show the distribution as function of χ for $r \in \{-0.6, -0.3, 0.0, 0.3, 0.6\}$.

large number of measurements covering virtually all directions in velocity space. The problem is considerably simplified if, as above, it is assumed that the velocity distribution is rotationally symmetric about the direction of the magnetic field, i.e. gyrotropic. In this case, with the magnetic field, $\mathbf{B}$, as the polar axis, the distribution is independent of the azimuthal angle. Directions of measurement need then only cover a range for the polar angle, $\phi = \angle(\mathbf{B}, \mathbf{k}^\delta)$. Ongoing work shows that anisotropic features may be identified with reasonable accuracy from just two measurements. A possibly surprising result is that the two directions of measurement should differ by no more than 30^0. A suitable choice for the geometry in such measurements would be $\angle(\mathbf{B}, \mathbf{k}_1^\delta) \simeq 45^0$ and $\angle(\mathbf{B}, \mathbf{k}_2^\delta) \simeq 75^0$.

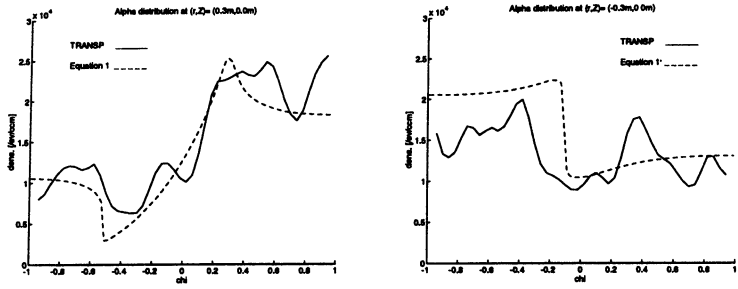

Figure 13: Velocity distributions of alpha particles at $(r, Z) = (0.3, 0.0)$ and $(r, Z) = (-0.3, 0.0)$. The full lines are obtained by TRANSP representing the distribution averaged over the energy interval [3.0, 3.6] MeV. The dashed lines, calculated by the simple model considered above, were also shown in the previous figure.

5 Conclusions

The initial operation of the diagnostic was useful to test the system, to demonstrate its viability and to identify areas where further improvements can be made. The results confirmed expectations and signal to noise ratios were in satisfactory agreement with theory.

Performance of the fully operational system has been assessed and compared with the needs in the coming DT campaign. This has identified a range of operational limits and the need for a viewing dump.

At the high electron temperatures expected during the heating phase of the high performance DT experiments relativistically downshifted ECE emission in direct view of the receiver makes it desirable to operate at 3.4 Tesla or above, and impossible to obtain useful alpha information at fields below 3.3 Tesla. Successful detection of the alpha distribution by CTS at such high temperatures is thus only possible at fields where the cyclotron resonance at 140 GHz is in the plasma, giving rise to strong ECE radiation which through wall reflections can enter the receiver. Under these conditions it is therefore necessary to operate with a viewing dump which is presently being constructed.

Finally we have shown that fast ion distributions must be ex-

pected to be anisotropic even in the case of thermonuclear fusion products with isotropic birth rates. This is to a large extent attributable to the inhomogeneous birth and slowing down rates.

References

BINDSLEV H (1993) *Plasma Physics and Controlled Fusion*, **35**, 1615.

BINDSLEV H (1995) *Proc. 7th Int. Symp. on Laser-Aided Plasma Diagnostics*, Fukuoka, Japan p. 60. (also available as JET preprint JET–P(95)66.

BINDSLEV H (1996*a*) *J. Atmospheric and Terrestrial Physics*, **58**, 983.

BINDSLEV H (1996*b*) Manuscript in preparation

COSTLEY A.E., ET.AL. (1988) JET Report R(88)08

GOLDSTON ET AL. (1981) *J. Computational Physics*, **43**, 61.

HOEKZEMA J.A., ET.AL. (1992) *Proc. 17th Int. Conf. on IR and mm Waves*, Colchester, UK pp 579, 588 and 244.

HOEKZEMA J.A., ET.AL. (1993) *Proc. 2nd Int. Workshop on Strong Microwaves in Plasmas*, Volga, Russia .

HOEKZEMA J A, ET.AL. (1995) *Proc. 22nd EPS Conference on Controlled Fusion and Plasma Physics*, Bournemouth, UK Vol. 19C, part II, p. 445. EPS JET Joint Undertaking, UK.

KOLESNICHENKO YA. (1995) *Nuclear Fusion*, **37**, 363.

SPITZER L. JR. (1962), *Physics of Fully Ionized Gases* 2nd Revised edition. Interscience, New York.

MICROWAVE ENHANCED SCATTERING MEASUREMENTS IN LOWER HYBRID WAVE EXPERIMENT IN FT-1 TOKAMAK

V.V. Dyachenko, M.M. Larionov, K.M.Novik, V.Yu.Shorikov

A.F. Ioffe Physical-Technical Institute, 194021, St. Petersburg, Russia

The original method of contactless diagnostics of oscillations and waves in a plasma is developed in A.F. Ioffe Institute - the enhanced scattering (ES) of microwaves [1,2]. The scattering of the extraordinary probing wave on the small-scale plasma oscillations is strongly increased near the upper hybrid resonance (UHR) zone, due to strong increase of a wave amplitude and reduction of wavelength there.

In the tokamak experiments, probing and reception of backscattered signal are realized by the pair of closely-placed horn antennas, from the strong magnetic field side of a torus. The accessibility condition of UHR for the probing wave must be fulfilled, otherwise the regime of reflectometry takes place. Good spatial resolution and high sensitivity to the small-scale plasma oscillations are reached by ES measurements. Frequency spectrum of scattered signal reflects the spectrum of plasma oscillations. The disadvantage of ES is the limited accuracy in the measurement of wavelength spectrum of oscillations. The upper limit of it is $l \leq 1/2\ \lambda_o$ (l- the wavelength of oscillations, λ_o - the vacuum wavelength of a probing wave, f_o - its frequency). The theory predicts the scale of the most effective scattering oscillations. $l^* = 1/2\ \lambda_o (V_{Te}/C)^{1/2}$, (V_{Te} -the thermal velocity of plasma electrons, C - the velocity of light). In our measurements, λ_o ~1cm, 10 eV < T_e<500 eV, l^*=0.04 - 0.1 cm. More complicated measurements, using fast modulation of a probing wave, allow to study the wavelength spectrum more exactly [3,4].

In FT-1 tokamak (R= 62 cm, a=15 cm, I=30-50 kA, B_0 =0.6-1.2 T), ES measurements were realized recently. Formerly, some ES experiments were carried out in FT-2 [1,2]. The scheme of experiment is shown in Fig.1. A pair of horn antennas with diagram width about 20°, are placed in a limiter shadow. Backward wave tubes of special type, operating at 24 GHz and 29.7 GHz, about 1 W, are used as a source of probing signal. The backscattered signal at the level of 10^{-10} W was amplified by the broadband superheterodyne receiver and analyzed by the spectrum

analyzer, $\Delta f = 75$ MHz over 2 ms. The measurements were fulfilled partly by the narrow-band receiver, tuning it in shot-to-shot regime. In this case 1000 Hz amplitude modulation of a probing signal was used to separate it from the ECE radiation of a plasma and from the pickups of powerful RF generators for lower hybrid (LH) pumping. In ohmic discharges of FT-1, without any external RF pumping, signals of scattering were disclosed, produced by the own small-scale plasma oscillations in a broad frequency range of 70-250 MHz. Their spectrum is shown in Fig.2. In ohmic discharge, at I=30 kA, central electron and ion temperatures are $T_e(0)$~ 450 eV, $T_i(0)$~100 eV. If the density is low, $n_e(0) \leq 1.3 \times 10^{13}$ cm^{-3}, UHR zone for f_o =24 GHz is accessible and is localized near the periphery, at r=12-15 cm, depending on the toroidal magnetic field, B_o=0.7-1.2 T. ES measurements are realized in this case. At higher density, $n_e = 1.8 \times 10^{13}$ cm^{-3} the second cut-off zone arises in the central region, leading to the reflectometric regime of probing. However the reflected signal has similar strong spectral broadening to 250 MHz, as the ES signal, Fig.2. The oscillations observed in this experiment probably are the strongly slowered lower hybrid (oblique Langmuir) waves excited by run-away electrons (the fan instability of a tokamak plasma).

Enhanced scattering measurements were carried out also in discharges with external pumping of LH waves. FT-1 is supplied by two magnetron generators, operating at 360 MHz and 920 MHz. The power absorbed in a plasma was 20-60 kW in 5-10 ms pulses. The antenna for electrostatic wave excitation was supplied by a slow-wave structure and was fed by a coaxial line [5,6]. Antenna was mounted in the same crossection as the horns for microwave probing but on the external side of a torus, Fig.1. Two different types of wave interaction with a hot tokamak plasma are found if different frequencies were used. Under 360 MHz pumping the intensive generation of fast ions, W_i=0.5-5 keV, in a plasma with T_i=100-140 eV was registered by the charge exchange analyzer. Under pumping by 920 MHz, the fast ion generation was strongly reduced, but strong increase of soft X-ray emission was found, with nonthermal spectrum. It shows the generation of a group of electrons with effective T_e about 10 keV. Similar types of wave interaction are found in many experiments on LH heating and current drive in tokamaks.

Scattering measurements were fulfilled also, as RF-pumping was applied to the low-temperature plasma of a toroidal discharge with limited current, I≤5 kA. In this case, $T_e(0)$~10-20 eV, $n_e(0) < 5 \times 10^{12}$ cm^{-3}.These

plasma parameters are very far from LH resonance, particularly for 920 MHz. However in a "cold" plasma both 360 MHz and 920 MHz RF pumping produce intensive generation of fast ions, as charge exchange measurements show. Their energy distributions reach W_i=5 keV, under 360 MHz pumping and W_i=2,5 keV under 920 MHz pumping.

The results of spectral analysis of scattered microwave signal at different RF-pumping frequencies and in different types of a discharge are shown in Fig.3. The case of application of 920 MHz, 60 kW RF-power to the normal tokamak discharge with I=30 kA is shown in Fig.3A. There are only two narrow lines, shifted from probing frequency f_o=24 GHz in both sides at ±920 MHz. The line of a probing frequency f_o also is very strong. ES shows that the waves of a pumping frequency are propagating in a plasma, and they are strongly slowered waves. The scale of strongly scattering oscillations is supposed to be l^*~0.1 cm. Taking into account the relation $N_{11} = (\omega / \omega_p) N_\perp$ for oblique Langmuir wave, the indexes of refraction are: $N_\perp$~300, N_{11}~20-30. The radial dependence of ES signal is shown in Fig.4. It was measured by changing the UHR position, if the magnetic field is varied from 0.6 T to 1.2 T. The scattered signal exists in a whole accessible volume, r >10 cm, but sharply increases at r=15 cm, near the position of antenna, strongly slowered waves are very intensive around it. If B_o<0.7 T, the cut-off surface appears for probing signal, leading to the reflectometric regime of measurements. The second maximum in Fig.6, at r= -14 cm, presents the reflected signal. Its spectrum also consists of the same lines: f_o; f_o±920 Mhz..

If the waves of 920 MHz, 60 kW, were excited in a "cold" discharge, I=3 kA, T_e~10 eV, $n_e(0)$~3.5×10^{12} cm^{-3}, the complicated spectrum of ES signal was observed. Not only narrow lines at f_o±920 MHz, but also broad maximums around f_o±300 MHz, f_o±600 MHz were found in it, Fig.3 B. Evidently they reflect the development of a parametric instability in a powerful LH wave. In a plasma with low electron temperature and density the threshold of this instability can be strongly reduced.

ES spectra measured in experiments of RF pumping by 360 MHz are shown in Fig.3 C (normal discharge, I=30 kA) and Fig.3 D ("cold" discharge, I=3 kA). In both cases, the regime of generation of fast ions was found by charge exchange measurements. In a high-temperature plasma, only lines shifted at the pumping frequency, f_o±360 MHz, are found in a spectrum. Their broadening in a plasma was detected by the spectrum analyzer. The line width is increased from 2 MHz at r=13 cm to 20 MHz at r=9 cm. This broadening is due to the interaction of LH wave

with low-frequency plasma oscillations. In a "cold" discharge, more complex spectra are found, reflecting the parametric instability of a wave in this case (Fig.3 D, Fig.5). There are several lines shifted in the low-frequency side from the initial one, $f_o \pm 360$ MHz. The distance between these lines is about the ion-cyclotron frequency. The structure of spectral lines depends on the radial point of measurement,choosed by the. B_o value. The most intensive lines are observed at r=8 cm, Fig.5.

Observation of ES signals, produced by the small-scale plasma oscillations, $l^* \sim 0.1$ cm, confirms the fact, that strongly slowered waves exist in a plasma volume. In the case of 360 MHz, their indexes of refraction shall be: $N_\perp \sim 800$, $N_{11} \sim 10\text{-}30$. The waves are observed in all accessible for ES measurements radial points, including the periphery. The maximum of scattered signal not corresponds to the position of LH resonance zone, in the case of its realization in the conditions of a discharge. We suppose that these waves are excited not in the LH resonance zone. They are excited under the action of radiofrequency polarization phenomena in a plasma surrounding the antenna and then are propagating inward the plasma volume. Strongly slowered waves can be absorbed by electrons and ions in the peripheral part of a discharge [6].

The equipment for ES measurements is under reconstruction now. The traveling wave tube, operating in the range of 27.5-28.5 GHz, with the output power of 30-100 W, will be used as a source of probing signal. Its excitation will be done by the generator capable for fast frequency and amplitude modulation. According to [3,4] more exact measurements of wavelength spectrum of plasma oscillations can be carried out by modulated probing signals. We suppose to fulfill such measurements in conditions of a tokamak discharge.

References

1. K.M. Novik, A.D. Piliya. Plasma Phys.Contr.Fusion 1993,35,357.
2. V.N. Budnikov. Nuclear Fusion 1991,31,611.
3. E.Z. Gusakov , A.D. Piliya. Sov.Tech.Phys.Lett., 1992,18,325.
4. Archipenko V.I., Bruesehaber B, Budnikov V.N. et al. Plasma Phys.Control. Fusion, 1995,37,A 347.
5. Gladkovsky I.P., Golant V.E., Dyachenko V.V., Larionov M.M.et al, Zh.Techn.Fiz.,1973,18,1632.
6. Dyachenko V.V., Larionov M.M., Novik K.M., Shorikov V.Yu. Proc.of 2nd International Workshop "Strong Microwaves in Plasmas", Nizhny Novgorod, 1994,1,121.

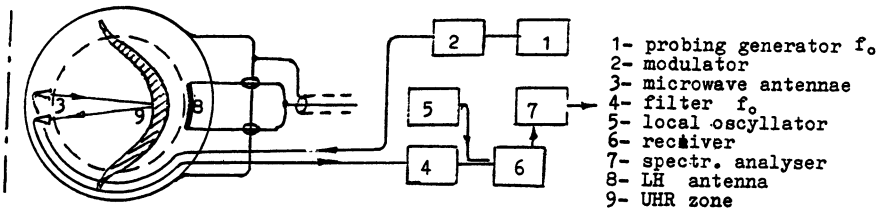

Fig.1 Sceme of ES measurements.

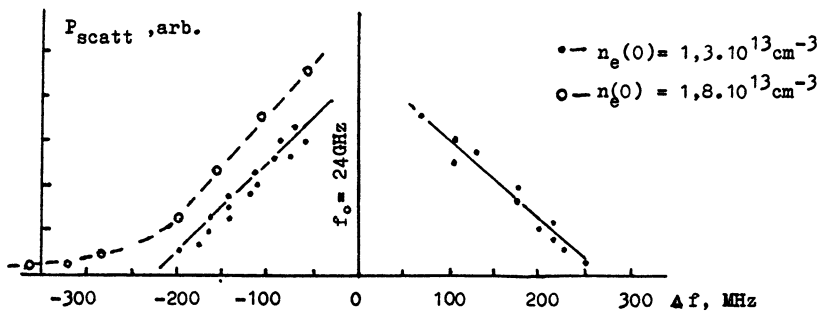

Fig.2 ES spectra of oscyllations in ohmic discharge.

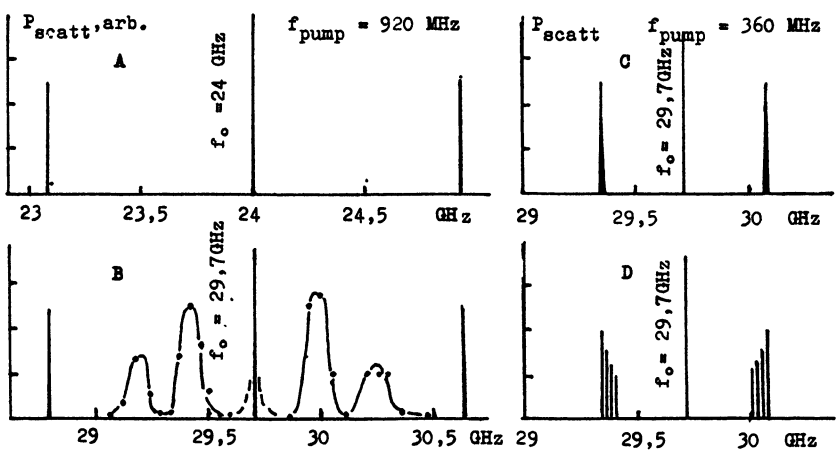

Fig.3 types of ES spectra under LH pumping.
A,C - normal discharge. B,D - "cold" discharge.

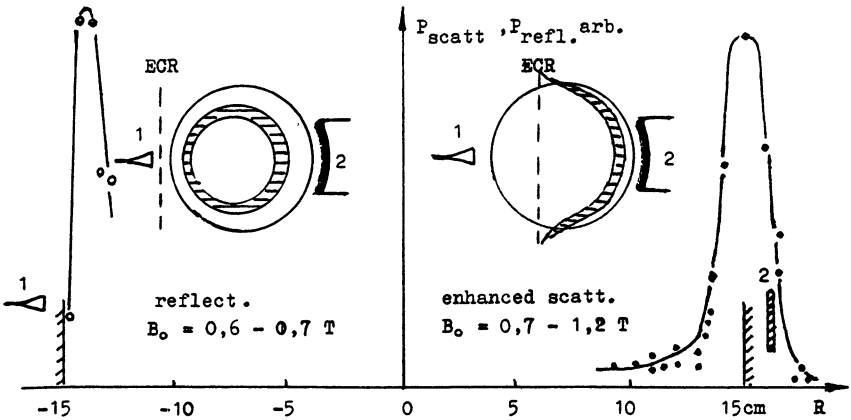

Fig.4 A Radial distribution of P_{scatt}, P_{refl}, f_o + 920MHz
f_o = 24GHz, f_{pump}= 920MHz
1 - microwave horn antenna
2 -LH antenna

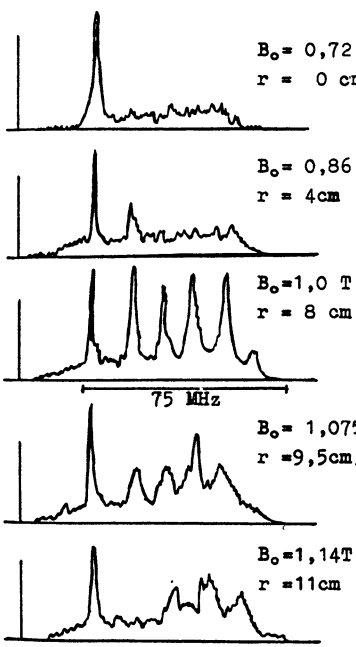

Fig.5 Radial dependence of ES spectra (case Fig.3 D).

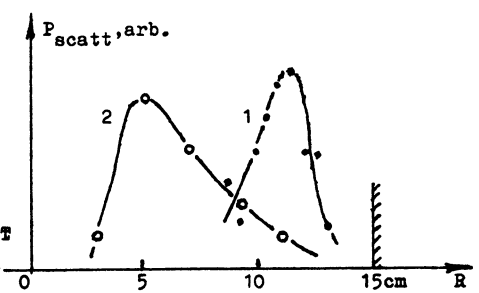

Fig.4 B Radial distribution of P_{scatt}, f_o + 360 MHz.
f_o= 29,7GHz, f_{pump}= 360MHz
1 - normal discharge
2 - "cold" discharge

MECHANISM OF LOWER HYBRID HEATING OF IONS AND ELECTRONS IN FT-2 TOKAMAK

V.N.Budnikov, M.A.Irzak

A.F.Ioffe Physico-Technical Institute, 194021, St. Petersburg, Russia.

1. Introduction.

Lower hybrid (LH) heating has not been as successful as other heating methods. The interest to it was lost due to the contradictory, unstable or irreproducible results and to the absence of heating. Since 1986 LH heating has been used only in JT-60 [1], but the study of the interaction mechanism has been carried on in FT-2 all these years.

The limitations of the LH heating are well known: the waves with longitudinal refractive index $N_{\parallel} > 1$ cannot penetrate in the central part of the fusion plasma because of the electron Landau damping, but for medium-size tokamaks it may appear a convenient method of heating. Now there is some interest to the study of the LH heating mechanisms due to the possibility of using LH waves for obtaining regimes with reversed shear [2], and LH current may be driven even in the absence of electron or ion heating.

LH heating is based on the interaction of the strongly slowed down waves with plasma ions and electrons. The ion heating is carried out by the so called stochastic wave damping on the ions with perpendicular velocities higher than the wave phase velocity [3, 4]. It was shown in theory that effective absorption of RF energy in the plasma requires a very low wave phase velocity [5, 6]

$$\omega / k_{\perp} \leq 2\sqrt{2} v_{Ti} \qquad (1)$$

This condition is satisfied near the LH resonance, i.e. in the region n_{LH} of linear transformation of the slow LH wave into a hot LH plasma wave.

There is also a non-linear mechanism of wave slowing down in the plasma associated with parametric instabilities [6, 7]. The pump wave f_0 launched into the plasma can decay into 2 daughter waves f_1 and f_2 (satisfying the conservation laws $f_0 = f_1 + f_2$, $\boldsymbol{k}_0 = \boldsymbol{k}_1 + \boldsymbol{k}_2$) which can be slower than the pump wave. The momentum conservation law $|\boldsymbol{k}_0| = |\boldsymbol{k}_1|$, $|\boldsymbol{k}_2|$ can be satisfied by the opposite direction of the vectors $\boldsymbol{k}_1$ and $\boldsymbol{k}_2$. And it appears that the short wavelength oscillations $\omega / k_{\perp} \approx 2\sqrt{2}\, v_{Ti}$ (which

interact with ions most effectively) are excited most easily (if the conservation law allows it) [7].

The interaction of LH waves with electrons is based on the parallel Landau damping mechanism. The condition of the parallel Landau damping is similar to (1):

$$\omega / k_{\parallel} \leq 2\sqrt{2} v_{Te} \tag{2}$$

Quasilinear effects can modify the electron Landau damping mechanism at high power levels [5]. The criterion (2) is then slightly modified $\omega / k_{\parallel} \leq 2.4\, v_{Te}$ and is usually presented in the form

$$N_{\parallel} \geq \frac{6.4}{\sqrt{T_e,\ \text{keV}}} \tag{3}$$

2. LH heating in 1986.

In the period of much interest to LH heating the LH experiments were carried out on more than 10 tokamaks and the results appeared to be contradictory. C.Gormezano commented it at Schliersee Conference in 1986 in such a way: a significant heating of ion component was observed in JFT-2 [8], Wega [9], Petula-B [10]; unstable heating was observed in PLT [11] and Versator [12]; poor heating was observed in ASDEX [13, 14] and no heating at all — in Alcator-C [15, 16] and FT [17].

In the work of V.E.Golant and V.I.Fedorov [6] these results were summarized as follows: "The conditions under which parametric instabilities develop and their effect on the penetration of waves to the plasma center ... are not completely understood." J.G.Wegrowe and G.Tonon [18] commented: "Whenever it has been observed, ion heating is thus consistent with the theoretical expectations. An open question is however to understand its absence in some experiments for which the prerequisites were apparently fulfilled."

Thus, the peculiarity of the situation was in the point that all the wave-plasma interaction mechanisms were known, but at the same time the heating was not observed in a larger part of the experiments.

3. Parametric instabilities.

The excitation of parametric instabilities in the peripheral plasma regions has been observed in many studies. The most detailed investigation of it was carried out in JFT-2 [19, 20, 21] and FT [22]. The frequency

spectra in these experiments were obtained by RF probes placed in the scrape-off layer. Two types of the decay instabilities have been observed. One of them was associated with the excitation of a whistler wave and ion quasi-mode (i.e. with a process of induced scattering of the pump wave on ions). The other was a resonant decay into an electron plasma wave and an ion cyclotron wave.

The contradictions in LH experiments results were explained by these parametric instabilities. If ion heating was observed, it was associated with the stochastic absorption in LH resonance. If there was no ion heating and only fast ions generation at the plasma periphery was observed, then it was explained by peripheral parametric instabilities which cause the wave energy absorption and acceleration of ions which are poorly confined. This point of view was demonstrated in F.Santini paper [23] at the Rome symposium in 1984 and was also presented in [6].

Opposite to this, M.Porkolab et al. [7] explained central ion heating in ATC device by the instability observed also by the peripheral probes. However, this point of view was not accepted then. Though, while counting the unsolved problems concerning LH heating it was noted in [6] that "the conditions of the development of parametric instabilities and their effect on the wave penetration to the plasma center can not be considered as absolutely clear".

4. Parametric instability in FT-2 tokamak.

A parametric instability in the plasma center was observed on FT-2 in 1988 [24, 25, 26]. It was made possible by using the technique of enhanced scattering of microwave oscillations [27], which allows to study short wavelength oscillations inside the plasma.

The main characteristics of FT-2 experiments are: major radius $R =$ 55 cm, minor radius (by the limiter) $a = 8$ cm, toroidal magnetic field $B_t \leq$ 2.5 T, plasma current $I_p \leq 40$ kA, plasma density $n = (0.5–3)\cdot 10^{13}$ cm^{-3}, electron temperature $T_e \approx 500$ eV, ion temperature $T_i \approx 100$ eV. LH waves were excited by a 300 kW magnetron generator at a frequency $f_0 =$ 920 MHz. RF power was launched into the plasma by a two-waveguide grill from the low field side at $N_{\|} \approx 2–3$. The short wavelength oscillations were probed by a 1 W microwave beam at a frequency 60 GHz.

The spectrum of the enhanced scattering signal is presented in Fig. 1. A slow daughter wave was observed here at a frequency near $f_1 \approx 0.7 \cdot f_0$, where $f_0 =$ 920 MHz is the frequency of the wave launched into the

plasma. The spectrum consisted of a single line with a few MHz width, which indicated at a highly coherent parametric process. (Unfortunately, the other daughter wave with lower frequency $f_2 = f_0 - f_1$ was not registered due to the absence of necessary equipment.) The instability was localized in a narrow spatial region along the radius with the width of a few mm at a local density $n_d \approx (0.3–0.5) \cdot n_{LH}$ (Fig. 2). In the decay region the condition of a local LH resonance is satisfied for the daughter wave f_1 which is therefore very slow and can effectively interact with the ions. Initially the instability appears in the center, when the central density (largest in the poloidal cross-section) attains a threshold value n_d. At further density increase the decay region is shifted to the periphery, and its local density is also increased but very slightly. Therefore, this instability is inherently "internal", as it cannot be moved to the low density region near the limiter $n_g << n_0$ by central density increase. Just the opposite, it tends to higher local density.

Such variation of the local density at the usual radial profiles of the tokamak parameters is predicted for a decay of a LH wave into another LH wave with lower frequency and a quasi-mode: LH $\rightarrow$ LH′ + QM [7].

The experiment demonstrated that the wave absorption and fast ions generation in the central regions are associated with the excitation of this instability. Fig. 3 shows that the pump wave with the frequency $f_0 =$ 920 MHz is exhausted in the region where the short wavelength oscillations at the frequency 660 MHz are localized. Fig. 4 shows the correlation between the start of 1 keV fast ions generation and the excitation of the oscillations at the shifted frequency. The fast ions generation begins at a minimum energy $E_{\min} \approx 8T_i$, which corresponds to the condition of the phase resonance of the ions with a wave having a phase velocity $\omega / k_\perp \approx 2\sqrt{2}\, v_{Ti}$. It agrees with the condition of an effective absorption and fast ions generation by the stochastic mechanism (1). Thus, to obtain an effective central ion heating in this case, the central density should be equal to n_d rather than to n_{LH}, when the parametric instability is developed in the center.

5. Unstable, irreproducible heating.

Though the observed parametric instability helped to understand which regimes should be chosen for an effective ion heating, in the following experiments the heating was very badly reproduced. This irreproducibility can be characterized by the threshold density n_d at which the fast ions gen-

eration appears. The threshold densities for 1 keV ions generation in various experiments are shown in Fig. 5, where one can see that the densities differed by a factor of 3. Evidently, the optimum density will be different in each case.

As the fast ions generations begins in the center, it is evident that the parameter which determines it is also related to the central plasma. Electron temperature T_{e0} appeared to be such a parameter [28]. T_e data is shown in Fig. 5 for the experiments when it was measured (by SXR diagnostics). One can see that n_d is approximately proportional to T_e. The temperature was not varied by purpose in these experiments. It had the values which depended on the degree of vacuum cleaning after opening the vacuum chamber or after the accidents. Thus, one of the reasons of bad reproducibility of LH ion heating is the variation of the initial ohmic plasma temperature during the experiments.

6. Oscillations at frequencies $f_0 - nf_{ci}$.

The oscillations at frequencies shifted by one or several ion cyclotron harmonics were observed by RF probes in many experiments [19, 20, 21, 22], including FT-2 [29]. In this experiment they were discovered in the inner plasma region in regime 3 by the enhanced scattering. The oscillations spectrum (Fig. 6a) included not only the generator frequency f_0 = 920 MHz, but also the frequencies shifted from f_0 by an ion cyclotron frequency and its 2nd and 3rd harmonics $f_0 - f_{ci}$, $f_0 - 2f_{ci}$, $f_0 - 3f_{ci}$, where f_{ci} = 30 MHz is a local ion cyclotron frequency at a low field side of the torus. One can see from Fig. 6a that the power measured at the shifted frequency exceeds the one at f_0. Apparently, it follows from the fact that the daughter waves $f_0 - nf_{ci}$ are slower than f_0 and the enhanced scattering signal must rise significantly at the increase of the wave refractivity index. These oscillations were observed at the radii r = 5.5–7 cm at local densities (0.6–1.5)·10^{13} cm^{-3}, see Fig. 6b. While scanning along the chords with CX analyzer it was established that 1 keV fast ions appear in the center both at $n_0 = 2 \cdot 10^{13}$ cm^{-3} slightly exceeding n_d and at $n_0 = 3 \cdot 10^{13}$ cm^{-3}. This experiment shows that the oscillations at the shifted frequencies $f_0 - nf_{ci}$ excited at the periphery at $r > 7$ cm propagate to the plasma center. The ion generation in the center indicates at the fact that the waves reach the central region.

The lowest LH density for $f_0 - nf_{ci}$ at the highest $N_{||} = 9$ possible in this case (see (3)) is $2.2 \cdot 10^{13}$ cm^{-3}, while the ion generation starts at

$n_d = 1.8 \cdot 10^{13}\,\mathrm{cm}^{-3}$. So, probably the waves $f_0 - nf_{ci}$ decay further, for instance, according to the scheme described in Section 2, and only after that they interact with the ions.

7. Transition from current drive to fast ions generation.

An important step in understanding the absorption mechanism was made at a detailed study of the transition region, when the current drive is still observed and at the same the fast ions appear [30]. The general dependence of the loop voltage drop (characteristic of current drive efficiency) and of the 1 keV CX flux on the density is presented in Fig. 7. The current drive cut-off correlates with the increase of the fast ions generation, and in these experiments the threshold density n_d is very close to the one in regime 3 (Fig. 5). This transition can be observed even during a single pulse. The plasma density usually increases during the RF pulse. At a certain initial density it can pass the threshold value n_d in the middle of the pulse. The transition dynamics is shown in Fig. 8: the appearance of the fast ions is accompanied by the disappearance of the loop voltage drop. Besides, as the density exceeds n_d, the energy of the electron beams (measured by SXR diagnostics) changes significantly. Together with the energies 30–40 keV typical for $n_0 < n_d$, the energies 3–4 keV appear and the energy spectrum at $n_0 > n_d$ becomes more sophisticated. Simpler spectra observed at densities far from n_d are presented in Fig. 9.

The electrons with energy 30–40 keV are in the phase resonance with the wave, excited by the grill ($N_\parallel \approx 2.5$). Such electron beams introduce into current drive. The energies 3–4 keV, approximately equal to $E_e \approx 8T_e$, correspond to the velocity $v_e \approx 2\sqrt{2}\,v_{Te}$. These electron beams can be associated with the slowed down oscillations. The simultaneous observation of both the fast ions with $E_i \approx 8T_i$ and the electrons with $E_e \approx 8T_e$ indicates at a single (parametric) mechanism of LH waves interaction with plasma ions and electrons. As the parametric instability is excited, a sharp change of the wave $k_\parallel$ spectrum takes place: instead of $N_\parallel \approx 2$–3 excited by the grill, $\omega / k_\parallel \approx 2\sqrt{2}\,v_{Te}$ appear. As a result the wave interacts with electrons having $v_{e\parallel} \approx 2\sqrt{2}\,v_{Te}$ and produces electron beams with the energy $E_e \approx 8T_e$. These are the slowest electron beams that can be produced by the wave and so they can effectively transfer their energy to the bulk electrons by the collisions, i.e. produce the heating. They absorb now RF energy instead of the superthermal electrons $v_{e\parallel} \approx c / N_\parallel$, which results in the switch-off of the current drive. Thus the current drive switch-off can take place

due to a competition between two groups of electrons, and not only as a result of a competition between ion and electron absorption [18, 31].

It should be noted that in current drive regimes the electron component is cooled due to the decrease of the ohmic energy input. As the density exceeds the threshold value n_d a significant electron heating is observed which can be considered as an indication at the change of the interaction mechanism.

8. Ion and electron heating.

The most effective ion and electron heating was obtained in regime 5 (Fig. 5) at the highest threshold density n_d [32, 33]. This result is evident as the heating efficiency is proportional to the density squared. Unfortunately the enhanced scattering could not be applied here because of the high densities.

The general picture of the wave interaction with the plasma is presented in Fig. 10. Here the relative loop voltage drop $\Delta U_L / U_L$, CX fluxes with energies 1.5 and 3.7 keV, the time derivative dT_e/dt at the beginning of RF pulse and the increase of the electron and ion temperatures in the end of the pulse are presented against the current central density n_0. $\Delta U_L / U_L$ is proportional to the current drive efficiency, and dT_e/dt — to the bulk electron heating power. Current drive disappears at that very plasma density when the fast ion generation and electron heating dT_e/dt appear simultaneously. A 4-fold increase of the ion temperature (from 100 eV to 400 eV) and 2-fold increase of the electron temperature (from 500 eV to 1000 eV) were observed in the experiment at 100 kW RF power comparable with the ohmic power level.

The heating efficiency $\eta = (\Delta T_e + \Delta T_i) n / P_{RF}$ attained $10 \cdot 10^{13}$ eV cm^{-3} kW^{-1} and did not depend on the power. However, such a heating was observed in a very narrow density range $\Delta n \approx 0.2 n$, and the largest electron heating took place at a density slightly lower than the ion heating. Aside from the fact of the effective heating itself, the following experimental results should be noted:

1. Simultaneous start of the fast ions generation and bulk electron heating from $n_0 = 2.9 \cdot 10^{13}$ cm^{-3}.

2. Switch-off of the electron heating ($dT_e/dt = 0$) as the electron temperature reached its maximum (Fig. 10) correlated with the appearance of the LH resonance for the pump wave in the plasma center. The density

$n_0^* = 4.3 \cdot 10^{13}\,\mathrm{cm}^{-3}$ was a LH density for the current plasma parameters. The electron heating was switched off before the end of RF pulse.

3. The most effective ion heating was observed after the electron heating was switched off. Then either the LH resonance conditions could be satisfied at the plasma center (point $n_0 = 4.3 \cdot 10^{13}\,\mathrm{cm}^{-3}$) or n_0 could be less than n_{LH}. The density $n_0 = 4.9 \cdot 10^{13}\,\mathrm{cm}^{-3}$ corresponded to the last case as n_{LH} at that moment increased to $5.5 \cdot 10^{13}\,\mathrm{cm}^{-3}$ due to Z_{eff} increase. Therefore, if in the beginning of the pulse we had the parametric mechanism features (beginning of fast ions generation at $n_0 < n_{LH}$ and their sequence: the less energetic ions appear at lower densities), then in the end of the pulse the ion heating could result from the energy absorption in LH resonance.

9. Effect of electron temperature on the heating

This change of interaction mechanism can be explained by the electron heating. The threshold of parametric instabilities $P_{th} \propto T_e^{\alpha}/n_e^{\beta}$, where α, $\beta = 1$–2 depending on the type of the instability, i.e. the threshold density $n_{th}^{\beta} \propto T_e^{\alpha}/P_{RF}$ [7]. From here follows that the local density at which the instability is excited rises with T_e increase. A strong effect of the electron temperature on the wave-ion interaction was observed in the experiments. The dependence of the threshold density n_d on T_e has been already discussed (Fig. 5). The localization of the ion heating also depends on the electron temperature. The chord T_i measurements by CX spectra are presented in Fig. 11. A narrow profile indicating at a central heating was observed at high T_e. It was in this experiment that the maximum ion heating was obtained. At lower T_e the T_i profiles became broader which is, evidently, due to a non-central wave absorption.

The electron heating taking place during RF pulse should result in a rise of a local density in the region of interaction (parametric decay). As it was mentioned above, the decay region is a LH resonance region for the daughter wave, and, therefore, its frequency should vary as $f \propto \sqrt{n_e}$. We have some experimental data on the variation of f_1 during RF pulse for the distribution of short wavelength oscillations (1) in Fig. 2, case 1. During RF pulse the localization of these oscillations changed very slightly (from $r = 3.1$ cm to 3.25 cm), but at the same time the local density increased and, consequently, the observed frequency increased, too. The dependence of the frequency on the density is presented in Fig. 12, it correlates with the curve of LH resonance frequency. So, it is demonstrated that such in-

teraction regimes exist when the spatial localization of the interaction does not change, but the local density increases, which results in the variation of the daughter wave frequency. One can believe that at a high electron temperature, when the instability threshold is high, the wave can reach the LH resonance without any parametric decay and be absorbed by the stochastic mechanism. The slow waves $\omega/k_\perp \approx 2\sqrt{2}\,v_{Ti}$ necessary for the interaction with ions will be produced by a linear mechanism and the oscillations providing the interaction with electrons $\omega/k_\parallel \approx 2\sqrt{2}\,v_{Te}$ will not be excited then. The electron heating will be switched off. The switch-off of the electron heating even before the end of RF pulse is very clearly demonstrated in Fig. 13, curves 2, 3. The density range where the electron heating is possible lies between n_d and n_{LH}: $n_d < n_0 < n_{LH}$.

10. Mechanisms of RF energy transport and absorption.

In spite of the fact that in our experiments we were unable to observe the second, low-frequency daughter wave due to some technical reasons, one can believe that these experiments demonstrated the excitation in the inner plasma region of the daughter waves corresponding to a decay of an electron plasma wave into a LH wave (either cold or hot plasma mode) and a quasi-mode: LH $\rightarrow$ LH′ + QM or into a LH wave and ion cyclotron harmonics: LH $\rightarrow$ LH′ + IC. Both types of instability had been predicted by M.Porkolab [7] and, apparently, they present the main channels of the development of parametric instabilities in a tokamak plasma. M.Porkolab considered various convective mechanisms of the instability development.

But in our experiment observed spectra consisted of a single narrow line, which indicates at a coherent process and at the development of an absolute parametric instability. As we have no suitable theory now, we can discuss it only qualitatively on the basis of general properties of parametric instabilities. There are two ways to transfer the RF energy excited by the grill inside a tokamak.

1. The wave at a frequency f_0 penetrates directly into the inner region where the parametric decay and absorption take place (Fig. 14a). In the decay region the wave is sufficiently slow, and the daughter wave being strongly slowed down is absorbed immediately.

2. The wave f_0, not very slow yet, undergoes a decay at the periphery at a low local density producing the waves with frequencies $f_0 - nf_{ci}$ which are close to the pump wave frequency (Fig. 14b). However, the daughter waves have higher $N_\parallel$ than the pump wave and so they have higher per-

pendicular refractive indices: $N_\perp \approx N_\parallel \sqrt{n/n_c}$. They propagate inside and are absorbed at lower densities as their LH resonance density is lower: $n_{LH}(f_0 - nf_{ci}) < n_{LH}(f_0)$. But what is most important — they leave the decay region at the periphery and reach the center where they produce fast ions (Fig. 6b). And these daughter wave may, evidently, undergo a further decay (of the first type) as the ion generation in the center starts at a density lower than $n_{LH}(f_0 - nf_{ci})$. So, though the wave decays at the periphery, we did not observe there any fast ions generation, all the same they appear in the center. Peripheral fast ions would appear if the central density is equal to or higher than the LH resonance density for the initial wave f_0 and the interaction (decay) region is shifted from the center.

Another important result of the experiments is that the parametric mechanism provides the wave interaction not only with ions, but also with electrons. Due to the change of the spectrum of the oscillations accompanying the development of a parametric instability the wave absorption switches from the superthermal electrons with $v_{e\parallel} \approx c/N_\parallel$ to the electrons with $v_{e\parallel} \approx 2\sqrt{2}\, v_{Te}$. It results in the current drive switch-off and in heating of the electron component. The dependence of the parametric instability threshold on T_e leads to the increase of the local density in the decay region n_d at the rise of T_e. This can take place not only at an independent change of T_e in the initial plasma, but also in the process of RF pulse when the electron heating results in the switch-off of the parametric instability and in the wave absorption in the LH resonance. It is shown schematically by an arrow in Fig. 14a. So the electron temperature is the main parameter which changes the absorption conditions. This is that very "hidden" parameter which determines irreproducibility and contradictory results of the LH heating.

References

1 Ushigusa K., Imai T., Ikeda Y. et al. In: Plasma Physics and Controlled Nuclear Fusion Research 1988 (Proc. 12th Conf, Nice, 1988), v.16 IAEA, Vienna (1989), p.621.

2 Levintin F.M. et al. Phys. Rev. Lett. 75 (1995) 4417.

3 Karney C.F.F. Phys. Fluids, 1978, v.21, No 9, p.1584-1599.

4 Karney C.F.F. Phys. Fluids, 1979, v.22, No 11, p.2188-2209.

5 Brambilla M., Chen Y.P. In: Heating in Toroidal Plasmas (Proc. 3rd Joint Varenna-Grenoble Int. Symp., Grenoble 1982) v.2, p.565-569.

6 Golant V.E. and Fedorov V.I. "RF Plasma Heating in Toroidal Fusion Devices", Consultants Bureau, New York and London, 1989. Golant V.E., Fedorov V.I., in High Frequency Plasma Heating in Toroidal Thermonuclear Devices, Ehnergoatomizdat, Moscow (1986), 69-96, 116-141, (in Russian).
7 Porkolab M. Phys. Fluids, 17 (1974) 1432; 20 (1977) 2058.
8 Uehara K., Nagashima T., in Heating in Toroidal Plasmas (Proc. 3rd Joint Varenna-Grenoble Int Symp. Grenoble, 1982), v.2, CEC, Brussels (1982) 485.
9 Gormezano C., Blanc P., Mel Shaer N. et al. ibid., p.439.
10 Van Houtte D., Agarici G., Blanc P. et al., in Heating in Toroidal Plasmas (Proc. 4th Int Symp. Rome, 1984) v.1, International School of Plasma Physics, Varenna (1984) 554.
11 Stevens I.E., Bernabei S., Bitter M. et al., in Heating in Toroidal Plasmas (Proc. 3rd Joint Varenna-Grenoble Int. Symp. Grenoble, 1982) v.2, CEC, Brussels (1982), 455.
12 Porkolab M., Lloyd B., Schuss I.I. et al., in Heating in Toroidal Plasmas (Proc. 4th Int. Symp. Rome, 1984) v.1, International School of Plasma Physics, Varenna, p.529-545.
13 Söldner F., Eckhartt D., Leuterer F. et al., in Controlled Fusion and Plasma Physics (Proc. 12th Eur. Conf. Budapest, 1985) v.9F, Part II, European Physical Society (1985) 244.
14 Eckhartt D., Leuterer F., Münich M. et al., in Heating in Toroidal Plasmas (Proc. 4th Int. Symp. Rome, 1984) v.1, International School of Plasma Physics, Varenna (1984) 501.
15 Porkolab M., Lloyd B., Schuss I.I. et al., ibid, p.529.
16 Porkolab M., Blackwell B., Bonoli P. et al., in Plasma Physics and Controlled Nuclear Fusion Research 1984 (Proc. 10th Int. Conf London, 1984) v.1, IAEA, Vienna (1985) 463.
17 Alladio F., Crisanti F., Bardotti G. et al., in Heating in Toroidal Plasmas (Proc. 4th Int Symp. Rome, 1984) v.1, International School of Plasma Physics, Varenna (1984) 546.
18 Wegrowe J.G., Tonon G., in Heating in Toroidal Plasmas (Proc. 4th Int. Symp. Rome, 1984) v.1, International School of Plasma Physics, Varenna (1984) 601.
19 Gormezano C. Plasma Physics and Controlled Fusion, v.28, p.1365-1376 (1986).

20 Nagashima T., Fujisawa N., in Heating in Toroidal Plasmas, Grenoble 1978, v.2, p.281-292.
21 Imai T. et al., in Heating in Toroidal Plasmas (Proc. 2nd Joint Grenoble-Varenna Int. Symp. Como, 1980) v.1, p.377- 384.
22 De Marco F. et al., in Heating in Toroidal Plasmas (Proc. 4th Int. Symp. Rome, 1984) v.1, International School of Plasma Physics, Varenna (1984) 546.
23 Santini F., in Heating in Toroidal Plasmas (Proc. 4th Int. Symp. Rome, 1984) v.2, International School of Plasma Physics, Varenna (1984), p.1303.
24 Budnikov V.N., Esipov L.A., Irzak M.A. et al., in Plasma Physics and Controlled Nuclear Fusion Research 1988 (Proc. 12th Int. Conf. Nice, 1988) v.1, IAEA, Vienna (1989) 645.
25 Budnikov V.N., Esipov L.A., Irzak M.A. et al. Pis'ma Zh. Eksp. Teor. Fiz., v.48, No 9, (1988) p.480.
26 Budnikov V.N. Nuclear Fusion, v.31, No 4 (1991) 611.
27 Novik K.M., Piliya A.D. Plasma Physics and Controlled Fusion, v.35 (1993) 357-381.
28 Budnikov V.N., Chashina G.I., Dyachenko V.V. et al., in Controlled Fusion and Plasma Physics (Proc. 22nd Eur. Conf. Bournemouth, 1995) v.19C, part II, European Physical Society (1995) 85.
29 Budnikov V.N., Dyachenko V.V., Esipov L.A. et al. "Investigation of Lower Hybrid Heating of Ions in the Tokamak FT-2" Preprint of the Ioffe PTI No 1296, 1988.
30 Budnikov V.N., Dyachenko V.V., Esipov L.A. et al., in Controlled Fusion and Plasma Physics (Proc. 22nd Eur. Conf. Bournemouth, 1995) v.19C, part IV, European Physical Society (1995) p.385.
31 Wegrowe J.G., Engelman F. Comments Plasma Physics Controlled Fusion, 1984, v.8, No 6, p.211-227.
32 Budnikov V.N., Dyachenko V.V., Esipov L.A. et al., in Controlled Fusion and Plasma Physics (Proc. 21st Eur. Conf. Montpellier, 1994) v.18B, part II, European Physical Society (1994) 1028.
33 Budnikov V.N., Dyachenko V.V., Esipov L.A. et al. Pis'ma v Zh. Tekh. Fiz., 1995, v.21, No 10, p.34-39.

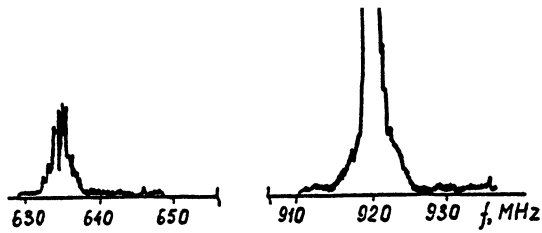

Fig. 1. Scattered radiation spectrum.

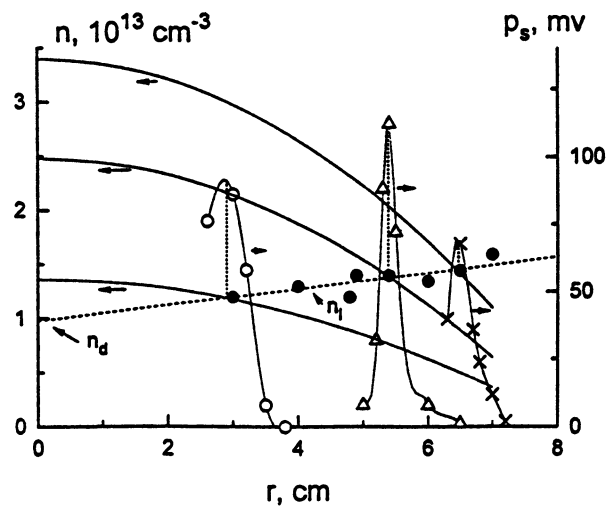

Fig. 2. Localization of the short-wavelength oscillations at various maximum plasma densities. The local density in the decay region is shown by closed circles and the dashed line.

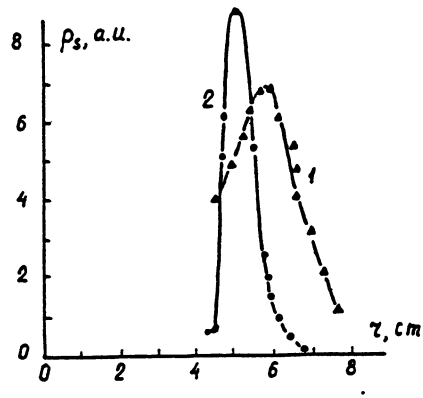

Fig. 3. Correlation of scattered signals at (1) 920 MHz and (2) 660 MHz.

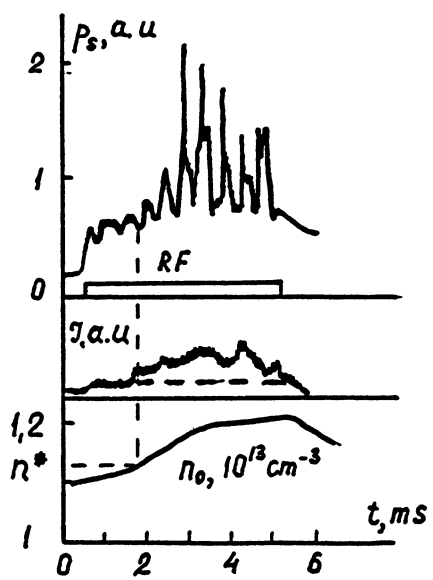

Fig. 4. Time correlation of the enhanced scattered signal, the start of 1 keV ion generation and plasma density.

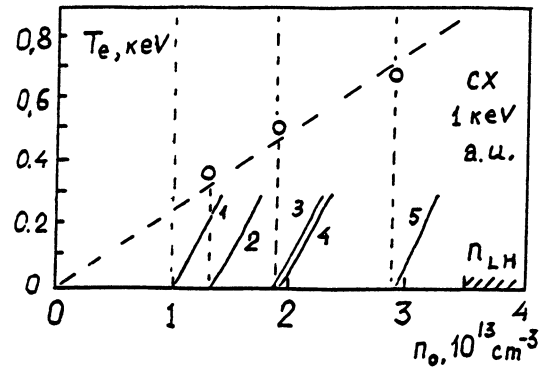

Fig. 5. Irreproducibility of the discharge. Different discharge regimes are indicated by numbers.

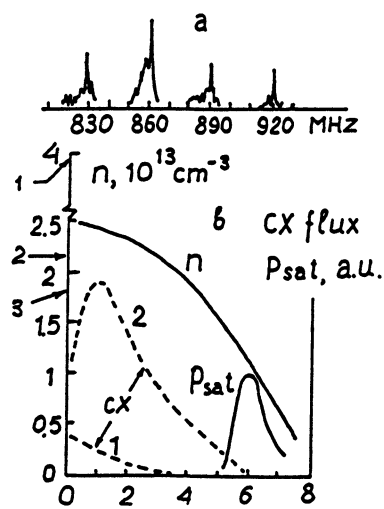

Fig. 6. (a) — spectrum of the scattered radiation. (b) — distributions of plasma density, scattered radiation power (in satellites) and 1 keV CX flux: 1 — $n = 2 \cdot 10^{13}$ cm^{-3}, 2 — $n = 3 \cdot 10^{13}$ cm^{-3}. The arrows show at: 1 — LH density at $N_{\parallel} = 2.5$; 2 — LH density at $N_{\parallel} = 9$; 3 — threshold density of fast ion generation.

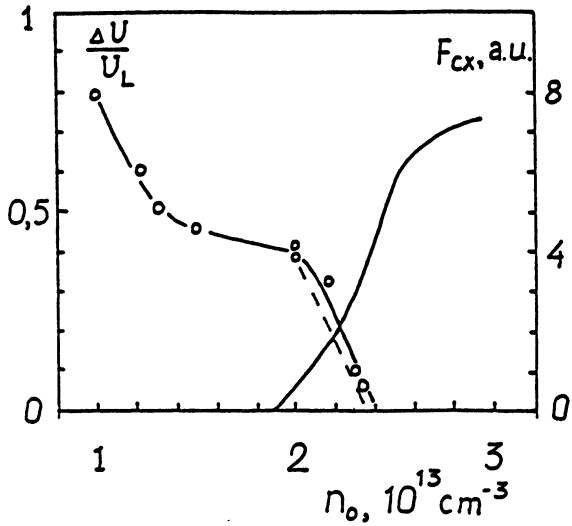

Fig. 7. Loop voltage drop versus the density.

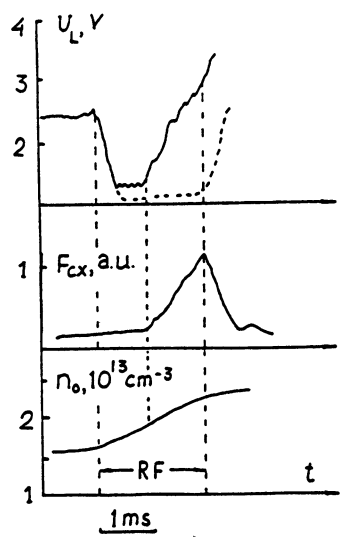

Fig. 8. Time behavior of the loop voltage drop, of the CX flux with the energy 1 keV and of n_0.

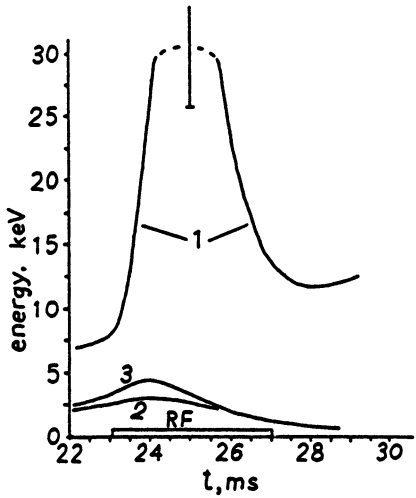

Fig. 9. Energy of electron beams during LH pulse. 1 — $n = 10^{13}$ cm^{-3}, r = 0 cm; 2 — $n = 2.5 \cdot 10^{13}$ cm^{-3}, r = 0 cm; 3 — $n = 2.5 \cdot 10^{13}$ cm^{-3}, r = 1 cm

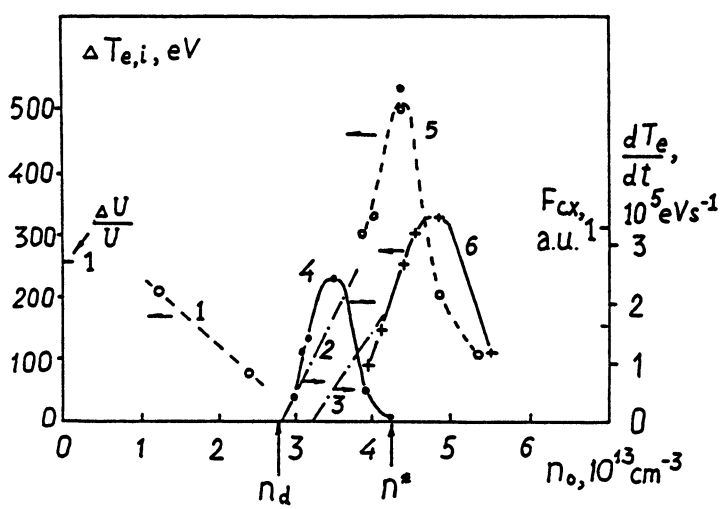

Fig. 10. The general picture of the LH wave – plasma interaction regimes: 1 — loop voltage drop; 2, 3 — CX fluxes with energies 1.0 and 3.7 keV, respectively; 4 — time derivative of T_e; 5 — rise of T_e; 6 — rise of T_i.

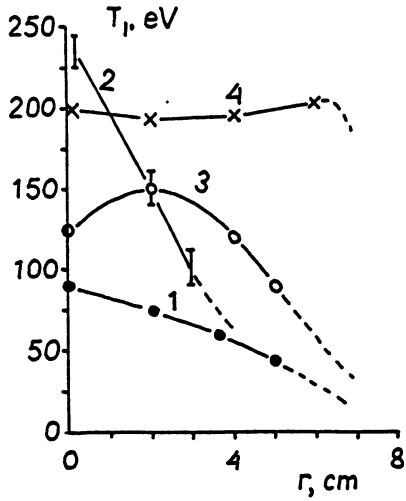

Fig. 11. Chord distribution of T_i at various T_e in the ohmic regime. 1 — ohmic regime; 2 — $T_e = 700$ eV; 3 — $T_e = 500$ eV; 4 — $T_e = 350$ eV.

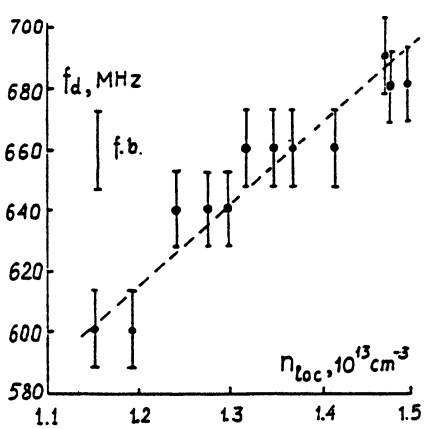

Fig. 12. Daughter wave frequency versus local density of parametric decay region. Dashed line is the $f \propto \sqrt{n}$ dependence.

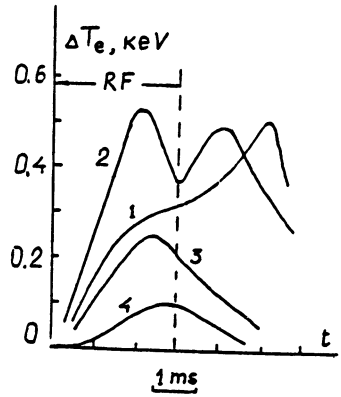

Fig. 13. Time behavior of electron temperature at various densities n_0: 1 — $n = 3.1 \cdot 10^{13}$ cm^{-3}, 2 — $n = 3.5 \cdot 10^{13}$ cm^{-3}, 3 — $n = 3.9 \cdot 10^{13}$ cm^{-3}, 4 — $n = 4.3 \cdot 10^{13}$ cm^{-3}.

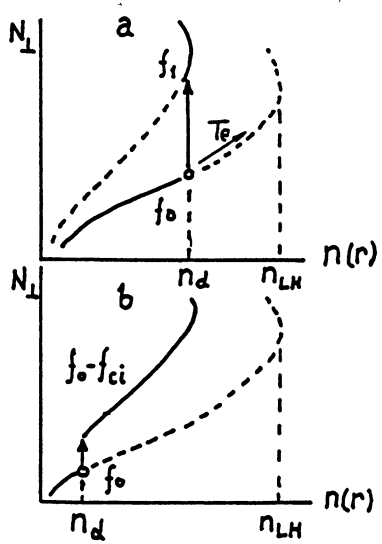

Fig. 14. Models of energy transport.

NEW TRANSPARENCY REGIONS FOR WAVES IN A NON-UNIFORM MAGNETIZED PLASMA

E.Z.Gusakov, M.A.Irzak, A.D.Piliya

A.F.Ioffe Physico-Technical Institute, 194021 St.Petersburg, Russia

New transparency regions may exist in a non-uniform magnetized plasma which can not be handled by a conventional WKB approach. Here we derive a generalized WKB equations describing adequately the waves propagation in such regions.

The WKB method is effectively used for the analysis of the wave propagation in a non-uniform plasma [1]. When the plasma is non-uniform only in one direction the method is based on representation of the field $E_i(x,t) = E_i(x)\cdot\exp(i\omega t)$ as an asymptotic series

$$E_i(x) = \sum_n E_i^{(n)}(x)\cdot\exp\left[i\frac{\omega}{c}\left(\int^x N_x(x')dx' + N_y y + N_z z\right)\right] \qquad (1)$$

where the terms $E_i^{(n)}(x)$ are assumed to decrease as $(k_x L)^{-n}$ (where L is the plasma inhomogeneity scale) and can be found by substituting (1) into the Maxwell equation

$$\Delta\vec{E} - \text{graddiv}\,\vec{E} + \frac{\omega^2}{c^2}\hat{\varepsilon}\vec{E} = 0, \qquad (2)$$

and equating the terms proportional to the same powers of the small parameter. In the 0-th order approximation the dependence $E_i^{(0)}(x)$ is neglected and one can determine both the dispersion relation

$$D_0(\omega,\vec{k},x) = 0 \qquad (3)$$

binding the wave vector with the frequency and coordinate and the wave polarization. These results coincide with corresponding expressions of the uniform plasma theory. In the next orders approximations one can find the dependencies $E_i^{(0)}(x)$ and then $E_i^{(0)}(x)$. The WKB approximation is applicable only to a weakly inhomogeneous plasma. Usually, by analogy with a non-magnetized plasma case, the applicability criterion is considered as

$$\frac{1}{k_x^2}\frac{dk_x}{dx} << 1 \qquad (4)$$

though, strictly speaking, the necessary condition to be fulfilled is

$$\left|E_i^{(0)}\right| >> \left|E_i^{(1)}\right| \qquad (5)$$

The importance of this observation can be illustrated by the following example. Let us assume that the plasma is non-uniform across the external magnetic field ($\vec{B} = B_0\vec{e}_z$). Then the dispersion relation (3) is especially simple in the case of transversal wave propagation at $N_z = 0$. For an extraordinary wave in the cold plasma model it looks like

$$N_x^2 = \frac{\varepsilon^2 - g^2}{\varepsilon} - N_y^2, \quad \text{where} \quad \varepsilon \cong 1 + \frac{\omega_{pe}^2}{\omega_{ce}^2} - \frac{\omega_{pi}^2}{\omega^2}; \quad g \cong \frac{\omega_{pe}^2}{\omega\omega_{ce}}. \qquad (6)$$

From this equation it follows, in particular, that the LH resonance is inaccessible from the plasma periphery and that the waves with $N_y > 1$ (i.e. slowed down in the direction perpendicular to the density gradient and the magnetic field) do not propagate. In the last case according to (6) the electric field decays exponentially inside the plasma:

$$E_y \propto \exp\left(-\frac{\omega}{c}\int^x \sqrt{N_y^2 - 1 + g^2}\,dx\right). \qquad (7)$$

According to (4) this is valid if $|g'| << (\omega/c)N_y^2$ (Here and further on the prime denotes d/dx).

However, this conclusion is sometimes quite contradictory with the results of numerical solution of (2). For example, in Fig. 1 we present the spatial distribution of the field component E_y, excited from the plasma periphery at the frequency 500 MHz. For the magnetic field $B =$ 18 kGs and density gradient $\nabla n_e = 10^{12}$ cm^{-4} the LH resonance is located at approximately 7 cm from the plasma surface. One can see that at some values of $N_y >> 1$ satisfying the criterion (4) a sequence of eigenmodes is excited in the plasma. As N_y increases the modes penetrate deeper inside and their wave length decreases. At $N_y > 16$ the propagation region reaches the LH resonance where a strong damping takes place. Such a contradiction between the WKB behavior described by (7) and the numerical modeling is due to breaking the necessary condition of WKB applicability criterion (5) which in our case has the form: $|g'| << (\omega/c)N_y$.

The possibility of strong damping of the LH waves at their transversal propagation has been pointed out before in the paper [2], where the absorption of the LH waves in a non-uniform plasma cylinder was investigated numerically. The accessibility of the LH resonance in [2] was confirmed qualitatively by the analysis of the differential equation describing an extraordinary wave and then it was concluded that this effect could not be described in the WKB approximation and the numerical solution of (2) was necessary.

But let us note that the solution of (2) presented in Fig. 1 for various N_y are "WKB-like", i.e. they can be represented by a sine function with a slowly varying wavelength and amplitude. At $N_z = 0$ fast and slow modes are decoupled

and then the analytical expression for this function can be obtained from the equation describing E_y component of the field:

$$E_y'' + \frac{\varepsilon' N_y^2}{\varepsilon(N_y^2-\varepsilon)} E_y' + \frac{\omega^2}{c^2}\left[\frac{\varepsilon^2-g^2}{\varepsilon} - N_y^2 - \frac{g' N_y}{\varepsilon}\frac{c}{\omega} - \frac{\varepsilon' g N_y}{\varepsilon(N_y^2-\varepsilon)}\right] E_y = 0$$

which is a second order differential equation. Applying the WKB method for the solution of this equation E_y can be represented in the form (1), but the difference is that now the refractivity index N_x must satisfy to a relation including the terms which are usually neglected in a conventional WKB analysis:

$$N_x^2 = \frac{\varepsilon^2-g^2}{\varepsilon} - N_y^2 - g' \frac{N_y}{\varepsilon}\frac{c}{\omega}, \qquad (8)$$

Here we assumed that $|g'| >> |\varepsilon'|$, which usually holds in the intermediate frequency range $\omega_{Bi} << \omega << \omega_{Be}$. The relation (8) is valid while the criterion (4) is satisfied and it follows from it that the LH resonance is accessible for the waves with positive $N_y > 0$ under the following conditions:

$N_y \frac{c}{\omega}|g'| > N_y^2$ at the plasma surface and $N_y \frac{c}{\omega}|g'| > g^2$ near the LHR.

According to (8) the maximum extent of the propagation region $\mathcal{L} = c/2\omega$ is achieved at $N_y = (c/2\omega_{ce})(\nabla n_e / n_{cr})$. The LH resonance becomes accessible at $L_n = (n_e'/n_{e0})^{-1} < c/\omega$.

The non-WKB terms may also lead to essentially new effects at $N_z \neq 0$. The method of taking them into account can be illustrated in a potential case $E = -\nabla\varphi$, when the field is described by $\mathrm{div}\,\vec{D} = 0$. In this case the equation for the field potential φ has the form:

$$\varepsilon\varphi'' + \varepsilon'\varphi' - \left(\frac{\omega}{c} N_y g' - \frac{\omega^2}{c^2} N_y^2 \varepsilon - \frac{\omega^2}{c^2} N_z^2 \eta\right)\varphi = 0 \qquad (9)$$

Making here the WKB substitution of the type (1) and neglecting $\varepsilon_{ik}' << (\omega/c) N_x \varepsilon_{ik}$ we obtain the dispersion relation

$$\varepsilon\left(N_x^2 + N_y^2\right) + \eta N_z^2 + \frac{c}{\omega} N_y g' = 0 \qquad (10)$$

Here the term $(c/\omega) N_y g'$ was kept because the terms proportional to $N_y N_x g$ were canceled in (9). The condition $(\omega/c) N_x L_n >> 1$ is not sufficient in this case.

We can proceed in the same way in the general case. Let us divide the field into the potential part and the curl $E_i = -\nabla_i\varphi + \mathcal{E}_i$. Then introducing WKB representations of these fields (1) into (2) we obtain the equation for the field potential. In so doing let us keep the terms with spatial derivatives of the dielec-

tric tensor elements only if the corresponding main (classical) terms (proportional to the tensor elements) are canceled and let us always neglect the derivatives of the field amplitudes. As a result we get a modified dispersion equation in the form:

$$D_0(N, \omega, x) + \delta D = 0, \text{ where} \tag{11}$$

$$\delta D = \frac{\varepsilon - N^2}{N^2}\left(\eta - N^2\right)\left\{\frac{c}{\omega}\nabla g \cdot \left[\vec{N} \times \frac{\vec{B}}{|\vec{B}|}\right] - g\vec{N}\frac{c}{\omega}\,\mathrm{rot}\,\frac{\vec{B}}{|\vec{B}|}\right\};$$

The dispersion curves $N_x(x)$ obtained from (11) for $N_z = 0.4$ at various N_y for the parameters of the previous numerical modeling are shown in Fig. 2. The transparency region at high $|N_y|$ exists only at $N_y > 0$. The conditions for eigenmodes of Fig. 1 localized in this region is similar to the quantum number law relating the refractive indices N_y and N_z:

$$\frac{\omega}{c}\oint N_x \mathrm{d}x = \frac{3\pi}{2} + \mathrm{n}\pi\,, \tag{12}$$

The analogous relation is obtained from the numerical solution of (2) as a condition of the plasma matrix impedance components equality to zero. These two predictions are compared in Fig. 3 where one can see a good agreement between them.

The plasma inhomogeneity can also change the dispersion characteristics of fast magnetosonic waves with frequencies several times the ion cyclotron frequency. In Fig. 4 we present the map of the zeros of the plasma surface impedance and the curves corresponding to the quantum number law (12), where N_x values were calculated both from the conventional dispersion equation (3) and from the modified one (11) for the frequency 20 MHz, magnetic field 0.5 T and $\nabla n_e = 10^{12}\,\mathrm{cm}^{-4}$. A reflecting metal wall placed at the distance 4.8 cm from the plasma surface produced the configuration necessary for the excitation of eigenmodes of a plasma waveguide. The results obtained from the modified dispersion equation agree very well with the numerical calculation while the conventional formula contradicts to them.

The good agreement of the modified dispersion equation (11) and the numerical modeling allows to use (11) in ray tracing calculations of the current generated by LH waves in the tokamak plasma. In Fig. 5 we present radial profiles of the RF current density computed with the use of dispersion relations (3) — curve 1 and (11) — curves 2 and 3 for co- and counter-injection of the current in FT-2 tokamak ($a = 8$ cm, $R = 55$ cm, $n_e(0) = 3\cdot10^{13}\,\mathrm{cm}^{-3}$, $T_e(0) = 450$ eV, $I_p = 30$ kA, $B = 20$ kGs, $P_{RF} = 400$ kW, $2 < N_z < 4$). A significant difference in the value and localization of the RF current is due to the different accessibility conditions for the waves with opposite signs of N_y.

Thus non-WKB terms resulting from the plasma inhomogeneity can significantly modify the dispersion characteristics of the waves in the intermediate frequency range. They have a noticeable effect on the ray-tracing trajectories and on the RF driven current profiles in small tokamaks. Besides, they can be important for providing the accessibility conditions for some parts of the wave spectra excited in the plasma.

References

1V.L.Ginsburg. "Propagation of electromagnetic waves in plasma." Moscow, Nauka, 1967.

2Yu.N.Dnestrvsky, D.P.Kostomarov et al. *Fizika Plasmy*, 1975, **1**, p. 623.

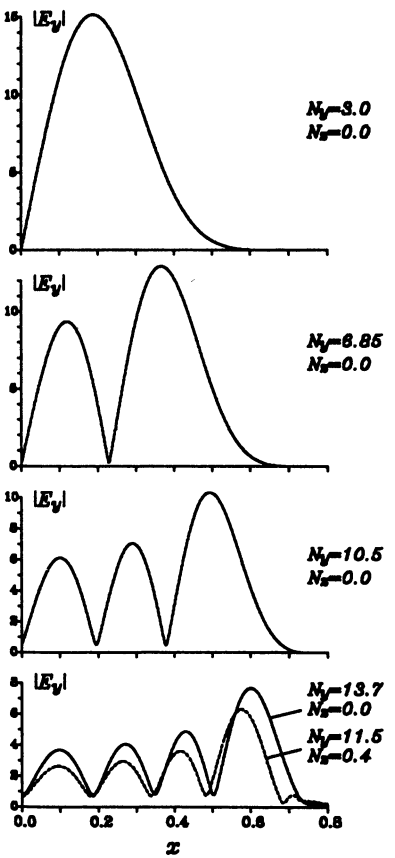

Fig.1. Electric fields structure in plasma. f = 500 MHz, B = 18 kGs, dn/dx = 10e12 cm−4

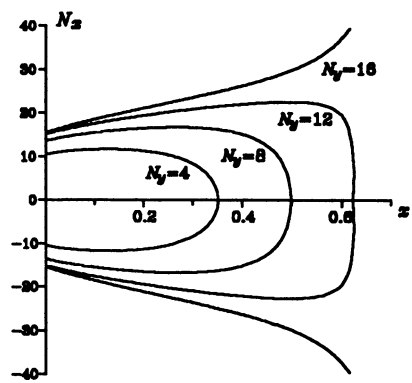

Fig.2. Dispersion curves for the same parameters; $N_z = 0.4$

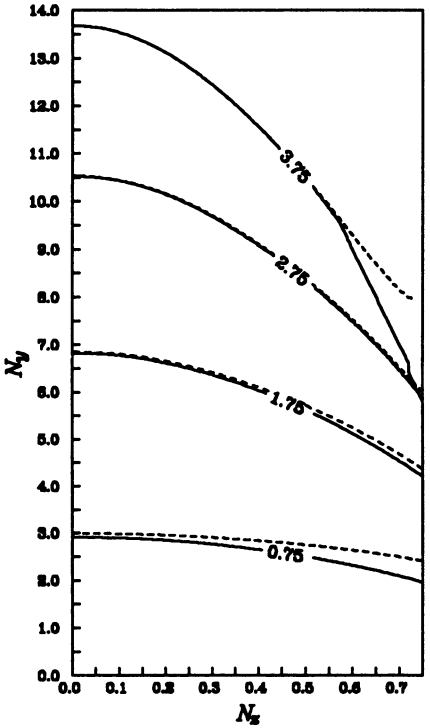

Fig.3. Phase integrals over WKB loops (solid lines) and zeros of plasma surface impedance Ey/Bz (dashed lines).

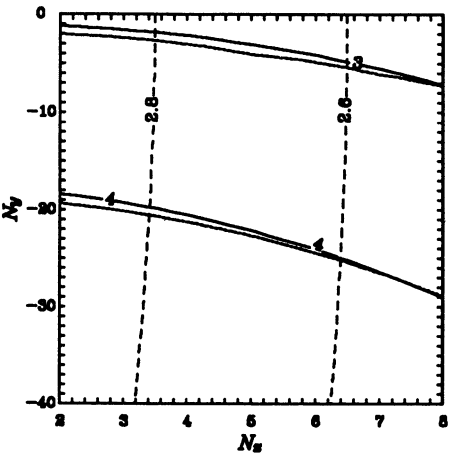

Fig.4. Zeros of plasma surface impedance (dots) and phase integrals over WKB loop: classical (dashed) and modified (solid line) cases. f = 20 MHz, B = 0.5 kGs, dn/dx = 10e12 cm−4. Reflecting mirror at 4.8 cm from the edge.

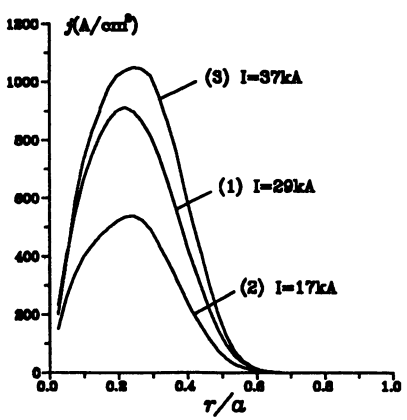

Fig.5. RF current profiles in FT−2 tokamak. (1) − using Eq.(3); (2) and (3) − co and counter injection respectively using Eq.(11).

On the influence of nonlinear correction on ECCD efficiency

A.Yu. Kuyanov†, A.A.Skovoroda†, M.D.Tokman‡

†INF, RRC I.V.Kurchatov Institute, Moscow, Russian Federation
‡ IAP, N. Novgorod, Russian Federation

1. In modern ECCD experiments on tokamaks essential deviation of the distribution function of resonant electrons from the Maxwellian one is achieved [7,19]. Calculations show that this can lead to sufficient changes in of the linear CD efficiency [1,5,10,23].

The increase in the characteristic perpendicular energy of resonant particles in the course of intensive ECR heating plays different roles depending on the experimental conditions. It is, therefore, of significant practical interest to analyze the regimes, in which the increase in local CD efficiency at large power levels is possible without decrease in the absorption coefficient of EC-wave. In work [10] the scaling for the power threshold of a quasi-linear increase in the local CD efficiency is obtained. In the present work we calculate the scaling for the maximum possible increase of CD global efficiency at high-power EC-heating for the parameters of the T-10 tokamak.

2. To obtain the scaling for CD efficiency at high level of EC-power we shall use the stationary quasi-linear equation for the electron distribution function. Within the approximation of the zero inductive electric field this equation has the following form [4,11,14,18,21]:

$$\left(\hat{Q} + \hat{S}\right) f = 0, \tag{1}$$

where $\hat{Q}$ is diffusion operator in the phase space under the EC-resonant condition, and $\hat{S}$ is operator of Coulomb collisions. We shall consider electron distribution function $f = f(v, \mu)$, where v is absolute value of electron velocity, and μ is cosine of the pitch angle.

In works [11,14,18,21] various $\hat{Q}$ representations with quasi-linear diffusion coefficient D were discussed. We use the following simplest form (see, e.g. [14,21]):

$$\hat{Q} = \hat{L} D \hat{L}, \tag{2}$$

$$\hat{L} = \frac{1}{v}\left(\frac{\partial}{\partial v} + \left(\Delta(v) - \mu^2\right)\frac{1}{v\mu}\frac{\partial}{\partial \mu}\right), \tag{3}$$

where $\Delta(v) = 1 - n\omega_r/\omega$, and ω_r is relativistic gyrofrequency, and n is number of a cyclotron harmonic.

The structure of function $D(v,\mu)$ is determined by spatial distribution of a microwave field over the considered flux surface and by the character of electron motion in a non-uniform magnetic field [14,18]. Generation of the EC-driven current is possible if D is an asymmetric function of variable μ [8]. Bounce averaging produces essential pitch angle symmetry of f and D in the banana region, where

$$|\mu| \leq \mu_c = \sqrt{\frac{2\varepsilon}{\varepsilon+1}}; \tag{4}$$

here $\varepsilon = r/R$ is local inverse aspect ratio. Consider LFS input of EC-waves in a tokamak with large enough optical depth of the plasma column. In this case it is possible to choose $D = 0$ for passing (untrapped) electrons with negative μ.

One can obtain all possible mechanisms of ECR current j generation having integrated quasi-linear equation (1) over $dvd\mu$ with weighting function $v^6\mu$:

$$j = j_{FB} + j_{||} + j_{fr} + j_{Okh} \tag{5}$$

The first term in Eq.(5) is the standard Fisch-Boozer current, j_{FB}, related to production of anisotropic electron resistivity under EC-heating [8]; $j_{||}$ is current produced by introduction of the longitudinal momentum of EC-wave into resonant electrons [8]; the third term, j_{fr}, describes current degradation due to the so-called neoclassical friction between the passing and trapped particles [9], the last term, j_{Okh}, is current connected with the wave–induced push of passing particles into the banana area in the phase space (Okhawa current [17]).

For the qualitative analysis we shall restrict the scope of this investigation to the case of the Lorentz gas approximation. It is convenient to introduce the function of distribution of the absorbed wave power and the averaging procedure over this function in the resonant region of the phase space (see the works [14,22,23])

$$p(v,\mu) = -mD\hat{L}f; \langle U(v,\mu)\rangle_r = P_u^{-1}\int_0^\infty\int_{\mu_c}^1 U(v,\mu)v^2p(v,\mu)dvd\mu, \tag{6}$$

where P_u is power density absorbed only by passing particles (P is total density of absorbed power deposition in the coordinate space), U is arbitrary function, and m is electron mass. We can obtain a simple expression for the total current density:

$$j = \frac{3eP_u}{m(4+2Z)D_c}\left(\left\langle v^2\mu\right\rangle_r - \frac{4\mu_c}{3}\left\langle v^2\right\rangle_r + \frac{1}{3}\left\langle\frac{\Delta(v)v^2}{\mu}\right\rangle_r\right), \tag{7}$$

where $D_c = v_e v_T^3$, v_e is frequency of Coulomb collisions for electrons, v_T is electron thermal speed, $Z = (1+Z_{eff})/2$, and Z_{eff} is effective charge of ions.The last term in the brackets describes the transfer of the wave longitudinal momentum

to electrons and will be ignored below. The second term describes the current degradation due to the trapped particles. It should be noted that the last expression gives a qualitatively correct description of the tendency of sharp reduction of EC-current with the characteristic value $\langle\mu\rangle_r$ of approaching the boundary of trapping cone μ_c for arbitrary Z_{eff}. In numerical calculations this effect was found, e.g., in work [23].

Equation (7) yields the following relation for the CD efficiency:

$$\eta = \frac{j}{P_u} \approx \eta_{FB} \frac{1 - \frac{\alpha\mu_c}{\langle\mu\rangle_r}}{\langle\mu\rangle_r}. \tag{8}$$

Here η_{FB} is standard Fisch-Boozer efficiency [8], and α is numerical factor of the order of unity. It follows from equation (8) that in the area of $\langle\mu\rangle_r \gg \mu_c$ efficiency of ECCD increases with increasing of the averaged pitch angle of resonant electrons (i.e. with falling $\langle\mu\rangle_r$ in the process of quasi-linear distortion of the distribution function). This effect was obtained from numerical calculations in works [5,10,15,23].

The regimes of EC-heating are very interesting and promising, when quasi-linear relaxation produces an increase in the CD efficiency without considerable decrease of the absorption coefficient of EC-wave.

There are two regimes of this type. First, it is the autoresonance regime, in which the longitudinal refraction index is equal to $N_\parallel = 1$ [13,15,24].

For ECR plasma heating in a toroidal device another attractive regime can be easily realized [20], namely, heating of subrelativistic electrons at the following conditions:

$$1 - \frac{n\omega_r}{\omega} - N_\parallel \frac{v_\parallel}{c} = 0, \tag{9}$$

$$\frac{v_r^2}{2c^2} \ll N_\parallel \frac{v_{\parallel r}}{c}. \tag{10}$$

Here index r marks all variables on the EC resonant line (9) and c is speed of light. In this limit resonant lines and quasi-linear diffusion curves in the phase space are close to vertical straight lines:

$$v_{\parallel r} = \frac{c\Delta(0)}{N_\parallel} = c\frac{\omega - n\omega_{r0}}{\omega N_\parallel}, \tag{11}$$

where ω_{r0} is nonrelativistic gyrofrequency. Under these conditions, the wave-induced diffusion cannot essentially reduce absorption of waves [20]. It should be noted that as energy of the particles grows, the shift of the relativistic mass changes the EC resonant lines stronger than quasi-linear diffusion lines. This shift leads, in the long run, to formation of a quasi-linear plateau.

The finite width of the spatial or temporal spectrum of microwave radiation and magnetic field inhomogeneity within the area of a microwave beam results in

formation of a resonant "belt" with width $\Delta v_{\|r}$ in the phase space [11,14]. For the sake of definiteness we shall consider the effect of the finite angular spectrum $\Delta N_\| \ll N_\| \ll 1$. One can obtain from simple geometrical considerations that the "belt" width $\Delta v_{\|r} \simeq \frac{\Delta N_\|}{N_\|} v_{\|r}$ determines the maximum value of perpendicular velocity $v_{\perp r}^2 = 2cN_\| \Delta v_{\|r}$ in the region of parameters described by equation (10).

From estimation for $\langle \mu \rangle_r$,

$$\langle \mu \rangle_r \approx \frac{1}{\sqrt{1 + \frac{v_{\perp r}^2}{v_{\|r}^2}}} \approx \frac{1}{\sqrt{1 + \frac{2N_\|^3 \Delta v_{\|r}}{c\Delta^2(0)}}}, \tag{12}$$

and relation (8) it is clear that the gain in efficiency increases with the increase of "belt" width $\Delta v_{\|r}$. The optimum width of the resonant "belt" is $\Delta v_{\|r} \simeq \frac{v_{\perp r}^2}{2v_{\|r}}$. In this region the electron distribution function over longitudinal velocities decreases significantly. For wider resonance region the whole number of electrons within this zone cannot grow significantly and, hence, CD efficiency cannot increase further.

For the quasi-Maxwellian electron distribution function the absorption of the main part of microwave power occurs in the area described by equation (10) at the following condition [16,22]:

$$\left(\frac{cN_\|}{v_T} \right)^2 > \ln \tau, \tag{13}$$

where τ is optical depth of plasma column for the considered EC-wave. At this condition the characteristic value of the normalized resonance detuning in the region of main absorption of microwave power is equal to

$$|\Delta(0)| \approx \frac{N_\| v_T \sqrt{\ln \tau}}{c}. \tag{14}$$

In the limit of a small inverse aspect ratio, $\varepsilon \to 0$, expressions (8),(12),(14) yield the following relation for the CD efficiency for the case of reasonably small $N_\|$:

$$\frac{\eta_{\max} - \eta_{FB}}{\eta_{FB}} \approx \frac{cN_\|}{2v_T (\ln \tau)^{3/2}}. \tag{15}$$

It is clear from equation (15) that the relative gain is proportional to the launching angle (which determines $N_\|$) almost inversely proportional to the temperature and has a logarithmically weak dependence on plasma density.

3. Estimation (15) was obtained for the local ECCD efficiency (i.e., for fixed flux surface). In practice, the global efficiency, $\langle \eta \rangle$, determined as the ratio of the total current I to the total absorbed power W, $\langle \eta \rangle = I/W$, is also very important. One of the objectives of our calculations is to check the possibility of expansion of

the local scaling (15) to global ECCD efficiency. There is an important question when profile effects are essential.

Another objective of the calculations is to obtain a quantitative relation for the expected probable nonlinear gain in efficiency in real experiments on tokamak T-10. The necessary level of microwave power for this gain is also determined.

The calculations were carried out with the use of the OGRAY kinetic code [15] at fixed plasma parameters and their profiles. The profiles and values of electron temperature $T_{eo} = 4.3$ keV and density $n_{eo} = 1.7 \cdot 10^{13}\text{cm}^{-3}$ on the toroidal axis agreed with experimental conditions in tokamak T-10 for 0.6 MW power and on-axis heating (see [15]). The effective charge of ions Z_{eff} was taken to be independent on radius ($Z_{eff} = 2$).

The microwave power (frequency of 70 GHz or 140 GHz) was concentrated in a gaussian beam with characteristic half-width $6cm$.

In the Figure we present dependencies of the maximum relative nonlinear gain in CD efficiency on: (a) the longitudinal refraction index in the region of the ECR absorption, (b) the on-axis temperature, and (c) the on-axis plasma density. To obtain these dependences, the on-axis ECR heating was considered. The level of input power was up to 5 MW. There is a reasonable agreement between the curves in the Figure and the scaling:

$$\frac{\langle\eta\rangle_{\max} - \langle\eta_0\rangle}{\langle\eta_0\rangle} \approx 5\frac{N_{\parallel}}{T_{eo}(keV)}. \qquad (16)$$

4. The presented analysis of ECCD in tokamaks at LFS launch of microwaves shows that the sufficient nonlinear ECCD efficiency gain is possible at the modern experimental level of microwave power. For this gain the oblique wave launching and a reasonably low temperature (see the condition (13) and scalings (15) and (16)) are preferable. Such regimes allow an increase in the EC-driven current in the off-axis region.

The work is supported by Russian Foundation for Basic Research Grants 95-02-03503-a, 95-02-04999-a.

References

[1] Alikaev V.V. and Vdovin V.L. (1983) *Fizika Plasmy* **9**, 928.

[2] Alikaev V.V. *et al* (1992) *Nuclear Fusion* **32**, 1811.

[3] Alikaev V.V. and Suvorov E.V. *Application of High-Power Microwaves* p.111. Artech House, Boston - London, (1994).

[4] Cohen R.H.(1967) *Phys. Fluids* **30**, 2443.

[5] Dnestrovskij Yu.N. *et al* (1988) *Nuclear Fusion* **28**, 267

[6] Dnestrovskij Yu.N. *et al* (1990) *Fizika Plasmy* **16**, 1286.

[7] Esipchuk Yu.V. (1995) *Plasma Physics and Controlled Fusion* **37** Suppl. 11 A, A279.

[8] Fisch N.J. (1987) *Rev. Mod. Phys.* **59**, 175.

[9] Cordey J.G. *et al* (1982) *Plasma Phys.* **24**, 73.

[10] Harvey R.W. *et al* (1989) *Phys. Rev. Lett.* **62**, 426.
[11] Harvey R.W. and McCoy M.G. (1992) GA Comp. Report, GA-A20978.
[12] Harvey R.W. *et al* (1995) Proc.9th Joint Workshop on ECE and ECH, Wold Scientific Publishing, Singapore, p. 63.
[13] Kuyanov A.Yu. *et al* (1992) Proc.14th International Conference on Plasma Physics and Controlled Nuclear Fusion Research, v.1, p.733.
[14] Kuyanov A.Yu. *et al* (1993) *Plasma Phys. Rep.* **19**, 683.
[15] Kuyanov A.Yu. *et al* (1994) Proc.15th International Conference on Plasma Physics and Controlled Nuclear Fusion Research, v.2, p.177.
[16] Litvak A.G. *et al* (1994) *Phys. Lett.* **A.188**, 64.
[17] Okhawa T. (1976) GA Comp. Report., GA-A13847.
[18] O'Brien M.B. *et al* (1986) *Nuclear Fusion* **26**, 1623.
[19] Razumova K.A. *et al Physics of Plasmas* **1**, 1554.
[20] Suvorov E.V. and Tokman M.D. (1983) *Plasma Phys.* **25**, 723.
[21] Timofeev A.V. and Tokman M.D. (1994) *Plasma Phys. Rep.* **20**, 336.
[22] Tokman M.D. (1995) Proc. 9th Joint Workshop on ECE and ECH, World Scientific Publishing, Singapore, p.51.
[23] Yoshioka K. and Antonsen T.M. (1986) *Nuclear Fusion* **26**, 839.
[24] Zvonkov A.V. *et al* (1995) Preprint IAE-5941 / 6, Moscow.

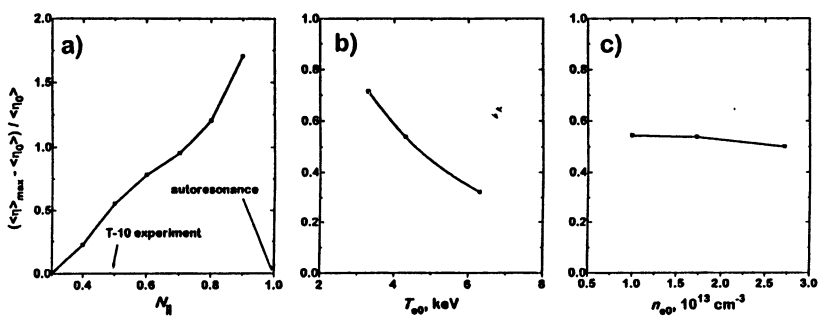

ELECTRON QUASILINEAR DIFFUSION UNDER ECR INTERACTION AT THE SUPERADIABATIC REGIME

A.V.Timofeev, A.V.Zvonkov

RNC Kurchatov Institute, Moscow, Russia

Gyrotrons used for ECR heating and current drive in thermonuclear devices generate almost monocromatic electromagnetic waves. However the electron distribution function evolution is described by the quasilinear diffusion equation based on random phase approximation. Larmor phase randomization can due either to the phenomenon of resonance overlapping or to Coulomb collisions. The bounce resonances are overlapped if the wave amplitude is sufficiently large, see for example [1]. Usually this condition is fulfilled for main part of the electrons with energy $\varepsilon \approx 1$-10keV. However, it can be violated for relativistic electrons ($\varepsilon \approx$ 0.1-1Mev). In some situations these electrons can provide the main part of the ECR current, for example in autoresonance mode of the current drive [2].

If the bounce resonances are "separated", electrons oscillate on the phase plane under ECR interaction regularly. This regime of the ECR interaction is named usually as superadiabatic regime. In this regime Coulomb collisions induce some weak electron diffusion on the phase plane. But synergetic effect of the Coulomb collisions and regular oscillation is more important. This effect is similar to the neoclassical diffusion.

This regime is analysed in [3], see also [1], for the problem of ECR in the magnetic traps and for abstract problem of standard mapping [4]. In both papers the simplest model of random impacts acting on Larmor phase is considered. The quasilinear diffusion coefficients obtained in these papers turn out identical. However, in real conditions random variations of the motion integrals ε, $\mu = p^2 \sin^2\theta / 2m\omega_{e0}$ are more important than direct Larmor phase randomization. (Here ε - electron energy, ω_{e0} - nonrelativistic electron cyclotron frequency, θ - pitch angle.) For relativistic electrons μ-variation due to the pitch angle scattering is most important. This process determines the Larmor phase dispersion.

We shall analyse in detail the most interesting case of weak collisions $D_\theta \langle\langle (\Delta\theta)^{3/2} \Omega_\theta'^{1/2}$. Here D_θ - diffusion coefficient on pitch angle, $\Delta\theta = (\frac{\omega_{e0}}{\omega} - \sin^2\theta \frac{\varepsilon}{mc^2}) \frac{2m\Delta\varepsilon}{p^2 \sin 2\theta}$ - pitch angle increment under one ECR interaction act, Ω - wave phase change on the electron trajectory during one bounce period. In this case Coulomb collisions distort the electron trajectory on the phase plane weakly. However inverse influence of the regular oscillations on Coulomb collisions can be strong. In particular, Coulomb collisions term transformed by regular oscillations describes some effects which can be considered as quasilinear diffusion due to ECR interaction.

The similar problems arise at the describing of the evolution of finite amplitude plasma oscillations [5] and of the charged particles dynamics in the magnetic traps [6]. The procedure of Coulomb collisions term transformation was worked out, see for example [6]. It is necessary to introduce the variables action - phase angle and to average Coulomb collision term on the phase.

We shall consider the electrons near the bounce resonance curve on phase plane $\Omega(\varepsilon, \mu) = 2\pi N$. Let us introduce Cartesian coordinates (p_1, p_2), p_1 -axis is directed along pitch angle. In this variables Coulomb collisions term takes the form

$$St = D_\theta p^2 \frac{\partial^2 f}{\partial p_1^2}. \qquad (1)$$

As it is known, electrons are displaced along lines $\varepsilon - \mu\omega = const$ under ECR action. The unit vector directed along this line is equal to $\vec{e} = (b,1) / (b^2 + 1)^{1/2}$, here $b = 2(\omega_e / \omega - \sin^2\theta) / \sin 2\theta$.

Let us introduce the new coordinate system (ς, η) with ς - axis along $\vec{e}$ -vector

$$\varsigma = p_1 e_1 + p_2 e_2,$$
$$\eta = p_1 e_2 - p_2 e_1.$$

Near bounce resonance curve ($\Omega(\varsigma, \eta) = 2\pi N$) the motion equations have standard form

$$\dot{\Phi} = \Omega'_\varsigma \varsigma + \Omega'_\eta \eta,$$

$$\dot{\varsigma} = \Delta_\varsigma \sin\Phi.$$

Here $\Delta_\varsigma = (\varepsilon / c^2 p)(1 + b^2)^{1/2} \Delta\varepsilon$, $\Delta\varepsilon$ - energy increment in one cyclotron interaction act, time is measured in $2\pi / \omega_b$ units.

The Hamiltonian

$$H = \varsigma'^2 / 2 - \cos\Phi$$

corresponds to this equation system, here $\varsigma' = (\varsigma - \varsigma_0) / g$, $g = (\Delta_\varsigma / \Omega'_\varsigma)^{1/2}$.

The motion described by this Hamiltonian was studied in detail, see for example [5]. We shall consider only so-called transit trajectories with unlimited phase change

$$\Phi = 2am(\alpha K(k) / \pi),$$

$$\varsigma' = (2 / k) dn(\alpha K(k) / \pi).$$

Action variable conjugated to α is given by the expression

$$I = 4E(k) / \pi k.$$

Here $K(k)$, $E(k)$ - complete elliptic integrals.

Let us transform (1) to the variables (I, η, α)

$$St = D_0 p^2 \left(\frac{\partial}{\partial I}\frac{\partial I}{\partial p_1} + \frac{\partial}{\partial \eta}\frac{\partial \eta}{\partial p_1}\right)\left(\frac{\partial I}{\partial p_1}\frac{\partial}{\partial I} + \frac{\partial \eta}{\partial p_1}\frac{\partial}{\partial \eta}\right) f.$$

Here we crossed out the terms $\frac{\partial}{\partial \alpha} C_1 \frac{\partial f}{\partial I}, \frac{\partial}{\partial \alpha} C_2 \frac{\partial f}{\partial \eta}$ vanished after α-averaging and the terms with derivative $\frac{\partial f}{\partial \alpha}$ as we assume that distribution function is independent on the phase. Jacobian $\frac{D(I, \alpha, \eta)}{D(p_1, p_2, \Phi)} = -\left(\frac{\Omega'_\varsigma}{\Delta_\varsigma}\right)^{1/2}$ dropped from this expression as it is almost constant near bounce resonance curve.

As the transformation $(\varsigma', \Phi) \to (I, \alpha)$ is canonical we obtain $\partial I / \partial p_1 = A \partial \Phi / \partial \alpha$, where $A = (e_1 + e_2 \Omega'_\eta / \Omega'_\varsigma)^{1/2}$. Derivative $\frac{\partial \eta}{\partial p_1}$ is equal to e_1. Also using relations $\langle \partial \Phi / \partial \alpha \rangle_\alpha = 1$, $\langle (\partial \Phi / \partial \alpha)^2 \rangle_\alpha = 4KE / \pi^2$ we obtain averaged Coulomb collision term

$$St = D_\theta p^2 (A^2 \frac{\partial}{\partial I} (\frac{4KE}{\pi^2} - 1) \frac{\partial}{\partial I} + + (A \frac{\partial}{\partial I} + e_1 \frac{\partial}{\partial \eta})^2) f. \quad (2)$$

In (2) the first term describes the diffusion on I, the second - along characteristics $dI / d\eta = e_2 / A$ on plane (I, η). Both processes have the comparable intensity near bounce resonance curve. However, the diffusion coefficient on the action $D_I = D_\theta p^2 A^2 (4KE / \pi^2 - 1)$ diminishes abruptly $D_I \propto I^{-4} (I \rangle\rangle 1)$ far from this curve. In real problems characteristic scales exceed distance between resonance curves greatly. Therefore electron distribution function is levelled off along characteristics and averaged diffusion coefficient can be used for describing the diffusion

$$\langle D_I \rangle_I \approx \frac{1}{2\pi} D_\theta p^2 A^2 (\Omega'_\varsigma \Delta_\varsigma)^{1/2} \int_0^1 dk \frac{K}{k^2} (\frac{4KE}{\pi^2} - 1). \quad (3)$$

Here the distance between resonances is evaluated as $\Delta I \approx 2 / k_{\min} \approx 2\pi (\Omega'_\varsigma \Delta_\varsigma)^{-1/2}$.

Collision term with averaged diffusion coefficient (3) assumes the form

$$St = [\langle D_I \rangle_I \frac{\partial^2}{\partial I^2} + D_\theta p^2 (A \frac{\partial}{\partial I} + e_2 \frac{\partial}{\partial \eta})^2] f. \quad (4)$$

It must be transformed to the variables p_1, p_2. This variables have no one to one correspondence with I, η as electrons blur because of oscillations on phase plane. However, only the processes with characteristic scales exceeding the distance between bounce resonances are of interest. This distance in turn exceeds the oscillation amplitude.

Therefore we can assume $I \approx (\Omega'_\varsigma \Delta_\varsigma)^{1/2}(\varsigma + \eta\Omega'_\eta / \Omega'_\eta)$ with precision $\Delta I \approx 1$.

Transforming (4) to the variables ς, η, we obtain

$$St = [\langle D_I \rangle_I \frac{\Delta_\varsigma}{\Omega'_\varsigma} \frac{\partial^2}{\partial \varsigma^2} + D_\theta p^2 (e_1 \frac{\partial}{\partial \varsigma} + e_2 \frac{\partial}{\partial \eta})^2] f.$$

Finally, using variables p_1, p_2, we find

$$St = [\langle D_I \rangle_I \frac{\Delta_\varsigma}{\Omega'_\varsigma} (e_1 \frac{\partial}{\partial p_1} + e_2 \frac{\partial}{\partial p_2})^2 + D_\theta p^2 \frac{\partial^2}{\partial p_1}] f.$$

Comparing this expression with (1) we see that additional diffusion along characteristics $e_2 p_1 - e_1 p_2 = const$ or equivalently along curves $\varepsilon - \mu\omega = const$ arises due to ECR interaction. This process can be characterized by the diffusion coefficient on energy

$$D_\varepsilon \approx \frac{1}{2\pi} D_\theta \varepsilon^{1/2} c p^{3/2} e_2 A^2 (\Omega'_\varsigma \Delta)^{1/2} \int_0^1 dk \frac{K}{k^2} (\frac{4KE}{\pi^2} - 1).$$

In the opposite case of the strong Coulomb collisions $D_\theta \rangle\rangle (\Delta\theta)^{3/2} \Omega'^{-1/2}_\theta$ is given by the usual quasilinear expression, see for example [1].

References

1. Timofeev A.V.// Reviews of the Plasma Theory./ Ed. Kadomtzev B.B. M.: Energoatomizdat. 1985. V.14. P.56.
2. Kujanov A.Yu., Skovoroda A.A., Timofeev A.V., Zvonkov A.V.// Plasma Phys. and Contr. Nucl. Fus. Res. Vienna: IAEA. 1993. V.1. P.733.
3. Timofeev A.V.// Fizika plazmy. 1975. V.1. P.88.
4. Rochester A.B., Rosenbluth M.N., White R.B.// Phys. Rev. 1981. V.A23. P.2664.
5. Budker G.I., Beljaev S.T.// Fizika plazmy i problemi upr. termojad. reak./ Ed. Leontovich M.A. AN SSSR . 1958. V.2. P.330.
6. Zaitsev T.S., O'Brien M.R., Cox M.// Phys. Fluids. 1993.V.B5. P.509.

NUMERICAL STUDY OF ECCD IN TOKAMAKS WITH OGRAY CODE

A.Yu.Kuyanov, A.A.Skovoroda, A.V.Timofeev, A.V.Zvonkov

INF, RRC Kurchatov Institute, Moscow

1. OGRAY code

Objectives. Numerical code OGRAY has been developed for study of ECR heating and current drive. Main requirements to the code were: adequate description of ECR interaction; flexibility; possibility of fast calculations on personal computers.

The OGRAY code is used for modeling of experiments in T-10, T-15 tokamaks, optimization of EC heating and current drive systems, searching for opportunities of nonlinear CD efficiency enhancement (autoresonance regime of CD).

Capabilities. The code provides computation of steady-state profiles of power deposition and induced current for arbitrary launching position and oblique launching angles for both O and X modes with simultaneous account for the absorption on several cyclotron harmonics.

Physical model. The Gaussian microwave beam with the width smaller than the plasma inhomogeneity scale is considered. The expression for the quasilinear diffusion coefficient for such a beam has been derived [1]. The calculation of the central ray trace is sufficient for the code. The electron distribution function found by solution of the stationary 2D quasilinear equation determines the absorption power density and induced current density on the given magnetic surfaces. Both the collision and quasilinear operators incorporate relativistic effects, trapped particles and are bounce-averaged.

Advantages. The quasilinear diffusion coefficient accounts for inhomogeneities of magnetic field and wave amplitude during the resonance interaction. The wave power on the trajectory is calculated with the account for quasilinear absorption. Ray tracing accounts for divergence (convergence) and diffraction of the wave beam [2]. Calculations on widely available computers are possible.

Drawbacks. The linearized collision operator is used, the momentum conservation is accounted approximately.The quasilinear equation does not incorporate the inductive electric field, so the induced conductivity is not accounted.

2. Study of equatorial launch in ITER

For microwave beam with frequency 170 GHz and power 50 MW at three values of magnetic field 5.68; 4.85; 4 T we computed radial profiles of power deposition *dP/dV* and driven current *J*, as well as total CD efficiency $\langle\gamma\rangle$ as a function of launching angle θ for an ordinary wave at equatorial launching. The main parameters of ITER and EC heating and the current drive system used in the calculations are presented in the Table. The plasma profiles were fixed. In the calculations the launching angle was varied with increment 5^0. The absorption on three harmonics of EC frequency was taken into account simultaneously.

Major radius, m	8.14
Small radius, m	2.8
Magnetic field on axis, T	4; 4.85; 5.68
Current, MA	14; 17; 21
q	3.1 - 3.2
Elongation (k_{95})	1.6
Electron temperature on axis, keV	20; for Ohmic stage 3.5
Electron density on axis, 10^{20} m^{-3}	1.3; for Ohmic stage 0.47
Gyrotron frequency, GHz	170
Gyrotron power, MW	50
Width of the wave beam at ECR point, m	0.4
Launching angle at radius 10.94 m, ^{0}.	0 (normal to an axis) - 50
Wave mode	Ordinary
EC harmonic	Fundamental
Effective charge	1.6

For magnetic field 5.68T at all launching angles EC power is absorbed almost entirely at the fundamental frequency and absorption is located at small radii from -50cm to +150cm (negative values correspond to position inside the magnetic axis). The location of

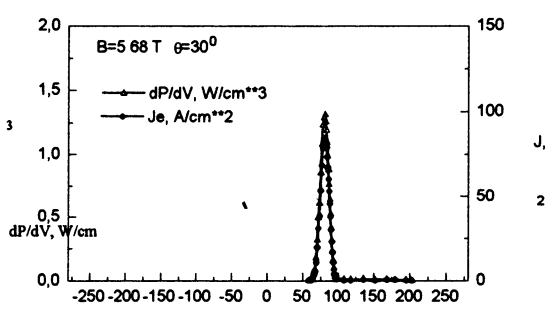

Fig.1 The profiles of power deposition and driven current for launching angle 30^0 and axis magnetic field 5.68T

absorption is shifted outside and the profile broadens as the launching angle increases. Note that for angle 40^0 the off-axis (on 1/2 of small radius) current drive is realized with rather high efficiency. The calculated profiles for the launching angle 30^0 are shown in Fig. 1.

In Fig. 2 the dependence of total CD efficiency and the share of total power absorbed at fundamental frequency on the launching angle is shown.

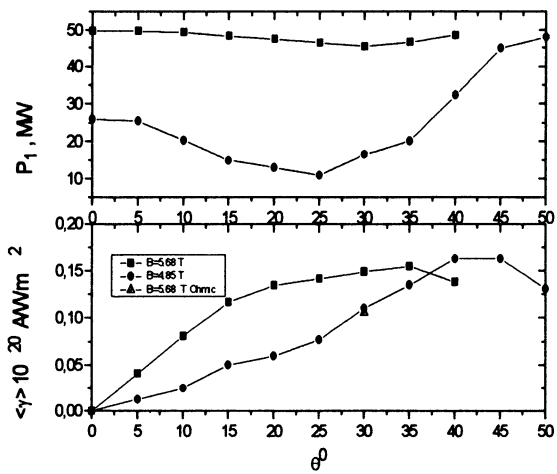

Fig.2 The dependence of CD efficiency and share of total power, absorbed on fundamental frequency, on launching angle

The efficiency increases with the rise of the launching angle up to 35^0 and achieves the value of $0.15 \cdot 10^{20} A/Wm^2$. For angles greater than 40^0 the power is not absorbed on one pass through the plasma due to decrease of absorption for a small angle between the wave vector and magnetic field. The density of driven current was found to be comparable with the density of inductive current, which gives the opportunity to control the profile of total current.

For magnetic field 4.85T a substantial part of EC power is absorbed at the second harmonic on the plasma periphery. For normal launching approximately half of the total power is absorbed before the wave reaches the fundamental harmo-

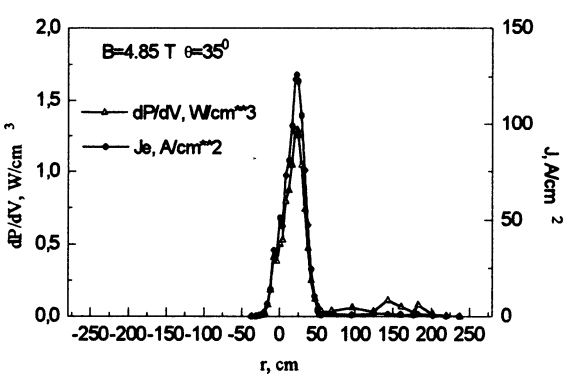

Fig.3 Power deposition and driven current profiles for launching angle 35^0 and magnetic field 4.85T

nic. The increase of the launching angle up to 25^0 rises the share of the power absorbed at the second harmonic. This is what explains significantly lower efficiency for these angles as compared with greater magnetic field.

For magnetic field 4T very large absorption is observed on the outer periphery of plasma at the second harmonic. The CD efficiency is very small: $0.014 \cdot 10^{20}$ A/Wm^2. The wave with frequency 170 GHz is hardly suitable for heating and current drive in magnetic field 4T.

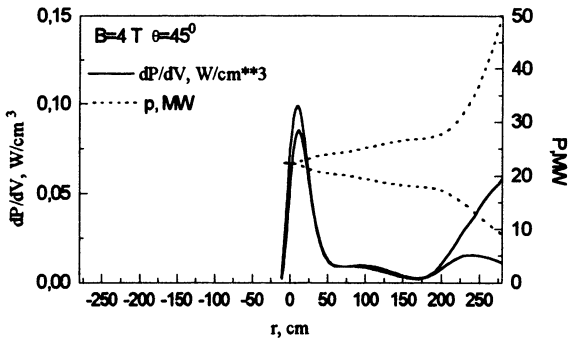

Fig.4 The profiles of power deposition and wave power for magnetic field 4T and launching angle 45^0 (wave leaves plasma through the outer boundary)

The refraction of the wave beam turns out to be insignificant for all considered angles. The dependence of CD efficiency on total EC power delivered from wave to plasma was not observed.

For the same values of magnetic field we calculated power deposition profiles at the Ohmic stage for launching angles close to optimal for the final stage and modeled transition from the Ohmic to the final stage with additional heating. The evolution of plasma equilibrium and radial profiles of plasma parameters for the Ohmic and transition stages were computed with the use of the ASTRA code by V.Leonov (INF, Kurchatov Institute).

We concluded that launching angles optimal for final stage provide effective plasma heating and transition from Ohmic to final stage. In the case of lower values of magnetic field (and inductive current) the corresponding calculations have shown that 50 MW of EC power is not enough to achieve the same parameters of the final stage. For 4.85T magnetic field 70 MW of EC power is required, whereas for 4T, 350MW.

3. Autoresonance regime of ECR CD in T-10

In [3,4] it was offered to use the phenomenon of autoresonance for ECR current drive. According to [5,6] the interaction of electrons with electromagnetic waves in an external magnetic field occurs in the autoresonance regime, if $N_\parallel = 1$ ($N_\parallel$ is component of refractive index along a magnetic field). In this regime parameters of a particle during

ECR interaction vary in such a manner that the resonant condition is not violated and consequently resonance acceleration of electrons can proceed for an extremely long time.

In this case the electron trajectory on the velocity plane coincides with the resonant curve. It makes the establishment of a plateau impossible and creates conditions for unlimited acceleration of electrons. Due to such acceleration a "jet" extended along the resonant curve tends to be generated in phase space. This distortion of the electron distribution function should be accompanied by intensive generation of an electric current. In the considered mechanism the current is driven by direct transfer of the momentum of electromagnetic waves to electrons. It is the difference from the known mechanism of Fisch - Boozer and similarity with low hybrid method of current drive.

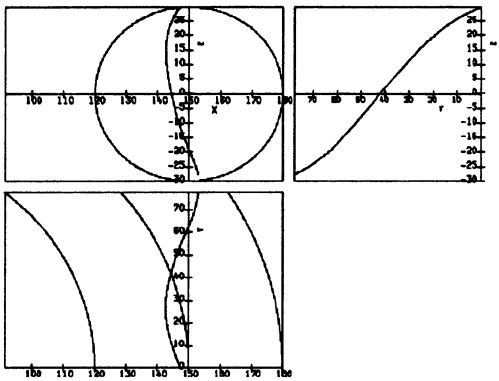

Fig.5 Beam trajectory suitable for autoreso-nance regime of current drive in a tokamak

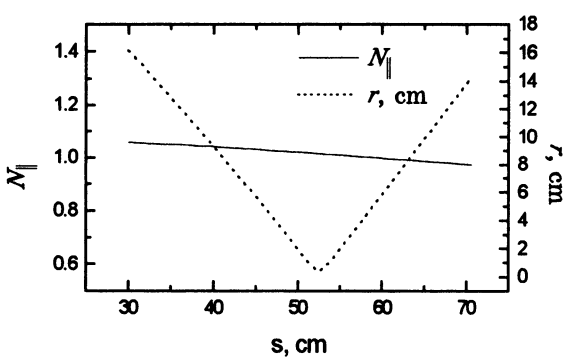

Fig.6 $N_\parallel$ as a function of distance along a ray for trajectory shown in Fig.5 (dotted line - small radius)

It was established earlier, that condition $N_\parallel = 1$ in the range of frequencies $\omega \approx \omega_e$ can be satisfied for extraordinary waves launched to the tokamak from above (or below). The launching angle with respect to magnetic field should be rather small. An example of the beam trajectory suitable for realization of the autoresonance regime is shown in Fig.5.

Figure 6 shows that on the whole trajectory $N_{\parallel} \approx 1$. In tokamak T-10 launching of the extraordinary wave from above at angle 20^0 to magnetic field appeared to be optimal. In Fig.7 the autoresonance regime is compared with the conventional, when the ordinary wave is launched from the outer side of torus at a rather large angle to magnetic field, the value $N_{\parallel}$ being in the interval 0.2 - 0.3. For large EC power the CD efficiency of the auto resonance regime can be twice that of the conventional regime.

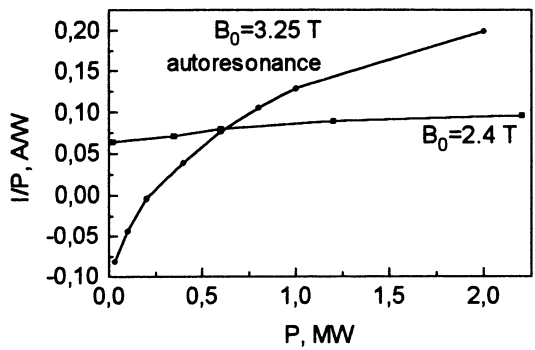

Fig.7 CD efficiency as a function of microwave power: 1-conventional regime ($N_{\parallel} = 0.2$), 2-autoresonance regime

Thus, the numerical analysis shows, that the ECR autoresonance regime of current drive has good prospects, at least in small tokamaks like T-10. The possibility to use the autoresonance regime in large tokamaks, like ITER, requires additional study.

References

[1] Kuyanov A.Yu., Skovoroda A.A., Timofeev A.V. // Fizika plasmy. 1993. V.19. P.1299.

[2] Timofeev A.V. // Fizika plasmy. 1994. V.20. P.1028.

[3] Kuyanov A.Yu., Skovoroda A.A., Timofeev A.V., Zvonkov A.V.// EPS Conf. Contr. Fus. and Plasma Phys.. Contrib. Papers. 1992. Pt.2. P.1521.

[4] Kuyanov A.Yu., Skovoroda A.A., Timofeev A.V., Zvonkov A.V. // Plasma Phys. and Contr. Nucl. Fus. Res. IAEA. Vienna. 1993. V.1. P.733.

[5] Davidovskiy V.A. // JETP. 1962. V.43. P.886.

[6] Kolomenskiy A.A., Lebedev A.N. // JETP. 1962. V.44. P.261.

ON THE POSSIBILITY TO USE "RADIO WINDOW" EFFECT FOR ECR CURRENT DRIVE IN LARGE-SCALED TOROIDAL DEVICES

O.B.Smolyakova and M.D.Tokman

Institute of Applied Physics, Russian Academy of Sciences,
Nizhny Novgorod, Russia

The problem we deal with is to analyze the possibility of improving ECCD efficiency in a large-scale tokamak using electron Bernstein waves (EBW) excited by linear coupling of normal waves in a magnetized plasma.

According to [1] EC current drive in tokamak by Bernstein modes has some advantages; we mark two of them. First, significant slowing down of EBW in magnetic field direction may be achieved. The longitudinal (parallel to magnetic field **B**) refractive index n_{II} can be determined [1] as $n_{II} \approx n_{\perp} B_{\theta}/B_{\varphi}$, where B_{φ} is the toroidal magnetic field, B_{θ} is the poloidal one and $n_{\perp}$ is the transverse component of refractive index. In the region of Bernstein mode absorption $n_{\perp}$ can be estimated as $n_{\perp} \sim \beta_T^{-1}$ (here $\beta_T = v_T/c = (2T_e/mc^2)^{1/2}$), so the value $n_{II} \approx \frac{1}{\beta_T}\frac{B_{\theta}}{B_{\varphi}}$ can became noticeable and influence essentially to variations of pitch angles of resonant particles reducing the negative effect of trapped electrons.

Second, the efficiency of current drive by a B-mode can be higher than that by electromagnetic waves. Due to the fact that absorption coefficient is approximately mc^2/T_e times higher than that of normal electromagnetic modes, the greatest part of the wave power has resonant absorption in the inhomogeneous magnetic field with more energetic electrons, so ECCD efficiency η, which is proportional to squared resonant electron velocity v_r^2, is enhanced.

When applied to large-scale devices, these points have some peculiarities. At first, for the parameters typical for hot plasma the estimated value of n_{II} is not much higher than unity, and some applications (for example, estimation of the influence of the particles trapping effect during ECRH), require more accurate calculation. Second, the usual ("classical")

way to excite the Bernstein mode [2] by launching the X-mode from the high field side is inefficient due to strong cyclotron absorption of power before the UHR region. So the so-called O-X-B mode conversion scheme seems to be more attractive. It was proposed in 1973 [3] for the heating of overdense plasma and efficiently realized in the large-scaled device W7-AS now [4][1].

In this scheme the O-mode is injected from the low field side at some optimal launching angle. If in the cut-off layer the longitudinal (parallel to the magnetic field) refractive index is determined by expression

$$n_z = n_{zopt} = \left(\frac{\sqrt{u}}{1+\sqrt{u}}\right)^{1/2}, \qquad (1)$$

(where $u = \omega_H^2/\omega^2$), there is no evanescent region for transverse refractive index $n_\perp$ and the O-wave is fully coupled to X- mode. It propagates towards the torus center, reflects there and goes to the UHR region where converts to the Bernstein mode. In the case of non-optimal angle transmission through the evanescent region is determined by coefficient

$$T = \exp\left(-pk_0 L\sqrt{\frac{\sqrt{u}}{2}(2(1+\sqrt{u})(n_{zopt}-n_z)^2 + n_y^2)}\right), \qquad (2)$$

where n_z and n_y are longitudinal and poloidal refractive indices, k_0 is vacuum wave number and, L is spatial density scale. The problem to provide the sufficient power coupling for a wave beam with a certain angular spectrum is the peculiar one, and may be that was the reason that O-X-B scheme performance for efficient heating was open to question for a long time. But the successful experiments on W7-AS show that the problem of beam matching can be solved. We can suppose that it also can be solved in principle on large-scale devices. It follows that increasing the scale of device under constant relation to beam aperture d rise up the coupling efficiency for beam width $\Delta n \sim \lambda/d$. But with no doubt this problem which stays now beyond the scope of our consideration needs more detailed investigation.

Such, a rather sophisticated scheme as O-X-B needs careful numerical simulation .

---

[1] The same mode coupling near plasma cut-off was observed in earlier ionospheric experiments in the radio frequency range ("radio window")[5].

To find out possible parameters of the mode excited in O-X-B scheme, the numerical code was elaborated and calculations were performed. Plasma modeled was considered to be a cylinder with radial dependence of density, temperature and current density:

$$n = n_0(1 - r^2/a^2)^q, T_e = T_0(1 - r^2/a^2)^p, j = j_0(1 - r^2/a^2)^s \qquad (3)$$

Ray trajectories and power absorption were calculated within the usual geometrical optics approximation:

$$d\xi_i/ds = \partial G/\partial\eta_i, \quad d\eta_i/ds = -\partial G/\partial\xi_i, \quad \tau = \int_0^l 2\,\mathrm{Im}\mathbf{k}\cdot d\boldsymbol{l}. \qquad (4)$$

Here ξ_i, η_i are generalized coordinates and momenta, τ is optical depth, and G is dispersion relation which was chosen different for different plasma regions. For the cold plasma approximation it is taken according to Appleton-Hartree formula:

$$G = n^2 - n_{o,e}^2 =$$

$$= n^2 - 1 + \frac{2\upsilon(1-\upsilon)}{2(1-\upsilon) + u\sin^2\vartheta \pm \sqrt{u^2\sin^4\vartheta + 4u\cos^2\vartheta(1-\upsilon)^2}}, \qquad (5)$$

where ϑ is angle between magnetic field and wave vector $\mathbf{k}$, the upper sign corresponds to the ordinary wave and the $\upsilon = \omega_p^2/\omega^2$, the lower one to the extraordinary wave, respectively.

Near the upper hybrid resonance the "warm" correction are taken into account:

$$G = G_{cold} + O(\beta_T^2) = (n^2 - n_o^2)(n^2 - n_e^2) - \beta_T{}^2 \cdot \upsilon \cdot n^6 \cdot D,$$

$$D = 3\cos^4\vartheta(1-\upsilon) + \frac{6 - 3u + u^2}{(1-u)^2}\cos^2\vartheta\cdot\sin^2\vartheta + \frac{3}{1-4u}\sin^4\vartheta. \qquad (6)$$

After increasing the value of parameter $\chi = \frac{n_\perp^2\beta_T^2}{2u}$ up to 0.1-0.2 calculations are continued according to the Bernstein mode dispersion relation:

$$G = 1 + \frac{2\upsilon}{n^2\beta_T{}^2}\{1 + \sum_{-\infty}^{\infty} i\sqrt{\pi}Z_0 I_l(\chi)\exp(-\chi)W(Z_l)\}, \qquad (7)$$

where I is modified Bessel function, W is plasma dispersion function and $Z_1 = (1 - 1\sqrt{u})/n_{II}\beta_T$.

In calculations, the starting point is taken in the cut-off region where the wave is assumed extraordinary and have wave vector **k** directed along the magnetic field; in this case 100% transformation takes place. Calculation stops when the optical depth of B-mode absorbed reaches $\tau \approx 1$. The corresponding O-wave trajectory is calculated from the cut-off point backward to vacuum to determine launching parameters.

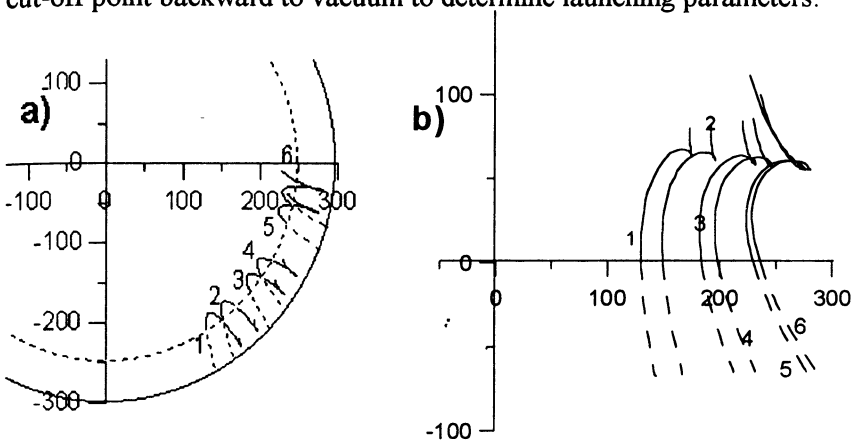

Figure 1 a, b.

Ray trajectories in the minor cross section (a) and in the equatorial one (b); dashed lines correspond to ordinary branches and solid to extraordinary and Bernstein branches; central parameters are u_0=1, υ_0=2.28, T_0 =5 keV; n_{II} in the absorption region equal respectively for different curves: 1 - n_{II} = 2.44, 2 - n_{II} = 2.02, 3 - n_{II} = 1.63, 4 - n_{II} = 1.47, 5 - n_{II} =1.22, 6 - n_{II} = 0.94; dashed circle in a) is the line of υ =1.

In Fig.1 a set of ray trajectories is presented in the minor (a) and equatorial (b) cross sections of tokamak for some hypothetical large-scale installation which has size, magnetic field and plasma current typical for ITER (the major radius R=800cm, the minor radius a=300cm, B_0 =5.8T, complete plasma current is 22 MA), but higher density to have the plasma cut-off inside the column. Different positions on the cut-off surface correspond to different launching angles. Plasma parameters at the center of the column are u_0=1, υ_0=2.29, T_0 =5 keV, density and

temperature profiles are determined by eq.(3) with q=0.8, p=2, s=2. Values of n_{II} in the absorption region (where $\tau \approx 1$) are shown for each trajectory. It is evident that, according to analytical predictions, values of n_{II} in the absorption region do not exceed the value of 1-2.

The most important parameter to characterize current drive efficiency is shift $Z=(1-\sqrt{u})/n_{II}\beta_T = v_{res}/v_T$ determining the energy of resonant electrons. In all variants computed this value is $Z \approx 3$, so particles with $3v_T$ velocities undergo resonant interaction. Such an efficiency proportional to v_{res}^2 can be compared with that of electromagnetic waves with the same parameters. According to [1], for O-mode $v_{res}/v_T \approx (\ln)^{1/2}\ \tau_o$. These values are estimated for calculated ray trajectories and give the B-mode ECCD efficiency to be approximately 1,5-2 times higher: for curves 1-6 corresponding values of optical depth give $\ln \tau_o \approx$ 4.5-8, whereas for B-mode $Z^2 \approx 9$.

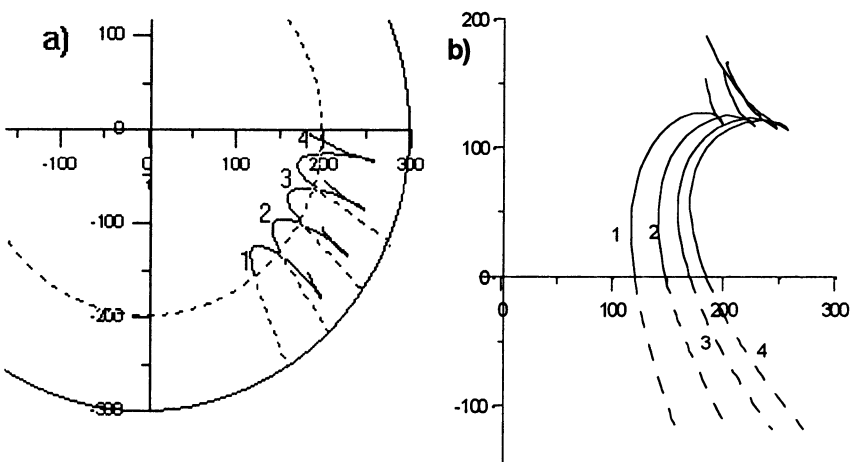

Figure 2 a, b.

Ray trajectories in the minor (a) and equatorial (b) cross-sections; central parameters are u_0=0.91, υ_0=1.4, T_0 =5keV; n_{II} in the absorption region equal respectively for different curves: 1 - n_{II} =1.39, 2 - n_{II}= 1.20, 3 - n_{II} =1.00, 4 - n_{II}=0.80.

It must be mentioned that the range of parameters suitable for such scheme of B-mode excitation is not too wide. It is restricted by the possibility of strong absorption on "cold" ray trajectories. So the trajectories

must lie close to the plasma periphery and not near to resonance layer. Using "nonresonant" parameter in the center of plasma column, $u_0 < 1$, trajectories with low "cold" absorption can be moved from outskirts (see Fig.2, a, b), but in this case the benefit in efficiency of B-mode compared with O-mode is smaller (for example, for $u_0=0.91$, $\upsilon_0=1.4$ and $T_0 = 5$keV the relation between resonant velocity and thermal one $Z=v_{res}/v_T$ is practically equal for both Bernstein and electromagnetic modes: for O-mode with the parameters corresponding to curves 1-4 $\ln\tau_o \approx 7\text{-}8$ while for B-mode $Z^2 \approx 9$).

Summary

It is shown that within some plasma parameter range in large-scale devices with overcritical densities it is possible to use the O-X-B scheme to excite the Bernsteim mode which is absorbed by resonant electrons with energies 1.5-2 times higher than in the case of electromagnetic modes. It should be noted that the absorption region is rather far from the center of the plasma column ($r_{abs}>2/3$ a). It imposes some restrictions to current drive but can be interesting from the point of view of suppressing MHD instabilities at the plasma periphery.

Acknowledgments

The work is supported by RFBR (Grant No 95-02-04999-a) and INTAS (Grant No 94-2815).

The authors would like to thank E.V.Suvorov for useful discussion and encouragement.

References

1. Litvak A.G. *et al,* Phys.Letters., 1994, A188, 64.
2. Baranov Ju.F. , Fedorov V.I. , Fizika Plasmy (Sov.), 1983, 4, 6 77.
3. Prienhalter I. and Kopecky V., J. Plasma Phys., 1973, 10, 1.
4. Laqua H. *et al,* Contrib. Papers of the 23rd EPS Conf . on Contr. Fusion and Plasma Physics , Kiev (Ukraine), 1996 (to be published).
5. Budden K.G. Radio waves in ionosphere. Cambridge University Press, 1961.

TWO KINDS OF WAVE PROCESSES UNDER POWERFUL ECH IN T-10 TOKAMAK

V.I.Poznyak, A.A.Bagdasarov, V.V.Piterskii, A.N.Yakovets

Russian Research Cebtre "Kurchatov Institute", Nuclear Fusion Institute, Moscow, Russian Federation

1. Introduction. The knowledge of the nature of transport processes and instabilities is necessary for the effective realisation of ECH, ECCD and instability control. We suppose that the driving force of those are the potential high frequency (HF) electron plasma waves [1-3]. An excitation of the coherent electromagnetic waves can take place under powerful ECH [1,2]. Plasma-wave processes were investigated in different regimes of T-10 tokamak (n_e=0.5-4x10^{13}cm^{-3}, I=100-400KA, B=14-28KGs, P_{ECH}=1.2MW).

2. Theoretical background. In most cases of an additional heating, the electric field for the creation of target plasma is used. Fig.1 shows the example of a stationary nonuniform distribution function on the longitudinal velocities of electrons.

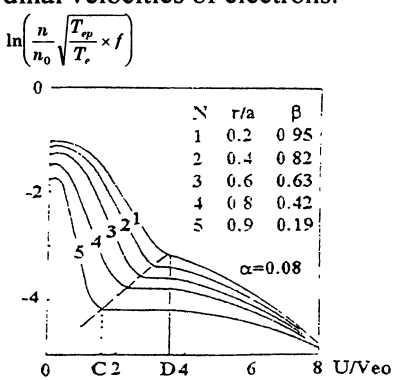

Fig. 1. Space-dependent electron distribution function normalized by the central value of the parameters

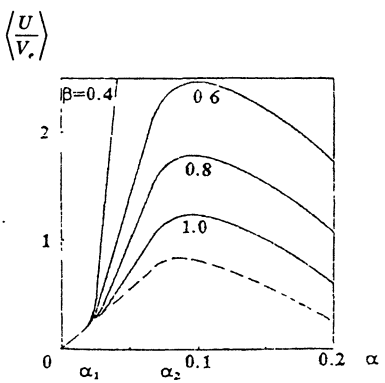

Fig. 2. Average direct velocity (local current density) versus b. Dotted line - main body part.

It was suggested that the local shape of distribution function is similar to the quasylinear solution [4,5]. Empirical distributions on the perpendicular velocities were selected with taking into account the real experimental data [2]. The working parameters of calculations are $\alpha = E_z/E_D$ and $\beta = \omega_{pe}/\omega_{be}$. Here, E_z = const. The beginning of Cherenkov area coincides with the critical velocity $C = v_e\alpha^{-1/2}$ (v_e - thermal velocity). Doppler mode is provided with the area $u > D = C/\beta$. The classical collisions are took into account in the body part $u < C$. The flux of acceler-

ated electrons $\Gamma \sim e^{-\alpha/4}$, them current and noise energy increase with α, but distribution function is compressed in the longitudinal direction owing to the reverse impact of the electron plasma waves. The corresponding dependence of the local current density on α is shown in Fig.2. In the region $\alpha > \alpha_2$, the current density is a fallen down function. A transition over the point $\alpha \sim \alpha_2$ leads to an instability in consequence of the positive feedback between current and electric field E_z. The determinate modification of E_z is secured by the electrodynamic compression of the current channel (pinch-effect). It is essential what the plasma pinch velocity v_r is connected with runaway phenomenon by the positive feedback ($v_r \sim E_z B_\theta / c B_z$, $E_z \sim v_r B_\theta / c$, $j \sim (c/r) d(rB_\theta)/dr$, $dj/dt \sim e\langle u \rangle \Gamma \sim e v_{col} \langle u \rangle \exp(-\alpha/4)$. This effect was lost sight in previous works [4,5 et al.].

The oscillations of high amplitude can be realised if them spectrum is high coherent, that is, certain spectral components amongst possible must have some advantages. We assume that plasma in the vicinity of the resonance magnetic surfaces $q = 1,2,3\ldots$ where the magnetic field structure is regular, possesses such property. The oscillations with the natural plasma frequencies of the corresponding zones is intensified in a direction of the resonance particles gradient. Most important property of the oblique Langmuir waves is transport of the longitudinal momentum across the magnetic field. Corresponding fluctuations of the poloidal magnetic field secure the plasma diffusion. Under instability $\alpha >= \alpha_2$ plasma flows out the excitation area, which is surrounded with the resonance surface r_{sm}, to the absorbing area (outside r_{sm} with a drift velocity of more cold plasma component. Energy of the electric field is passed to the oscillations. Oscillations damp under the realisation of the uniform space distribution inside the resonance magnetic surface r_{sm}.

The important peculiarity of the oblique ECH is a creation of the hot electron flux to the uptermal region of distribution function [2]. An additional nonuniformity of the hot particles in space is the reason for the strengthening of potential oscillations. Moreover, ECH can realise the inverse distribution on the transverse velocities which is unstable to a generation of EC harmonics. The electron scattering on the potential waves and space plasma diffusion can effort this effect, especially in the first stage of ECH.

3. Experiment and discussion. Fig.3 shows some characteristics of the discharge with different development of the instability. Measurements of the plasma noises were fulfilled in region band 0.5-7.5GHz[1]. All investigated discharges are accompanied by the intensive splashes of the HF oscillations

in the beginning of current (1-st time window), when we deal with a cold-plasma and flux of accelerating electrons. The instability is finished by the establishment of the quasistationary spectrum. Fluctuations have a chaotic character and grow with plasma current. Before the ELM-like instability on q = 3 (2nd window), ECE and HF signals are being regular. HF signal is enhanced shortly before the breakdown mainly in low frequency region, but diminishes in high frequency region. The instabilities are stopped under ECH (3rd window), but a total intensity of the oscillation increases several times. The disruptive form of the instability on $q = 2$ is shown in 4th window. As result, temperature and density drop very fast and disruption transforms spontaneously in the fan instability, when body plasma is cold, energy and current are concentrated in a runaway component. The characteristic energy region of tail for any kind of discharge is relatively narrow and soft (15-30KeV, by ECE and SXR).

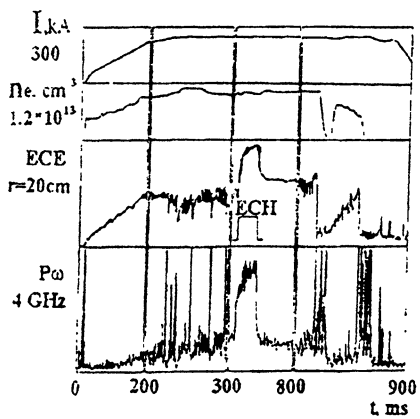

Fig. 3. ECE and HF oscillations in discharge with different form of the instability and with ECH

In Fig.4., the exponential dependence of oscillations around the maximum of them spectrum on the discharge current is shown. Elm-like instabilities are absent under low current. Than, first crash is appeared in the end of discharge and moves to the beginning of discharge with a current rise. Oscillations are saturated under some critical value of current. Disruption is being very probable. The rise of the noises correlates with the appearance of the hot electron flux on the plasma periphery. Apparently, the instability of this flux is the reason of the global ELM-like instability.

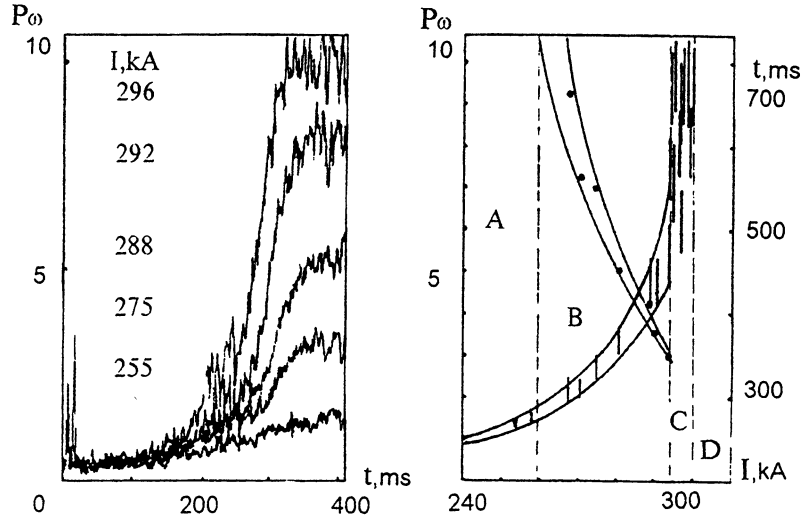

Fig. 4. Dependencies of noise level and time of first ELM-like instability on the discharge current. A - free ELM-instability regions, B - with ELM-like instability, C - high risk of disruption, D - disruptive always.

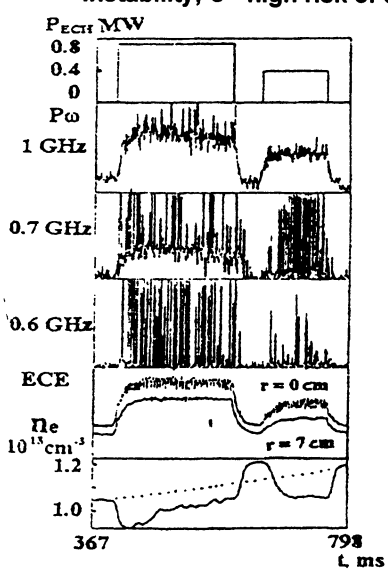

Fig. 5. Different behavior of spectral components of the plasma oscillations in discharge with sawtooth oscillations under ECH

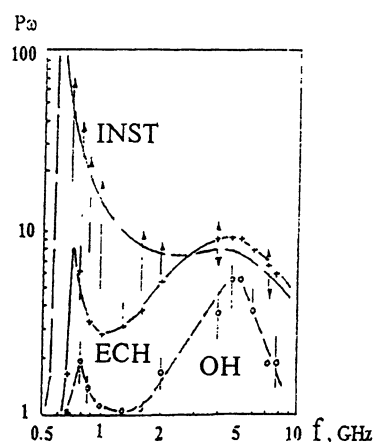

Fig. 6. Spectra of the electron (Langmuir) oscillations for stable OH, ECH and in the instability $q = 1$.

Fig.5 shows the regime with saw-tooth oscillations. Average density increases monotonously without ECH. Under ECH, the modulation of it is determined by a rebuilding of the density profile. HF signal in a high frequency region has a noise-like shape. Under the successive reduction of frequency (or the rise of density under fixed frequency), the sharp splashes are appeared in the moment of each breakdown. This splashes can reach several order of value close to low frequency boundary of HF mode. Fig.6 shows spectra of oscillation under OH, ECH and in the instability. The semibreadth of spectrum $\Delta\omega_s$ is essentially narrow then ω_{pe}. For the low frequency maximum, $\Delta\omega_m << \Delta\omega_s$. Its position shifts to the left then more, then the amplitude modulation of ECE is more deep. We believe that this maximum is the result of the non-linear scattering of the intensive Langmuir waves on electrons and ions and its stationary frequency corresponds to the ion plasma frequency w_{pi}. Thus, we can find the space location of zone which plays the role of the carrier trigger generation.

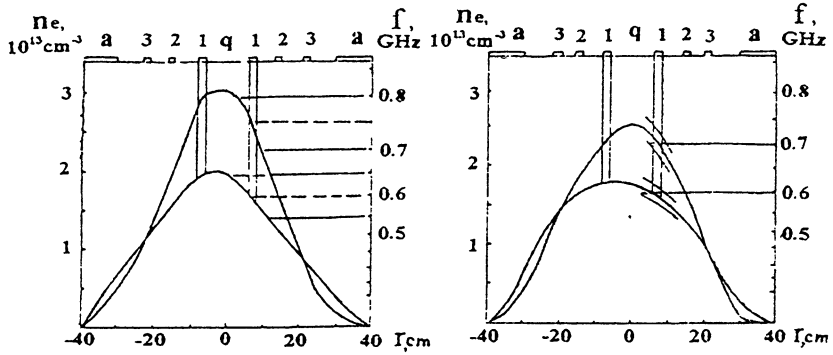

Fig. 7. The determination of the space-boundary conditions for mode $q = 1$

Fig.7A was obtained due to many frequency measurements in the regimes with quasistationary density before and in ECH. The horizontal lines show a probable interval of frequency of the stable maximum. Fig.7B illustrates two moments under ECH with increasing average density when the noise part of spectrum is appeared in the band of receivers with fixed frequencies. It can see that correlation between the obtained radial co-ordinates and the location of r_{sl} zone (by ECE and SXR) is satisfactory. Specific violation of the poloidal symmetry under a high level of turbulence (density profile shifts inside, temperature profile-outside) can be explained by the

dependence of the resonance conditions on the magnetic field ($\omega_k = k_{\parallel} v_{\parallel} - \omega_{be}$). The action of plasma waves can be more then that of the rotation transformation. In this case, distribution must be non-uniform along the magnetic force lines then more then level of the oscillation is higher (in particular, for instability). It should to add that such almost ideal picture for $q = 1$ mode can be essentially complicated by the processes of another kind (radiation, ionisation, charge exchange), which are important for more high mode number. Apparently, the impurity flux from wall and limiter plays the most important role for ELM-like instability.

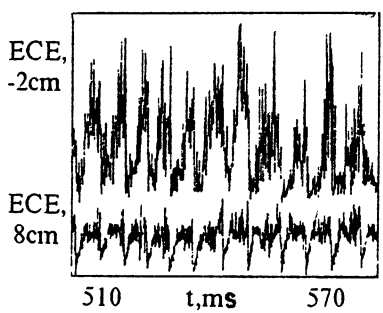

Fig. 8

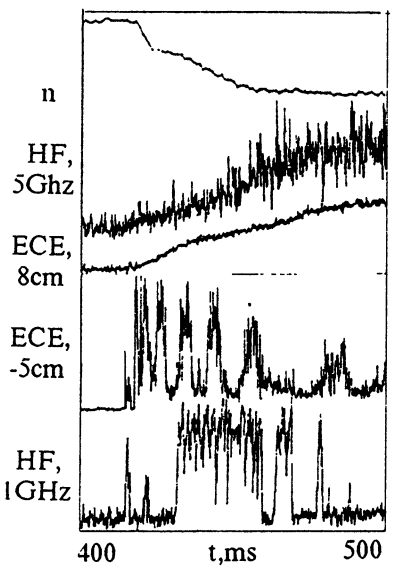

Fig. 9

EC-instability were discovered [1,2] by means of the 1st, 2nd and, some times, 3rd harmonics of ECE. Instability has a threshold and is observed, as rule, under input power above 300-400 kW for average density up to $3x10^{13}cm^{-3}$. Space location of the high splash-like ECE, evidently, coincides with 0- and π - points of the absorbing plasma ring. Characteristic energies from specific frequency shift (rough evaluation) are no more than 15-30 keV. For central ECH, splash-like emission with frequencies shifted up and down is observed. It can be explained by absorption of secondary waves in the plasma periphery directly or after wall reflection. The instability is accompanied by various modulating effects. In Fig.8, correlation between amplitude of EC-instability and saw-tooth period can be explained by the

increase of the amount of hot electrons under joint action of input EC- and potential HF-waves.

Fig.9 illustrates some peculiarities in the first stage of ECH when density and temperature profiles are rebuilt. Unstable ECH is begun just after the gyrotron switch-off. The amplitude pulsation is connected, perhaps, with the diffusion processes which are most effective under maximal density gradient. It should mark that low frequency HF components have unstable shape, but plasma under ECH is stable on the whole.

4. Conclusion. The presented phenomenological model is not contradict to the data obtained on the T-10 tokamak. More over, it gives possibilities to explain logical and relatively easy many experimental results on different tokamaks: non-local transport phenomena, fast pinch of heat and particles, similarity and difference between instabilities. Actually, several know instabilities can be generation by the unit term - current kinetic instability. Its main reason is instability of the accelerating electrons under common action of the pinch and potential waves. In order to realise the complete model, it is necessary to analyse the ion behaviour, drift processes, to take into account the peculiarities of magnetic field structure. We believe that main reason of suppression of instabilities is replacement of the inductive current source by the source which has not the positive feedback with current. The analysis of the hot electron behaviour together with the spectral measurements of the plasma oscillations gives, at least, in some cases the possibility to obtain certain signs of the coming instability essential before the time of breakdown. EC instability under powerful ECH can be reason of additional heat transport and impurity flux.

Authors are very grateful for the collaboration with T-10 Team.

References

1. V.I.Poznyak, A.A.Bagdasarov, V.V.Piterskii at al., Proc. in Intern. Conf. on Plasma Phys. and Contr. Fusion, Seville, 1994 IAEA, Vienna, 1995, 2, 169.
2. V.I.Poznyak, A.A.Bagdasarov, V.V.Piterskii at al., Proc. of the Ninth Joint Workshop on ECE and ECH, Borrego Springs, California, 1995, World Scientific Publishing Co. Pte., **137**.
3. V.I.Poznyak, A.A.Bagdasarov, V.V.Piterskii, A.N.Yakovets, Proc. in 23rd EPS Conf., Kiev, 1996, a078.
4. V.V.Parail. O.P.Pogutse, Sov. Plasma Physics, 1976, **22**, 228.
5. Muskietti L., Appert K., Vaclavk K., Appl.Phys., 1982, 2512.

STUDY OF LOW FREQUENCY INSTABILITIES IN A MICROWAVE PRODUCED TOROIDAL PLASMA

P.K.Sharma, J.P.Singh and D.Bora
Institute for Plasma Research,
Bhat, Gandhinagar 382 424, India.

ABSTRACT

Investigation of spatially localised low frequency flute and drift waves in a toroidal Electron Cyclotron Resonance (ECR) produced plasma is reported here. Hydrogen plasma using 2.45 GHz microwave is produced in a toroidal device BETA [1]. Equilibrium density, floating potential and plasma temperature in a poloidal cross section of toroidal plasma are measured. Contours of density and floating potential exhibits slab nature in the vertical direction of the poloidal cross section. Plasma is formed with a peak density of 4×10^{11} cm $^{-3}$. The electron temperature is about 4 - 7 eV. Fluctuating component of density and floating potential is also measured. Radially localised low frequency (LF) electrostatic instabilities are observed. Presence of both, flute modes and drift modes is reported. Our measurements reveal that the excitation of LF fluctuations depend strongly on the sign of product $\nabla n.\nabla B$. LF coherent fluctuating modes are observed in the region where $\nabla n.\nabla B > 0$ and turbulent spectra is observed where the condition $\nabla n.\nabla B < 0$ is satisfied. Our measurements reveal that drift modes could be excited when $\eta_e < 0$ (where $\eta_e = (\nabla \ln T_e) / (\nabla \ln n_e)$), whereas R - T modes could be excited when $\eta_e > 0$ and density gradient is antiparallel to `g',effective gravity due to curved magnetic field.

1. INTRODUCTION:

A series of experiments [1-5] on study of LF instabilities have been conducted in the toroidal device BETA [1]. During,these experiments it has been shown that magnetised low-β plasma embedded in a pure toroidal magnetic field is subjected to the R-T instability (simulating effective gravity `g') with density gradient (∇n) antiparallel to it [1,4]. In all the experiments [1-5] reported earlier, the plasma production scheme has been similar. Plasma is primarily produced using hot cathode discharge method. An incandescent filament, placed in the toroidal vacuum vessel is biased with respect to the vessel, thus initiating a hot cathode discharge. In order to overcome

problems, related to the physical presence of the cathode in the plasma volume, existence of primary energetic electrons and complicated electric field, Electron Cyclotron Resonance (ECR) breakdown has been used to produce plasma in the experiment described in this communication.We report here on the equilibrium profiles of ECR produced hydrogen plasma along with the characteristics of the LF electrostatic fluctuations present in this plasma

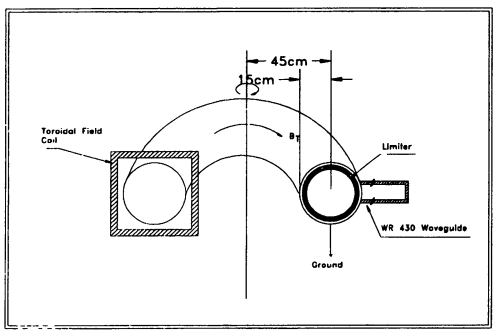

fig 1. Schematic of BETA machine

2. EXPERIMENTAL SET-UP AND METHODS:

The device, shown schematically in figure 1, is described in detail elsewhere [1]. A toroidal magnetic field of 0.06 T and 0.08 T, at the minor axis is produced for a duration of 3.5 second. The toroidal magnetic field rise

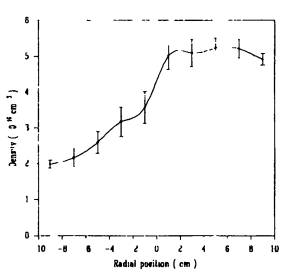

fig 2.Radial profile of density at B_t = 0.06 T

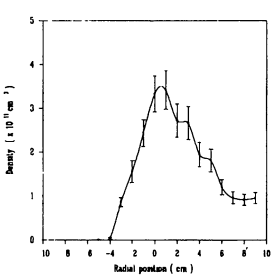

fig 3. Radial profile of density at B_t = 0.08 T

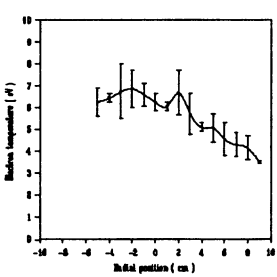

fig 4. Radial profile of electron temperature

within 50 milliseconds and remains constant (ripple < 2%) there after upto 3.5 seconds. A radio frequency source at a frequency of 2.45 GHz, capable of

delivering 700 W, is used to form plasma. ECR breakdown at this frequency occurs at a toroidal magnetic field (B_t) of 0.0875 T. By varying the strength of the toroidal magnetic field, we change radial location of the ECR region and hence density profile could be tailored. Hydrogen plasma is produced with a toroidal magnetic field of 0.06 T and 0.08 T at the minor axis. The vessel is evacuated to a base pressure of 8×10^{-4} Pascal. Plasma is produced at a working pressure of 6.67×10^{-3} Pascal. Equillibrium density, floating potential and plasma temperature of the plasma are measured. Hydrogen plasma is formed with a peak density of 4×10^{11} cm $^{-3}$. Electron temperature is about 4-7 eV. A limiter of diameter 18 cm is used to short circuit the electric field established due to the curvature and ∇B drift to provide equilibrium to the plasma. Both the vessel and the limiter are grounded. A radially movable cylindrical Langmuir multi-probe system with exposed tips of 10 mm in length and 0.5 mm in diameter, is used to measure the equilibrium plasma density, floating potential and electron temperature at different locations in the poloidal cross section.

Fluctuating components of density and floating potential have also been measured at these locations. Two probes separated by a distance of 1 cm are used to measure the density and the floating potential fluctuations simultaneously. The data are analysed using a standard fast Fourier transform technique (FFT) [6] to obtain the power, phase and coherence spectrum of the fluctuations.

3. RESULTS AND DISCUSSIONS:

Equal density and equal floating potential contours are generated from the measurements of density and floating potential in the poloidal cross section. The contours exhibits slab nature in the vertical direction within z = +8 cm to z = -8 cm. The extent of slab nature in the vertical direction

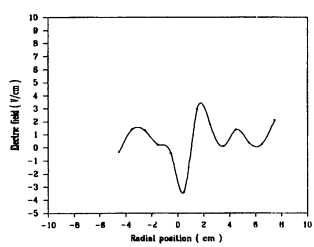

Figure 5. Radial profile of electric field at B_t = 0.08 T

could not be controlled during these experiments, unlike in the case of filament produced plasma experiments [5], where the filament length decided the extent of the slab nature of the plasma in the vertical direction. At B_t = 0.06 T, plasma is observed over the entire radial location , i.e. -9 cm $\leq r \leq$ +9 cm, as shown in figure 2, whereas at B_t = 0.08 T we could observe the plasma

in the region -4 cm ≤ r ≤ +9 cm as shown in figure 3. The density is higher in the second case, almost by an order of magnitude. In our earlier work it has been reported [5] that in BETA the toroidal magnetic field lines are open. Therefore, when ECR region is located near the inner edge of the minor radius (R ~ 31 cm), the open field lines enhance the loss of plasma particles. This explains why plasma density is more in the former case and less in the latter case. We have also measured the radial electron temperature profile. Plasma is formed with a peak temperature of about 7 eV. The radial profile, shown in figure 4, is broad and shows a weak fall (about 3 eV over a distance of 6 cm) in the outer region.. Floating potential is also measured at different radial locations. Space potential (φ_s) is obtained from floating potential and electron temperature. The radial electric field, as shown in figure 5, is spatially oscillating in nature. The peak value is about 3 V/cm , otherwise it is typically around 1 V/cm.

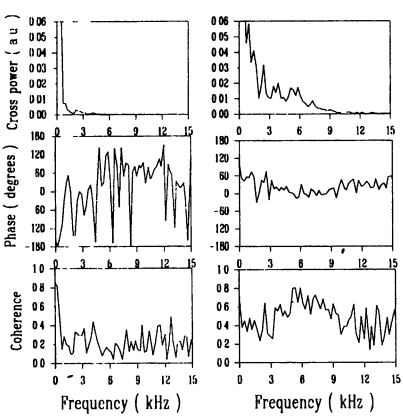

fig 6. Cross power, phase and coherence spectrum at (a) r = -2 cm and (b) r = +2 cm.

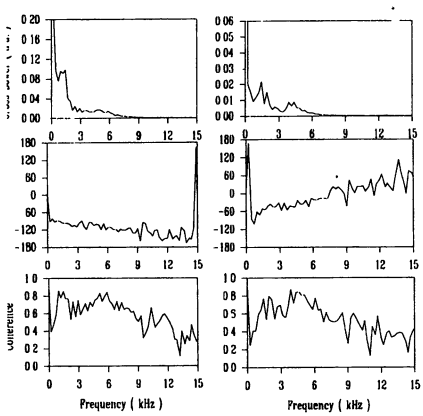

fig 7. Cross power, phase and coherence spectrum at (a) r = 4 cm and (b) r = 8 cm

Fluctuating component of density and floating potential shows presence of turbulent spectra in the region where the condition $\nabla n.\nabla B < 0$ is satisfied. Coherent low frequency electrostatic fluctuations are observed in the region where the condition$\nabla n.\nabla B > 0$. Region A extends from -4 cm ≤ r ≤ 0 cm and it is here that the condition $\nabla n.\nabla B < 0$ is satisfied, where we observe turbulent spectra. A typical cross power , phase and coherence spectra

between density and floating potential fluctuations at r = -2 cm is shown in figure 6(a). In region B, which extends from 0 cm ≤ r ≤ +9 cm,we find $\nabla n.\nabla B > 0$ and observe, both flute modes and drift modes.

The presence of flute modes and drift modes depends on the sign of η_e, where η_e is defined as $\eta_e = (\nabla \ln T_e)/(\nabla \ln n_e)$. Radial plot of η_e for our experimental parameters is shown in figure 8. It is observed that drift modes are observed in the region where η_e is negative. It is evident that $\eta_e < 0$ in the region -1 cm ≤ r ≤ 2 cm and r ≥ 8 cm. In other region we observe flute modes. Figure 6(b) shows a typical cross power,

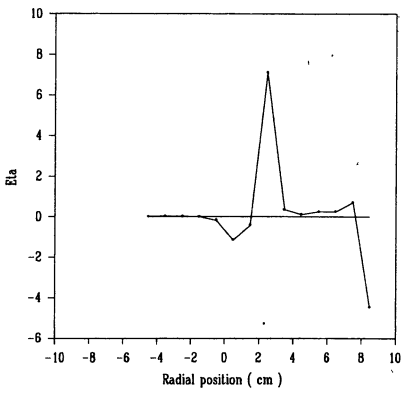

Fig 8 Radial profile of η_e

phase and coherence spectra between density and floating potential fluctuations at r = 2 cm. In this region the cross power spectrum exhibits a well defined peak centred around 5.0 kHz. The peak shows high degree of coherence (around 0.8). The phase difference between the density and the floating potential fluctuations at this frequency is between 0° and 50°. It is well known that gradient driven drift instability shows a phase difference close to 0° between the density and floating potential fluctuations at the same location [1]. Our measurements suggest presence of drift modes in this region. Figure 7(b) shows a typical cross power, phase and coherence spectra between density and floating potential fluctuations at r = 8 cm. In this region the cross power spectrum exhibits well defined peaks centred around 2 kHz and 4 kHz. The phase difference at this frequency between the density and the floating potential fluctuations is around 40°, showing drift nature of the instability. In the region, 3 cm ≤ r ≤ 6 cm we observe LF fluctuations showing flute nature. A typical cross power, phase and coherence spectra between density and floating potential fluctuations at r = 4 cm is shown in figure 7(a). The cross power exhibits a well defined peak centred around 1.3 kHz. The phase difference at this frequency between the density and the floating potential fluctuations is around 100°. As density gradient is antiparallel to the effective gravity , this region is more favourable for the

excitation of R-T instability. Also the phase difference observed in this region indicates the presence of a flute mode

4. CONCLUSION

We have formed hydrogen plasma using ECR method. Plasma is formed with a peak density of 4×10^{11} cm $^{-3}$. Electron temperature is in the range of 4 - 7 eV. Contours of density and floating potential exhibit slab nature of the plasma in the vertical direction of the poloidal cross section. Turbulent spectra is observed where the condition $\nabla n.\nabla B < 0$ is satisfied. LF coherent fluctuating modes are observed in the region where$\nabla n.\nabla B > 0$. Both R-T modes and drift modes are observed in the region where $\nabla n.\nabla B > 0$. To conclude, our measurements reveal that drift modes could be excited when $\eta_e < 0$ whereas R-T modes could be excited when $\eta_e > 0$ and density gradient is antiparallel to `g'.

5. REFERENCES

One N., Phys. Lett., 1989, 139A, 308
Two N., Geophys. Res. Lett., 1992, 19(3), 245
Three N., Geophys. Res. Lett., 1992, 19(3), 241
Four N., Plasma Phys. Contr. Fusion., 1995, 37, 387
Five N., Plasma Phys. Contr. Fusion., 1995, 37, 1003
Six N., IEEE. Trans. Plasma Sci., 1974, PS-2, 261

FREQUENCY-TUNING IN ECRH CURRENT DRIVE

H. Bindslev[1], O. Dumbrajs[2], and J.A. Heikkinen[3]

[1] JET Joint Undertaking, Abingdon, OXON OX14 3EA, U.K.
[2] Helsinki University of Technology, FIN–02150 Espoo, Finland.
[3] VTT Energy, P.O. Box 1604, FIN–02044 VTT, Finland.

We have evaluated the magnitude of localized current modification for intense off-axis RF heating in nearly burning reactor plasmas. The modification consists of the bootstrap current perturbation and of the current driven by RF momentum transfer and asymmetric heating. The results are used in a transport code to study the dynamics of current generation and its response to source frequency tuning.

Introduction

In the present work, the problem of modifying the plasma current density profile with fast tunable RF sources is addressed for tokamak configurations in the presence of localized microwave power deposition. Current modification is beneficial for stabilizing MHD modes, and may even enhance confinement by reverse shear generation. The fast frequency tuning of microwave sources can also provide a novel way to control the power deposition profile in the plasma. To investigate the limits of such frequency tuning for moving the current generation region, the current rise and decay times have to be evaluated and compared with the tuning rate. The requirements of frequency tuning should then be contrasted to the present stage of art of tuning technology of microwave sources.

At the same time, for strong wave absorption the characteristics of the current have to be assessed. Since the RF heating can be well localized, the resulting perturbation in the bootstrap current may become large. This is because the radial gradient of the local perturbation in the plasma stress is steep, even though the perturbation is much smaller than the background pressure.

Current drive model

Models for the RF-induced bootstrap current have been recently developed for ICRF heated minority ions [1], ECRF-heated electrons

[2], and for LH-heated alpha particles [3]. In order to obtain the total driven current, the bootstrap current perturbation due to the heated particles is added to the current driven by momentum transfer and asymmetric heating. For ECCD, there exist analytical expressions for the driven current by the latter mechanisms in terms of power absorption [4].

ECRF model.

For ECRH, the quasilinear diffusion coefficient D for the electron interaction with the microwave is evaluated from [2,5]

$$D = \frac{\pi}{16\tau}[(\frac{eE_{||}}{m})^2(\frac{k_\perp v_{||}}{\omega})^2\frac{e^{-2y^2/L^2}}{Wv_{||}^3}]_{\theta_{res}}\frac{K}{\oint d\theta/v_{||}}, \quad (1)$$

where $E_{||}$ is the parallel wave field component with respect to the magnetic field, K is the resonance integral, τ is the average time between successive passes through the RF, θ is the poloidal angle, θ_{res} indicates the angle at which the resonance condition $\omega - \Omega_0(r,v,\theta) - k_{||}v_{||}$ is satisfied at radius r, $y = r\sin\theta_{res}$, L is the radius of the microwave beam, e, m denote the electron charge and mass, $v_\perp$ and $v_{||}$ are the electron perpendicular and parallel velocity with respect to the magnetic field, respectively, $\oint d\theta$ denotes the integral over one complete bounce in the particle orbits, and one has defined $W^2 = \sin^4\alpha/L^4 + (\Omega_T'/2v_{||})^2$. Here, ordinary wave mode propagation is assumed having fundamental cyclotron resonance with the electrons, ω is the wave angular frequency, Ω is the relativistically corrected cyclotron frequency, $k_{||}$ and $k_\perp$ are the parallel and perpendicular wavenumber components, respectively, $\Omega_T' = (\Omega_c y/qR^2)(1 - k_{||}v_\perp^2/2\Omega_c v_{||})$, Ω_c is the cyclotron frequency at $\theta = \pi/2$, R is the major radius, and q is the safety factor, α is the wave propagation angle with respect to the magnetic field. The above diffusion coefficient is limited by relativistic heating out, giving the maximum $D = (c^2\Delta k_{||}v_{||}/L\omega v_\perp)^2/(2\tau_1)$, where $\Delta k_{||}$ is the spread in the parallel wavenumber spectrum, and $\tau_1 = \tau 2\pi Rq/L$.

In the present model the wave power absorption density is given by $p_{RF} = \int_0^c 4\pi m[\partial(v^3\hat{D})/\partial v]f dv$, with distribution function $f(r,v)$ obtained from the isotropic Fokker–Planck equation $\partial f/\partial t = (1/v^2)(\partial/\partial v)[v^2\hat{D}(\partial f/\partial v)] + (\partial f/\partial t)_{coll}$, where $(\partial f/\partial t)_{coll}$ denotes the electron-electron collision operator, v is the total electron

velocity, and $\hat{D} = (1/2)\int_{-1}^{1}(1-\mu^2)D d\mu$ is the pitch averaged diffusion coefficient with $\mu = v_{||}/v$.

Transport model

The transport code ASTRA[6] is used to follow the temporal evolution of plasma temperature, inductive electric field, and the thermal bootstrap current. The power input to the code is the absorbed power density given by the RF models, and the current input consists of the currents driven by the asymmetric wave heating and momentum transfer also given by the RF models. In the cases considered, no significant fast electron tail formation is found for ECRF heating. For thermal diffusion in space, a combination of anomalous thermal conductivities for the Alcator and η_i modes [7] has been applied.

Results

Dynamics of current generation

Figure 1 shows the results from an ASTRA simulation of ECRF heating for a reactor-scale tokamak. Reactor-scale parameters are used: $R = 7.75$ m, $a = 2.8$ m, $B = 6.2$ T, $I = 15$ MA, $T_{e,i} = 20$ keV, and $n_e = 0.84 \times 10^{20}$ m^{-3}. Equal deuterium and tritium concentrations are assumed. Here, B is the toroidal magnetic field on the axis, I is the total plasma current, and T_i is the ion temperature for each ion species. The density and temperature profiles are given by $n, T = n_0, T_0 \times (1 - r^2/a^2)^{\alpha_n, \alpha_T}$ with $\alpha_n = \alpha_T = 0.5$; the current density profile is parabolic. Here, a fixed density profile has been assumed. The electron cyclotron resonance (in the low velocity limit) for 156 GHz frequency is at $r = 0.8$ m, and the beam radius is $L = 0.1$ m. Fifty 2 MW beams with oblique propagation ($k_{||} = 1000$ m^{-1} with $\delta k_{||} = 60$ m^{-1}) are assumed. The power absorption is localized near $r = 0.9$ m. The plasma profiles are shown for $t = 10$, 100, 200 ms, and 400 ms, as well as 10 ms after a rapid frequency change from 156 GHz to 149 GHz at $t = 200$ ms.

One can see in Fig. 1 that the electron (and ion) temperature grows locally near the absorption regime and leads to the formation of a bidirectional bootstrap current on the time scale of tens of milliseconds characteristic to the heating rate. The bootstrap current density j_B is found to be a significant fraction of the total driven current j_T. The time scale for the corresponding local changes in the

total current is $50 - 100$ ms, restrained by induction. Similarly, the total current density profile does not seem to respond to the fast frequency change until about 200 ms after the change. This is partially due to the slow decay of the temperature perturbation, and partially due to the inductive delay. At the lower frequency, the current density profile is found to be strongly deformed at $r = 1.3$ m corresponding to the electron cyclotron resonance layer at that frequency. A current drive efficiency of about 0.005 A/W is found.

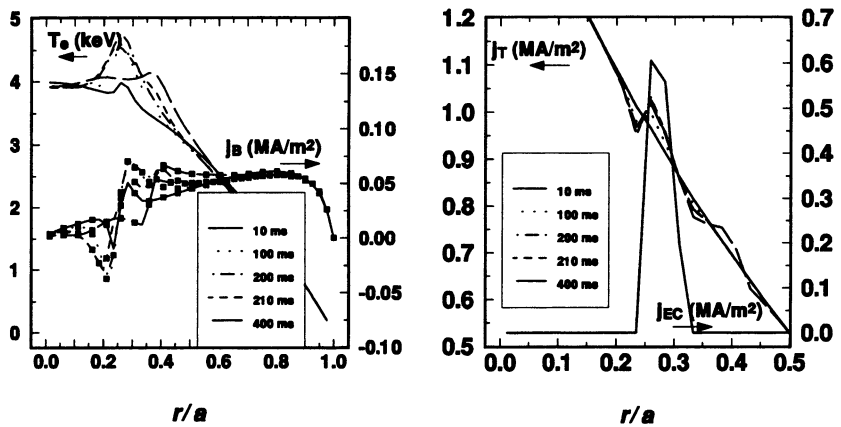

Figure 1: *The evolution of plasma temperature and current density profiles obtained from the ASTRA transport simulation for ECCD*

Figure 2 presents the evolution of the ECCD case without a frequency jump but including additional LH heating of 100 MW. The LH launching parameters have been optimized for electron current drive. Interestingly, the local ECRH heating tends to attract the LH power deposition to the EC resonance region. The increase in the local temperature by ECRH at $r = 0.9$ m, although relatively small, appears to increase the local LH-wave absorption and, consequently, localize the LH-driven current there. This mechanism might be useful for applying LHCD in synergy with either ICRH minority or mode conversion current drive, or with ECCD. The observed synergy appears to be lost when the electron temperature grows too much and, consequently, the LH absorption regime moves suddenly to the peripheral region.

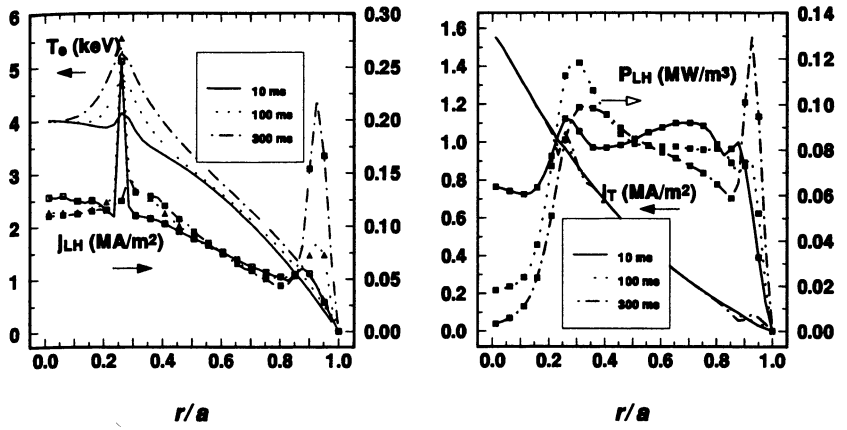

Figure 2: *The evolution of plasma temperature and the current density profiles obtained from the ASTRA transport simulation for synergic ECCD and LHCD*

Summary

For intense, local off-axis RF current drive, the local heating of the plasma may create a bidirectional local perturbation in the bootstrap current profile. According to the transport analysis presented here, the achieved local perturbations in the plasma stress can be sufficiently large to produce a significant bootstrap current perturbation – provided that such modifications remain MHD stable. A stability analysis is therefore needed in the future. It should be emphasized that this well-localized bootstrap current of bipolar profile is excited even with symmetric $k_{||}$ spectrum, thus requiring no directivity in the antenna system, and that it is not degraded by the trapped particle effect, but is even enhanced by it.

Considering fast tuning of the power deposition, a strict time constraint of about 100 ms is observed for the response in the total current modification. The frequency tuning of high-power microwave sources can be accomplished in several ways. For example, in the case of a gyrotron it has been shown theoretically [8] that the frequency of a high-power gyrotron could be changed very fast (in microseconds), in steps of a few GHz, by changing the accelerating and modulation voltages. This requires a very sophisticated power supply. In Ref. [9]

this method has been demonstrated experimentally, although for a low-power gyrotron. Another way of tuning the gyrotron frequency is to change the magnetic field. In the experiment of Ref. [10] it was demonstrated that this way it was possible to step-tune a high-power coaxial gyrotron between 116 GHz and 164 GHz. Also, output powers of around 1 MW have been achieved. Unfortunately, due to the large inertia of the magnetic field, this process may take several minutes. Much faster tuning should be possible in a smaller frequency range of a few GHz by keeping the main magnetic field constant and varying only an additional magnetic field produced by an extra small solenoid. It is much easier to tune the frequency of a free electron laser where only the accelerating voltage needs to be changed. For example, the high-power (1 MW) free electron laser developed for fusion purposes [11] offers a fast continuous tuning in the entire frequency range from 130 GHz to 260 GHz.

References

1. Heikkinen J.A. et al., to appear in Plasma Phys. Contr. Fusion.
2. Heikkinen J.A. et al., 23rd EPS Conf. on Contr. Fusion and Plasma Physics, Kiev, 24-28 June 1996, paper E051.
3. Heikkinen J.A. and Sipilä S.K., to appear in Nuclear Fusion.
4. Fisch N.J., Rev. Mod. Phys., **59** (1987) 175.
5. O'Brian M.R. et al., Nuclear Fusion **26** (1986) 1625.
6. Pereverzev G.V. et al., Max-Planck-Institut für Plasmaphysik, Report IPP 5/42, Garching, August 1991.
7. Romanelli F. et al., Nuclear Fusion **26** (1986) 1515.
8. Dumbrajs O. and Nusinovich G.S., IEEE Trans Plasma Sci., **20** (1992) 452.
9. Idehara T. et al., Physics of Plasmas, 1 (1994) 1774.
10. Piosczyk B., Proceedings of the 21st International Conference on Infrared and Millimeter Waves, Berlin, July 14-19, 1996, p. AM2.
11. Verhoeven A.G.A. et al., in these proceedings.

ON ENERGY FLUX AND RAY TRAJECTORIES OF ELECTROMAGNETIC WAVES IN A PLASMA IN THE LANDAU CYCLOTRON DAMPING REGION

A.I.Smirnov and M.D.Tokman

Institute of Applied Physics, Russian Academy of Sciences,
Nizhny Novgorod, Russia

I. Introduction

It is well known that for energetic characteristics of macroscopic electric field in the dissipative media there is not, generally speaking, any common correct phenomenological[1] expression [1].

There are difficulties in determination of the energy flux in the dissipative medias with spatial dispersion. In the "hot" magnitoactive plasma this problem manifests itself by the fact that standard geometrical optics provides in the ECR zone rays in the complex space [2]. Such rays, generally speaking, has no clear physical sense. In the absence of dissipation rays trajectories are directed along the lines of the energy flux $\mathbf{S}$ [2,3]:

$$\mathbf{S} = \frac{c^2}{16\pi\omega} E_p^* E_m \frac{\partial D_{pm}}{\partial \mathbf{k}} = \mathbf{\Pi} + \mathbf{K}, \tag{1}$$

where E_m stands for Cartesian components of the complex amlitude of the electric field;

$$D_{pm} = \delta_{pm} k^2 - k_p k_m - \frac{\omega^2}{c^2} \epsilon_{pm}(\omega, \mathbf{k}), \tag{2}$$

$\epsilon_{pm}(\omega, \mathbf{k})$ is dielectric tensor depending on frequency ω and wave vector $\mathbf{k}$;
$\mathbf{\Pi}$ is Poynting vector (electromagnetic part of the energy flux);

$$\mathbf{K} = -\frac{\omega}{16\pi} E_p^* E_m \frac{\partial \epsilon_{pm}}{\partial \mathbf{k}}$$

[1] I.e. free from consideration of microscopic structure of media.

where **K** is density of the energy flux carryed by the media ("kinetic" or sloshing flux).

In case of significant anti-Hermitian tensor[1] ϵ_{pm} relation (1) provides physically senseless complex vector **S**.

In the present work the quasi-linear theory method is used to calculate EC-waves energy flux.

II. Quasi-linear theory of kinetic processes in quasi-optical beams of EC-waves

Let us consider cyclotron interaction between electrons and a monochromatic quasi-optical wave beam. We shall define the complex amplitude of the HF-field as

$$\mathbf{E}(\mathbf{r}) = \mathbf{e}(\mathbf{k})A(\mathbf{r}) - i\frac{\partial \mathbf{e}}{\partial k_j}\frac{\partial A}{\partial r_j}; \tag{3}$$

here $\mathbf{e}(\mathbf{k})$ is unit vector of polarization of the normal mode under consideration; $A(\mathbf{r})$ is scalar amplitude[2]. Further let us substitute relation (3) to the kinetic equation averaged over high frequency. After calculation of respective moments of the distribution function we shall get relations for components of the kinetic energy flux which we shall demonstrate for the simplest case of the quasi-transverse (or transverse) waves propagation:

$$div\mathbf{K} = Q - div\left\{\frac{\omega}{16\pi}|A|^2 e_j^* e_n \frac{\partial \epsilon_{pm}^{(H)}}{\partial \mathbf{k}}\right\}, \tag{4}$$

$$Q = -\frac{i\omega}{8\pi}|A|^2\left[\left(1 + \frac{\partial}{\partial r_m}(argA(\mathbf{r}))\frac{\partial}{\partial k_m}\right)e_j^* e_n \epsilon_{jn}^{(aH)}\right], \tag{5}$$

$$K_x = -\frac{\omega}{16\pi}e_j^* e_n \frac{\partial \epsilon_{jn}^{(H)}}{\partial k_\perp}|A|^2, \tag{6}$$

[1] Such situation takes place at the center of the cyclotron absorbtion line [2,4].

[2] The second term in (3) takes into account the finite width of the spatial Fourier-spectrum; it disappears in the plain wave limit.

$$K_y = -i\frac{\omega}{16\pi}e_j^* e_n \frac{\partial \epsilon_{jn}^{(aH)}}{\partial k_\perp}|A|^2, \qquad (7)$$

In (4–7) $\epsilon_{jn}^{(aH)}$ and $\epsilon_{jn}^{(H)}$ are anti-Hermitian and Hermitian components of the standard dielectric tensor of the plasma (see [4]) and $k_\perp$ is transverse component of the wave vector of the beam **k**. Vector **k** is oriented in the (x,z) plane, and magnetic field $\mathbf{H}_o$ is directed along axis z.

From expression (7) one can see that transfer of the kinetic energy of particles along the axis perpendicular to the plane of vectors **k** and $\mathbf{H}_o$ takes place due to anti-Hermitian component of the dielectric tensor. This transfer leads, for example, to the respective displacement of the energy profile deposition as compared to the profile of the beam in the poloidal cross-section of the toroidal installation.

By combining relation (4) with the law of the full energy flux conservation one can obtain relation

$$div\mathbf{S} + Q = 0, \qquad (8)$$

where Q is determined by the relation (5),

$$\mathbf{S} = \frac{c^2}{16\pi\omega}\left(e_j^* e_n \frac{\partial}{\partial \mathbf{k}} D_{jn}^{(H)}\right)|A|^2, \qquad (9)$$

$D_{jn}^{(H)}$ is the Hermitian part of tensor D_{jn} determined by the relation (2).

According to (8) the direction, in which intensityof the HF field spreads, may be determined by the real part of the standard relation (1) even if Hermitian and anti-Hermitian components of the dielectric tensor are of the same order. The last conclusion refers to the solution of the electrodynamic problem for slab geometry given in [5,6].

Also from relations (8,9) and (5) it follows that in the general case the correct calculation of the spatial dispersion leads to the appearance of terms $\sim \frac{\partial \epsilon_{ij}}{\partial \mathbf{k}}$ not only in expression for the energy flux but also in the expression for energy loss Q.

III. Conclusion

In conclusion we shall formulate the results following from the presented investigation:

1. At the center of the cyclotron resonanse line HF field stimulates extra transfer of the energy by plasma particles along the axis perpendicular to the plane of vectors of the external magnetic field and phase velocity of the propagating EC wave. There is no such transfer under the approach of "pure Hermitian" dielectric tensor.

2. The use of the real Hamiltonian to find the trajectory of the wave beam in the region of the cyclotron absorption line is possible in the case of not too long traces of propagation. Corrections to the field caused by the anti-Hermitian components of the dielectric tensor are of the same order as the difraction effects.

References

1. V.L.Ginzburg, "Propagation of Electromagnetic Waves in Plasmas", *Pergamon*, Oxford, 1964.

2. V.V.Alikaev, A.G.Litvak, E.V.Suvorov and A.A.Fraiman, "Electron-Cyclotron Resonance Heating of Toroidal Plasmas", in *High-Frequency Plasma Heating*, ed. A.G.Litvak, New York, 1992, pp.1 - 61.

3. E.Westerhoff, Proc. of the workshop on 'Theory of Fusion Plasmas', Varenna, 1994 (to be published).

4. A.I.Akhiezer, I.A.Akhiezer, R.V.Polovin, et al. "Plasma Electrodynamics", *Pergamon*, Oxford, 1975.

5. E.Westerhoff, Proc. 23rd EPS Conf. on Contr. Fusion and Plasma Physics, Ed: Kiev (Ukraine) 24 - 28 June, 1996.

6. A.I.Smirnoff, M.D.Tokman, *ZhETF*, 1996, N 8.

DEVELOPMENT OF LOW FREQUENCY MICROTURBULENCE DURING LH CURRENT DRIVE SWITCHING OFF IN FT-2 TOKAMAK

V.V.Bulanin, V.N.Budnikov, V.V.Dyachenko*, E.Z.Gusakov*, L.A.Esipov*, E.R.Its*, A.V.Petrov, A.V.Vers*

State Technical University, St.Petersburg, Russia
* A.I.Ioffe Institute, St.Petersburg, Russia

Introduction

It has been known for a long time that nonlinear interaction between pump wave and tokamak plasma results the LH driven current switch off and the subsequent fast ion generation. In recent years the detailed study of the transition from the LH current drive to the fast ion generation has been carried out on the FT-2 tokamak [1]. The parametric decay at low plasma density at $\omega_0 \approx 2\omega_{LH}(0)$ is conceded to be reasonable for the transition (Here: ω_0 is the frequency of the injected pump wave and $\omega_{LH}(0)$ is the lower-hybrid frequency evaluated at the plasma centre). The small-scale fluctuations behaviour during this transition has been studied with the collective CO_2-laser scattering. The concern experimental data are presented in this paper. The CO_2-laser scattering has been previously employed to investigate the short-wave fluctuations at the pump wave frequency [2] and at the ion gyrofrequency [3] presumably excited through the parametric mechanism. However, the study of the low frequency turbulence has not been attempted.

Experimental Setup

The FT-2 tokamak OH discharge in hydrogen (R = 55 cm, a = 8 cm, I_p up to 43 kA , B = 24 kGs) has been preceded the RF switch on [1]. The plasma parameters $\langle n_e \rangle = (1.3\text{-}4)\cdot 10^{13}$ cm^{-3}, T_e = 500-600 eV, T_i = 100 eV have been got at this moment. The RF power launched from the low magnetic field side with two-waveguide grill was from 20 to 140 kW at a frequency 920 MHz. The pulse duration was nearly 4 ms.

The CO_2-laser scattering diagnostics with paralleled K-analysis has been used to study small-scale fluctuations. The incident laser beam is directed along vertical chord of minor cross-section of the torus. The beam could be positioned at value x of 0, ±3, ±5, +6 cm (here $x = R - R_0$, where R_0 is the major radius of the device). Scattering is measured in the plane perpendicular to the toroidal magnetic field. This plane is located 180° around the torus from the grill. For our case of near-forward scattering the laser beam couples only to fluctuation wavevectors $\mathbf{K}_\perp$ oriented nearly perpendicular to the incident beam. The diagnostic setup is able to gauge simultaneously the radiation scattered from fluctuations at four different $K_\perp$-values in the range from 8 to 40 cm^{-1} and in the frequency band up to 2 MHz. An optical mixing homodyne techniques was used for the detection. The wavevector resolution was constant and equal to 6.5 cm^{-1}. The spatial resolution was about ± 1 cm in the direction transverse to the laser beam. For super small scattering angles the length of scattering volume along the incident beam was about minor cross-section diameter. Thus the scattered signal power spectrum $P_S(K_\perp,\omega)$ can be conveniently regarded as an integral of local power spectrum of fluctuations along the laser beam direction.

Experimental Results.

The specific feature of the FT-2 tokamak experiment consists of the fact that the plasma density increase accompanying RF pulse makes it possible to observe the transition from the current drive to the fast ion generation in a single tokamak shot [1]. The typical traces of plasma parameters and the frequency-integrated scattered power waveforms for such a discharge are shown in Fig 2. The waveforms for two $K_\perp$-values represent the scattering power averaged in a frequency band 0.06-1 MHz and are plotted in the same arbitrary units to be compared between. One can see that the loop voltage drop associated with the current drive remains nearly fixed until the CX-flux is starting up. The drastic increase of the microturbulence has been observed just after the current drive switching off. The fluctuations behave in quite a different manner for the lower and higher level of density preceded RF pulse. At lower plasma density (see Fig.1) the LH current drive displayed as the loop voltage drop is observed to be nearly the same during the whole RF pulse. The

significant changes of P_s values have been observed neither during nor after the RF pulse. Under the higher density (see Fig3) the LH current is not driven at all, the CX-flux is starting from the beginning of RF pulse,

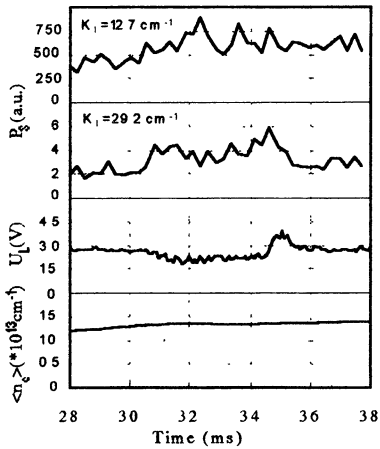

Fig 1. Time evolution of P_S and plasma parameters in a discharge with LH driven current (X=+5 cm, I_p=40 kA)

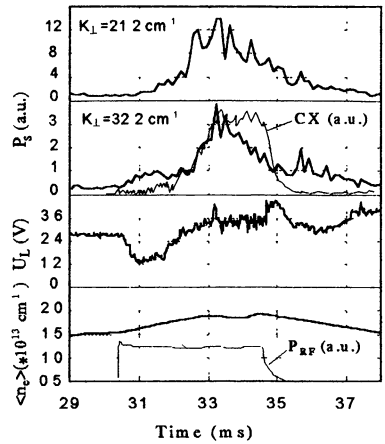

Fig 2. Same as Fig.1 but for the tokamak shot with the current drive switch off (X=-3 cm, I_p=30 kA)

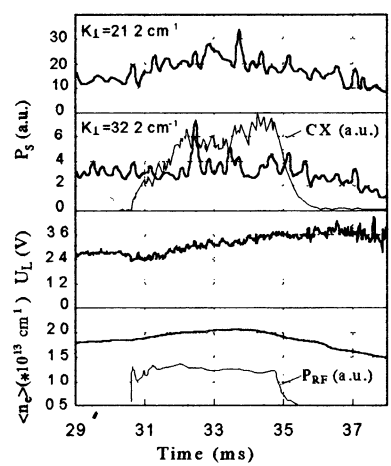

Fig 3. Same as Fig.1 but for a discharge in the absent of LH current drive (X=-3 cm, I_p=30 kA)

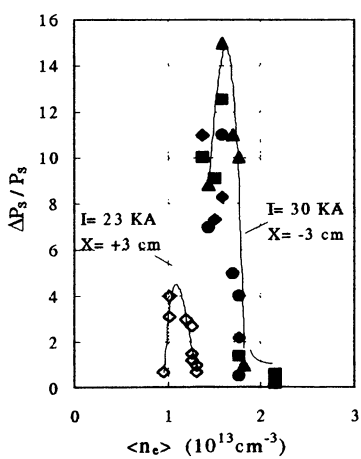

Fig 4. The relative increment of the scattering power versus $(\langle n_e \rangle)_{OH}$. Different symbol correspond to different $K_\perp$-values.

while the scattering power increases a little bit. Thus the turbulence was excited only in the narrow range of plasma densities $(<n_e>)_{OH}$ preceding the RF pulse. This plasma density interval is correlated with the conditions when the current drive switch off and fast ion generation are observed simultaneously during a RF pulse. The fluctuation intensity increment ΔP_S over the OH level of P_S as a function of the initial density $(<n_e>)_{OH}$ is shown in Fig 4. It worth noticing that the experiments on the tokamaks of quite different geometry show the ion temperature increase [4] and the ion gyrofrequency short wave excitation [3] in the same narrow density range to satisfy the condition $\omega_0 \approx 2\omega_{LH}(0)$.

The ratio $\Delta P_S/P_S$ as a function of injected RF power is shown in Fig 5. The RF power threshold of nearly 20 kW is evidently seen for the case of low initial density $(<n_e>)_{OH}$. At higher densities the threshold is not observed at all. A slight increase of fluctuations in these conditions may be merely accounted for plasma density increasing during RF pulse. The multichannel scattering detection has let to discover that shorter wave fluctuations are of greater rate increase as compared to the larger scale ones (see Fig 6) .

The frequency integrated scattering power waveforms were found to be similar under the different incident laser beam x-positions. This refers equally to the different dependencies presented in Figs 4..6. However the frequency spectra are essentially dependent on the incident beam location. As the elongated scattering region is moved towards the plasma periphery, the scattering intensity is increased while the ω-spectra are shifted to lower frequency range. As an example two frequency spectra are shown in Fig 7 for the both central and peripheral scattering volume positions. One has to keep in mind that the orientation of **K**-vector relative to the plasma poloidal velocity $\mathbf{V}_\theta$ has to be changed under the incident beam displacement. Therefore the expected Doppler frequency shift $\mathbf{K}\cdot\mathbf{V}_\theta$ of scattering signal has to decrease as the laser beam chord is moved towards the plasma edge. This effect may be a reason of the observed ω-spectrum displacement to lower frequency range. It is particularly remarkable that an unusually sharp frequency spectra are discovered in the interval of $0 < | x | < 5$ cm. The peak nature of spectra remained quite appreciable even after the ensemble average. Thus the frequency peaks are accounted for the scattering from "quasicoherent" small-scale modes. These modes are to be associated with high frequency "quasicoherent"

bursts which are evidently seen in output signals of detectors. These spectra are sampled in Fig 8 for x = -3 cm. Under the symmetrical probing (x = + 3 cm) the spectra are found to be the same shaped accept the

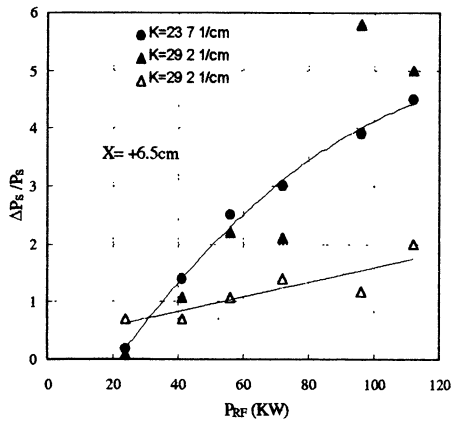

Fig 5. The relative increment of the scattering power versus injected RF power. Solid symbols correspond to $(\langle n_e \rangle)_{OH}=1.5\cdot10^{13}cm^{-3}$, open - $(\langle n_e \rangle)_{OH}=1.8\cdot10^{13}cm^{-3}$

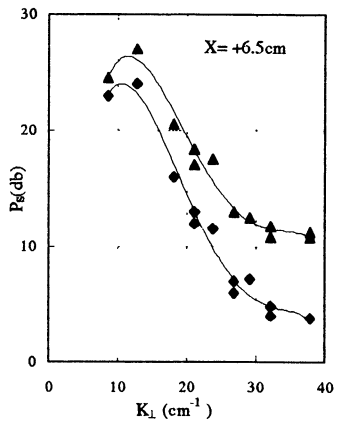

Fig 6. Power $K_\perp$ -spectra for different periods of time: before RF pulse (squares) and after the current drive switch off (triangles)

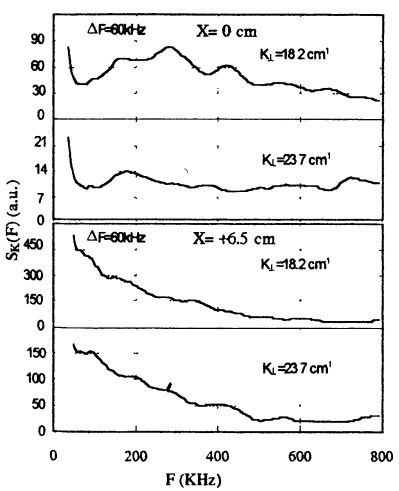

Fig 7. Comparison of the smoothed power spectra for different incident beam positions; I_p = 30 kA

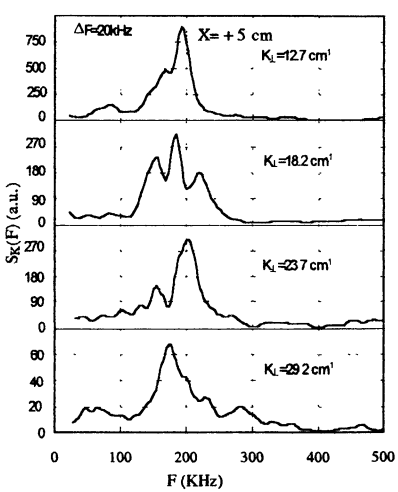

Fig 8. The smoothed power spectra for X= -5 cm; I_p = 40 kA.

broad band back ground intensity. Taken together the data are fitted to a model of the fluctuation development to minor radius interval $4 < r < 6$ cm.

Conclusion

The experimental results are summarised as follows. The short-wave low-frequency turbulence with a "quasicoherent" mode is drastically increased just after LH current drive switch off. The increasing of electron density turbulence is strongly correlated with the RF wave slowing down and the fast ion appearance and exhibits the existence of the RF power threshold. The intensive slowed down RF wave may be an immediate cause of fluctuation excitation or else indirect reason of drift turbulence enhancement through the evolution of plasma parameter radial profiles. However the fact that the small-scale fluctuations are increased faster than larger size ones is not characteristic of drift instability in tokamak. The most plausible process reasonable for this excitation is the pump wave decay into lower-hybrid and drift type waves [5]. It is possible as well that the RF wave is scattered from low-frequency fluctuations near plasma periphery [4], then RF wave is slowed down under the intensity increase. The non-linear interaction between this wave and interior plasma may cause a short -wave fluctuation enhancement.

Acknowledgements

This work was supported in part by INTAS Contract No 94-2236 and RFBR Contract No 94-02-04759-a.

Reference

[1] V.N.Budnikov et.al., 22nd EPS Conference, Bournemouth, 1995, ECA, **19C**, IV-385
[2] C.M.Surko et.al., 2nd Joint Grenoble-Varenna Int. Symp. on Heating in Toroidal Plasmas, 1980, **1**, 393
[3] Y.Takase et.al., Phys. Fluids, 1985, **28**, 983
[4] J.J.Schuss et.al., Nuclear Fusion, 1981, **21**, 427
[5] A.K.Sundaram, P.K.Kaw, Nucl. Fusion, 1973, **13**,901

MICROWAVE DISCHARGES

ATMOSPHERE BREAKDOWN PRODUCED BY MICROWAVE NANOSECOND RADIATION FOR CREATION OF OZONE LAYER

A.L.Vikharev, O.A.Ivanov and A.G.Litvak

Institute of Applied Physics, Nizhny Novgorod, Russia

Introduction

This paper deals with one of environmental problems which has recently arisen, namely, the problem of the stratospheric ozone layer, widely discussed. Appearance of regions with ozone contents in them 20-50 % lower than the usual level, the so-called ozone "holes", has become a regular event in Antarctic and Arctic regions and over large industrial centers. The main reason that causes destruction of the ozone layer is now considered to be pollution of the atmosphere with chlorofluorocarbons (CFCs). CFCs molecules have low chemical activity and can reach the heights of the ozone layer, where they are destroyed by the ultraviolet component of sunlight. The chlorine atoms freed by CFC dissociation enter catalytic reactions with ozone and, in their turn, destroy it.

Currently the world community takes measures to prevent atmosphere pollution with gaseous wastes of industrial enterprises and to reduce production of CFCs with long life times. However, these measures are insufficient. The matter is that typical lifetimes of CFCs in the atmosphere are tens of years, and that means that destruction of the ozone layer will go on for many years, even after the use of CFCs has been completely stopped. That is why the methods for ozone regeneration in the region of ozone "holes" by means of actively affecting the Earth atmosphere are extensively searched for now. The proposed projects consider two different approaches: atmosphere purification from CFCs [1] and regeneration of ozone to the initial natural level [2, 3]. These projects are planned to be carried out by means of an artificial ionized layer (AIL) produced in the atmosphere at different heights with nanosecond microwave pulses injected from ground-based antennas. This paper contains a detailed discussion of the second research line. Here we consider the plasma-chemical way to artificially regenerate the ozone layer in the stratosphere by means of air

ionization. In the ionized region electrons dissociate oxygen molecules, and then the latter are converted into ozone.

Scheme of AIL formation

A possible way to produce an AIL in the atmosphere is shown in Fig.1. Ground-based antennas send two focused beams of powerful electromagnetic waves (with wavelength from 0.8 to 10 cm) into the atmosphere. In the region where the beams cross a microwave discharge is produced (i.e. an AIL is formed) at power density above the breakdown threshold.

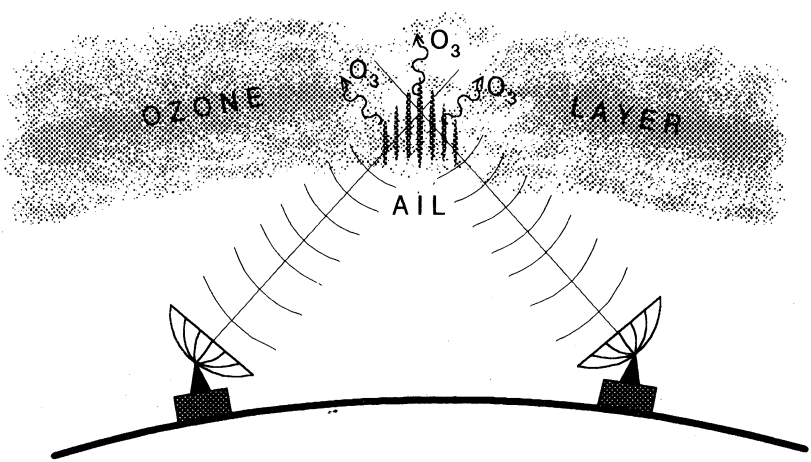

Fig.1. Scheme of an artificial ionized layer formation

Advantages of this scheme of AIL formation are: high efficiency of energy transmission and ease of localization of the breakdown region and ease of positioning an AIL in a preset region of the ozone "hole". As it has been already mentioned, the most efficient ozone generation will be achieved when one uses short (nanosecond) pulses with τ= 10-100 ns. Air ionization in such short times requires high intensities of electric fields in the beams. Estimations show that production of an AIL at the height of 30 km by means of antennas 60 m in diameter placed at the distance of 35 km and emitting waves within the 3-cm wavelength range would require pulsed microwave power in the wave beams higher than $P = 4 \cdot 10^9$ W.

Such power level has been already achieved by modern microwave generators in laboratory experiments. Thus, production of an AIL in the atmosphere is possible even at the current level of technological development.

Now let us analyze this project using results of estimations, numerical calculations and laboratory experiments.

Laboratory modeling

The IAP team has developed and built an experimental set-up for laboratory modeling of plasma chemical reactions in an AIL produced by means of nanosecond wave beams. This complex was used to perform a series of experiments using different sources of microwaves.

In the first experiment [4] the relativistic carsinotron operating within the 8-mm wavelength band was used with power P = 20 MW, pulse duration τ = 5 ns and pulse repetition frequency F = 1-5 Hz.

The second experiment [5] was performed using a 3-cm wavelength band magnetron with power P = 50 kW at pulse duration τ = 500 ns. The magnetron could operate at a high pulse repetition rate, up to $F = 10^3$ Hz. In the second case a cavity-based microwave pulse compressor was also used. This device transformed pulses of the magnetron into pulses with duration τ = 6 ns and P = 800 kW.

In this series of experiments [3] ozone generation was investigated at the pressures and temperatures of air that corresponded to the conditions of the upper atmosphere. The schematic drawing of the experimental set-up is shown in Fig. 2.

A mirror formed a wave beam focused at the center of a spherical quartz retort with its volume about 900 cm^3. The retort walls could be cooled with liquid nitrogen. The gas temperature was set to equal the temperature of the walls and was changing in the range from 200 to 300^0K. The discharge was ignited at the mirror focus as a set of plasmoids situated at antinodes of the standing wave formed by the electromagnetic wave incident on the mirror and reflected from it. The experiments were performed in air within the pressure range from 10 to 90 Torr. The values of pressure and temperature corresponded to the atmospheric conditions at the height of 15-30 km.

Figure 3 represents schemes of other experiments. The discharge was

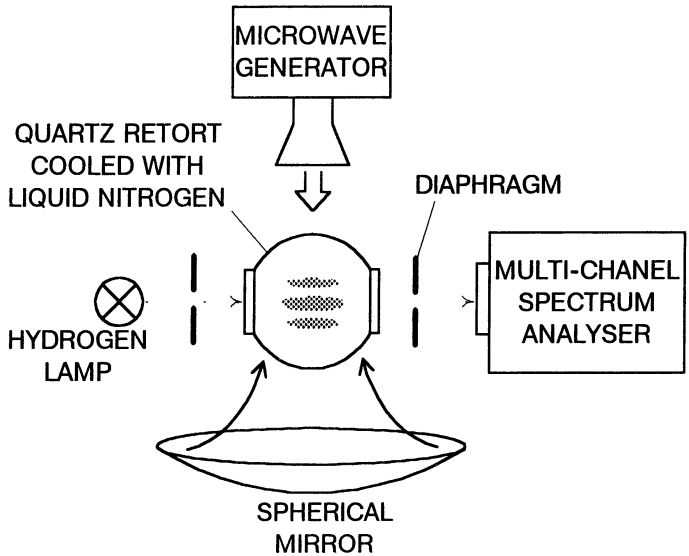

Fig.2. Scheme of the experimental set-up for ozone measurements at low temperature

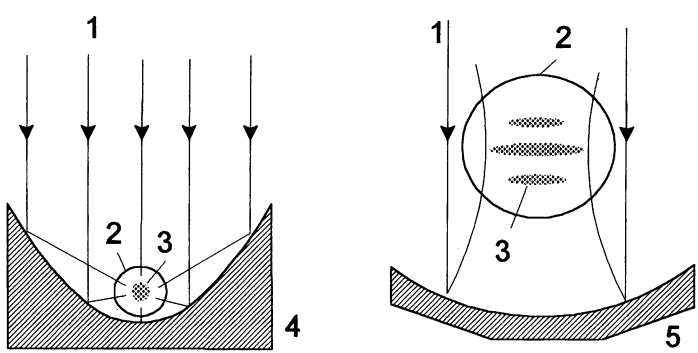

Fig.3. Different schemes for creation of microwave discharges:
1- microwave radiation, 2- quartz retort, 3- discharge plasma,
4- parabolic cylinder, 5- spherical mirror

ignited in two basically different electrodynamic systems. In the first case microwave radiation was focused with a parabolic cylinder, so that the electromagnetic field in the breakdown region was close to a standing cylindrical TE mode. The discharge was shaped as a cylinder several millimeters in diameter and about 30 cm long. In the second case a quasi-planar standing electromagnetic wave was formed by means of a spherical mirror. Then the discharge was a set of plasmoids about 3 cm in diameter localized at the antinodes of the standing wave. The experiments were performed at the room temperature of the air in the pressure range p = 10-250 Torr.

Thus, in the experiments the following factors varied: air density (pressure p = 10-250 Torr) and temperature (T = 200-300^{0}K), radiation parameters, namely, pulse duration (τ = 5, 6 and 500 ns), repetition rate (F = 1-1000 Hz), power (P = 1-20 MW) and the discharge structure.

Densities of ozone and nitrogen dioxide were measured by observing absorption of hydrogen lamp radiation at wavelengths $\lambda \approx 260$ nm and $\lambda \approx 360$ nm, respectively, basing on the known relation:

$$I(\lambda) = I_0(\lambda) \exp(-\sigma N_a L), \qquad (1)$$

where $I(\lambda)$ and $I_0(\lambda)$ are transient and incident intensities of the diagnostic radiation at wavelength λ, L is length of the optical path, σ is absoption cross-section for O_3 or NO_2 and N_a is density of the absorber. When processing the results we made use of absorption cross-sections given in [6-8].

Experimental results

The following regularities of ozone production at room temperature of the air (T = 300^{0}K) were observed.

In the nanosecond microwave discharge the effective dissociation of molecules of O_2 and N_2 (the effective production of O and N atoms) takes place. As a result, the concentration of O_3 increased linearly during the first pulses, Fig.4. The main way for O_3 formation in air is the following reaction taking place in the after-discharge period [7, 8]:

$$O + O_2 + M \rightarrow O_3 + M, \qquad (2)$$

where the reaction constant is $k_1 = 6.2 \cdot 10^{-34} (T/300)^{-2}$ cm^6/s for $M = O_2$ and $k_1 = 5.7 \cdot 10^{-34} (T/300)^{-2.8}$ cm^6/s for $M = N_2$.

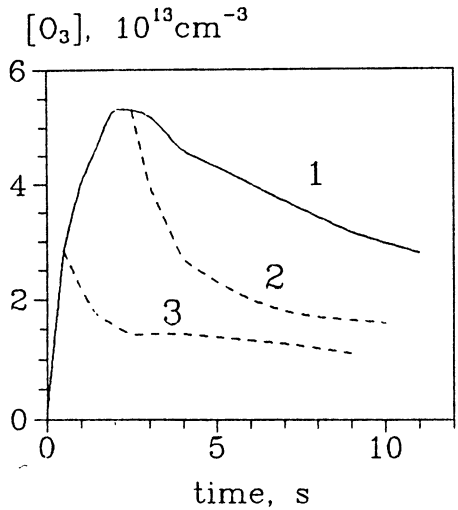

Fig.4. Time evolution of ozone concentration in different number of pulses in series: 1) N =200, 2) N =15, 3) N =3; air pressure p = 45 Torr, repetition frequency F = 4 Hz.

The dynamics of ozone depended on the number of microwave pulses or on duration of the discharge maintenance. The density of O_3 reached its maximum and then gradually fell down to the low level. As series is made shorter the ozone quickly decreases to some definite stationary level, Fig.4. The higher is the number of pulses in the series, the less is the time of transition to the stationary level. It testifies to the fact that the concentration of particles destroying the ozone is accumulated in the ionized region during maintenance of the discharge. Having taken into consideration the rate of ozone destruction, one can estimate of the reaction constant, which is $k \approx 2 \cdot 10^{-14}$ cm^3/s . This constant characterizes the reaction of nitrogen oxide with ozone [7, 8]:

$$NO + O_3 \rightarrow NO_2 + O_2 , \qquad (3)$$

where $k_2 = 4.3 \cdot 10^{-12} \cdot \exp(-1560/T)$ cm^3/s .

This reaction results in an accumulation of nitrogen dioxide, which at sufficiently high densities withdraws atomic oxygen from the process of ozone formation in the following reaction [7]:

$$NO_2 + O \rightarrow NO + O_2, \qquad (4)$$

where $k_3 = 6.5 \cdot 10^{-12} \exp(120/T)$ cm^3/s .

Density of NO_2 exceeds the detection threshold at the moment when ozone density passes through its maximum. Further, as O_3 becomes less dense, NO_2 density grows, reaches its maximum and falls to a certain level, Fig.5.

Initially, nitrogen oxides may be produced in reaction [7, 8] with participation of nitrogen atoms:

$$N + O_2 \rightarrow NO + O, \qquad (5)$$

where $k_4 = 4.4 \cdot 10^{-12} \exp(-3200/T)$ cm^3/s .

Due to its high rate, the reverse reaction,

$$NO + N \rightarrow N_2 + O, \qquad (6)$$

where $k_5 = 1.05 \cdot 10^{-12} \cdot T^{0.5}$ cm^3/s , limits formation of nitrogen oxides. At low energy contributions, when NO production is determined mainly by reaction (5), one can estimate from reactions (5) and (6) stationary density of NO at long series of pulses:

$$[NO] \approx [O_2] \cdot k_4/k_5 \approx 10^{17} \cdot T^{-0.5} \cdot p \cdot \exp(-3200/T) \qquad (7)$$

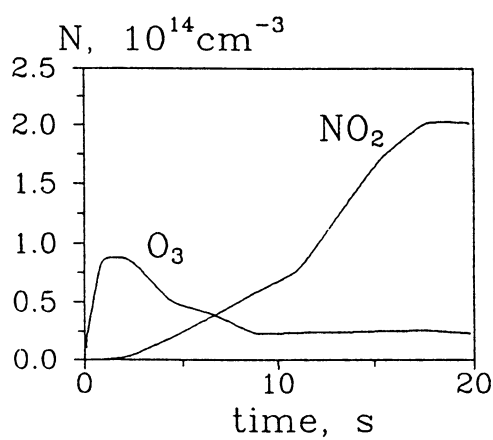

Fig.5. Time dependence of the densities of ozone and nitrogen dioxide at $T \approx 300^0$K, p = 45 Torr, F = 4 Hz.

Thus, one can achieve the maximum possible density of ozone and minimum amount of nitrogen oxides at $T \approx 300^0$K only when the number of microwave pulses is small, $N \approx 1$-5. In this case the amount of accumulated nitrogen oxides does not reach the value that would limit ozone formation.

The majority of the above reactions is strongly dependent on the gas temperature, T. Therefore, under the real stratosphere conditions at T = 200-250^{0}K the corellations between the main processes of ozone formation may change. Figure 6 shows the time dependence of O_3 density for p = 30 Torr as the gas temperature decreases. The experiment described in [3] showed that when the temperature decreased to 215^{0}K, ozone density in all the range of pressures grew by more than an order, and no decrease in ozone content was observed even when the effect was long. Figure 7 shows time dependence of ozone density at fixed density of neutrals, $N = 2 \cdot 10^{18}$ cm^{-3}, for various gas temperatures. The maximum ozone density under the studied pressures was growing in proportion to the air pressure.

The analysis shows that a decrease in T leads to higher velocities of ozone production in reaction (2) and, at the same time, reduces strongly the efficiency of nitrogen oxides production in reaction (5). It follows from Eq.(7) that NO density cannot exceed the value about $9 \cdot 10^8 \cdot p$ at T= 220^{0}K.

Estimations of ozone and nitrogen dioxide production at the stage of linear ozone growth show that the density produced in the retort during one pulse in experiment under pressure p= 90 Torr is about $(2\text{-}3) \cdot 10^{12}$ cm^{-3} for O_3 and for $NO_2 < 10^{10}$ cm^{-3}.

Thus, generation of a microwave discharge in the atmosphere may provide such conditions, under which nitrogen dioxide density will not exceed the natural level of NO_2 [9], and O_3 density will correspond to or exceed the density at the maximum of the ozone layer.

An important parameter that makes the microwave discharge rather advantageous for generation of ozone in the atmosphere is amount of energy going into production of one ozone molecule. The energy cost of that was determined in the following way [5]. Ozone density was measured in a short series of pulses, when it grew linearly and the influence of nitrogen oxides was low. The measurements were performed some time after the pulse series was over, when O_3 filled all the volume of the vacuum chamber, V_k, uniformly. The energy cost was determined basing on the total energy of the microwave pulse, $W = P \cdot \tau$, and using the following formula:

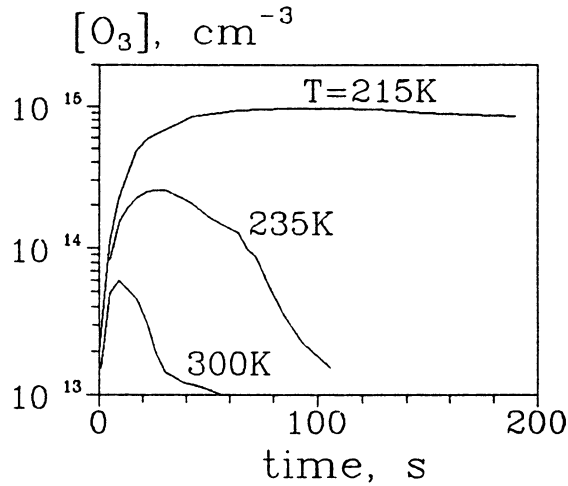

Fig.6. Time variation of ozone density at p = 30 Torr and F = 3 Hz at various air temperatures

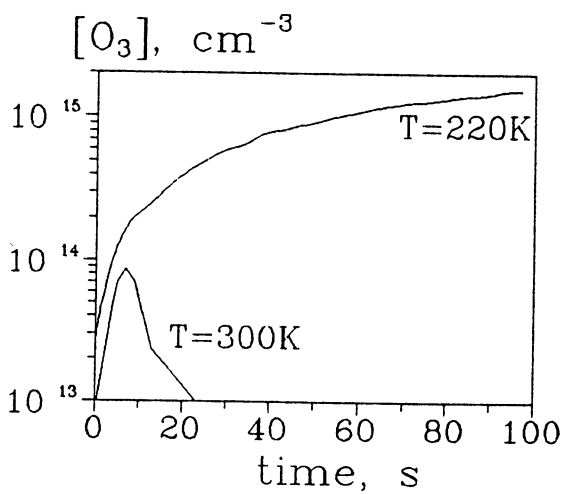

Fig.7. Dependence of ozone density on time at density of neutrals $N = 2 \cdot 10^{18}$ cm^{-3}, F = 3 Hz and various gas temperatures

$$\delta = P \cdot \tau \cdot n_p / [O_3] \cdot V_k \qquad (8)$$

where n_p is number of microwave pulses, and $[O_3]$ is ozone density after n_p pulses. The results of measuring the energy cost of ozone formation for two different types of the microwave discharge is shown in Fig.8 [10]. The energy cost was 2-3 times lower in a discharge created by standing waves than in a discharge formed by a converging cylindrical TE-mode. This shows that efficiency of ozone formation depends essentially on the electrodynamic system producing the discharge. For systems operating with standing waves or crossing wave beams efficiency turns out to be higher.

These experiments showed that the energy cost of production of one ozone molecule is lower in that type of the microwave discharge, in which the maximum of its energy goes into dissociation of oxygen molecules. Oxygen atoms are produced and then converted into ozone mainly in dissociation of O_2 molecules by an electron impact:

$$e + O_2 \rightarrow O_2^* \rightarrow O + O + e \qquad (9)$$

and in collisions of O_2 with metastable N_2 molecules:

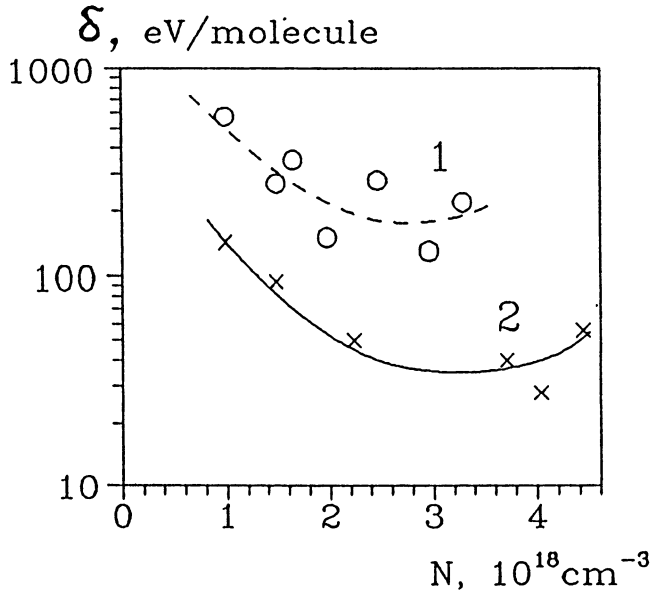

Fig.8. Experimental dependence of energy cost of ozone formation on air density for discharges created by a converging cylindrical TE-mode (1) and by standing wave (2).

$$e + N_2 \rightarrow N_2(A^3\Sigma_u^+) + e, \quad (10)$$

$$N_2(A^3\Sigma_u^+) + O_2 \rightarrow O + O + N_2. \quad (11)$$

The velocity constants for processes (9) and (10) are determined by the function of electron distribution over energies and depend on intensity of the electric field in plasma. The value of O_2 dissociation rate for process (9) in air, k_d, is rather well known for a constant electric field. Let us use these data and estimate the energy cost of production of one ozone molecule in the microwave discharge. We assume that all oxygen atoms are formed in the process of direct dissociation of oxygen (9), and then they enter the reaction of ozone synthesis (2). Estimates will be made basing on the equation describing accumulation of oxygen atoms during a pulse:

$$d[O]/dt = 2 \cdot k_d \cdot [O_2] \cdot N_e. \quad (12)$$

Equation (12) yields the following expression for ozone density produced in one microwave pulse:

$$[O_3] = [O] = 2 \cdot k_d(E_e/N) \cdot [O_2] \cdot N_e \cdot \tau. \quad (13)$$

The energy cost of one ozone molecule is found from the ratio of the microwave energy absorbed in plasma to ozone density:

$$\delta = \sigma \cdot E^2 \cdot \tau / 2 \cdot k_d \cdot [O_2] \cdot N_e \cdot \tau = 5/2 \cdot (e^2/m) \cdot (\nu/N)^{-1} \cdot (E_e/N)^2 / k_d, \quad (14)$$

where $\sigma = e^2 N_e \nu / m (\nu^2 + \omega^2)$ is specific plasma conductivity, ν is rate of electron-molecule collisions, and ω is the wave frequency, $E_e = E \cdot \nu / (\nu^2 + \omega^2)^{1/2}$ is efficient electric field. Using equation (14) it is easy to determine optimal conditions, when at the preset energy of the microwave pulse the number of oxygen atoms produced in the ionized region is maximal. The value of $(E_e/N)^2 / k_d$ is minimal when the value of reduced efficient electric field E_e/N is determined by the following expression:

$$E_e/N = 2 \cdot k_d / dk_d/d(E_e/N) \quad (15)$$

Figure 9 shows the plot for dependence of δ on the reduced electric field, E_e/N (curve 2). The calculations employed the contants of O_2 dissociation rates for process (9) in air from [11]:

$$k_d = 10^{-(A + B/(E/N))}, \quad (16)$$

where A and B are numerical coefficients [11]. It was taken into account that dissociation of ozone molecules in reaction (9) goes on from three electronic levels. For calculation of δ the total constant k_d was used.

Figure 9 shows also the experimental data from [5]. The value of efficient field E_e was determined from intensity of the electric field in the discharge region before the breakdown starts, and the rate of electron collisions in air was assumed equal $\nu = 5{,}3 \cdot 10^9 \cdot p\ (c^{-1})$ [12].

As seen from Fig.9, experimental values of δ are lower than the calculated ones. It witnesses that the channel of O_2 dissociation associated with excitation of electronic levels of N_2 molecules plays a significant part in the plasma of a nanosecond microwave discharge in air. Using the results of [13], we added curve 3 to Fig.9 to represent the results of calculating the energy cost of ozone formation with account for indirect channel of O_2 dissociation due to processes (10) and (11).

Thus, there are optimal conditions for oxygen dissociation in air. The above estimates dealt with determination of optimal conditions for production of oxygen atoms. In the case of a discharge produced by a single nanosecond pulse (or a short series of microwave pulses) they are valid also for ozone, since the process of accumulation of ozone destroying

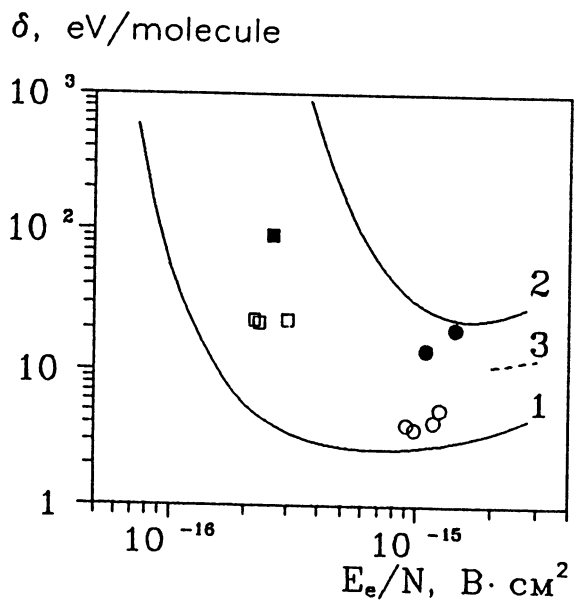

Fig.9. Dependence of energy cost of one ozone molecule on the reduced electric field. Calculation: 1- oxygen, 2, 3- air.
Experiment: oxygen: o- τ=6ns, □- τ=500ns; air: ●- τ=6ns, ■- τ=500ns

particles is too low, and gas is heated insignificantly. By that, the energy cost of ozone formation is determined by electrodynamics of the discharge and depends on how fast the optimal conditions for oxygen dissociation are achieved and for how long they will be sustained in the discharge region.

The results of the performed modeling experiments make it possible to conclude that an efficient way to produce ozone in the atmosphere has been found. A nanosecond microwave discharge can efficiently generate ozone. The laboratory experiments demonstrated sufficiently low energy costs of producing one ozone molecule: $\delta = 15\text{-}20$ eV/molecule, which corresponds to production of 100 g of O_3 per 1 $kW \cdot h$ of consumed energy. The energy cost of ozone generation in an AIL produced by two wave beams crossing in the atmosphere may be found by means of approximate calculations.

Numerical calculations

In order to estimate energy cost of ozone generation in an AIL, let us use the one-dimensional model, which is often used to describe the dynamics of a discharge in crossed TE-beams [14]. Within this model the field distribution is described by the following equation:

$$\partial^2 E/\partial x^2 + k^2 (\sin^2\Theta - (1 + i \nu/\omega) N_e/N_c) E = 0 , \qquad (17)$$

where 2Θ is angle between beams' axes, and the X-axis is perpendicular to the besector of this angle and lies in the plane of the beams' axes. Equation (17) was solved for interval $-L \le x \le +L$, where L is coordinate of an arbitrary point out of the AIL. At $x = \mp L$ at the boundary such conditions were set, which corresponded to incidence of two opposite waves on the discharge region.

It was assumed that AIL was produced at heights H = 20, 25 and 30 km by two ground-based antennas at the distance of 30 km from each other. The calculations were performed for microwave wavelength λ = 3 cm. Figure 10 shows dependence of the energy cost on the value of initial electric field E_0 in AIL [10]. It is seen that the minimum energy cost (30 - 40 eV) is achieved at heights H = 25 km at initial field intensity E_0 =4 kV/cm . Such value of the electric field may be achieved by focusing two beams by antennas 100 m in diameter with microwave power transmitted in each beam equal P = 5 GW .

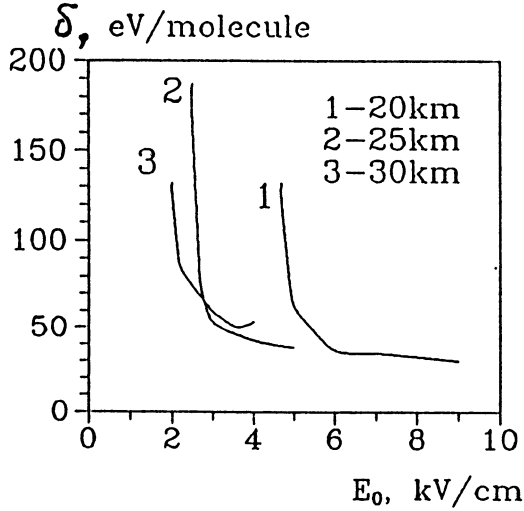

Fig.10. Dependence of the energy cost on the value of initial electric field in artificial ionized layer

Note that the obtained value of the initial electric field E_0 is close to the value of the field, in which the maximum share of the microwave pulse energy goes into ionization E_0/E_k = 5-7 at pulse duration: $\tau_i = \ln(N_{ek}/N_{eo})/\nu_i(E_0)$. Here $E_k(V/cm) \approx 10^{-15} \cdot N(cm^{-3}) \cdot (1+\omega^2/\nu^2)^{1/2}$ is critical field corresponding to the condition of equality of the electron impact ionization rate to the rate of electron attachment to oxygen molecules $\nu_i(E_k) = \nu_a$. However, achievement of the maximum number of oxygen atoms requires that duration of microwave pulses should be several times higher than τ_i.

Estimations of the potential of the microwave method for ozone replenishment in the region of ozone "holes"

As it has been found, the nanosecond discharge is an efficient way to produce ozone in the atmosphere. However, the processes in real atmosphere are determined by a multitude of physico-chemical processes, which can be hardly reproduced under laboratory conditions. A number of questions arises: at what heights accumulation of ozone is most efficient,

what is the ratio between ozone densities and nitrogen oxides in the ionized region, and what will happen to the ozone injected into the atmosphere ? Let us consider these problems in detail.

Numerical calculations in [15] modeled conditions of the real atmosphere and showed that it is most profitable to increase ozone density in the region of its natural maximum. Figure 11 shows the vertical profiles of variations in stationary ozone density due to the effect of an additional ozone source. Intensity of the source was assumed to be $6{,}8 \cdot 10^5$ molecule/cm^3. The maximum gain of general ozone contents was 11% when such an additional ozone source was placed at the height of 18 km.

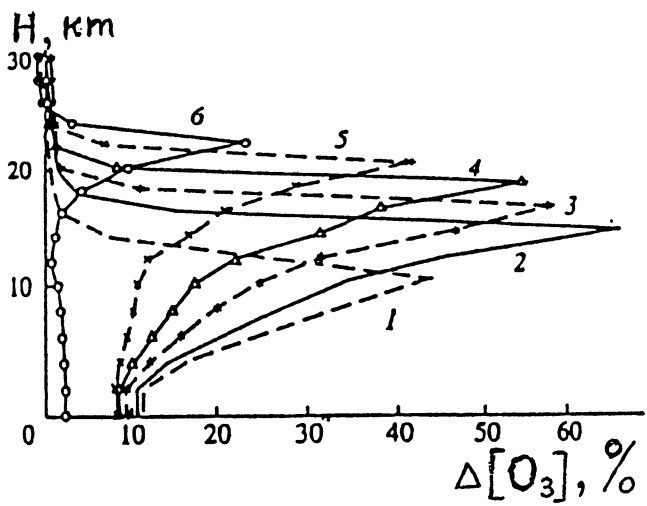

Fig.11. Vertical profiles of variations in stationary ozone density due to the effect of an additional ozone source placed in a 2 km layer with centers at: 1- 10, 2- 14, 3- 16, 4- 18, 5- 20, 6- 22 km

The project of making an atmospheric ozone generator has to be analyzed in terms of side effects, in this case, accumulation of nitrogen oxides should be estimated. At long series of pulses stationary density of NO molecules in AIL is determined by expression (7). After one microwave pulse the ratio of $[O_3]$ to $[NO_x]$ depends on energy contribution in discharge plasma. Figure 12 shows the results of calculations of ratio $[O_3]/([NO]+[NO_2])$ in dependence on specific energy at optimal condition for ozone generation in AIL (Fig.10). The calculations were performed for

wavelength $\lambda = 3$ cm and pulse duration $\tau = 100$ ns, for two ground-based antennas 100 m in diameter at the distance of 30 km from each other. It is seen that the maximum ratio of $[O_3]$ to $([NO]+[NO_2])$ may be achieved.

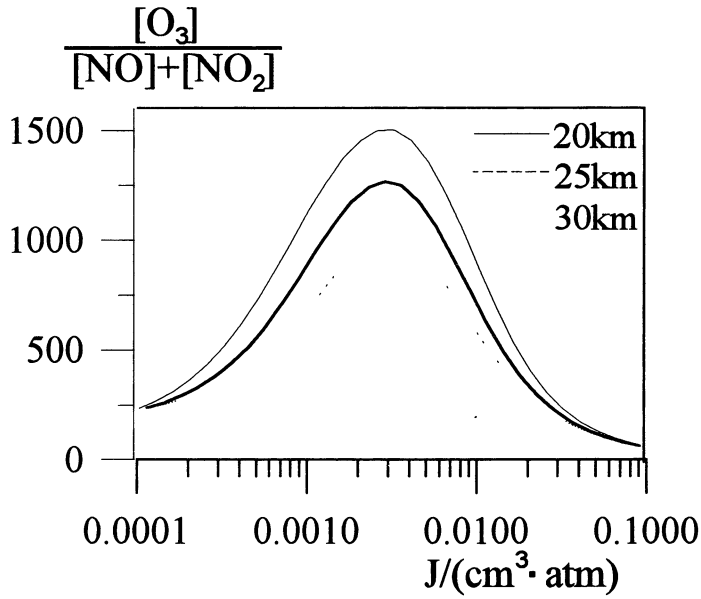

Fig.12. Dependence of the ratio of ozone density to nitrogen oxides density on specific energy in the ionized region

The possibility to realize such a project depends on the level of the required energy costs. These costs are not high when ozone is replenished in the region of local "holes" that appear over large industrial centers. In such "holes" ozone may be replenished using one microwave complex shown in Fig.1.

The problem of ozone "holes" over the poles is more complicated, since replenishment of ozone there would require accumulation of ozone comparable with the general contents of ozone in the atmosphere, and, correspondingly, higher energy costs. And these energy costs depend on the characteristic time of destruction of additionally produced ozone in the ozone "hole".

Ground-based observations yield data on seasonal variations of the general ozone contents in different regions of the Earth [16]. Figure 13 and Figure 14 show seasonal variations of the general ozone contents at the Southern and Northern Poles. The ozone "hole" phenomenon is manifested as a stable decrease in the general ozone contents in the polar regions in September-October. As seen from these Figures, one can determine the characteristic time of ozone destruction during "hole" formation, which is τ_{oz}= 86 and τ_{oz} = 250 days for the Antarctic and Arctic, respectively.

Using these data, let us estimate the required mean power for ozone replenishment in different ozone "holes". Required power P for ozone replenishment to the natural level $[O_3] = 2 \cdot 10^{12}$ cm^{-3} at the height of 18 km in a layer ΔH = 2 km depends on the area of "hole" S and characteristic time of ozone destruction τ_{oz} :

$$P = [O_3] \cdot \Delta H \cdot S \cdot \delta / \tau_{oz} \qquad (18)$$

The values of P which were determined from equation (18) (at δ =20 eV) are presented in the Table for Arctic and Antarctic ozone "holes", respectively.

Table

"Holes"	Local	Arctic	Antarctic	
S, km^2	10^3	10^6	10^7	
τ_{oz}, days	10	250	86	200
P, W	10^7	$6 \cdot 10^8$	$17 \cdot 10^9$	$3 \cdot 10^9$

It should be noted that the above estimates determine the maximum required mean power for Antarctic ozone "hole". In reality, the mean power can be significantly lower. The matter is that an AIL in the region of the ozone "hole" will change the chemical balance, which will result in a longer time of ozone destruction. In order to explain this statement, let us consider the processes leading to destruction of ozone and formation of the Antarctic "hole". In winter time the atmosphere conditions over the Antarctic are characterized by a stable cyclone. That is why the polar

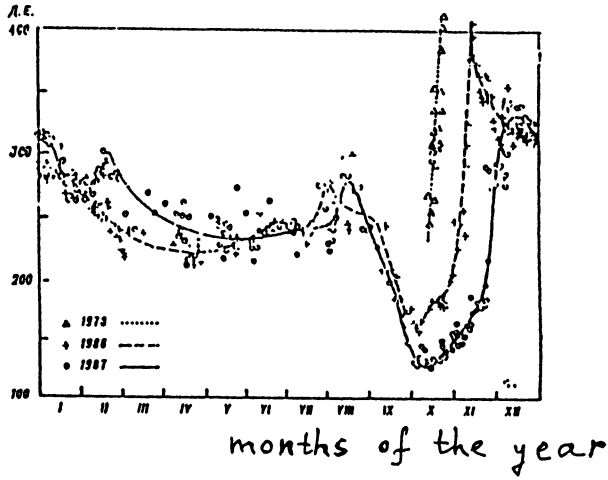

Fig.13. Seasonal variations of the general ozone contents in the Antarctic

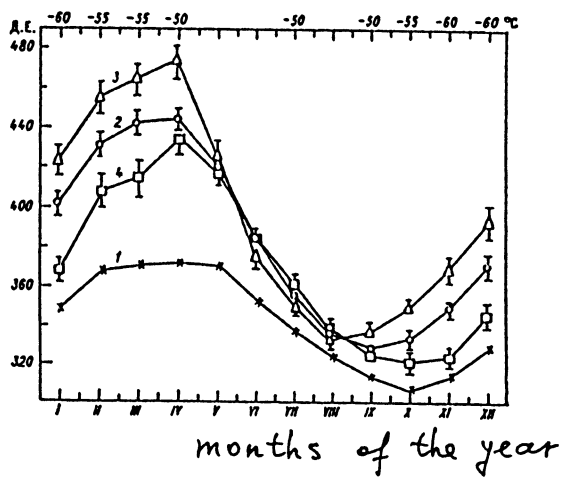

Fig.14. Seasonal variations of the general ozone contents in the Arctic

stratosphere does not exchange air with the stratospheric regions over middle latitudes. Besides, the polar stratospheric clouds over the Antarctic, which in winter consist of ice crystals and fluid drops, accumulate nitrogen oxides in themselves. That results in a break in the influence of the nitrogen and chlorine cycles on each other. The content of nitrogen oxides, NO_x, decreases, and concentration of chlorine oxides, ClO_x, increases, which, in their turn, make the role of the chlorine cycle more important, and cause ozone destruction and formation of ozone "holes".

As it is known, at the usual stratospheric conditions over middle latitudes the nitrogen and chlorine cycles,

$$NO + O_3 \rightarrow NO_2 + O_2, \qquad (19)$$

$$NO_2 + O \rightarrow NO + O_2, \qquad (20)$$

and

$$Cl + O_3 \rightarrow ClO + O_2, \qquad (21)$$

$$ClO + O \rightarrow Cl + O_2, \qquad (22)$$

make their mutual influence on ozone weaker due to active formation of molecules of nitrosyl chlorate:

$$NO_2 + ClO \rightarrow ClONO_2. \qquad (23)$$

Molecules of $ClONO_2$ are not dangerous for ozone. However, their destruction during formation of stratospheric clouds over the Antarctic leads to an increase in the ClO_x content and a corresponding decrease in the O_3 content.

It should be noted that an AIL in the region of an ozone "hole" will generate small amounts of nitrogen oxides (at the level of the natural background). Thus, an AIL will restore the balance of the nitrogen and chlorine cycles. Concentration of the chlorine oxide will get lower, which will lead to longer life times of the additionally produced ozone.

It is known from [17] that in pure oxygen atmosphere the characteristic time for stabilization of balanced ozone concentration depends on height and is sufficiently long. For example, at the height of 20 km it is τ_{oz}= 200 days. At this characteristic time the ozone replenishment will require the minimum mean power (see the Table for Antarctic ozone "hole"). In reality, such a process will require mean power in the range from estimated using τ_{oz} = 86 days, to estimated using τ_{oz} = 200 days.

The value of mean power for ozone replenishment in local ozone "hole" is also presented in the Table. The life time of regenerated ozone in local "hole" depends on the velocity of wind. At the area of "hole" $S = 10^3$ km^2 the characteristic time equals approximately to $\tau_{oz} = 10$ days.

Conclusion

We intended to show in this paper that there are good prospects of creating an efficient atmospheric ozone generator at admissible energy costs, which would solve the problem of the stratospheric ozone.

Acknowledgements

This paper is based in part on the project supported by the Russian Fund for Fundamental Investigations (grant 96-02-19467).

References

1. Askaryan G.A. et al., Sov. J. Plasma Phys., 1992, **18**, 625-631
2. Vikharev A.L. et al., Proc. ICPIG -21, Bochum, 1993, **1**, 123-124
3. Akhmedzhanov R.A. et al., Phys. Lett., 1995, **A207**, 209-213
4. Akhmedzhanov R.A. et al., Pis'ma v Zh. Tech. Fiz., 1995, **21**, N9, 26
5. Akhmedzhanov R.A. et al., Zh. Tech. Fiz., 1997, **67**, N2
6. McEwan M.J., Phillips L.F., Chemistry of the Atmosphere. London: Edwards Arnold Ltd., 1975
7. Baulch D.L. et al., J. Phys. Chem. Ref. Data, 1982, **11**, 327-497
8. Atkinson P.et al., J. Phys. Chem. Ref. Data, 1989, **18**, 881-1097
9. Brasseur G., Solomon S., Aeronomy of the Middle Atmosphere. Dordrecht, Holland: Reidel Publ. Co., 1984
10. Akhmedzhanov R.A. et al., Plasma Physics Reports, 1997, **23**, N1
11. Aleksandrov N.L. et al., High Temperature, 1981, **19**, 485-490
12. MacDonald A.,Microwave breakdown in gases.New York:Wiley,1966
13. Aleksandrov N.L. et al., Pis'ma v Zh. Tech. Fiz., 1990, **16**, N6, 4-7
14. Matveyev A.A., Silakov V.P., Proc. of General Physics Institute (Moscow), 1994, **47**, 58-73
15. Karol' I.L., Kiselev A.A., Frol'kis V.A. Izvestiya, Atmospheric and Oceanic Physics, 1995, **31**, 120-122
16. Aleksandrov E.A., Izrael' Yu.A., Karol' I.L. and Khrgian A.Kh., The Ozone Layer of the Rearth and its Transformation, St.Petersburg, Gidrometeoizdat, 1992
17. Okabe H.,Photochemistry of Small Molecules.New York: Wiley, 1978

POWER FOR COMPENSATION OF OZONE DEFICIENCY IN THE OZONE "HOLES"

G.M.Batanov, I.A.Kossyi, A.A.Matveyev and V.P.Silakov

General Physics Institute of Russian Academy of Sciences, Moscow, Russia.

I. INTRODUCTION

During the last years, the idea of reconstructing the ozone layer of the Earth by action on the stratosphere is increasingly discussed in the literature [1]. I.L.Karol' et al. in [2] examined methods of repairing ozone "holes" and come to the conclusion that all of them (mechanical, optical and chemical) are unpromising.

In the present work, we once again turn to the problem of the generation of artificial ozone layers. We focus on the gas-discharge methods, which were not analyzed in paper [2], and consider the laser method of repairing ozone holes from a somewhat different angle. Our main purpose here is to analyse ecological, economical and engineering aspects of these, seemingly promising, methods for solving one of the most pressing ecological problems - preservation of the ozone layer.

II. GAS-DISCHARGE AND OPTICAL METHODS OF RECONSTRUCTIN THE OZONE LAYER.

We can mention the following, seemingly evident, advantages of the gas-discharge and optical methods of ozone production in the stratosphere:

- the possibility of generating O_3 molecules directly in the ozone layer without additional energy expenditure for ozone (or oxygen) transport from the Earth surface and the corresponding pollution of the atmosphere;
- relatively high efficiency of ozone production (i.e., low energy cost of forming O_3 molecules).

Let us first consider the gas-discharge method. Note that the most promising, ecologically pure, and feasible (by means of modern engineering) discharge is that produced in the stratosphere by a powerful microwave beam (or beams). Vikharev et al. [3] were the first to propose the use of microwaves in order to produce artificial ozone layers. Figure 1 shows a scheme for the implementation of this proposal. Freely localized discharges are exited in the stratosphere in a scanned region, where powerful pulsed microwave beams intersect. The basic idea is that the bulk of the microwave-pulse energy is expended on the ionization and dissociation of molecules without a noticeable heating of a gaseous

medium. It is also assumed that short (nanosecond) microwave pulses do not lead to an appreciable production of nitrogen oxides, which, along with chlorofluorocarbons (CFCs), are capable of destroying ozone molecules in catalytic reactions.

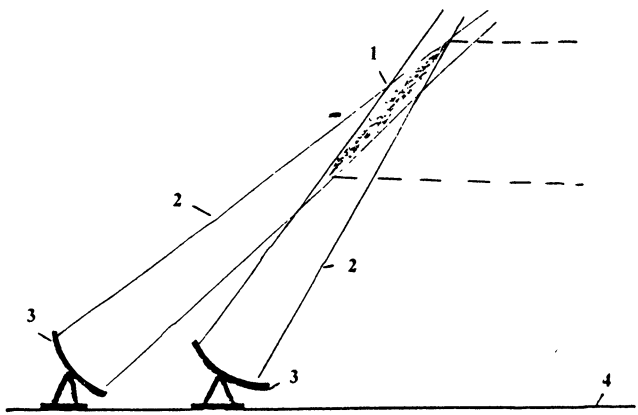

Fig. 1. Scheme for the generation of an artificial ozone layer by means of powerful microwave beams.
1 - artificial ozone layer; 2 - microwave beams, 3 - antennas; 4 -the Earth

Paper [3] and subsequent papers [4-6] describe experiments on laboratory modelling of discharges freely localized in the stratosphere and study the possibility of using these discharges to produce ozone. For this purpose, microwave pulses with the wavelength $\lambda_f = 0{,}8$ cm, peaked power $P_f \cong 10\text{-}15$ MW, and duration $\tau_f = 5$ ns were employed. In experiments, the energy cost of ozone production turned out to be $\varepsilon_{O3} \geq 100$ eV per molecule. The concentration of ozone molecules produced in the course of the discharge reached $n_{O3} \cong 10^{15}$ cm^{-3}. At the same time, the concentration of NO_2 molecules produced in discharges was not larger than 10^{13} cm^{-3} ($n_{NO2} < 10^{13}$ cm^{-3}).

The measurements carried out by Vikharev et al. [3-6] lead authors to the conclusion that the excitation of nanosecond microwave discharges in the stratosphere can be considered as a possible method of repairing large-scale ozone holes.

Gurevich et al. [7] were the first to analyze this problem theoretically. They arrived at the conclusion that the gas-discharge method for restoring the ozone layer is decidedly promising and can be implemented with modern equipment.

Using the "oxygen" photo-chemical model of the atmosphere (when the influence of nitrogen and other components of the air is neglected) the authors of paper [7] determined the optimum altitude for the artificial ozone layer. Their analysis was based on the calculation of the photo-chemical lifetimes of nitrogen, τ_{O3}, and the choice of stratosphere altitudes at which this lifetime is maximum. As a result, the altitude $H \cong 20$ km, at which the calculated lifetime is $\tau_{O3} \cong$ 200-300 days, was shown to be optimum for the artificial ozone layer.

From this lifetime, Gurevich et al. [7] determined the power of a microwave source capable of reconstructing the ozone layer over the entire Antarctic (the area is $S \cong 10^8$ km^2).

They made an encouraging conclusion that the power $P \cong 15$ - 20 GW is sufficient to restore such a significant reduction in the total ozone content (TOC) as $\Delta N_{O3} \cong 50$ D (the natural TOC being of order 300 D, where D is the Dobson unit equal $2{,}7.10^{16}$ cm^{-2}). According to the initial assumptions adopted in [7], it is easy to fill the ozone hole over the Antarctic: ozone molecules should be produced only in a small region whose area S_0 is substantially less than the total area of the Antarctic, S, and then they fill the entire space over the Antarctic owing to the winds (with the velocity $v \cong$ 5 m/s) and transverse (with respect to the winds) diffusion (the turbulent-diffusion coefficient is assumed to be $D_t \cong 10^9$ cm^2 s^{-1}).

In analyzing the possibility for producing the artificial ozone layer over the Earth, it is useful to consider the idea proposed by Starik et al. [1]. They questioned the energetic and ecological aspects of the gas-discharge method for producing the lacking ozone and turned to the method of laser pre-excitation of oxygen molecules followed by the transformation of O_2 into O_3 due to the "free" energy of the solar radiation.

Essentially, this method consists of the following: the stratosphere is irradiated by powerful lasers at altitudes higher than 25 km. The laser radiation causes the resonant excitation of oxygen molecules from the ground electron state $O_2(X^3\Sigma_g^-,v')$ to the metastable states $O_2(a'\Delta_g,v'')$ and $O_2(b^3\Sigma_g^+,v'')$ where v' and v'' are the quantum vibrational numbers of the ground and metastable electron states, respectively. Consequently, under the action of laser irradiation, a large amount of the O_2 molecules are transferred to the metastable electron states. The rate of photodissociation from these states under the action of solar radiation is much higher (by a factor of several hundreds) than that from the ground state. As a result of

recombination between atomic oxygen produced during photodissociation and molecular oxygen, there arise ozone molecules, and a deficit of ozone is thus compensated. The estimates made in [1] show that the power of laser radiation required for the production of the same amount of ozone molecules as was lost from the ozone layer is 5 GW.

III. ECONOMICAL AND ENGINEERING ASPECTS OF GAS-DISCHARG AND OPTICAL METHODS FOR RESTORING THE OZONE LAYER.

The problem of restoring the ozone layer is of current interest, and its solution involves global methods and powerful energy sources. That is why we must analyse once more whether the gas-discharge and optical methods of creating artificial ozone layers are promising from the economic standpoint and whether the optimistic conclusions drawn in [1, 3-7] are justified.

As a criterion for economical efficiency, we use the following obvious condition:

The total power P_0 of the system of ozone production required for the repairing of large-scale ozone holes should satisfy the relation:

$$P_0 << P_c \ , \qquad (1)$$

where P_c is the level of the present-day power production in the developed countries (e.g., in the USA, $P_c \cong 600$ GW).

The power P_0 needed for the gas-discharge method can be estimated from the simple relationship

$$P_0 \cong \Delta n_{O3} \, S \, \Delta H \, \varepsilon_{O3}/\tau_{O3} \equiv \Delta N_{O3} \, S \, \varepsilon_{O3}/\tau_{O3} \equiv Q_{O3} \, S \, \varepsilon_{O3} \ , \qquad (2)$$

where Δn_{O3} is the level of the deficient ozone concentration averaged over the ozone layer, S is the area over which an artificial ozone layer is formed, ΔH is the thickness of the artificial layer, ε_{O3} is the energy cost of forming one ozone molecule, τ_{O3} is the characteristic lifetime of ozone molecules, and Q_{O3} is the rate of ozone production (measured in molec/s cm^2) required for maintaining the artificial ozone layer.

Following papers [3-7], we assume that gas discharges in the stratosphere are excited by the microwave beam (or beams) as shown in Fig. 1. Then, the power of the ground microwave generator determined from (2) depends on the choice of a scheme for forming the artificial ozone layer. First, we examine the scheme used in paper [7]. The microwave beam (or a system of beams) excites a discharge in the stratosphere in a region whose area is much less than of the ozone hole ($S_0/S << 1$). Then,

ozone molecules produced by the discharge fill the entire ozone hole owing to the wind and diffusion.

According to the estimates of Gurevich et al. [7], the power P_0 turned out to be fairly low ($\approx$ 15 - 20 GW), because they assumed that the lifetime τ_{O3} is as long as 200 days. However, in the problem of reconstruction of the ozone layer, this value of τ_{O3} seems to be unreasonably overestimated due to the following circumstances:

(1) The lifetime of ozone molecules in ozone holes in the stratosphere differs strongly from the lifetimes calculated in terms of the oxygen model;

(2) In ozone holes, both the spectrum and intensity of the ultraviolet solar radiation that penetrates into the lower stratosphere can significantly vary. This, in turn, changes the nature of photo-chemical processes and decreases the photo-chemical lifetime of O_3 molecules produced by gas-discharge or optical methods;

(3) Ozone production by the gas-discharge method is inevitably accompanied by the generation of new products in plasma-chemical processes occurring in the discharge. These products can also strongly affect the state of the excess ozone produced in the layer.

We will illustrate these general considerations by the calculations carried out using a versatile kinetic model of a nonequilibrium discharge in a mixture of oxygen and nitrogen (this model is described in [8]).

The kinetic scheme includes a vast set of reactions with a participation of the following plasma components: $N_2(X^1\Sigma_g^+)$, $N_2(A^3\Sigma_u^+)$, $N_2(B^3\Pi_g, W^3\Delta_u, B'^3\Sigma_u^-)$, $N_2(a'^1\Sigma_u^-, a^1\Pi_g, w^1\Delta_u)$, $N_2(C^3\Pi_u, E^3\Sigma_g^+, a''^1\Sigma_g^+)$, $O_2(X^3\Sigma_g^-)$, $O_2(a^1Dg)$, $O_2(b^1\Sigma_g^+)$, $O_2(c^1\Sigma_u^-, C^3\Delta_u, A^3\Sigma_u^+)$, $N(^4S)$, $N(^2D)$, $N(^2P)$, $O(^3P)$, $O(^1D)$, $O(^1S)$, O_3, NO, NO_2, NO_3, N_2O, N_2O_4, N_2O_5, e, O^-, O_2^-, O_3^-, O_4^-, NO^-, NO_2^-, NO_3^-, N_2O^-, N^+, N_2^+, N_3^+, N_4^+, O^+, O_2^+, O_4^+, $O_2^+ \cdot N_2$, NO^+, $NO^+ \cdot NO$, $NO^+ \cdot N_2$, $NO^+ \cdot O_2$, NO_2^+, N_2O^+. This set describes the kinetics of electron-impact electronic excitation, dissociation and ionization of neutral particles; processes of associative ionization with a participance of electronically excited particles; processes of electron attachment and detachment; chemical kinetics of neutral particles; ion conversion; reactions of electron-ion and ion-ion recombination.

In chemical transformations of neutral components of the mixture, processes with a participation of unexcited and electronically excited

particles are taken into account. The most complete and reliable information on chemical reactions between unexcited neutral particles of nitrogen-oxygen mixture, in our opinion, contains in the review [9]. Rate constants of more than 25 reactions between atoms and molecules of nitrogen and oxygen and products of their interactions were taken from this review.

Reactions between unexcited particles are supplemented by more than 65 reactions between electronically excited molecules and atoms of the components of the initial gaseous mixture and products of their interactions.

Lastly, an essential block of the kinetic scheme consists of reactions (more than 100) describing conversion of positive and negative ions of initial components (nitrogen and oxygen) as well as of products of chemical reactions between them.

Electron energy distribution function determining the kinetic coefficients of electrons was calculated by means of a numerical solution of the quasi-stationary Boltzmann equation in a two-term approximation. A formulation of the Boltzmann equation takes into account the processes of elastic scattering of electrons from heavy particles; processes of excitation of rotational, vibrational and electronic degrees of freedom of the N_2 and O_2 molecules; ionization and attachment.

The Boltzmann equation was numerically solved by the iterative finite-difference method [10] with an inhomogeneous (exponential) energy grid. The kinetic model reduces to a stiff system of ordinary differential equations that was solved with the use of the Gear method.

The computational scheme [8], being of universal character and applicable practically to any pulsed non-equilibrium discharge in nitrogen-oxygen mixture, is used in the present work for an analysis of experiments [3-6] modeling a natural realization of atmospheric microwave discharge under laboratory conditions. At the same time this scheme is used also for calculations describing a hypothetical effect of plasma-forming powerful microwave beam upon the atmosphere. In this case a presence of water molecules in the composition of real air is taken into account, because hydrogen-containing components may exert an essential influence on charged particles' and chemical dynamics of the air mixture excited by the microwave discharge. Besides, the kinetic scheme is supplemented by the processes of photodissociation of gaseous molecular components under the action of solar radiation. At the same time, since characteristic duration of microwave pulses is small, in modeling plasmachemical processes at the active stage of the discharge we neglect photodissociation processes as well as the processes of diffusion and wind transport.

Before analyzing the calculated results, we should note that the authors of papers [3-7] neglected the production of nitrogen oxides (NO_2, NO, N_2O_5 and N_2O) in the course of any (in particular, microwave) discharge in the stratosphere. This circumstance was frequently mentioned during the analysis of ecological consequences of creating artificial radio-reflecting plasma mirrors in the atmosphere (see, e.g., [11-13]). Here, we again consider the plasma-chemical consequences of exciting discharges in the stratosphere. We start with the assumption that the lifetime of the discharge-produced ozone molecules can be smaller due to the ozone destruction in catalytic reactions involving nitrogen oxides NO_x that are generated in the same discharge region.

The amount of these oxides can be calculated for each case of discharge excitation by using the kinetic scheme developed in paper [8]. Analysis of the results of previous calculations for microwave discharges excited by long (microsecond) pulses in the stratosphere [11-13] and a comparison with the experimental data [12] allow us to conclude that, in essentially all the investigated regimes, the production of ozone in the discharge region is accompanied by the generation of nitrogen oxides whose concentration turns out to be higher than or close to 0,5% of the ozone concentration.

In order to analyze whether this conclusion is valid for "short" (nanosecond) microwave pulses, we carried out the calculations (using the scheme developed in [8]) for conditions close to those of experiments described in [3-6]. In calculations we used the wavelength $\lambda_f = 0,8$ cm, the air pressure $p = 90$ Torr, the temperature $T = 220$ K, and the parameter $E/n_m = 6,25.10^{-15}$ V cm^2. The microwave-pulse duration ranged as $\tau_f = 1,67 - 4$ ns. Accordingly, the specific energy input into the discharge ranged as $w = 9.10^{-5} - 0,5$ J/cm^3 atm.

Figure 2 displays the characteristic results for $\tau_f = 4,00$ ns. We can see that the production of excess ozone is accompanied by the generation of nitrogen oxides NO, NO_2, N_2O, and N_2O_5. The rapid disappearance of NO molecules in the post-discharge period occurs as a result of production of a large amount of atomic nitrogen (at high values of the parameter E/n_m). The final state of the medium treated by the microwave pulse is characterized by the presence of two stable components, N_2O and N_2O_5, which were not recorded in the experiments [3-6]. (The diffusion of nitrogen dioxides from the discharge region and their transformation into N_2O_5 (Fig. 2) in the experiments [3-5] can reduce the concentration of NO_2 to values lower than those that can be recorded by the measurement equipment (~ 10^{13} cm^{-3}))

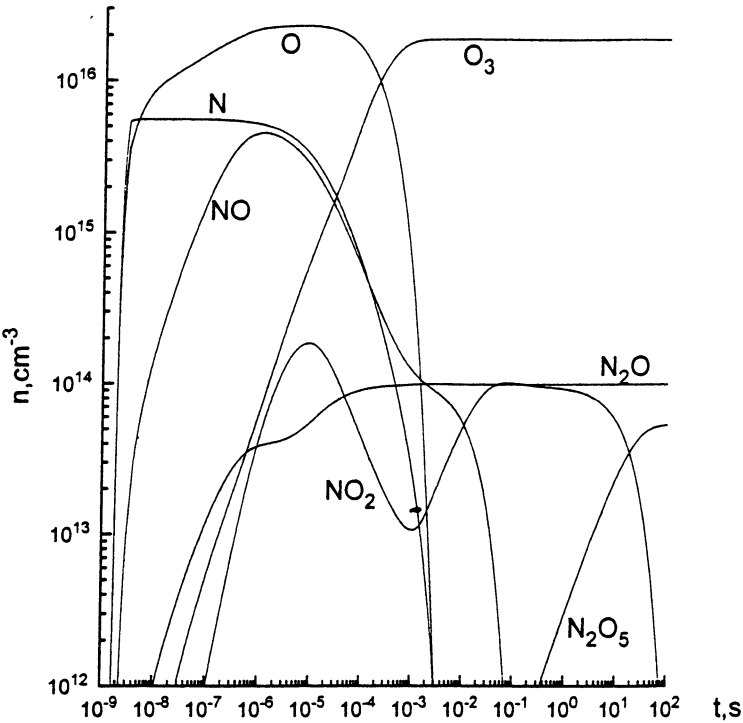

Fig. 2. Results of calculations of the evolution of the products produced in the course of a microwave discharge under conditions close to those of experiments in [6]:

$\lambda_f = 0{,}8$ cm; $E/n_m = 6{,}25.10^{-15}$ V cm^2; $\tau_f = 4$ ns; p = 90 Torr and T = = 220 K

It should be noted that, in the calculations that were performed for a comparison with the laboratory experiments, no account was taken of photo-chemical processes, which are responsible for the transformation (under natural stratospheric conditions) of N_2O and N_2O_5 molecules into NO_2 and NO and can maintain the concentration of the latter at the same level for a long time. The Table 1 lists the calculated results for the concentrations of ozone and nitrogen oxides generated by means of nanosecond microwave pulses with different duration.

The table shows that, in all the cases under consideration (as in the case of microwave pulses [11-13]), the concentration of NO_2 is not less than 0,5% of the ozone concentration.

The concentration of ozone that should be produced in the discharge region to compensate for the losses of O_3 molecules from the ozone hole can be estimated (in order of magnitude) as $n_{O3} \cong \Delta n_{O3}\ (S/S_0)\ (\tau/\tau_{O3})$, where $\tau \cong a/v$ and a is characteristic linear size of ozone production

Table 1

τ_f, (ns)	n_{emax}, (cm^{-3})	w, (J/cm^3 atm)	n_{O3}, (cm^{-3})	n_{NOx}, (cm^{-3})	n_{O3}/n_{NOx}
1,67	$1,06.10^{12}$	$9,00.10^{-5}$	$8,97.10^{12}$	$3,40.10^{11}$	26
1,80	$8,30.10^{12}$	$7,40.10^{-4}$	$8,33.10^{13}$	$7,30.10^{11}$	115
1,90	$3,17.10^{13}$	$3,26.10^{-3}$	$3,86.10^{14}$	$2,09.10^{12}$	185
2,00	$7,80.10^{13}$	$1,07.10^{-2}$	$1,25.10^{15}$	$6,15.10^{12}$	200
3,00	$1,63.10^{14}$	0,225	$1,81.10^{16}$	$1,06.10^{14}$	170
4,00	$1,72..10^{14}$	0,459	$2,97.10^{16}$	$1,80.10^{14}$	165

region ($a \sim \sqrt{S_0}$). For $a \cong 1$ km, $v = 5$ m/s and $\tau_{O3} = 10$ days we obtain $n_{O3} \cong 2.10^{16}$ cm^{-3}.

Description of the dynamics of stratospheric air components during the microwave discharge and at the post-discharge stage was performed on the basis of the kinetic scheme [8] outlined above. In doing so, a presence of hydrogen-containing neutral components (H_2O, H, H_2, OH, HO_2, H_2O_2, HNO_2, HNO_3, HNO_4), positive and negative ions in air mixture was taken into account. Data on rate constants of reactions with a participance of these components were taken for the most part from [14-16]. In addition to purely chemical processes, the processes of photodissociation of the molecules O_2, O_3, NO_2, N_2O, N_2O_5, HNO_3 etc. under the action of solar radiation [17,18] were also considered. Due to low relative content of hydrogen-containing components their influence on electron energy distribution function was neglected.

As an example, Fig. 3 shows the results of calculations of plasma-chemical parameters for the field experiment on microwave discharges freely localized in the stratosphere (H = 20 km). A microwave pulse with the parameters $\lambda_f = 0,8$ cm, $\tau_f = 4,0$ ns, and $E/n_m = 6,25.10^{-15}$ V cm^2 makes it possible to obtain the ozone concentration $n_{O3} \cong 2.10^{16}$ cm^{-3}. Performing calculations similar to those in Fig. 2, we can determine the products of the plasma-chemical reactions in the discharge region. We observed the evolution of these products for a long period after the discharge phase. The density modulation of the components under study is related to the day-night alternation. We calculated the photo-chemical reactions under the

assumption that the stratosphere is unperturbed. Diffusion of air mixture components was accounted in zero-dimensional approximation by introducing effective terms of diffusive losses into kinetic equations for each component. We also assumed that, for the altitude of interest, the diffusion coefficient is $D_t \cong 3.10^5$ cm^2/s. This value corresponds to the literature data (see, e.g., [17]) and seems to be closer to the real one than the unreasonably high value (~ 10^9 cm^2/s) adopted in paper [7].

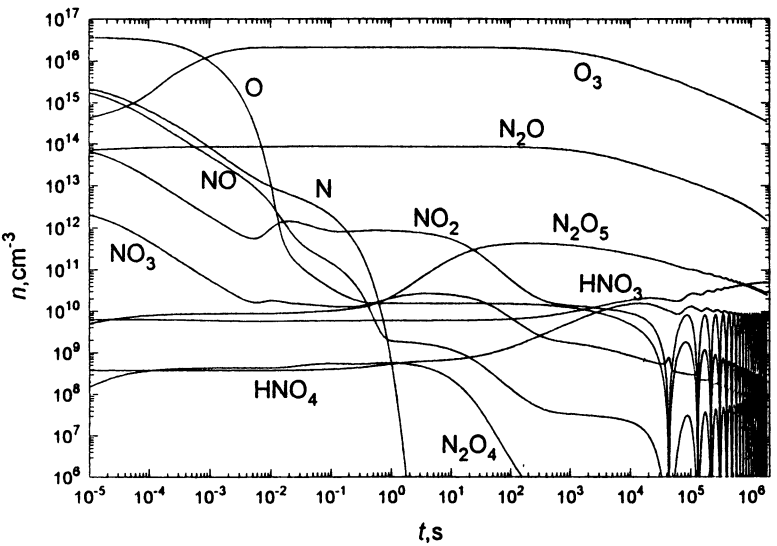

Fig. 3. Results of calculations of the evolution of the products, produced in the course of a microwave discharge excited in the unperturbed stratosphere.
λ_f = 0,8 cm; $E/n_m = 6{,}35.10^{-15}$ V cm^2; τ_f = 4 ns; H = 20 km and D = $= 3.10^5$ cm^2/s
The characteristic size of the discharge region is 1 km.

After the microwave pulse is switched off, the ozone concentration grows to $n_{O3} \cong 2.10^{16}$ cm^{-3} and then begins to decrease; the characteristic time of the decrease in the total number of the resulting O_3 molecules is τ_{O3} ≅ 15-20 days. It justifies our choosing of value of lifetime and shows that in the case being considered τ_{O3} begins to depend on the production of nitrogen oxides in the region of ozone generation.

Using relationship (2) we can easily estimate that, for the O_3 lifetimes $\tau_{O3} \cong$ 10-20 days, (measured [19] or determined from our calculations) and for the energy cost $\varepsilon_{O3} \cong 100$ eV (determined in the experiments [6]), the power level required for the reconstruction of a large-scale ozone hole (e.g., over the Antarctic) is as large as

$$P_0 \cong 8.10^3 - 1{,}6.10^4 \text{ GW}.$$

This value is larger or even much larger than the present-day power production all over the world ($\sim 3.10^3$ GW)

Now, we consider a scheme for the global (rather than local) ozone generation over the entire hole. This method is unlikely to be feasible from the engineering standpoint. Nevertheless, we will also estimate the possible consequences of its implementation, because it might seem to be attractive owing to possibility of compensating for ozone losses ΔN_{O3} over the entire ozone hole by means of a uniform production of a small amount of O_3 molecules..

To do this, we use relationship (2) and take into account the fact that the rate Q_{O3} should be equal (in absolute value) to the rate of a seasonal decrease in the total amount of ozone in the hole. For definiteness, we again consider the hole over the Antarctic. Then, the maximum rate Q_{O3} is observed in spring (August, September, and October). According to [19], in 1986-1990, in latitude 80-90° south, this rate was equal to $(0{,}93 - 0{,}62).10^{12}$ molec/s cm^2. Using these values of Q_{O3}, we can estimate the power required for uniform ozone production.

For $Q_{O3} = 0{,}93.10^{12}$ molec/s cm^2, this power is $P_0 \cong 1860$ GW (for $\varepsilon_{O3} = 50$ eV and $S \cong 2{,}5.10^7$ km^2) and $P_0 \cong 1{,}5.10^4$ GW (for $\varepsilon_{O3} = 100$ eV and $S = 10^8$ km^2).

For $Q_{O3} = 0{,}62.10^{12}$ molec/s cm^2, we obtain $P_0 \cong 1240$ GW (for $\varepsilon_{O3} = 50$eV and $S = 2{,}5.10^7$ km^2) and $P_0 \cong 10^4$ GW (for $\varepsilon_{O3} = 100$ eV and $S = 10^8$ km^2).

Thus in the case of "uniform" production , the power level of the gas-discharge source of ozone is also comparable to or even larger than the present-day power production all over the world.

At first glance, the use of the optical method (proposed by A.M.Starik et al. [1]) for repairing the ozone layer will require a substantially lower input than in the case of gas-discharge production. However, a simple analysis shows that actually this power should be even higher than that for the freely localized microwave discharge. The power P_0 required for laser repairing of the ozone hole can be estimated through the following relationship, which is similar to (2):

$$P_0 \cong \Delta n_a \, S \, \Delta H \, \varepsilon_a/\tau_a \quad , \qquad (3)$$

where Δn_a is the desired concentration of oxygen molecules excited by laser radiation to the state $O_2(a'\Delta_g)$ (below, we will denote this state as $O_2(a)$), ε_a is the energy cost of excitation, and τ_a is the characteristic lifetime of an excited oxygen molecule.

The lifetime τ_a can be estimated from the relationship

$$\tau_a^{-1} = k_5 n_{O3} + k_6 n_{N2} + k_7 n_{O2} + k_8 n_O + k_9 n_{NO} \qquad (4)$$

Here, k_5, ..., k_9 are the constants of the following processes [8]:

$$O_2(a) + O_3 \rightarrow O_2 + O_2 + O; \qquad k_5 = 9{,}7.10^{-13} \exp(-1564/T) \ cm^3 s^{-1} \qquad (5)$$

$$O_2(a) + N_2 \rightarrow O_2 + N_2; \qquad k_6 = 3.10^{-21} \ cm^3 s^{-1} \qquad (6)$$

$$O_2(a) + O_2 \rightarrow O_2 + O_2; \qquad k_7 = 2{,}2.10^{-18}(T/300)^{0,8} \ cm^3 s^{-1} \qquad (7)$$

$$O_2(a) + O \rightarrow O_2 + O; \qquad k_8 = 7.10^{-16} \ cm^3 s^{-1} \qquad (8)$$

and

$$O_2(a) + NO \rightarrow O_2 + NO; \qquad k_9 = 2{,}5.10^{-11} \ cm^3 s^{-1} \qquad (9)$$

At the altitude H = 30 km, for the natural concentrations of O_2, N_2, O_3, O, and NO molecules and $T \cong 220$ K, we obtain

$$\tau_a \cong 10 \text{ s}.$$

Since the rate of the photodissociation (by ultraviolet solar radiation) of O_2 molecules from the $O_2(a)$ state is higher than that from the ground electronic state [1] by a factor of 300, we can assume that $\Delta n_a \cong 1/300 \, n_{O2}$; i.e., at the chosen altitude, we have $\Delta n_a \cong 2.10^{14} \ cm^{-3}$. Assuming that $\varepsilon_a \cong 1$ eV, $\Delta H \cong 1$ km, and $S = 10^8 \ km^2$ (for the Antarctic), we obtain from (3):

$$P_0 \cong 2.10^8 \text{ GW}$$

This value is so high that it is inexpedient to use the optical method to reconstruct the ozone layer.

IV. CONCLUSION

Thus, in present paper, we have shown that, for both the gas-discharge and optical methods of creating artificial ozone layers, the power level of ozone sources should be comparable to or even much higher than the present-day power production all over the world. For example, the power required for repairing the ozone hole over the Antarctic is

$$P_0 \cong 10^4 - 10^8 \text{ GW}.$$

Hence, we can conclude that the implementation of the methods proposed in [1, 3-7] is impossible from both the engineering and economical standpoints.

The results of our analysis are in complete agreement with the conclusion drawn by I.L.Karol' et al. [2] that none of the methods involving the introduction of ozone molecules in the ozone layer can be used to repair ozone holes.

At the same time, since the idea of generating artificial ozone layers turned out to be unpromising, interest is growing in a fundamentally new approach to the ecological problem under study. We mean the global troposphere cleaning from ozone-destroying contamination by means of gas-discharges, which will prevent the income of these products into the ozone layer [20,21]. The implementation of this method, which requires (according to preliminary estimates) relatively low powers and energy costs, can lead to a substantial decrease in the concentration of ozone-destroying components in the stratosphere and, as a result, the self-reconstruction of the ozone layer.

ACKNOWLEDGEMENTS

We are grateful to G.A.Askar'yan for fruitful discussions.

This work was supported in part by the Russian Foundation for Fundamental Investigations (Project No 96-02-16037a).

REFERENCES

1. A.M.Starik, O.N.Favorskii, O.S.Khabarov and B.N.Amelin, Vestn. Rus. Akad. Nauk, 1993, **63**, No 12, 1082.

2. I.L.Karol', A.A.Kiselev and V.A.Frol'kis, Izv. Akad. Nauk SSSR, Ser.: Fiz. Atmos. Okean., 1995, **31**, No 1, 120.

3. A.L.Vikharev, A.M.Gorbachev, O.A.Ivanov, A.L.Kolisko and A.G.Litvak. XXI ICPIG, Proceedings, Bochum, 1993, **1**, 123.

4. A.L.Vikharev, O.A.Ivanov, A.G.Litvak, Microwave Plasma and its Applications, Invited Papers, Moscow Physical Society, 1995, 391.

5. A.L.Vikharev, A.M.Gorbachev, O.A.Ivanov, A.L.Kolisko and A.G.Litvak, J. Geophys. Res., 1994, **99**, No D10, 21057.

6. R.A.Akhmedzhanov, A.L.Vikharev, A.M.Gorbachev, O.A.Ivanov, N.G.Kolganov, A.L.Kolisko and M.M.Ofitserov, Physics Letters, 1995, **A207**, 209.

7. A.V.Gurevich, N.D.Borisov, S. Montecinos Geisse and P.Hartogs, Physical Letters, 1995, **A207**, 281.

8. I.A.Kossyi, A.Yu.Kostinsky, A.A.Matveyev and V.P.Silakov, Plasma Sources Sci. Technol., 1992, **1**, 207.

9. O.E.Krivonosova, S.A.Losev, V.P.Nalivayko, Yu.K.Mukoseyev and O.P.Shatalov, Plasma Chemistry, 1987, No 14, B.M.Smirnov, Ed., Moscow: Energoatomizdat.

10. N.A.Dyatko, I.V.Kochetov and A.P.Napartovich, Fizika Plazmy, 1992, **18**, 888.

11. I.A.Kossyi, A.Yu.Kostinsky, A.A.Matveyev and V.P.Silakov, Comments Plasma Phys. Controlled Fusion, 1991, **14**, No 2, 73.

12. G.A.Askar yan, G.M.Batanov, D.F.Bykov, S.I.Gritsinin, I.A.Kossyi, A.Yu.Kostinsky, A.A.Matveyev and V.P.Silakov, ISPP-7 "Piero Caldirola", Controlled Active Global Experiments (CAGE), E.Sindoni and A.Y.Wong (Eds), SIF, Bologna, 1991, 239.
13. G.A.Askar'yan, G.M.Batanov, A.E.Barkhudarov, S.I.Gritsinin, E.G.Korchagina, I.A.Kossyi, V.P.Silakov and N.M.Tarasova, J. Phys. D, Appl. Phys., 1994, **27**, No 6, 1311.
14. D.L.Baulch, R.A.Cox, P.J.Crutzen, R.F.Hampson, J.A.Kerr, J.Troe and R.T.Watson, J. Phys. Chem. Ref. Data, Supplement I, 1982, **11**, 327.
15. B.M.Smirnov, Complex Ions, Moscow: Nauka, 1983.
16. V.G.Anicich and W.T.Huntress, Astrophys. J. Suppl., 1986, Ser. **62**, 553.
17. G.Brasseur and S.Solomon, Aeronomy of the Middle Atmosphere, Dordrecht, Holland, D.Reidel Publ. Co., 1984.
18. J.W.Chamberlain, Theory of Planetary Atmospheres, N.-Y., Academic Press, 1978.
19. E.A.Aleksandrov, Yu.A.Izrael', I.L.Karol' and A.Kh.Khrgian, The Ozone Layer of the Earth and its Transformation, St. Petersburg, Gidrometeoizdat, 1992.
20. G.A.Askar'yan, G.M.Batanov, S.I.Gritsinin, I.A.Kossyi, A.A.Matveyev and V.P.Silakov, Comments Plasma Phys. Controlled Fusion, 1994, **16**, No 1, 43.
21. G.M.Batanov, I.A.Kossyi and V.P.Silakov, Preprint No 11, General Physics Institute, Moscow, 1995.

PHYSICS OF SUPER UNDERCRITICAL STREAMER DISCHARGE AND ITS APPLICATION FOR OZONE LAYER SAFETY

G.I.Batskih, K.V.Khodataev

Moscow Raduotechnical Institute, RAS
Warshavskoe shosse, 132, Moscow 113519, Russia
Fax: (095) 314 1053, e-mail: khodataev @ glas.apc.org

Introduction

According to the observation data[1] the present ozone layer global depletion is -6% of natural level. The grows rate of ozone layer depletion is -4% per decade. It was found that the ozone layer depletion is antropogenic. The major cause of the depletion are the pollutions of the chlorofluorocarbons (CFCs, or freons) into the atmosphere [2],[3]. The industrial freons released in the atmosphere are driven by the convective flux at height 12-20 km corresponding to the lower boundary of the ozone layer. Under the influence of the ultraviolet radiation CFCs educe chlorine which serves as catalyst to destroy ozone taking part repeatedly (up to 10^5 cycles) in the decay reaction. The freons rate in air equals approximatelly 10^{-9} in troposphere and on altitudes higher 15 km quikly decreases with decrement ~-0.7 km^{-1}. The annual pollution of freons equals ~0.5-0.6 Mt/year.

In view of ecologically unacceptable exhausting of the ozone layer the countries joining Vienna Convention and Montreal Protocol (including Russia) carry out the curtailing of the ozone-destroying freons production.

Nevertheless at recent time a considerable mass of the industrial freons accumulated in atmosphere is able to cause the catastrophic from the ecological point of view reduction of the ozone layer. The mass of the freons accumulated in atmosphere and its life-time in atmosphere approximatelly equals 20 Mt and 100 years accordingly. The problem of the removal of the ozone-destroying freons released in the atmosphere is important to the same extent as one of the freon production curtailing.

There are the row of proposals of cleaning atmosphere from ozone destroing freons by means of discharge in UHF radiations [4],[5]. We will

concretize the goals of the cleaning global system, requarements on it and type of cleaning discharge.

The requarements on global cleaning system

Let the cleaning global system production is 2 Mt CFCs per year. It means that after stop of the CFCs pollution the system will have cleaned the atmosphere through T=10 years. During T the main part of air must pass through active zones of cleaning stations by means of natural wind convection. Since major part of CFCs is placed in troposphere the cleaning active zone must be placed in troposphere too. The products of CFCs destruction have a good physical-chemical activity and consequently small life-time in atmosphere. If the average wind velocity in troposphere is V_w= 10 m/s, the cross section of station active zones S must be equal

$$S = S_E \cdot \frac{h}{T \cdot V_W \cdot N}, \qquad (1)$$

(h-altitude of troposphere, S_E--Earth area, N - number of stations.). The S can't be more than ~ 10 km^2. Consequently the number of stations can be estimated as N≥200.

The supposed scheme of cleaning station work is shown on Fig.1. The diverged radiation beam is scaned in the plane which is orthogonal to the wind velocity. So as electric field of radiation invers rates a distance and air density decrease exponentially, electric field normalysed on its critical value (critical factor Ψ) have a maximum at some altitude h_d. A discharge is excited in radiation beam at altitude h_d where critical factor is maximum. The h_d depend on radiation power. The power modulation gives us a possibility of scaning discharge region along the beam. Usual value of moved discharge velocity is $V_S \approx$ 1 km/s [6],[7]. One can see that diameter of discharge rigion must be equal

$$d \approx \sqrt{S \cdot V_W / V_S} \approx 0.3 km, \qquad (2)$$

If the mean value of active zone altitude is 8 km and wave-length of radiation is 10cm the spot with diameter d can be created by means of mirror with diameter 3-5 m.

The system power depend on the energetic cost of CFCs destroying. It was defined experimentally [8] that in upcritical pulse discharge energetic

cost of CFCs molecula destruction equals $\varepsilon \approx (0.1 \div 20)$ keV/molecula CFC. It is naturally to suppose that in undercritical discharge $\varepsilon \approx 1$keV/molecula CFC. Then the average radiation power of system and one station must be equal 40 GWt and 0.2 GWt consequently. The radiation field at middle altitude of active zone is super undercritical: $\Psi \approx 0.002$. It is important to point that applying of pulse regime of radiation with $\Psi \approx 1$ is not realizable because average V_s is very small in this case and condition (2) can't be satisfied. The main question are: can discharge exist if $\Psi << 1$?

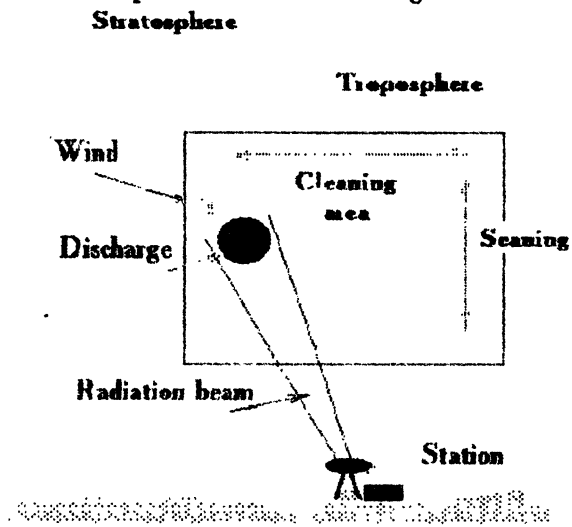

Fig.1 The scheme of cleaning station work

The super undercritical discharge

It is known that the streamer discharge in dense air can exist in undercritical UHF field after initial ignition (so called initiated discharge). The phenomenon is observed very dood in long wave-length part of UHF diapason. In a dense gas an electrodeless UHF discharge has a complicated filamentary structure [9],[10]. After creation it can be supported by radiation with $\Psi << 1$ by means of streamer effect. The discharge consists of thin filaments selfformed into electrodynamic resonant dipoles and loops, rising one from another and propagating away from the initiating points. It was found experimentally [11] that the streamer discharge initiated by resonant

metal vibrator can continiously exist even if $\Psi \leq 0.02$. The phenomenon was observed under conditions: air pressure is 0.1-1 atm., radiation wave length is 8.5 cm. The dependence breakdown value of inversed critical factor $1/\Psi_b$ upon radius of vibrator is shown on Fig.2. We hope to ignite the streamer discharge if $\Psi \rightarrow 0.001$.

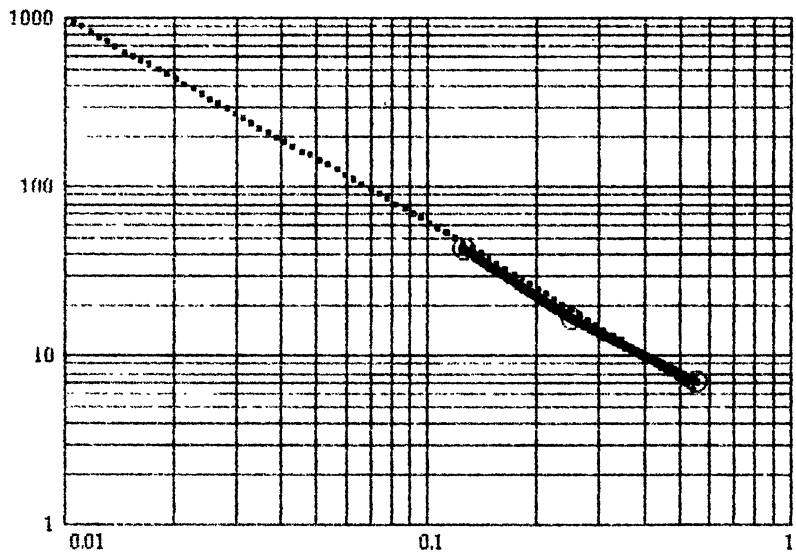

Fig.2 Dependence breakdown critical factor $1/\Psi_b$ upon resonant initiator radius a [cm] (solid - measurements, dots - estimation)

The results of numerical simulation of initiated streamer discharge in undercritical UHF electric field are shown on Fig.3. The model is taking into account the elementary chemical processes (ionization by electron impact, dissociative attachment), electron diffusion, ambipolar field, gas heating, finite wave-length. The cilindrical initiator is oriented along electric field. The radius and length of initiator equal 0.1 and 1 cm, gas pressure - 1 atm, wave-length - 8.5cm, $\Psi = 0.25$. The typical simulation example illustrate the first step of discharge ignition. Electric field maximum on both ends of initiator exceed the critical value and the streamer discharge starts to

germinate in both direction. Electric field maxima move with streamer ends together. The gas into the streamer is heated. The electric field maximum maximorum corresponds to resonant value of summary length of initiator and streamer brunchs. In this point the streamer velocity is maximum and equals approximatelly 10^5 cm/s. After resonant point the streamer velocity decreases and streamer stops. The heated gas in the stoped streamer (with accordingly small gas density) will play role of initiator for next step of discharge. And so on step by step. The streamer undercritical discharge in active zone of a cleaning station will be ignited by means of resonant metallic vibrators which will be lifted (by balluns, rocket or plane) on altitude h_i once for station work start.

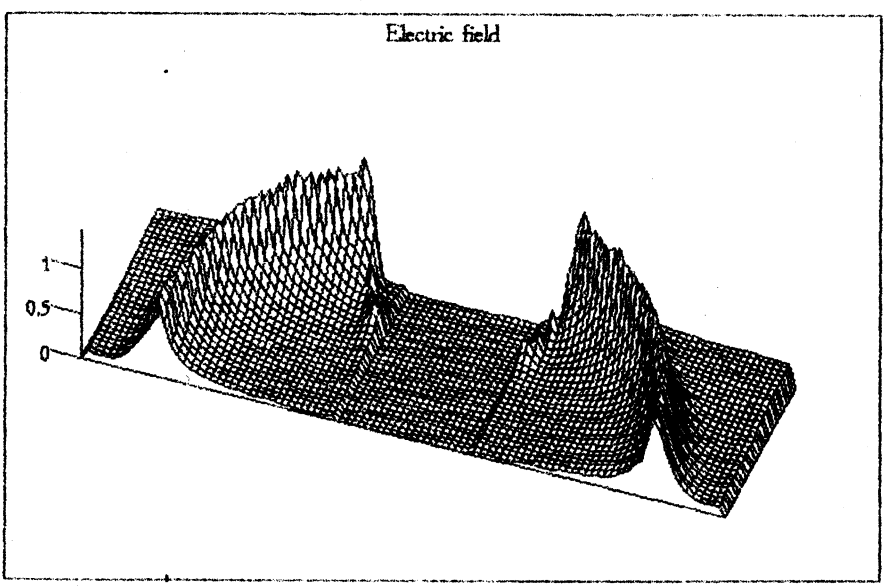

ee

Fig.3. The temporal evolution of electric field distribution along initiator axis

Conclusion

The idea of ozone layer reservation by means of stored freon decomposition in UHF discharge is technically realizable. The more applicable discharge for this goal is super undercritical streamer discharge in continuous UHF radiation. The two problems must be investigated: 1)can a streamer UHF discharge exist if critical factor much less 0.01, 2)what is the real cleaning efficiency of super undercritical streamer discharge.

References

[1] Scientific assesment of ozone depletion. Global ozone research and monitoring project, Report No.37, 1994

[2] M.J.Molina, F.S.Rowland. *Nature* **249**, 810 (1974)

[3] J.C.Farman, B.G.Gardner, J.D.Shanklin. *Nature* **315**,207 (1985)

[4] K.T.Tsang, D.D-M Ho, A.Y.Wong, R.J.Sivenson. ISSP-7 "Piero Cardirola", Controlled Active Global Experiments (CAGE), E.Sindoni and A.Wong (Eds.), SIF, Bologna 1991, p.143-156.

[5] G.A.Askar'yan, G.M.Batanov, S.I.Gritsinin, I.A.Kossyi et al.J.Phys. D: Appl. Phys., 27, No.6, pp. 1311-1318, (1994).

[6] L.P.Grachov, I.I.Esakov, G.I.Mishin, K.V.Khodataev. Zhurnal Technicheskoi Fiziki, (in Russian), 1995, **65**, No5, pp. 21-30.

[7] L.P.Grachov, I.I.Esakov, G.I.Mishin, K.V.Khodataev. Zhurnal Technicheskoi Fiziki, (in Russian), 1995, **65**, No11, pp. 86-92.

[8] G.M.Batanov, S.i.Gritsinin, E.G.Korchagina, I.A.Kossyi et al. Comments Plasma Phys. & Control Fusion, 16, No.2, pp. 113-127 (1994)

[9] L.P.Grachov, I.I.Esakov, G.I.Mishin, K.V.Khodataev, V.V.Tsyplenkov. Zh. Tekh .Fiz. , **64**, pp. 74-88 (January 1994), (in Russian), Tech. Phys. 39 (1), January 1994, pp.40-48.

[10] A.L.Vikharev, A.M.Gorbachov, A.V.Kim, A.L.Kolysko. Fizika Plasmy 1995, **18**, 8, pp. 1064-1075.

[11] L.P.Grachov, I.I.Esakov, G.I.Mishin, K.V.Khodataev. Zhurnal Technicheskoi Fiziki, (in Russian), 1995, **65**, No7, pp. 60-67

EXPERIMENTAL AND NUMERICAL STUDIES OF MICROWAVE HEATING OF CERAMICS

J.H. Booske, S.A. Freeman, and R.F. Cooper

University of Wisconsin, Madison, WI, USA

Introduction

Microwaves came of age with the development of radar during World War II. At that time it was discovered that microwave energy from radar could dry large ceramic bodies. However, serious efforts to process ceramics with microwave energy did not appear until the late 1960's [1,2] and early 1970's [3-6]. In recent years, many researchers have studied high-temperature processing of ceramics such as firing, sintering, joining, and melting [7-16]. The initial stimuli for their efforts were the unique benefits that microwave heating could provide that conventional furnace heating could not. These potential benefits included more precise and controlled volumetric heating, faster ramp-up to temperature, lower energy consumption, and improved quality and properties of the processed materials. As it turned out, researchers working with different processes and materials have found an additional (and unpredicted) benefit of enhanced process rates. As these enhancements were not initially well-understood, they came to be generically described as the "microwave effect."

In the particular case of ionic crystalline solids (e.g., ceramics), a growing body of experimental data supports the observation that microwave heating leads to enhanced mass transport rates when compared with conventional heating at the same temperature. The empirical evidence spans a range of thermal processes and material types. However, direct comparison of different experiments is difficult due to varying process conditions from laboratory to laboratory, such as the microwave field strengths, field orientations and patterns, processing temperature, ramp-up rates, materials and initial material conditions, etc. Nevertheless, the sheer bulk of the evidence of microwave enhancements compellingly suggests that an unknown, non-thermal, microwave effect that induces enhanced mass transport in ceramics does indeed exist.

Ceramic sintering and heating in microwave furnaces have been widely studied. Densification rates (and therefore the mass transport rates) are sometimes enhanced an order of magnitude or more. Process times and temperatures are dramatically lowered. Specific observations exist for pure and blended alumina [17-24], blends of zirconia [25-28], and other ceramics such as hydroxyapatites [29], barium titanate [24], mullite [30], phosphates [31], borides [32], and nitrides [33-35]. Microwave enhancements have also been reported in reaction sintering of mullite and aluminum titanate ceramics [36] and in lead-barium titanate [37], as well in grain growth in alumina [38]. Finally, observations of diffusion rates of radioactive tracer O^{18} isotope ions into the surface of sapphire single crystals heated in microwave ovens and conventional ovens indicate diffusion rate enhancements of up to two orders of magnitude.[18]

Besides sintering, many other solid state thermal processes have been studied in microwave furnaces and compared to conventional processes. Several research groups have reported microwave-enhanced joining of ceramic parts [12,39,40]. Other processes studied span a wide range -- nucleation and crystallization [41-43], grain growth [38], annealing [42,44], combustion synthesis [45], calcination [46], and other solid-state reactions [47,48]. In addition to the the O^{18} tracer-isotope-ion-diffusion-into-sapphire, other fundamental studies of chemical diffusion in glasses [49] and ceramics [50] have shown microwave-enhanced surface penetration by the diffusing species. A review of recent and emerging materials processing applications is described in the paper by Bykov and Semenov, also presented at this conference.

Mass Transport in Ceramics

Processess such as sintering, joining, chemical and tracer diffusion, and even ionic conductivity involve mass (or ionic) transport. Because of the high density, close-packed arrangement of the ions in the solid state, solid state transport is always diffusive. Furthermore, ions may only move in the solid state by shifting from their initial occupation site to a nearby vacant (defect) or open site in the microstructure. To shift to this new position typically involves a certain potential energy barrier that the particle's kinetic energy must exceed (e.g., by pushing through close-packed neighboring ions). This "activation energy" barrier

represents the major difference between diffusive transport in a solid and in a fluid (such as a plasma).

The diffusive transport rate J of ions in ceramic solids can be generally described by the product of a transport coefficient (such as a mobility) and a "driving force" (such as a potential energy gradient):

$$\mathbf{J}\left(\frac{ions}{m^2 \cdot s}\right) = -\underbrace{\frac{Dc}{kT}}_{\substack{transport\\ coefficient}} \underbrace{\frac{kT}{c}\nabla c}_{\substack{driving\ force\\ (Newtons)}} - \underbrace{\frac{Dc}{kT}}_{\substack{transport\\ coefficient}} \underbrace{q\nabla\phi}_{\substack{driving\\ force}} \qquad (1)$$

where D is a diffusion coefficient, c is the concentration (density) of the mobile species, k is Boltzmann's constant, T is the sample's temperature, q is the electric charge of the mobile species, and ϕ is the electric potential. Note that in crystalline solids, the ions move by "jumping" into neighboring vacant lattice sites (vacancies), and often one describes net ionic diffusion by following the apparent counter-diffusion of these vacancies (which also possess local electric charge in ionic crystalline solids). Again, because of the potential energy barriers for ionic diffusion and for creating vacancies in the microstructure, diffusion coefficients and vacancy concentrations in ionic crystalline ceramics are typically temperature dependent.

Based on Eq.(1), one can predict how various types of microwave effects on ionic transport should physically manifest. For example, if the microwave fields were to anomolously enhance the ionic *mobility* (transport coefficient), then, according to Eq. (1), this should manifest as a *multiplicative* increase of transport flux in the presence of a pre-existing conventional driving force (such as a gradient in the mobile species concentration or electric potential). On the other hand, if the microwave fields were to introduce a new, additional *driving force* for diffusion, then the "microwave effect" should manifest as an *additive* increase of transport flux in the presence of a pre-existing conventional driving force. Finally, diffusion coefficients and vacancy concentrations are temperature sensitive. Hence, under-measured bulk temperatures due to inaccurate diagnostics or spatially non-uniform (inverted) temperature profiles must also be considered as candidate explanations for the apparent rate increases during microwave heating of ceramics.

Temperature mismeasurement issues

Non-perturbative temperature measurement in a microwave field environment is a non-trivial problem. Thermocouples must be dielectrically shielded, thereby decreasing their sensitivity. Moreover, temperature gradients exist in the material being microwave-heated, so a thermocouple contacting the surface may not accurately measure bulk temperature. Pyrometry appears to be the preferred method, especially when the emitted light is collected via a light pipe from the bottom of a "black-body well" drilled into the sample. Questions still remain, however, on whether even this technique yields an accurate measure of the true bulk temperature at the center of the heated object. Some researchers found good agreement between thermocouple and pyrometer measurements [43,51], others found significant differences [52].

Since microwave energy is absorbed volumetrically, and is dissipated by convective and radiative heat loss at the surface, inverted temperature profiles (center hotter than the surface) may result. Surface temperature diagnostics may therefore under-indicate the "true" interior temperature.

In many of the experiments mentioned above, the process rates in microwave furnaces are often 10 or more times faster than in the conventional control experiments. To explain such apparent enhancements solely on the basis of temperature profiles or mismeasurement would require measurement errors of up to 200-400 °C out of an average temperature of 1000-1800 °C. From the more comprehensive and careful studies of temperature diagnostic techniques cited above, it appears beyond credibility that 25% errors were involved. Furthermore, drastic microstructure differences are not found across the cross-sections of the processed samples, indicating that the center-to-surface temperature differences are considerably less than the 25% variations needed to explain the most dramatic "microwave effects." The most convincing evidence that temperature mismeasurement (due to inverted temperature profiles) is unlikely to be the sole explanation for all microwave effects comes from the surface penetration diffusion experiments [18,49,50], which measure a physical process which takes place within microns of the surface. In this case, an accurate surface temperature measurement would be an accurate measurement of the temperature in the region being studied.

Athermal energy distributions

An early candidate theoretical explanation for microwave-enhanced solid state transport consisted of microwave-driven athermal energy distributions.[53,54] Such effects could explain the experimental observations, since even if the temperature (average thermal energy) was accurately measured, a non-Boltzmann, high-energy tail would increase the probability of diffusion events beyond the probability predicted by Boltzmann (thermal) statistics. This phenomenon is more common in rf-heated plasmas, but rare in the solid state due to extremely fast energy relaxation rates. Simplified model calculations [55] indicate that microwave-heated crystalline ceramics may achieve a slightly but adequately (to explain tenfold increases in diffusion) perturbed ion energy distributions, at least for certain material types.

Experimental Evaluation

An ideal and straightforward experiment to test for this possibility is to measure the effects of strong microwave fields on ionic currents in ceramic crystals subjected to a static emf. Halide salts represent an excellent choice of ceramic for this purpose, since their wide-electronic-bandgaps and comparatively small activation energies for ionic mobility mean that electric currents in response to applied voltages will be dominated by ionic transport rather than electronic. Consequently, an experimental configuration was assembled similar to the schematic in Fig. 1. A detailed description of the apparatus can be obtained from Refs. [55-57].

In response to an external bias voltage, mobile ions in a crystalline ceramic specimen conduct a current:

$$I = A\sigma E_{bias} = qA \times \frac{Dc_v}{kT} \times q\frac{V_{bias}}{L} \qquad (2)$$

where A is the crystal's cross-sectional area, σ is the sample's conductivity, E_{bias} is the applied bias electric field ($E_{bias} \sim V_{bias}/L$), q is the mobile ion charge, D is the ion (or ion vacancy) diffusion coefficient, c_v is the ion vacancy concentration, V_{bias} is the applied bias voltage, and L

is the length of the crystal sample. The appropriate experiment is to apply a bias voltage across the length of a crystalline ceramic specimen and measure the ionic current. During the measurement, a brief pulse of microwave radiation is applied. Any increase in the diffusion coefficient due to a microwave-induced athermal ion energy distribution should lead to a *proportionate* (i.e., multiplicative) increase in the ionic current during the microwave pulse.

Figure (2) displays typical results of such experiments. In the top frame, a 10 V external bias voltage is applied to a NaCl specimen (for 5 ms duration) and an ionic current results, as expected. Two ms after the bias voltage is applied, the crystal is also illuminated by a 400 μs pulse of 14 GHz microwave energy, with peak power ~1 kW in a Ku-band waveguide applicator. The microwave pulse is chosen to be much longer than diffusion timescales, but too brief to significantly heat the specimen (specimen temperature is controlled by external heating tapes). It is evident that the ionic current increases significantly during the microwave pulse.

According to Eq.(1) or (2), if the ionic current enhancement results from increased mobility, then a doubling of the bias voltage should coincide with a doubling of ionic current before, during, and after the microwave pulse (i.e., a multiplicative effect). However, as shown in the middle and lower frames, the ionic current enhancement magnitude due to microwave fields is independent of the bias voltage, i.e., an *additive* effect. It was this discovery that led to the conclusion that *strong microwave fields introduce a new driving force for ionic diffusion in ionic ceramics.* Moreover, detailed measurements established that the effect scales linearly with $|E|^2$, indicating that the new driving force is a nonlinear phenomenon.

Ponderomotive force model

Close to the completion of these early experiments, a theoretical model for microwave-enhanced diffusion was proposed by Rybakov and Sememov [58]. The basic idea is that a high frequency (HF) harmonic electric field drives a HF flux of charge mobile species (e.g., vacancies or ions) within the crystal. In the bulk of the crystal the fluxes are spatially uniform. Near the surface, however, the medium discontinuity results in a

harmonic oscillation of the ionic (or vacancy) concentration, as it alternately accumulates and depletes during a HF cycle. According to the model, these oscillations in the near-surface vacancy (or ion) concentrations are in phase with the HF electric field oscillations. Referring to the second term in Eq.(1), in-phase oscillations of electric field (or potential) and mobile charge concentration multiply to yield a rectified, quasi-stationary flux of charge carriers that does not cancel when averaged over a HF cycle. In particular, a second-order expansion analysis of the combined transport, continuity, and Poisson's Equations:

$$\mathbf{J}_i = -D_i \nabla c_i + \frac{D_i c_i}{kT} q_i \mathbf{E} \tag{3}$$

$$\frac{\partial c_i}{\partial t} = -\nabla \cdot \mathbf{J}_i \tag{4}$$

$$\nabla \cdot \mathbf{E} = \frac{1}{\varepsilon} \sum_i q_i \left(c_i - c_i^{(0)} \right) \tag{5}$$

yields the quasi-stationary ionic flux

$$\mathbf{J}_i^{(1)} \approx -D_i \nabla c_i^{(1)} + \frac{D_i c_i^{(1)}}{kT} q_i \mathbf{E}^{(1)} + \frac{D_i c_i^{(0)}}{kT} \left\langle \left(\frac{c_i^{(2)}}{c_i^{(0)}} \right) q_i \mathbf{E}^{(2)} \right\rangle \tag{6}$$

where $\mathbf{J}$, c, and $\mathbf{E}$ have been expanded as

$$X(t) \approx X^{(0)} + X^{(1)} + X^{(2)} \tag{7}$$

with $X^{(0)}$ representing static (equilibrium) solutions, $X^{(2)}$ representing HF fluctuation terms, and $X^{(1)}$ representing the HF-period-averaged, quasi-stationary components. The $\langle\ \rangle$ brackets indicate a time-average over a HF-cycle. The "i" subscripts denote different mobile species. The microwave-induced ponderomotive driving force (or pmf) is identified as the time-average piece of the last term of Eq(6):

$$pmf \equiv \left\langle \left(\frac{c_i^{(2)}}{c_i^{(0)}} \right) q_i \mathbf{E}^{(2)} \right\rangle \tag{8}$$

There are many similarities and some differences between this ponderomotive effect in solids and that conventionally discussed for plasmas. A thorough discussion of this topic is described in the paper by Rybakov and Semenov, also presented at this Workshop. At a very simplified level, the conventional plasma ponderomotive force problem assumes a nonuniform field and uniform medium (or transport) properties. The solid state ponderomotive force problem, however, typically, assumes a uniform field and an (abruptly) nonuniform medium or transport properties (e.g., at a free surface or grain boundary).

There were several aspects of significant agreement between this model and the early experimental measurements. First, the model predicted a nonlinear effect, properly scaling with the square of the electric field amplitude. Second, the model predicted an additive new driving force for diffusion, rather than a multiplicative enhancement of the transport coefficient. Third, the model predicted the effect should predominate near material surfaces or medium discontinuities, in agreement with a number of experimental observations.[55]

Further Experimental Confirmation

Motivated by the promising agreement between the preliminary results and the ponderomotive model, a collaboration was undertaken (Booske, Cooper, Freeman, Rybakov, and Semenov) to compare theoretical predictions and experimental measurements of ionic currents in both NaCl and AgCl crystals for longer microwave pulses. The details of this work are described in a forthcoming publication [59] and we just summarize a few illustrative examples here.

An extended theory was developed by Rybakov and Semonov, analyzing the bulk crystal, the metallic electrode, a contact-interface region between the electrode and crystal, and the external circuit. This theory predicted that the ponderomotive force (and ionic current) in a AgCl crystal with Ag electrodes should decay from initial transient to steady state according to an inverse square root dependence on time, $I(t) \propto |E|^2 / \sqrt{t}$. Figure 3 illustrates a typical ionic current response to a 20 ms microwave pulse. Observe how the ionic current has an initial transient spike that decays over 5-10 ms to a steady state value that depends on the microwave power. Also, at the end of the microwave

pulse, there is a transient spike (of opposite polarity to the first one) and a decay to zero current. For these experimental data, best fit was achieved by plotting the decaying current versus $1/\sqrt{t}$, as shown in Fig. 4, and in agreement with the theory. For long pulse experiments with NaCl crystals with Pt (sputter-deposited) electrodes, the theory predicted that the current should decay as an exponential function, $I(t) \propto |E|^2 \exp(-t/\tau)$. Again, there was quite good agreement between this prediction and experimental observations.

A final experimental investigation concerned the question of why we should be observing *any* net current in the external circuit. According to the model, if the *pmf* forces mobile charges to diffuse inward (surface-to-bulk), then this action should occur symmetrically at both ends, producing mutually canceling currents (i.e., unobservable) in the external circuit. The external observation of microwave-induced currents, therefore, predicates that the end conditions of the two crystals are not precisely identical. There are several reasons why this is expected to be true for realistic experimental conditions.[55] One example is illustrated in Fig. 5, showing Rutherford Backscattering Spectroscopy (RBS) spectra for the two ends of a single NaCl crystal with sputtered platinum electrodes. Both ends have some intermixing of Pt, Na, and Cl within several hundred Angstroms from the interface. However, the Pt concentration, for example, is not identical at the two ends. Note that Pt^{++} impurity ions in the NaCl can have significant influence on the local equilibrium Na vacancy concentration. The difference between the two spectra also offers strong corroborating evidence for our claim that the asymmetry of properties at the ends of the crystal leads to our measurement of a net current rather than two equal and opposing currents.

Numerical Modeling

The same sensitivity to crystal end conditions that made experimental observations possible also made further experiments of this type problematic. While microwave power and sample temperature could be adequately controlled, attempts to vary sample properties (such as bulk impurity concentrations) were frustrated by the fact that the end condition effects were always a more dominant factor. Moreover, sufficiently precise control of all the relevant end condition factors was, for practical

purposes, impossible. [55] Other experimental limitations included practical challenges to varying frequency and several other physical parameters over large dynamic ranges. Nevertheless, the extent of agreement between the ponderomotive theory and our experimental results lent sufficient credibility to the model that further investigation seemed warranted. Consequently, we selected to pursue further study by means of numerical simulations.

The numerical simulations involved computer solution of Eqs. (3)-(5), with appropriate boundary conditions. The major assumptions included a one-dimensional model (motion in "x") with E-field parallel to x and the long-wavelength (quasi-static) limit. A principal objective of this work was to obtain *quantitative* predictions of the magnitude of the *pmf* for various values of physical parameters. To facilitate this capability, we adopted values for the material defect chemistry parameters (i.e., activation entropies and enthalpies) consistent with the well-documented properties of NaCl (one of the materials used in our experiments).

A comprehensive description of the simulations can be found in Ref.[55], as well as forthcoming publications. Here we will just summarize the parameters or effects investigated, and a few representative results. Effects accounted for in the simulations included: (1) equilibrium nonuniformities in anion and cation vacancy concentrations (and space charges) near the boundaries, (2) divalent impurity concentrations, (3) both anion and cation mobile species, and (4) several boundary conditions, including free surfaces and vacancy sources (or sinks) at the boundaries.

Figure 6 illustrates the near-surface, microwave-driven oscillations of mobile (Cl) vacancies during the first two cycles of the microwave excitation. Sodium vacancies demonstrated similar behavior. Figure 7 illustrates the product of the harmonically-oscillating microwave field and the (Na) vacancy concentration. The rectified, $\cos^2(\omega t)$, nonlinear behavior is evident. As explained earlier, the is the basis for the time-averaged *pmf*. In the simulations, the *pmf* was observed to drive fluxes of *both* Na and Cl vacancies into the crystal bulk, i.e., true mass transport. [55]

With these simulations, it was possible to calculate magnitudes of the microwave *pmf* as functions of several variables, including electric field strength, temperature, frequency, and impurity concentration. To

illustrate, Fig. 8 shows the predicted linear dependence of the *pmf* on the square of the microwave electric field magnitude. Also, one observes that the magnitude of the *pmf* ranges from 10^{-18} to 10^{-16} N in NaCl for strong microwave field intensities, $|E| \sim 10^5 - 10^6$ V/m. For typical variations of other parameters, values of the *pmf* were also observed between 10^{-19} and 10^{-15} N. Table 1 below compares typical values of various natural driving forces (in NaCl) to the achievable *pmf* magnitude. For materials other than NaCl, the absolute values of the driving forces may change but the relative comparisons are expected to be the same.

From Table 1, one may observe that for strong microwave field strengths, i.e., $|E| > 10^4$ V/m, the *pmf* can compete with or dominate many natural driving forces for ionic mass transport in ceramic materials.

Table 1. Comparison of microwave and natural driving forces for ionic diffusion in NaCl ceramic

diffusion driving force	typical magnitude (N)
sintering (1 μm powder)	~ 10^{-18} to 10^{-16}
joining (identical material)	< 10^{-18}
temperature gradients	~ 10^{-19}
chemical inter-diffusion	~ ∞ to 10^{-16}
tracer isotope diffusion	<< 10^{-18}
microwave pmf	10^{-19} to 10^{-15}

Conclusions

It has been demonstrated that high-power microwave fields can enhance mass transport in ionic crystalline solids. Experiments measuring short pulse and long pulse dynamics of microwave-irradiated halide salt ceramics show that the microwave fields do not enhance the ionic mobility, but rather are responsible for an additional driving force for ionic diffusion. The data are in good agreement with qualitative

predictions of a nonlinear ponderomotive force model. This force arises at any abrupt nonuniformity in medium transport properties, such as free surfaces, grain boundaries, or amorphous-crystalline structure interfaces.

Numerical simulations have provided additional insight into the details of this phenomenon. In particular, illustrative simulations of NaCl show that opportunities to observe and take advantage of enhanced mass transport due to strong microwave fields depend on the application and physical circumstances. The determining issue is whether the microwave *pmf* exceeds or is smaller than other "natural" driving forces. Microwave-enhanced transport should be observable in the sintering of ionic ceramics whenever strong field intensities (e.g., $\geq 10^4$ V/m) and moderate-to-large grain powders (e.g., ≥ 1 μm) are used. Applications involving chemical inter-diffusion are unlikely to observe any "microwave effects" unless the process is continued long enough to significantly reduce the initially strong concentration gradient of the diffusing species (thereby depleting the natural driving force). On the other hand, microwave joining and radioactive tracer isotope diffusion applications are prime candidates to observe microwave effects, due to their typically small natural driving forces.

Acknowledgments

The authors gratefully acknowledge support for this work by the U.S. National Science Foundation, both through the PYI program (ECS-9057675) as well as grant CTW-9526035, the Electric Power Research Institute, PYI equipment donations by Tektronic Corporation, and the U.S. National Aeronautics and Space Administration.

References

1. M.L. Levinson, U.S. Patent No. 3,585,58 (15 June 1971), original application 19 October, 1965.
2. J.M. Osepchuk, IEEE Trans. Micr. Thy. Tech. 32(9), 100 (1984).
3. A.C. Metaxas and R.J. Meredith, *Industrial Microwave Heating*, (Peter Peregrinus Ltd., London, 1983).
4. W.R. Tinga, "Interactions of Microwave and Materials," *IMPI, Proc. on Short Course for Users with Microwave Power*, Nov. 1970.

5. W.H. Sutton, MRS Symp. Proc. **124**, ed. by W.H. Sutton, M.H. Brooks, and I.J. Chabinsky, 287 (1988).
6. A.J. Berteaud and J.C. Badot, *J. Micr. Power* **11**[4], 315 (1976).
7. N.W. Schubring, "Microwave Sintering of Alumina Spark Plug Insulators," *Tech. Rep. GMR-4471, General Motors Research Laboratory*, 1 (1988).
8. J.F. MacDowell, *Am. Cer. Soc. Bull.* **63**[2], 282 (1984).
9. Y. Haessler and L. Johansen, MRS Symp. Proc. **124**, 273 (1988).
10. W.H. Sutton, *Am Cer. Soc. Bull.*, **63**[2], 376 (1989).
11. T.T. Meek and R.D. Blake, *J. Mat. Sci. Lett.* **5**, 270 (1986).
12. D. Palaith, R. Silberglitt, C.C.M. Wu, R. Lkeiner, and E. Libelo, *Am Cer. Soc. Bull.* **68**[9], 1601 (1989).
13. H. Fukushima, T. Yamaka, M. Matsui, *J. Mater. Res.* **5**[2], 397 (1990).
14. L. Sheppard, *Am. Cer. Soc. Bull.* **67**[10], 1556 (1988).
15. J.D. Katz, *Ann. Rev. Mater. Sci.* **22**, 153 (1992).
16. D.L. Johnson, *Ceramics International* **17**, 95 (1991).
17. Y.L. Tian, D.L. Johnson, and M.E. Brodwin, *Cer. Trans.* **1** 95 (1988).
18. M.A. Janney and H.D. Kimrey, *MRS Symp Proc* **189**, 215 (1990).
19. L. Schuh, A. Gasch, F. Harbach, "Microwave Sintering of Ceramic Components," **Ceramics-Addiing the Value, Vol. 1,** AUSTCERAM 92, Proc. Int. Ceram Conf. Melbourne, Australia, 130 (1992).
20. J. Samuels and J.R. Brandon, *J. Mat. Res.* **27**, 3259 (1992).
21. D.J. Grellinger, J.H. Booske, S.A. Freeman, and R.F. Cooper, *Cer. Trans.* **59**, 465 (1995).
22. J. Cheng, J. Qui, J. Zhou, and N. Ye, *MRS Symp Proc.* **269**, 323 (1992).
23. B. Swain, *Adv. Mat. and Proc. Incorporating Metal Progress*, September (1988).
24. Y. Bykov, A. Eremeev, and V. Holoptsev, *MRS Symp Proc.* **347**, 585 (1994).
25. R. Wroe, A.T. Rowley, to be published in *J. Mat. Res.* (1996).
26. M.A. Janney, M.L. Jackson, and H.D. Kimrey, *Ceram Trans* **36**, 101 (1993).

27. M.A. Janney, C.L. Calhoun, H.D. Kimrey, *Cer. Trans.* **21**, 311 (1991).
28. M.A. Janney, H.D. Kimrey, *Adv. in Sintering*, Ed. by Bleninger and Handwerker, (Am. Ceram. Soc., Westerville, OH, 1990).
29. Y. Fang, D.K. Agrawal, D.M. Roy, and R. Roy, *Cer. Trans* **21**, 349 (1994).
30. J. Cai, C.Y. Song, B.S. Li, X.X. Huang, J.K. Guo, and Y.L. Tian, *MRS Symp. Proc.* **347**, 545 (1994).
31. Y. Fang, D.K. Agrawal, D.M. Roy, and R. Roy, *Cer. Trans.* **36**, 109 (1993).
32. C.E. Holcombe and N.L. Dykes, *J. Mat. Sci.*, **26**[14], 3730 (1991).
33. J. Zhang, L. Cao, F. Xia, *MRS Symp Proc.* **269**, 329 (1992).
34. T.N. Tiegs, J.O. Kiggans, H.T. Lin and C.A. Wilkens, *MRS Symp. Proc.* **347** , 501 (1994).
35. Y.C. Kim, S.C. Koh, D.K. Kim, and C.H. Kim, *Cer. Trans.* **59**, 415 (1995).
36. P. Boch, N. Lequeux, and P. Piluso, *MRS Symp. Proc.* **269**, 211 (1992).
37. J. Cheng, Y. Fang, D.K. Agrawal, and R. Roy, *MRS Symp. Proc.* **347**, 513 (1994).
38. M.A. Janney, H.D. Kimrey, M.A. Schmidt, J.O. Kiggans, *J. Am Cer. Soc.* **74**[7], 1675 (1991).
39. J.G.P. Binner, P.A. Davis, T.E. Cross, J.A. Fernie, *Cer. Trans.* **59**, 335 (1995).
40. S. Al-Assafi, D.E. Clark, *MRS Symp Proc* **269**, 335 (1992).
41. A. Boonyapiwat and D.E. Clark, *Cer. Trans.* **59**, 505 (1995).
42. T.N. Tiegs, K.L. Ploetz, J.O. Kiggans, R.L. Yeckley, *Cer. Trans.* **36**, 59 (1993).
43. A.D. Cozi, Z. Fathi, D.E. Clark, *Cer. Trans.* **36**, 317 (1993).
44. T.N. Tiegs, M.K. Ferber, J.O. Kiggans, K.L.. More, C.M. Hubbard, D.W. Coffey, *Cer Trans* **21**, 411 (1991).
45. T. Yiin and M. Barmatz, *Cer. Trans.* **59**, 541 (1995).
46. H.Y. Kim and J.Y. Jeon, *MRS Symp. Proc.* **347**, 507 (1994).
47. I. Ahmad, D.E. Clark, *Cer. Trans.* **21**, 605 (1995).
48. M. Willert-Porada, *Cer. Trans.* **36**, 277 (1993).
49. Z. Fathi, I. Ahmad, J.H. Simmons, D.E.Clark, *Cer. Trans.* **21**, 333 (1991).

50. Z. Fathi, D.E. Clark, and R. Hutcheon, *MRS Symp. Proc.* **269**, 347 (1992).
51. D.J. Grellinger and M.A. Janney, *Cer. Trans.* **36**, 59 (1993).
52. T.T. Meek, S.S. Park, M.A. Nehls, C.W. Kim, *MRS Symp. Proc.* **155**, 267 (1989).
53. J.H. Booske, R.F. Cooper, I. Dobson, and L. McCaughan, *Cer. Trans.* **21**, 185 (1991).
54. J.H. Booske, R.F. Cooper, L. McCaughan, S.A. Freeman, B. Meng, *MRS Symp Proc* **269**, 137 (1992).
55. S.A. Freeman, "Investigations of Non-Thermal Interactions Between Microwave Fields and Ionic Ceramic Materials," Ph.D. Thesis, University of Wisconsin-Madison (Published by University Microfilms International, Ann Arbor, MI, 1996).
56. S.A. Freeman, J.H. Booske, and R.F. Cooper, *Rev. Sci. Instrum.* **66**[6], 3606 (1995).
57. S.A. Freeman, J.H. Booske, and R.F. Cooper, *Phys. Rev. Lett.* **74**[11], 2042 (1995).
58. K.I. Rybakov and V.E. Semenov, *Phys. Rev. B* **49**[1], 64 (1994).
59. K.I. Rybakov, V.E. Semenov, S.A. Freeman, J.H. Booske, R.F. Cooper, "Dynamics of Microwave-Induced Currents in Ionic Crystals", to be published in *Phys. Rev. B* (1996).

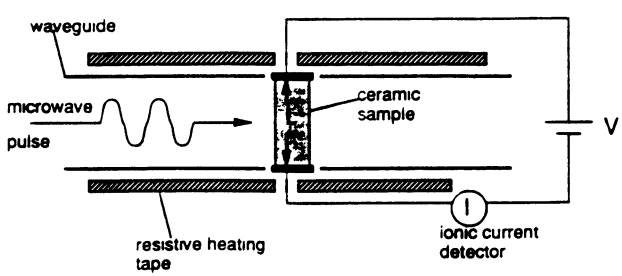

Fig. 1. Experimental schematic for ionic current measurements during microwave irradiation

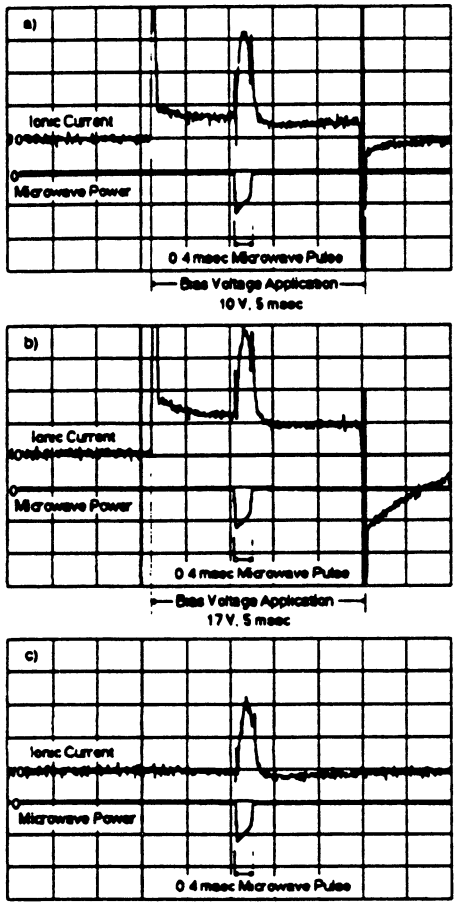

Fig. 2. Oscilloscope traces showing the effect of microwave irradiation on ionic currents in a NaCl crystal at 150 °C. In all three frames, upper trace is the ionic current, lower trace is the microwave power. Horizontal scale is 1 ms/div.

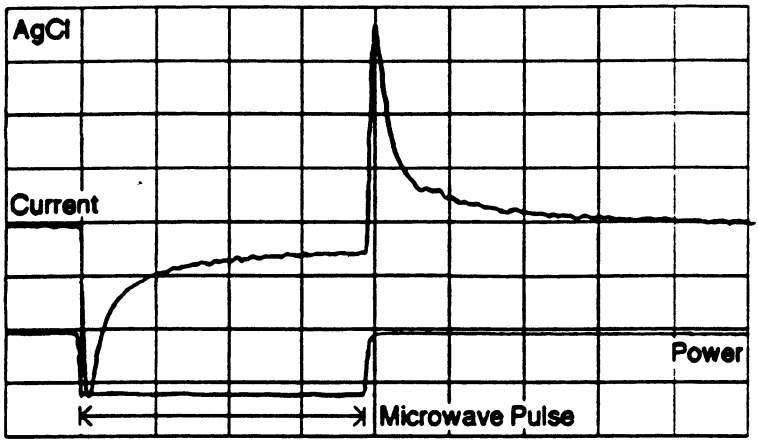

Fig. 3. Oscilloscope traces of the ionic current (upper trace) in a AgCl crystal at 180 °C due to a pulse of microwave radiation (lower trace). The horizontal scale is 0.5 ms/div.

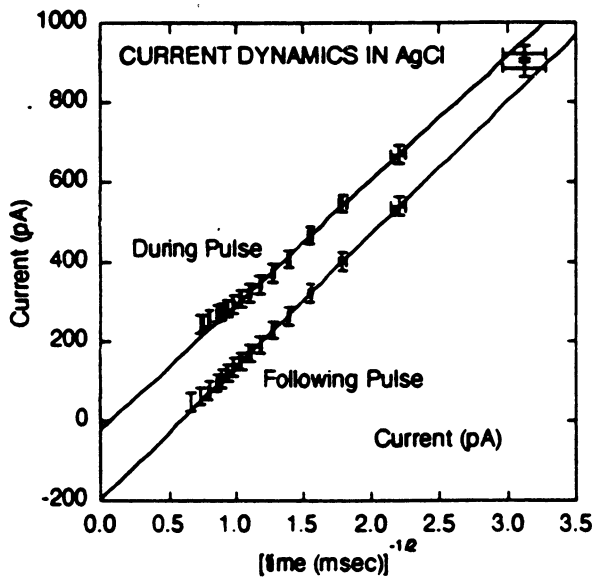

Fig. 4. The ionic current dynamics in AgCl show a $(t)^{-1/2}$ dependence during decay to asymptotic, steady state value.

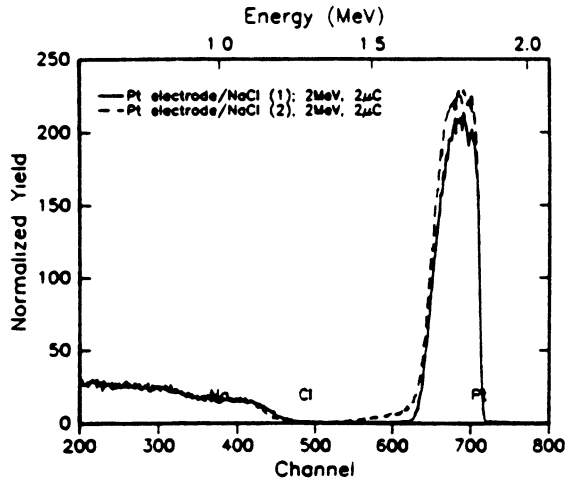

Fig. 5. RBS spectra from the two ends of a NaCl crystal with plasma-sputtered platinum electrodes showing slight differences in the Pt concentration profiles.

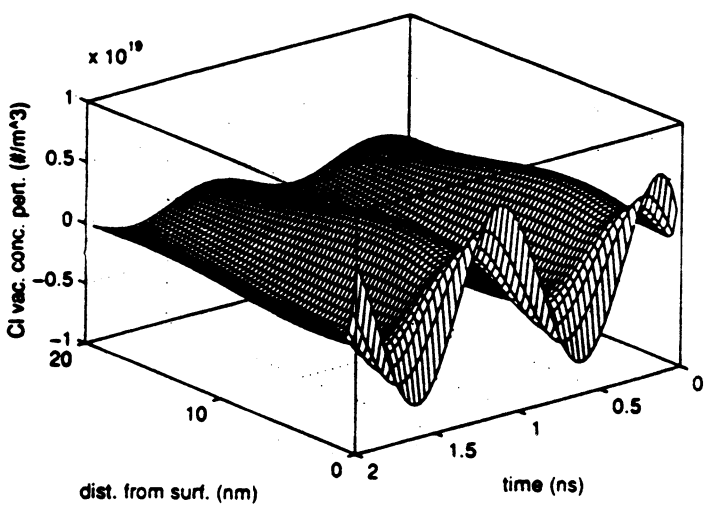

Fig. 6. The HF fluctuations of the chlorine vacancy concentration near the free surface boundary.

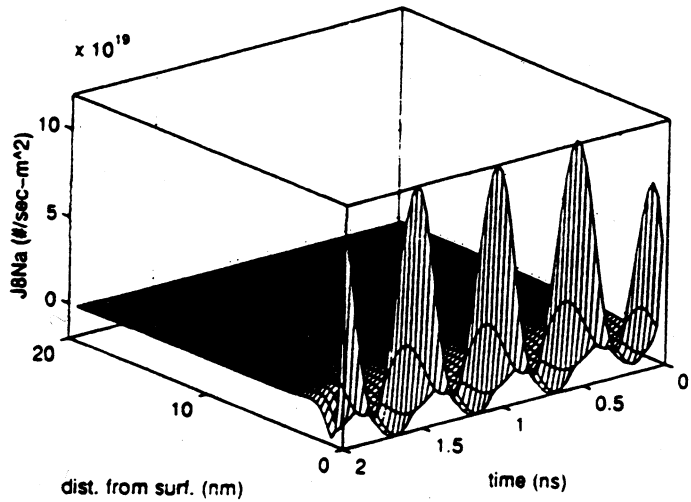

Fig. 7. The fast timescale variation of the product of the Na vacancy concentration and microwave electric field oscillations.

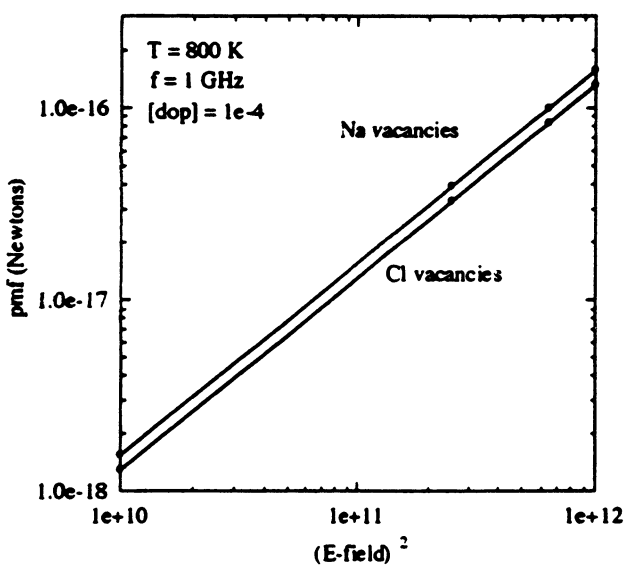

Fig. 8. The pmf characterized (in simulations) versus the microwave electric field strength

MUTUAL-CONCENTRATING EFFECTS OF FIELD AND PLASMA IN MICROWAVE AND OPTICAL GAS DISCHARGES

V.B.Gil'denburg, A.G.Litvak, I.A.Shereshevskii*, A.A.Solodov, N.K.Vdovicheva*, N.V.Vvedenskii, N.A.Zharova

Institute of Applied Physics, RAS, N. Novgorod, Russia
*Institute of Physics of Micro-structures, RAS, N. Novgorod, Russia

A remarkable feature of the ionization-type nonlinearity in the nonlinear plasma electrodynamics is existence of the so-called mutual-concentrating (mutual-enhancement, joint localization) effects of the field and plasma in electromagnetic-wave-created discharges. These effects result in the formation of localized plasma-field structures and change wave propagation and plasma production conditions drastically. One of the main effects of this kind is due to the plasma resonance phenomenon and is manifested as the local ionization-field (LIF) instability (it is designated also as plasma-resonance or quasi-static instability). In this paper we present the findings of an investigation of these effects for different models of the small-scale LIF-instability (including its linear and nonlinear stages) in the microwave and optical discharges. The results considered are of interest for the applications relating to the problems of intensive wave propagation in gases, as well as of production and use of the microwave and laser plasma (plasma-chemistry, laser technique, wake-field particle acceleration, artificial ionized regions in atmosphere, and material processing).

The self-consistent electric field in our treatment is taken to be quasi-monochromatic and given by the expression $\mathcal{E} = \frac{1}{2}\mathbf{E}e^{-i\psi} + \text{c.c.}$ with slowly varying in time (but arbitrarily varying in coordinates) complex amplitude $\mathbf{E}(\mathbf{r}, t)$ and constant (or slowly time-varying) frequency $\omega(t) = \partial\psi/\partial t$. As to the concrete physical mechanism of plasma production, we center mainly (Section 1-3) on the case of electron-impact (avalanche-type) ionization; in Section 4 we consider LIF-instability under the alternative ionization mechanism: direct (tunneling) ionization of atoms by the intense laser field.

1. Linear stage of small-scale instability in the quasi-static (potential) field

1.1. Instability of space-periodical perturbations in the homogeneous discharge

As the starting point we use the balance equation for the plasma density N

$$\partial N/\partial t = D\Delta N + (\nu_i - \nu_a)N - \alpha N^2 \tag{1}$$

with ordinary approximations: the diffusion (D) and recombination (α) coefficients and the attachment frequency (ν_a) of electron are supposed to be constant; the ionizing collision frequency of electrons, $\nu_i(|E|)$ is a fast growing function of electric field amplitude $|E|$. At first, we study the plasma-field structures with its scale-length small compared to the wavelength λ. In this case the electric field can be considered potential and described by the quasi-static equations:

$$\mathbf{E} = -\nabla\varphi, \ \nabla(\varepsilon\mathbf{E}) = 0. \tag{2}$$

Here φ is the electrical potential, $\varepsilon = 1 - (N/N_c)(1 - i\nu/\omega)$ is the complex plasma permittivity, $N_c = m(\omega^2 + \nu^2)/4\pi e^2$ is the critical density, ν is the electron collision frequency. Let the discharge plasma and electric field, in the unperturbed steady state, be homogeneous and characterized by the following parameters: $N = N_0$, $\mathbf{E} = \mathbf{x}_0 E_0$, satisfying to the stationary condition of $\nu_{i0} = \nu_i(E_0) = \nu_a + \alpha N_0$ ($\mathbf{x}_0$ is the unit vector in the x-direction). Consider the stability of this steady state with respect to small space-periodical perturbations. Setting $N = N_0 + N_1$, $\mathbf{E} = \mathbf{E}_0 + \mathbf{E}_1, \mathbf{E}_1 = -\nabla\varphi_1$ and linearizing Eqs. (1),(2), we obtain the following equations for the perturbations $N_1(x,t)$, $E_{1x}(x,t) = -\partial\varphi_1/\partial x$:

$$\frac{\partial N_1}{\partial t} = D\Delta N_1 + \frac{\beta\nu_{i0}N_0}{2E_0}(E_{1x} + \text{c.c.}) - \alpha N_0 N_1, \tag{3}$$

$$\frac{\partial E_{1x}}{\partial x} - \frac{1}{\varepsilon_0 N_c}E_0(1 - i\frac{\nu}{\omega})\frac{\partial N_1}{\partial x} = 0. \tag{4}$$

Here $\varepsilon_0 = 1-(N_0/N_c)(1-i\nu/\omega)$, $\beta = d(\ln\nu_{i0})/d(\ln E_0)$ (for air $\beta \simeq 5$). For perturbations of the form $N_1, E_1 \sim \exp(\gamma_k t + i\mathbf{kr})$ we can find, based on the system (3),(4), a dispersion equation describing the time

constant γ_k (growth rate of instability) as a function of longitudinal (k_x) and transverse ($\mathbf{k}_\perp$) components of the perturbation wave vector $\mathbf{k}$. In the simplest (and the most interesting) case of low collision frequency, $\nu \ll \omega$, this dispersion equation is as follows:

$$\gamma_k = \beta\nu_{i0}\frac{N_0 k_x^2}{N_c\varepsilon_0 k^2} - (Dk^2 + \alpha N_0), \tag{5}$$

where $k^2 = k_x^2 + \mathbf{k}_\perp^2$. In the case of $\alpha = 0$ and $k\lambda \ll 1$, this result agrees with that obtained formerly for the recombination-free discharge in the plane wave field [1]. If the plasma density lies in the range $N_t < N_0 < N_c$, the perturbations with not too large wave number $k < k_t$ (the value of k_t is defined by diffusion) are unstable ($\gamma_k > 0$). The maximum growth rate of instability

$$\gamma_m = \gamma_0 - \alpha N_0, \ \gamma_0 = \beta\nu_{i0}\frac{N_0}{N_c\varepsilon_0} \tag{6}$$

is achieved under conditions $k_x = k$, $Dk^2 \ll \beta\nu_{i0}N_0/(\varepsilon_0 N_c)$, that is, for the large-scale density perturbations in the form of layers perpendicular to the vector $\mathbf{E}$. The lower threshold density N_t depends on the ratio $q = \beta\nu_{i0}/\alpha N_c$: $N_t = 0$ at $q > 1$, $N_t = 1 - q$ at $q < 1$.

1.2. Evolution of 3D localized perturbations in the homogeneous discharge

Generalization of 1D linear Eqs.(3),(4) to the 3D perturbations $N_1(\mathbf{r}, t)$, $\varphi_1(\mathbf{r}, t)$ leads to the following equations (as in the previous paragraph we consider the case of $\nu/\omega = 0$):

$$\frac{\partial N_1}{\partial t} = D\Delta N_1 - \frac{\beta\nu_{i0}N_0}{E_0}\frac{\partial\varphi_1}{\partial x} - \alpha N_0 N_1, \tag{7}$$

$$\Delta\varphi_1 = -\frac{E_0}{\varepsilon_0 N_c}\frac{\partial N_1}{\partial x}. \tag{8}$$

Taking the Fourier transform of Eqs.(7) and (8) we find:

$$\begin{Bmatrix}\varphi_1\\ N_1\end{Bmatrix} = \iiint_{-\infty}^{+\infty}\begin{Bmatrix}\varphi_k\\ N_k\end{Bmatrix}\exp(\gamma_k t + i\mathbf{kr})d\mathbf{k}, \tag{9}$$

with γ_k given by Eq.(5), $\varphi_k = ik_x N_k E_0/(\varepsilon_0 N_c k^2)$, and N_k given by the initial conditions.

Let the initial ($t = 0$) distribution of the density perturbation $N_1(\mathbf{r}, 0)$ be characterized by two parameters: some unified scale-length L_0 and the total particle number $N_{1\Sigma} = \int \int\limits_{-\infty}^{\infty} \int N_1 d\mathbf{r}$. Thus, in the spectral region $k^2 \ll 1/L_0^2$, we can set $N_k \simeq N_{1\Sigma} = \text{const}$, and the Fourier-expansion (10) for N_1 at the final stage of the process ($Dt \gg L_0^2$, $\gamma_0 t \gg 1$) can be transformed in the following way ($\mathbf{r} = \mathbf{x}_0 x + \mathbf{r}_\perp$):

$$N_1 = e^{\gamma_m t} \iiint\limits_{-\infty}^{+\infty} N_k \exp[(-\gamma_0 \frac{k_\perp^2}{k^2} - Dk^2)t + i\mathbf{kr}] d\mathbf{k} \simeq$$

$$N_{1\Sigma} e^{\gamma_m t} \iiint\limits_{-\infty}^{+\infty} \exp\{i(\mathbf{k}_\perp \mathbf{r}_\perp + k_x x) - [k_\perp^2 (\frac{\gamma_0}{k_x^2} + D) - Dk_x^2]t\} d\mathbf{k}_\perp dk_x \simeq$$

$$\pi N_{1\Sigma} \frac{1}{\gamma_0 t} e^{\gamma_m t} \int\limits_{-\infty}^{+\infty} k_x^2 \exp[ik_x x - k_x^2 (\frac{\mathbf{r}_\perp^2}{4\gamma_0 t} + Dt)] dk_x =$$

$$\frac{\pi^{3/2} N_{1\Sigma} e^{\gamma_m t}}{2\gamma_0 D^{3/2} t^{5/2} F_1^{3/2}} (1 - \frac{x^2}{2DtF_1}) \exp(-\frac{x^2}{4DtF_1}), \tag{10}$$

where $F_1(\mathbf{r}_\perp, t) = 1 + (\mathbf{r}_\perp^2/4\gamma_0 Dt^2)$. It follows from (10) that the longitudinal (L_x) and transverse ($L_\perp$) scale-lengths of perturbation at large t are the following time-functions: $L_x = (2Dt)^{1/2}$, $L_\perp = 2(D\gamma_0)^{1/2} t$. In the case of slight diffusion, we can find an intermediate-time asymptotic solution on the time interval $1/\gamma_0 \ll t \ll (L_0^2/D)$). For example, the evolution of initially Gaussian perturbations $N_1 = N_{10} \exp(-\mathbf{r}^2/L_0^2)$ at this intermediate stage is as follows:

$$N_1 = \frac{N_{10} e^{\gamma_m t}}{2\gamma_0 t F_2^{3/2}} (1 - \frac{2x^2}{L_0^2 F_2}) \exp(-\frac{x^2}{L_0^2 F_2}), \tag{11}$$

where $F_2(\mathbf{r}_\perp, t) = 1 + (\mathbf{r}_\perp^2 L_0^2 \gamma_0 t)$. The longitudinal and transverse scale-length at this stage are $L_x = L_0$, $L_\perp = L_0(\gamma_0 t)^{1/2}$. In both cases (that is, at $\gamma_0 t \gg 1$) the ratio of these lengths $L_\perp/L_x$ is growing as $(\gamma_0 t)^{1/2}$.

1.3. Instability of plasma slab in the perpendicular electric field

Let a homogeneous steady-state discharge occupies the region between two planes, $x = \pm L$. Unperturbed parameters are: $N = N_0$, $\varepsilon = \varepsilon_0 = 1 - N_0/N_c$, $E_x = E_c$ at $|x| < L$; $N = 0$, $\varepsilon = 1$, $E_x = \varepsilon_0 E_c$ at $|x| > L$. For simplicity we suppose that $\nu = \alpha = D = 0$. The evolution of small perturbations obeys to: Eq.(7),(8) for the values N_1, φ_1 in the discharge, Laplace equation $\Delta\varphi_2 = 0$ for additional term φ_2 in the field potential outside the discharge ($|x| > 0$), and the following boundary conditions at $|x| = \pm L$:

$$\varphi_2 = \varphi_1, \quad \frac{\partial\varphi_2}{\partial x} = \varepsilon_0 \frac{\partial\varphi_1}{\partial x} + \frac{N_1 E_c}{N_c}. \tag{12}$$

There are two types of the normal ($\sim \cos(ky)\exp(\gamma t) f(x)$) solutions of the stated problem: with the symmetrical ($N_1 \sim \mathrm{ch}(pkx)$) and antisymmetrical ($N_1 \sim \mathrm{sh}(pkx)$) distribution of the density perturbation. In both cases

$$\gamma = \frac{\beta\nu_{i0}(1-\varepsilon_0)}{\varepsilon_0(1-p^{-2})}. \tag{13}$$

The variable p is defined by equation

$$\mathrm{cth}(pkL) = -(p/\varepsilon_0)^{\pm 1}, \tag{14}$$

Signs + and − relate to the symmetrical and antisymmetrical solutions respectively. The roots of Eq.(14) are either pure imaginary (Re $p = 0$) or pure real (Im $p = 0$). The first case corresponds to the x-periodical perturbation which is unstable ($\gamma > 0$) in the same region $N_0 < N_c$ as in the absence of discharge boundaries. The second case corresponds to the x-aperiodical perturbations which are unstable only in the region $N_0 > N_c$. In particular, the symmetrical perturbations can be unstable in interval $N_c < N_0 < 2N_c$ if its wave number k exceeds some critical value: $\mathrm{th}(kL) > N_0/N_c - 1$; at the critical point the growth rate $\gamma \to \infty$; at $kL \gg 1$ it becomes $\gamma = -\beta\varepsilon_0/(\varepsilon_0 + 1)$. The results obtained allow an understanding of why the plane layers originated due to the LIF-instability during the initial stage of microwave discharge in the experiments [2], then were disintegrating into a set of small plasmoids.

2. Nonlinear stage of small-scale instability in the 1D quasi-static (potential) field

Nonlinear evolution of 1D x-periodical perturbations was studied numerically based on a simple solution of Eq.(2) for the field amplitude $\mathbf{E} = \mathbf{x}_0 E(x,t)$ with the assumption that the average (over the spatial period L) field amplitude is a given (time-independent) constant E_0:

$$E = \frac{E_0 \varepsilon_{eff}}{\varepsilon}\ , \quad E_0 = L^{-1}\int_0^L E(x)dx = \text{const}, \quad \varepsilon_{eff}^{-1} = L^{-1}\int_0^L \varepsilon^{-1}dx \tag{15}$$

Here ε_{eff} is so-called effective permittivity determining average polarizability of plasma. In balance equation (1), we used the ordinary approximation,

$$\nu_i - \nu_a = \nu_{i0}[(|E|/E_c)^\beta - 1), \tag{16}$$

with given constants ν_{i0} and E_c.

Some results of computation of system (1),(15),(16) are presented in dimensionless variables $x \to x/L_a$, $t \to \nu_{i0}t, \mathcal{N} = N/N_c (L_a = (D/\nu_{i0})$ in Fig.1. The computations were performed at the initial condition $\mathcal{N}(x,0) = \mathcal{N}_0 + \mathcal{N}_1 \cos(2\pi x/L)$ for the parameters: $E_0/E_c = 0.95$, $\nu/\omega = 0.5$, $L/L_a = 10$, $\mathcal{N}_0 = 0.8$, $\mathcal{N}_1 = 0.04$, $\alpha = 0$, $\beta = 4$. We can see that discharge evolution is characterized (at $E_c - E_0 \ll E_c$) by several pulsations with deep spatio-temporal modulation of plasma density. Each pulsation consists of two stages: fast and slow. At the first of them development of the instability leads to formation of the over-critical density pike, which is very sharp initially and then expands fast yielding the breakdown waves. This stage ends in the establishment of an almost uniform state with $\mathcal{N} > 1$ which is stable in terms of perturbations considered. At the second stage the density decreases slowly and finally reenters the zone of instability ($\mathcal{N} < 1/[1 + (\nu/\omega)^2]$ after which the nonuniform component of the density (if it has not had time to relax too strongly as at the end of the last pulsation in Fig.1) increases again and the process repeats. It is obvious that in the presence of a weak random source of ionization (which can be taken into account by introducing an additional

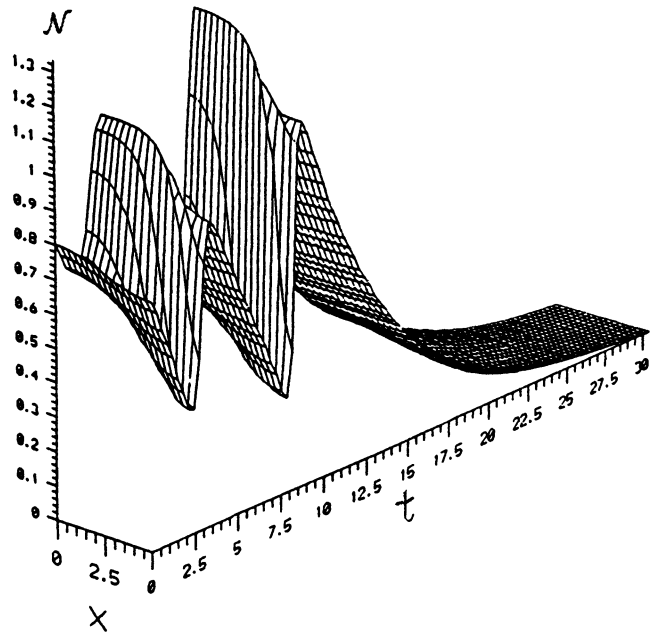

Fig. 1: Spatio-temporal evolution of the plasma density $\mathcal{N}(x,t)$ in the absence of an external source of ionization.

term into the right-hand side of eq.(1)) the pulsations outlined above should become non-stop and take the stochastic form [3].

3. Nonlinear stage of LIF-instability in the 2D wave problem

Consider the evolution of discharge produced by the plane electromagnetic wave, $\mathcal{E}_0 = (1/2)\mathbf{x}_0 E_0 \exp[i(\omega t - kz)] + \text{c.c.}$ $(k = \omega/c)$ propagating in a nonuniform gas in $+z$ direction. The critical (threshold for breakdown) field in the gas is a given smooth function $E_c(z)$, and the wave amplitude E_0 exceeds E_c in some restricted region. As is clear from the preceding Sections, the discharge formed in this region is unstable towards the spatial modulation in the direction of the electric field $\mathbf{x}_0$. The electric field in the x-modulated discharge has the components E_x and E_z depending, together with the plasma

density N, on the variables x, z, t. The magnetic field has only the y-component; its complex amplitude $H_y(x,z,t)$, assuming a reasonably low ionization rate, $\nu_i \ll \omega$, obeys the stationary equation:

$$\nabla(\varepsilon^{-1}\nabla H_y) + k^2 H_y = 0 \tag{17}$$

The field components $E_x and E_z$ determining the ionization rate can be expressed in terms of H_y using the Maxwell equations:

$$E_x = \frac{ic}{\omega\varepsilon}\frac{\partial H_y}{\partial z}, E_z = -\frac{ic}{\omega\varepsilon}\frac{\partial H_y}{\partial x}. \tag{18}$$

Notice that this 2D model describes also the dynamics of the discharge created in the uniform gas by the focused wave beam with given ray trajectories; in the latter case E_c = const, $E_0 = E_0(z)$.

Equation system (1),(17),(18) was solved numerically in the region $0 < x < L_x$, $0 < z < L_z$ with x-periodicity conditions at $x = 0$ and $x = L_x$ and radiation or boundedness conditions for the spatial (in the x-direction) Fourier harmonics of the reflected and transmitted waves at the boundaries $z = 0$ and $z = L_z$. For the difference $\nu_i - \nu_a$ the same approximation (16) was used as in the previous Section. The function $E_c(z)$ in our model was chosen in the form $E_c(z) = E_{c0}[1 + (z - z_0)^2/l_2]$. The initial condition for the plasma density was similar to that in the above 1-D quasi-static model: $N = N_0 + N_1\cos(2\pi x/L_x)$.

As the computation demonstrates, the typical scenario of discharge evolution in the parameter range where the instability exists is as follows. Initially, nearby the minimum of the breakdown field $E_c(z)$ ($z = z_0$), a near-homogeneous (in the x direction) crest of a breakdown wave arises moving towards the incident electromagnetic wave (in the $-z$ direction). Then, because of the instability of the small initial modulation of the density in the x direction, the breakdown wave disintegrates into small separate plasma clusters (2-D plasmoids) with over-critical plasma density continuing to move towards the $-z$ direction. The plasmoids contain the regions of the plasma resonance, where the electric field component parallel to ∇N has sharp resonance peaks exceeding (at small collision frequency $\nu \ll \omega$) the amplitude of the incident wave E_0 by the factor ω/ν. The arising structure is illustrated by Fig.2(a,b) showing the plasma density and electric field

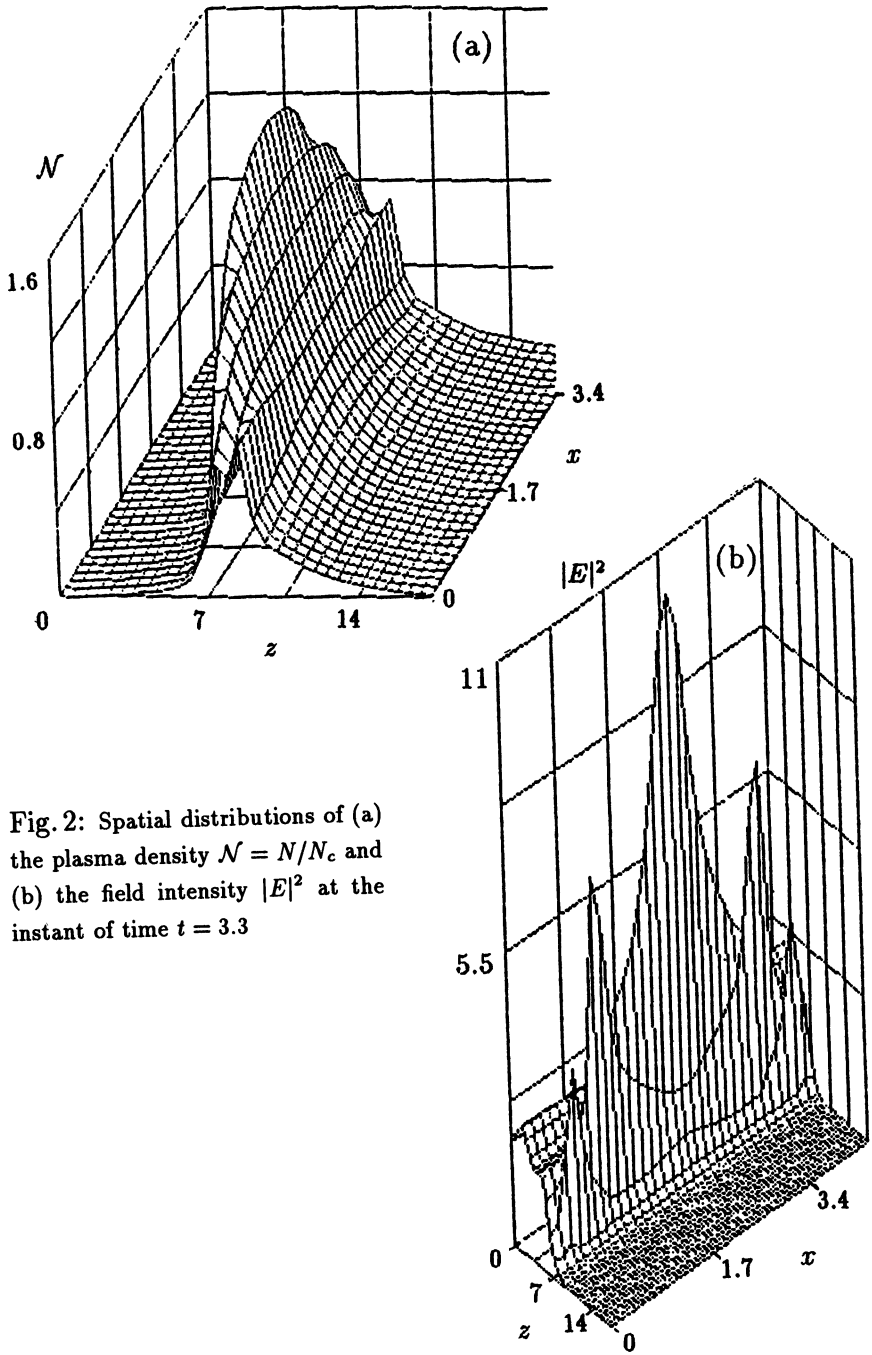

Fig. 2: Spatial distributions of (a) the plasma density $\mathcal{N} = N/N_c$ and (b) the field intensity $|E|^2$ at the instant of time $t = 3.3$

amplitude distributions at time instant $t = 4$ (we use the dimensionless variables $t \to \nu_a t,\ x, z \to kx, kz,\ N \to N/N_c, |E|^2 \to |E/E_c|^2$). Entering the region with $E_c(z) > |E|$, the plasmoids stop and decay, after that a new breakdown wave arises at the region $z \simeq z_0$ and repeats the evolution of the previous one.

Generation of the moving resonance regions with high peaks of the field amplitude at the nonlinear stage of the LIF-instability is a remarkable feature of the process considered. These small-sized regions are the zones of enhanced activity, where the local electron energy, the rate of ionization and molecular-excitation process are much higher than in the surrounding plasma. Thus it is the dynamics of this active (resonance) zones that defines the energy transfer and kinetic process rate in the low-pressure microwave discharge.

4. Microfilamentation in the optical-field-induced ionization process

In this Section, we consider the linear and nonlinear stages of the LIF-instability in the optical discharge, produced by a high intense laser in the uniform gas with high density under the tunneling ionization conditions. The statement of electrodynamic problem we solve here is simpler than in the previous Section: this is the initial (but not boundary) problem in which the plasma density $N(x,t)$ and field amplitude $|E|(x,t)$ are the periodical functions of the transverse coordinate x, but does not depend on the longitudinal (parallel to the wave propagation) coordinate z. The wavelength λ in the z-direction and spatial period L of the traverse modulation of the density and amplitude are the constants, given by the initial conditions. The transverse distribution $N(x,t)$, $|E|(x,t)$, as well as the field frequency ω, are the slow (on the scale $1/\omega$ time functions.

We take, as the model equation for the instantaneous plasma density $n(t)$, the known static expression for the rate of tunneling ionization of the hydrogen atom [4]:

$$\partial n/\partial t = w(\mathcal{E}, n) = 6\Omega(N_g - n)\frac{E_a}{|\mathcal{E}|}\exp\left(-\frac{E_a}{|\mathcal{E}|}\right) . \qquad (19)$$

Here $\Omega = me^2/h^3 = 4.16 \times 10^{16}$ s^{-1} is atomic frequency unit, h is Planck's constant, $E_a = (2/3)E_{a0}, E_{a0} = m^2e^5/h^4 = 5.14 \times 10^9$ V/cm is field strength at the first Bohr radius, and N_g is the density of

neutral atoms of the gas before the ionization process.

Equation (19) is applicable to describe ionization in a laser field with frequency ω and amplitude E (see also [5 - 9]), when the following conditions are fulfilled: $\omega \ll \Omega$, $I \ll q$, $E \ll E_a$, where $q = e^2E^2/2m\omega^2$ is quiver energy of electrons, and I is ionization potential of the atom. The growth of the average plasma density, $N = \langle n \rangle$, are determined by the expression $\partial N/\partial t = \langle w(\mathcal{E}) \rangle$ (here and further angle brackets denote averaging over the field period $2\pi/\omega$).

We seek the solution of equations for the electric ($\mathcal{E}$) and magnetic ($\mathcal{H}$) fields in the form of a p-polarized wave

$$\left\{ \begin{matrix} \mathcal{E} \\ \mathcal{H} \end{matrix} \right\} = \frac{1}{2} \left\{ \begin{matrix} \mathbf{E}(x,t) \\ \mathbf{H}(x,t) \end{matrix} \right\} \exp[ikz - i\varphi(t)] + \text{c.c.}, \; N = N(x,t) \; , \quad (20)$$

with a fixed longitudinal wave number $k = 2\pi/\lambda$, slow time-varying frequency $\omega(t) = \partial\varphi/\partial t$ and x-periodic amplitudes of the field components $\{E_{x,z}, H_y, N\}(x,t) = \{E_{x,z}, H_y, N\}(x + L, t)$. The range of interest for the lengths λ and L is $L/\lambda < 1$. The wave frequency ω, as well as the transverse structures of the field and the plasma, may change significantly in a long (on the scale of $1/\omega$) time.

At a sufficiently low ionization rate the stated problem can be solved within the adiabatic approximation based on two comparatively simple equations for the field. The first one determines the transverse structure and the frequency of the wave, which correspond to the instant distribution of the density, $N(x)$, at every instant t, as if this distribution was stationary. For the magnetic field of the form (20) this stationary equation, as it follows from the Eq.(17), is

$$\varepsilon \frac{\partial}{\partial x} \left(\frac{1}{\varepsilon} \frac{\partial H_y}{\partial x} \right) + \left(\frac{\omega^2}{c^2} \varepsilon - k^2 \right) H_y = 0. \quad (21)$$

Using the stationary equations (17) and (21) without the terms containing temporal derivatives of the amplitude and the density we actually neglect group lagging in the transverse direction and excitation of natural plasma oscillations at frequency ω_L in time-varying plasma. This is valid for perturbations with the transverse scale $L < \lambda$, if a characteristic time of variation in the complex amplitude, $\tau_e = |\mathbf{E}||\partial\mathbf{E}/\partial t|^{-1}$, is great compared to the period corresponding to

the beat frequency, $\tau_d = (\omega - \omega_L)^{-1}$. With the given x-periodicity condition, the solution of Eq.(21) determines, at each instant of time t (for known distribution of the density $N(x,t)$), the eigenfunction $H_y(x,t)$ and eigenvalue $\omega(t)$.

The time-dependent normalization factor in the determination of eigenfunction H_y must be calculated by means of the evolution equation that describes variation of the wave energy in a plasma with growing density:

$$\frac{\partial}{\partial t}\int_0^L |\mathbf{E}|^2\, dx = -\frac{4\pi e^2}{m\omega^4}\int_0^L \langle Q\rangle\, dx\ ,\ Q = \frac{\partial n}{\partial t}\left(\frac{\partial \mathcal{E}}{\partial t}\right)^2. \qquad (22)$$

This equation is a generalization of the intensity transport equation obtained earlier for a homogeneous quasi-monochromatic wave [7,9] with transverse modulations of the field and density taken into account. It may be derived directly from Poynting's theorem for the quasi-monochromatic field by using the x-periodicity condition for the fields and the known equation for the instantaneous electron current $\mathcal{J}$:

$$\partial \mathcal{J}/\partial t = (e^2 n/m)\mathcal{E}. \qquad (23)$$

Eq.(23) is valid at any ionization rate w. It is easily derived from the kinetic equation under realistic assumption that the free electrons are born with zero (or isotropically distributed) velocity. The right-hand side of the Equation (22) determines energy losses caused by energy transfer to newly born electrons [5,7,9]. Direct energy losses by electrons' detachment, as well as collision losses, can be neglected, assuming $\varepsilon = 1 - N/Nc$, in the validity region of the static formula (19) ($I \ll q$) and at small collision frequency of electrons ($\nu \ll wN_c \ll \omega$).

The dynamics of a homogeneous breakdown (in the absence of space modulations) produced by the field of a linearly polarized transverse wave $\mathcal{E} = \mathbf{x}_0 E_0(t)\cos(kz - \varphi(t))$ in the case of $|E| \ll E_a$ is described by smooth functions $E_0(t), \omega(t), and \omega_L(t)$ [6]. The average rates of ionization, $\langle w\rangle$, and dissipation, $\langle Q\rangle$, in Eq. (22) and the long-time asymptotic solution are determined in this case by the following expressions: $\langle w\rangle = w(E_0)\sqrt{E_0/E_a}$, $\langle Q\rangle = \langle w(\partial\mathcal{E}/\partial t)^2\rangle =$

$\langle w \rangle \omega^2 E_0^3/E_a$, $\omega_L^2(t) = \omega^2(t) - \omega^2(0) \sim t^{2/3}$, $E_0(t) \sim (\ln \omega)^{-1}$. Let us study stability of this process to small perturbations that modulate the wave amplitude and plasma density in the x-direction. Representing the expressions for field components and plasma density as $E_x = E_0(t) + E_1(x,t)$ and $N = N_0(t) + N_1(x,t)$, and linearizing Eqs. (18), (19) and (21) against the homogeneous (but non-stationary) background, E_0 and N_0, we obtain the following equations for the small perturbations E_1 and $\varepsilon_1 = -N_1/N_c$:

$$\frac{\partial^2 E_1}{\partial x^2} + \frac{E_0}{\varepsilon_0}\frac{\partial^2 \varepsilon_1}{\partial x^2} + \left(\frac{\omega}{c}\right)^2 \varepsilon_1 E_0 = 0 \ , \ \frac{\partial \varepsilon_1}{\partial t} + \gamma_0 \varepsilon_1 + \alpha E_1 = 0, \quad (24)$$

where $\varepsilon_0 = 1 - (N_0/N_c), \alpha = N_c^{-1}(d\langle w \rangle / dE_0), \gamma_0 = \langle w \rangle (N_g - N_0)^{-1}$. For perturbations of the form $E_1, \varepsilon_1 \sim \cos(2\pi x/L) \exp \int \gamma(t)\, dt$ we find, based on system (24), the following expression for the growth rate of instability, γ:

$$\gamma = \gamma_0 \left[\frac{N_g - N_0}{N_c - N_0} \frac{E_a}{E_0} \left(1 - \frac{L^2}{\lambda^2}\right) - 1 \right]. \quad (25)$$

It follows from Eq.(25) that perturbations with the spatial period L shorter than the length of the electromagnetic wave, $\lambda = 2\pi/k$, can be unstable ($\gamma > 0$). The instability is caused in fact by the plasma resonance phenomenon and can be understood in the framework of a simple quasi-static (plain capacitor) model which is valid for the small scale $L \ll \lambda$. As the undercritical plasma density $N < N_c$ increases in a thin plane layer, the normal field component increases according to the quasi-static relation $E_x = \text{const}/\varepsilon$. It results in the growth of the ionization rate $\langle w \rangle$ and the further growth of the density. At the same time, defocusing of the wave by the dense plasma is negligible on this small scale (but it suppresses the instability with the scale $L > \lambda$). When the condition of $(N_g - N_0)E_a \gg (N_c - N_0)E_0$ is fulfilled, the maximum of γ reached in the limit of $L/\lambda \to 0$ is $\gamma_{max} = (\langle w \rangle E_a)/(N_c E_0 \varepsilon_0)$. The lower limit of the instability scale, L_{min}, cannot be found in the framework of local relations (1) and (2), and, probably, must be determined either by the amplitude of electron oscillations in the optical field, or by the Debye lengths. In a gas with high density ($N_g > N_c$) the value of γ grows infinitely as the density

N_0 approaches the critical value, N_c. However, it begins to exceed the growth rate of the homogeneous background ($\gamma > \langle w \rangle / N_0$) even at the values of the background density, N_{0S}, which are much smaller than the critical one: $N_{0S}/N_c \simeq E_0/E_a \ll 1$. If at such values of N_0 the electron or neutral density fluctuations or an external random source of ionization produce a "seed" small-scale perturbation with a sufficiently great value N_{1S}, then the spatial modulation of the plasma density $N(x)$ may become significant even in the region of $\varepsilon \sim 1$, i.e. much earlier than the point of plasma resonance is achieved. For example, in the case of $N_{1S}/N_{0S} = E_0/E_a = 0.1$ the value of $N_1(0,t)$ calculated by means of the above linear theory becomes of the order of $N_0(t)$ at $N_0/N_c \simeq 0.3$.

The dynamics of the field and plasma at the nonlinear stage of instability (at large ε_1 and E_1) was studied by computer simulation. The system of Eqs. (18),(19),(21), and (22) was integrated numerically in the interval $0 < x < L$ with the periodic boundary conditions and the following initial conditions: $N(x,0) = N_{00} + N_{10}\cos(2\pi x/L), H_y(0,0) = H_0$, and $\partial H_y/\partial x(0,0) = 0$; at small N_{00} and N_{10} the field at the initial instant $t = 0$ is an almost transverse wave with amplitudes $E_x \simeq H_y \simeq H_0$ and frequency $\omega_0 \simeq kc$. The results of numerical calculations for the values of dimensionless parameters $N_{c0}/N_g = 0.8$, $\lambda/L = 2\pi/kL = 3$, $H_0/E_a = 8.25 \times 10^{-2}$, $N_{00}/N_{c0} = 0.1$, and $N_{10}/N_{c0} = 0.01$ ($N_{c0} = N_c(\omega_0)$) are shown in Figs. 3 and 4. Figure 3 (a and b) presents spatial distributions of the electric field components $E_x(x)$ and $E_z(x)$, the plasma density $N(x)$ and permittivity $\varepsilon(x)$ at various time moments t. We see that the nonlinear stage is characterized by formation of sharp maxima in the transverse field and density; the electric field in a thin layer with $\varepsilon \ll 1$ increases significantly, whereas outside this layer it significantly decreases as compared to the initial unperturbed value, $E_0(0)$. At a certain point, this process acquires the explosion character and goes on until the gas is almost completely ionized at the maximum point, where the difference $\omega - \omega_L$ reduces to the minimum (positive) value. Thereafter the produced layer with increased density extends slowly, and the field maximum becomes lower.

Figure 4 shows the time-dependencies of the frequency $\omega(t)$, field energy $K(t)$, average energy flux $P(t)$ (related to their initial values),

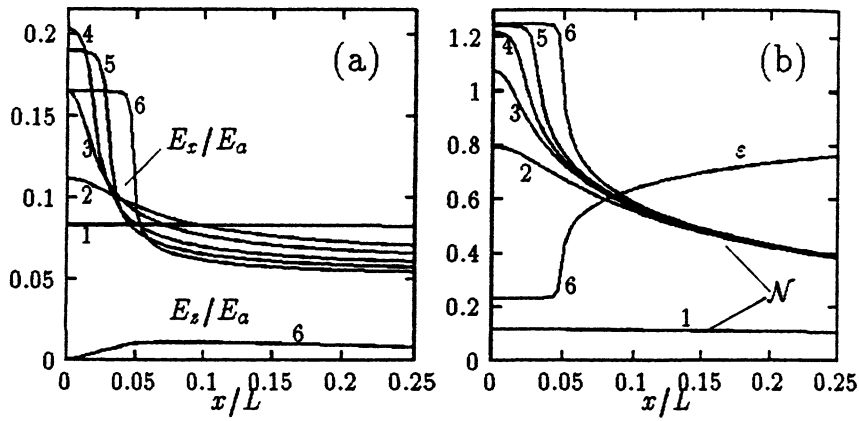

Fig. 3: Spatio-temporal evolution of the field and plasma at the nonlinear stage of LIF instability: (a) transverse, $E_x(x)$, and longitudinal, $E_z(x)$, field components, (b) dimensionless plasma density, $\mathcal{N}(x) = N/N_{c0}$, and permittivity, $\varepsilon(x)$, at various instants of time; the curves 1 – 6 correspond to the values of $\omega t \times 10^{-3} = 0$; 7.39; 7.96; 8.45; 10.2; 25, respectively; the period of initial transverse modulation is $L = \lambda/3$.

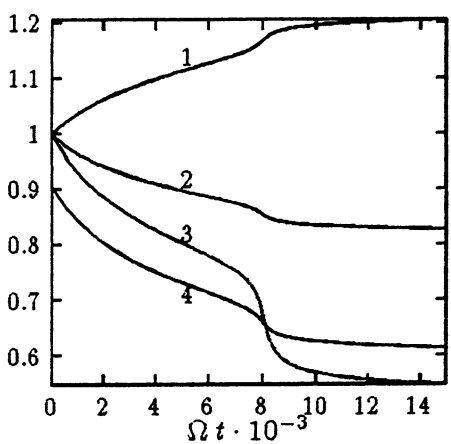

Fig. 4: Wave frequency, ω/ω_0, energy, K/K_0, energy flux, P/P_0, and effective permittivity, ε_{eff} (curves 1 – 4 respectively) as time functions.

and the real part of the effective permittivity, $\varepsilon_{eff}(t) = (ck/\omega)^2$, which determines characteristics of average (over the x coordinate) fields. These dependencies are rather steep at the stage of fast growth of the field and density and slow down sharply after ionization is saturated at the maximum point.

The studied numerical example may correspond to different sets of dimensional parameters of the problem. Specifically, the framework of the approximations used above includes, with a sufficient accuracy, the case of H-gas with the density $N_g = 1.4 \times 10^{20}$ cm^{-3} (the pressure $p \simeq 5.8$ atm) ionized by a laser pulse with wavelength $\lambda = 3$ μm ($\omega_0 = 6.3 \times 10^{14}$ s^{-1}, $N_{c0} = 1.1 \times 10^{20}$ cm^{-3}), initial intensity $S = 10^{14}$ W/cm^2, and duration $\tau_p > 200$ fs. An analysis of the calculation results shows that for the above example $\tau_d/\tau_e \simeq 10^{-1}$, i.e. the condition of validity of adiabatic approximation (4)-(6) is fulfilled in this case. Note, however, that the maximum rate of the explosion process that is achieved near $N = N_g$ grows as the parameter N_g/N_{c0} increases; thus, at a sufficiently high gas density (actually, starting from $N_g/N_{c0} \simeq 2$) the adiabaticity condition, $\tau_e \gg \tau_d$, must be inevitably violated near the sharpening point. By that, evidently, the effective refractive index $\varepsilon_{eff}^{1/2}$ must change step-wise and this change must be accompanied by shock excitation of a reflected wave and generation of intense plasma oscillations. In this case the theory developed makes it possible to conclude only that the explosion process is inevitable and to describe the first (adiabatic) stage of the process in a "temporal" problem. More specific conclusions on the character of LIF instability manifestation in actual conditions of an optical breakdown produced by focused laser pulses in a limited gas region could be made by means of solving a more complicated (two- or three-dimensional) spatio-temporal problem within the non-adiabatic approximation.

To conclude this Section, we have shown that in the process of optical-field-induced ionization the field and plasma cannot stay homogeneous even on scales small compared to the wavelength. Due to the effect of LIF instability, on such scales development of the periodic plasma-field microstructure occurs with gradients parallel to the wave electric field. At a sufficiently high gas density, the sharpening regime is realized at the nonlinear stage of the instability, the

process acquires the explosion character and leads to formation of thin resonance layers, in which the electric field of the wave concentrates. In this regime the processes of scattering and generation of higher radiation harmonics must be strongly intensified, and this is highly important for problems of production and diagnostics of laser plasmas with high density.

This work was supported by the International Scientific Foundation (grant No. R8A300), and the Russian Basic Research Foundation (grant No. 96-02-17467).

References

1. V.B.Gil'denburg, A.V.Kim, Sov.Phys.JETP, 1978, **47**, 72.
2. A.L.Vikharev, V.B.Gil'denburg, O.A.Ivanov, and A.N.Stepanov, Fiz. Plazmy **10**, 165 (1984); Sov.J.Plasma Phys. **10**, 96 (1984).
3. V.B.Gil'denburg, A.A.Solodov, JETP Lett., 1995, **62**, 551.
4. L.D.Landau and E.M.Lifshitz, *Quantum Mechanics*, 3rd ed. (Pergamon, London, 1978).
5. P.B.Corkum, N.H.Burnett, and F.Brunel, Phys.Rev.Lett., 1989, **62**, 1259.
6. M.C.Downer, W.M.Wood, and J.T.Trisnadi, Phys.Rev.Lett.,

MICROWAVE REFLECTION FROM A SHEET PLASMA

R. F. Fernsler, J. Mathew, R. A. Meger, W. M. Manheimer, J. A. Gregor, D. P. Murphy, and R. E. Pechacek***

Naval Research Laboratory, Washington, DC, USA
*University of Maryland, College Park, MD, USA
**SFA Inc., Landover, MD, USA

- As is well known, a plasma is a good reflector of electromagnetic radiation up to the plasma frequency, but unlike a metallic reflector, a plasma has low mass and can therefore be repositioned or recreated quickly. Manheimer [1] has suggested that these properties be exploited to produce an agile plasma mirror for steering radar beams rapidly over wide angles. Such a mirror would have the directional capability of phased-array antennas, but with broad instantaneous bandwidth and potentially lower cost. To explore this possibility, the Naval Research Laboratory has been conducting experiments using a sheet plasma to reflect 10 GHz microwaves. As discussed by Robson *et al.* [2] and Meger *et al.* [3], the plasma is created using a hollow-cathode discharge in a low-pressure gas (~ 100 mtorr). Mathew *et al.* [4] have shown that these discharges operate in an unusual "enhanced glow" mode, in which a low-current beam of energetic electrons formed at the cathode propagates all the way to the anode. The beam ionizes the gas and creates the dense plasma responsible for reflecting microwaves.

In this paper we determine the plasma properties needed to reflect microwaves, and then consider how to produce such a plasma using an energetic beam of electrons. Included in the calculations are estimates of the absorptive and radiative properties of the plasma, the maximum microwave power that can be tolerated, and the requirements for plasma flatness and surface motion. We then discuss the experimental apparatus and results achieved thus far, as well future plans. Included in the latter is the production of a sheet plasma more than a square meter in cross-sectional area. The experiments described here were performed with a plasma 50 cm across by 60 cm long and roughly 2 cm thick.

Plasma Requirements

In this section we determine the plasma properties needed to reflect microwaves of frequency $f_o \leq 15$ GHz. We start by considering the current induced in the plasma by the microwave electric field E. If the plasma electrons are treated as cold and there is no dc magnetic field, the electron current density is given from the momentum equation by

$$j_e = \frac{e^2 n_{pe} E}{m(\nu_{pe} + i\omega)} . \qquad (1)$$

Here n_{pe} is the plasma electron density, e and m are the electron charge and mass, respectively, ν_{pe} is the momentum-transfer collision frequency, and $\omega = 2\pi f_o$ is the angular microwave frequency. The power absorbed equals the real part of $j_e \cdot E$, and for normal incidence, Eq.(1) combined with Maxwell's equations and the WKB approximation yields the dispersion relationship,

$$k^2 c^2 = \omega^2 - \frac{\omega\, \omega_{pe}^2}{(\omega - i\nu_{pe})} . \qquad (2)$$

Here c is the speed of light, k is the wave number, and $\omega_{pe} = (4\pi e^2 n_{pe}/m)^{1/2}$ is the plasma frequency. The neglect of the magnetic field B is justified provided the electron cyclotron frequency $\omega_{ce} = eB/mc << \omega$. This corresponds to fields B < 1 kG for frequencies of interest.

Wave absorption is determined by the imaginary part of k, and Eq. (2) indicates that this absorption is small only if $\nu_{pe} << \omega < \omega_{pe}$. In a singly ionized plasma with an electron temperature $T_e \sim 1$ eV, the electron-ion collision frequency is $\nu_{ei} \sim 3x10^{-5} n_{pe}$, while the electron-neutral collision frequency is $\nu_{en} \sim 10^{-7} N$, where N is the neutral gas density. The total collision frequency ν_{pe} equals the sum of these, and it is less than ω only if $n_{pe} < 3x10^{15}$ cm^{-3} and $N < 10^{17}$ cm^{-3}. As we shall show, plasma densities well below $3x10^{15}$ cm^{-3} are sufficient to reflect microwaves, and thus a weakly ionized plasma can be used in a cold background gas at pressures below 1 torr. A weakly ionized plasma in a cold gas is advantageous, because the plasma density n_{pe} decays rapidly once the ionization source is removed.

To determine the plasma size and density needed, consider first a uniform sheet plasma of thickness x_o. For $\nu_{pe} << \omega$, the imaginary part of k is given from Eq. (2) by

$$k_i^2 \approx \frac{\omega_{pe}^2 - \omega^2 - \nu_{pe}^2}{2c^2} + \sqrt{\left(\frac{\omega_{pe}^2 - \omega^2 - \nu_{pe}^2}{2c^2}\right)^2 + \left(\frac{\nu_{pe}\omega_{pe}^2}{2\omega c^2}\right)^2} \quad . \qquad (3)$$

If $\omega < \omega_{pe}$, the waves are evanescent and propagation effectively ceases if $x_o > 5c/\omega_{pe} \sim 1$ cm. The rate of energy absorption equals the integral of $j_e \cdot E$ over x_o, and dividing by the incident power, $cE^2/4\pi$, gives the fraction of power absorbed:

$$f_a = \frac{\nu_{pe}}{2k_i c}\frac{\omega_{pe}^2}{\omega^2} \quad . \qquad (4)$$

Maximum absorption occurs at the plasma frequency, and there $f_a = (\nu_{pe}/2\omega)^{1/2}$. However, for frequencies $\omega < 0.9\omega_{pe}$, the fraction drops to

$$f_a < 1.5\frac{\nu_{pe}}{\omega_{pe}} \quad . \qquad (5)$$

The power absorbed is then less than 2% if $\nu_{pe} < 10^9$ s^{-1}. This corresponds to gas densities $N < 10^{16}$ cm^{-3}.

Additional absorption occurs in the plasma wings where the density n_{pe} falls off. The fraction of power absorbed in the wings is given by $4\int dz\, k_i(z)$ for the round trip, where $k_i \approx \nu_{pe}\omega_{pe}^2/2\omega c(\omega^2 - \omega_{pe}^2)^{1/2}$ according to Eq. (3). If n_{pe} falls linearly from critical density to zero over a distance Δx, the fraction of power absorbed in the wings is given by

$$\Delta f_a \approx \frac{8}{3}\frac{\nu_{pe}\Delta x}{c}. \qquad (6)$$

Typically $\Delta f_a > f_a$, meaning that most absorption occurs in the wings. The sum of Δf_a and f_a gives the total absorption coefficient, and it is less than 5% if $\Delta x < 1$ cm and $\nu_{pe} < 6\times10^8$ s^{-1}. The latter corresponds to gas densities $N < 6\times10^{15}$ cm^{-3}, or pressures below 200 mtorr at room temperature. We thus conclude that high reflectivity requires low gas density and a dense plasma more than a cm thick, with wings not much more than a cm wide. In addition, the plasma surface should be smooth and stationary to within a tenth of a wavelength, $0.1\lambda \cong 2$ mm, during a pulse. The flatness criterion is generally well satisfied, since spatial fluctuations in a plasma are typically confined to a few Debye lengths, $\lambda_D = (2T_e/m)^{1/2}/\omega_{pe} \sim 10^{-2}$ mm. Motion of the plasma surface will be addressed later.

Non-Normal Incidence and Refraction

The preceding calculations confirm the well-known reflective properties of plasmas at frequencies $\omega < \omega_{pe}$. Waves with $\omega > \omega_{pe}$ can reflect as well, however, provided they strike the plasma at an angle. To show this, let us ignore absorption and set $\nu_{pe} = 0$. The phase velocity of waves in a uniform plasma is then given from Eq. (2) by

$$v_{ph} = \frac{\omega}{k} = \frac{\omega c}{\sqrt{\omega^2 - \omega_{pe}^2}} . \tag{7}$$

This velocity exceeds c, and thus the waves refract. Complete reflection occurs when the angle of incidence satisfies

$$\theta > \sin^{-1}(c/v_{ph}) . \tag{8}$$

Combining the last two equations, we find that reflection occurs when the plasma frequency satisfies

$$\omega_{pe} > \omega \cos\theta . \tag{9}$$

This equation shows that plasmas can reflect high-frequency waves incident off axis.

Microwave Emission

To be useful as a receiver, the plasma should be a poor microwave emitter, with an equivalent radiation temperature ideally at or below room temperature. This condition appears to be difficult to meet, given the 1 eV temperature of the plasma electrons. However, Kirchoff's law (detailed balance) relates emissivity to absorptivity, and it dictates that a good reflector is a poor emitter. To estimate the radiation temperature, we observe that the microwave quantum energy $\hbar\omega$ is well below the gas kinetic energy at room temperature, and thus that the microwave emission is proportional to the plasma temperature times the plasma absorptivity. Because the plasma electrons are the hottest species in the plasma and the source of the microwaves (through bremsstrahlung), the radiation temperature is given by

$$T_\omega \approx (f_a + \Delta f_a)\, T_e , \tag{10}$$

where the absorptivity $(f_a+\Delta f_a) << 1$ by design. If we assume an electron temperature $T_e \cong 1$ eV and an absorptivity ~ 0.05, the microwave radiation temperature is $T_\omega \sim 600$ K, or roughly twice room temperature. This temperature can be reduced by lowering the gas density to reduce

ν_{pe}, until $\nu_{pe} \rightarrow \nu_{ei} > 5x10^7\ s^{-1}$. In principle, radiation temperatures T_ω well below room temperature are possible, according to Eqs. (5) and (6).

Maximum Microwave Power

As discussed above, the use of a weakly ionized plasma has several advantages, and one of these is the ability to handle high microwave power. The principal requirement is that the microwaves should not appreciably affect the plasma volume or density. This is generally true as long as $\nu_a\tau_p < 2$, where ν_a is the electron avalanche rate due to microwave heating and τ_p is the microwave pulse duration. The finite magnitude of the electron ionization cross section limits the avalanche rate to $\nu_a < 10^{-7}N$ in most gases, where ν_a is in s^{-1} and N is in cm^{-3}. There is then no limit on microwave power, provided $N\tau_p < 10^7\ s/cm^3$.

To determine the maximum microwave power for long pulses, we express ν_a as the gas density N times the average of the electron velocity times the ionization cross section. That average is a function of the plasma electron temperature T_e, and in equilibrium T_e is determined by a balance between electron collisional cooling and Joule heating, given by the real part of $j_e \cdot E$. Balancing the two rates, we find that T_e is a strong function of E_e/N, where E_e is the equivalent dc electric field giving the same heating rate:

$$E_e = \frac{E}{\sqrt{1+\omega^2/\nu_{pe}^2}}\ . \qquad (11)$$

In this equation E is the rms (rather than peak) microwave electric field. If we set $\nu_{pe} << \omega$ to minimize absorption, Eq. (11) reduces to $E_e \cong (\nu_{pe}/\omega)E$. Allowing for constructive interference outside the plasma, the rms field is related to the incident microwave intensity I_o by $E \leq 4(\pi I_o/c)^{1/2}$, and thus $E_e \leq 4(\nu_{pe}/\omega)(\pi I_o/c)^{1/2}$.

Using swarm data tabulated by Dutton [5], the reduced avalanche rate in air can be approximated by

$$\nu_a/N \approx \begin{cases} 10^{-8}\exp(-960N/E_e) - 7x10^{-13}, & \text{for } E_e/N \leq 370\ Td \\ 5x10^{-8}\exp(-1550N/E_e), & \text{for } E_e/N \geq 370\ Td\,. \end{cases} \qquad (12)$$

Here ν_a/N is in cm^3/s and E_e/N is expressed in Townsends (Td), where 1 Td = 10^{-17} V-cm^2. Using Eq. (12) and approximating the collision frequency by $\nu_{pe} \cong 10^{-7}N$, we find that there is no limit on the pulse

duration if the microwave intensity $I_o < 3$ MW/m^2. Conversely, for pulse lengths $\tau_p < 50$ μs, intensities well above 3 MW/m^2 are permitted.

Plasma Creation

Although several different schemes for creating the agile-mirror plasma have been considered, the present device uses a high-voltage, hollow-cathode discharge. The hollow cathode used for most of the experiments described herein consists of a three-sided rectangular cavity, 50 cm long and 1.2 cm deep by 1.6 cm wide. The operating characteristics of the discharge are sensitive to the cavity size and shape, as well as to the voltage, gas pressure and magnetic field. Typical parameters used to reflect 10 GHz microwaves were: anode-cathode length ℓ = 60 cm; solenoidal field B ~ 200 G; air at P ~ 100 mtorr; and discharge voltage $\Phi_o > 3$ kV. In this parameter regime, the discharge operates in an enhanced glow mode, in which a low-current electron beam is created in the hollow cathode and propagates all the way to the anode. The beam, rather than field-driven avalanche ionization, is responsible for producing the dense plasma used to reflect microwaves. Such a discharge differs from conventional glow discharges in terms of the current density achieved, and it differs from most hollow-cathode discharges, in that the beam continues to propagate from cathode to anode throughout the pulse. For purposes of discussion, we shall treat the beam as a source of known current density j_b and energy $e\Phi_o$. Operation of the hollow cathode itself will not be addressed.

Beam self-forces are negligible because j_b is small, and the electric field is weak (except near the cathode) because of shorting by the plasma. The advance of the beam toward the anode is then determined primarily by the applied magnetic field B and by collisions with the gas molecules. If collisions are temporarily neglected, the transverse motion of the ith beam electron is described by

$$x_i(t) = x_{ci} + \frac{v_{\theta i}}{\omega_{ce}} \sin(\omega_{ce} t + \phi_i) \ , \qquad (13)$$

where x_{ci} denotes the location of the guiding center, $v_{\theta i}$ is the rotation speed, ϕ_i is a phase factor, and $\omega_{ce} = eB/mc$ is the cyclotron frequency. The mean-square beam width is obtained by averaging x_i^2 over space and time for all beam electrons in a given lateral slice, giving

$$\delta x_b^2 = \langle x_i^2 \rangle = x_c^2 + \frac{\varepsilon_\perp}{m\omega_{ce}^2} , \qquad (14)$$

where x_c^2 is the average of x_{ci}^2 and $\varepsilon_\perp$ is the average of the transverse energy, $mv_{\theta i}^2/2$. Note that δx_b is the beam half-width.

Inelastic collisions create the plasma, but small-angle elastic collisions occur more often. The elastic collisions increase x_c and $\varepsilon_\perp$, thus causing the beam to expand. The increase in x_c occurs because redirection of a particle displaces its guiding center x_{ci} by $r_{ci}\delta\theta_\perp$, where r_{ci} is the particle gyroradius and $\delta\theta_\perp$ is the transverse deflection angle. As a result, x_c^2 increases by the number of collisions times the mean-square scattering angle, $\delta\theta_c^2$, per collision. For planar discharges, only half of the deflection is normal to the discharge, and thus

$$\frac{dx_c^2}{dt} \approx \frac{v_b N \sigma_{el} r_c^2}{2} \delta\theta_c^2 , \qquad (15)$$

where v_b is the beam speed, σ_{el} is the elastic scattering cross section, and r_c is the rms gyroradius. At the same time, scattering transfers longitudinal beam energy to transverse energy at a rate

$$\frac{d\varepsilon_\perp}{dt} \approx v_b N \sigma_{el} \frac{m v_{bz}^2}{2} \delta\theta_c^2 , \qquad (16)$$

where v_{bz} is the axial beam velocity.

For small-angle scattering, one can set

$$\sigma_{el}\, \delta\theta_c^2 \approx 2 \int d\Omega\, (1 - \cos\theta) \frac{d\sigma}{d\Omega} \equiv 2\sigma_m , \qquad (17)$$

where $d\sigma/d\Omega$ is the differential cross section and σ_m is the momentum-transfer cross section. Combining Eqs. (14)-(17), we find that scattering spreads the beam at a rate

$$\frac{d}{dt} \delta x_b^2 \approx v_b N \sigma_m [r_c^2 + (v_{bz}/\omega_{ce})^2] . \qquad (18)$$

The term in brackets is related to the total beam energy by

$$r_c^2 + (v_{bz}/\omega_{ce})^2 = \frac{2\varepsilon_b}{m\omega_{ce}^2} . \qquad (19)$$

If the energy ε_b is a constant equal to $e\Phi_o$, we obtain

$$\frac{d}{dt} \delta x_b^2 \approx v_b N \sigma_m r_m^2 , \qquad (20)$$

where $r_m = (2e\Phi_o/m\omega_{ce}^2)^{1/2}$ is the maximum gyroradius possible. In practice, inelastic collisions lower ε_b as the beam propagates, and thus the expansion rate gradually slows.

Momentum loss from elastic scattering limits the forward advance of the beam to distances

$$z < z_m = (n_o \sigma_m)^{-1} . \tag{21}$$

The time taken to reach this distance is z/v_{bz}, and thus Eq. (20) indicates that

$$\Delta(\delta x_b^2) \approx \frac{v_b}{v_{bz}} \frac{z}{z_m} r_m^2 . \tag{22}$$

For Φ_o = 3 kV and B = 200 G, the maximum radius increase is ~ 1 cm. This is comparable to the initial plasma width, based on the size of the cathode. The increase is smaller, of course, if the discharge length $\ell < z_m$. For example, the momentum-transfer cross section for a 3 keV electron in air is $\sigma_m \cong 1.2 \times 10^{-18}$ cm^{-2}, and the gas density at 100 mtorr is $N \cong 3.3 \times 10^{15}$ cm^{-3}. The beam range is then $z_m \cong 4\ell$ for ℓ = 60 cm. In that case, a beam starting with a 1 cm half-width would broaden by only 2 mm or so.

At sufficiently small voltages, the range z_m becomes shorter than the discharge length ℓ. In the example cited, this occurs at voltages below 2 kV, depending on gas pressure. At distances $z > z_m$, the discharge takes the form of a positive column sustained by avalanching. Avalanching requires a high electric field, and associated with this field is a high electron drift velocity. The large drift velocity necessitates a small plasma density, in order to maintain current continuity with the negative-glow region where the drift velocity is small. The low plasma density of the positive column makes it nearly transparent to microwaves, and consequently the discharge is a good microwave reflector only if an enhanced glow is maintained over virtually the entire volume. To achieve the latter, the discharge voltage must be high and the gas pressure low.

Let us next consider the beam needed for an enhanced glow to produce plasmas capable of reflecting microwaves. To reflect 15 GHz waves, the plasma density should satisfy $n_{pe} \geq 2.8 \times 10^{12}$ cm^{-3}, while for 10 GHz the requirement is $n_{pe} > 1.2 \times 10^{12}$ cm^{-3}. To determine the plasma density, we use the plasma-electron continuity equation,

$$\frac{\partial n_{pe}}{\partial t} = \frac{j_b}{e} \frac{1}{w_i} \frac{d\varepsilon_b}{dz} + D_a \nabla_\perp^2 n_{pe} - \beta n_{pe}^2 . \tag{23}$$

Here j_b is the axial beam current density, $d\varepsilon_b/dz$ is the beam energy deposited axially per cm in the gas, w_i is the average beam energy deposited per electron-ion pair created, D_a is the ambipolar diffusion coefficient, and β is the electron-ion recombination rate. In this equation we have dropped electron attachment relative to recombination because of the high plasma density, and we have dropped avalanching because the plasma keeps the electric field well below breakdown.

For beam energies of interest, the inelastic loss function can be approximated by

$$\frac{d\varepsilon_b}{ds} \approx \frac{2\pi NZ(r_c mc^2)^2}{\varepsilon_b}[\ln(\varepsilon_b/W_o) + 0.15], \qquad (24)$$

where s is the path length, Z is the atomic number of the molecules, r_c is the classical electron radius, and W_o is the mean molecular excitation energy. The loss function per *axial* cm, $d\varepsilon_b/dz$, equals $d\varepsilon_b/ds$ times (v_b/v_{bz}), where v_b is the speed of the beam electrons and $v_{bz} \le v_b$ is the axial beam velocity. The total path length is limited to

$$s < s_m(\varepsilon_b) = \int_0^{\varepsilon_b} d\varepsilon_b' \left(\frac{d\varepsilon_b}{ds}\right)^{-1} \approx 0.5\frac{\varepsilon_b}{(d\varepsilon_b/ds)} . \qquad (25)$$

This distance is comparable to the elastic range z_m given by Eq. (21), so that the neglect of energy loss in Eq. (22) is not truly justified. Both s_m and z_m increase quadratically with beam energy ε_b to lowest order.

Let us now consider the loss terms in Eq. (23), starting with electron diffusion. Because the plasma Debye length λ_D is much shorter than the plasma width x_o, the plasma electrons are electrostatically tied to the ions, and the diffusion is ambipolar. Ignoring negative ions, the diffusion coefficient is given by

$$D_a = \frac{T_e + T_i}{[1+(\omega_{ce}/\nu_{pe})^2]\, m\nu_{pe} + [1+(\omega_{ci}/\nu_i)^2]\, M_i\nu_i}, \qquad (26)$$

where T_i, M_i, ω_{ci} and ν_i are the temperature, mass, cyclotron frequency, and collision frequency, respectively, of the ions. Collisions with the gas molecules keep the ions cold, $T_i << T_e$, and for magnetic fields less than 250 G and gas pressures ~ 100 mtorr, typical values are $\omega_{ci} < 5\text{x}10^5\ s^{-1}$, $\nu_i \sim 2\text{x}10^6\ s^{-1}$, $\omega_{ce} < 5\text{x}10^9\ s^{-1}$, and $\nu_{pe} \sim 3\text{x}10^8\ s^{-1}$. The diffusion coefficient then satisfies $D_a \sim 10^4\ cm^2/s$ for $T_e \sim 1$ eV.

The last term in Eq. (23) represents electron-ion recombination. In molecular gases like air, the dissociative recombination coefficient is large: $\beta \cong 5x10^{-8}/T_e^{-0.39}$ cm^3/s. For $n_{pe} \sim 10^{12}$ cm^{-3} and $T_e \sim 1$ eV, the recombination loss rate is $\beta n_{pe} \sim 5x10^4$ s^{-1}. This is large compared with the diffusion loss rate, $D_a/x_o^2 \sim 10^4$ s^{-1}, and thus the steady-state plasma density in Eq. (24) can be approximated by

$$n_{pe} \approx \sqrt{\frac{j_b}{e\beta w_i}\frac{d\varepsilon_b}{dz}} \ . \qquad (27)$$

For 3 keV electrons in 100 mtorr of air, $d\varepsilon_b/dz$ exceeds 7 eV/cm, depending on v_b/v_{bz}. The axial beam current density needed to produce $n_{pe} > 10^{12}$ cm^{-3} is then

$$j_b \gtrsim 30 \ mA/cm^2 \ . \qquad (28)$$

Equations (21)-(28) indicate that an electron beam with an energy of 3 keV and a current of 30 mA/cm^2 or more can produce a dense plasma capable of reflecting microwaves, over lengths up to 2 m in 100 mtorr of air. The beam profile should be roughly flat-topped over a cm or more, and it can be kept from spreading excessively by applying a longitudinal magnetic field ~ 200 G. Note that beam ionization produces a stable stationary plasma, as long as the beam itself is stable. In addition, after the beam turns off, the plasma density decays, halving in a time $\tau_{½} = 1/\beta n_{pe}$. During this decay, the plasma electrons cool so that T_e falls and β rises; as a result, $\tau_{½}$ is less than 10 μs for plasma densities $n_{pe} > 10^{12}$ cm^{-3}. After $9\tau_{½}$, the density decreases by an order of magnitude. A new plasma mirror can thus be created and destroyed as rapidly as every 20 μs or so.

Higher plasma densities can be obtained by using an atomic gas like argon, in place of molecular gases like air, so that diffusion rather than recombination is the major loss mechanism. However, the decay time is then longer and the plasma profile is more rounded.

In the present device, the beam is created as ions bombard the cathode and liberate secondary electrons. The ion current is converted to plasma electron current past the cathode, through gas ionization. If one beam electron is produced for every ten incident ions on average, the ion current striking the cathode must be ten times the beam current. A plasma current density $j_p \cong 0.3$ A/cm^2 is therefore needed to produce $j_b = 30$ mA/cm^2. To sustain the plasma current in the bulk plasma, the electron drift velocity must be ~ 10^6 cm/s, for plasma densities $n_{pe} \sim 10^{12}$ cm^{-3}.

Such a drift velocity requires an axial electric field $E_o \sim 0.1$ V/cm in 100 mtorr of air. This field is well below the breakdown strength, and the beam energy gained from it is negligible compared with the inelastic loss function, $eE << d\varepsilon_b/dz \sim 7$ eV/cm, as assumed earlier. Thus, as long as the cathode can supply the necessary current, a dense plasma capable of reflecting microwaves can be produced and sustained.

Left out of this analysis are space-charge effects in the sheaths near the cathode. Space-charge effects keep j_p below the Child-Langmuir limit, which decreases with sheath thickness. For planar cathodes, j_p is small because the sheath must be thicker than an ionization mean free path. In a hollow cathode, however, two opposing cathodes develop on the inner side walls, and electrons reflex transversely between the two walls. Such reflexing increases the gas ionization rate, which increases the plasma density and reduces the sheath thickness. Much higher currents can therefore be drawn from hollow cathodes than from planar ones. The current drawn depends on the cathode dimensions, gas pressure, voltage and magnetic field, but analysis of these effects is outside the scope of the present paper.

We close the theoretical analysis with an estimate of the gas temperature rise. Such a rise causes the gas to expand and rarefy in a time $x_o/c_s \sim 50$ μs, where $c_s \sim 3x10^4$ cm/s is the sound speed. If heating and expansion are appreciable on this time scale, thermal instabilities and arcing are likely. In the present system, there are two sources of energy deposition in the bulk plasma. The beam deposits energy at a volumetric rate $(j_b/e)(d\varepsilon_b/dz) \cong 0.2$ W/cm^3, while the ohmic heating rate is $j_pE_o \cong 0.03$ W/cm^3. The total heating rate per molecule is ~ 0.5 keV/s, and thus ~ 0.5 eV per molecule is deposited in a pulse $\tau_p = 1$ ms long. This energy is eight times the initial thermal energy and will eventually lead to appreciable gas heating and expansion.

Fortunately, little of the deposited energy goes directly into gas heating, so that the temperature rise and expansion occur only slowly. For example, most of the ohmic energy goes into vibrational excitation of the molecules, and that energy is recovered only slowly (over minutes to hours) through vibrational-translational relaxation. For the beam, roughly two-thirds of the deposited energy goes into ionization and dissociation, with the remainder going into gas excitation and electron heating. The ionization energy is later recovered through dissociative recombination, but this process converts only a few percent of the total deposited beam energy into gas heating. The dissociation energy is itself later recovered

as the atoms recombine, but atomic recombination takes minutes or more, based on a three-body rate coefficient ~ 10^{-33} cm^3/s. Thus, only a few percent of the total deposited energy goes into gas heating during a pulse, and consequently the gas temperature during a pulse is modest. Gas heating and expansion are therefore unimportant, as long as the gas is refreshed between pulses and each pulse is less than 1 ms long. However, gas heating can become a problem for long pulses or a continuous train of closely-spaced pulses. We point that in the present system most of the energy supplied (nearly 100 kW peak) is deposited not in the gas but on the cathode, by energetic ions crossing the high-voltage sheath. The use of an externally generated electron beam, with zero voltage applied across the plasma, would reduce this consumption by roughly an order of magnitude.

Experimental Apparatus

A schematic of the system used is shown in Fig. 1. The cylindrical vacuum chamber is made of lexan 1.2 cm thick, capped by acrylic endplates 10 cm thick. The chamber is 81 cm long and has an inner diameter of 79 cm. A brass anode 67 cm in diameter is mounted on a conducting rod through the bottom of the chamber, and the height of the rod can be adjusted to change the anode-cathode separation ℓ. In the experiments reported here, ℓ was 60 cm. The cathode is brass and contains a hollow rectangular channel on the bottom. The behavior of the discharge is strongly influenced by the dimensions of the channel, and for the results given here the channel was 50 cm long by 1.6 cm wide and 1.2 cm deep, recessed in rectangular acrylic plate 58 cm long by 10 cm wide. A rectangular mask with a slot 50 cm long and 1.8 cm wide was placed over the channel, to suppress the formation of plasma outside the hollow. The cathode structure is attached to a conducting rod though the top plate of the vacuum chamber, enabling the cathode to be rotated while under vacuum. A longitudinal magnetic field up to 500 G is produced using two, 110-turn Helmholtz coils, 120 cm in diameter and 60 cm apart. The cathode is pulsed negative by a Crossatron switch connected to a high-voltage power supply in series with an 80 Ω resistor. Square voltage pulses with a duration between 20 μs and 1 ms have been produced, at repetition frequencies up to 10 Hz. The device has also been operated in a ten-pulse burst mode at 10 kHz, with pulse lengths τ_p between 30 and 70 μs. Typical operating parameters for the discharge are voltage ~ 4 kV,

current ~ 20 A, magnetic field ~ 200 G, and air at a pressure ~ 100 mtorr. Diagnostics include various microwave receivers and sources (at 8, 10 and 140 GHz), a calibrated microwave noise source, an energy analyzer, Langmuir probes, and optical spectroscopy.

Results

Figure 2 shows typical results for the discharge current and voltage in an eight-pulse burst at 10 kHz. Each voltage pulse is 60 μs long, and the repetition rate of the burst is 0.5 Hz. The bottom trace shows the microwave signal reflected off the plasma from a 10 GHz, continuous source. Reflection occurs only while the mirror is on, and the signal is nearly flat-topped with a rise time ~ 6 μs and a decay time ~ 10 μs. In burst mode as well as for long-duration single pulses, there was a transient period lasting ~ 100 μs, during which the discharge current was higher. During this phase, the plasma surface contracted by ~ 2 mm, according to microwave interferometry. After the transient period, the surface was essentially stationary. Time-resolved digital images of the plasma confirmed this behavior. The transient phase of the discharge current and surface movement is believed to be associated with processes occurring within the hollow cathode.

The reflective properties of the plasma were compared with those of a flat aluminum plate 10 cm wider than the plasma. This data was taken by rotating the plasma or plate while keeping the microwave source and receiver at fixed locations. The microwave dish had a 30 cm diameter and was 96 cm from the mirror, so some of the radiation missed the mirror. As shown in Fig. 3, the peak power reflected from the plasma is virtually indistinguishable from that reflected from the metal plate, which indicates high reflectivity from all portions of the plasma. Moreover, the sidelobes of the two signals are similar and down by more than 20 db, which indicates a surface flatness better than $\lambda/8$. The small differences in the sidelobes can be attributed, at least in part, to the larger size of the aluminum plate, and/or to reflections from the walls of the vacuum chamber. No significant dependence on microwave polarization has been found.

The plasma density was measured independently using Langmuir probes and a 140 GHz microwave interferometer. These diagnostics confirmed that the density exceeded 10^{12} cm^{-3}, and higher densities have been obtained using other cathodes and gases. In addition, the Langmuir

probe indicated an electron temperature $T_e \sim 1$ eV and a dc longitudinal electric field $E \sim 0.1$ V/cm. The behavior of the plasma afterglow was determined as well, after the voltage turned off. Plots of the inverse of the plasma density versus time were linear, giving a rate coefficient $\beta \cong 2 \times 10^{-7}$ cm^3/s. This value is in good agreement with that expected for dissociative recombination of cold electrons.

An energy analyzer was constructed using a biased Faraday cup behind a hole in the anode. This device measures longitudinal energy only, and it confirmed the presence of a low-current, energetic electron beam reaching the anode. Near the cathode, the beam energy essentially equaled the full discharge voltage, and it dropped by only a few hundred volts at the anode. The beam full-width was ~ 2 cm, while the plasma full-width was ~ 2.5 cm. The one unexpected result was a low beam current density, $j_b \sim 3$ mA/cm^2. This result represents the only major discrepancy with theory, and additional efforts to repeat the measurement are planned.

A pulsed transverse magnetic field was added to the longitudinal dc field, in order to tilt the plasma. Pulsed fields up to 80 G were applied, and this enabled the plasma to be tilted by as much as $\pm 20^\circ$, at which point the ends of the plasma struck the chamber walls. Such deflection should redirect the microwave beam by twice as much, or 80° overall. Calculations indicate that the magnetic field is uniform to within a few percent within the plasma, and the plasma appeared to remain planar when deflected. Microwave reflection from the deflected plasma has yet to be demonstrated, however.

The radiation emitted at 10 GHz from the plasma was compared with that from a known noise source, and the comparison indicates a radiation temperature $T_\omega \sim 600$ K. This result is only preliminary, however, because it was taken with a different cathode and because a non-random component was detected in both signals. Efforts to refine the measurement are underway.

Summary

Experiments supported by theory demonstrate that a stable, flat and mobile plasma can be constructed to reflect microwaves nearly as well as a metallic plate. The plasma can be created and destroyed in times as short as 10 μs, be maintained for 1 ms or longer, and be reoriented magnetically. In addition, microwave emission from the plasma was

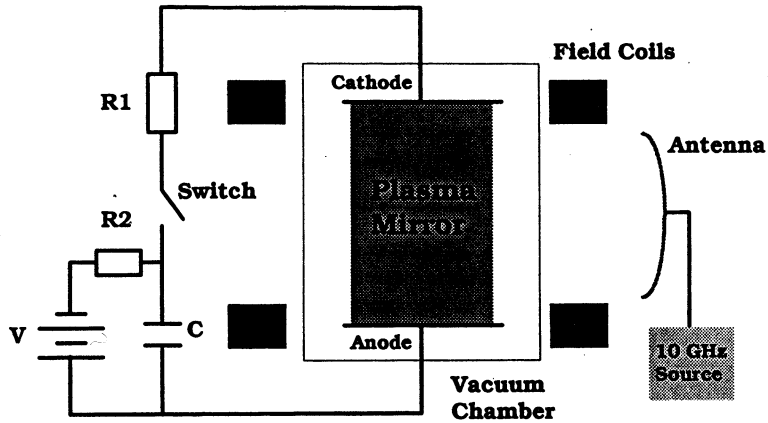

Fig. 1. Experimental apparatus.

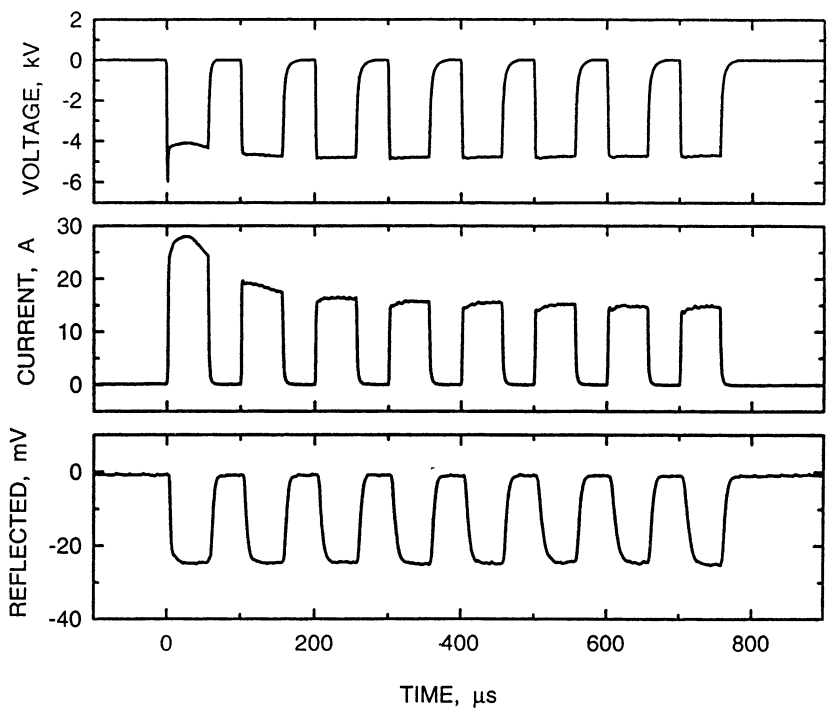

Fig. 2. Discharge voltage, current, and reflected microwave signals for an eight-pulse, 10 kHz burst.

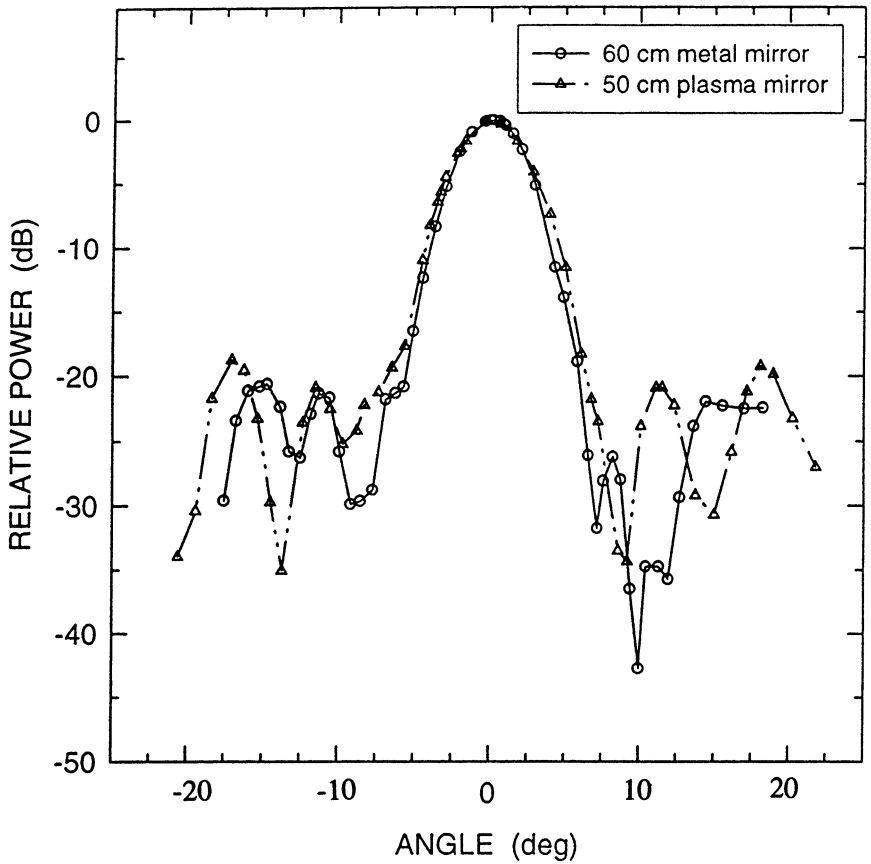

Fig. 3. Microwave power reflected from a sheet plasma, compared with that from an aluminum mirror, versus mirror rotation angle. Zero degrees corresponds to 90° reflection between source and receiver.

shown to be low, with an equivalent radiation temperature well below the electron temperature. The experimental results are in generally good agreement with theory, except for measurements of the beam current density. Those measurements are believed to be in error, based on several independent measurements of the plasma density and the known plasma production and loss rates. In addition to the efforts already described, several new studies are underway, including: the use of different gases and cathode designs, in order to increase the plasma density while decreasing power consumption; microwave reflection from magnetically tilted plasmas; refined measurements of plasma emission; and the construction of a larger chamber for producing plasmas more than a square meter in area. And last, an effort is underway to eliminate the linear hollow cathode by using one or more externally generated electron beams. With external beams, a high-current discharge is no longer needed, thus reducing gas heating and power consumption by roughly an order of magnitude.

Acknowledgment

The authors thank A. E. Robson, J. P. Hansen, J. B. Rao and M. I. Skolnik for helpful discussions, and A. Noll for technical assistance. This work was supported by the Office of Naval Research, USA.

References

1. W. M. Manheimer, IEEE Trans. Plasma Sci., 1991, **19**, 1228.
2. A. E. Robson, R. L. Morgan, R. A. Meger, IEEE Trans. Plasma Sci., 1992, **20**, 1036.
3. R. A. Meger, J. Mathew, J. A. Gregor, R. E. Pechacek, R. F. Fernsler, W. Manheimer, A. E. Robson, Phys. Plasmas, 1995, **2**, 2532.
4. J. Mathew, R. F. Fernsler, R. A. Meger, J. A. Gregor, D. P. Murphy, R. E. Pechacek, W. M. Manheimer, submitted to Phys. Rev. Lett., 1996.
5. J. Dutton, J. Phys. Chem. Ref. Data, 1975, **4**, 577.

FAST HIGHLY NONLINEAR VOLUMETRIC MEDIUM FOR MILLIMETER WAVES BASED ON THE PLASMA OF THE POSITIVE COLUMN OF Cs-Xe DC GAS DISCHARGE

Bogatov N.A., Gitlin M.S., Dikan D.A., Luchinin G.A.

Institute of Applied Physics, Russian Academy of Sciences, Nizhny Novgorod, Russia

Abstract

A plasma of the positive column of DC discharge in a cesium and xenon mixture was shown to provide an effective volumetric nonlinear medium for microwaves. In such a gas-discharge plasma under a xenon pressure 30 Torr and an electron density $N_e > 10^{12}$ cm^{-3}, a homogeneous spatial distribution of electron density with width about 0.8 of the discharge tube diameter was achieved. Using a 35 GHz microwave beam with intensities up to 0.25 W/cm^2, it has been found that the plasma of the positive column Cs-Xe discharge has a very high nonlinear refractive index, n_2 = - 0.1 cm^2/W, and a relatively fast response time of about several microseconds.

Introduction

There has recently been considerable interest in nonlinear microwave quasi-optics [1-7]. This interest arises from the fundamental scientific significance of nonlinear microwave quasi-optics as well as enormous number of possible applications, for example, in passive self-limiters [8], power-controlled switches [9], spatial modulators [10], image correlators [11], bistable devices [12], for beam deflection and steering [13], nonlinear phase shifting [2], real-time holography and phase conjugation (PC) [12-15], microwave beam combining and amplification via two- and four-wave mixing (FWM) [12-15], etc. These processes can be used in radar, microwave communications, beamed microwave power transmission, etc. However, the lack of appropriate nonlinear materials for microwaves is considered a bottleneck in achieving potential of the field [16].

Artificial Kerr media, saturable-absorbing molecular gases, and plasmas have been proposed as nonlinear media for microwaves. However,

values of nonlinear refractive index coefficient, n_2, less than 10^{-3} cm^2/W have been attained in the microwave region for artificial Kerr media [1-3], saturable-absorbing molecular gases [4], collisionless plasma with ponderomotive force nonlinearity [5,6,7]. For such a small value of the nonlinear refractive index effective self-action and interaction of microwaves are possible only with participation of powerful beams (microwave intensity W more than 10 W/cm^2 and, hence, pump beam power more than 1 kW). Therefore, artificial Kerr media, saturable-absorbing molecular gases, and collisionless plasma can be used for control and analysis of rather powerful microwave signals. Besides, these nonlinear media have a number of other shortcomings. Artificial Kerr media have slow response times (> 1 s) and therefore generally cannot be used as a real-time quasi-optical element for microwaves. Saturable-absorbing molecular gases and collisionless plasmas have fast response times, 0.1-10 μs, but these nonlinear media are applicable in a severely limited frequency range. Saturable-absorbing gas media are applicable only for microwaves with selective wavelengths in the submillimeter and short-millimeter wave region ($\lambda < 2$ mm), where there is high resonance absorption by rotational transitions of dipole molecules [4]. Collisionless plasma with ponderomotive force nonlinearity was used as a nonlinear medium for the middle-centimeter wave region [6,7], but for efficient interaction of radiation in the short-centimeter and millimeter wave region, plasma with high electron density, $N_e > 10^{11}$ cm^{-3}, and low electron temperature, $T_e < 1$ eV, is required. Generation of homogeneous strongly ionized collisionless plasma with such parameters in a large volume (10^3 - 10^4 cm^3) is a rather complicated problem. This proves that further study and optimization of the mentioned nonlinear media, as well as the search for novel nonlinear materials for centimeter and millimeter waves, are necessary. One good prospect for nonlinear media for microwaves would be a non-equilibrium weakly ionized gas discharge plasma [17]. The mechanism of nonlinearity in a weakly ionized plasma is caused by the dependence of plasma kinetic coefficients (generation and loss rates of charged particles, their mobility, diffusion coefficient, etc. [18]) on electron temperature T_e. In such a gas-discharge nonlinear medium the heating of electrons under the action of microwaves leads to variation of electron density, N_e, and their mobility; therefore, complex high-frequency permittivity of the plasma depends on the intensity of the microwave radiation, W.

In this work we have shown experimentally that a non-equilibrium weakly ionized plasma. of a positive column of the DC discharge in a mixture of cesium and a rare gas can provide an effective and fast volumetric nonlinear medium for microwaves. In our opinion, such a gas discharge medium can be used for fast control and analysis of relatively weak CW microwave signals in the broad region of centimeter and millimeter waves.

The experimental apparatus

Figure 1 illustrates the basic experimental arrangement used to study discharges in a mixture of cesium vapor with a rare gas. The plasma was

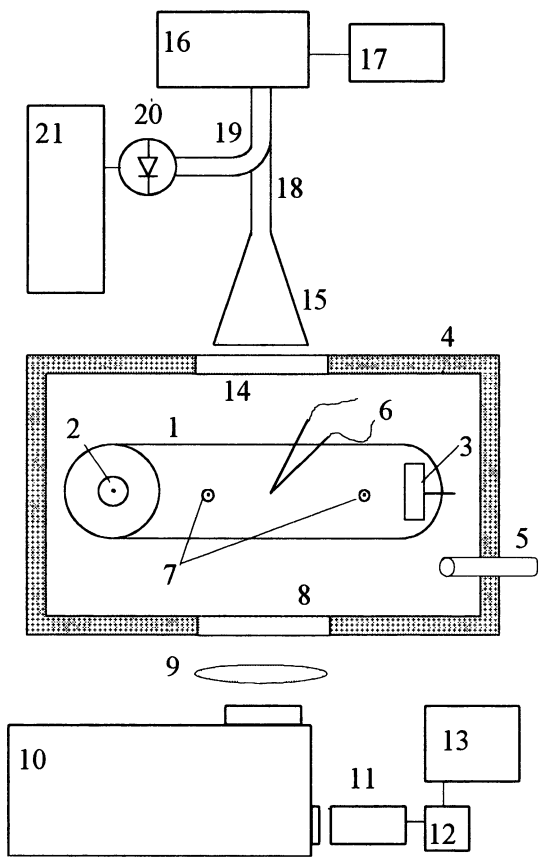

Fig. 1. Experimental set-up (top view).

produced in the sealed cylindrical glass gas-discharge tube 1 with a heated cathode. The lowest energy losses in elastic electron-atom collisions takes place in xenon due to its maximum, among stable rare gases, atomic mass. For this reason, gas discharge tubes filled with xenon were generally used in the experiments reported here. The xenon gas pressure at the room temperature was 30 Torr (xenon number density N_{Xe} is 10^{18} cm^{-3}). The discharge tube had a sidearm, in which a drop of cesium was placed. To obtain the required density of cesium vapor, the gas-discharge tube was heated in special oven 4 with hot air supplied through tube 5. The temperature of the discharge tube wall, T_w, was controlled by means of thermocouples 6 with accuracy ± 2 degrees. The big bend of the L-shaped gas discharge tube 1 of length 40 cm and internal diameter 48 mm was placed horizontally, and the distance between cathode 2 and anode 3 was 38 cm. The gas discharge tube was provided with two single probes 7, placed at the tube axis and spaced 10 cm apart. The longitudinal electric field E in the positive column of the discharge was determined by the difference of potentials between the two probes using a high-impedance voltmeter. Through quartz window 8 and lens 9 the emission of the positive column of the gas discharge was sent to monochromator 10. The light was detected with photomultiplier 11. Its output signal was fed to the input of an oscilloscope, or, through amplifier 12, to X-Y recorder 13. A microwave beam was fed into the oven perpendicularly to the discharge tube axis through quartz window 14. The microwave beam was formed by pyramidal horn antenna 15 which measured 50 cm in length with aperture dimensions 8×6 cm. The 35 GHz CW magnetron 16 fed by power supply 17, was used as a microwave source with maximum output power 10 W. The microwaves were fed to horn antenna 15 by means of rectangular waveguide 18. The waveguide directional coupler 19 branched off a small part of the microwave radiation to microwave diode 20 which was used to control the power of millimeter waves. The signal from the diode entered the oscilloscope 21.

Experimental results

Parameters of the plasma of the positive column of Cs-Xe DC gas discharge

The electron temperature and relative variation of electron density in the positive column of the discharge were deduced from the emission

spectrum of radiative recombination of electrons and cesium atomic ions Cs^+ with formation of a cesium atom in a state 6P (6P-recombination continuum of cesium) [18,19,20]. In the range of electron energy, ε, where the Maxwellian electron energy distribution function took place (ε < 1.39 eV), the intensity of the recombination continuum is described by the following expression [18, 20]:

$$I(\nu) = A \cdot N_e \cdot N_{Cs^+} \cdot T_e^{-3/2} \cdot \nu \cdot (\nu - \nu_0) \cdot \sigma_r(\nu - \nu_0) \cdot exp\{-h(\nu - \nu_0)/kT_e\}, \qquad (1)$$

where N_{Cs+} is number density of cesium atomic ions, ν is radiation frequency, ν_0 is boundary frequency of the continuum, $\sigma_r(\nu - \nu_0)$ is the cross section of radiative recombination into the 6P atomic state of cesium, and A is constant. For the 6P-recombination continuum of cesium the product $(\nu - \nu_0) \cdot \sigma_r(\nu - \nu_0)$ is constant with good accuracy [19,20] and therefore the electron temperature may be obtained by the slope of the straight line approximating the dependence of $\ln[I(\nu) / \nu]$ on ν.

The positive column of the Cs-Xe discharge was studied experimentally in the range of tube wall temperatures from 350 to 400 degrees K (partial pressure of cesium vapor 10^{-4} - $2 \cdot 10^{-3}$ Torr) and at discharge current densities from 20 mA/cm^2 to 200 mA/cm^2. At a preassigned value of the discharge current three different forms of the positive column were observed depending on the temperature of the tube wall. At high wall temperatures the positive column was constricted and occupied only the upper part of the horizontally placed bend of the tube; this is denoted as the first discharge form. For this discharge form the longitudinal electric field and the electron temperature were low (E < 0.4 V/cm, T_e < 0.3 eV) and the optical emission lines of atomic cesium and cesium recombination continuum were observed only in the spectrum of the positive column discharge. When the tube temperature was reduced, the diameter of the positive column discharge increased gradually. Finally its glow filled the entire tube volume; this is denoted as the second discharge form. In the spectrum of the second form of the discharge xenon atom emission lines are also present along with the cesium atom emission lines and cesium recombination continuum. Appearance of the xenon lines reveals that except cesium, xenon also plays an important role in the energy and ionization balance of this form of the positive column of the discharge [21-23]. When the tube

was cooled further, a bright filament about 5 mm in diameter strongly emitting xenon lines appeared in its upper part; this we denote as the third discharge form. The expansion of the positive column of the discharge with decreasing tube temperature resulted from considerable cesium atom depletion which is most pronounced in the region of the current density maximum owing to ionization of cesium atoms and the inhomogeneity of the gas density due to heating by discharge current and heat conduction of the gas [21,22]. Consequently, the longitudinal electric field and the electron temperature increased noticeably (E = 0.5 - 0.7 V/cm, T_e = 0.35 - 0.4 eV). Figure 2 shows the plot of the longitudinal electric field in the positive column as a function of the tube wall temperature for discharge current

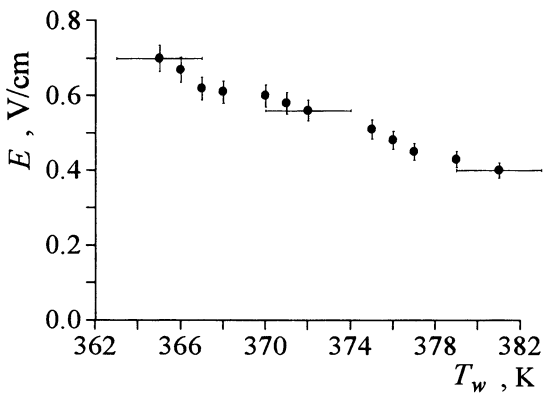

Fig. 2. The longitudinal electric field in the plasma of the positive column of Cs-Xe DC gas discharge on the tube wall temperature for J =1.5 A.

J = 1.5 A. Figure 3 shows dependence of the electron temperature in the positive column on the tube wall temperature. The study of the spatial distribution of electron density in the positive column of the discharge was peformed using movable single probes. It showed that the spatial distribution of electron density in the second form of the discharge is nearly uniform and its width (FWHM), d, reaches 0.8 of the tube diameter in the vicinity of a boundary of the third discharge form (T_w = 365-370 K). A similar result was obtained for a discharge tube with inner diameter of 98 mm. Therefore, the use of the second form of the positive column of the Cs-Xe discharge should be especially advantageous for the creation of a homogeneous nonlinear medium with dimensions significantly exceeding

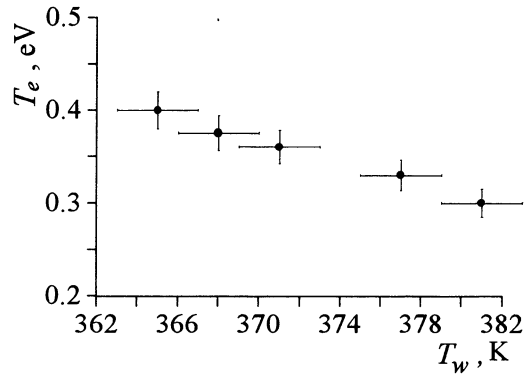

Fig. 3. The electron temperature in the plasma on the tube wall temperature for J = 1.5 A.

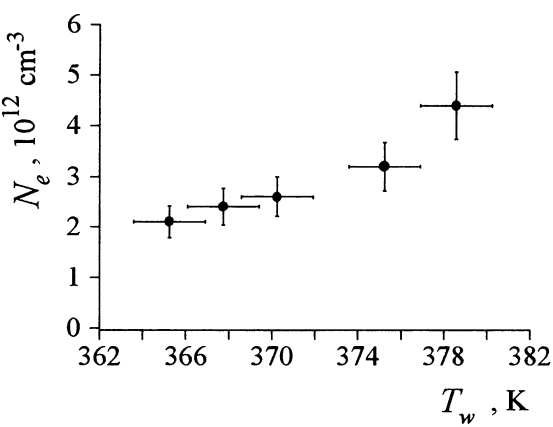

Fig. 4. The electron density in the plasma on the tube wall temperature for J = 1.5 A.

the microwave wavelength. The absolute value of electron density in the positive column of the discharge was determined from discharge current J on the basis of measuring the longitudinal electric field, E, the electron temperature, T_e, and the width of the spatial distribution of the electron density, d, according to

$$N_e = 4J / \pi d^2 e \mu(T_e) E , \qquad (2)$$

where $\mu(T_e)$ is electron mobility in the longitudinal electric field, which have been calculated as a function of the electron temperature for the momentum transfer cross-section of the electron-xenon atom collision as given in [24]. Figure 4 shows electron density in the positive column as a function of the tube wall temperature at J = 1.5 A.

Microwave interaction with the plasma

The action of microwaves on the plasma of the noncontracted positive column of the Cs-Xe discharge was studied at discharge current 1.5 A, tube wall temperature 368 K. For such conditions T_e = 0.37 eV and the electron density is $2.5 \cdot 10^{12}$ cm^{-3} which is about one-seventh of the critical plasma density, N_c, for microwaves with λ = 8 mm. The ratio of mean electron-xenon atom collision frequency for momentum transfer, ν_m [18], to the angular frequency of the microwave field, ω, equals ν_m / ω = 0.05. The absorption coefficient of microwaves in the plasma at these conditions is 0.05 cm^{-1}, and the reflection coefficient of microwave beam from the plasma boundary is less than 1%. Therefore, intensity of microwaves propagating normally to the axis of the positive column Cs-Xe discharge 40 mm in diameter can be assumed to be approximately constant. Variation of the electron density and temperature under the action of the microwaves could be found from the variation of the emission of 6P-recombination continuum of cesium. Figure 5 shows the plot of relative intensity I/I_0 of the recombination continuum at wavelength 490 nm as a function of microwave intensity W; here I_0 is intensity of the continuum in the absence of the microwave field. The variation of electron temperature was less than the 5% experimental error, even at the maximum 0.25 W/cm^2 intensity of the microwaves. This is caused evidently by the fact that the atomic excitation and ionization rate coefficients depend strongly on T_e and small variation of the electron temperature is sufficient to

change the electron density significantly. To clear up the ionization mechanism of the nonlinearity of the positive column of the Cs-Xe discharge and to determine the response time of the nonlinear media, we study

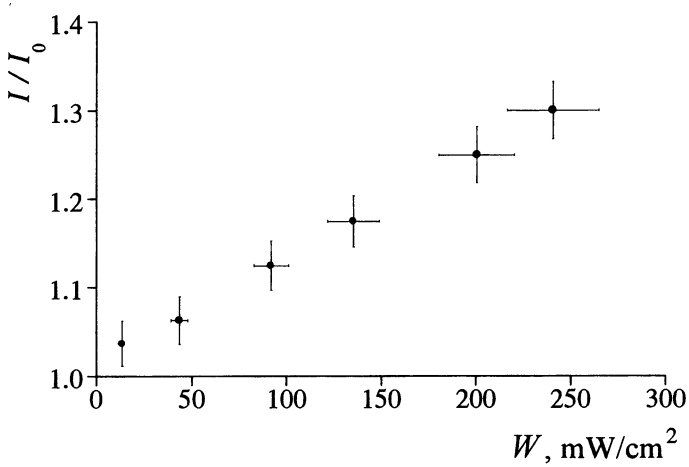

Fig. 5. The relative intensity of the 6P-recombination continuum of cesium vs the microwave intensity.

relaxation of the charged particle density up to the unperturbed level after switching off the microwave source instantaneously. Figure 6 shows the time history of the microwave intensity and the intensity of the cesium

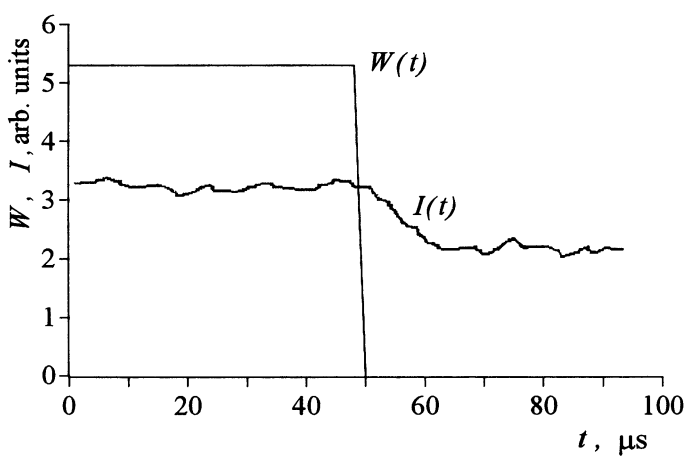

Fig. 6. The time history of the microwave intensity and the intensity of the 6P-recombination continuum of cesium.

6P-recombination continuum at the 490 nm wavelength. The intensity of CW microwave radiation was 0.25 W/cm^2. As may be observed from the oscillogram the response time of the nonlinear medium determined as the time of electron density relaxation, is several microseconds and it is approximately equal to the time of formation of Xe_2^+ ions, which are fast destroyed in the discharge by dissociative recombination [25,26]. Dimer ions, Xe_2^+, appear due to three-body association reaction between xenon atoms and atomic ions Xe^+ formed by stepwise ionization of xenon atoms. Thus one may conclude that the main variation of the density of charged particles in the noncontracted positive column under the action of the microwave radiation occurs due to additional ionization of xenon atoms. Variations of electron density and the density of Cs^+ ions due to additional ionization of cesium atoms under the action of microwaves were rather small, so that slow relaxation of charged particle density to the unperturbed level caused by recombination of electrons and Cs^+ ions was not observed over the noise background of the measured history of the cesium recombination continuum [25]. Since in the noncontracted positive column the density of Cs^+ ions and the electron temperature were little affected by the microwaves, the relative variation of the electron density, N_e/N_{e0}, as it follows from relation (1), equals the relative variation of the intensity of the recombination continuum I/I_0 ; here N_{e0} is electron density in the absence of microwave radiation. Figure 7 shows the plot of the value of variation of electron density in the plasma,

$$\Delta N_e = N_e - N_{e0} = (I / I_0 - 1)N_{e0} \tag{3}$$

as a function of the microwave intensity. It follows from this plot that the variation of the electron density is approximately in direct proportion to the microwave intensity,

$$\Delta N_e = q \cdot W, \tag{4}$$

where coefficient q equals $2.5 \cdot 10^{12}$ (W cm)$^{-1}$. The intensity-dependent refractive index, $n(W)$ [12], for plasmas in the limit $\nu_m << \omega$ is given by the following expression

$$n(W) = (1 - N_e(W)/N_c)^{1/2} = (n_0 - \Delta N_e/N_c)^{1/2} \tag{5}$$

[18]; here n_0 is linear refractive index of the plasma. When $\Delta N_e << N_c\, n_0$, plasma intensity-dependent refractive index equals $n(W) = n_0 + n_2 W$, were the nonlinear refractive index of the plasma of the positive column Cs-Xe discharge is $n_2 = - q/(2N_c\, n_0) = - 0.1$ cm^2/W.

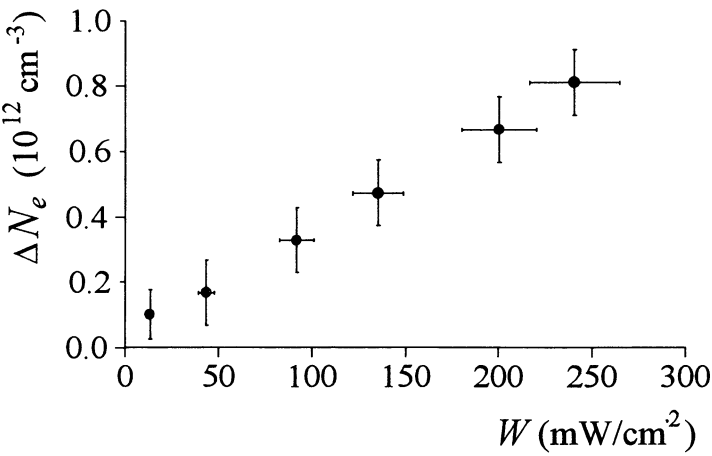

Fig. 7. Variation of the electron density in the plasma as a function of the microwave intensity.

As an example, using the measured value of the nonlinear refractive index we have estimated phase conjugate reflectivity via FWM [12-15] in a homogeneous slab of the plasma of the positive column of the Cs-Xe discharge. For microwaves with $\lambda = 8$ mm PC power reflectivity of the slab of Cs-Xe plasma 10 cm long at xenon pressure 30 Torr, electron density $N_{e0} = 2.5 \cdot 10^{12}$ cm^{-3} and equal intensities of the pump waves, $W_1 = W_2 = W = 30$ mW/cm^2, should be about 10%.

Conclusion

Thus, our study has shown that the plasma of the positive column of a DC discharge in the cesium - xenon mixture provides a stationary, homogeneous nonlinear medium for microwaves with sizes much larger than the microwave wavelength, a high nonlinear refractive index, and fast response time.

Acknowledgments

The authors are grateful to S.V.Golubev and A.G.Litvak for their interest to the work. This work has been performed in the framework of Scientific Program "Physics of Microwaves" and partially supported by the International Science Fundation, Grant R8C300 and the Russian Fund of the Basic Researches, Grant 94-02-04165.

References

1. McGraw R., Rogovin D.N., Ho W.W. et al. Phys. Rev. Lett., 1988, **61**, 943.
2. Bobbs B., Shin R., Fetterman H. R., Ho W.W. Appl. Phys. Lett., 1988, **52**, 4.
3. Shin R., Fetterman H. R., Ho W.W. et al. Phys. Rev. Lett., 1990, **65**, 579.
4. Bogatov N.A., Gitlin M.S., Litvak A.G. et al. Phys. Rev. Lett., 1992, **69**, 3635.
5. Steel D.G., Lam J.F. Opt. Lett. 1979, **4**, 363.
6. Pawley C.J., Huey H.E., Luhmann N.C., Jr. Phys. Rev. Lett., 1982, **49**, 877.
7. Domier C.W., Luhmann N.C., Jr. Phys. Rev. Lett., 1992, **69**, 3499.
8. Justus B.L. Huston A.L., Campilo A.J. Appl. Phys. Lett., 1993, **63**, 1483.
9. Bloembergen N. J. Nonlinear Opt. Phys. & Materials, 1996, **5**, 1
10. Thoma R., Hampp N., Brauchle C., Oesterhelt D. Opt. Lett., 1991, **16**, 651.
11. Blagglo I., Partanen J.P., Al B., Knize R. J., Hellwarth R. Nature, 1994, **371**, 318.
12. Boyd R.W. Nonlinear Optics. London: Academic Press, 1992.
13. Eichler H.J., Gunter P., Pohl D.W. Laser-Induced Dynamic Gratings. Berlin: Springer-Verlag, 1986.
14. Zeldovich B.Ya., Pilipetsky N.F., Shkunov V.V. Principle of phase conjugation. Heidelberg: Springer-Verlag, 1985.
15. Optical Phase Conjugation /Ed. by R.A. Fischer, Academic Press, New York, 1983.
16. Rogovin D.N., McGraw R., Ho W.W et al. IEEE Transactions on Microwave Theory and Techniques, 1992, **40**, 1780.

17. Bogatov N.A., Gitlin M.S., Golubev S.V. Sov. Tech. Phys. Lett., 1992, **18**, 760.
18. Raizer Y.P. Gas Discharge Physics, Berlin: Springer-Verlag, 1991.
19. Sayer B., Jeannet J.C., Lozingot J. et al. Phys. Rev. A, 1973, **8**, 3012.
20. Wetzer J.M. Physica C, 1984, **123**, 247.
21. Meyer H.J.G., Ahsmann G., v.d. Laarse et al. Philips Res. Rep., 1967, **22**, 209.
22. Waszink J.H., Polman J. J. Appl. Phys., 1969, **40**, 2403.
23. Morgulis N.D., Polushkin I.N. Teplofizika Vysokikh Temperatur (in Russian), 1966, **4**, 745.
24. Pack J.L., Voshall R.E., Phelps A.V., J. Appl. Phys., 1992, **71**, 5363.
25. Morgulis N.D., Polushkin I.N. Journal of Technical Physics (in Russian), 1966, **36**, 542.
26. Mitchell J.B.A. Phys. Rep., 1990, **186**, 216.

TAIL EROSION OF HPM PULSES

K. Madsén, D. Andersson, M. Lisak* and V. Semenov***

National Defence Research Establishment, Linköping, Sweden
*Chalmers University of Technology, Göteborg, Sweden
**Institute of Applied Physics, Nizhny Novgorod, Russia

Introduction

High power microwave (HPM) pulses propagating in gases may experience tail erosion, i.e. the trailing part of the pulse is suppressed by self-induced absorption and reflection. The basic physics of tail erosion is discussed in this work, together with two technical aspects and experimental results. Extreme tail erosion takes place in microwave transmit receive (TR) switches, which have been studied theoretically and experimentally [1,2]. Tail erosion of HPM pulses propagating in air has been studied both experimentally [3] and theoretically [4]. As a continuation of these studies, HPM aspects of microwave induced air breakdown has been analyzed further in the present work. A 37 GHz microwave generator which produces 15 MW, 4 ns pulses, has been used to demonstrate breakdown and tail erosion in a focused beam. The breakdown field strength and turn-on time have been experimentally determined and shown to be in good agreement with predictions in [4].

Basic physics involved in the tail erosion phenomenon

The nonlinear coupling between the wave and the properties of the medium is given by the equation of continuity for the electron density, n, which determines the time evolution of n,

$$\frac{\partial n}{\partial t} = \nu_{net} n \qquad (1)$$

where ν_{net} denotes the net ionization frequency, which is a function of gas composition and pressure but particularly also of wave power P. From eq (1) one infers that if $\nu_{net} > 0$, the electron density will exponentiate to very high values and obviously the continous wave breakdown criterion determining the critical microwave power P_b, where breakdown occurs is given by $\nu_{net} = \nu_{net}(P_b) = 0$. For short pulses, the pulse length,τ, becomes important and the breakdown criterion is qualitatively determined by the requirement that the pulse length, τ ,

should be longer than the turn-on time, τ_s , which is defined as the time needed for the electron density to exponentiate to the critical value n_{cr}, at which the concomitant plasma frequency equals the wave frequency, i.e.

$$\int_0^{\tau_s} \nu_{net}(P(t))dt = \ln\frac{n_{cr}}{n_0} \tag{2}$$

where n_0 is the initial electron density. In the case when P can be considered constant in time eq (2) implies that the turn-on time , τ_s , is

$$\tau_s = \frac{\ln(n_{cr}/n_0)}{\nu_{net}(P_b)}. \tag{3}$$

The breakdown condition for a microwave pulse of length τ then becomes $\tau_s = \tau$. For $\tau > \tau_s$, parts of the trailing portion of the pulse will be suppressed, the suppressed part increasing as τ increases.

Tail erosion in the microwave TR-switch

Extreme tail erosion takes place in the microwave TR-switch, in which a number of measures have been taken to obtain a turn-on time shorter than the rise time of the incident pulse. Field enhancement cones are used, together with a keep-alive arrangement, which ensures continous presence of a first electron to trigger the breakdown. The gas pressure within the TR-switch is chosen to correspond to the minimum of the Paschen curve. Experiments have shown [1], that sub-ns turn-on times are achieved and that only a narrow spike pulse is transmitted through the TR-switch. It can be shown [1] that the peak leakage power, $\hat{P}_t$, is equal to the incident power at the turn-on time, which yields:

$$\hat{P}_t = \frac{\gamma G}{\nu_i(P_b)} P_b \tag{4}$$

where γ is the exponential growth rate of the the incident power, $G=\ln(n_{cr}/n_0)$=const, ν_i is the ionization rate and P_b is the breakdown power. Predictions based on (4) have shown good agreement with experiments [1].

Tail erosion of HPM pulses propagating in air

Microwave breakdown in ambient air at atmospheric pressure has been demonstrated, using a 37 GHz BWO-oscillator, which produces 15 MW peak power, 4 ns pulses. A cylindrical tapered open end horn was

used to concentrate the microwave power. The big opening of the horn was placed adjacent to the 37 GHz radiating horn, cf. Fig 1. The length of the horn was 350 mm. A 4 mm wide slot was made in the output part of the horn, to provide a window for visual inspection of the breakdown.

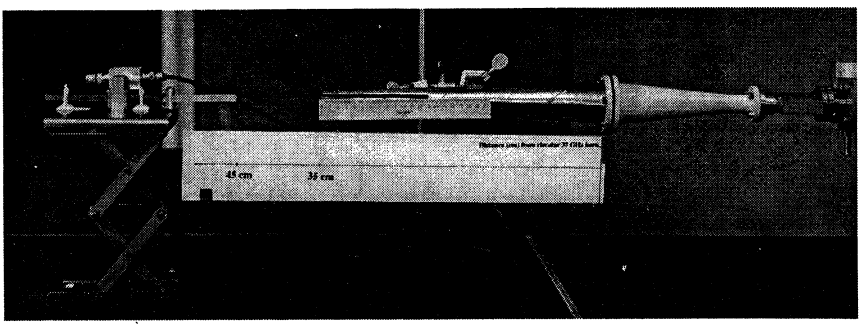

Fig. 1 - Cylindrical field concentrating horn and detector

A recording of air breakdown inside the concentrating horn was made, using a standard S-VHS video camera. A burst of pulses at 10 Hz repetition rate and peak power of 15 MW was injected into the horn and a microwave induced breakdown pattern was observed, cf. Fig. 2.

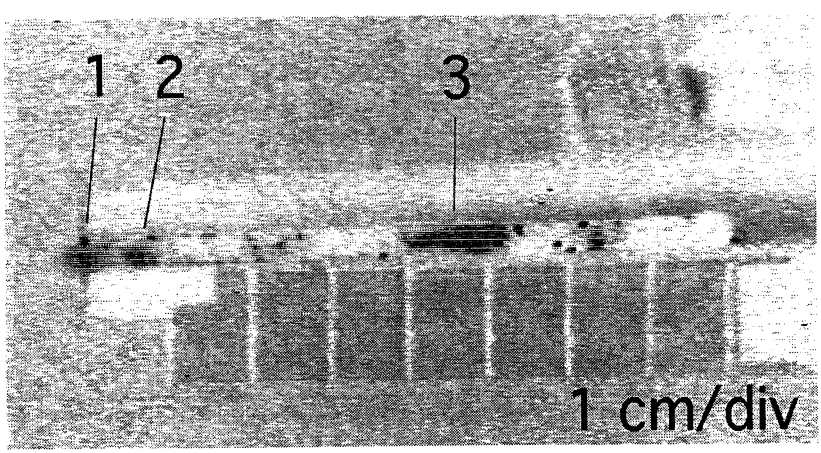

Fig. 2 - Inverted image of microwave breakdown in the horn

The black breakdown "clouds" in Fig. 2 have been numbered 1-3 and their volumes estimated to be 13 mm^3, 2 mm^3 and 38 mm^3, respectively. The fact that a standing wave is formed at the output

section is infered from the 5 mm separation between breakdown no 1-2, which shows reasonable agreement with the oscillator 4 mm half wavelength. The field strengths at the breakdown points 1-3 have been estimated to be E_1= 6.4 MV/m, E_2= 6.1 MV/m and E_3= 5.0 MV/m.

A theoretical model for the breakdown field strength of air was published in [4]. The model, which is based on an empirical approximation for the air ionization frequency, predicts that the breakdown field at 1 atm, 37 GHz and 4 ns pulse width is 5.3 MV/m, in reasonable agreement with the observed value E_3 at the first strong breakdown formation. The pulse from the 37 GHz generator, as measured by the detector is shown in Fig 3a and Fig 4a. Shown in Fig 3b and Fig 4b are also the pulses when affected by tail erosion, measured by the detector placed 10 cm from the receiving horn output, cf. Fig. 1.

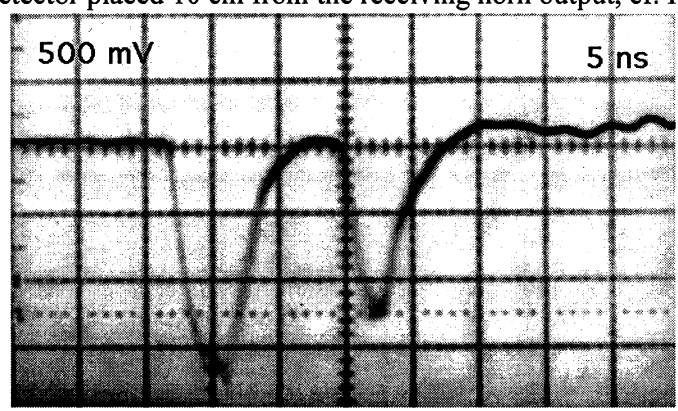

Fig. 3a - 37 GHz pulse measured without breakdown horn

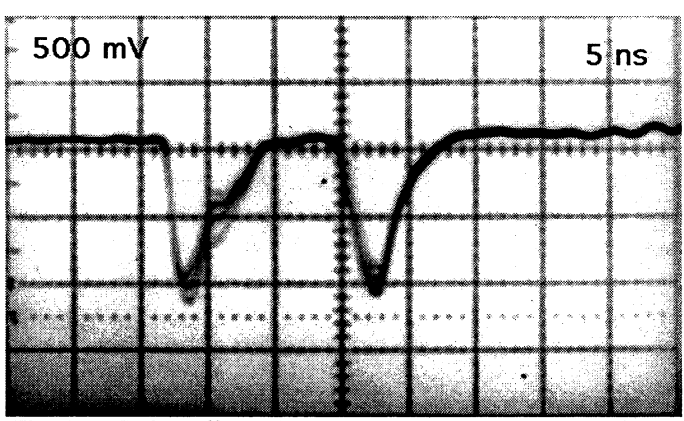

Fig. 3b - Pulse affected by tail erosion in breakdown horn

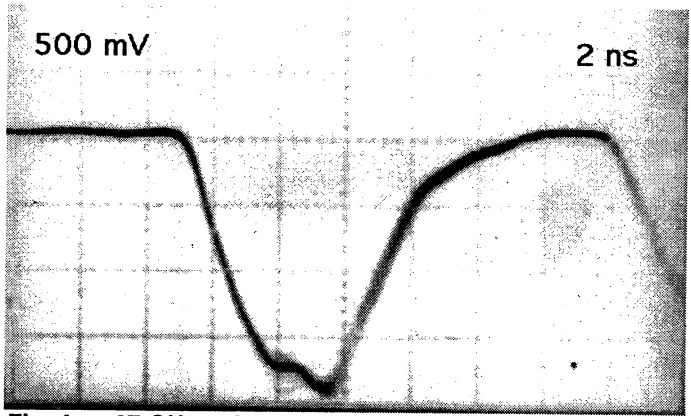

Fig. 4a - 37 GHz pulse measured without breakdown horn

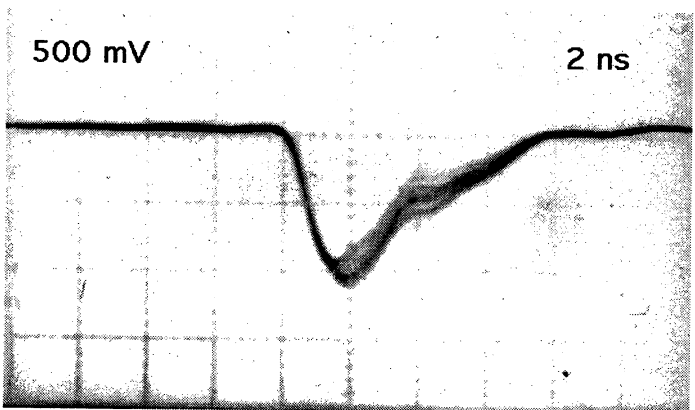

Fig. 4b - Pulse affected by tail erosion in breakdown horn

The tail erosion effect is clearly seen in Fig. 3b and Fig. 4b above. The leading edge sneaks through and the trailing part of the incident pulse energy is transfered to plasma formation. Tail erosion only has a minor effect on the second pulse in Fig 3b, which has a peak amplitude 4 dB below the first pulse. The turn-on time jitters between 1.5 ns and 2 ns, cf. Fig. 4b. An estimate of the energy in the trailing part of the first pulse which is dissipated in plasma formation can be made by integrating the difference between the curves in Fig. 4a and Fig 4b, which results in an energy transfer to the breakdown plasma of 50 mJ per pulse. The turn-on time observed in Fig. 4b can be compared with

the predicted turn-on time from a model previously published [4], which basically is similar to eq. (3), with an empirical model for ν_{net} for air,

$$\tau_s \approx \frac{\ln(n_{cr}/n_0)}{5.14 \cdot 10^{11} p} \exp\left(\frac{73\left(p^2 + p_c^{\,2}\right)^{0.22}}{E^{0.44}} \right) \qquad (5)$$

where, $p_c = 1.26 \cdot f_{GHz}$. Using p = 760 Torr, E = 6.4 MV/m and $\ln(n_{cr}/n_0)$ = 20 we obtain the switch time $\tau_s \approx 1.7$ ns, in excellent agreement with the observed turn-on time in Fig. 4b. Note that the field strength estimated at the very output of the breakdown horn E_1 was used in the above evaluation, since the pulse form was measured after propagation of the wave through the entire horn.

Conclusions and further work

An experimental demonstration of short pulse microwave induced breakdown of air and concomitant pulse tail erosion has been made and the experimentally determined breakdown field strength and turn-on time have been shown to be in good agreement with theoretical models. The fact that the half wavelength periodic breakdown pattern is not clearly visible along the entire slot in Fig. 2 can be explained by strong tail erosion of the pulse in breakdown no 3. The pulse that penetrates the breakdown no 3 is shortened and the power density needs to achieve a higher value for breakdown to occur. The observed breakdown pattern, will be analyzed further and compared with models for air ionization, induced by short high-power microwave pulses.

References

1. Madsén K, Andersson D, Lisak M, Lundgren L, Semenov V, Theoretical and experimental investigation of leakage power in microwave transmit-receive switches, subm. to J. Appl. Physics.
2. Löfgren M, Andersson D, Bonder H, Hamnén H, Lisak M, Breakdown phenomena in microwave TR-switches, J. Applied Physics, **69** (4), 1981 (1991).
3. Kuo S P, Zhang Y S, Physics Fluids B **2**, 667 (1990).
4. Löfgren M, Andersson D, Lisak M, Breakdown-induced distortion of HPM pulses in air, Phys. Fluids B **3** (12), 3528 (1991).

ION CHARGE STATE DISTRIBUTION IN THE ECR SOURCE WITH PUMPING BY MILLIMETER -WAVE GYROTRON RADIATION

S.V. Golubev, V.G. Zorin, S.V. Razin

Institute of Applied Physics of Russian Academy of Sciences
Nizhny Novgorod, Russia

The sources using microwave discharge plasma sustained in an open magnetic trap under the conditions of electron-cyclotron resonance (ECR) recently has began to be considered as the most perspective sources of multi-charged ions (MCI). Such ECR sources are intended mostly for ion injection into cyclotron accelerators, the efficiency of which strongly depends on the efficiency of the ion source [1,2].[1]

An essential increase in operation efficiency of the ECR source, i.e. increasing charge and ion beams intensity, is possible with the increase of pumping frequency. These investigations started to develop after a series of experimental works had been published (see, e.g. [5]), in which the sufficient increase of MCI output was demonstrated with the increase of pumping frequency from *10* to *18 GHz*: ion current mean with respect to charge state distribution had increased proportionally to the square of the pumping frequency ($I_{MCI} \sim f^2$). At the same time, the ion charge state distribution almost did not change (see Fig. 2). This can be explained in the context of an elementary model. Plasma density N_e increases with microwave pumping frequency increase, the plasma losses increase in proportion to N_e due to Coulomb collisions. Plasma confinement time in trap τ is inversely proportional to N_e. In this case the ion charge state distribution determined by $N_e\tau$ doesn't change, while MCI current determined by N_e/τ is proportional to f^2 if $N_e \sim f$. In connection with the above consideration the interest to investigations of the ECR discharge pumped by high frequency and according increase of MCI current is understandable. Moreover, the use of millimeter wave radiation of modern gyrotrons makes it possible to hope for such increase of plasma density

[1]ECR discharge is presented as a possible source of soft incoherent X-ray radiation [3, 4].

that allows changes in the character of plasma confinement in the trap. The so-called quasi-gas-dynamic regime of plasma confinement realized [6] when plasma lifetime weakly depends on its density [2].

The realization of such a regime means not only the growth of MCI beam intensity, but mainly the growth of confinement parameter $N_e\tau$ that leads to a sufficient shift of ion charge state distribution to the region of large ionization states.

This paper contains first experimental data on ion distribution over charge states in high-power pulsed ECR discharge sustained by short-wave gyrotron radiation. An experiment scheme is shown in Fig. 1.

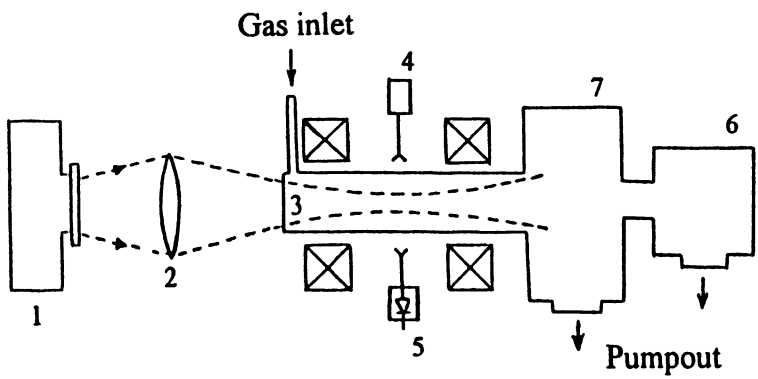

Fig. 1. The experiment scheme.

Microwave radiation from pulse-mode gyrotron (1) (frequency *37.5 GHz*, pulse duration 1 ms and power *130 kW*) was focused by dielectric lens (2) into vacuum discharge chamber (3). The wave was linearly polarized. The discharge chamber with an input window *70 mm* in diameter was placed

[2] The lifetime in the quasi-gas-dynamic regime of dense plasma confinement with magnetized collisionless electrons and cold ions, in the case when the electron scattering into a loss cone due to interaction with a resonant microwave pump controls the losses, is determined according to [7] by relation $\tau = L\,K\,/\,V$, where L is characteristic size of the trap, V is ion sound velocity, and K is coefficient that weakly depends on plasma density.

into a mirror magnetic trap formed by two solenoids (duration of the magnetic field pulse was about *13 ms*). The trap length was *25* cm, mirror ratio was *3.2*. The maximum value of magnetic field strength in the plug was *2.3 T*. To evaluate plasma density in the discharge, the factor of transmission of the diagnostic microwave through the plasma (4, 5) was measured. The diagnostic microwave radiation with frequency *35.52 GHz* and polarization corresponding to the ordinary wave was injected into the trap center perpendicularly to the magnetic field. The ions coming out from the plasma along the magnetic field lines were investigated with a two-step (magnetic and electrostatic analysis) five-channel analyzer (6) with mass resolution *3* attached to the discharge chamber through coupling section (7). The pressure of used gas (Argon) was set using a pulse valve and was about or over $3 \cdot 10^{-5}$ *Torr*. Gas inlet put in practice into discharge chamber (see Fig. 1) while pressure in the analyzer and coupling section was low (about 10^{-6} *Torr*). The peculiarity of these experiments was that efficiency of MCI generation was investigated at rather high plasma density (an order of magnitude higher than in traditional ECR sources of MCI). In these experiments the total shielding of diagnostic and high-power microwaves by the discharge was observed, thus testifying that plasma density with value more that $4 \cdot 10^{13}$ cm^{-3} was obtained.

The efficiency of MCI generation and ion energy depend essentially on the gas pressure and power of microwave radiation. Energy of ions flown out from plasma was between *100 eV* and *10 keV*. The typical ion charge state distribution at optimum gas pressure (about 10^{-4} *Torr*) is shown in Fig. 2. For the comparison in the same figure the ion charge state distributions for traditional ECR continuous mode operation sources of MCI with pumping by centimeter wave radiation (from *6* to *18 GHz*) [5, 8, 9, 10] are shown. As it is seen from this figure, the distribution obtained in our experiments is shifted to the larger ionization states (maximum corresponds to ion charge *11-12* while in traditional sources it is about *8*).

Thus, using more powerful and more short-wavelength gyrotron radiation we suppose to succeed in realization of the quasi-gas dynamic regime of plasma confinement that increased $N_e\tau$ parameter and provided the corresponding shift of ion charge state distribution in the direction of larger ionization states.

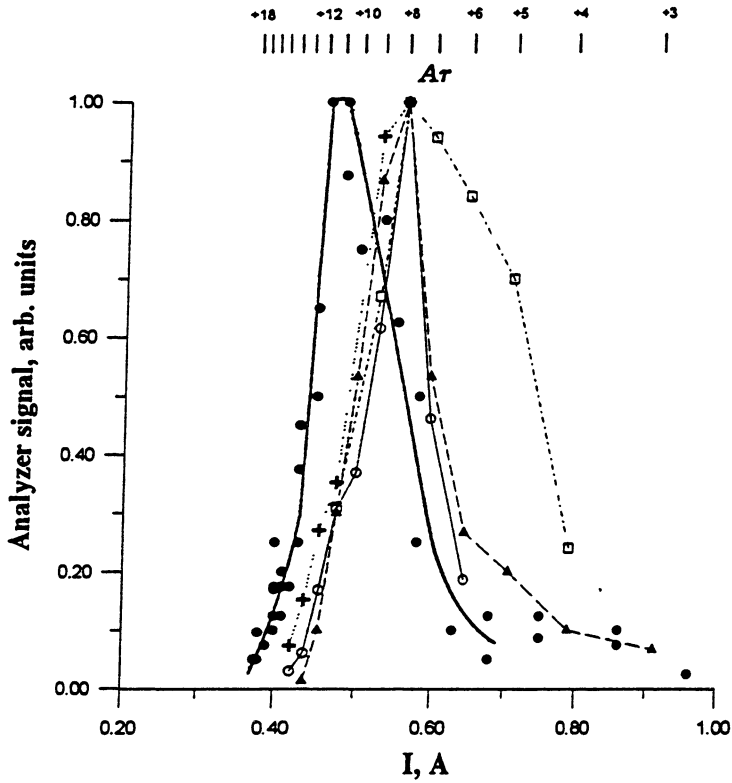

Fig. 2. Dependence of ion analyzer signal on current of analyzer magnet. The magnet currents corresponding the Argon ions with different charges are shown on upper part of the picture. Points are result of our experiments, ▲ - data on charge state distribution of [5], ✚ - [8], ◻ - [9], ○ - [10].

References

1. R. Geller. Colloque de Physique. Supplement au Journal de Physique. 1989. V. 50. C. 1. P. C1-887 - C1-892.
2. Y. Arata, S. Miyake, H. Kishimoto, N. Abe, Y. Kawai. Jap. J. Appl. Phys. 1988. V. 27. №7. P. 1281-1286.
3. J.H. Booske, F.A. Aldabe, R.F. Ellis, W.D. Getty. J. Appl. Phys. 1988. V. 64. № 3. P. 1055-1067.

4. S.V. Golubev, Yu.Ya. Platonov, S.V. Razin, V.G. Zorin. Tech. Phys. Lett. 1994. V. 20. №2. P. 135-137.
5. R.Geller, B.Jacquot, P.Sortais. Nuclear Instruments and Methods in Physics Research. 1986. A 243. P. 244-254.
6. S.V.Golubev, V.G.Zorin, T.N.Zorina, S.V.Razin. Proc. Int. Workshop on "Strong Microwaves in Plasmas". Nizhny Novgorod. 1991. V. 1. P. 485-489.
7. S.V. Golubev, V.E. emenov, E.V. Suvorov, M.D. Tokman. Proc. Int. Workshop on "Strong Microwaves in Plasmas". Nizhny Novgorod. 1994. V. 1. P. 347-375.
8. H. Beuscher. Review of Scientific Instruments. 1990. V. 61. № 1. P. 262-264.
9. T.A. Antaya, S. Gammino. Proc. Int. Workshop on "Strong Microwaves in Plasmas". Nizhny Novgorod. 1994. V. 1. P. 399-413.
10. G.G. Gulbekian, I.V. Kolesov, V.V. Bekhterev, et. al. Joint Institute of Nucler Research Rapid Communication. 1995. №4(72)-95. P. 63-74.

THE MICROWAVE DISCHARGE IN A PLASMA NEUTRALIZER OF ITER INJECTOR

A.A.Skovoroda, V.A.Zhil'tsov

INF, RRC Kurchatov Institute, Moscow, Russia

INTRODUCTION. The basis of the injection method for heating and current drive in tokamak is neutralization of negative hydrogen ions accelerated up to MeV energies. Efficiency of neutralization N (the ratio of H^0 flow to H^- ion current) determines the total efficiency of NBL η (ratio of neutral beam power, P_b, to electric power, P) in many respects. In **Fig.1** is shown, how N varies on linear density, $(n_e+n_a)l$, at high i=0.9 (plasma neutralizer, PN) and low i=0.01 (gas neutralizer, GN) ionization degrees of a target, $i=n_e/(n_e+n_a)$. It is seen that efficiency of neutralization reaches the maximum value for PN at optimum linear density of a target about $2\cdot10^{15}$cm^{-2}. At the characteristic length of ITER PN l=3m we obtain the characteristic density of plasma n_e ~$7\cdot10^{12}$cm^{-3}.

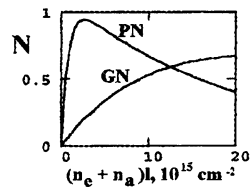

Fig.1. Efficiency of neutralization of 1 MeV ion H^- in hydrogen plasma

At the moment GN with low peak N~60% is used. This is caused by low power efficiency of the known discharge systems for plasma production, when the whole gain in N is spent on plasma production. The problem consists in creation of a system for producing plasma with high efficiency.

REQUIREMENTS AND CONCEPT OF PN. We shall show as the necessity of requirements fulfilment has defined our concept.

Effective confinement of plasma

For ITER conditions we shall estimate the power needed for plasma production, P_{pn}, , at which PN remains effective. We shall proceed from the following quantities: one NBL module power P_b=12.5MW; η with GN, η_{gas}=0.43; η with PN, $\eta_{pn}=0.6(1-P_{pn}/P)$; the total beam cross-section 1.45×0.5m^2 is determined by an existing current density (20mA/cm^2) of negative ions source.

When accepting efficiency enhancement factor η_{pn}/η_{gas}=1.27, then it is allowable to spend on plasma production less than **2MW** of electrical power. The volume of high-ionized plasma with density $7\cdot10^{12}$cm^{-3} will

make more than $10m^3$ and, hence, the power density will make less than **0.2 W/cm^3**. From simple power balance $P_{pn} = n_e V \alpha T_e / \tau \eta_{mw}$ by accepting the following magnitudes of factors: α=10 - cost coefficient, η_{mw}=0.5 - performance coefficient of microwave generator (for reduction of plasma losses and for maintenance of steady state work we use the electrodeless microwave discharge), we shall obtain the following condition on plasma confinement: $T_e[eV]/\tau[ms] < 10$. Two approaches are basically possible: the hot plasma, when the time of life,τ, grows faster then temperature, and the cold plasma, when it is necessary to obtain rather large τ. We consider, that the latter opportunity is more real. At T_e~10 eV τ should be more than 1ms. It can be reached, for example, at plasma confinement in a multipole mirror, where the confinement time does not depend on plasma density and grows with reduction of temperature under the scaling

$$\tau[s] \sim 3 \frac{B_s[T] V[m^3] A^{0.25}}{L_s[m] T_e^{3/4} T_i^{1/4}[eV]},$$

B_s, L_s - magnetic field and total length of magnetic slits. It is visible, that by use of large B_s~1T at rather large volume rather large τ can be realized.

Deviations of ions in PN

The necessary use of 3D plasma confinement results in a problem, connected to the requirement of small (<5 mrad) deviations at passage of ions through PN magnetic system. Fortunately, the magnetic system of the multipole trap allows to use the effect of auto-compensation of large deviations at passage of the end wall in practically complete absence of a magnetic field in the basic volume of a PN [1]. Numerical calculations confirm this opportunity.

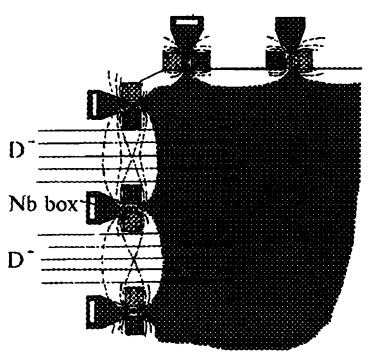

Fig.2. Plasma in multipole mirror

Large ionization degree

The problem consists in obtaining plasma with high ionization degree at low T_e. It is important also to strongly reduce gas flows from PN, than even more to improve parameters of PN in comparison with GN. The geometry

of a multipole trap (see **Fig.2**) allows to use the following opportunities: (a) gas screening in PN centre due to large volumes of a plasma; (b) small gas pressure in the PN chamber at large pressure in gas boxes; (c) use of a superpermeation of Nb boxes for direct absorption of plasma flows on the PN walls.

The absence of a magnetic field in the basic volume of a trap provides a free movement of charged particles, that makes it possible to use gas ionization mainly on the plasma periphery.

Concept of PN

In **Table 1** the basic requirements to PN for the single ITER NBL module are specified.

Table 1

l / V	3m / >10m^3
n_e / T_e	7 10^{12}cm^{-3} / <10eV
τ	> 1 ms
dP/dV	~ 0.1 W/cm^3
i	> 0.3
divergence	< 5 mrad

Our **concept** is based on use of a multipole magnetic trap with the following properties: (a) closed ∇B drift of electrons, (b) large B_s>1T, (c) large magnetic field on a plasma surface 1kG, (d) large PN volume V>10m^3. The plasma will be produced in steady state by the electrodeless microwave discharge at gas pressure less than 10^{-4}torr at mainly collisionless character of microwave energy absorption.

MICROWAVE DISCHARGE IN MULTIPOLE TRAP. Use of the electrodeless discharge provides steady-state work of PN by the most effective transfer of energy to electrons (for example, in ECR conditions), the ionization ability of which provides plasma production. The physics of such discharges in multipole traps is *not investigated* practically.

A major factor determining character of such discharges is the value of the cut-off density, when the microwaves cannot freely propagate through PN. This fact defines the necessity of use in ITER of the microwaves with high frequencies, 20-30 GHz, i.e. the gyrotrons. However, of large interest is the research of the opportunity to use the klystron type generators with lower frequency, 7 GHz.

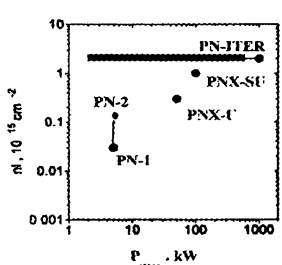

Fig.3. PN installations line.

Installations of PN line

For an experimental investigation of the above questions in INF RRC Kurchatov Institute there is the line of PN type installations, shown in **Fig.3**.

In **Table 2** the modern status of these installations is shown.

The experiment on PN-1 device (see **Fig.4**) has shown, that by stationary work in 70l chamber the plasma density $5 \cdot 10^{11} cm^{-3} = 7 n_{cut\text{-}off}$ was produced at low absorbed power density $0.02 W/cm^3$. Thus at T_e=4-10eV the ratio T_e/τ=10 was obtained at the ionization degree 0.1.

Table 2

Device	Status	$n_e l$, $10^{15} cm^{-3}$	V, m^3	P_{mw}, kW	f, GHz	B_{ss}, T	i	Type of mag.system
PN-1	exp.95-96	0.03	0.07	5	2.45	0.2	0.1	Perm.Magn.
PN-2	exp.07.96	>0.03	0.07	5+2	2.5+7	0.2	>0.1	Perm.Magn.
PNX-U	constr.96	0.3	0.7	50	7	0.5	0.2	CopperCoils
PNX-SU	beam exp. proposal	>1	1	100	7	1	0.3	SuperCond. +Copp.Coils
N-ITER	design	2	>10	>500	>18	>1	>0.3	SuperCond.

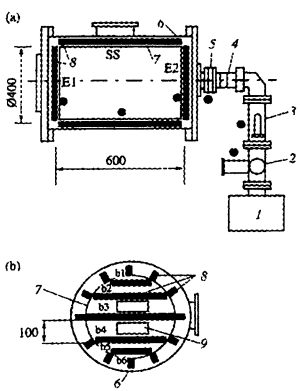

Schematic of the PN-1 device (a) top view, (b) E2 end view (1) magnetron (2) ferrite circulator (3) tunable attenuator, (4) matching transformer, (5) vacuum-sealed quartz waveguide window (6) vacuum chamber, (7) insert, consisting of isolated cylindrical side surface (SS) and plane end surfaces (E1 and E2), (8) permanent magnets and (9) MW input. b1–b6 are the belt numbers. Points note the locations of calorimeters

Fig.4. PN-1 device

The original surface-type discharge was realized, when the microwaves were excited in *plasma wavequides* a×b, formed by plasma surface and in a metal chamber wall see **Fig.5**. The plasma was heated on periphery in conditions of upper hybrid plasma resonance. The gas ionization takes place on periphery. The detail investigation of this discharge can be found in work [2].

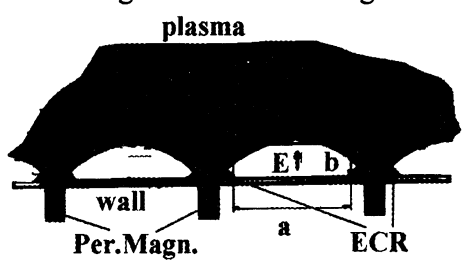

Fig.5. Formation of plasma waveguide in multipole mirror PN-1 [2].

On PN-1 the opportunity to use superpermeation of Nb tubes 0.1 mm thick for pumping hydrogen was checked too. At fall of 0.25A plasma flow on a tube in stationary conditions up to 33 % of the flow penetrated inside the tube. Thus the gas pressure inside the tube in 1000 time exceeded pressure in the discharge chamber.

In **Fig.6** constructing installation PNX-U is shown. On this larger device three variants of the microwave discharge is planned to test.

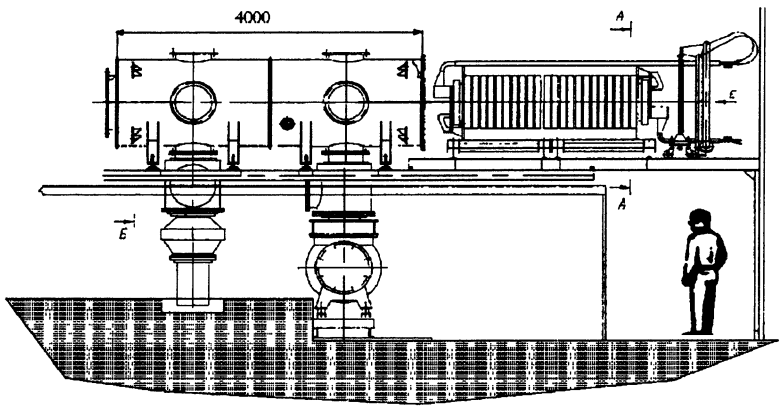

Fig.6. PNX-U installation (multipole magnetic system is moved out from vacuum vessel).

Various types of the microwave discharge

In **Fig.7** PNX-U microwave system is shown.

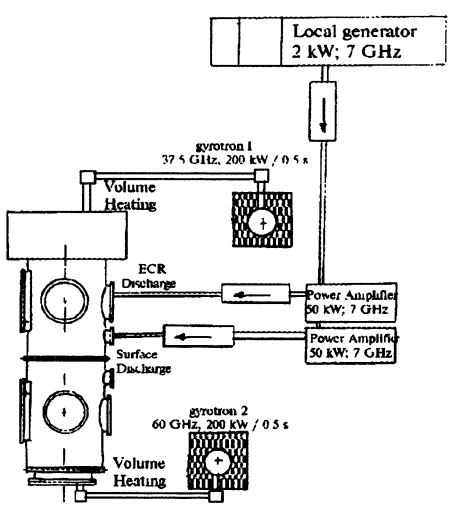

Fig.7. PNX-U microwave system.

GEOMETRY OF SURFACE & ECR DISCHARGES

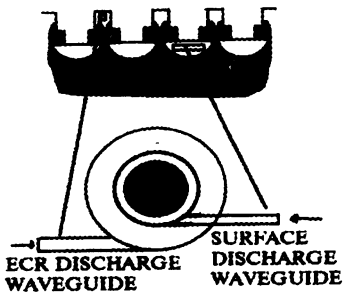

GEOMETRY OF VOLUME HEATING

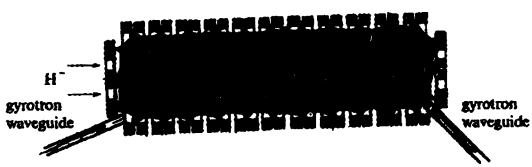

Fig.8. Various types of the microwave discharge in PN.

The *first* type of discharge organization is the same as in PN-1 installation and uses the excitation of circular plasma wavequides in conditions, when plasma density is higher then the cut-off density. In **Fig.8** geometry of such discharge is shown.

The *second* type uses ECR for electron heating at plasma density close to critical. The ECR area is concentrated close to gas boxes, therefore, microwave power is favourable for entering direct into these boxes. Experiments on such discharge organization are not known. The *third* type is associated with opportunity of volumetric heating of electrons on collisions at multipass (1-2 wall reflections) propagation of microwaves. For these purposes gyrotrons is planned to use.

References

1. Skovoroda A.A. Preprint IAE-5544 / 6, Moscow, 1992
2. Zhil'tsov V.A., Kosarev P.M., Skovoroda A.A. Plasma Phys. Reports, 1996, v.**22**, No.3, pp. 246-258

CHARGE AND MASS TRANSPORT IN INHOMOGENEOUS SOLIDS INDUCED BY MICROWAVE FIELDS

K.I. Rybakov and V.E. Semenov

Institute of Applied Physics, Russian Academy of Sciences,
Nizhny Novgorod, Russia

In recent years, many independent experiments in materials science and technology have established the presence of significant nonthermal influence of microwave electromagnetic fields of moderate intensity on the mass and charge transport in solids [1]. In our previous papers [2,3] we proposed a theoretical explanation of these observations based on the concept of the averaged ponderomotive action of the microwave field. This theory has received a recent experimental confirmation [4]. In this paper, the theoretical results are reviewed with an emphasis on the methodology of defining and obtaining the averaged ponderomotive force.

The fact that the spatially nonuniform high-frequency electromagnetic field influences the time-averaged motion of charged particles is well known in physics. The slowly varying force acting on a particle in such a field is called the averaged ponderomotive force [5]. In general, it is quadratic with respect to the field strength and depends on the degree of its nonuniformity. However, an exact definition of the ponderomotive force can be given only within a chosen mathematical model of the dynamic system. Consequently, several different physical quantities may be called the ponderomotive force. The most important cases are reviewed below.

1. The *Euler hydrodynamics approach* uses the following basic equations:

$$\begin{aligned} &\frac{\partial N}{\partial t} + \nabla \cdot (N\mathbf{v}) = 0; \\ &m\left[\frac{\partial \mathbf{v}}{\partial t} + (\mathbf{v}\cdot\nabla)\mathbf{v}\right] = e\mathbf{E} + e\left[\frac{\mathbf{v}}{c}\times\mathbf{H}\right] - \nu\mathbf{v}, \end{aligned} \tag{1}$$

where N is concentration of particles (per unit volume), $\mathbf{v}$ is hydrodynamic velocity, m and e are mass and charge of particles, $\mathbf{E}$ and

$\mathbf{H}$ are electric and magnetic vectors of the field ($\mathbf{E}$, $\mathbf{H} \propto \exp(i\omega t)$), and ν is friction coefficient, or collision frequency.

Defining within this approach the ponderomotive force (per unit volume), $\mathbf{f}_1$, as the total averaged force exerted by the electromagnetic field,

$$\mathbf{f}_1 = m\langle N\rangle \left[\frac{\partial\langle\mathbf{v}\rangle}{\partial t} + (\langle\mathbf{v}\rangle\cdot\nabla)\langle\mathbf{v}\rangle + \nu\langle\mathbf{v}\rangle\right], \tag{2}$$

where angular brackets denote time averaging, and solving Eqs.(1), we obtain the following expression for $\mathbf{f}_1$:

$$\mathbf{f}_1 = -\frac{\omega_p^2}{\omega^2+\nu^2}\nabla\left\langle\frac{\mathbf{E}^2}{8\pi}\right\rangle + \frac{\omega_p^2}{\omega^2+\nu^2}\frac{\nu}{c^2}\left\langle\frac{c}{4\pi}[\mathbf{E}\times\mathbf{H}]\right\rangle, \tag{3}$$

where $\omega_p = \sqrt{4\pi e^2 N/m}$ is Langmuir frequency. The average ponderomotive force calculated within the Euler hydrodynamics approach thus consists of two terms, the first of which is known as the Miller force, and the second can be interpreted as the absorbed momentum of the electromagnetic field.

2. The equation of motion for the *single particle approach* has the following form:

$$m\frac{\partial^2\mathbf{r}}{\partial t^2} = e\mathbf{E}(\mathbf{r},t) + \frac{e}{c}\left[\frac{\partial\mathbf{r}}{\partial t}\times\mathbf{H}(\mathbf{r},t)\right] - \nu\frac{\partial\mathbf{r}}{\partial t}, \tag{4}$$

where $\mathbf{r}$ is radius-vector of the particle. The ponderomotive force is defined within this approach as

$$\mathbf{f}_2 = m\langle N\rangle\left(\left\langle\frac{\partial^2\mathbf{r}}{\partial t^2}\right\rangle + \nu\left\langle\frac{\partial\mathbf{r}}{\partial t}\right\rangle\right). \tag{5}$$

The expression for $\mathbf{f}_2$ obtained from the solution of Eq. (4) can be presented in the following form:

$$\mathbf{f}_2 = \mathbf{f}_1 + \frac{\omega_p^2}{\omega^2+\nu^2}\frac{\nu}{4\pi\omega^2}\left\langle(\mathbf{E}\cdot\nabla)\frac{\partial\mathbf{E}}{\partial t}\right\rangle. \tag{6}$$

Thus, in the presence of friction the ponderomotive force obtained within the single particle approach is different from the previous case.

3. Consider now the same hydrodynamics equations (1) but written in terms of *particle fluxes* $\mathbf{J} = N\mathbf{v}$:

$$\frac{\partial N}{\partial t} + \nabla \cdot \mathbf{J} = 0;$$
$$m\left\{\frac{\partial \mathbf{J}}{\partial t} + \left[(\mathbf{J}\cdot\nabla)\frac{\mathbf{J}}{N} + \mathbf{J}\left(\nabla\cdot\frac{\mathbf{J}}{N}\right)\right]\right\} = eN\mathbf{E} + \frac{e}{c}[\mathbf{J}\times\mathbf{H}] - \nu\mathbf{J}. \tag{7}$$

The ponderomotive force is

$$\mathbf{f}_3 = m\left\{\frac{\partial\langle\mathbf{J}\rangle}{\partial t} + \left[(\langle\mathbf{J}\rangle\cdot\nabla)\frac{\langle\mathbf{J}\rangle}{\langle N\rangle} + \langle\mathbf{J}\rangle\left(\nabla\cdot\frac{\langle\mathbf{J}\rangle}{\langle N\rangle}\right)\right]\right\} + \nu\langle\mathbf{J}\rangle, \tag{8}$$

and solving Eqs.(7) gives

$$\mathbf{f}_3 = \mathbf{f}_2 + \frac{1}{\omega^2+\nu^2}\frac{\nu}{4\pi\omega^2}\left\langle(\mathbf{E}\cdot\nabla)\left(\omega_p^2\frac{\partial\mathbf{E}}{\partial t}\right) + \mathbf{E}\left(\nabla\cdot\omega_p^2\frac{\partial\mathbf{E}}{\partial t}\right)\right\rangle. \tag{9}$$

In the presence of friction this expression differs from both (3) and (6). It can be seen that if the electric field has linear polarization, i.e.,

$$\mathbf{E} = \mathbf{A}(\mathbf{r})\exp[i\varphi(\mathbf{r})]\exp(i\omega t) + \text{c.c.}, \quad \mathbf{A} = \mathbf{A}^*, \tag{10}$$

then the last term in Eq. (9) is zero, and $\mathbf{f}_3 = \mathbf{f}_2$. Another interesting observation is that the ponderomotive force defined within the flux hydrodynamics approach exists even in the uniform quasielectrostatic field, when $\mathbf{f}_1 = \mathbf{f}_2 = 0$.

The physical nature of the difference between expressions (3), (6), and (9) can be illustrated with the following considerations. When friction is significant, Eqs. (2), (5), and (8) reduce, respectively, to

$$\begin{aligned}\mathbf{f}_1 &= m\nu\langle N\rangle\langle\mathbf{v}\rangle;\\ \mathbf{f}_2 &= m\nu\langle N\rangle\langle\partial\mathbf{r}/\partial t\rangle;\\ \mathbf{f}_3 &= m\nu\langle\mathbf{J}\rangle.\end{aligned} \tag{11}$$

Since generally $\langle\mathbf{J}\rangle \neq \langle N\rangle\langle\mathbf{v}\rangle$, there is a difference between the ponderomotive forces calculated within the Euler and flux hydrodynamics approaches:

$$\mathbf{f}_3 - \mathbf{f}_1 = m\nu\langle(N - \langle N\rangle)(\mathbf{v} - \langle\mathbf{v}\rangle)\rangle. \tag{12}$$

When comparing the single particle and flux hydrodynamics approaches, we should note that $\langle\mathbf{J}\rangle \neq \langle N\rangle\langle\partial\mathbf{r}/\partial t\rangle$ when there is rotational motion of particles. An analysis of Eq. (9) shows that if ν is

spatially uniform, then $\nabla \cdot (\mathbf{f}_3 - \mathbf{f}_2) = 0$, and the particle fluxes generated by the ponderomotive force do not redistribute matter within the system. Conversely, in systems with nonuniform transport properties the ponderomotive force can cause directional mass transport – even if the electric field is uniform.

As shown below, for solid state applications the following limiting case is of special interest:

$$\nu \gg \omega_p \gg \omega. \tag{13}$$

In this limit, the ponderomotive force defined according to the flux hydrodynamics approach takes an especially simple form [3],

$$\mathbf{f}_3 = \langle \rho \mathbf{E} \rangle, \tag{14}$$

when calculated within the free quasielectrostatic problem

$$\begin{gathered} \nabla \times \mathbf{E} = 0; \\ \nabla \cdot (\epsilon \mathbf{E}) = 0; \\ \epsilon = 1 - \frac{\omega_p^2}{\omega(\omega - i\nu)}. \end{gathered} \tag{15}$$

In Eq. (14) $\rho = (\nabla \cdot \mathbf{E})/4\pi$ is density of the field-induced space charge.

It should be also mentioned that in most common cases a reasonable estimate for the magnitude of the ponderomotive action is the value of the radiation pressure of the field,

$$p \sim \mathbf{E}^2/8\pi. \tag{16}$$

The transport properties of solids are determined by their microstructure. In crystalline solids, one of the predominant mechanisms of mass transport is vacancy transfer. As long as relative concentration of vacant sites in the crystalline lattice is low, it is convenient to apply the ideal gas treatment to the vacancies. In ionic crystals, the vacancies carry an effective electric charge and, therefore, comprise the so-called vacancy plasma. Condition (13) translates for such plasma into

$$\omega\tau \ll \frac{d}{\lambda} \ll 1, \tag{17}$$

where τ is time interval between atom hops, d is interatomic distance, $\lambda = \sqrt{4\pi e^2 N/kT}$ is Debye–Hückel radius, N is vacancy concentration. This condition is valid for most ionic crystalline solids in the temperature and frequency ranges used in microwave processing technologies.

According to our previous work [2,3], the action of the ponderomotive force on ionic crystals can generate mass transport much more efficiently than the mechanical stresses equal to the field radiation pressure (16) do. Such enhanced performance results from selective nature of the ponderomotive action in solids. This selectivity manifests itself in a number of aspects. One of them is selectivity with respect to recipients of the action. Specifically, the field acts on the charged vacancies, i.e. directly on the atoms neighbouring an empty site of the lattice (the only atoms that are able to move), whereas the mechanical stresses are applied to the entire crystal in which most of the atoms are fixed. Due to this effect, the ponderomotive action is equivalent to the action of the mechanical stresses which are $(N\Omega)^{-1}$ times greater than the radiation pressure (Ω is the vacancy volume) [2].

Another aspect of the selectivity of the ponderomotive action is associated with the spatial distribution of this action in inhomogeneous solids. An analysis of the distribution of the ponderomotive force (14) within a crystalline body having a thin near-surface amorphized layer with higher vacancy diffusivity shows [3] that predominant in such body are the matter flows driven by the tangential component of the field within this layer. The ponderomotive action is therefore applied to the spatial region with the highest mobility of vacancies, unlike the mechanical stresses which are applied uniformly to the entire body. The enhancement factor derived from this effect is $(D_b/D_a + a/\Lambda)^{-1}$, where D_b is bulk diffusivity, D_a is characteristic value of the vacancy diffusivity in the amorphized layer, a is thickness of the layer, and Λ is characteristic size of the crystal.

The total enhancement factor is therefore

$$[N\Omega(D_b/D_a + a/\Lambda)]^{-1}. \tag{18}$$

For example, in the conditions of microwave sintering of ceramics, (18) can be as high as 10^8. This means that the ponderomotive action

of the microwave field of 1 kV/cm (which is a typical magnitude for the microwave processing technologies), its radiation pressure being about 0.1 Pa, results in the matter fluxes (e.g., in plastic deformation of ceramic particles) comparable to those caused by mechanical stresses of 10^7 Pa. It is known that stresses of similar or even smaller magnitude govern the conventional oven sintering. Thus, the ponderomotive action of microwave field on solids is highly significant and must manifest itself in the experiment.

Acknowledgement

This work was supported in part by the Russian Basic Research Foundation through Grant No. 95-02-05000-a.

References

1. S.J. Rothman, in *Microwave Processing of Materials IV*, edited by M.F. Iskander, R.J. Lauf, and W.H. Sutton, MRS Symposium Proceedings Vol. 347 (Materials Research Society, Pittsburgh, 1994), pp. 9 – 18.

2. K.I. Rybakov and V.E. Semenov, Phys. Rev. B **49**, 64 – 68 (1994).

3. K.I. Rybakov and V.E. Semenov, Phys. Rev. B **52**, 3030 – 3033 (1995).

4. K.I. Rybakov *et al.*, "Dynamics of microwave-induced currents in ionic crystals", submitted to Phys. Rev. B (1996), *see also* J.H. Booske, this Proceedings.

5. A.G. Litvak, in *Reviews of Plasma Physics*, edited by M.A. Leontovich (Consultants Bureau, New York, 1986), Vol. 10, p.294.

CHLOROFLUOROCARBONS (CFC's) DESTRUCTION AND TRANSFORMATION IN A MICROWAVE GAS DISCHARGE

S.I.Gritsinin, I.A.Kossyi, M.A.Misakyan, V.P.Silakov

General Physics Institute, Moscow, Russia

The present work is devoted to the experimental investigations of microwave pulse discharges in nitrogen or argon mixtures with chlorofluorocarbons (CFC's). It is known that such discharges at high gas pressure and subthreshold electric fields are strongly contracted, and contraction regions are the sources of intensive radiation in IR, visible and UV ranges. This radiation excites the electron and vibrational levels of molecules and induces their dissociation and ionization. Our recent investigations of such discharges have shown their high plasma-chemical efficiency. We supposed that such discharges could effectively transform freons into modifications which would be more safe for ozone layer of the Earth.

The present experimental work was carried out to determine the efficiency of modification of ozone-destroying freons into safe for ozonosphere compounds with the help of microwave discharges. The investigations of transformation dynamics have been carried out for freons introduced as an admixture into different diluting gases under the action of pulse microwave discharges. The identification of produced products and particle balance of evolutionating gas-chemical mixture were realized.

The glass retort (diameter was *ac* 10 cm and volume was *ac* 1.4 litter) used as a reactor was placed in the focal region of converging microwave beam. Microwave parameters were: irradiating wavelength 2.5 cm; pulse power **P**=300 kW (S=30 kW/cm^2); pulse repetition frequency 0.5-1 Hz. The discharge in the retort was initiated by metal needles and spread towards the radiation source. The discharge appears as the series of sharply nonuniform and bright shining filaments.

We investigated the behaviour under discharge action of simple freons - chlorofluoromethanes - such as F-10, 11, 12 and 13, mixed with argon, nitrogen and air. Main attention was turned to the investigation of 10% mixture of F-12 with argon at total pressure about 100 Torr.

Both active and passive emission spectroscopic techniques were used. The Cl_2 concentration was measured by an absorption of the diagnostic radiation

near 3400 A wavelength. The complex products of freon decomposition were examined by an absorption of diagnostic IR radiation.

In fig. 1 the behaviour of parent F-12 and destruction products concentrations is shown in time.

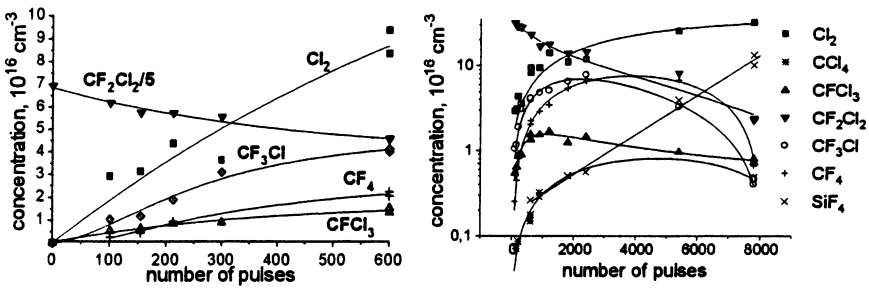

Fig. 1. The concentrations of parent F-12 and products of transformation.

The main products of F-12 decomposition are chlorofluoromethanes of CF_nCl_{4-n}, type, n=0÷4. There were also a more complex compounds, for example C_2F_4, C_2F_6, $C_2F_4Cl_2$ and others, but their concentrations were small and did not exceed 10^{16} cm^{-3}. Besides, the considerable amount of Cl_2 was registered. At a small number of pulses F-13 predominates. In this case the number of F-13 particles represents around 40% of parent F-12 destroyed molecules. The considerable quantity of CF_4 particles was produced too. From these data we can conclude that the transformation degree of F-12 to F-13 and F-14 reached 70%, the chlorine-enriched freons F-10 and F-11 being produced in lower quantities.

In fig. 2 the quantity change of C, Cl and F atoms which were integrated over all identified compounds is shown. Cl and F atoms were registered almost completely. If any unregistered compounds were also present in this case, then their concentration may be neglected. As for C atoms we have the great disbalance - carbon atoms concentration decreased.

It was shown in the course of measurements that emission intensity of Swan band of C_2 molecules was dropping. The intensity of this emission owes its origin to the carbon-containing molecules in gas phase. Thus, this fact is attributable either the erraping of carbon atoms from gas phase onto the retort walls, or to the forming of molecules with stronger bonding of carbon atoms. Thus, on the initial stage practically all losses of parent freon are connected with the transformation to fluorine-enriched modifications of freon.

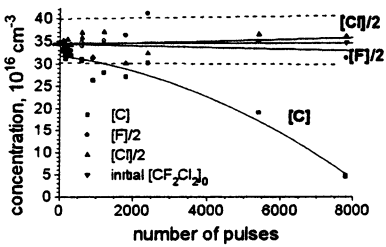

Fig.2. Balance of atoms.

The released surplus chlorine is mainly in the molecular form. Further the growth of the concentration all these products except of molecular chlorine stops. Besides SiF_4 appears. Under prolonged microwave action the degradation of both parent freon and all products was observed excepting the Cl_2 and SiF_4 whose concentrations increased all time and reached their maximum possible values.

It is known from our experiments that initiated microwave gas discharge at high pressure has complicated space-time structure which is universal for all gases and gas mixtures [1,2]. Such discharge represents the series of high ionized channels (filaments) stretched along the electric field vector. The filament appearance is associated with kinetic and ionization instabilities. Filament plasma is a strong source of radiation in UV, visible and IR spectral ranges. Around the filaments the gas molecules are appreciably excited on vibrational and electron states and gas medium is heated by shock wave.

It is natural to suppose that freon molecules mainly decay in the regions where plasma concentration and temperature have maximum values, that is within filaments. The characteristic number of pulses for freon decay is around 1000 and if in each pulse freon is completely destroyed in any volume, then this volume should be no less than 1.4 cm^3. This value essentially exceeds the total filament volume which is around 0.1 cm^3 [3].

Thus we come to the conclusion that for explanation of freon decay it is necessary to suppose the presence of plasma-chemical transformation processes

$$CF_2Cl_2^* + CF_2Cl_2^{**} \Rightarrow CF_3Cl + CFCl_3$$

$$\Rightarrow CF_4 + CCl_4 .$$

Chlorine appears in filaments and around the filaments due to photodissociation of chlorine-containing products. Fast recombination leads to molecular chlorine formation. The stable carbon radical CF_2 takes part in the reactions forming complex compounds:

$$CF_2 + CF_4 + M \Rightarrow C_2F_6 + M$$

$$CF_2 + CF_2Cl_2 + M \Rightarrow C_2F_4Cl_2 + M$$

It is important that after fairly long-time of microwave action we observe formation of considerable quantity of SiF_4. Finally, almost all fluorine atoms

transforms from parent freon into SiF_4. We can suggest the following known reactions with generation of oxygen or carbon oxide:

$$2CF_2+SiO_2 \Rightarrow SiF_4+2CO$$

$$2F_2+SiO_2 \Rightarrow SiF_4+O_2$$

The geterogenic reactions on the retort walls are possible too:

$$2\ CF_2Cl_2+SiO_2 \Rightarrow SiF_4+CO_2+CCl_4$$

where one reagent must be excited at least. These reactions can help to solve the problem of removing of carbon atoms, because of the high bond energy of carbon atoms in these oxides.

Conclusion:

1. The type and quantity of detected products after microwave action on freon mixtures sends us in supposition that major channel of parent freon destruction are chemical transformation processes in nonequilibrium plasma resulting in interaction between vibrationally or/and electron excited molecules of freons.
2. The gas volume which the destruction takes place in essentially exceeds the released energy volume (filament volume), but exactly the discharge contraction regions play the dictating role due to the fact that dense and hot plasma in these regions is the source of radiation exciting the gas in near-filament regions.
3. The UV radiation from filaments realizes not only initiation and intensification of plasma-chemical processes but performs the function of rejection of chlorine-containing products. As a result the main products of transformation are fluorine-enriched products such as F-13 and F-14 freons. These freon modifications almost are not subjected to photodissociation under sun UV radiation action.

Thus, we can suppose that the microwave discharges show considerable promise as a means for cleaning of atmosphere from ozone-destroying freons and for industrial transformation of these freons into the safe modifications.

References.

1. Batanov G.M. et al.//in:"Plasma Physics and Plasma Electronics" Ed. by L.M.Kovrizhnykh, 1989, Nova Science Publishers, Commack, pp241-282.
2. Askaryan G.A., Batanov G.M. et all.// - J. Phys. D: Appl. Phys., 1994, Vol. 27, No 6, pp. 1311-1318.
3. Akhvlediani Z.G., Barkhudarov E.M. et al. Sov. Phys. Plasma J., 1996, v. 22, N 5.

Characteristic Properties of the Microwave Breakdown Wave in Nitrogen and Oxygen

G. M. Batanov, I. A. Kossyi, N. I. Malykh *, *A. A. Matveev* **, *A. V. Sapozhnikov, V. P. Silakov* **

General Physics Institute, Moscow, Russia
*Phys. Technical Institute, Sukhumy, Georgia
**App. Mathemetics Institute, Moscow, Russia

Recently the role of various elementary processes in dynamics of the discharge development has become to be taken into account in studying microwave discharges in molecular gases. So far the most attention was devoted to the electron detachment from negative oxygen ions during the plasma decay [1--3]. As it was shown in [1], the plasma decay in the air is retarded with increase in the energy deposition. In [2] the electrone detachment was used to explain the electron density growth in nonself-sustaining discharge. In [3] the electrone detachment effect was explained by reactions with atomic and excited oxygen. Meanwhile, it has been shown in [4--7] that associative ionization leads not only to maintaining the "long-living" plasma but to the explosive growth of the electron density in the microwave field, which changes the discharge electrodynamics.

One can expect that, in addition to the associative ionization caused by the storage of metastable atoms and molecules excited by the electron impact, the storage of the negative ions in discharges including oxygen or water vapor can also lead to the explosive growth of the electron density. In this connection, it is interesting to follow the time evolution of the electron density in discharges in nitrogen and oxygen, which proceed in wide-aperture microwave beams. For a pressure in the range 10--20 Torr the discharge in these gases is a breakdown wave in character (see, for example, [8, 9]); in the case of weakly converging beams, the effect of ionization-field instabilities leading to the plasma stratification and increase in the electron density up to and above the critical value is reduced. Therefore, in such discharges the role of the kinetic processes can manifest itself most clearly.

Experiments were performed with gyrotron radiation with a wave length of 8 mm and a power of 500 kW. A Gaussian beam with weak ellipticity was focused inside the vacuum chamber with a polistirene lens

and had the characteristic radius a_F = 1.8 cm in the focal plane and the characteristic caustic length $l_F = ka_F^2$ = 25 cm. The variable quantities were the working gas pressure (10--20 torr) and the microwave pulse duration.

Typical photos of the discharge in nitrogen and oxygen are shown in Fig. 1. For small pulse duration the discharge is a single or several uniformly luminous plasmoids aligned along the microwave beam axis (Figs. !a, 1c). Cross dimension of plasmoids is somewhat less than 1 cm. With increase in the radiation pulse duration (Figs. 1b, 1d) plasmoids appear in the region behind the focal plane, both in nitrogen and oxygen. In other aspects the discharge luminosity in these gases is different in character. In oxygen a weakly nonuniform wide luminosity region (with a cross section of about 3 cm) appears, which occupies both the focal region and the region behind the focal plane. With increase in the pulse duration the luminosity region moves along the beam towards the radiation flux. In the nitrogen we did not observe the expansion of the luminosity in the focal region. In addition to the plasmoids located along the axis, chaotically located plasmoids appear outside and behind the focal regions; the brightness of these plasmoids is larger than that of the axial objects. The time behavior of the discharge luminosity from the focal region, which is registered by the photomultiplier, is also different in both gases (Fig. 2). In nitrogen the intense luminosity is seen at the leading edge of the microwave pulse followed by the almost constant weak signal during the rest of the discharge (Fig. 2a). In oxygen the second peak with the sharp leading edge appears after the first one, then the luminosity decreases down only to half the initial value. Sometimes, a third peak of radiation is registered.

The plasma density was measured by the phase shift with help of the interferometer with a wave length of 2 mm. The space resolution was 1 cm. The diagnostic beam axis was placed at a distance of 5 cm from the center of the caustic towards the lens. As it is seen in the oscilloscope traces of the interferometer phase detector signals (Fig. 3), evolution of the electron density is different in discharges in nitrogen and oxygen. In the case of nitrogen, the electron density reaches its maximum during the leading edge duration of the gyrotron pulse (1 μs) followed by the smooth density decrease during the powerful radiation pulse and exponential decay after the end of the pulse. In oxygen the electron

density has a spike during the breakdown and becomes to drop even before the end of the microwave pulse. If the pulse duration is sufficiently large ($\tau_i > 3\ \mu$s), the second spike twice as large as the first one appears, as a rule. This increase in the electron density begins at the instant when the discharge luminosity is maximum. The electron density growth is then replaced by the exponential decrease with the characteristic time equal approximately to 3 μs. The third spike can follow the second one, as it can be seen in Fig. 3d. It should be note that if the microwave pulse is shortened, the second spike of the electron density, which usually appears before stopping the action of the electric field, reaches its maximum value after this action has stopped.

After having observed all the totality of the experimental results, we assume the following pattern of development of the microwave discharge in nitrogen and oxygen.

If the experiment is performed in the regime typical of our measurements (the field amplitude is 6 kV/cm), in which the field is much greater than the threshold one, then the gas breakdown occurs at the leading edge of the microwave pulse. This is confirmed by the spike at the leading edge of the signal from the detector located at the backside wall of the vacuum chamber at the beam axis (this detector registers the intensity of radiation passed through the discharge) (Figs. 3b, 3d) and by the sharp leading edge of the photomultiplier signal (Figs. 2a, 2b). Growth of the plasma density in all the region located along the caustic length leads to the field attenuation in the focal region due to refraction and absorption. In this case, the plasma acts as a diversing lens and shifts the focal region of the Gaussian beam further from the lens. Similar effect has been observed by I.A. Kossyi and co-authors in 1972. The formation of plasmoids in the region behind the focal plane and increase in the power registered at the beam axis behind the discharge (Figs. 3b, 3d) confirm this conclusion. Attenuation of the field in the focal region results in limiting the electron density in the first maximum at a level of $2\text{--}3.10^{12}$ cm^{-3} and in its decreasing during the continuing action of radiation. The strong decrease in the discharge luminosity in nitrogen seems to be due to the larger field attenuation in the focal region by refraction and absorption. One can assume this effect to be caused by the associative ionization resulting in the slower decay of the plasma density with time [10]. Earlier we observed similar retarded relaxation of the nitrogen gas-discharge plasma [11].

In the oxygen discharge the radiation "refocusing" and drop in the plasma density cause the repeated breakdown wave. Ionization caused by the active particles storage is clearly seen, as the growth of the electron density continues even after the end of the microwave pulse. For the discharge in oxygen numerical calculations were performed by the simplified kinetic procedure [12] for conditions similar to the experimental conditions (Fig. 4). The calculations show that after the field is switched off, the electron density spike appears on account of the electron detachment, when the dissociative attachment in the high field is replaced by the weak three-particle attachment.

Thus, a substantial distinction is observed in dynamics of the development of the microwave ionization wave in nitrogen and oxygen. The results similar to those obtained in the discharge in oxygen we obtained also by using the air, water vapor as well as water vapor--nitrogen and water vapor--oxygen mixtures as a working gas.

This work was supported by the Russian Foundation for Basic Research, project no. 96-02-16162a.

REFERENCES

1. Vikharev, A.L., Ivanov, O.A., and Stepanov, A.N., Zh. Tekh. Fiz., 1984, vol. 64, no. 8, p. 1617--1619.

2. Golubev, S.V., Gritsinin, S.I., Zorin, V.G., et al., High-Frequency Discharge in Wave Fields, Gorkii, 1988, p. 136--197.

3. Baiadze, K.V., Kulikov, V.N., and Mitsuk, V.E., VIII All-Union Conf. on Physics of Low-Temperature Plasma, Minsk,1991, p. 45--46.

4. Silakov, V.P., Fiz. Plazmy, 1988, vol. 14, no. 10, p. 1209--1213 [Sov. J. Plasma Phys. (Engl. Transl.), 1988, vol. 14, no. 10, p. 708].

5. Silakov, V.P., Preprint of Moscow Engin. Phys. Institute, Moscow, 1990, no. 10, p. 12.

6. Bezmenov, I.V., Rusanov, V.V., and Silakov, V.P., Preprint of Keldysh Institute of Appl. Mathematics, Russ. Acad. Sci., Moscow, 1992, no. 30, p. 28.

7. Bezmenov, I.V., Rusanov, V.V., and Silakov, V.P., Trudy IOFAN (Transact. of Inst. General Phys., Russ. Acad. of Sci., Moscow: Nauka, 1994, vol. 47, p. 74--107.

8. Vikharev, A.L., Gil'denburg, V.B., Kim, A.V., Litvak, A.G., and Semenov, V.E., High-Frequency Discharge in Wave Fields, Gorkii, 1988, p. 41--135.

9. Inovenkov, I.N., Kim, A.V., Rakova, E.I., Semenov, V.E., and Chukhin, A.E., Preprint of Inst. of Appl. Phys., Russ. Acad. of Sci., Moscow, 1990, no. 271, p. 28.

10. Gritsinin, S.I., Kossyi, I.A., Silakov, V.P., Tarasova, N.M., and Terekhin, V.E., Teplofiz. Vys. Temp., 1986, vol. 24, no. 4, p. 663--667.

11. Askar'yan, G.A., Batanov, G.M., Gritsynin, S.I., Korchagina, E.G., Kossyi, I.A., Malykh, N.I., Misak'an, M.A., Silakov, V.P., and Sapozhnikov, A.V., Zh. Tekh. Fiz., 1996, vol. 66, no. 3, p. 19--27.

12. Kossyi, I.A., Kostinskii, A.Ya., Matveyev, A.A., and Silakov, V.P., Plasma Sources Sci. Tekhnol., 1992, vol. 1, p. 207--220.

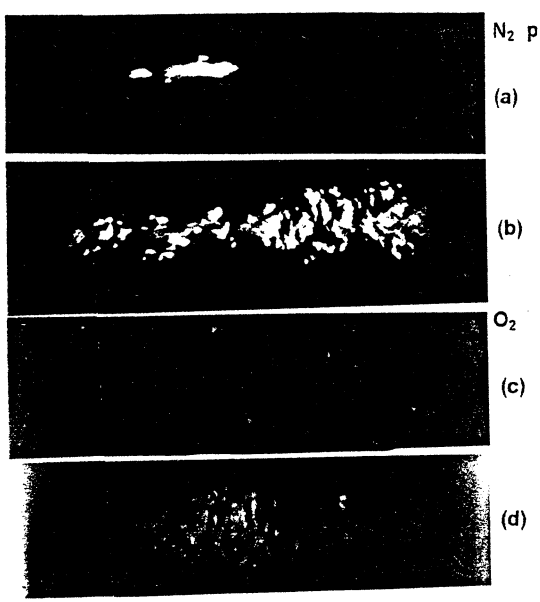

Fig. 1 Photos of the discharge in nitrogen (a, b) and oxygen (c, d). The pressure is 10 Torr and the microwave pulse duration is (a) 2; (b) 6; (c) 3; and (d) 8 μs.

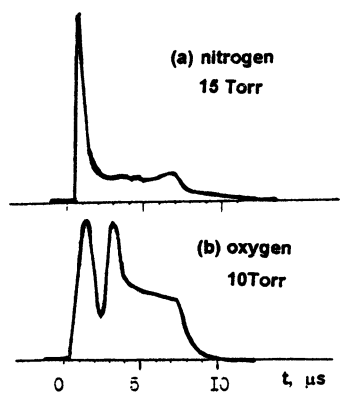

Fig. 2 Oscilloscope traces of the photomultiplier signal.

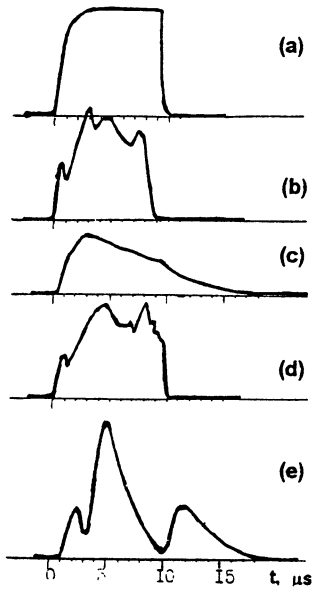

Fig. 3 Oscilloscope traces of the radiation power at the beam axis registered at the backside wall of the chamber (a, b, d) and those of the phase shift measured by the interferometer (c, e): (a) signal measured in the absence of the discharge; (b, c) nitrogen, 10 Torr; (d, e) oxygen, 10 Torr.

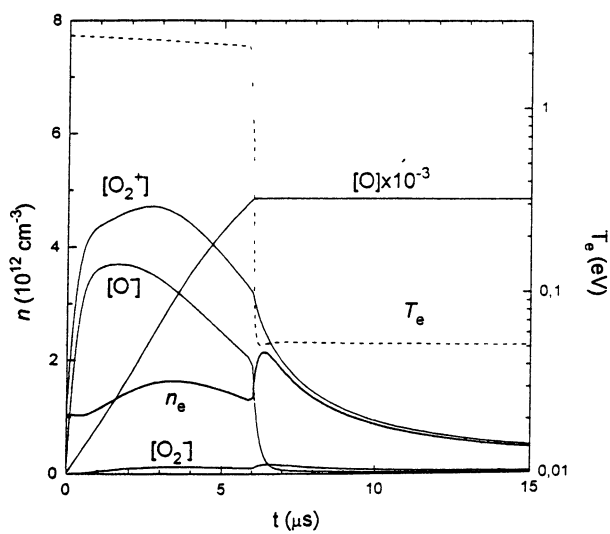

p=10 Torr, $\langle E(t)\rangle/N$=(6.9-3·10^5 t) 10^{-15} V·cm^{-2}, λ=8 mm
Isohoric discharge, τ=6 μs

Fig. 4 Calculation of the discharge kinetics in oxygen.

HIGH-FREQUENCY ELECTRICAL BREAKDOWN IN ELECTRONEGATIVE GASES WITH FAST ELECTRON ATTACHMENT AND DETACHMENT PROCESSES

N.L.Aleksandrov, S.A.Guz, A.M.Konchakov, A.P.Napartovich, A.M.Okhrimovskyy*

Moscow Institute of Physics and Technology,
Dolgoprudny, Russia
*Troitsk Institute for Innovation and Fusion Research,
Troitsk, Russia

The development of high-frequency electrical breakdown in a gas depends on a variety of parameters such as the field strength and frequency, the gas properties and the electrode geometry. At sufficiently high gas densities when the field angle frequency ω is lower than the frequency of the electron momentum relaxation ν_m electrons are in an oscillatory drift motion with the amplitude $A = e E_0/(m \omega \nu_m)$, where e and m are the electron charge and mass and E_0 is the field strength amplitude. If $A < d/4$ (d is the distance between electrodes), the main mechanism of electron loss which governs the breakdown voltage in an electropositive gas is the free electron diffusion to the boundaries of the discharge volume. In an electronegative gas, an electron attachment to neutral species also becomes important.

Aints *et al* [1] have shown that if fast electron detachment from negative ions compensates for the electron loss through attachment to neutral species, the breakdown voltage is lowered at $A \ll d$ and resulting losses could be described as due to the process of pseudo diffusion of electrons with rate that might be up to several orders of magnitude greater than that of the normal diffusion. This was invoked to explain a decrease in the radio frequency (RF) breakdown voltage with increasing ω and d which was observed experimentally in the atmospheric-pressure

air [1].

The mechanism of the pseudo diffusion process may be explained in the following way. An electron which is in the oscillatory drift motion with the amplitude A along the field attaches to a molecule to form a negative ion which is essentially at rest. Then, at a random moment the electron detaches from the ion and oscillates around the new midpoint which is displaced by a distance of the order of A because the electric field is now phase shifted. If $A \ll d$ the process is repeated many times. The direction of the displacement along the field direction is also random. Therefore, the considered transport of electrons can be treated as pseudo diffusion of the charged particles. For the coefficient of the common electron diffusion, we have $D \sim \lambda^2 \nu_m$, where λ is the electron mean free path for momentum transfer. Similarly the pseudo diffusion coefficient is of the order of $D^* \sim A^2 \nu$, where ν is the value of the order of attachment and detachment frequencies.

The aim of this paper is to derive consistently the criterion of breakdown in a high-frequency uniform electric field in an electronegative gas with fast electron attachment and detachment processes. In addition, we generalize the discussion [1] in order to take into account negative ion species which is not involved in electron-detachment processes. This model is more adequate to describe the breakdown in air.

We consider gas breakdown in a uniform electric field $\mathbf{E} = \mathbf{E}_a \cos \omega t$ and assume the following model of negative-ion kinetics

$$e + A \xrightarrow{\nu_a} A^-,$$

$$A^- \xrightarrow{\nu_d} e + A$$

and

$$A^- \xrightarrow{\nu_c} B^-.$$

In addition, we assume that the frequencies obey following inequalities

$$\nu_a, \nu_d \gg d/w \gg \nu_{ion}, \nu_c, \tag{1}$$

where w is the electron drift velocity in the field E_0, and ν_{ion} is the ionization frequency; that is, there are fast processes (electron attachment and detachment) and slow processes (ionization and negative-ion conversion), whereas electron drift is intermediate in rate.

The balance equations for electrons and the A^- ions are

$$\frac{\partial n_e}{\partial t} = -\nu_a n_e + \nu_d n_i - w \cos \omega t \frac{\partial n_e}{\partial x} + \nu_{ion} n_e \qquad (2)$$

$$\frac{\partial n_i}{\partial t} = \nu_a n_e - \nu_d n_i - \nu_c n_i \qquad (3)$$

For simplicity we assume that, with the exception of ν_{ion}, the other collisional frequencies and the electron mobility are time-independent ones.

It follows from (1) that in the right-hand side of equations (2) the first two terms are much greater than the third one which in turn is much greater than the fourth one. However, the fourth term can not be neglected because it determines the breakdown threshold.

In a short time of about ν_a^{-1} and ν_d^{-1} the densities of electrons and A^- ions reach the quasi-steady state

$$n_e^0 = \frac{\nu_d}{\nu_a + \nu_d} n_\Sigma , \quad n_i^0 = \frac{\nu_a}{\nu_a + \nu_d} n_\Sigma ,$$

where n_Σ is a sum of the densities of these particles which is determined by the slow processes.

When solving equations (2) and (3) we account for the electron drift term in the right-hand side in perturbation theory and neglect the slower processes. To the first order, the quasi-steady solution of equations (2) and (3) should be sought in the following form

$$\begin{pmatrix} n_e \\ n_i \end{pmatrix} = \begin{pmatrix} n_e^0 \\ n_i^0 \end{pmatrix} + \begin{pmatrix} a_e \\ a_i \end{pmatrix} \cos \omega t + \begin{pmatrix} b_e \\ b_i \end{pmatrix} \sin \omega t \qquad (4)$$

where a and b are proportional to $\frac{\partial n_e}{\partial x}$ and change only slowly with time. These quantities are determined by substituting (4) into equations (2) and (3).

In order to derive the breakdown criterion we add the equations (2) and (3) and average the resulting equation over the field period. Then, the attachment and detachment terms cancel each other and the drift term vanishes on averaging at $A \ll d$. Therefore, the breakdown threshold is governed by the slow collisional processes. In so doing we should account for the small correction to the drift term which follows from (4). This correction is much less then the drift term which vanishes on averaging but no less than the surviving terms which describe the slow processes.

As a result, we have the equation

$$\frac{\partial \overline{n}_\Sigma}{\partial t} = \overline{\nu}_{ion}\overline{n}_e + \frac{\partial^2}{\partial x^2} D^* \overline{n}_e - \nu_c \overline{n}_i$$

and the breakdown criterion

$$\overline{\nu}_{ion} = \frac{\pi^2}{d^2} D^* + \nu_a \frac{\nu_c}{\nu_d} \tag{5}$$

where the overline denotes time averaging and the pseudo diffusion coefficient is

$$D^* = \frac{w^2}{2} \frac{\nu_a}{\omega^2 + (\nu_a + \nu_d)^2} \quad . \tag{6}$$

The latter term in the right-hand side of equation (5) describes the electron loss due to the indirect formation of B^- ion through the attachment to A molecule. Aints *et al* [1] neglected this term. However, our estimate which is based on the available data [2,3] upon the rates of negative-ion processes shows that this term is much greater in air than the pseudo diffusion term. It means that the electron pseudo diffusion has little or no effect on high-frequency breakdown in air, but, more importantly, concept of pseudo diffusion fails in air because of slow electron detachment.

This contradicts the interpretation by Aints *et al* [1] of their experimental data.

However, the influence of the electron pseudo diffusion on high frequency breakdown can become more important as the rate of electron detachment increases. This can be observed for repetitive breakdown in air when a substantial number of active neutral particles such as atoms O, radicals and electronically excited molecules are accumulated from impulse to impulse. Collisions between active particles and negative ions result in fast electron detachment in air.

High frequency breakdown can also be controlled by the electron pseudo diffusion in NO and N_2O. The dominant attachment and detachment processes in NO are

$$e + NO \longrightarrow O^- + N$$

$$O^- + NO \longrightarrow e + NO_2 \quad k = 2 \times 10^{-10} cm^3/s \quad [4]$$

and those in N_2O are

$$e + N_2O \longrightarrow O^- + N_2$$

$$O^- + N_2O \longrightarrow NO^- + NO \quad k = 2.2 \times 10^{-10} cm^3/s \quad [5]$$

$$NO^- + N_2O \longrightarrow e + NO + N_2O \quad k = 5.1 \times 10^{-12} cm^3/s. \quad [5]$$

The similar effect is anticipated to take place in gas mixtures in which the dominant electron attachment process results in formation of O^- if the mixture contains components (NO, CO, H_2, SO_2, C_2H_4, etc.) which effectively destroy O^-.

References

1. Aints M., Haljaste A., Kudu K., Adamson V., J. Phys. D: Appl. Phys., 1995, 28, 81
2. Wetzer J. M., Wen C., J. Phys. D: Appl. Phys., 1991, 24, 1964
3. Akishev Yu. S., Derygin A. A., Elkin N. N., Kochetov I. V., Napartovich A. P., Tsyshkin N. I., Fiz. Plazmy, 1994, 20, 487
4. Smirnov B. M., Negative Ions, 1992 (New York: Mc Graw - Hill)
5. Parkes D. A., J. Chem. Soc. Farad. Trans. I, 1978, 11, 2103

LONG PLASMA COLUMNS WITH HIGH ELECTRON DENSITIES PRODUCED BY PULSED SURFACE WAVE DISCHARGES

A.L. Vikharev, A.M. Gorbachev, O.A. Ivanov, V.A. Isaev, V.A. Koldanov, A.L. Kolisko

Institute of Applied Physics, Nizhny Novgorod, Russia

Discharges produced by surface waves (SW) are subject of many investigations because of their technological application and their use in fundamental research [1-2]. Concerning the latter aspect the steady state of SW produced discharges especially at low pressures (< 5 Torr) and low frequencies (< 5 GHz) is studied extensively. On the other hand, for many applications long homogenous plasma columns generated in short times are required. The electron density in SW produced discharges exceeds the critical value, $N_e \geq N_c \cdot (1 + \varepsilon_g)$, where $N_c = m(\nu^2 + \omega^2)/4\pi e^2$, ω is wave frequency, ν the collision frequency, ε_g is dielectric permitivity of the tube (at f $\approx$ 40 GHz , $N_c \geq 10^{14}$ cm^{-3}). Consequently, it grows significantly as the frequency of the exciting field increases. The maximum frequency, at which up to now one has managed to obtain a short-wave discharge, does not exceed 10 GHz. In this wavelength band the SW is usually launched by a surfaguide [3]. Its operating power is limited by the gas breakdown in the SW excitation region of the rectangular waveguide.

Generation of long plasma columns in the centimeter wavelength band requires high microwave power typically of the order of ten kilowatts. We suggest two novel types of launchers which allows the use of much larger microwave power and high wave frequency for generation of a discharge in a pulsed regime.

The E-plane junction set-up

For excitation of high power surface waves in the 3-cm wavelength band we used a novel type of launcher (E-plane junction) [4] which allows to generate a long plasma column in a quartz tube placed in a single-mode waveguide. The microwave power is coupled to this waveguide at an E-plane junction. Energy passes through a circulator to the E-plane junction via a transmitting waveguide. The electric field of a TE_{01} mode in this

waveguide is parallel to the tube axis. To match the impedance of the plasma-filled waveguide to the power-transmitting waveguide a movable short circuit is used at the H-plane junction. The launcher proposed by us is especially efficient at a high level of microwave power, since it does not contain inhomogeneities, at which a breakdown could develop out of the discharge tube. At low levels of power (in the continuous regime) when discharge ignition requires special elements (narrowing of the waveguide, gaps, etc. [3]) that increase the field to the breakdown level, this method may prove less efficient. A tube with inside diameter 4 mm, outside diameter 6 mm and length of 50 cm is used. The tube is filled with various gases: air, He, Ar and mixtures at pressures p = 1-60 Torr. The experiments are performed using microwave radiation with wavelength λ = 3 cm, pulse duration τ = 1-15 μs, pulse power P = 30-150 kW, a repetition frequency F = 0.1-1 Hz. Power P_{ab} absorbed in the discharge was measured with a directional coupler with respect to the difference between the power reflected from the launcher with no discharge present, P_{in}, and the power P_{ref} reflected when the discharge was ignited: $P_{ab} = P_{in} - P_{ref}$. A high degree of absorption (~ 70-90 %) is observed over a wide range of gas pressures assuming no drastic influence of losses by radiation and in the waveguide structure. Thus, a novel microwave SW launcher allows extension of the operating microwave power level.

It was shown also that at high pressure ($\nu \geq \omega$) a discharge in the waveguide is built up in the field of the main waveguide mode and the SW propagate on the background of this pre-ionized plasma along the discharge.

The E^{O}_{01} mode -based set-up

Another type of launcher is shown in Fig.1. In this launcher for excitation of SW we used the E^{O}_{01} mode of a circular waveguide. In the experiment surface waves were excited by radiation in the 8-mm wavelength range. A magnetron with output power P = 30–60 kW was used as a microwave generator. Duration of the microwave pulse varied in the range of τ = 0.5–10 μs, and pulse repetition rate was $F = 10–10^3$ Hz. Radiation generated by the magnetron in the form of the $H^{\square}_{10}$ mode of a rectangular waveguide was first converted into the H^{O}_{11} mode of a circular waveguide, and then,

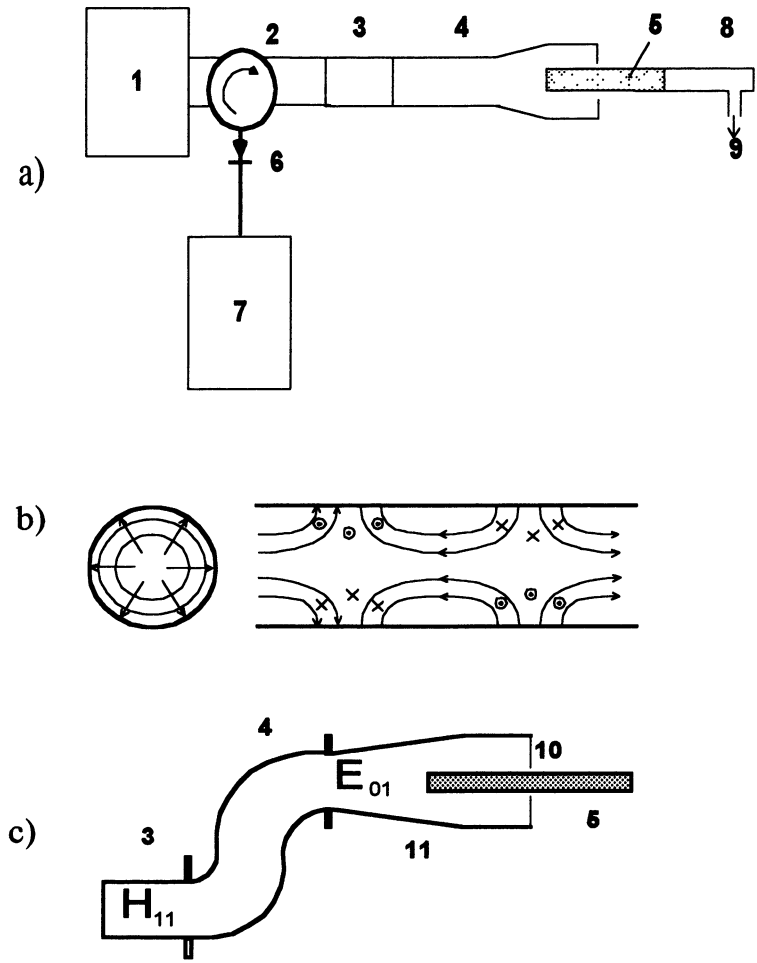

Fig. 1 (a) Scheme of the experimental set-up; (b) structure of electromagnetic fields in E^{o}_{01} mode ($\rightarrow$ *E*, $\times$ - *H*); (c) design of launcher: 1 - magnetron, 2 - circulator, 3 - mode convertor $H^{\square}_{10} \rightarrow H^{o}_{11}$, 4 - mode convertor $H^{o}_{11} \rightarrow E^{o}_{01}$, 5 - discharge, 6 - detector, 7 - oscilloscope, 8 - quartz tube, 9 - pumping, 10 - diaphragm, 11 - horn

by means of the mode converter described in [5], into the E^{o}_{01} mode of an oversized circular waveguide. The discharge was produced in quartz tubes

with external diameters 6 mm or 9 mm and length L = 30 cm, which were situated along the axis of the circular waveguide.

Design of the exciter and the field structure in the waveguide at the mode converter output is shown in Fig. 1. The $H^{O}_{11} \rightarrow E^{O}_{01}$ mode converter is based on a circular bent waveguide 8 mm in diameter with sign-alternating curvature. The structure of the E^{O}_{01} mode is such that the maximum of the E_z component of the electric field is situated at the waveguide center, and direction of E_z coincides with the axis of the waveguide and the gas-discharge tube. Direction of other components of the electromagnetic field (E_r and H_φ) is also close to the field structure in an axially symmetric surface wave. That is why direction of the electromagnetic fields relative to the axis of the discharge tube seems to be advantageous for efficient excitation of a surface wave.

A thin metal diaphragm with diameter D_1 somewhat larger than the diameter of the gas discharge tube was set at the output of the exciter. The diameter of the diaphragm aperture was chosen such as to reflect a significant part of the power transmitted in the E^{O}_{01} mode in the absence of a discharge. At the same time, the surface wave propagating along the tube and localized near its walls penetrated freely through the aperture in the thin diaphragm. For efficient excitation of a surface wave there are optimal correlations between the radius of the discharge tube and diameters of the output waveguide and the diaphragm. They stay within the ranges $D/2R \sim$ (1.3-2) and $D_1/2R \sim$ (1.2-1.5). Additional matching may be done by varying the length of the section of the discharge tube in the exciter.

Using this launcher for the first time the high power SW were excited in 8-mm wavelenght band. The electron density in the discharge in this experiment achieved 10^{14} cm^{-3}. In Fig. 2 the fraction of absorbed power is plotted versus the air pressure for different tube diameters. Measurements showed a sufficiently high level of excitation efficiency in a wide range of gas pressures and incident microwave powers. The lower absorption coefficient at higher pressure can be explained by the increasing breakdown field and the resulting longer time of discharge creation. Figure 2 shows also the length of the microwave discharge versus pressure. At fixed duration of the microwave pulse this dependence has a characteristic maximum, which is determined by the velocity of ionization front propagation.

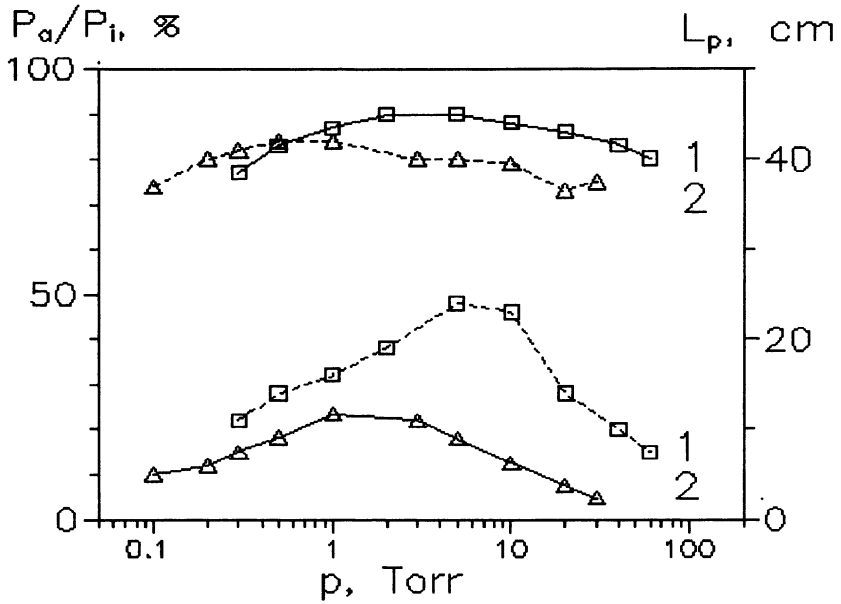

Fig.2 Variation in the fraction of absorbed power and discharge length with air pressures (pulse duration τ = 5 μs): 1 - tube diameter 2R = 9 mm, P_i = 50 kW; 2 - 2R = 6 mm, P_i = 40 kW.

Ionization front advanced

The full length of the plasma column depends on the pulse duration, τ ,and ionization front velocity, V_f.

$$L = \int_0^{\tau} V_f \, dt$$

The temporal evolution of the discharge along the tube was studied on the bases of the plasma light emission. A maximum value for the ionization front velocity as a function of pressure is observed. The corresponding gas pressure of this maximum value, V_f ,is different for different gases and increases with increasing incident microwave power.

The measured velocities were compared with the values calculated on the basis of three different models. These models describe the ionization

front propagation dominated by the ponderomotive force action, the breakdown wave mechanism and the electron diffusion, respectively [4]. The experiments performed in the short wavelength band ($\lambda \sim 8$ mm) confirmed the results described in [4], i.e. that ionization front motion could be interpreted to be based on the formation of a breakdown wave.

Conclusion

1. The experiments performed demonstrated that E-plane junction is an efficient launcher for SW at high incident microwave power. At high pressure $(\nu \sim \omega)$ the gas breakdown occurs primarily in the field of the main waveguide mode. The plasma in the waveguide mode acts as a pre-ionization for the SW.
2. It is shown that using the E^{O}_{01} mode of a circular waveguide allows to create SW discharge under much higher frequency than in well known launchers. For the first time the high-power SW were excited in the 8-mm wavelength band.
3. A new interpretation of the ionization front advanced of SW produced discharge is suggested. The mechanism of ionization front motion was interpreted to be based on the formation of a breakdown wave.

This work was supported by the Russian Fund for Fundamental Investigations (grant 95-02-05586a).

References

1. Moisan M., Zakrzewski Z., J.Phys.D.: Appl.Phys. 1991, **24**, 1025
2. Moisan M, Ferreira C M, et al. Rev. Phys. Appl.,1982, **17**, 707
3. Moisan M., Zakrzewski Z., Pantel R. and Leprince P., IEEE Trans. on Plasma Phys., 1984, **12**, 203.
4. Bohle A., Ivanov O., et al., J.Phys.D.: Appl.Phys., 1996, **29**, 369
5. Vinogradov D.V., Denisov G.G., Radiofizika (in Russian) 1990, **33,** 726

LUMINESCENCE OF SHORT - LIVED COLOR CENTERS IN LiF CRYSTALS EXCITED BY SECONDARY – ELECTRON EMISSION MICROWAVE DISCHARGE

G.M.Batanov [#], *V.A.Ivanov**, *M.E.Konyzhev**

[#] General Physics Institute of the Russian Academy of Sciences, Russia, Moscow
* Science and Technology Center PLASMAIOFAN, Russia, 117942 Moscow, Vavilova str. 38. E-mail:ivanov@plasma.gpi.msk.su

1. Introduction

The problem of high-power-microwave transmission through the dielectrics is one of the urgent problems of the modern microwave physics and technology.

High power microwave radiation initiates different types of microwave discharges on a surface of an insulating crystal in vacuum. The discharges produce the electronic excitations in the near-surface layer of the crystals. Relaxation of metastable state of the ensemble of nonequilibrium excitations leads to a microwave breakdown of the crystal and the damage of the surface [1, 2].

This report devotes to the luminescence kinetics of solid-state excitations induced due to the interaction of pulsed microwave radiation with lithium fluoride (LiF) crystals in vacuum.

2. Classification of microwave discharges along a surface of a crystal and experimental layout

It is known three types of electrodeless microwave discharges along a single surface of an insulating crystal in vacuum:

- secondary - electron emission microwave discharge (SEEMD) [3],
- microwave breakdown (MB) in the form of a contracted discharge on the surface of the crystal [1],
- plasma-flare microwave discharge (PFMD) [4].

The SEEMD transforms to the PFMD passing through the stage of the microwave breakdown on the surface of the crystal in vacuum:

SEEMD → microwave breakdown → PFMD.

The mechanisms of these transformations have a great importance for the understanding of the exitation and evolution of different types of microwave discharges. We study these mecanisms experimentaly.

Fig. 1 shows the experimental layout. Cleaved or polished LiF crystals are positioned through a cutoff section at the electric-field maximum of a standing TE_{10} wave of a rectangular waveguide with a cross section of 120 × 57 mm^2. The waveguide is evacuated by titanium pumps to a pressure of 10^{-4} Pa. A microwave pulse with a length τ from 1 to 60 μs and a power P_0 up to 2 MW is delivered from the magnetron to the vacuum section along a microwave line. The wavelength of microwave radiation in the waveguide is $\lambda_g = 20$ cm.

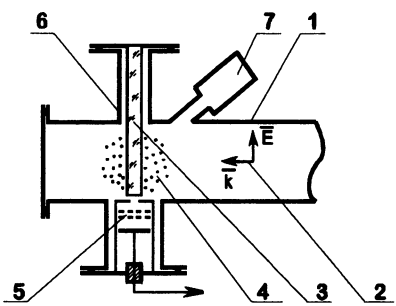

Fig. 1.

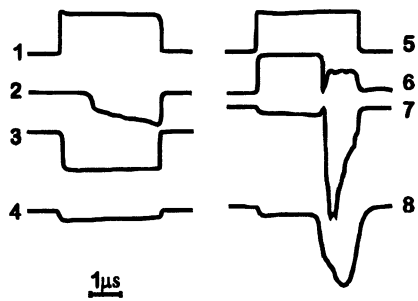

Fig. 2.

Fig. 1. Experimental layout. 1 - Waveguide; 2 - incident microwave radiation; 3 - LiF crystal; 4 - microwave discharge; 5 - multigrid electrostatic analyzer; 6 - cutoff section with a diameter of 24 mm; 7 - photomultiplier with optical filters.

Fig. 2. Typical oscillograms of the signals during the microwave discharges at the surface of a LiF crystal. SEEMD: 1-incident microwave power; 2-electron current from the discharge region near the threshold for the onset of the SEEMD (P_0 = 45 kW, E_0 = 2.3 kV/cm); 3, 4 - electron current and light emission from the discharge region when the threshold for a SEEMD is exceeded considerably (P_0 = 280 kW, E_0 = 5.7 kV/cm).

The discharge transformations (SEEMD → MB → PFMD): 5, 6 - Power of the incident and reflected microwave radiation; 7, 8-electron current and light emission from the discharge region for the transition from a SEEMD to a PFMD due to a microwave breakdown (P_0 = 300 kW, E_0 = = 5.9 kV/cm). The gain levels for traces 2, 3, and 7 form the rations 260:13:1, respectively.

3. Secondary - electron emission microwave discharge (SEEMD) [5]

The SEEMD arises when $\mathcal{E} = e^2 E_0{}^2 / 2 m \omega^2 > W_1$. and exists during the breakdown delay time $\Delta\tau < \tau$. Corresponding threshold electric field $E_{0\,thr}$ is determined from the condition: $e^2 (E_{0\,thr})^2 / 2 m \omega^2 = W_1$.

$\mathcal{E}$ is the oscillation energy of electron, E_0 is the electric field amplitude of microwaves, e and m are the specific charge and mass of an electron, ω (= 1.23 x 10^{10} s^{-1}) is the angular frequency of microwaves, W_1.(≈ 15 eV for the LiF crystal) is the first critical potential for the surface, τ is the time duration of the microwave pulse, $\Delta\tau$ is the time duration of SEEMD, $E_{0\,thr}$ (≈ 2 kV/cm for the LiF crystal) is the threshold electric field for the onset of the SEEMD. Electrons of SEEMD have energies on the order of the oscillation energy. High pulsed electron current densities reach the value $j_e \sim 1$ A /cm^2. Microwave absorption coefficient (per unit area of the crystal) in the stage of the SEEMD is low:

$$\eta \sim e E_0 / m \omega c \sim 10^{-2}.$$

A few thouthands of SEEMD pulses create an optically dense layer (on the surface of the LiF crystal) containing induced color centers. The density of F, F_2 and F_3^+ centers (stable at room temperature for years) may reach the value of 10^{20} cm^{-3}, and the thickness of the layer is not larger than 10^{-4} cm [2, 5].

A high intensity luminescence of the LiF crystals appears in a wide optical range (380 - 750 nm) during the microwave pulse. This luminescence is uniform over the crystal surface. In this report we consider some experimental results on the luminescence decay kinetiks of the LiF crystals excited by the electrons of SEEMD.

4. Microwave breakdown on the surface of the crystals

Microwave breakdown is initiated by the SEEMD [1]. The breakdown delay time $\Delta\tau < \tau$ obeys the empirical law: $(S - S_{thr}) \times \Delta\tau$ = const, where S_{thr} is the threshold intensity for the onset of the SEEMD. The value of the constant is determined by the nature of the crystal: const ≈ ≈ (0.04 - 0.8) J cm^{-2}, const ~ ω. The breakdown is accompanied by the absorption of microwave energy up to 100 % with a time scale $\delta\tau \sim 0.1\mu$s, an intense flash of light, and a burst of electron and ion currents from the discharge region [1, 4].

When the electrons of the SEEMD bombard the crystal, high density of electronic excitations (electron-hole pairs, excitons, plasmons) arises in the surface layer. Decay of the excitations leads to creation of short-lived color centers with lifetime ~ 1 μs at room temperature. During the breakdown delay time $\Delta\tau$ an accumulation of these centers takes place.

Recombination of the short-lived centers may lead to the formation of an electron-hole plasma with a such high carrier density, that a local electric field intensification arises near inhomogeneities in the plasma density. The SEEMD electron density in the conduction band of the crystal required to initiate this process is $n_e \sim 10^{15}$ cm^{-3}. The concentrations of stable centers on the order of 10^{17} cm^{-3} are reached during the one microwave pulse in our experiments [2]. Accodingly, the concentrations of short-lived centers must be much more than 10^{17} cm^{-3}. Although the 10^{17} cm^{-3} values are sufficient here, but what is the real value of concentration of these centers reached under SEEMD during the microwave pulse in our experiments?

5. Luminescence of short-lived color centers in the LiF crystals

The main purpose of this experiments was to find a luminescence of short-lived color centers and to estimate their concentration in the surface layer of the LiF crystal during the secondary–electron emission microwave discharge (SEEMD). We proposed to mesure this concentration using the luminescence diagnostics.The luminescence of LiF crystals was detected at room temperature in the spectral ranges of 375±10 nm, 463±10 nm, and 686±10 nm using narrow-band optical filters, and in the range 620-750 nm using wide-band optical filter. We found that the characteristic times of luminescence growth/decay are about 1–2 μs (Fig.3,4,5). The luminescence intensity and decay time increase when microwave power increases. The luminescence intensity in the 686 nm band is more than one order larger than that in the 375 nm and 463 nm bands. It is shown, that luminescence decay kinetiks (for the four spectral ranges) is notecably dependent on the SEEMD–irradiation dose. In particular, the "fast" glow components appear in addition to "slow" glow components. The intensity ratio of the former to the latter reachs the value of 0.2–0.5. The main result is the observation of high intensity of red-band luminescence of LiF crystals unduced by SEEMD. Based on the sensitivity of the photomultiplier and on the measured transparant coefficients of the optical filters we could estimate the absolute luminescence intensity of short-lived

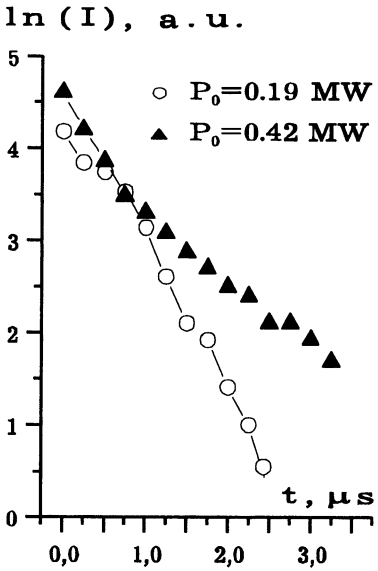

Fig. 3.

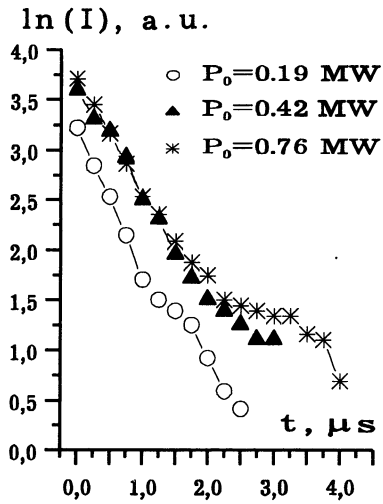

Fig. 4.

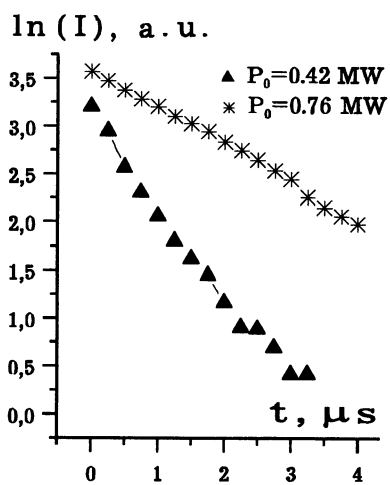

Luminescence decay kinetics of short-lived color centers in LiF crystals:

Fig. 3: $\lambda = 463 \pm 10$ nm,
Fig. 4: $\lambda = 686 \pm 10$ nm,
Fig. 5: 620 nm $< \lambda <$ 750 nm,

P_0 – microwave power
I - luminescence intensity,
t - time duration after the end of microwave pulse.

color centers in the LiF crystals. The calculations gave the concentrations of the centers more than the value of 10^{19} cm^{-3} during the microwave pulse. Such high concentration of short-lived centers is sufficient to produce (due to the recombination process) the electron density in the conduction band of the crystal much more than $n_e \sim 10^{15}$ cm^{-3}. So, recombination of the centers leads to the formation of an electron-hole plasma with a such high carrier density, that a local electric field intensification arises near inhomogeneities in the plasma density. Absorption of microwave energy in these plasma regions produces phonons and local heating of the crystal lattice which stimulate the explosive color center recombination process and plasma production again. As a result of these processes a plasma channel intergrow in a surface layer of the crystal and stretchs out along the electric field vector of the wave. That is why the microwave breakdown on the surface of the crystal is realized.

6. Summary

So, based on the experimental measurements of color center luminescence we found the high concentration of the non-stable short-lived centers in LiF crystals during the SEEMD and consequently experimental confirmation of the recombination mechanism of microvawe breakdown on the surface of the LiF crystal in vacuum [1].

References.

1. Batanov G.M., Ivanov V.A., Konyzhev M.E. Russian JETP Lett., 1994, 59, 690.
2. Batanov G.M., Ivanov V.A., Konyzhev M.E. et al., Russian Tech. Phys. Lett., 1993, 19, 653.
3. Grishin L.V. et al. Trudy FIAN, 1977, 92, 82.
4. Batanov G.M., Ivanov V.A. Trudy IOFAN, 1988, 16, 46.
5. Batanov G.M., Ivanov V.A., Konyzhev M.E. et al. ISPP-13 "Piero Caldirola". Ed. by G.Bonizzoni, W.Hooke and E.Sindoni. SIF, Bologna, 1993. P. 521-525.
6. High-Energy Solid-State Electronics [in Russian], Ed. by D.I.Vasburd. Nauka, Novosibirsk, 1982.

These researches were supported by Russian Fund of Fundomental Investigations, grant № 96-02-17647-a.

HELICON WAVE PLASMA SOURCE IN A TRUE LARGE VOLUME TOROIDAL DEVICE

Aparajita Mukherjee & D. Bora

Institute for Plasma Research
Bhat, Gandhinagar - 382428
India

ABSTRACT

Dense, large volume plasma is produced in a true toroidal device BETA [1] using radio-frequency (rf) excitation of helicon waves. Experiments are mainly conducted to study the equilibrium profiles and low frequency electrostatic fluctuations in a collisionless regime. Radial wave magnetic field profiles look different than observed elsewhere in cylindrical systems. Existence of coherent peaks at 960 G is observed. Phase information suggests two different types of low frequency instabilities exist in the bad as well as in the good curvature region. Percentage of density fluctuations normalized to their equilibrium value increases in the bad curvature region.

1. INTRODUCTION

The plasma production by radio-frequency (rf) waves using either inductive or capacitive coupling methods are well known. Boswell [2-5] developed an efficient radio frequency discharge in the frequency region of helicon waves, $w_{ci} \ll w \ll w_{ce}$ for basic and applied plasma experiments. Shoji [6] has obtained almost the same result with a different antenna from that used by Boswell. In a theoretical analysis, Chen [7] has suggested that the rate of energy absorption by wave damping is due to collisional and Landau damping of the helicon wave. Plasma production by helicon waves is characterized by various advantages compared with other high frequency plasma production methods: (a) the phase velocity of the helicon wave is of the order of the electron thermal velocity or the ionization energy, so high energy electrons coupled to the fast phase velocity are not needed for maintaining the discharge as in the plasma production by lower hybrid

waves, (b) plasma production for various kinds of ion species in the wide range of magnetic fields is possible with the same frequency, because the damping of the helicon waves does not depend on ion species and is not directly connected to the cyclotron frequency as in ICR and ECR.

In a toroidal device BETA, helicon wave is excited to get a large volume dense plasma by a helical antenna. In the present paper detailed measurements of the rf produced plasma are reported. Low frequency electrostatic fluctuations are also observed at different radial locations.

In Sec. 2, we describe the experimental apparatus. Observations are presented with possible interpretations in Sec. 3. Conclusions are summarized in Sec. 4.

2. EXPERIMENTAL SETUP & MEASURING TECHNIQUES

Experimental device which has been used to produce large volume rf plasma is shown in figure 1, consists of a torus with a major radius of 45 cm and minor radius of 15 cm. A pure toroidal magnetic field is produced by 16 toroidal field coils surrounding the torus. Maximum toroidal magnetic field of 0.1 T can be produced for 1.0 s. A limiter of diameter 18 cm is used to short-circuit the electric field established due to the curvature and ∇B drift. Both the limiter and vessel are grounded.

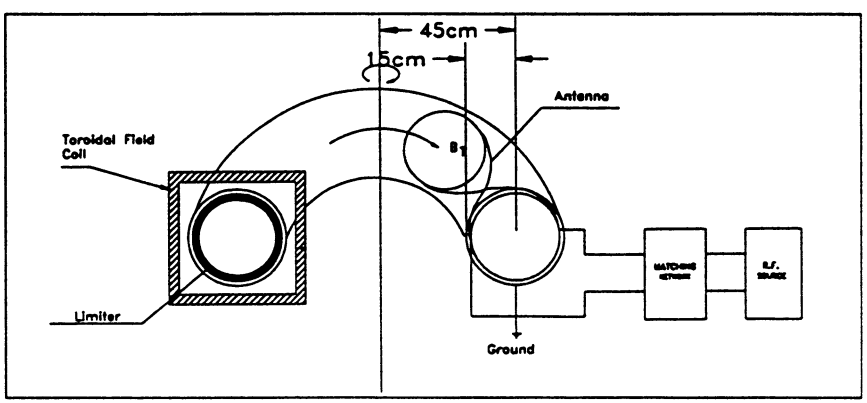

Fig. 1: Schematic of experimental apparatus

Argon plasma is produced with a broad band helical antenna which operates in axial mode ($0.75 < c/\lambda < 1.25$). The antenna consists of two

copper strips of 2.5 cm wide, 0.3 cm thick with one helical pitch, in order to excite m = 1 mode, is placed at a radial position of 10 cm (plasma radius = 9 cm). The length of the antenna is chosen to be 25 cm. Since the antenna length is much smaller than the free space wavelength of the rf signal, the current pattern is established almost instantaneously. The design of the antenna is such that the return path of the current is through plasma. 1 kW rf power at 8.0 MHz is supplied from an oscillator-amplifier system. The power P_{rf} is delivered to the plasma via a coaxial cable and is matched to the antenna with inductors and a variable capacitor. The base pressure is kept at less than 7×10^{-6} T and the working pressure is 1×10^{-4} T, so that the plasma remains collisionless.

Radial profiles of plasma parameters are measured at 90 cm away in the toroidal direction from the antenna using Langmuir probe which has a tungsten tip 1.0 mm in diameter and 3.0 mm long. Center tapped magnetic probes are used to measure wave magnetic fields at different radial locations. Magnetic probes consist of single layer solenoidal coils of 4.0 mm in diameter, 10.0 mm in length with 10 windings and are placed at 22.5 degrees away in the toroidal direction from the antenna. Katsumata probe is used to measure ion temperature. Fluctuating components of the density and floating potential are simultaneously measured using double Langmuir probes. The data are analysed using a standard fast Fourier transform (FFT) technique [8] to obtain frequency, phase, coherence and power spectrum of the fluctuations. The data are acquired on a dual channel Lecroy digital oscilloscope which are then processed on a VAX 8810 computer. During experiment rf current fed to the antenna is monitored with the help of current transformer.

3. RESULTS & DISCUSSION

RF plasma is produced in a toroidal chamber with a confining toroidal magnetic field B_T of 960 Gauss at 1×10^{-4} Torr. Measurement reveals almost flat radial density profile with shallow radial gradients which is shown in figure 2. Figure 3 shows the radial profile of T_e, which is around 25 eV, much higher compared to other experimental results conducted in cylindrical devices. At 3.0 cm minor radial position electron temperature shows a maximum value. It is observed that in a toroidal system the particles remain confined for a longer time than in a cylindrical system. The electrons being in the rf field for a longer time, gain energy while

traversing the torus several times before they are lost to the chamber wall, hence a rise in temperature is observed. Ion temperature is measured using Katsumata probe which is around 3.5 eV.

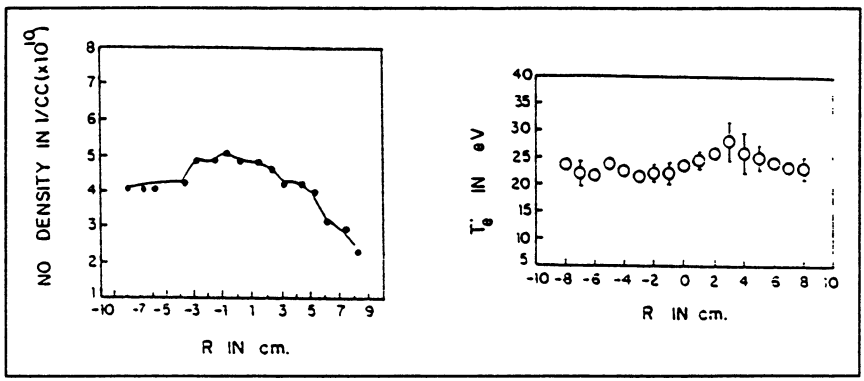

Fig. 2: Radial profile of no. density **Fig. 3: Radial profile of T_e**

The radial profiles of the wave magnetic fields for m = 1 mode at 22.5° (17.7 cm) away in the toroidal direction from the antenna are plotted in figure 4. Profiles look different than observed and reported elsewhere for cylindrical system [9]. Since the wavelength of the excited helicon wave is comparable to the major radius R, one should consider toroidal effects. The modes couple thereby modifying the power deposition radially in the plasma volume.

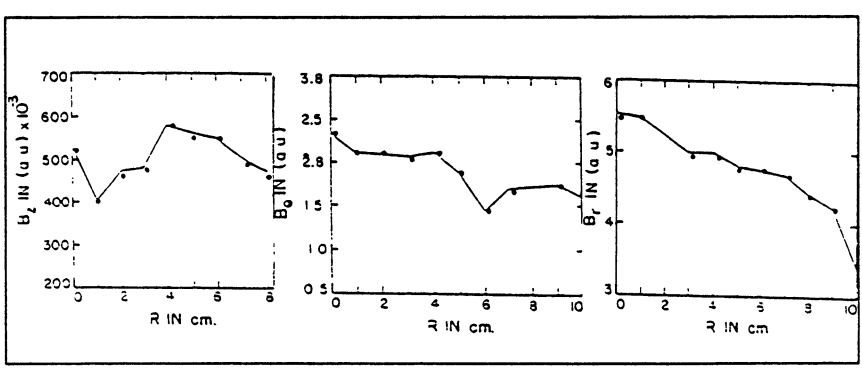

Fig. 4: Radial profiles of wave magnetic fields for m = 1 mode

Investigations of gradient and curvature induced low frequency instabilities in a toroidal system are of great interest. It is well known that the simple curved magnetic field has a region of bad curvature as well as good curvature. The plasma in the bad curvature region is unstable to flute perturbations which is due to the centrifugal force acting on the particles that gives rise to Rayleigh-Taylor gravitational instability. The plasma in the good curvature region is unstable to drift kind of perturbations which is due to the radial pressure gradient that gives rise to the drift instability.

Fluctuations in density and floating potential are measured simultaneously at different radial locations. Coherent peaks are observed at 960 Gauss magnetic field. The cross power spectrum exhibits well defined peaks centered around 1.09 ± 0.4 kHz, 2.68 ± 0.3 kHz, 4.07 ± 0.7 kHz and 5.44 ± 0.4 kHz. Phase information reveals the presence of mixed characteristics of R-T and drift instabilities. One such scenario for 5.44 ± 0.4 kHz case is illustrated in figure 5. If fluctuations in density and floating potential are in phase (~ 0°), instability is of drift kind, where as if they out of phase (~180°), R-T predominates. The R-T instability is more prevalent in the bad curvature region (B.C.R) and the drift instability in the good curvature region (G.C.R). Drift instability is stable in the good curvature region i.e. radially inner positions if the following condition is satisfied: $- 2/\alpha R \left(1+T_i/T_e \right) > 1$, where, α is the inverse density scale length. At -3.5 cm minor radial location α comes out to be -0.1276 cm^{-1}. Condition for stability is not satisfied for our experimental situation (T_i ~ 3 eV and T_e ~ 22 eV). This suggests the existence of drift instability in the good curvature region. Most of the peaks show the coherence level above

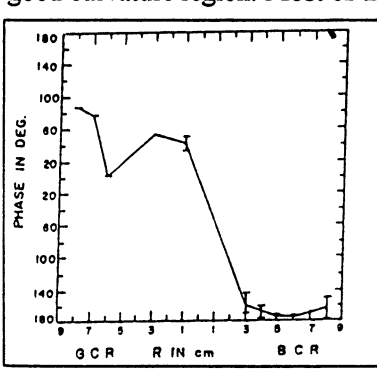

Fig. 5: Radial phase variation

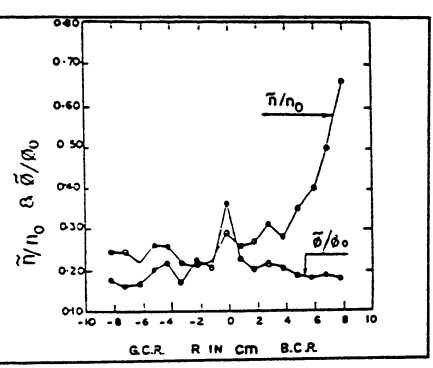

Fig. 6: Radial variation of $\tilde{n}/n_0$ & $\tilde{\phi}/\phi_0$

0.5 except at the center where the spectrum is turbulent. Figure 6 shows the density and floating potential fluctuations normalized to their equilibrium value as a function of minor radius. Fluctuation in density increases at the bad curvature region, where as floating potential fluctuation maximizes near the plasma center.

4. CONCLUSION

Results of an experimental work on rf produced plasma in a toroidal device is reported. Unlike in cylindrical system, the plasma density profile observed in the radial direction is almost flat. The electron temperature is higher than in cylindrical devices. Components of the wave magnetic field have been measured and a strong effect of toroidicity is observed. Low frequency oscillations are observed in rf produced toroidal plasma. Phase information reveals different types of instabilities exist in the bad as well as in the good curvature region. Driving forces for such instabilities are curvature in the magnetic field and plasma density gradient. Good coherence levels are reported everywhere except at the plasma center.

We thank Prof. P. K. Kaw for fruitful discussions and encouragement during the work.

REFERENCES:

One N., Phys. Lett., 1989, 139A, 308
Two N., Plasma Phys. Controlled Fusion, 1984, 26, 1147
Three N., Appl. Phys. Lett., 1989, 55, 148
Four N., J. Vac. Sci. Technol., 1989, A7, 3345
Five N., Phys. Fluids, 1991, B3, 869
Six N., AIP document No. PAPS-PFBPE-03-893-7, Institute of plasma physics, Nagoya University, Japan, 1986, 67
Seven N., Plasma Phys. Controlled Fusion, 1991, 33. 339
Eight N., IEEE Trans. Plasma Sci., 1974, PS-2, 261
Nine N., Plasma Sources Sci. Technol., 1993, 2, 5

CONTENTS OF VOLUME 1

MICROWAVE DISCHARGES